PRO-TEM network

Process Industry Thermal Energy Management

Focussing on Interdisciplinary Research, Promoting Future Research, Transferring Knowledge, Sharing Opinions and Stimulating Interactions among Stakeholders to Ensure the UK Achieves World Leading Status in Thermal Energy Management

http://research.ncl.ac.uk/pro-tem

The 1st PRO-TEM Network Conference

Sustainable Thermal Energy Management in Process Industry (SusTEM2010)

Conference Proceedings

Compiled by Janie Ling Chin (Network Co-ordinator)

Gratitude and Welcome to SusTEM2010

It is my pleasure to welcome you all to Newcastle University and the Sustainable Thermal Energy Management 2010 (**SusTEM2010**) Conference.

The **SusTEM2010** conference has been organised by the Process Industries Thermal Energy Management (**PRO-TEM**) Network, which is a research network whose aim is to promote and disseminate internationally recognised research and support knowledge transfer to all stakeholders. I am grateful to the **EPSRC Energy Programme** for funding the **PRO-TEM** network and also to our conference sponsors, **Newcastle Science City** and **Newcastle Institute for Research on Sustainability**, for their additional financial support which has made this conference possible.

As a consequence of government targets to reduce CO_2 emissions by 80% by 2050, energy intensive sectors, such as the process industries, have been increasingly the focus of attention and where significant reductions can be made. The current **EPSRC Energy Programme** portfolio of awards in the area of energy efficiency is over £63M. Through these projects, academic research and industrial support is brought together to develop the novel technologies and approaches in energy management needed if we are going to make a significant contribution to this challenge.

Newcastle Science City is an initiative which promotes Newcastle as a city of science across the world. It is one of only six cities in the UK to be given the status as a focal point for transforming the best ideas and discoveries into new products and services. As part of city-wide partnership, it aims to maximise the potential of the science base by helping to create new businesses, attract investment, strengthen science networks and ensure that local people can become part of our continued scientific achievement. As a key partner in **Newcastle Science City,** Newcastle University's contribution is rooted in research excellence in sustainability, ageing and health and stem cell and regenerative medicine.

Newcastle Institute for Research on Sustainability brings researchers together from across Newcastle University to develop sustainable responses to the great challenges of our age: ensuring that everyone has access to a fair share of the world's resources in perpetuity. The focus of this Institute is on delivering solutions to major challenges in areas including: urban living, low-carbon energy and transport, food security, water management, and clean manufacturing

SusTEM2010 is organised in parallel sessions covering, Barriers and Challenges; Heat Exchangers; Industrial Applications; Process Modelling and Thermal Power, which are important themes in the quest to improve thermal energy management. The research presented is applicable to a number of sectors and processes used in the industry, for example, aluminium casting, lactic acid production, papermaking, food processing, and oil refining. I would like to thank the authors for preparing their papers and presentations and sharing their stimulating and interesting research with us. I hope you all enjoy today and that you will also join us next year for **SusTEM2011**.

Professor Tony Roskilly
Chair of the PRO-TEM Network

PRO-TEM network

Process Industry Thermal Energy Management

Focussing on Interdisciplinary Research, Promoting Future Research, Transferring Knowledge, Sharing Opinions and Stimulating Interactions among Stakeholders to Ensure the UK Achieves World Leading Status in Thermal Energy Management

research.ncl.ac.uk/pro-tem

Sustainable Thermal Energy Management Conference
(SusTEM2010)

Conference Dinner at Newcastle Civic Centre on Tuesday Evening **2nd November**
Conference at Great North Museum, Newcastle upon Tyne, UK on Wednesday **3rd November**

The aims of SusTEM2010 are closely aligned with those of the Process Industry Thermal Energy Management (PRO-TEM) Network, i.e. to incorporate knowledge and experience among stakeholders and furthermore disseminate future research challenges. Therefore, participants are expected from all the main UK universities and a large selection of industries to discuss and share the latest ideas to effectively manage energy use in process industries.

Objectives
The objective of SusTEM 2010 is to disseminate research which addresses sustainable thermal energy management which is applicable to improving energy utilisation in the process industries.

Scope
The scope of SusTEM 2010 includes whole systems analysis, optimisation of equipment and processes, process integration, low grade heat, modelling, sensor and control systems, use of novel technology and cycles, energy maintenance and diagnostics, and any other relevant topics.

Main Topics
Based on the abstracts submitted to this conference, the following draft conference agenda is proposed so that the structure of the conference will cover different research topics, namely Barriers and Challenges; Heat Exchangers; Industrial Applications; Process Modelling and Thermal Power.

Conference Agenda (Tuesday and Wednesday, 2-3 November 2010)

SusTEM 2010 Conference		
Tuesday, 2 November	1730 - 1830	**Registration at Newcastle Civic Centre**
	1830 - 1840	**Welcome**
	1840 - 1900	**Keynote Speech** by Professor Dermot Roddy
	1900 - 2100	**Conference Dinner**

			Track 1	Track 2
Wednesday 3 November		0900 - 0930	**Arrivals & Registration at Great North Museum, Newcastle** (via the Claremont Road side entrance)	
		0930 - 0940	**Welcome Address** by Professor Tony Roskilly	
			Track 1	**Track 2**
	Section 1		**Barriers & Challenges Chairperson: Professor Dermot Roddy**	**Heat Exchangers Chairperson: Professor David Reay**
		0940 - 1005	Review of Low Grade Thermal Energy Sources and Uses from the Process Industry in UK Speaker: **Dr Yasmine Ammar (Newcastle University)**	Identifying Optimal Cleaning Cycles for Heat Exchangers Subject to Fouling and Ageing Speaker: **Mr Thomas Pogiatzis (Cambridge University)**
		1005 - 1030	Don't Lock Me in: Public Opinion on the Prospective Use of Waste Process Heat for District Heating Speaker: **Dr Paul Upham (University of Manchester)**	Fouling Thresholds in Bare Tubes and Tubes Fitted with Inserts Speaker: **Professor Barry Crittenden (University of Bath)**
		1030 - 1055	Heat pumps and energy storage - the challenges of implementation Speaker: **Professor Neil Hewitt (University of Ulster)**	Application of Intensified Heat Transfer for the Retrofit of Heat Exchanger Network Speaker: **Mr Yufei Wang (The University of Manchester)**
		10 minutes	**Refreshment 1**	
	Section 2		**Industrial Applications Chairperson: Mark Lewis**	**Process Modelling Chairperson: Professor Barry Crittenden**
		1105 - 1130	Potential Energy Savings by Application of the Novel CRIMSON Aluminium Casting Process Speaker: **Dr Xiaojun Dai (Birmingham University)**	Physical and Operating Conditions Effects on Silica Gel/Water Adsorption Chiller Performance Speaker: **Mr Ahmed Rezk (Birmingham University)**
		1130 - 1155	Significant Thermal Energy Reduction in Lactic Acid Production Process Speaker: **Professor Iqbal M Mujtaba (University of Bradford)**	Operation Window and Part-Load Performance Study of a Syngas Fired Gas Turbine Speaker: **Assistant Professor Ma Linwei (Tsinghua University)**
		1155 - 1220	Sequential Modelling of Thermal Energy: New Potential for Energy Optimisation in Papermaking Speaker: **Dr Paul Austin (Cambridge University) and/or Dr Puya Afshar (The University of Manchester)**	Condensing Boiler Applications in the Process Industry Speaker: **Dr Qun Chen (The University of Sheffield)**

		70 minutes	**Lunch & Posters**	
Wednesday 3 November	**Section 2**	1330 - 1355	Modelling of Energy Flows in Potato Crisp Frying Processes Speaker: **Professor Savvas Tassou (Brunel University)**	Dynamic Modelling of a Two-Phase Thermofluidic Oscillator for Efficient Low Grade Heat Utilization: Effect of Fluid Inertia Speaker: **Miss Roochi Solanki (Imperial College)**
		1355 - 1420	Novel Model Reduction Techniques for Refinery-Wide Energy Optimization Speaker: **Mr Taoufiq Gueddar (London's Global University)**	Computational Fluid Dynamic Investigation of Liquid Rack Cooling in Data Centres Speaker: **Dr Jon Summers (University of Leeds)**
		1420 - 1445	Computational Fluid Dynamic (CFD) Investigation of Air Flow and Temperature Distribution in a Small Scale Bread-Baking Oven Speaker: **Dr Zinedine Khatir (University of Leeds)**	Identifying and Quantifying Energy Savings on Fired Plant Using Low Cost Modelling Techniques Speaker: **Dr Bob Tucker (Zerontec Ltd)**
		15 minutes	**Refreshment 2**	
	Section 3		**Thermal Power** **Chairperson: Dr Colin Harrison**	
		1500 - 1525	The Effect of Hydrogen Containing Fuel Blends upon Flashback in Swirl Burners Speaker: **Professor Nicholas Syred (Cardiff University)**	
		1525 - 1550	An Integrated Solar-Cryogen Hybrid Power System Speaker: **Mr Yongliang Li (University of Leeds)**	
		1550 - 1615	An Investigation of a Household Size Trigeneration Running with Hydrogen Speaker: **Dr Yaodong Wang (Newcastle University)**	
		1615 - 1630	**Closing Address**	

Organising Committee:

Professor Tony Roskilly Newcastle University, UK	Professor Dermot Roddy Newcastle University, UK	Miss Janie Ling Chin Newcastle University, UK

Scientific Committee:

Professor Tony Roskilly (Organiser) Newcastle University, UK	Professor Ignocio Grossmann Carnegie Mellon University, USA	Associate Professor Yang-Cheng Shih Tsukuba University of Technology, Japan
Professor Dermot Roddy (Organiser) Newcastle University, UK	Professor Chonghun Han Seoul National University, South Korea	Professor Vida Sharifi The University of Sheffield, UK
Professor Brian Agnew Newcastle University, UK	Dr Aly A Hassan Minia University, Egypt	Assistant Professor Stan Shire University of Warwick, UK
Professor Tariq Al-Shemmeri Staffordshire University, UK	Dr Terry Heppenstall The Pipe Dream Company Ltd, UK	Dr Andrew G.F. Stapley Loughborough University, UK
Prof Diran Apelian Metal Processing Institute, Worcester, USA	Professor Neil Hewitt University of Ulster, UK	Dr David Swailes Newcastle University, UK
Associate Professor George C Bakos Democritus University of Thrace, Greece	Professor Simone Hochgreb University of Cambridge, UK	Professor Jim Swithenbank The University of Sheffield, UK
Professor Dilip Ballal, USA The University of Dayton, USA	Dr Ye Huang University of Ulster, UK	Professor Luca Tagliafico University of Genoa, Italy
Dr Justin Bishop University of Oxford, UK	Associate Professor Peter Arendt Jensen Danmarks Tekniske Universitet, Denmark	Dr Kate Theobald Northumbria University, UK
Dr Leslie Bolton BP UK	Professor Wooju Kim Yonsei University, South Korea	Dr Patricia Thornley The University of Manchester, UK
Dr Grant Campbell The University of Manchester, UK	Dr Jiri Klemes University of Pannonia, Hungary	Dr Guohong Tian Newcastle University, UK
Professor John Chew University of Surrey, UK	Professor Jacob Klimstra Jacob Klimstra Consultancy, The Netherlands	Dr Petar Varbanov University of Pannonia, Hungary
Dr Nyuk Ling Chin Universiti Putra Malaysia, Malaysia	Professor Siau Ching Lenny Koh The University of Sheffield, UK	Assistant Professor R Velraj Anna University, India
Professor Barry Crittenden University of Bath, UK	Professor Chang Sik Lee Hanyang University, South Korea	Dr Vishwas Wadekar AspenTech Ltd, UK
Professor Yulong Ding University of Leeds, UK	Professor Jae Kyu Lee Korea Advanced Institute of Science and Technology	Professor Michael Waller Miami University, USA
Dr Urmila Diwekar Vishwamitra Research Institute, USA	Dr Jonathan Lee Newcastle University, UK	Dr Li-Wei Wang Shanghai Jiao Tong University, China
Dr Hongbiao Dong University of Leicester, UK	Professor Ronnie Magee Queen's University Belfast, UK	Dr Yaodong Wang Newcastle University, UK
Professor Thomas F Edgar University of Texas, Austin USA	Dr Rikard Mikalsen Newcastle University, UK	Professor Paul Watkinson The University of British Columbia, Canada
Professor Mahmoud M. El-Halwagi Texas A&M University, USA	Professor Bahram Moshfegh Linköping University, Sweden	Professor John Weisend Michigan State University, USA
Professor Zhongyun Fan Brunel University, UK	Professor Iqbal Mujtaba University of Bradford, UK	Dr Dawei Wu Newcastle University, UK
Professor Tom Fletcher Brigham Young University, USA	Professor Kim Choon Ng National University of Singapore, Singapore	Professor JinYue Yan Malardalen University, Sweden
Professor Eric Fraga University of College London, UK	Professor Toby Norris Aston University, UK	Associate Professor Yuying Yan The University of Nottingham, UK
Professor Peter Fryer University of Birmingham, UK	Professor Carlos Ordonez The University of Texas at Austin, USA	Professor Kunio Yoshikawa Tokyo Institute of Technology, Japan
Associate Professor Guohui Gan The University of Nottingham, UK	Dr Ian Potts Newcastle University	Professor Yang Zhang The University of Sheffield, UK
Dr Yunting Ge Brunel University, UK	Professor Mark Price Queen's University Belfast, UK	Associate Professor Chang-Ying Zhao University of Warwick, UK
Dr Audley Genus Newcastle University, UK	Professor David Reay Heriot-Watt University Edinburgh, UK	Professor Toshko Zhelev University of Limerick, Ireland

Contents

Track 2 Section 2: Process Modelling

Section 3: Thermal Power

Track 1 Section 1

Barriers and Challenges

Don't Lock Me in: Public Opinion on the Prospective Use of Waste Process Heat for District Heating

Paul Upham*, Fiona Chisholm, Chris Jones

Tyndall Centre Manchester, University of Manchester, Manchester, M13 9PL, United Kingdom

*Corresponding author. paul.upham@manchester.ac.uk Tel +44(0)161 306 3258

Abstract

While the available resource in terms of waste process heat in the UK is substantial, there are a wide variety of issues to consider and barriers to overcome in order to realise its potential. This paper discusses one particular factor, namely the opinions of consumers and citizens. We describe the results of two focus groups with a potential domestic client group, namely elderly people, and the postal questionnaire responses of 312 individuals living in the proximity of a large potential heat source, namely the Corus steel-works in Port Talbot, Wales. While those questioned were broadly supportive of the idea of district heating, particularly if this would involve reductions in domestic heating costs, both the qualitative and quantitative work revealed concern about long-term contractual lock-in. In direct contrast, the stability of long-term demand, involving some degree of consumer lock-in to some degree, is likely to be a pre-requisite for commercially viable district heating systems. We conclude that price inducements will be required to overcome consumer concerns in this context.

Keywords   district heating; process heat; distributed heat; public opinion; perceptions

1   Introduction

District heating distributes heat to consumers in industrial, commercial and domestic sectors through closed-circuit pipe networks that transfer heat to end-users via heat exchangers. Although the technology is mature and is deployed effectively in other Northern European countries (DECC, 2009), it is little used in the UK (Macadam et al. 2008). District Heating coverage of the UK's heating demand is at present estimated at 4%, with the largest share in communally operated installations, such as universities, hospitals, and industrial sites (Koehler, 2009). For comparison, district heating provides some 60% of the total heat supply in Denmark, and 49% of the total heat supply in Finland (Davies and Woods, 2009). Use is also high in countries including Sweden, Poland, Estonia, Latvia, Lithuania, Romania, Belarus, the Czech Republic and Russia (Werner, 2004) - in short, in countries where the state has been significantly involved in housing planning.

Despite the many challenges of retrospectively installing district heating in the UK, not least of which are currently dispersed responsibilities and perceived investment returns (DECC, 2009), there is now increasing policy attention to energy efficiency options in the UK. This reflects stringent, long term greenhouse gas emissions reduction targets (HM Government, 2008) and is supported by the publication of several recent UK Government policy documents acknowledging the potential role of district heating: the 'Heat and Energy Saving Strategy' (HM Government, 2009), the 2009 'Heat and Energy Saving Strategy Consultation' (DECC, 2009); and 'Warm Homes, Greener Homes: A Strategy for Household Energy Management' (HM Government, 2010). As dwellings account for some 70% of the UK's heat demand, compared to (perhaps surprisingly) 1.7% for the sum of all other non-domestic and non-process heat demand (Koehler, 2009), it is the domestic sector that merits closest attention for district heating, with non-domestic demand more likely playing the role of 'heat anchors', in the sense of providing base load (i.e. relatively constant) heat demand (ibid). It should be noted that not all domestic housing areas are equal in terms of their suitability for district heating: with heat density defined as the annual heat demand divided by the number of hours in a year, the proportion of total heat demand for UK dwellings in 'high' heat density regions is 20%, which could equate to about 90% of the flats and about 20% of the terraces in these areas (ibid, p.7). Social housing is also likely to comprise an important portion of relevant housing stock (ibid).

While there is a large literature on human perceptions of thermal comfort, including those of older individuals (e.g. Day and Hitchings, 2009), little of this work relates directly to public perceptions of installing and using district heating, particularly for the UK. One of the few UK studies on the significance of consumer opinion for publicly-installed heat infrastructure serves as a salutary indicator that this deficit needs remedying. This relates to the partial failure to install free central heating in Lambeth, London (Armstrong et al, 2006). Armstrong et al (ibid) found that even though a new heating system was viewed as a significant improvement by the local council and there were to be no installation costs for the consumer, the majority of those approached to take part in the scheme declined. Given the relative unfamiliarity of district heating in the UK, any project endeavouring to make use of waste process heat for domestic and commercial space and water heating will likely be more difficult, if not impossible, without consumer support.

Our main objective here is to add to the limited empirical evidence on UK citizen and consumer opinion on the use of waste process heat for district heating. We also discuss this in terms of related theoretical literature, psychological and sociological. We firstly describe we describe the results of two focus groups on district heating with potential, older users in Newcastle. While this involved consideration of hypothetical installation, the participants engaged closely with the issues. The second set of results consist of resident opinion on the prospective use of waste process heat for district heating in the local authority area of Neath Port Talbot in Wales, where waste process heat from Corus, a local integrated steelworks, could potentially be used to provide local buildings with space and water heating. This is a relatively 'live' context, in which opinions may be more actualised and reliable than in hypothetical consideration (Shackley *et al.,* 2004). Although at the time of the study there were no definite plans for district heating, this is being given serious consideration by local agencies.

2   Research design and methods
2.1   Theoretical considerations
In developing questions for both the focus groups and questionnaire survey, we have considered primarily two social science literatures. First are insights from environmental psychology. This literature tells us that we should expect only a small percentage of potential users of district heating to commit to district heating for environmental reasons. Health, security and social issues consistently feature higher in the UK public's concerns than environmental issues (Bord et al, 2000; DEFRA, 2002; Poortinga and Pidgeon, 2003; MORI, 2005). Only 11% of UK citizens identify environment and pollution as one of the two or three issues affecting their quality of life, while more people cite money, health, crime, job, neighbours, transport and housing as their top priorities (DEFRA, 2002), (Ipsos-MORI, 2009). Moreover, studies suggest a relatively low salience for climate change in individuals' day-to-day choices and actions (Brook Lyndhurst, 2007; Giorgi et al, 2009). Growing awareness of environmental problems at an abstract or general level tends not to feed through to personally-relevant attitudes: most people do not think about energy consumption or environmental impact when buying appliances (Brook Lyndhurst, 2007), when buying and preparing food (Giorgi et al, 2009) or when travelling (King et al, 2009) (in Upham et al, 2009).

Consequently, we need to consider other motivations and factors, and other conceptual approaches, when seeking to identify and characterise public perceptions of district heating. A potentially useful literature in this regard is that relating to 'practices', concepts of which have been developed to investigate consumer behaviour within socio-technical regimes. The latter views technology and society as part of an indivisible whole: technology is seen as embedded in a social context that strongly influences the way that technologies are designed and function – e.g. (Cherns, 1976). In general, practice approaches view patterns of consumption, such as heat use, as an outcome of (a) routinised, socially-learned habits or practices; and (b) particular socio-technical infrastructure or 'sysTEMs of provision' (Upham et al, 2009). While this way of thinking does not deny individual psychology and autonomy, it does hold that habits and practices are primarily shaped by the day-to-day context of living within socio-technical systems, rather than, or as much as, conscious decision-making (ibid).

Several authors have worked within a practices paradigm on environmentally-relevant topics, much of this which has focussed on energy consumption in domestic households. For example, Shove and Southerton (2000) examined the adoption of the freezer in British households. Chappells and Shove (2005) examined the socially-constructed nature of indoor temperature comfort, considering whether design standards are 'self-fulfilling' in the sense that they inadvertently construct and reproduce increasingly standardised concepts and conventions of comfort (Baker, 1993; Humphreys, 1994; Shove, 2004). A key implication of the above is that opinion is shaped by individual context and informed by past experiences, as much as by the knowledge and information that consumers have access to. Hence the empirical work solicits information about current heating systems and practices, as well as investigating issues relating to 'lock-in'. This is the idea that heat users are likely to be locked into their existing energy systems by a range of institutional, infrastructure and cultural processes (Unruh, 2000). Lock-in itself is not problematic. What is problematic is lock-in to unsustainable systems and the immobility, or resistance to change that lock-in poses: disrupting socio-technological lock-in is notoriously difficult and in part explains why policy-makers tend to favour 'technological fixes' that at least appear to be easier to introduce than behavioural change. We discuss lock-in in more detail after presenting the results.

2.2   Empirical aspects

For the qualitative investigation, two focus groups were commissioned through the Institute of Aging and Health (IAH) of the University of Newcastle, who recruited sixteen 50 to 85 year olds from their Voice North Database. This age group was identified as being an above average heat use demographic. Fifteen households were represented, the majority of whom were homeowners, with two participants in either rented or retirement accommodation. Detached, semi, terrace and flat housing stocks were covered. The groups were held in April 2010 and there was an even gender split amongst group members. While a range of socio-economic backgrounds were represented, the majority of participants were mid to high socio-economic class: it is important to note this, as less affluent groups may view the potential cost reductions of district heating, and the trade-offs involved, more favourably. It is also worth noting that the preceding winter had been unusually protracted and cold and that the Newcastle location of the focus groups is somewhat colder than some of the UK. The majority of participants lived alone and were not in employment at the time of the study. As is normal practice, participants were paid a small incentive to attend. The focus groups were two hours in duration each and were split into two sections. In the first section, participants were asked about their existing heating arrangements and habits. This was then followed by a fifteen minute presentation on district heating and the second section, in which participants were asked to give their views on district heating. A common set of question prompts was used in each group. For present purposes, thematic analysis of the focus group transcripts was undertaken, which involved identification of themes and selection of supporting quotations.

For the quantitative investigation, 3,000 postal questionnaires were distributed to residences in Neath Port Talbot in the proximity of the Corus steel-works, with accompanying franked return envelopes and a prize incentive to encourage responses. A shorter version of the questionnaire was piloted in Port Talbot town centre and postal distribution was in July 2010, with specific postcodes targeted. The pre-amble to the questionnaire emphasised its local relevance, with the intention of encouraging reliable responses. In terms of background and regional context, Corus is an integrated steelworks located in the town of Port Talbot which produces approximately 4.7 million tonnes of steel a year. It is located in the West Wales and the Valleys region, comprising 15 local authority areas receiving approximately £1 billion from the European Regional Development Fund (ERDF) as part of the European Union Structural Funds Programming Round 2007-2013, to progress the sustainable and competitive development of the region's economy. This will include addressing climate change, improving transport and regenerating the region's most deprived areas (Welsh Assembly Government, 2009). As a result of its large scale manufacturing processes, Corus currently produces large quantities of waste process heat.

The questionnaire investigated awareness and support for using waste process heat for district heating, including views on key features of district heating schemes, such as domestic and street disruption

associated with installation and contractual issues. As district heating systems can make use of a wider range of energy sources (Ghafghazi et al, 2010), including waste heat from industrial processes, biomass energy, geothermal energy, waste incineration, nuclear energy and fossil fuels, attitudes to the hypothetical use of a range of heat sources were also assessed. The questionnaire response rate was a modest 11% and this should be borne in mind when considering the generalisability of the results.

3   Focus group results[1]
3.1   Existing heat practices
Bearing in mind our rationale that understanding the existing socio-technical system and heating practices are critical to an understanding of how district heating may be progressed and perceived, the first section of the focus groups was designed to identify the existing heating arrangements of participants, with particular reference to types of heating system and energy supplier. In total, fourteen participants (87.5%) had natural gas heating, including one member of group two, who had both natural gas and solar thermal heating. Two participants (12.5%), one in each group, had electric heating systems. The types of heating supply were therefore broadly in line with national trends of domestic heat supply; 81% natural gas and 9% electric heating (Koehler 2009).

In most cases the heating system had come with the property, and in the case of those with electric heating there was no option to change to natural gas. Several participants had installed new combination boilers and were happy with how they functioned, though one member of the first group refused a combination boiler in favour of replacing her previous boiler and water storage tank with a new one. Almost all the members of each group had central heating, except those with electric systems. All those with central heating had a supplementary heat source, such as electric convection or a gas fire in the living room. These additional heating systems were used to 'boost' the temperature in certain rooms; there was also an element of frugality involved in the sense of a dislike of heating the whole house via central heating, when only one room was occupied. Although one participant, with an electric storage heater system, was unhappy with his heating, the other participants were largely content with their current systems. Only one participant had made a significant modification to his system, by adding solar thermal water heating. The majority of members however, had been content to keep incumbent systems because they worked adequately. The major implication of this, for district heating, is that any change will need to be 'like for like', involving minimal change to habits and routines.

The participants were also asked about their energy suppliers and four influencing factors were identified. Several members of each group had changed supplier in the last few years. The most common reason was reducing cost. Simplifying energy bills through 'dual fuel' tariffs were popular with a minority of participants in each group. Whether the supplier was British or not was significant for the couple in group one, while a participant in the same group had changed to a supplier who promised to supply 'eco' gas and electricity. When asked to sum up what was the most important attribute of a heating system, cost, reliability, simplicity, comfort, efficiency, convenience and environmentally sensitivity were mentioned. In group one, efficiency and reliability were more frequently mentioned, whereas comfort was most popular in group two.

3.2   Opinion on district heating
Overall, both focus groups were broadly supportive of using process heat though district heating in principle. For example:

> "…I think if we're using heat that's a by-product I think that's an excellent idea because I think it's so ridiculous that so much is wasted in heat. Where we used to live there was Didcot Power Station and the amount of wasted heat there you could see it.

---

[1] Full details of the focus group and questionnaire survey results are available here: http://www.tyndall.ac.uk/research/energy/thermal-management This conference paper and a journal paper to follow synthesise but also extend the analysis.

> "…if it was available and if it was kind to the atmosphere and everything and low cost…."

However, this support was conditional on a range of technical, contractual and operational concerns being addressed. The strength of these concerns, each of which are considered below, should not be under-estimated. In both groups, district heating was seen as acceptable if it met all of the desirable attributes of current heating and hot water systems, at similar or lower cost, as well as being environmentally preferable to the current system. Project developers will need to clearly explain how district heating is capable of meeting these criteria.

In both groups, the initial discussion following the presentation on district heating focused on technical concerns about reliability. For example, one participant asked about the frequency of leakages throughout the system. Another wanted to know what effect improved industrial efficiency would have on supply in the long term if process heat was being used. One respondent cited an example he was aware of in Moscow, where those at the "end of the line" did not receive water at a temperature as high as other users. Another reminded us of the long history of this technology:

> "When I went to college District Heating was talked about in the 1940s: the brave new world of District Heating".

Nonetheless, the participants largely accepted the facilitators' reassurance on technical reliability (or at least, did not contest it further). A related demographic issue is worthy of note: while heat (or home temperature) may be more salient for those spending more time at home than those in a external work-place, of which elderly people will form a sizeable fraction, age may in some cases be a deterrent to incurring infrastructural change:

> "I think I would have to wait until it had proved itself to some degree before I would be willing to change. Because I don't think in the long term, and I think I'm talking for quite a lot of us here, we've got a finite number of years and therefore is it going to be worth changing or having a lot of upheaval?"

Most participants wanted assurance that the new system would be at least able to fulfil all the functions of their existing one:

> "…I think it's a very good idea if, as I said before, we can replace like with like with no disruption other than, you know, what you would expect."

The particular technical attributes expected of any new system were reliability and ability to control the temperature of the hot water supply. In terms of control, participants were sensitive to any association with storage heating, with which there was universally bad experience. For example:

> "My daughter has got night storage heaters and I mean at this time of the year it's absolutely tremendous - the temperature in her house - but she can't do anything about it."

While all participants stated that they prioritised comfort over heating cost – they could afford to make this choice - cost was nonetheless an issue. While the groups were directed away from a lengthy discussion of fuel poverty, they nonetheless discussed ways of managing cost at some length, despite most being from mid to high socio-economic backgrounds:

> "And putting extra clothes on…
>
> I put woollies on in the house…
>
> I put extra clothing on…
>
> I was going to say that…" (discussion sequence in group 2).

A second, important set of issues discussed in both groups relates to contracts and ownership. A considerable length of time was spent discussing these points and there was a greater range of opinion from within the groups; there was also perhaps greater opportunity for speculation, which to some extent may have fuelled opinion variety. One key concern in this respect, raised in both groups, is the possibility of contract lock-in. There was suspicion that the scheme may begin with a reasonable price, but then increase once customers are connected:

> "What happens next year you can put your price up once you've got me?"

> "Okay it's dead cheap for the first two years but what freedom have they got to change the price after the initial period? And so you would want some assurance about the long term pricing."

In some cases participants made explicit links to past experiences, firstly under the nationalised system and also under the current liberalised energy market. The lack of choice with British Gas in the nationalised era was mentioned by a member of group two, with support from others, as being negative, and he associated the single supplier nature of district heating as analogous to this. Indeed there was some concern about being forced into a district heating scheme:

> "And so when they install it for existing buildings, is it compulsory or can you keep independent sources?"

The need to be assured about long term cost led the discussion onto ownership and trust. The supplier was important for a number of reasons. Although there was an exception in group one, the majority of participants stated a preference for a well known company to act as the supplier. There were also, however, reservations about whether private companies should be trusted. One member of group two thought that a private company would be too profit-oriented and that customers would require some control of what suppliers could alter in the supply contract. For one group member, the prospect of a supplier being sold to another company was a concern, again emphasising that confidence and trust in a particular supplier will be important. The need for reassurance about contracts and financial reliability was a recurrent theme:

> "Would you say then it would be more likely to be applied in sort of council housing or conglomerate type of housing or a separate individual house? If you sort of left your house and signed over your lease or whatever the next person would be obliged to some extent to take it on without great cost to change."

> "These various communities in Europe how long have they been in operation? ….
> And none of them have failed or gone bankrupt or anything like that?"

The possibility of community ownership of the district heating scheme was mooted by the facilitator in group two and this drew broad support for reasons of knowing who owned and controlled the scheme. This enthusiasm was, however, qualified by a belief that community-owned schemes, such as those in Switzerland, would not work in the UK. This was attributed to the perception that people moved around the UK too often, although a form of co-operative in which people moving into the area would be obliged to join was suggested as a solution by one participant.

In group one, the discussion about suppliers also focused on security of supply, with the majority of the group agreeing with the idea of a 'British' energy company owning the system and ensuring "national autonomy" as positive. A sequence illustrating some of the above points:

> "I think again it would come down to cost and it would come down to whether you trusted them because as soon as you get a very private company in the most important thing that they

are looking for is profit. And would you have any control over the charges that they were going to make."

Facilitator: "If there was some system of local ownership, and I don't mean the local council I mean the people that are the users having a stake in it, would that make it any more appealing?"

"Definitely…"

"I think it would to me yes, yes, because they're always selling them off "

Facilitator: "And so if you felt you had some sort of stake in it?"

"If it was a sort of cooperative enterprise."

Disruption from installation was less of an issue than initially hypothesised. It was seen as a necessary nuisance no worse than disruption from the installation of broadband fibre optics and replacing water mains. This did, however, somewhat contradict the view held in both groups that district heating was better suited to new-build housing, rather than existing estates where retro-fitting might be costly and difficult:

"I hadn't heard of it and I think it's a good idea. But from a practical point of view from where I'm living I couldn't see it going into the neighbourhood other than new buildings or apartment blocks. It would be great for public buildings."

In general, throughout the discussion of district heating, participants were keen to understand how the new technology might affect their day to day lives. While manifesting some environmental concern as citizens, most appeared to think partly as consumers who needed to be materially satisfied at acceptable cost, and partly as people with existing routines and practices into which the service provision of district heating will need to fit if it is to be accepted. In short, socio-technical and practice concepts were helpful in eliciting and characterising responses.

4   Questionnaire survey results
4.1   Respondent characteristics
The respondents approximated 0.23% of the Neath Port Talbot population (312 of 134,468 residents). The large majority (97.1%) were resident in the Sandfields, Aberavon Sands and Aberavon areas of Neath Port Talbot. Although too small for the results to be considered to adequately, or represent the views of the local area as a whole, the responses nonetheless provide some valuable insights into local resident opinion. Of the 312 participants, there was a near-even gender split. Relative to the age distribution of the Neath Port Talbot population in the 2001 Census, those aged 15-24 and 25-34 are substantially under-represented; participants aged 35-44 are slightly under-represented; participants aged 45-54 are well represented; participants aged 55-64 and 65-74 are significantly over-represented; and participants aged 75+ are well represented.

In terms of other respondent characteristics, 81% of respondents agreed with the statement 'I am very concerned with environmental issues' (it is likely that social response bias rendered this question not useful for purposes of categorising and response correlation). Most respondents (66.6%) replied as a home-owner or business owner: 12.3% rented their home or business from a landlord and 21.1% rented their home or business from the council. The percentage owning their home or business premises is similar to the percentage of homeowners in the Neath Port Talbot population in the 2001 Census (71.3%). Only 0.7% responded as a business and 0.3% as both businesses and householders.

Respondents were also asked to indicate which of the following three statements best described their current position:

- 'I make most or all of the decisions in my household or business regarding energy bills.'
- 'I make decisions regarding energy bills with other members of my household or business.'
- 'Other members of my household or business make most of the decisions regarding energy bills.'

The purpose of this question set was to identify whether those responding would be (or at least considered themselves to be) responsible for taking the decision to sign up to a district heating scheme, should one be introduced. A majority of participants (66.3%) claimed to be solely responsible for making decisions regarding energy bills in their household or business; 30.1% of participants also claimed to make decisions with other members of their household or business and only 3.6% reported that decisions were mostly made by other members of their household or business.

4.2   Prior awareness of district heating

Participants were first asked whether they had previously heard of district heating, to ascertain the level of prior awareness of district heating technology amongst participants. This awareness was very low: only 27 of the 305 participants who responded to this question (8.9%) had previously heard of district heating.

4.3   Initial impressions of district heating

Participants were then presented with a short explanation of district heating, so that they could answer the remaining questions. In order to ascertain their initial impressions of the idea, they were asked to indicate the extent to which they agreed with the following statements:

- 'It (district heating) sounds like a good idea in principle.'
- 'It sounds like a good idea but I'd need to know more about it (district heating).'
- 'I'm not sure that I quite understand what district heating involves yet.'

Nearly 19 times as many participants indicated positive, rather than negative, responses towards the brief description of district heating presented to them: 86.6% of participants agreed with the statement 'It sounds like a good idea in principle' (47% strongly agreed; 39.6% tended to agree). A relatively small percentage of participants were neutral, neither agreeing nor disagreeing with the statement (7.4%); 1.4% responded 'No opinion/Don't know'.

Nonetheless, despite willing to express positive approval of the technology, respondents also clearly wanted more information before forming a firm opinion: 51.1% of participants strongly agreed and 35.3% of participants tended to agree with the statement: 'District heating sounds like a good idea, but I'd need to know a lot more about it.' 8.3% were neutral. 2.3% of participants tended to disagree and 1.5% of participants strongly disagreed. 1.5% of participants responded with 'No opinion/Don't know.' Similarly, 25% of participants strongly agreed and 31% of participants tended to agree with the statement: 'I'm not sure that I quite understand what district heating involves yet.' 21.8% of participants neither agreed nor disagreed. 8.5% tended to disagree and 8.9% strongly disagreed. 4.8% of participants responded with 'No opinion/Don't know.'

4.4   Tolerance of disruption and contract tie-in

Respondents were asked to consider how favourably they viewed four features that may pertain to a district heating scheme in their area: temporary street disruption for pipe laying; installation of a small heat exchanger in the home/business; being tied into a heating/hot water contract for 12 months; and being tied into a heating/hot water contract for 24 months. The questions were explicitly framed with the assumption of an annual heating bill reduction of 10-20% in return for the disruption and contract tie-in, a percentage value agreed as plausible (though by no means definite or assured) with the potential waste heat supplier. The objective of this group of questions was to investigate willingness to accept disruption, inconvenience and foregone contractual flexibility, in return for reduced heating bills.

Again in the context of an annual heating bill reduction of 10-20%, more than half of the participants (57.8%) viewed temporary street disruption for pipe-laying very favourably or favourably: 19.9% and 37.9% respectively. This form of disruption was viewed unfavourably or very unfavourably by only 8% and 4.7% of participants, respectively. 26.9% of participants also indicated a neutral response. With the same assumed heating cost reduction, installation of a heat exchanger in the home was viewed very favourably by 24.4% of participants and favourably by 41.1% of participants. Installation was viewed neutrally by 19.7% of participants, unfavourably by 6% of participants and very unfavourably by 4.7% of participants. 4% of participants responded with 'No opinion/Don't know.' Thus, six times as many participants responded favourably, rather than unfavourably, to the prospect of having a heat exchanger installed

Long term contractual tie-in, however, does appear to be a potential problem for district heating. Being tied into a heating/hot water contract for 12 months was viewed very favourably by 7.6% of participants and favourably by 28.6% of participants. It was viewed neutrally by 28.2% of participants, unfavourably by 17.3% of participants and very unfavourably by 12.3% of participants. 6% of participants responded with 'No opinion/Don't know.' Tie-in for 24 months was viewed as a much worse prospect, being viewed very favourably by only 4% of participants and favourably by 8% of participants, viewed neutrally by 23.6% of participants, and viewed unfavourably by 31.3% of participants and very unfavourably by 25.8% of participants. 7.3% of participants responded with 'No opinion/Don't know.' Thus more than half of the participants (57.1%) perceived being tied into a 24 month contract negatively, almost twice those negative towards being tied into a 12 month contract.

4.5 General, mid-point opinion
The next set of questions assessed willingness to accept district heating in general (in contrast to the preceding set, which assessed rather than willingness to accept specific aspects of the technology). The question set is positioned at approximately the mid-point of the questionnaire, allowing opinion to be compared to related earlier and later questions. Participants were asked to indicate the extent to which they agreed with the following statements:

- 'I'd be willing to accept district heating in return for a 10-20% cut in my heating bill.'
- 'I would not be willing to accept district heating.'
- 'I'm still unsure – I would need to know exactly what was being offered.'

Very positively, the large majority of participants (75.1%) agreed that they would be willing to accept district heating in return for a 10-20% cut in their heating bills (33.8% of participants strongly agreed and 41.3% of participants tended to agree). 14.3% of participants neither agreed nor disagreed. 2.7% of participants tended to disagree and 3.1% of participants strongly disagreed. 4.8% of participants responded with 'No opinion/Don't know.'

The second question of this set tested for unconditional acceptance in the negative, demonstrating reasonable consistency in terms of the positive support for district heating: only 3.2% of participants strongly agreed and 8% of participants tended to agree with the statement 'I would not be willing to accept district heating.' 28% of participants tended to disagree and 22.8% of participants strongly disagreed. However, a substantial 28.4% of participants neither agreed nor disagreed 9.6% of participants responded with 'No opinion/Don't know.'

Consistent with this, despite the general lack of opposition, the third question of this set evidenced substantial uncertainty related to the respondents' own knowledge base: 31.6% of participants strongly agreed and 31.2% of participants tended to agree with the statement 'I'm still unsure – I would need to know exactly what was being offered.' 20.3% of respondents were neutral, 5.6% of participants tended to disagree and 5.6% of participants strongly disagreed. 5.6% of participants responded with 'No opinion/Don't know.'

4.6   Attitudes to heating attributes and energy providers
The next set of six questions investigated perceptions of a variety of aspects of heat supply, in order to better understand the criteria that a district heating system should satisfy, from a domestic user perspective. Aspects tested are: reputation of the supplier; contract flexibility (i.e. being able to leave a contract without penalty); cost; degree of control over the heat supply (e.g. ability to adjust the thermostat); reliability of the heat supply; and environmental impact. Participants were asked to indicate the extent to which they considered each of these aspects to be important.

In terms of results, all of the above aspects were rated as having a high degree of importance for the large majority of respondents. Specifically, the percentage of respondents indicating a very important or important rating was 87.5% for reputation of the supplier (66% very important; 21.5% important); 94.4% for contract flexibility (73.4% very important; 21% important); 96.6% for cost (84.6% very important; 12.1% important); 93.7% for degree of control over the heat supply (74.3% very important; 19.3% important); 97% for reliability of the heat supply (83.7% very important; and 13.3% important); and 85.8% for environmental impact (55.7% very important; 30.1% important). Much smaller numbers of respondents indicated neutral, unimportant, very unimportant or 'No opinion/don't know' responses for all of the aspects of heating supply tested.

4.7   Attitudes to different heat sources
As mentioned, district heating systems can make use of a wide range of energy sources (Ghafghazi et al., 2010) and attitudes to the hypothetical use of a range of heat sources were assessed to identify any differing perceptions, particularly whether the use of waste process heat would be viewed differently to other sources of heat. Perhaps surprisingly given a number of opposition campaigns, waste incineration as a heat source was considered positively by nearly half of respondents (very favourably by 26.1% of participants and favourably by 22.9%). It was considered neutrally by 22.5% of participants, unfavourably by 8.1% of participants and very unfavourably by 9.9% of participants. 10.6% of participants responded with 'No opinion/Don't know.'

Coal and gas power stations as heat sources elicited a more mixed response: they were considered very favourably by 13.4% and favourably by 25.7% of participants. 29.3% of respondents considered coal and gas neutrally, 11.6% of participants considered them unfavourably and 11.2% of participants considered them very unfavourably. 8.7% of participants responded with 'No opinion/Don't know.' Nuclear power as a heat source received a more negative response, being considered very favourably by 10.1% of participants and favourably by 14.1% of participants. It was considered neutrally by 26% of participants, unfavourably by 17.3% of participants and very unfavourably by 25.3% of participants. 7.2% of participants responded with 'No opinion/Don't know.' Biomass energy as a heat source received a very substantial neutral/don't know response, perhaps for its relative unfamiliarity. It was considered very favourably by 11.9% of participants and favourably by 20.5% of participants; neutrally by 30.9% of participants; unfavourably by 10.4% of participants and very unfavourably by 11.5% of participants. 14.7% of participants responded with 'No opinion/Don't know.' Waste heat from industries was considered most favourably of all: very favourably by 37.5% and favourably by 29.1%; neutrally by 15.5%, unfavourably by 3.4% and very unfavourably by 6.1% of participants. 8.4% responded with 'No opinion/Don't know.'

4.8   House value perceptions
Respondents were asked to envisage a situation in which they were buying a new home. They were then presented with the following statements and were asked to indicate to what extent they agreed with each one, also assuming an annual heating bill reduction of 10-20%:

- 'I would be more likely to buy a property with district heating.'
- 'I would be less likely to buy a property with district heating.'
- 'District heating would have no impact on my decision to buy a property.'

Regarding the first question, 50.7% agreed that they would be more likely to buy a property with district heating (19% strongly agreed; 31.8% tended to agree). However, high proportion of participants neither agreed nor disagreed (40.5%), indicating a high degree of uncertainty or indifference. Only 4.4% tended to disagree and 4.4% strongly disagreed with the statement.

4.9   Overall disposition to district heating

Towards the end of the questionnaire, respondents were asked to indicate to what extent they would be likely to sign up for district heating, based on the information they had received through the preceding sections. Majority opinion was split between positive and undecided: 16% described themselves as somewhat likely, 20.5% likely and 12.4% very likely to sign up for district heating; 35.8%, however, were undecided. Relatively few, though not a negligible number, were negative about the technology: 8.1% said they would be very unlikely to sign up, 3.9% unlikely and 3.3% somewhat unlikely to sign up for district heating. Opinion thus seemed somewhat less positive than at the mid-point, though, importantly, this question did not offer a 10-20% heating bill reduction.

5   Discussion

Public support for new energy technologies, as identified in questionnaire surveys, rarely translates into universal support for new developments at the local scale (e.g. as reviewed in Upham et al., 2009; Devine-Wright and Howes, 2010). Moreover, support may be conditional and sometimes reluctant (Pidgeon et al, 2008) – more akin to tolerance or acceptance than positive, active support. Yet district heating does require 'active acceptance': residents must be willing to have the technology installed in their homes, in contrast to the 'passive acceptance' that may suffice in the case of macro-wind developments, for example (Sauter and Watson, 2007). Moreover, as DECC observe: "Once connected to a district heating network, customers are unlikely to be able to switch between heating suppliers in the way that gas consumers can" (DECC, 2009). Although customers will be free to use electric heating in particular, this would incur additional cost, as would switching out of district heating (ibid), if this were contractually possible at all.

From the consumer perspective, it is the issue of contract lock-in, plus the need to know more generally about what district heating would entail, that are probably the dominant concerns. Our results indicate support for district heating that goes beyond abstract, in principle support, and the prospect of a cost reduction does appear influential. Indeed, where feasible, some schemes in Europe do offer a guarantee of lower costs to the consumer than use of a domestic boiler (DECC 2009). However, there is an obvious tension between consumer concerns about lock-in and the way in which, as DECC state: "District heating networks are only commercially viable if they can be assured of large and consistent heat loads" (ibid). The lock-in challenge is thus two-fold: first there is the challenge of undoing lock-in to an individualised heating system involving domestic boilers in each home, with concomitant issues of sunk personal costs and the flexibility of moving between suppliers; and second is the challenge of creating lock-in to a new, more collectivised system, in which consumers, providers and other agencies are involved in a relatively long term arrangement. For this to be feasible, investors need to be convinced that an acceptable return is possible and consumers need to be convinced that the arrangement will be preferable to the status quo. Anticipating the concerns of consumers, DECC discuss the associated issues and facilitating measures, referring to the possible roles of heat demand and source mapping; obliging or incentivising potential heat anchors (large demand sources) to connect to district heating schemes; obliging or incentivising co-location of heat supply and demand, where appropriate for new build (reflecting the aspiration that all new UK homes be 'zero-carbon' from 2016); consumer connection subsidy and supporting regulation in general (DECC 2009).

Returning to the present findings, despite generally positive perceptions of district heating, participants were for the most part unwilling to commit to district heating without knowing exactly what it entailed and what was required of them as consumers. Moreover, people ascribed importance to attributes of heating and hot water supply that one would expect in a purchasing situation, where market ethics normally dominate: contract flexibility, cost, degree of control over the heat supply, reputation of the supplier and reliability, in addition to some concern about environmental impact. As

noted in a variety of public service contexts – e.g. (Livingstone et al. 2007) - people arguably move between different roles as they navigate daily circumstances, and these roles include being both a citizen and a consumer (Berglund and Matti, 2006; Johnston 2008). Somewhat bluntly put, as citizens, people will likely understand the need for and benefits of contractual lock-in to district heating; yet as consumers they will be aware that this potentially poses risks and costs to themselves. These may be amplified where the heat source is waste process heat, as such a heating system will rely the on-going commercial viability of an entity subject to changing market conditions. DECC acknowledge that consumer subsidies and discounts could be helpful in encouraging consumers to connect to district heating networks (DECC, 2009). At the very least, people will need key details on district heating schemes from credible sources. While information provision has been shown to substantially improve homeowners' attitudes towards district heating and increase uptake in Sweden (Mahapatra and Gustavsson, 2009), trust in the particular information source will surely also be critical.

6   Conclusions

Both the qualitative and quantitative studies described here provide an insight into some of the general end user criteria that district heating will need to meet. Focus groups with members of the public for whom heat is particularly salient, and a public questionnaire survey in a locality where a district heating scheme using waste process heat is plausible, both indicate that while 'citizen-consumers' are favourable to the idea, this support is conditional on a range of conventional purchasing criteria being met, including acceptable cost, reliability and flexible contractual arrangements. While these attributes are relatively easily anticipated in principle, there is remarkably little UK evidence on the subject. Gaining consumer support for changes from existing, individualised heat systems will not be easy – moving from one form of socio-technical lock-in to another rarely is. The more knowledge we have of consumer perceptions, the better able we will be to deal with concerns that may arise.

Bibliography

Armstrong, D., R. Winder, et al. (2006). "Impediments to policy implementation: The offer of free installation of central heating to an elderly community has limited uptake." Public Health 120.

Berglund, C. and S. Matti (2006). "Citizen and consumer: the dual role of individuals in environmental policy." Environmental Politics 15(4): 550 - 571.

Bord, R. J., R. E. O'Connor, et al. (2000). "In what sense does the public need to understand global climate change?" Public Understanding of Science 9: 205-218.

Brook Lyndhurst (2007). Public Understanding of Sustainable Energy Consumption in the Home. Final Report to the Department for Environment Food and Rural Affairs. London, DEFRA.

Clarke, J., Newman, J., Smith, N., Vidler, E., Westmarland, L. (2007) Creating Citizen Consumers: Changing Public & Changing Public Services, SAGE Publications Ltd, London.

Cherns, A. (1976). "The principles of sociotechnical design." Human Relations 29(8): 783-792.

Davies, G., Woods, P. (2009) The Potential and Costs of District Heating Networks: A Report to the Department of Energy and Climate Change. Available: http://www.decc.gov.uk/assets/decc/what%20we%20do/uk%20energy%20supply/energy%20mix /distributed%20energy%20heat/1_20090505121831_e_@@_204areportprovidingatechnicalanaly sisandcostingofdhnetworksv30.pdf (accessed 4th August 2010).

Day, R., Hitchings, R. (2009) Older people and their winter warmth behaviours: understanding the contextual dynamics. Available:

http://www.gees.bham.ac.uk/documents/Research/Older_People_in_Winter_Report_final.pdf
(accessed 26th August 2009).

DECC (2009). Heat and Energy Saving Strategy Consultation. London.

DEFRA (2002). Survey of public attitudes to quality of life and to the environment: 2001. London,
Department for Environment, Food and Rural Affairs.

Devine-Wright, P., Howes, Y. (2010) Disruption to place attachment and the protection of restorative
environments: A wind energy case study, Journal of Environmental Psychology (in press).

Elzen, B., F. W. Geels, et al. (2004). System Innovation and the Transition to Sustainability.
Cheltenham, Edward Elgar.

Ericsson, K. (2009) Introduction and development of the Swedish district heating systems: Critical
factors and lessons learned. Available:
http://miljo.lth.se/fileadmin/miljo/personal/KarinE/Swedish_district_heating_case-
study_KEricsson.pdf (accessed 4th August 2010).

Eurobarometer (2007). Energy technologies: knowledge, perceptions, measures, Special
Eurobarometer 262, European Commission, Brussels.

Foxon, T.J. (2002) Technological and institutional 'lock-in' as a barrier to sustainable innovation.
Available: http://www.iccept.ic.ac.uk/public.html (accessed 18th August 2010).

Foxon, T.J., Burgess, J., Hammond, G.P., Hargreaves, T., Jones, C.I., Pearson, P.J. (2010) Transition
pathways to a low carbon economy: Linking governance patterns and assessment methodologies.
Available: www.iaia.org (accessed 18th August 2010).

Giorgi, S., D. Fell, et al. (2009). EV0402 : Public Understanding of Links between Climate Change
and (i) Food and (ii) Energy Use: Final Report. A report to the Department for Environment,
Food and Rural Affairs. London, Brook Lyndhurst & Defra.

Ghafghazi, S., Sowlati, T., Sokhansanj, S., Melin, S. (2010) A multicriteria approach to evaluate
district heating system options, Applied Energy, 87, 1134-1140.

Heiskanen, E., Kasanen, P., Timonen, P. (2005) Consumer participation in sustainable development,
International Journal of Consumer Studies, 29 (2) 98-107.

HM Government (2008). Climate Change Act 2008, TSO, Norwich

HM Government. (2009a) The UK Low Carbon Transition Plan: National strategy for climate and
energy. Available:
http://www.decc.gov.uk/assets/decc/white%20papers/uk%20low%20carbon%20transition%20pla
n%20wp09/1_20090724153238_e_@@_lowcarbontransitionplan.pdf (accessed 10th July 2010).

HM Government. (2009b) Heat and Energy Saving Strategy: A Consultation. Available:
http://hes.decc.gov.uk/consultation/download/index-5469.pdf (accessed 1st August 2010).

HM Government. (2010) Warm Homes, Greener Homes: A Strategy for Household Energy
Management Supporting Papers. Available:
http://www.decc.gov.uk/assets/decc/What%20we%20do/Supporting%20consumers/Household%
20Energy%20Management/1_20100303145715_e_@@_warmhomessupportingdocs.pdf
(accessed 4th August 2010).

Ipsos-MORI (2009). Ipsos MORI Issues Index – Topline Results. http://www.ipsos-
mori.com/Assets/Docs/Polls/poll%20-%20July09%20Issues%20index.pdf.

Johnston, J. (2008). "The citizen-consumer hybrid: ideological tensions and the case of Whole Foods
Market." Theory and Society 37(3): 229-270.

King, S., M. Dyball, et al. (2009). Exploring public attitudes to climate change and travel choices:
deliberative research. Final report for Department for Transport.
http://www.dft.gov.uk/pgr/scienceresearch/social/climatechange/attitudestoclimatechange.pdf,
People Science & Policy Ltd & ITS, Leeds.

Koehler, B. (2009). District Heating; Economic Assessment and Evaluation of Evidence. DECC.
London.

Livingstone, S., P. Lunt, et al. (2007). "Citizens, consumers and the citizen-consumer: articulating the
citizen interest in media and communications regulation." Discourse & Communication 1(1): 63-
89.

Mahapatra, K., Gustavsson, L. (2009) Influencing Swedish homeowners to adopt district heating
systems, Applied Energy, 86, 144-154.

Macadam, J., G. Davies, et al. (2008). The Potential and Costs of District Heating Networks: a Report to the Department of Energy and Climate Change. DECC. Oxford, Poyry Energy.

McGowan, F., Sauter, R. (2005) Public Opinion on Energy Research: A Desk Study for the Research Councils, University of Sussex. Available: http://www.epsrc.ac.uk/pubs/reports/Documents/EnergyAttitudesDeskStudySussex2005.pdf (accessed 27th July 2010).

MORI (2005). Science in society: Findings from qualitative and quantitative research. London, MORI.

National Assembly for Wales Finance and Statistics Team (2008) Key Statistics for Neath Port Talbot. Available at: http://www.neath-porttalbot.gov.uk/PDF/Key%20Statistics%20for%20Neath%20Port%20Talbot.pdf (accessed 4th August 2010).

Nye, M., Whitmarsh, L., Foxon, T. (2010) Socio-psychological perspectives on the active roles of domestic actors in transition to a lower carbon electricity economy, Environment and Planning A, 42 (3), 697-714.

Office for National Statistics (2001) Neath Port Talbot Census 2001. Available: http://www.statistics.gov.uk/census2001/pyramids/pages/00nz.asp (accessed 4th August 2010).

Pidgeon, N. F., I. Lorenzoni, et al. (2008a). "Climate change or nuclear power - No thanks! A quantitative study of public perceptions and risk framing in Britain." Global Environmental Change-Human and Policy Dimensions 18(1): 69-85.

Pierce, M. (1995) Controlling urban climates: The need for local heat supply planning, Journal of Urban Technology, 2 (3), 59-79.

Poortinga, W. and N. F. Pidgeon (2003). Public perceptions of risk, science and governance. Norwich, UEA/ MORI.

Sauter, R., Watson, J. (2007). Strategies for the deployment of micro-generation: Implications for social acceptance, Energy Policy, 35 (5) 2770-2779.

Shackley, S., Reiche, A., Mander, S. (2004) The Public Perceptions of Underground Coal Gasification (UCG): A Pilot Study: Tyndall Centre Working Paper 57. Available: http://www.tyndall.ac.uk/sites/default/files/wp57.pdf (accessed 22nd August 2010).

Shove, E., Walker, G. (2007) CAUTION! Transitions ahead: politics, practice and sustainable transition management, Environment and Planning A, 39, 763-770.

Unruh, G. C. (2000). "Understanding carbon lock-in." Energy Policy 28(12): 817-830.

Upham, P., L. Dendler, et al. ""Carbon labelling of grocery products: public perceptions and potential emissions reductions"." Journal of Cleaner Production In Press, Accepted Manuscript.

Upham, P., Whitmarsh, L., Poortinga, W., Purdam, K., Darnton, A., McLachlan, C., Devine-Wright, P. (2009) Public Attitudes to Environmental Change: A Selective Review of Theory and Practice, A Research Synthesis for The Living with Environmental Change Programme, http://www.lwec.org.uk/news-archive/2009/30102009-report-published-public-attitudes-environmental-change

Walker, G., Cass, N. (2007). Carbon reduction, 'the public' and renewable energy: engaging with socio-technical configurations, Area, 39 (4), 458-469.

Welsh Assembly Government (2008) Welsh Index of Multiple Deprivation (WIMP) 2008 Summary Report. Available at: http://wales.gov.uk/docs/statistics/2010/100712wimd08summaryreviseden.pdf (accessed 4th August 2010).

Welsh Assembly Government. (2009) European Structural Funds 2007-2013 Strategic Framework: Climate Change; ERDF Convergence P4T1 and P4T2; ERDF Competitiveness: P3. Available: http://wales.gov.uk/docs/wefo/publications/strategicframeworks/100420climatechangeframeworken.pdf (accessed 7th July 2010).

Werner, S. (2004) District Heating and Cooling, Encyclop edia of Energy, 1, 841-848.

Heat Pumps and Energy Storage – The Challenges of Implementation

Neil J Hewitt

Centre for Sustainable Technologies, University of Ulster, Newtownabbey, Co Antrim, BT370QB, UK

Abstract
The wider implementation of variable renewable energy sources such as wind across the UK and Ireland will demand interconnection, energy storage and more dynamic energy systems to maintain a stable energy system that makes full use of one of our best renewable energy resources. However large scale energy storage e.g. pumped storage may be economically challenging. Therefore can thermal energy storage deployed domestically fulfil an element of such an energy storage role? Current electricity pricing is based on a ½ hourly timeframe which will be demonstrated to have some benefits for hot water heating from electrical water heaters in the first instance. However heat pumps linked to energy storage can displace fossil fuel heating systems and therefore the question is whether a renewable tariff based on "excess" wind for example is sufficient to operate heat pumps. An initial analysis of this scenario will be presented and its potential role in challenging aspects of fuel poverty.

Keywords   heat pumps; energy storage; large scale non-dispatchable renewable energy

1   Introduction

There is no denying the wider role that will be played by renewable energy and the UK has very significant renewable energy resources especially wind, wave and tidal, solar etc when pursuing a strategically secure and environmentally responsible energy future. The UK Government through the Energy White Paper [1] states that 20% of the UK's energy will be provided from renewable sources by 2020. Given wind energy's leading competitive position, it has been estimated that wind energy with utilisation factors of 35% will generate 80TWh from a capacity of 26GW i.e. about 20% of the overall annual UK electricity consumption [2]. Barthelmie et al [3] states that the accuracy of short-term forecasting is economically viable for large wind farms. However short-term is defined in the range 0-36 hours and these limitations will be explored in more detail to understand the challenges these place on the possibility of utilising non-dispatchable renewable energy as a socially-serving tariff for the alleviation of fuel poverty. Mueller and Wallace [4] review the wave and tidal energy systems and state that such technologies are 15 years behind wind energy but have considerably more predictability than that associated with wind. However there is a challenge associated with the available market space for non-dispatchable renewable energy without the necessary energy storage/interconnection investment and an understanding of the dynamics of electricity networks, buildings (as energy users) and demand side management in general. These elements must be combined into an energy system whose goals should be that of minimising carbon and minimising fossil fuel imports while maintaining energy affordability and ensuring UK competitivity.

Thus the objectives of this work are for a likely wind energy system, to consider the dynamics of the aging electricity infrastructure (including the existing thermal generating plant), consider the dynamics of the built environment and consider a mechanism for managing these dynamics as an electricity tariff that may alleviate some of the challenges associated with energy poverty.

2   Energy poverty and the new wind age?

OFGEM's Project Discovery [5] has four scenarios for future UK energy prices. These scenarios ("green transition", "green stimulus", "dash for energy" and "slow growth") predict the average domestic consumer electricity bill will rise according to the following scenarios by 2020:

"Green transition"	£500/annum
"Green stimulus"	£500/annum
"Dash for energy"	£575/annum
"Slow growth"	£600/annum

These scenario prices represent a 25% to a 50% increase in energy costs over the 2009 prices per home. Given that the UK definition of a home in fuel poverty is that the household spends more than 10% of its income on energy [6], and while it is believed that modern and future housing standards should ensure that there is no increase in hardship not unless there is a substantial increase in fuel prices, a minimum of a 25% increase in energy may represent a major challenge.

The UK Government and devolved administrations have targets to ensure that no household should be in fuel poverty by 2016 (2018 in Wales) [7]. The 2010 target is not expected to be met and the 2016/18 targets will be very challenging. If "Project Discovery" can be used as a basis, what would a 25% increase in energy prices do to fuel poverty? It is estimated that this will ensure that a further one million households, including about 500,000 pensioners, will be classified as being in fuel poverty [8]. Decentralised renewable energy [9] is still in its infancy and it is therefore difficult to ascertain the conditions under which it will provide the greatest benefit, given the potential for high system costs and improper performance claims.

Therefore what are the choices moving forward? If the UK and Ireland are moving towards an electric economy led by non-dispatchable wind (in the first instance), it seems appropriate to utilise electric heating, transport etc to balance the electricity network. However this must provide benefits to the participants as well as the electricity utilities.

3   Electricity network dynamics and energy pricing

This analysis brings together electricity network operation, the potential impacts of wind energy penetration on such a network, the role of energy storage and the role of thermal lags encountered in buildings. The approach requires indications as to the dynamics of the above processes, their responses to changes in demands and for how long that "stored" response can provide a useful contribution to the end-user and just in a network balancing role.
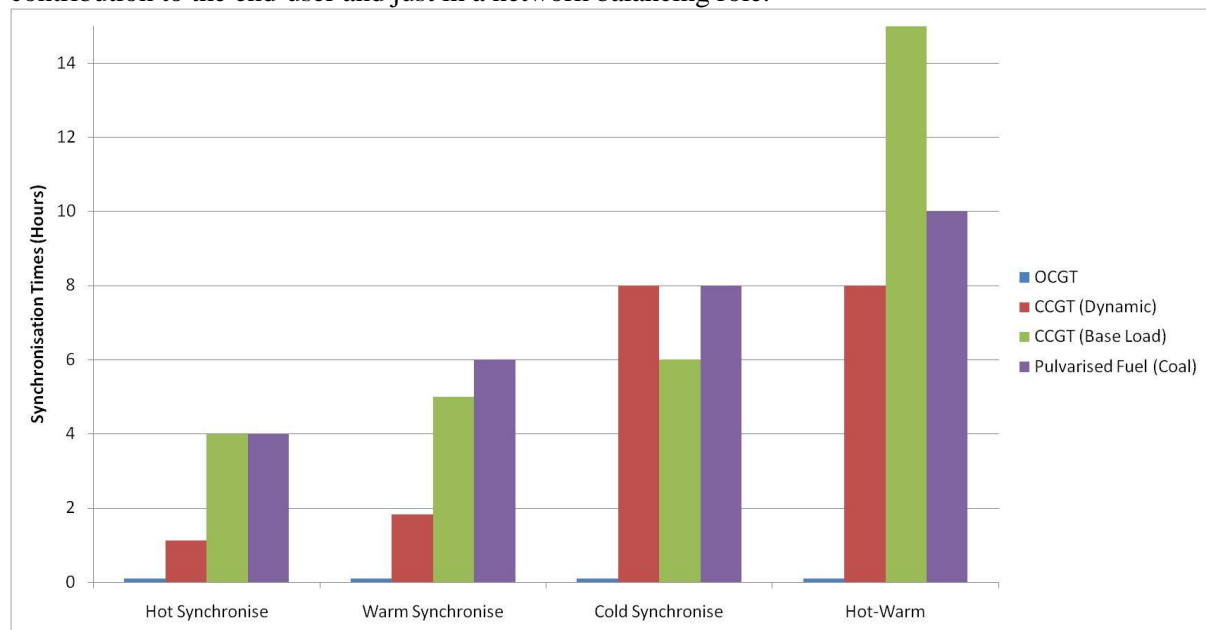
Figure 1: Typical times to synchronisation for combined cycle gas turbine (CCGT) and pulverised fuel (coal) power stations

Response times of thermal power stations (coal-fired pulverised fuel, combined cycle gas turbines, open cycle etc) differ somewhat according to technology but indicative response times are illustrated in Figure 1 for the three Northern Ireland power stations (as representative of the UK and Ireland fleet) as outlined by the Single Electricity Market Operator (SEMO) [10]. In addition, in UK and Ireland, spinning reserve plants are available within about 30 seconds i.e. not generating electricity but at operating temperature. The rates at which a thermal power station attains its operating temperature

are limited by for example expansion rates of the turbines etc as they heat up prior to electricity generation and synchronisation. A simplistic view is to relate this phenomenon to that of thermal mass i.e. base load systems (continuous operation) can be seen as "heavy" whilst the newer dynamic systems are seen as "light". The latter heats up faster and therefore can be synchronised to the needs of the network faster. This is often a challenging task for a conventional electricity distribution network based on centralised thermal power plant but is complicated further by the addition of large amounts of non-dispatchable wind based electricity. Plants are dispatched based on a merit order i.e. response characteristics, efficiency, network constraints etc. A sudden change in available wind energy may require a change in a power station status, an additional change that, as illustrated later, has a detrimental effect on the maintenance of the plant.

Figure 1 also barely notes the response times of the open cycle gas turbines used for quick responses (at 0.13 hours i.e. 8 minutes). These typically represent about 1/20th of the capacity of the power station they are associated with, but are a noted growth area in Irish terms to meet the potential growth in the numbers of dynamic interventions required to accommodate a considerably higher wind penetration of about 40% by 2020. Such interventions are paid a high price (Figure 8 illustrates peak system marginal prices for example) as they occur at times of high electricity demands and thus energy storage to reduce peaks in demands is seen as necessary. A caveat to this is that the price then paid for energy storage (as storage reduces the electricity price spikes) must therefore be competitive at a lower income rate.
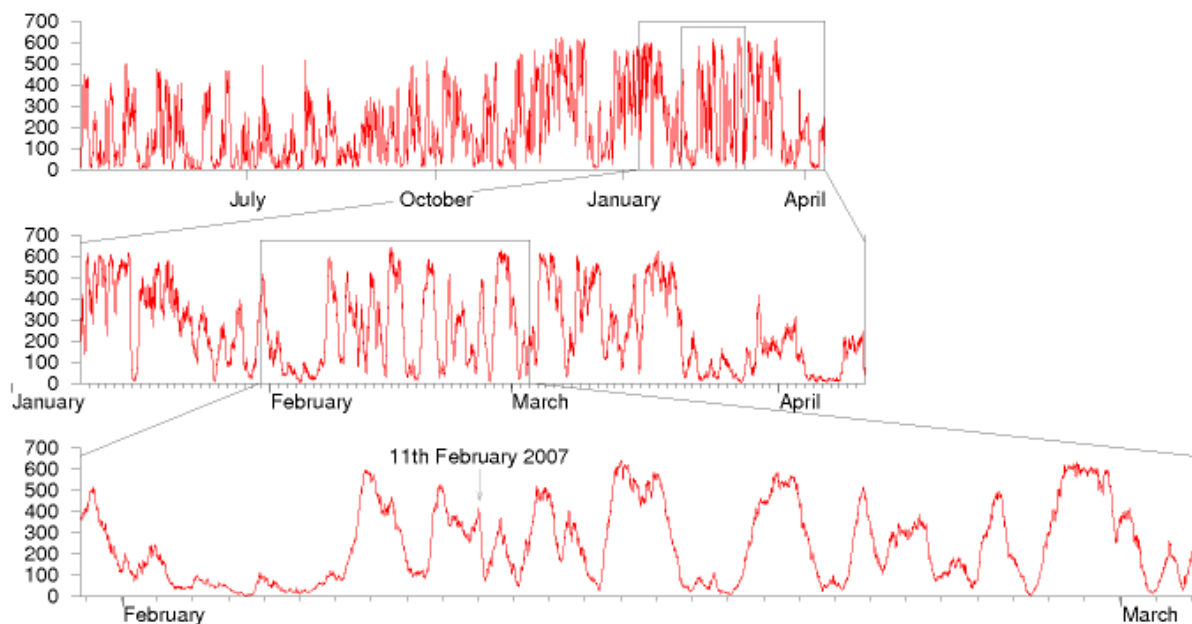
Figure 2: Wind Energy Dynamics

Wind penetration is increasing on the Irish network, subject to economic and technical constraints. Figure 2 illustrates the challenges wind places on the electricity network [10]. Similar conditions are expected on the UK network with 25GW offshore and 8GW onshore wind permissible by 2020 [11]. The rate of change of wind power noted is comparable with the response times of the fossil fuel units when operating under their "hot" boundary conditions i.e. restarting in a time period or no more than 8 hours since their last operation. Thus typically a four hour time until synchronisation (aided by fast starting open cycle gas turbines) appears practical. However cycling of large scale base load power stations is problematical [12]. The challenges that arise are increased capital spend for component replacement, increased operation and maintenance costs, lower availability due to increased failure rate and increased outage time and increased fuel cost arising from reduced efficiency and non optimum heat rate. Recent studies suggest that the average cold start cost is 70000 US$, warm start costs of 4000 US$, hot start costs of 3500 US$, based on 1000 MW nominal output of coal fired plant.
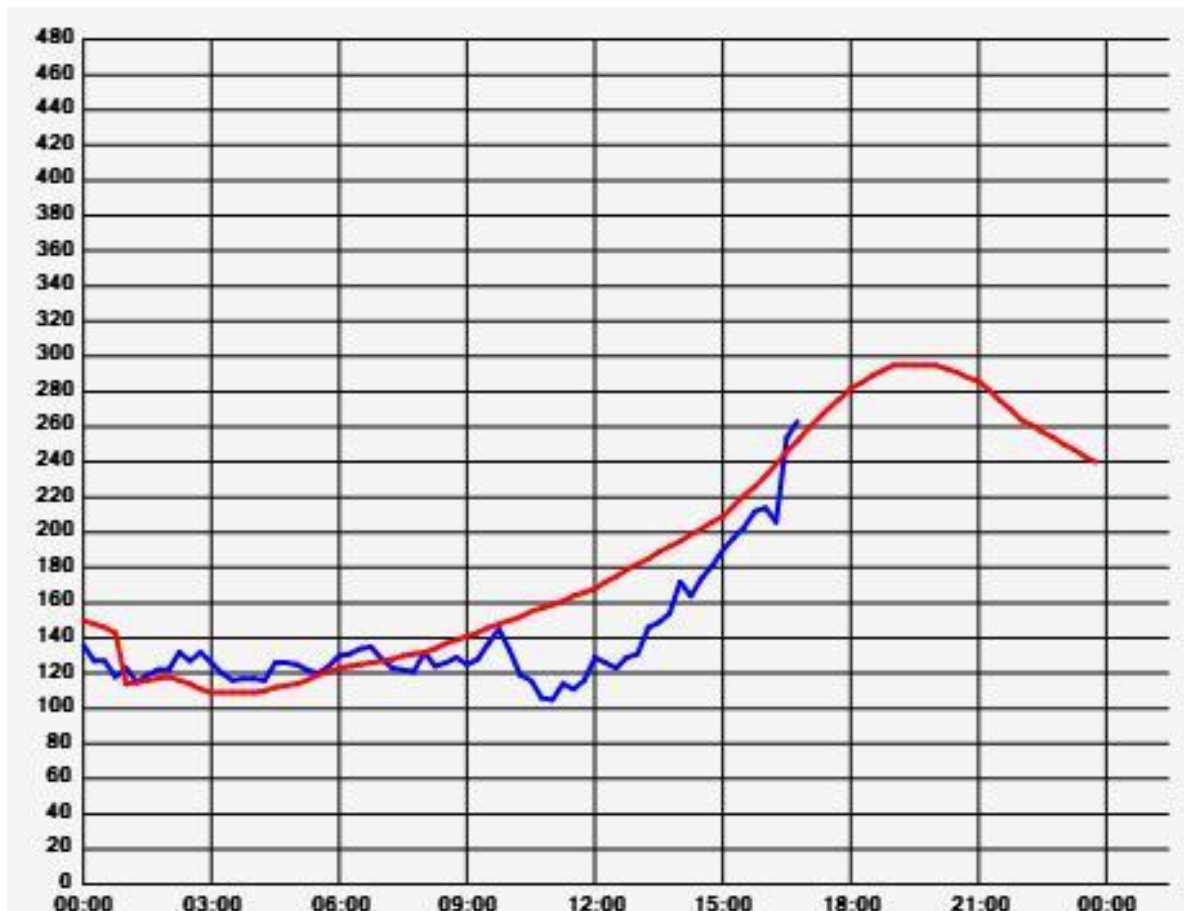
Figure 3: Forecast Wind (red) (MW) versus Actual Wind Generation (blue) in Ireland for a day [13]

So what of wind forecasting? In order to reduce large thermal plant starts, operate plant more efficiently and reduce the use of expensive open cycle peaking plant, can wind forecasts be produced that allow plant scheduling to occur in such a way as to allow existing fossil fuel plant to operate most effectively (or not at all)? Figure 3 illustrates the challenges for forecasting wind [13] and the need therefore to bring on conventional generation short notice or indeed, increase the use of expensive OCGT generation. Thus the inaccuracy associated with 0-36 hour prediction will require greater consistency.

4   The built environment, heat pumps and energy storage
Wind energy in particular presents challenges due to its variability in relation to the demand (and supply) side needs of an electricity network. If a large amount of wind energy is to be superimposed onto a traditional fossil fuel fired (or future nuclear) electricity network, the inherent smoothing associated with wind turbines widely dispersed across a geographical region may not be sufficient to manage the dynamics of existing fossil fuel and nuclear plant (in ramping up or down depending on network requirements). Therefore an element of storage is required.

Figure 4 summarises the role of electrical energy storage technologies [14]. While a number of these technologies can be considered as mature, it is only the recent growth in non-dispatchable renewable energy generation that energy storage deployment has become of interest. Furthermore the built environment with its thermal lags and electrical demands requires further investigation as a mechanism for adding to the portfolio of approaches illustrated. The key challenges are technology selection and development and the relationship between the technology capacity, the building energy process demand and the socio-economic acceptability of the storage medium. Thermal energy storage systems utilising phase change materials [15] are an option to enhance thermal storage (whether actively or passively) in buildings. *Table 1* illustrates some of the suppliers and their product range.

It is noted that many of these cover passive and active thermal comfort range and their supporting systems.
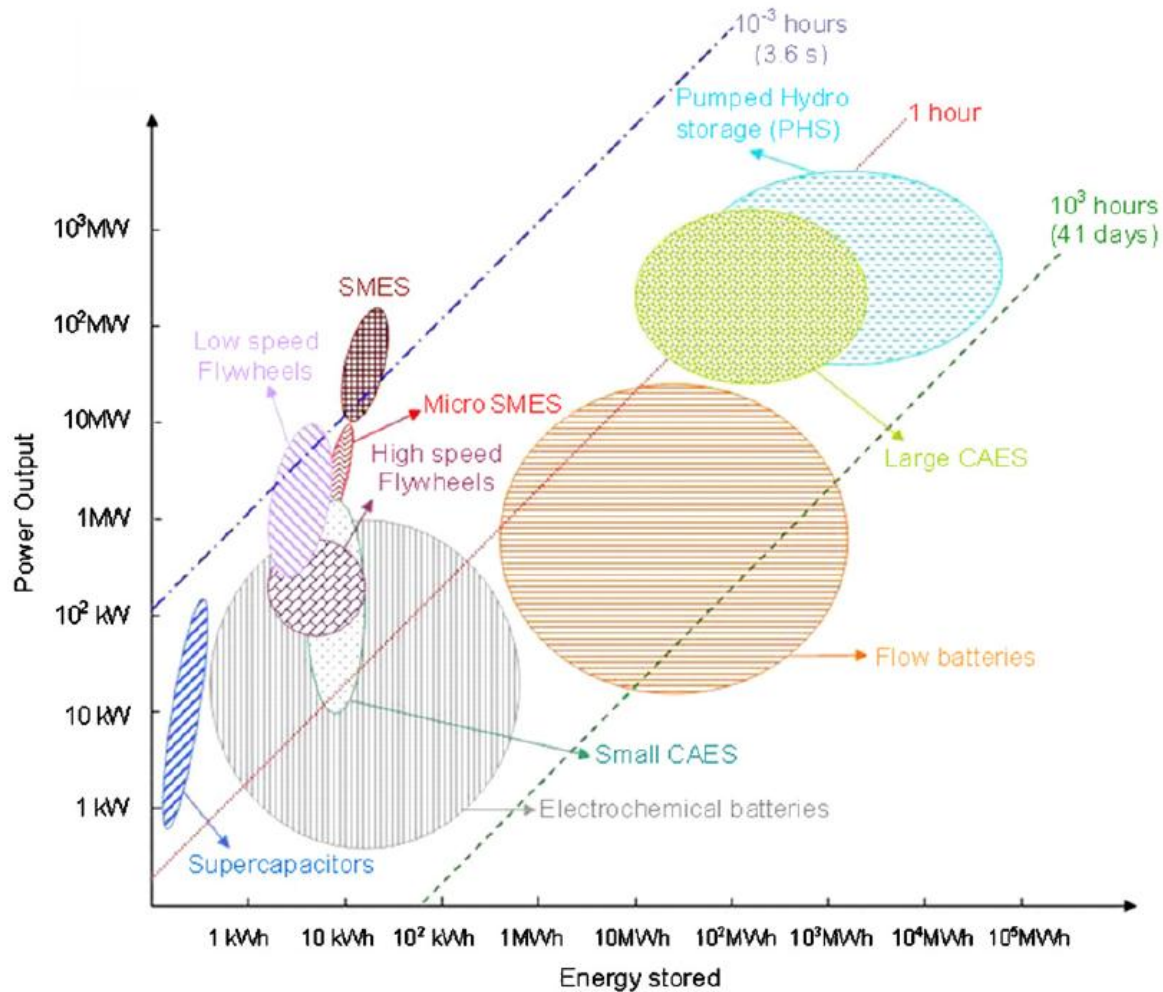
Figure 4: Energy Storage Response Times [14]

Table 1
Global Commercial PCM Manufacturers

Manufacturer	PCM Temperature Range °C	Number of PCM's Available
Rubitherm	-3 to 100	29
Crystopia	-23 to 27	12
TEAP	-50 to 78	22
Doerken	-22 to 28	2
Mitsubishi	9.5 to 118	6
Climator	-18 to 70	9
EPS	-114 to 64	61

The challenge is therefore energy storage. Large-scale storage has attraction for energy utilities and network operators alike due to the ease of communications and simplified response characteristics. The built environment on the other hand represents a virtual energy store that requires the development of a "smart grid" to enable its use in energy storage to its full potential and as it obviously already exists, potentially reducing capitals cost of energy storage creation.

4.1   The built environment as an energy store

The ability of a typical example of the local housing stock to retain heat after the heating system was utilised was examined. Figure 5 illustrates the type of results seen over usual winter conditions. While thermal comfort is a personal choice, for the illustrative nature of this study, ±2.0°C from a UK living space norm of 21°C [16] is assumed and therefore 3 hours storage is not unreasonable. Of course this varies widely dependant on building type, climate, solar orientation, passive gains, occupancy etc and requires more investigation but the concept of using our building stock to effectively store energy for a number of hours prior to use is available. This not only helps to balance the electricity network in times of higher wind forecast but allows the organisation/person who participates in such a scheme to see benefit by for example reduced electricity prices during such periods and less heating/cooling requirements due to a pre-cooling/heating period. Such "passive" systems can be augmented by for example wall-boarding systems impregnated with micro-encapsulated phase change materials (PCM) [17].
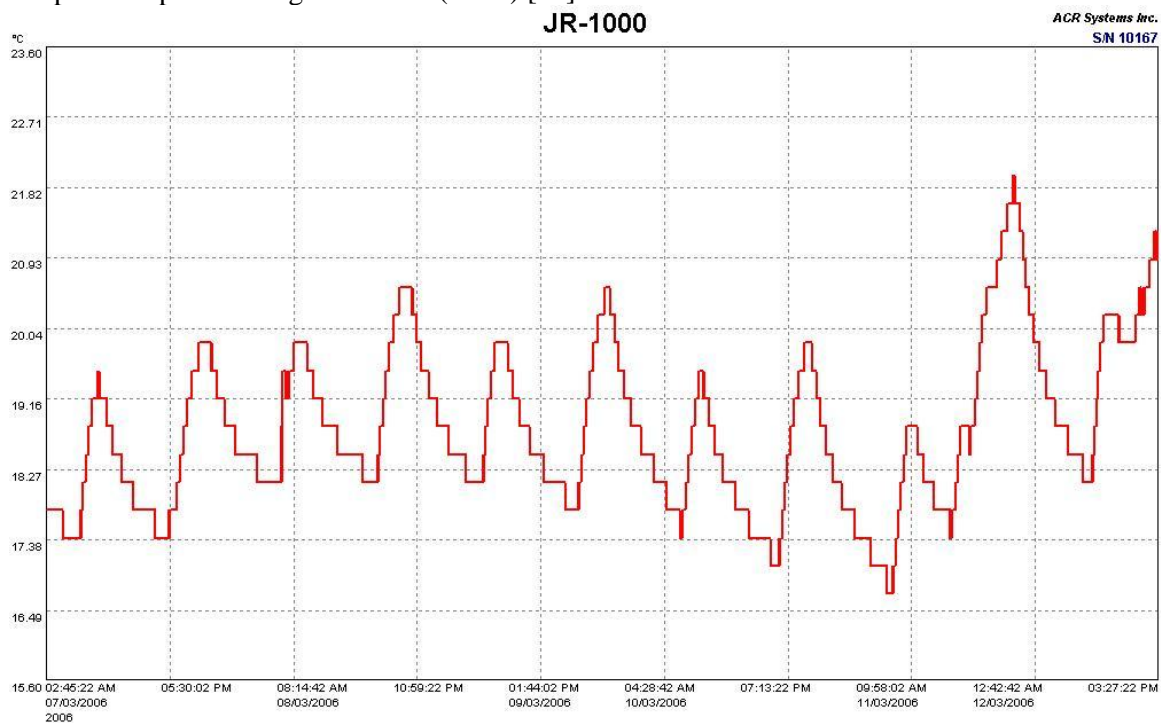
Figure 5: Thermal Response of a 100m^2 Semi-Detached Home built in 1995

4.2   Heat pumps, air-conditioners and energy storage dynamics

There are a number of methods available to balance the electricity network in times of high wind energy availability. It has been illustrated that the buildings themselves have some ability but this requires an individual building approach which may be augmented by PCM's where thermal mass is an issue. Commercial buildings are already awash with air-conditioning (reversible heat pumps) and the domestic market is growing. So what is their value in balancing an electricity network?

Figure 6 illustrates the performance curve from a heat pump heating the home whose thermal energy storage performance was briefly considered earlier in this study.   It takes approximately 30 minutes before the system cycles off from start up at 18:00 i.e. the hot water returning to the unit is sufficiently warm enough indicating that the home is no longer taking any heat. Adopting an alternative solution would for example, heat domestic hot water. The room space has not acquired the notional 21°C temperature in that time and therefore any storage capability would be compromised.

Energy storage systems are a challenge. Water is effective but bulky. PCMs have excellent storage characteristics but poor thermal conductivity characteristics i.e. they are reluctant in the most part to let heat in an out at the perceived demand and supply side rates. Salt based systems seem to suffer from complexity and material challenges and may be best suited to seasonal storage systems. An

example of PCM related activity is illustrated in Figure 7 where the response times for a higher temperature heat pump are considered [18]. In the same 30 minutes, the temperature of a typical UK 144 litre tank of water can be raised by 9°C. Thus the problem becomes this – what is the best use of this 30 minutes of energy and why is there a fixation with 30 minute time slices? To answer the question regarding 30 minutes, hot water may be the best solution, subject to hot water storage losses being minimised. Such storage technologies exist for solar thermal systems and have been evaluated [19] with positive results for hot water energy storage regarding solar energy and next morning usage.
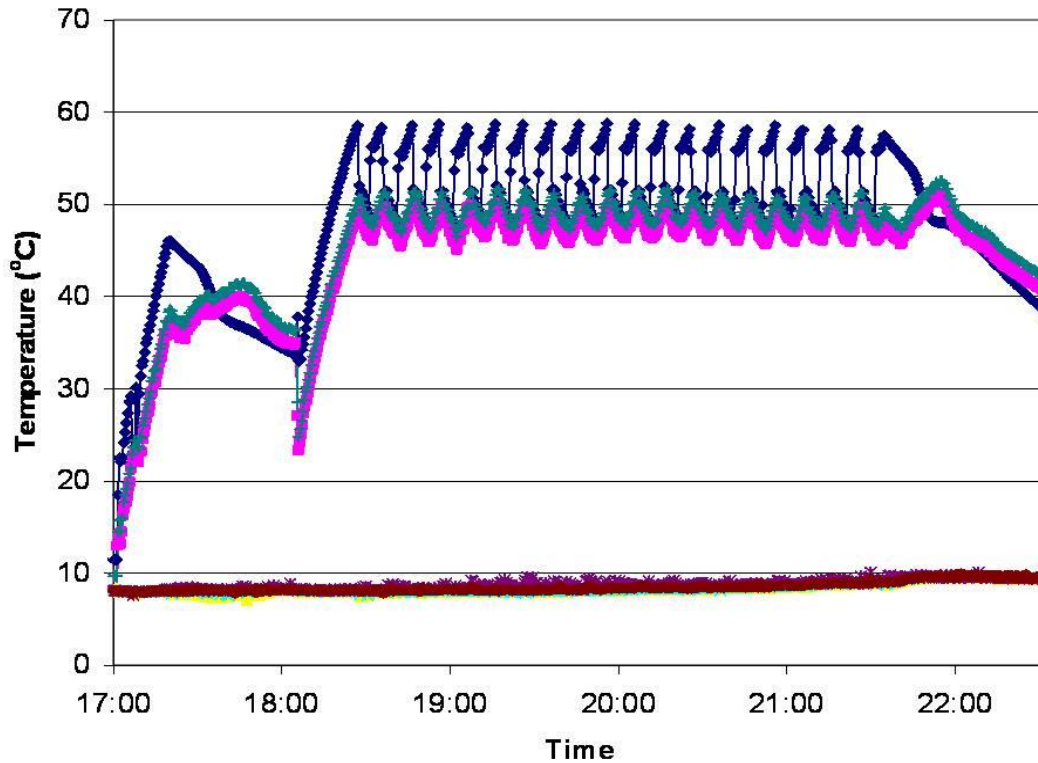
Figure 6: Air Source Heat Pump Response Time at Start Up
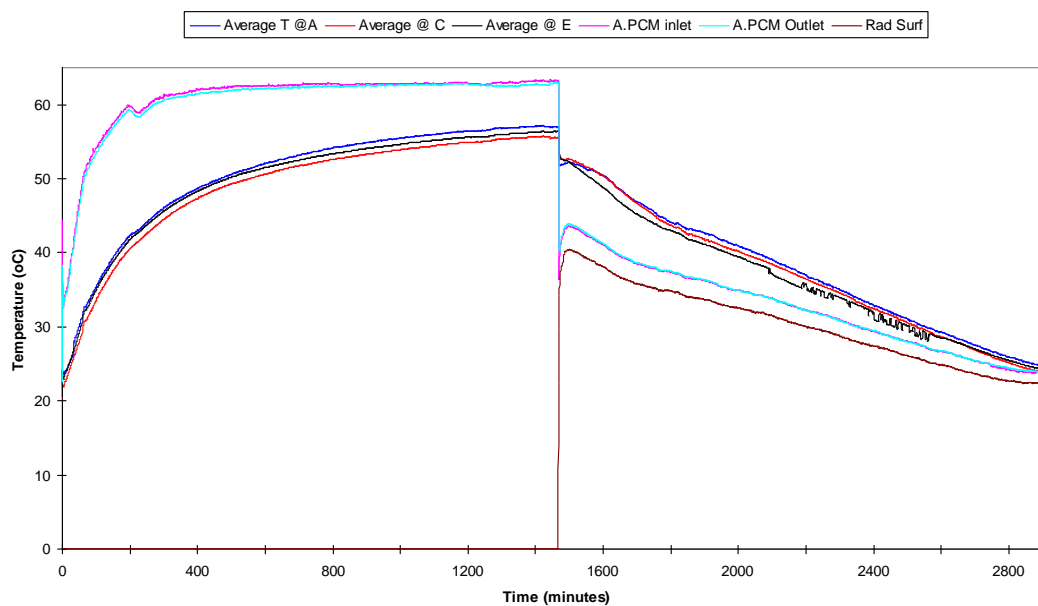
Figure 7: Paraffin Wax Based Solid PCM Response Times

The role of 30 minutes in making decisions as to the type of energy storage is also challenging. The system marginal price (SMP) for electricity from the supply network (as illustrated by the maximum SMP illustrated in Figure 8) is defined by 48 time steps in a 30 minute delimited electricity market day [10]. A model for flexible electricity tariffs based on SMP would be required to allow excess wind energy to be used for example, domestically to space or water heat.
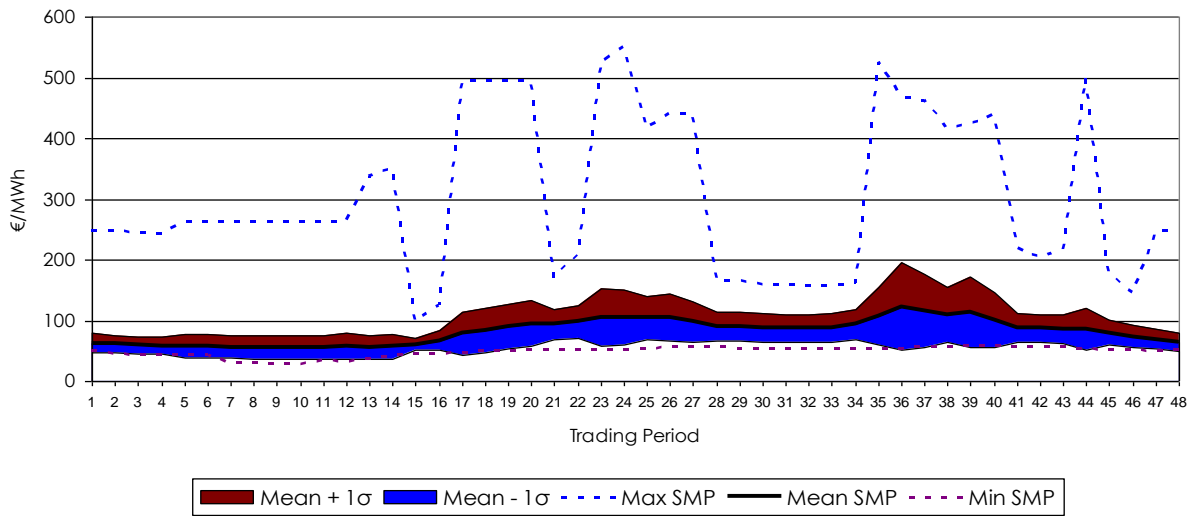
Figure 8: System Marginal Price Operation [10]

5   Alleviating fuel poverty

Water storage advantages will not be realised if the insulation associated with the hot water storage tank is not sufficient. Building Regulations require all hot water storage vessels to be insulated. BS 1566 and BS 3198 allow maximum heat loss for factory applied insulation of 1 watt/per litre of hot water storage capacity under test conditions. Heating to 60°C to minimise risk of legionella is required but equally to avoid scalding risk, the water delivery should be no higher than 44°C [20]. A typical shower temperature of 37°C is often considered as a useful baseline for domestic hot water applications and a model was developed for hot water storage heat loss (Figure 9). This model assumes that a night off-peak electricity pricing rate is used to change the hot water storage between 11pm and 7am.
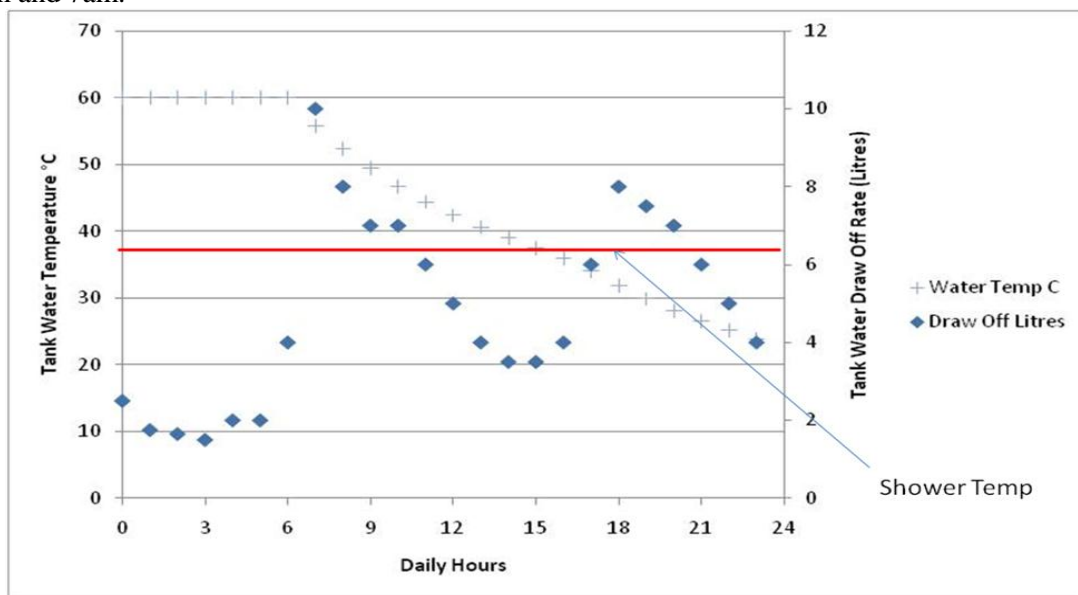
Figure 9: Water Storage and Daily Use without additional energy input after 6am

Applying a 30 minute boost at for example 3pm (a time where (a) the system marginal price is usually low and (b) from the selected hot water draw off profile [21], the hot water storage cylinder

temperature has dropped below 37°C), the added benefit can be seen until 7pm (Figure 10). A 60 minute boost at this period (Figure 11) can reveal added benefit of hot water at a temperature above 37°C until 10pm. If this tariff was effectively at zero cost to encourage participation, a saving of up to £0.40/day can be achieved.
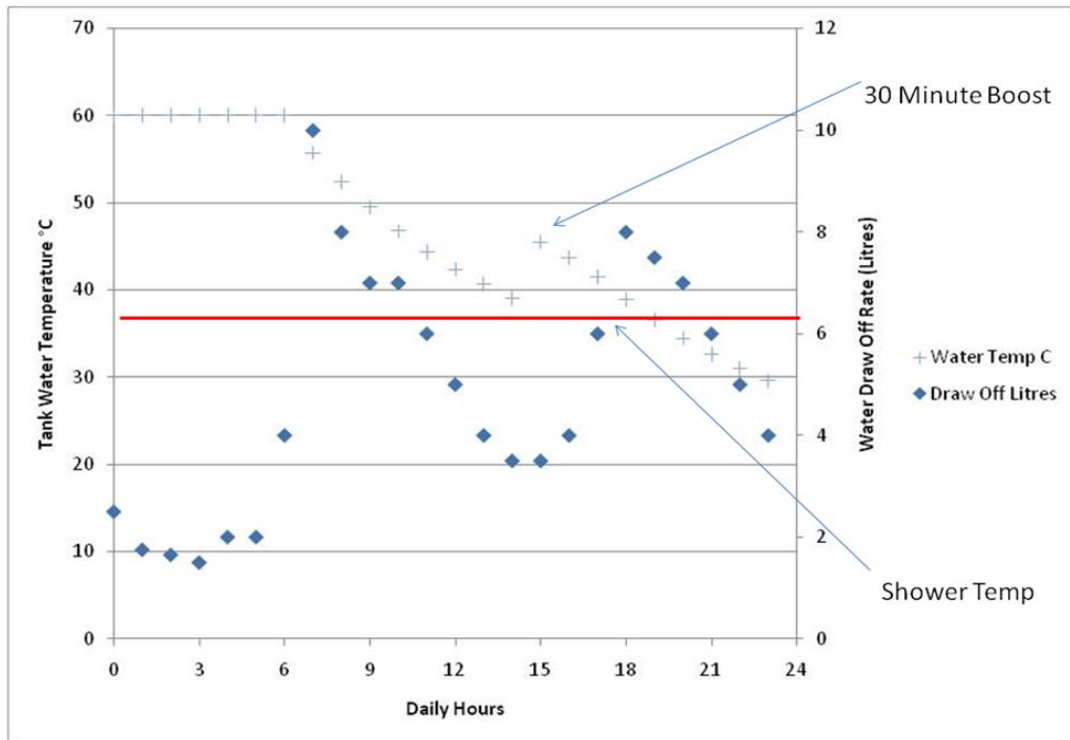
Figure 10: Impact of a low system marginal price boost to water heating for 30 minutes
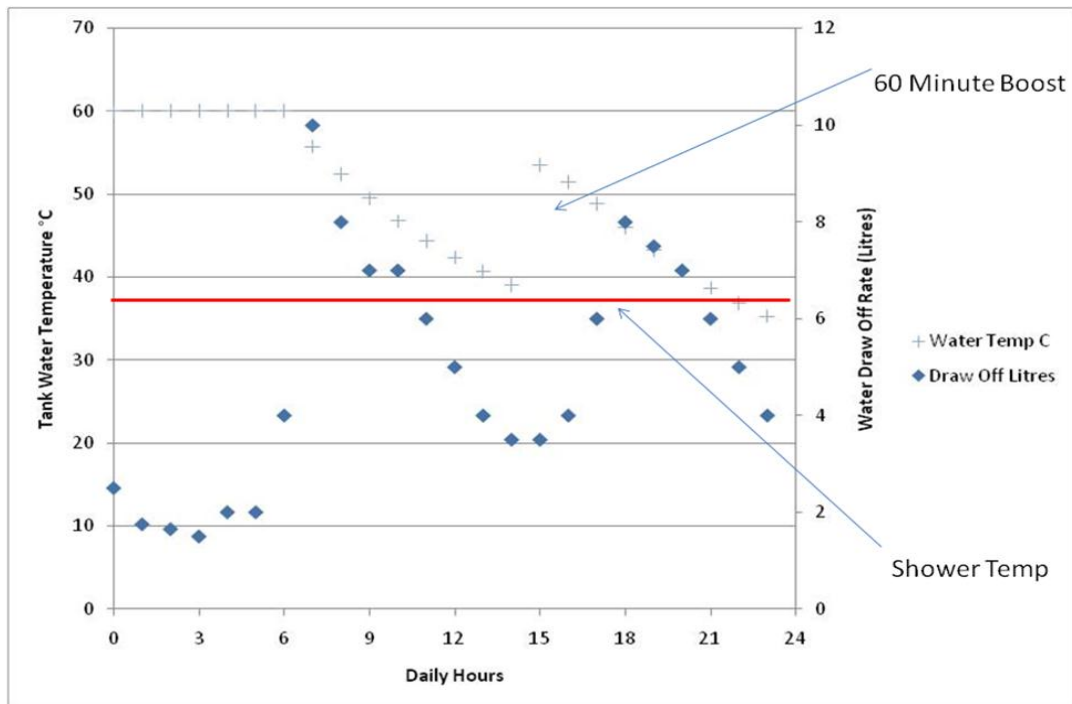
Figure 11: Impact of a low system marginal price boost to water heating for 60 minutes

Space heating is more complicated and the thermal mass of the heat pump has been demonstrated to be a drawback for 30 minute pricing.   60 minute pricing would allow up to three hours thermal

storage in this example and would potentially offset the 4pm-7pm peak system marginal pricing period. This can be augmented by energy storage including augmented hot water cylinders allowing contributions to space heating, targeted space/room controlling and more sophisticated energy storage in the form of phase change materials. Again savings of approximately £0.40/day can be achieved if such a tariff is low/zero cost to encourage participation.

In order to achieve such savings technologically, a "smart grid" is required. Low cost communications to operate water heaters, heat pumps, air-conditioners etc potentially based on the already extensive roll-out of broadband etc will be required. Communication and the development of the "soft grid" will be a new area that must compliment any user interaction and user acceptability issues. Having users accept that low cost energy will benefit when for example, they are not in the house and at work may be the greatest challenge of them all.

6   Conclusions

The role of heat pumps and hot water storage cannot be underplayed in the efforts to integrate greater amounts of electricity onto the network. The dynamics of even relatively simple buildings allows a degree of thermal management which can be augmented by for example phase change materials based wall materials. However the common electricity market mechanism of ½ hourly electricity pricing may influence the benefits such systems may have, especially when operating from ambient temperatures in the first instance. Systems that have been operating for a time before the required start under a low cost electricity tariff influenced by large amounts of non-dispatchable renewable energy generation will respond quicker and achieve greater benefits for the building user. The "smart grid" must take account of the dynamics of all participants to maximise benefits for all.

This challenge is set to increase [22]. The global wind market is still growing (14% for 2009 over 2008) in the current economic down turn and investment in the complimentary "Smart Grids" (34% for 2009 over 2008) has been developed to balance demand side management, thermal power station response times etc. Thus there is potentially a new energy paradigm on the horizon when this is integrated with the necessary communication and control strategies to allow demand side management to balance non-dispatchable wind generation.

References
[1]   Energy White Paper Our Energy Future, Creating a Low Carbon Economy, UK Government, 2003
[2]   Impact of wind generation on the operation and development of the UK electricity systems, Electric Power Systems Research, Volume 77, Issue 9, July 2007, Pages 1214-1227, Goran Strbac, Anser Shakoor, Mary Black, Danny Pudjianto, Thomas Bopp
[3]   The economic benefit of short-term forecasting for wind energy in the UK electricity market, Energy Policy, Volume 36, Issue 5, May 2008, Pages 1687-1696 R.J. Barthelmie, F. Murray, S.C. Pryor
[4]   Enabling science and technology for marine renewable energy, Energy Policy, Volume 36, Issue 12, December 2008, Pages 4376-4382, Markus Mueller, Robin Wallace
[5]   Project Discovery - Energy Market Scenarios - (Reference number: 122/09), 09/10/2009
[6]   Energy, equity and the future of the fuel poor, Energy Policy, Volume 36, Issue 12, December 2008, Pages 4471-4474, Simon Roberts
[7]   http://waleshome.org/2010/01/fuel-price-increases-have-outstripped-resources-for-tackling-fuel-poverty/
[8]   National Energy Action/Age Concern.
[9]   Decentralised systems and fuel poverty: Are there any links or risks? Energy Policy, Volume 36, Issue 12, December 2008, Pages 4514-4517, Gordon Walker
[10] Single All-Ireland Market Operator http://allislandmarket.com/
[11] The UK Renewable Energy Strategy, July 2009, HM Government.
[12] J Gostling (2002) Two Shifting of Power Plant: Damage to Power Plant Due to Cycling - A brief overview OMMI (Vol. 1, Issue 1) April 2002
[13] http://www.eirgrid.com/operations/systemperformancedata/windgeneration/

[14] H. Ibrahim, A. Ilinca, J. Perron (2008) Energy storage systems - Characteristics and comparisons Renewable and Sustainable Energy Reviews, Volume 12, Issue 5, June 2008, Pages 1221-1250

[15] Francis Agyenim, Neil Hewitt, Philip Eames, Mervyn Smyth (2010) A review of materials, heat transfer and phase change problem formulation for latent heat thermal energy storage systems (LHTESS) Renewable and Sustainable Energy Reviews, Volume 14, Issue 2, February 2010, Pages 615-628

[16] Yigzaw Goshu Yohanis, Jayanta Deb Mondol (2010) Annual variations of temperature in a sample of UK dwellings Applied Energy 87 (2010) 681–690

[17] Shane Colclough, Philip Griffiths, Stefan Gschwander (2009) Thermal Energy Storage and the Passive House Standard: How PCM incorporated into wallboard can aid thermal comfort, PLEA2009 - The 26th Conference on Passive and Low Energy Architecture, Quebec City, Canada, 22-24 June 2009

[18] Francis Agyenim, Neil Hewitt (2010) The development of a finned phase change material (PCM) storage system to take advantage of off-peak electricity tariff for improvement in cost of heat pump operation Energy and Buildings, Volume 42, Issue 9, September 2010, Pages 1552-1560

[19] Jayanta Deb Mondol, Mervyn Smyth, Aggelos Zacharopoulos, Trevor Hyde (2009) Experimental performance evaluation of a novel heat exchanger for a solar hot water storage system, Applied Energy, Volume 86, Issue 9, September 2009, Pages 1492-1505

[20] http://www.hse.gov.uk/lau/lacs/79-5.htm

[21] Energy Savings Trust, Measurement of Domestic Hot Water Consumption in Buildings, DEFRA, 2008

[22] Global Trends in Sustainable Energy Investment 2010, Analysis of Trends and Issues in the Financing of Renewable Energy and Energy Efficiency, UNEP, SEFI, Bloomberg New Energy Finance, 2010.

Track 2 Section 1

Heat Exchangers

Identifying Optimal Cleaning Cycles for Heat Exchangers Subject to Fouling and Ageing

Thomas Pogiatzis, Edward Ishiyama, William Paterson, Vassilis Vassiliadis, Ian Wilson*

Department of Chemical Engineering & Biotechnology, New Museums Site, Pembroke Street, Cambridge, CB2 3RA

* Corresponding author. Email: diw11@cam.ac.uk; Tel. +44(0) 1223 334 777; Fax. + 44(0) 1223 334 791

Abstract

Fouling of heat exchangers causes reduced heat transfer and other penalties. Regular cleaning represents one widely used fouling mitigation strategy, where the schedule of cleaning actions can be optimised to minimise the cost of fouling. This paper investigates, for the first time, the situation where there are two cleaning methods available so that the mode of cleaning has to be selected as well as the cleaning interval. Ageing is assumed to convert the initial deposit, labelled 'gel', into a harder and more conductive form, labelled 'coke', which cannot be removed by one of the cleaning methods. The second method can remove both the gel layer and the coke layer, but costs more and requires the unit to be off-line longer for cleaning. Experimental data demonstrating the effects of ageing are presented. The industrial application is the comparison of cleaning-in-place methods with off-line mechanical cleaning. A process model is constructed for an isolated counter-current heat exchanger subject to fouling, where ageing is described by a simple two-layer model. Solutions generated by an NLP-based approach prove to be superior to a simpler heuristic. A series of case studies demonstrate that combinations of chemical and mechanical cleaning can be superior to mechanical cleaning alone for certain combinations of parameters.

Keywords   ageing; cleaning; fouling; non-linear programming; optimisation; scheduling

1   Introduction

Many heat transfer systems are subject to fouling, reducing the efficiency of heat transfer and limiting productivity. Heat exchangers experiencing fouling are therefore cleaned regularly, with the length of an operating cycle being determined by an optimization involving cleaning costs and fouling-related losses, as outlined by Ma and Epstein [1]. Fouling and cleaning are, however, symbiotic processes, as outlined by Wilson [2]. The effectiveness of a cleaning operation dictates the initial conditions for subsequent fouling, while the state of the fouling deposit at the end of the production run determines the nature and dynamics of cleaning. 'State' here refers to factors such as the deposit microstructure and chemical nature, all of which contribute to the reactivity and rheology of the layer, which determine the layer's response to cleaning agents and mechanical action such as fluid shear.

In many food, water and chemical applications the deposit undergoes 'ageing', a transformation over the lifetime of the run from the initial precursor form to another, usually more cohesive, form. The extent of ageing determines the state of the layer and therefore the ease with which a fouling layer can be removed. Different cleaning methods are available to an operator (see [3]), and the cleaning efficiency will therefore be affected by ageing. In selecting a cleaning method, the operator must consider whether the method can remove aged as well as freshly formed material.

The experimental data in Figure 1 show local shear strength and density measurements for three calcium sulphate scale deposits, grown under identical conditions for different times. The deposit grows in thickness over time as material continues to be added at the deposit/solution interface. The profiles show the material near the interface to be less dense and weaker. Over time, the density and strength of deposit at a given location increases. Ageing is likely to occur irrespective of whether deposition continues, but this will depend on the operating conditions and processes involved. A cleaning method relying on fluid shear alone is unlikely to be able to remove the hardened deposit: either mechanical action will be required or exposure to chemical agents to convert it to a softer, soluble or more readily removable form.

It should be noted that the deposit thicknesses, δ, reported in Figure 1 are large: the thermal conductivity, λ, of mineral scales [4] are of order 1-2 W m^{-1}K^{-1}, so a slab of thickness 3 mm would correspond to a thermal resistance, R_f, of $\sim (\delta/\lambda) = 3\times10^{-3}$ m^{2}K W^{-1}, which is higher than the value quoted by the TEMA guidelines for heat exchangers handling cooling water [5]. These deposits were generated deliberately in order to allow property distributions to be measured: the deposit thicknesses involved in the current work were considerably smaller. The study by Bohnet *et al.* [6] represents one of the few detailed studies of deposit ageing in the heat transfer literature: deposit ageing has received noticeably more attention in the field of subsea oil pipeline deposition (*e.g.* [7]) where gelation and solidification of waxes can result in flow restriction and blockage.
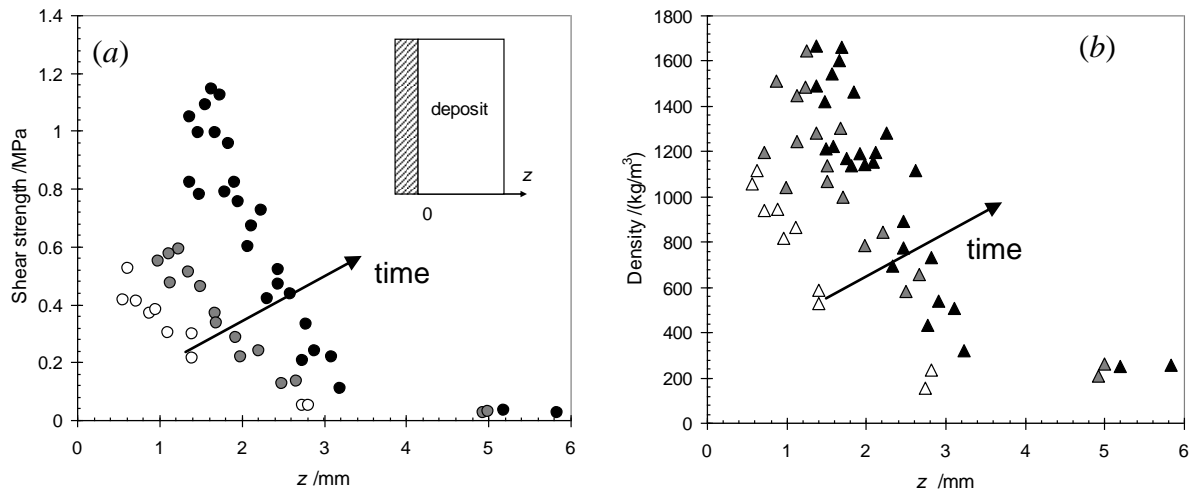
Figure 1: Distribution of (*a*) local shear strength and (*b*) local density in calcium sulphate scale fouling deposits formed on heat transfer surfaces. Ordinate z is the distance from the heat transfer surface, as depicted by the inset in (*a*). Symbol shading indicates age of deposit: open, total thickness $\delta = 2.9$ mm; grey, $\delta = 5.0$ mm; black, $\delta = 5.8$ mm. Reproduced from Bohnet *et al.* [6].

The impacts of ageing on fouling and cleaning dynamics have not received much attention, mainly due to the paucity of data available. The relationship between the extent of ageing and the dynamics of cleaning is important when a cleaning method is not completely effective or where two or more cleaning methods are available, with differing efficiencies. An example is the cleaning of refinery preheat train exchangers processing crude oil, which can either be cleaned completely using time-intensive and relatively costly mechanical actions (the tube bundle has to be removed from the unit), or can be cleaned in place by recirculation of detergent solution, which reduces the deposit layer thickness significantly - but not completely - while incurring lower downtime and cleaning costs. The scheduling of cleaning then becomes a combinatorial problem, as the operator has to decide *when* and *how* to clean an exchanger.

Previous analyses of scheduling cleaning in heat exchangers subject to fouling have usually assumed complete cleaning and have not considered more than one cleaning method. The use of intermittent cleaning by a less efficient but cheaper method can extend the operating period between shut-downs substantially: this combination of cleaning methods gives rise to a cleaning 'supercycle'. In this paper we extend the cleaning scheduling framework presented by Ma and Epstein [1] to the mixed cleaning (supercycle) problem. Two approaches are presented: (*i*) a heuristic-based method, and (*ii*) a non-linear programming approach, which can be applied to cases with severe constraints. The approaches are compared. The dependency on fouling and ageing rates are illustrated for a single shell-and-tube heat exchanger.

2   Development of the cleaning problem including ageing

2.1   Modelling ageing

The change in deposit microstructure caused by ageing has two important effects on fouling and cleaning. Figure 2 shows the effect of thermal ageing on the thermal conductivity and rheology of gums formed in autoxidation fouling: such gums are found in oxygenated olefin streams [8] and food frying applications.   The thermal conductivity increases with time, which changes the thermal resistance of the deposit layer and thereby the temperature distribution across the deposit. The rate of deposition is usually sensitive to the deposit surface temperature, so ageing and deposition are coupled. The visco-elastic parameters in Figure 2(b) show that the elastic modulus, G', is consistently greater than the viscous modulus, G'', so the material exhibits chiefly solid behaviour: its stiffness, quantified by G', similarly increases with time. Greater mechanical forces will be required to remove an aged deposit, as seen in Figure 1. The data in Figure 2 were collected at one temperature: ageing is expected to proceed faster at higher temperatures. Detailed modelling of ageing is not straightforward as different regions are formed at different times and are therefore of varying age: Ishiyama *et al*. [9] presented a model describing the impact of ageing on deposit thermal conductivity and reported solutions generated using a discretised form of the associated population balance. They did not consider rheological aspects, owing to the paucity of data available. Such a model is too computationally intensive to use in an optimisation.
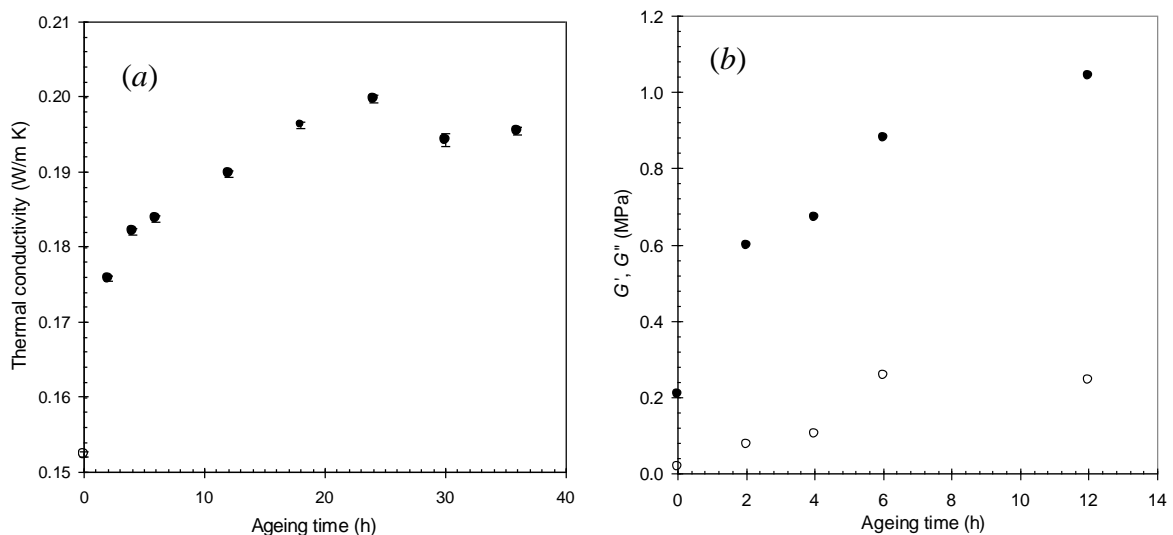
Figure 2: Evolution of (*a*) thermal conductivity, and (*b*) viscoelastic properties of fouling layer gums formed by autoxidation of linseed oil at 100 ℃, aged in air in an oven for up to 14 h at 100 ℃ [solid symbols - elastic modulus, G'; open symbols - viscous modulus, G'']. Data from Er and Lee [10], reproduced with permission.

For the purposes of optimising cleaning schedules, the key requirement is to be able to track the impact of ageing on heat transfer (and thus energy losses associated with fouling) and on cleaning effectiveness (which we reduce here to a simple criterion, as to how much of the fouling layer can be removed by a cleaning-in-place (CIP) method). We employ a new two-layer model to describe deposit ageing, inspired by the two-layer modeling concept presented by Crittenden and Kolaczkowski [11]. The two layers are described as (*i*) 'gel', being freshly deposited material, and (*ii*) 'coke', representing aged material, with the two differing in microstructure, thermal conductivity, and ease of removal. The terms 'gel' and 'coke' are borrowed from the crude oil fouling literature. For illustration, the thermal conductivity of gel fouling layers are close to that of the bulk oil, at 0.1-0.2 W m^{-1} K^{-1}, whereas that of coke is often reported as > 1.0 W m^{-1} K^{-1} [9]. Figure 3 illustrates the two-layer concept and its relationship to the distributed model.
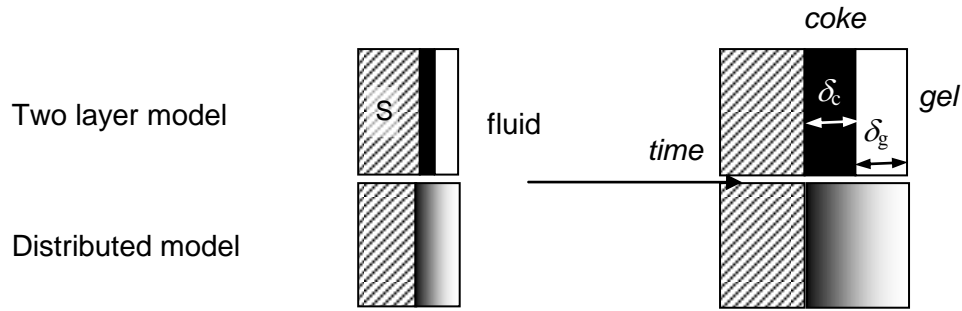
Figure 3: Schematic of a fouling deposit undergoing ageing on a heat transfer surface, labelled S. Darker shading indicates harder material: δ_c and δ_g are the thickness of the coke and gel layers, respectively.

The two-layer concept is used to explore aspects of fouling and cleaning dynamics whereby cleaning-in-place, which takes less time, may be used to remove the gel layer but extended cleaning is required to remove the 'coke' layer. Ishiyama *et al*. [12] have recently compared the agreement between the two-layer concept to their detailed, distributed model and identified regimes where it does give a reasonable estimate of the latter model's behaviour.

The (thermal) fouling resistance of the fouling layer, R_f, is evaluated by treating the layers as a pair of thin slabs of insulating material, *viz*.

$$R_f = \frac{\delta_g}{\lambda_g} + \frac{\delta_c}{\lambda_c}$$
(1)

where λ_g and λ_c are the thermal conductivities of the gel and coke layer, respectively. The change in thickness of each layer with time, t, is assumed to follow zeroth order kinetics, with

gel layer $$\frac{d\delta_g}{dt} = \lambda_g k_g - \frac{d\delta_c}{dt}$$
(2)

coke layer $$\frac{d\delta_c}{dt} = \lambda_c k_c \qquad \delta_g > 0:$$
(3a)

$$\frac{d\delta_c}{dt} = 0 \qquad \delta_g = 0$$
(3b)

The first term on the RHS of (2) describes the deposition of gel at the deposit/fluid interface, and the second term accounts for the conversion of gel to coke. The density of the deposit is assumed to remain constant when it is converted: ageing-related shrinkage (or expansion) is not considered.

The above kinetic scheme makes several assumptions which can be modified when supporting data become available. Ishiyama *et al*. [12] discussed the use of zeroth order rate expressions to represent the distributed ageing model [10]: deposition and ageing are treated here as fronts moving into the flow and gel, respectively. In contrast, Atkins [13] envisaged the growth of a hard coke layer in crude oil furnaces being determined solely by the temperature distribution in the deposit. The deposition rate constant, k_g, and ageing rate constant, k_c, as well as the values of the thermal conductivities, are all assumed to be independent of temperature in the work reported here as the aim is to illustrate the concept. These parameters – particularly the rate constants - are expected to be temperature sensitive (with differing sensitivities), and this coupling aspect is being considered in ongoing work.

The two-layer ageing model is well suited for the cleaning scheduling problem under consideration here. Figure 4(*a*) illustrates the growth of local deposit with total thickness, δ, showing the continuous growth of foulant due to deposition of gel on its surface, and development of a layer of a discernibly aged material, marked 'A'. The layers differ in their ability to be removed by a CIP process based on treatment with a given solvent (*e.g.* due to chemical bonding) or fluid shear (*e.g.* rheological properties). Figure 4(*b*) shows the result of a CIP action ('C'), where the aged layer remains on the

surface and fouling restarts from a layer of thickness δ_a. Figure 4(*c*) shows where the cleaning action removes the deposit completely. These methods often require access to the surface, *i.e.* dismantling of equipment, and is labelled 'M' as it includes mechanical action. The time taken to clean, τ_i, depends on the operation; τ_C and τ_M are the times taken for CIP and mechanical cleaning, respectively; one expects $\tau_C < \tau_M$. If $\tau_C \geq \tau_M$ the incentive for CIP action must arise from a lower cost of cleaning as it offers less process benefit.
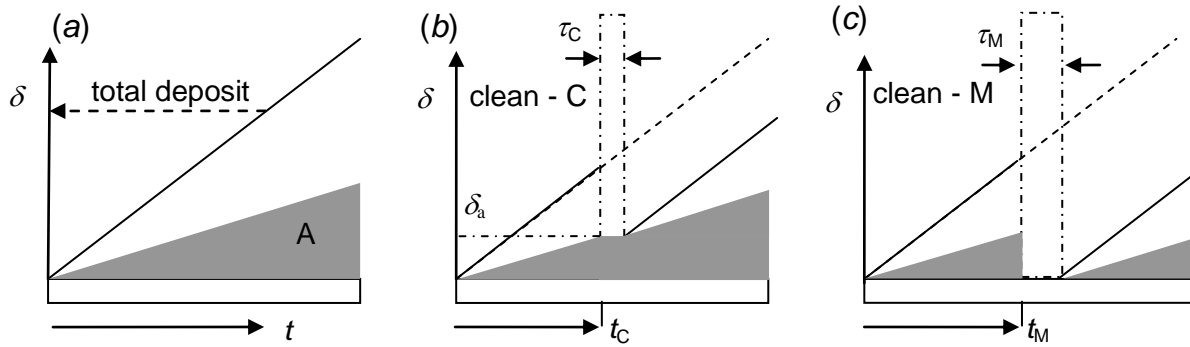
Figure 4: Schematic of the impact of ageing on fouling and cleaning. (*a*) deposit, thickness δ, grows and an aged layer (grey, labelled A) grows simultaneously; (*b*) cleaning-in-place at time t_C leaves the aged layer – fouling restarts from δ_a; (c) mechanical (ex-situ) cleaning at time t_M removes all deposit and fouling restarts from a clean surface.

2.2   Heat exchanger model

A simple shell-and-tube heat exchanger operating in counter-current mode subject to fouling and ageing is considered. Deposition (and ageing) is assumed to occur at a uniform rate across the exchanger, so that the unit can be described by a lumped parameter model. Heat transfer is modelled using the NTU-effectiveness method, where the overall heat transfer coefficient, *U*, is given by

$$\frac{1}{U} = \frac{1}{U_{clean}} + R_f \tag{4}$$

where U_{clean} is the value for a surface free from deposit. Fouling is assumed to occur only on the tube-side. The constant feed flow rate scenario is considered here, where the flow rates of the hot and cold streams do not change as a result of fouling: the pressure drop across the exchanger will increase. The number of transfer units, *NTU*, is given by

$$NTU = \frac{UA}{\left(w \cdot C_p\right)_{min}} \tag{5}$$

where *A* is the heat transfer area, *w* the mass flow rate and C_p the specific heat capacity for the stream (hot or cold) with lowest heat capacity flow rate ($w \cdot C_p$). The rate of heat transfer in the unit, *Q*, is given by

$$Q = \varepsilon \cdot Q_{max} = \varepsilon \cdot \left(w \cdot C_p\right)_{min} \cdot \left(T_{in,h} - T_{in,c}\right) \tag{6}$$

where Q_{max} is the thermodynamic limit for heat transfer in the unit, T_j^{in} the inlet temperature of the jth stream and ε the effectiveness (see [14]). The operating parameters are summarised in *Table 1*. The value of *NTU* when clean was 0.32, giving an effectiveness, ε, of 0.26, indicating that the unit would be sensitive to changes in *U* caused by fouling. The clean heat duty, Q_{cl}, was 1.95 MW.

Table 1
Process model parameters

Group	Parameter		Value
Exchanger	U	Overall heat transfer coefficient	600 W m^{-2} K^{-1}
[2 tube passes	A	Surface area	80 m^2
1 shell pass]	N_t	Number of tubes	100 per pass
	d_i	Tube inner diameter	0.0211 m
Cold stream	w_c	Mass flow rate	135 kg s^{-1}
	$T_{in,c}$	Inlet temperature	252°C
	$C_{p,c}$	Specific heat capacity	3125 J kg^{-1} K^{-1}
Hot stream	w_h	Mass flow rate	68 kg s^{-1}
	$T_{in,h}$	Inlet temperature	302°C
	$C_{p,h}$	Specific heat capacity	2200 J kg^{-1} K^{-1}
Fouling	k_g	Deposition rate, base case	5×10^{-6} m^{2}K W^{-1} day^{-1}
	k_c	Ageing rate, base case	2.5×10^{-7} m^{2}K W^{-1} day^{-1}
	λ_g	Gel thermal conductivity	0.1 W m^{-1} K^{-1}
	λ_c	Coke thermal conductivity	1.0 W m^{-1} K^{-1}

2.3 Scheduling model

The Ma and Epstein [1] approach for scheduling of cleaning of individual heat exchangers subject to fouling is adapted for this problem. Fouling reduces energy recovery, but taking units off-line for cleaning incurs further costs for cleaning, for lost production and/or additional energy to compensate for the unit being out of service. The objective function is written in terms of a daily averaged loss, *TAL*, over the cycle time, T_{cycle}:

$$TAL \equiv \frac{total\,cost}{T_{cycle}} = \frac{energy\,losses + cleaning\,cost}{operating\,time + downtime} \tag{7}$$

For the case of mechanical cleaning alone depicted in Figure 5(*a*), which is the scenario considered by Ma and Epstein, the optimal cycle time is well-defined as cleaning returns the exchanger to its initial, clean condition and the process repeats itself with $T_M = t_M + \tau_M$. The objective function in this case is

$$TAL \equiv \frac{cost}{T_M} = \frac{C_E \int_0^t [Q_{cl} - Q(t')]dt' + C_E Q_{cl}\tau_M + C_M}{t_M + \tau_M} \tag{8}$$

where C_E is the cost of energy, Q_{cl} the heat duty when clean and C_M the cost of mechanical cleaning. The optimal operating time t_M is identified by differentiating *TAL* with respect to operating time, t.

The mixed cleaning campaign in Figure 5(*b*) illustrates a case where chemical cleaning does not restore the unit to its clean performance ($Q < Q_{cl}$), but the penalty for cleaning is initially smaller than that associated with mechanical cleaning. Eventually the benefit of chemical cleaning is inferior to mechanical cleaning and the latter is performed, resetting the system to its clean state and restarting the supercycle.
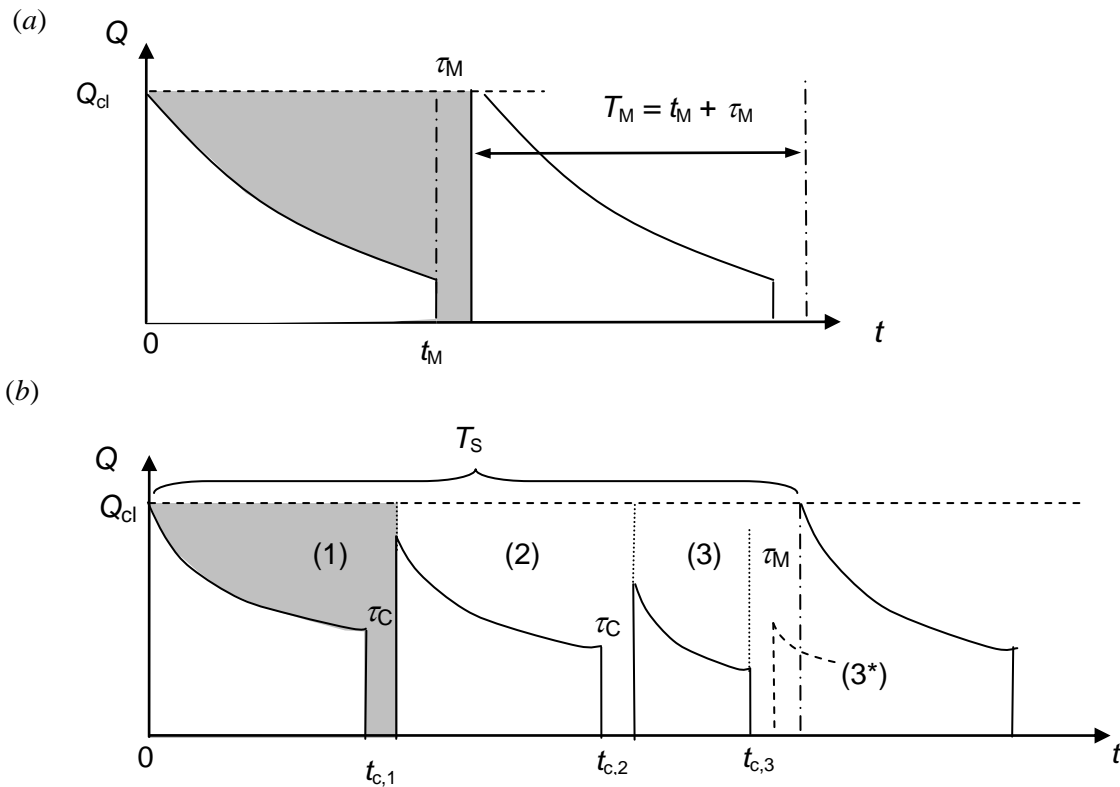
Figure 5: Schematic showing the impact of (*a*) mechanical cleaning, and (*b*) mixed chemical/mechanical cleaning on heat exchanger duty *Q*. The mixed cleaning supercycle shows 2 chemical cleaning actions, labelled (1),(2), followed by either a mechanical clean (3) or a third chemical clean (3*). The system starts in the clean state at $t = 0$. Shading in first cycle shows the energy loss due to fouling when operating and downtime while cleaning.

The objective function for the supercycle is an extended form of equation (6), *viz.*

$$TAL = \frac{1}{T_S \equiv \tau_M + j \cdot \tau_C + \sum_{i=1}^{j} t_{ci} + t_M} \left\{ \begin{array}{l} j \cdot C_C + C_M \\ + \sum_{i=1}^{j} C_E \cdot \int_{t_{c,i-1}+\tau_C}^{t_{c,i}} (Q_{cl} - Q(t'))dt' + C_E \cdot \int_{t_{c,j}+\tau_C}^{t_M} (Q_{cl} - Q(t'))dt' \\ + j \cdot C_E \cdot Q_{cl} \cdot \tau_C + C_E \cdot Q_{cl} \cdot \tau_M \end{array} \right\} \quad (9)$$

where j is the number of chemical cleaning actions, t_{ci} the operating period before the ith chemical clean, and C_C the cost of a chemical clean. Cleaning costs and cleaning intervals are assumed to be independent of the extent of fouling and ageing: in certain applications the cleaning time and cost are likely to be related to these factors.

2.4   Solution approaches

Two methods for generating solutions to the mixed cleaning scheduling problem are used. The first is a heuristic method based on the Ma and Epstein approach, employing a marching 'greedy' algorithm (see [15]). Following a cleaning action, the choice of whether to use chemical or mechanical cleaning in the next sub-period is determined by finding the optimal t_C, t_M and associated *TAL* values for that sub-period and selecting the action with the superior *TAL* value for that sub-period. A series of local decisions are made and eventually mechanical cleaning will be selected and the super-cycle restarts. These calculations were performed in Mathematica™ on a standard desktop PC. Time was discretised into time steps of 1 day and the performance of the heat exchanger evaluated at each interval.

In the second, deterministic approach, the length of each of the operating sub-periods was treated as a decision variable and solutions were generated for a selected number of j chemical cleaning actions. For example, in Figure 5, the values of $t_{C,1}$, $t_{C,2}$ and t_M were treated as continuous variables in searching for the optimal value of *TAL* evaluated over the whole supercycle. Heat exchanger performance was modelled as above. The value of j was varied from 0 (corresponding to mechanical cleaning only) up to 8, although the upper limit was reduced if an increasing trend was observed in the TAL_j values. This non-linear programming problem was evaluated using the CONOPT$^©$ optimiser in GAMS™ (General Algebraic Modelling System) on the desktop PC.

The costing parameters used in the case studies were: C_E = 1 £/kW day; C_C = 10 k£; C_M = 20 k£; τ_c = 1 day; τ_M = 5 days. These values are illustrative and will vary with the application. The results are sensitive to these parameters, as reported (albeit for mechanical cleaning alone) for scheduling in networks of heat exchangers by Ishiyama *et al*. [16]. Comparison of the two methods for the mechanical-cleaning-only scenario yielded good agreement for all case studies.

3   Results and discussion
3.1   Base case
The *TAL* values in Figure 6 shows that for the base case (k_g = 5×10^{-6} m^{2}K W^{-1} day^{-1}; k_c = $k_g/20$) the optimal combination of cleaning actions is three chemical cleans followed by a mechanical clean. The corresponding TAL value of 310 £/day, which is close to that obtained for 2 chemical cleans (311 £/day). The optimal region is therefore shallow and is not symmetric, which is also a feature of the mechanical-cleaning-only problem. The individual sub-period operating times were $t_{c,1}$ = 107 days, $t_{c,2}$ = 109, $t_{c,3}$ = 110 days and t_M = 116 days, giving a supercycle period of 442 days.
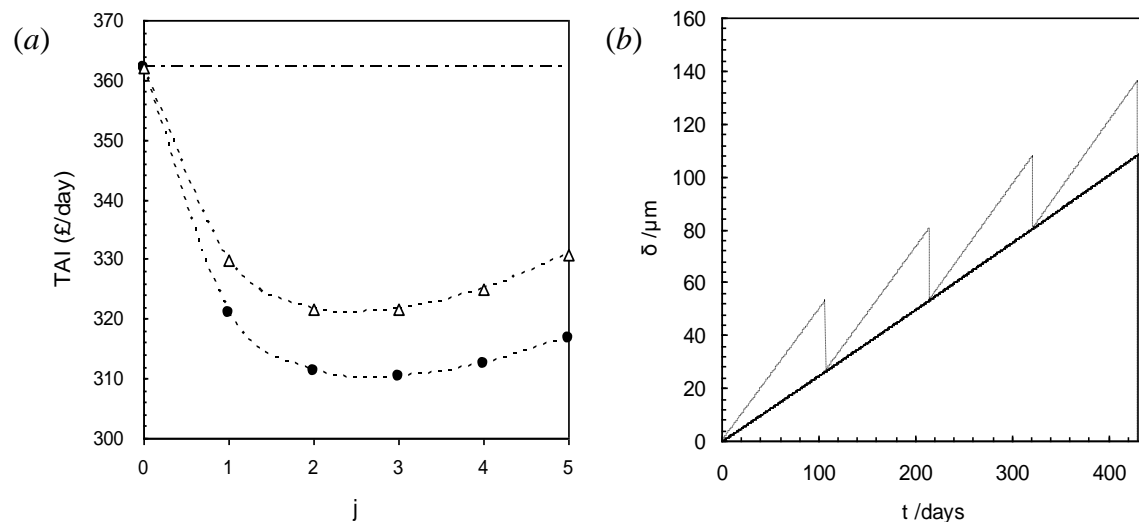
Figure 6: Optimal supercycle solutions for the base case scenario. (*a*) *TAL* values for different numbers of chemical cleans: dashed line is an interpolated guide to the eye, horizontal line the result for mechanical cleaning (j = 0; *TAL* = 362 £/day). Symbols: solid circles – NLP solution, open triangles – heuristic (greedy) algorithm; (*b*) Thickness profiles for best solution, j = 3: solid line, coke layer; dashed line, coke and gel layers, *i.e.* total deposit thickness.

The shallow nature of the optimal region suggests that approximate values of the physical model parameters will suffice. These could be obtained by experimental studies or analysis of plant operating data.

The deposit thickness profiles in Figure 6(*b*) show the sawtooth trend expected, with chemical cleaning regularly removing the gel layer and the coke layer growing steadily. It should be noted that although the gel and coke layers approach equal thickness for extended parts of the supercycle, the contribution of the gel to the overall thermal resistance dominates as its thermal conductivity is (with

the parameters used here) a tenth of that of the coke: the corresponding R_f–t profile is dominated by the gel contribution.

The figure shows that a mixed cleaning cycle is superior to mechanical-cleaning-alone for this scenario, owing to the effectiveness of the chemical cleaning method in reducing R_f. Figure 6(*a*) shows that the heuristic calculation approach was able to identify mixed cleaning cycles superior to the mechanical-cleaning-alone, but these had *TAL* values consistently larger than the deterministic (NLP) approach. The results were checked by using the different calculation engines to estimate the *TAL* values for the other schedule and these showed good agreement. The remaining plots of supercycle performance only show results obtained using the deterministic approach.

3.2 Effect of deposition rate

Here, the deposition rate was changed to (*i*) $2k_{g,base}$ and (*ii*) $0.6k_{g,base}$, with all other parameters (including the ageing rate k_c) constant. The results are summarised in Figure 7, alongside those obtained for the base case.
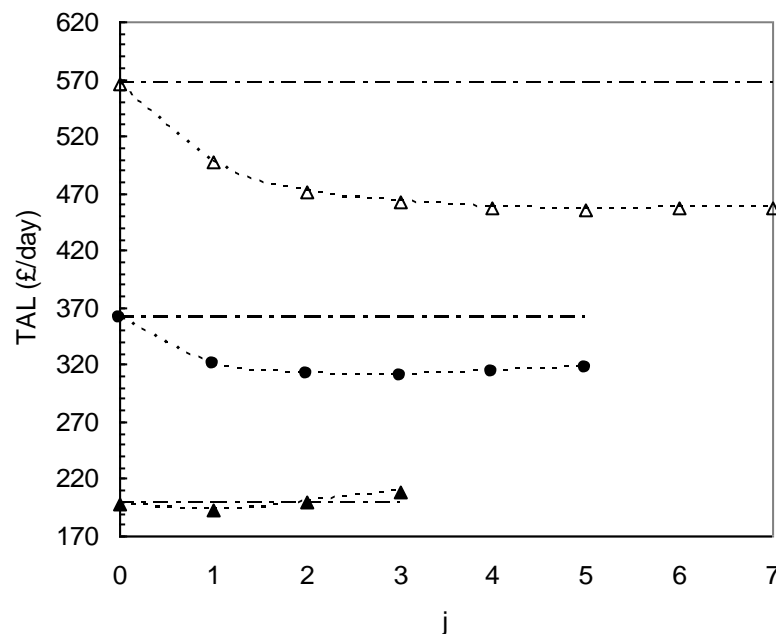
Figure 7: Effect of gel formation rate, k_g, on mixed cleaning. Symbols: circles - base case (Figure 6), $k_g = k_{g,base}$; open triangles, $k_g = 2k_{g,base}$; closed triangles, $k_g = 0.6k_{g,base}$. Dashed lines are interpolated guides to the eye, horizontal lines show *TAL* for mechanical cleaning.

The figure shows an increase in *TAL* as k_g increases, caused by the gel fouling layer developing more quickly and energy losses increasing. Chemical cleaning is, however, effective at removing the gel and so chemical cleaning is an attractive option: the optimal number of chemical cleans for $k_g = 2k_{g,base}$ is five, giving $T_S = 419$ days (*cf.* $T_S = 442$ days for the base case). The plot shows a more shallow optimum than the base case and it is clear that many more chemical cleaning actions could be used before mechanical cleaning became competitive.

For the slower fouling case, the optimal combination was one chemical clean followed by mechanical cleaning (giving *TAL* = 192 £/day, $T_S = 448$ days) which is close to that for mechanical cleaning alone (*TAL* = 198 £/day, $T_M = 310$ days). There is little difference between these *TAL* values, particularly given the inherent uncertainty in deposition (and ageing) parameters. The physical explanation here is that the rate of energy loss is slower, but the rate of coke formation is the same, so the contribution of the coke layer to R_f when cleaning is needed is larger and chemical cleaning has no effect on this contribution. There will clearly exist combinations of parameters when mixed cleaning offers no advantage over mechanical cleaning.

3.3   Effect of ageing rate

The ageing rate was changed to (*i*) $k_c = 1.3k_{c,base}$ and (*ii*) $k_c = 0.4k_{c,base}$, while keeping k_g constant. Increasing the ageing rate reduces both the thermal resistance of the deposit and the amount of deposit removed by a chemical clean. A lower k_c value reduces the rate of conversion to coke, and favours chemical cleaning. These effects are evident in the results presented in Figure 8. Increasing the ageing rate reduces the *TAL* for mechanical cleaning (to 317 £/day), as less energy is lost. The optimal number of chemical cleans compared to the base case declines from 3 to 2 (*TAL* = 290 £/day), while the supercycle time remains similar, at $T_S = 390$ days *cf.* 442 days. This apparent benefit of ageing is, however, sensitive to the cost parameters used: increasing C_M from the value used here ($C_M = 2C_C$) will shift the economics towards chemical cleaning, for instance.
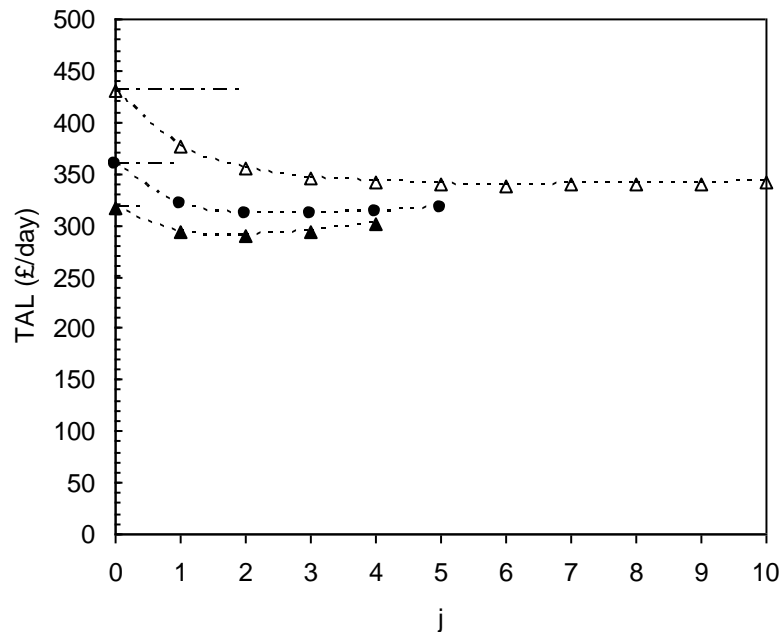
Figure 8: Effect of ageing rate on mixed cleaning performance. Symbols: circles - base case (Figure 6), $k_c = k_{c,base}$; open triangles, $k_c = 0.4k_{c,base}$; closed triangles, $k_c = 1.3k_{c,base}$. Dotted lines are interpolated guides to the eye, horizontal lines show *TAL* for mechanical cleaning.

A lower ageing rate increases the effect of deposition on heat transfer, reflected in the higher *TAL* value for mechanical cleaning, but favours chemical cleaning. The optimal region is again broad, with 6 chemical cleans (giving $T_S = 636$ days *cf.* $T_M = 147$ days) giving the numerical optimum. As with the high k_g case, regular chemical cleaning is superior to a mechanical-only regime.

3.4   Implications

In many crude oil and food applications, ageing and deposition are promoted by the use of high heat transfer surface temperatures. High wall temperatures are used to increase the temperature difference driving heat transfer, reducing the surface area required for heat transfer and thereby the capital cost of the unit. This work, however, shows that the use of high wall temperatures, by promoting ageing and deposition, affect the optimal operating costs when cleaning is used as the primary fouling mitigation method. In the limit, ageing can inhibit the use of cleaning-in-place techniques that would otherwise be more cost-effective over extended operating periods.

A two-layer ageing model has been used to make the calculation of mixed cleaning schedules, tractable. Parameterisation of this model and the associated deposition model requires experimental data, which in most cases will require new experimental studies. Conventional fouling studies, where thermal resistance is typically measured over time, are unsuitable for estimating the four parameters (λ_c, λ_g, k_c, k_g) in the two-layer model with sufficient accuracy. Independent measures of deposit thermal conductivity are needed, which will require reliable measures of deposit thickness obtained

either by (*i*) interrupting fouling tests and extracting these data in a manner similar to the study by Bohnet *et al*. [6]; (*ii*) using imaging methods; or (*iii*) using in-situ sensors such as the fluid dynamic gauging technique reported by Tuladhar *et al*. [17] for measuring fouling layer thickness and thermal conductivity, and by Chew *et al*. [18] for determining layer strength in real time. One of the aims of this work was to develop the numerical framework for exploiting such data. Another was to demonstrate the potential benefit of mixed cleaning campaigns, so that an operator could compare this with the cost of performing such experimental studies.

4   Conclusions

A two-layer ageing model has been used to quantify the effect of ageing on the thermal resistance of a fouling deposit and its susceptibility to removal by cleaning-in-place methods. The approach presented by Ma and Epstein [1] for calculating the optimal time for cleaning heat exchangers subject to fouling was extended to incorporate ageing and to evaluate mixed cleaning strategies combining cleaning-in-place and mechanical methods. A heuristic and an NLP solution method for the resulting optimisation problem showed the latter to be more successful. The scope for using mixed-cleaning campaigns for mitigating fouling was explored for different scenarios. The results showed that certain combinations of ageing rates, deposition rates and cost factors will favour mixed cleaning. For a given (gel) deposition rate, slow ageing favoured mixed cleaning regimes while for a given ageing rate, mixed cleaning was favoured when gel formation was rapid. The method is reliant on the availability of the parameters of the two-layer model. It is likely that the model will be highly sensitive to these parameters and reliable estimation of their values is going to be important in the application of the proposed methodology.

References
[1]   Ma, R., and Epstein, N. (1981). Optimum cycles for falling rate processes. *Canadian Journal of Chemical Engineering*, **59**, 631-633.
[2]   Wilson, D.I. (2005) Challenges in cleaning: Recent developments and future prospects, *Heat Transfer Engineering*, **26**(1), 51-59.
[3]   Müller-Steinhagen, H. (ed) (2000) *Fouling in Heat Exchangers*, publ. IChemE, Rugby.
[4]   Zhenhua, Q., Yongchang, C. and Chongfang, M.A. (2008) Experimental study of fouling on heat transfer surface during forced convective heat transfer, *Chinese J. Chem. Eng*., **16**(4), 535-540.
[5]   TEMA Standards (2007) 9th edition, publ. Tubular Exchanger Manufacturers Association.
[6]   Bohnet, M., Augustin, W. and Hirsch, H. (1999) Influence of fouling layer shear strength on removal behaviour, in Bott, T.R., Melo, L.F., Panchal, C.B. and Somerscales, E.F.C (eds.) *Understanding Heat Exchanger Fouling and its Mitigation*, publ. Begell House, 201-208.
[7]   Singh, P., Fogler, H.S. and Venkatesan, R.S. (2001) Morphological evolution of thick wax deposits during aging, *AIChEJ*, **47**, 6-18.
[8]   Wilson, D.I. and Watkinson, A.P. (1996) A study of autoxidation fouling in heat exchangers, *Canadian Journal of Chemical Engineering*, **74**(2), 236-246.
[9]   Ishiyama, E.M., Coletti, F., Machietto, S., Paterson, W.R., Wilson, D.I. (2010) Impact of deposit ageing on thermal fouling, *AIChE Journal*, **56**(2), 531–545
[10] Er, Y.L. and Lee, J. (2010) Part IIB Research Project, Department of Chemical Engineering and Biotechnology, University of Cambridge.
[11] Crittenden B.D. and Kolaczkowski S.T. (1979) Energy savings through the accurate prediction of heat transfer fouling resistances, in O'Callaghan W.O. *Energy for Industry*, 257-266.
[12] Ishiyama, E.M., Paterson, W.R. and Wilson, D.I. (2010) Exploration of alternative models for the ageing of fouling deposits, *AIChE Journal*, under review.
[13] Atkins, G.T. (1962) What to do about high coking rates. *Petro/Chem Engineer*, **34**(4), 20-25.
[14] Incropera, F.P. and De Witt, D.P. (2006) *Fundamentals of Heat and Mass Transfer*, Sixth Edition, publ. Wiley, New York.

[15] Ishiyama, E.M., Paterson, W.R. and Wilson, D.I. (2010) The effect of ageing on fouling-cleaning symbiosis, Fouling and Cleaning in Food Processing 2010, ISBN 978-0-09542483-2-1, publ. Dept of Chemical Engineering & Biotechnology, Cambridge, 128-135.

[16] Ishiyama, E.M., Paterson, W.R. and Wilson, D.I. (2009) A platform for techno-economic analysis of fouling mitigation options in refinery preheat trains, *Energy & Fuels*, **23** (3), 1323-1337.

[17] Tuladhar, T.R., Paterson, W.R. and Wilson, D.I. (2002) Thermal conductivity of whey protein films undergoing swelling: measurement by dynamic gauging, *Food Bioprod. Proc.*, **80**, 332-339.

[18] Chew, J.Y.M., Tonneijk, S.J., Paterson, W.R. and Wilson, D.I. (2006) Solvent-based cleaning of emulsion polymerisation reactors, *Chem. Eng. J.*, **117**, 61-69.

Nomenclature

English

A	Heat transfer area	m^2
$C_{p,c}$, $C_{p,h}$	Specific heat capacity cold/hot stream	$J\ kg^{-1}\ K^{-1}$
C_E,	Energy cost	$£\ J^{-1}$
C_M, C_C	Cleaning cost: mechanical, chemical	£
d_i	Tube internal diameter	M
G'	Elastic modulus	Pa
G''	Viscous modulus	Pa
k_c	Coking rate constant	$m\ s^{-1}$
k_g	Deposition (gel formation) rate constant	$m\ s^{-1}$
N_t	Number of tube passes	-
NTU	Number of transfer units	-
Q, Q_{cl}, Q_{max}	Duty, when clean, maximum	W
R_f	Fouling resistance	$W\ m^{-2} K^{-1}$
t	Time	day
t_c	Cleaning time, chemical cleaning	day
t_m	Cleaning time, mechanical cleaning	day
TAL	Time averaged loss	$£\ day^{-1}$
T_S	Supercycle time	day
U, U_{clean}	Overall heat transfer coefficient, clean	$W\ m^{-2} K^{-1}$
w, w_c	Mass flow rate, cold stream	$kg\ s^{-1}$
z	Distance from the heat transfer surface	m

Greek

δ, δ_c, δ_g	Layer thickness, coke, gel	m
ε	Effectiveness	-
λ_c	Thermal conductivity, coke	$W\ m^{-1} K^{-1}$
λ_g	Thermal conductivity, gel	$W\ m^{-1} K^{-1}$
τ_c	Time to clean, chemical cleaning	day
τ_M	Time to clean, mechanical cleaning	day

Fouling Thresholds in Bare Tubes and Tubes Fitted with Inserts

Mengyan Yang*, Barry Crittenden

Department of Chemical Engineering, University of Bath, Bath, BA2 7AY, United Kingdom

Corresponding author. Email: my223@bath.ac.uk;Tel: +44(0) 1225 386501; Fax. +44(0) 1225 385713

Abstract

Maya crude oil fouling reveals a straightforward dependency of initial fouling rate on surface temperature but a rather complex dependency on velocity in bare tubes, the initial fouling rate showing a maximum and then decreasing significantly towards zero as the velocity is increased. Surface shear stress clearly is an important parameter. CFD simulation of fluid flow in a tube fitted with a hiTRAN® insert reveals a complex distribution of surface shear stress. To compare the insert situation with the bare tube, an equivalent velocity concept is introduced on the basis that at a given average velocity the fluid flow results in the same average wall shear stress regardless of whether the tube is bare or is fitted with an insert. Using the equivalent velocity concept, the fouling data obtained using both a bare tube and a tube fitted with inserts can be correlated using a single model. Moreover, the fouling threshold conditions below which fouling is negligible, can be predicted for both situations.

Keywords   fouling; threshold conditions; crude oil; hiTRAN® inserts; CFD

1   Introduction

Most recent research on threshold conditions have been of the fouling on the inside surface of a bare round tube. Indeed, very limited work has addressed fouling threshold conditions in more complex geometries. Fouling threshold models [1, 2] can be difficult to use for predicting fouling rates for different operating conditions and crude oil types, and even more difficult for different configurations of heat exchanger surface. Based on the model developed by Epstein [3],Yeap et al. [4] proposed a model for bare round tubes incorporating the effects of mass transport and chemical reaction. A fouling suppression term, $Cu^{0.8}$, was included such that the model would be capable of predicting not only fouling threshold conditions as a function of velocity but also maxima in the fouling rate – velocity relationship [5, 6]. hiTRAN® in-tube inserts have been shown to be effective in mitigating crude oil fouling [7, 8] and increasing interest in their use in such applications is being shown by the oil industry [9] as well as by the water industries [10, 11]. A good review of applications and benefits of tube inserts in heat exchangers is provided by Ritchie and Droegemueller [8]. Ritchie et al. [12] studied the characteristics of fluid flow in the tube with inserts, and indicated that the flow near the wall resembled a turbulent profile even at a Reynolds number of 500. They also gave some theoretical analysis of the fouling on the wall of tube with inserts, auguring well for the development of suitable models for fouling of tubes containing inserts [12].

The use of inserts, however, raises a challenge in the application of fouling models, namely in the determination of Reynolds number and wall shear stress. Indeed, current fouling models are not capable of taking into account the complex variation of surface shear stress along the insert length. Whilst wall shear stress is easily calculated for bare round tubes using the friction factor approach, this method cannot be used with hiTRAN® inserts. The objective of this work therefore is to determine whether CFD simulation can offer a possible solution to this challenge such that a suitably modified fouling model can be used to predict the fouling rate and threshold conditions for tubes with and without inserts fitted.

2   Experiments and CFD simulation

2.1   Fouling experiments

Details of the experimental rig, the crude oil, the procedure and results with bare tubes are provided by Crittenden et al. [6]. The rig, as shown in Figure 1, comprised a 0.105 m^3 heated reservoir, a variable speed centrifugal feed pump and a by-pass for circulating crude oil through the reservoir whilst the oil was being heated. Flow rates to two 270mm parallel tubular test sections were individually controlled and monitored using rotameters. Three surface thermocouples placed in grooves on the tubing outer surface at 120° separation at each of two axial locations, at 70mm and 90mm from the tube outlet respectively, were used to record tube surface temperatures. The apparatus was maintained at a constant pressure of 15 bar and the crude oil temperature was maintained constant at 150°C. Surface temperatures up to 280°C were obtained by constant flux direct electrical heating. Unfiltered Maya crude oil was selected for study since it was expected to foul easily and because it contained a low percentage of light ends, making it easier to handle in the laboratory [6]. Typical properties were 21.1 API gravity, vapour pressure in the range 6.2-6.7 psig, 0.55% gas w/w, 4.03% total wax w/w, -21°C pour point, a calculated cloud point in the range 17-40°C, and viscosities of 161.5 and 54.80 mm^2/s at 30°C and 50°C, respectively. The overall composition of Maya crude oil and its physical properties are provided elsewhere [6, 13]. Its fluid properties were assumed to remain constant from run to run. The hiTRAN® tube inserts were provided by Cal Gavin Ltd (Alcester, UK; www.calgavin.com). Most experiments were conducted using a "medium density" insert signified as MDI in *Table 1*. The medium density inserts consist of about 420 wire loops per metre. The loop is of 12.2 mm diameter and made of 0.76 mm diameter stainless steel wire. The loop matrix occupied the entire test section.
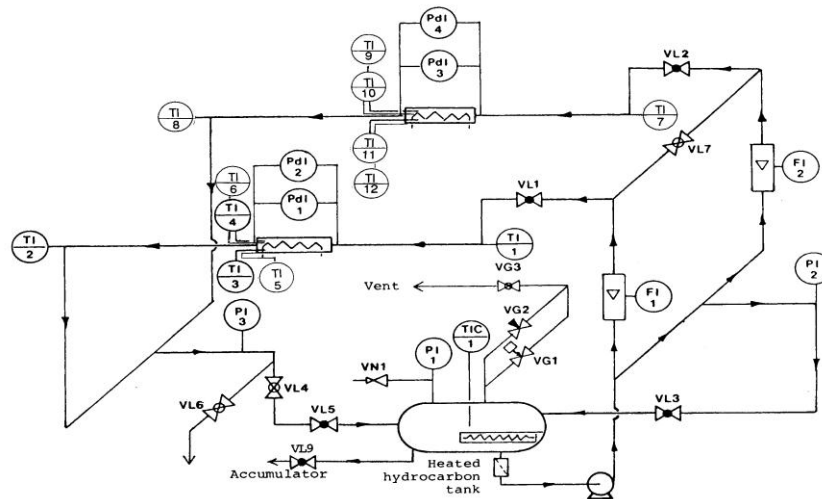
Figure 1: Schematic of the pilot-scale parallel tube apparatus [6]

Table 1
Experimental conditions

Velocity (m/s)	Re	Initial (clean) surface temperature			
		250°C	265°C	270°C	280°C
0.5	3600	Bare & MDI	Bare & MDI	NA	Bare
0.8	5800	Bare	NA	NA	Bare
1.0	7300	Bare & MDI	Bare & MDI	Bare	Bare
1.5	11000	Bare & MDI	Bare & MDI	Bare	Bare
2.0	14500	Bare & MDI	Bare	Bare	Bare
3.0	21800	Bare	Bare	Bare	Bare
3.6	26200	Bare	Bare	Bare	Bare
4.0	29000	Bare	Bare	Bare	Bare

Bulk temperature: 150°C; Reynolds number calculated for bare tube

2.2   CFD simulation

The CFD package Comsol (Burlington, MA, USA) is used to model the distributions of wall shear stress in bare tubes and tubes with the insert. The equations of the *k-ε* turbulence flow model can be found elsewhere [14, 15]. For the bare tube, the geometry is taken to be two-dimensional with axial symmetry, whilst for the tube fitted with the insert, the geometry must be considered to be three-dimensional. As seen later in Figure 5, hiTRAN® inserts comprise a series of loops equally spaced with a helical pattern and periodical pattern in the axial dimension. For CFD, the inserts are represented by closed round loops whose diameter and thickness are set to be the same as for the actual insert. In the CFD, the loops are placed in a cylinder so that the actual situation is closely simulated. The boundary conditions are set to be a logarithmic wall function for all walls, a constant linear velocity for the inlet and an open boundary for the outlet. The simulations were conducted for average inlet velocities in the range of the experimental values shown in *Table 1*. Under the conditions listed in *Table 1*, the fluid flow in the tube with inserts is in turbulent mode according to the study by Ritchie et al. [8]. The mesh size at the boundaries was set to be much smaller than in the bulk fluid. A series of simulations was conducted, beginning with a coarse mesh and then refined until the resulting velocity field and the velocity gradient near the wall were virtually independent of the mesh size. Further mesh refining caused significantly longer computational times.

3   Results and discussions
3.1   Experimental results – bare tube and tube with insert

As reported elsewhere [6], the average linear initial fouling rate was calculated using changes with time in the surface temperatures recorded by the thermocouples. Fouling rates at various initial surface temperatures with the bare tube are shown as a function of velocity in Figure 2. A maximum in the fouling rate as a function of velocity was also observed with experiments using a model chemical system of styrene polymerization [5]. As the velocity approaches zero, fouling rates follow the same trend as expected since as the velocity approaches zero, the fouling process would tend towards pure diffusion control. For tests using inserts, a velocity maximum in the fouling rate was not clearly observed, as shown in Figure 3.
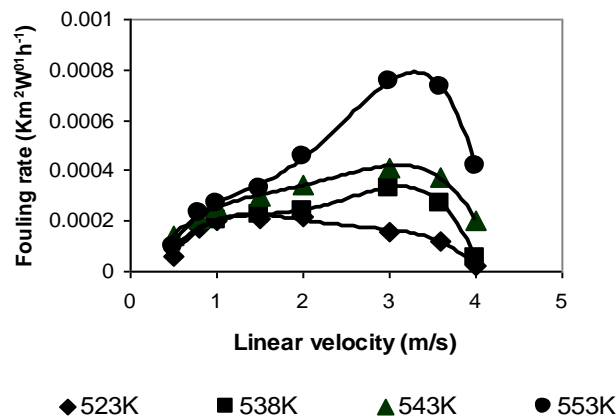
Figure 2: Initial fouling rates with the bare tube (bulk temperature: 423K)

Much interest has been shown recently in the concept of threshold fouling for crude oils and how this concept can be incorporated into the design of heat exchanger systems [1, 2, 4, 16]. The experimental fouling rate data obtained using either the bare tube or the tube with the insert show similar trends in that as the velocity is increased (beyond that for the maximum fouling rate for bare tubes) the initial fouling rates decrease towards zero. The threshold conditions can therefore be obtained by extrapolating the fouling curves to the axis (*Table 2*).
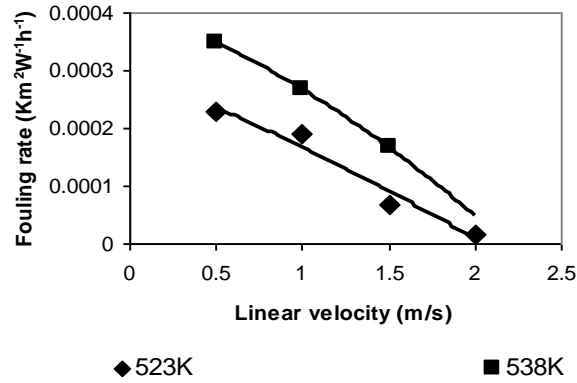
Figure 3: Initial fouling rates with medium density insert (bulk temperature: 423K)

Table 2
Fouling threshold conditions

Temperature (K)	Linear velocity – bare tube (m/s)	Linear velocity –tube with insert (m/s)
523	4.01	2.23
538	4.16	2.43
543	4.48	No data
553	4.58	No data

3.2 CFD simulation results
3.2.1 CFD simulation for fluid flow in a bare tube

The CFD simulation for the bare tube is straightforward and Figure 4 shows the resulting velocity field. In addition to velocity fields, the Comsol simulation provides solutions to the turbulent viscosity and velocity gradients from which the shear stress distribution can be obtained. *Table 3* shows that the values of shear stress obtained from the CFD simulation compare closely with those calculated using the friction factor method [17]. The results are for a tube of 19mm ID and a fluid of viscosity 0.0015 Pas at 150°C. The CFD data are taken at a *z* position of 0.4m where the turbulence is expected to be fully developed.

Axially symmetric geometry, the upper boundary representing the central axis.
Left end: inlet; Right end: outlet

Velocity scale (m/s)
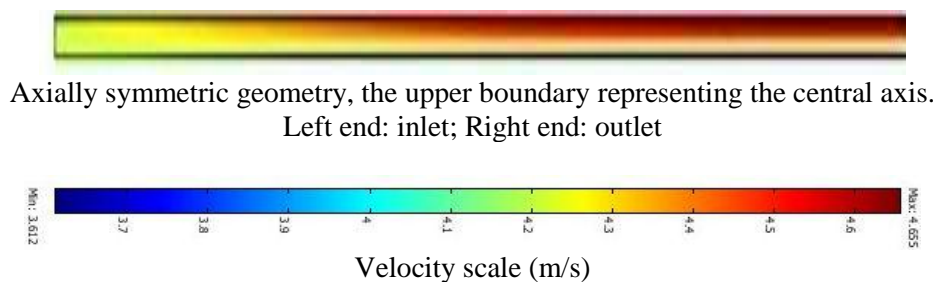
Figure 4: Velocity field obtained from CFD simulation for bare tube (linear velocity: 4m/s)

Table 3
Comparison of bare tube shear stresses using CFD and friction factor methods

Velocity (m/s)	Shear stress CFD results (Pa)	Friction factor calculation (Pa)	Re	Friction factor
0.5	0.78	0.82	6909	0.0087
1	2.89	2.77	13818	0.0073
2	9.88	9.31	27636	0.0061
3	19.2	18.93	41455	0.0055
4	32.2	31.33	55273	0.0052

3.2.2   CFD simulation for fluid flow in a tube with inserts

The CFD simulations for the tube fitted with a hiTRAN® insert are much more complicated. The insert loop significantly increases the number of mesh elements and therefore the number of loops to be considered must be kept as few as possible. Given its periodical pattern, the number of loops is taken in such a way that the periodical pattern repeats just once. The fluid flow pattern, including the shear stress, would be expected to repeat periodically along the axial direction. Figure 5 shows the resulting velocity field.

With inserts, the shear stress distribution varies significantly in all three dimensions, r, ϕ, and z. Figure 6 shows the shear stress distribution on the wall in the z direction from the edge of a loop located at $z = 0$ as shown in Figure 5 where the loop touches the wall to that over the next loop. The wall shear stress in between the two adjacent loops in the ϕ dimension is quite even compared with that in the z direction shown in Figure 6. Over all dimensions, the wall shear stress drops to the minimum at the wall area just behind the loop edge, as shown in Figure 6. As shown in *Table 4*, the values of the pressure drop obtained by integrating the CFD simulated data compare well with the experimentally measured values obtained by Cal Gavin. Differences are most likely to be due (i) to slight variations in the way the wires actually position themselves in the tube when compared with the theoretical interpretation in the simulation, and (ii) to how the pressure drop in the CFD simulation is integrated along the axial direction. It is inappropriate to use tube inserts at high velocity since not only would the pressure drop be high but as seen in Figure 2, the fouling rate would in any case be low.

To simplify the simulation, the temperature dependence of the viscosity was not incorporated. This may not significantly undermine the accuracy of the simulation, given the argument as follows: Firstly, the geometry region of relevance in the simulation is very limited. As seen in Figure 5 the horizontal length is just 0.026m. Within this short distance, the temperature variation can be assumed to be negligible. Secondly, for the turbulent flow the total viscosity is mainly determined by the turbulent viscosity, which is less sensitive to the temperature. However, the temperature effect on the molecular viscosity will be included in further work for CFD simulation of heat transfer in the tube with inserts.
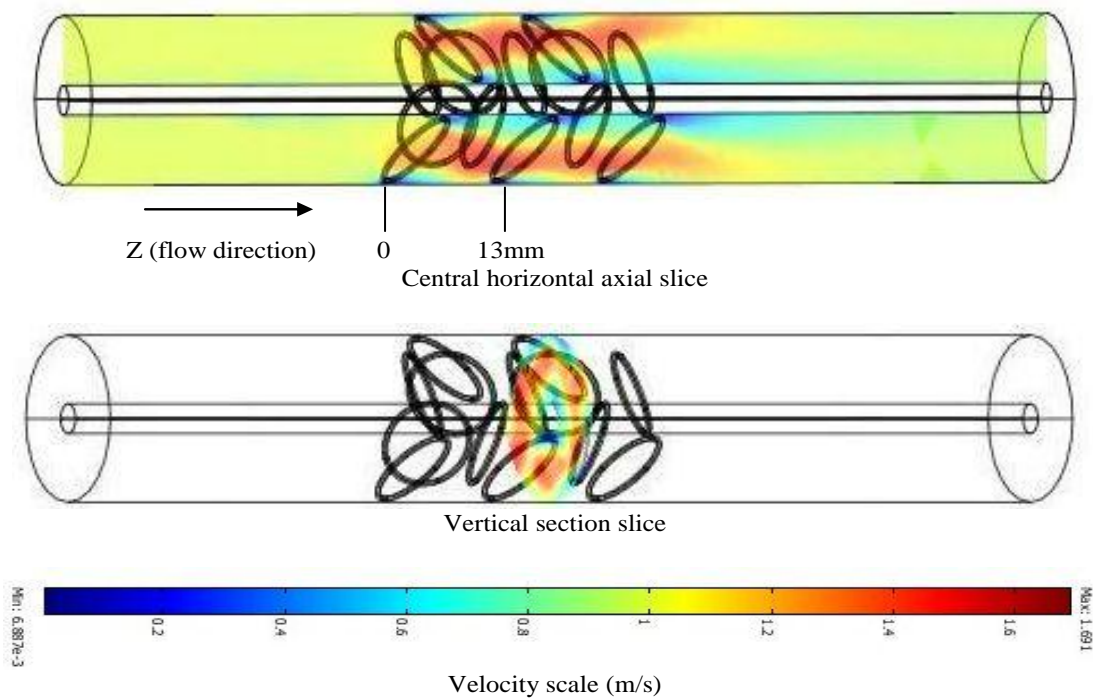
Figure 5: CFD simulation results for the velocity field (linear velocity: 1.0 m/s)
Left end: inlet; Right end: outlet

Table 4
Pressure drops obtained by CFD simulation and measured by Cal Gavin

Linear velocity (m/s)	Pressure drop (kPa/m) hiTRAN®	Pressure drop (kPa/m) CFD simulation
0.5	2.53	4.43
0.8	5.94	6.88
1.0	9.00	13.12
1.6	21.91	25.33
2.0	33.76	38.46
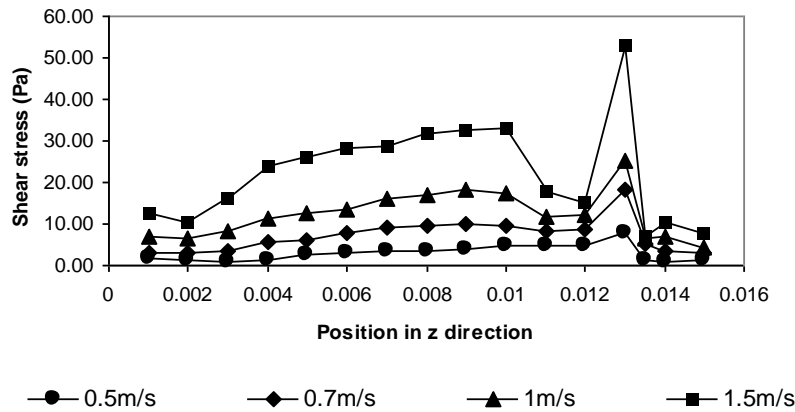
Figure 6: Wall shear stress distribution from the edge of one loop to that of the next

3.3   Modelling fouling rates and threshold conditions

3.3.1   Suppression term as a function of velocity

Attempts to fit a number of models of this type to the experimental data shown in the last section have been made. As an example, the use of Yeap's model [4] with the suppression term, $Cu^{0.8}$ is now described. Yeap's model has been tested since it has been claimed to take into account the effects of both mass transport and chemical reaction in fouling. Indeed, its form follows the fouling-velocity relationship shown in Figure 2:

$$\frac{dR_f}{dt} = \frac{A C_f u T_s^{2/3} \rho^{2/3} \mu^{-4/3}}{1 + B u^3 C_f^2 \rho^{-1/3} \mu^{-1/3} T_s^{2/3} \exp(E/RT_s)} - Cu^{0.8}$$

The first term of the right hand side of the model represents the fouling resistance increase due to the generation of the fouling deposit, and accounts for the effect of the temperature on the reaction rate as well as the effect of velocity on the mass transfer. Applying this model to all the experimental data (bare tube and tube with insert) yields a poor overall fit as shown in Figure 7. The model parameters obtained by regression are 51300 (kJ/mol), 8.98×10^{-10} (kg $^{2/3}$K$^{1/3}$ m$^{5/3}$(kW)$^{-1}$s$^{-1/3}$ h^{-1}), 3.81×10^{-5} (m$^{13/3}$kg $^{2/3}$ s$^{8/3}$ K$^{-2/3}$), 1.09×10^{-4} (m$^{6/5}$K s$^{4/5}$ K$^{-2/3}$ (kW)$^{-1}$ h^{-1}) for the model parameters *E*, *A*, *B*, and *C*, respectively. The poor fitting is not surprising since firstly no account is taken of the effect of the insert on the fluid flow pattern, and secondly the model does not account for the effect of the wall shear stress on local fouling rates.

To obtain the threshold conditions from the model, the threshold temperatures for the velocities listed in *Table 2* are obtained from the equation when the fouling rate is set to zero. Figure 8 shows that the fitting of threshold conditions is particularly poor. Indeed, it is not possible to draw a unique boundary between the fouling and non-fouling fields. The reason for this is that with mixed fouling data from

both bare tube and tube with insert experiments, the fouling threshold temperature is no longer a unique function of the threshold velocity. The threshold temperature may also depend on the tube situation, that is, whether it is bare or whether it is fitted with an insert.
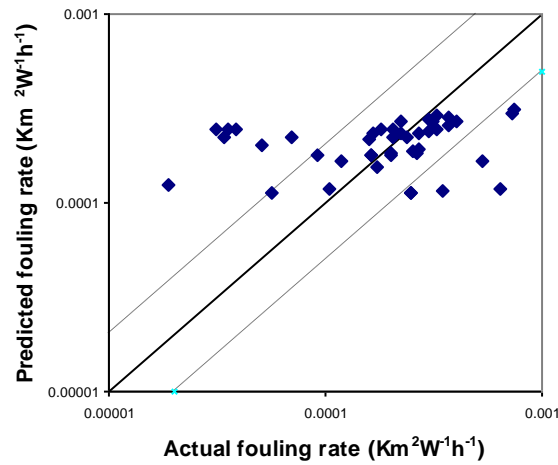
Figure 7: Comparison of experimental fouling rate data to the Yeap model predictions
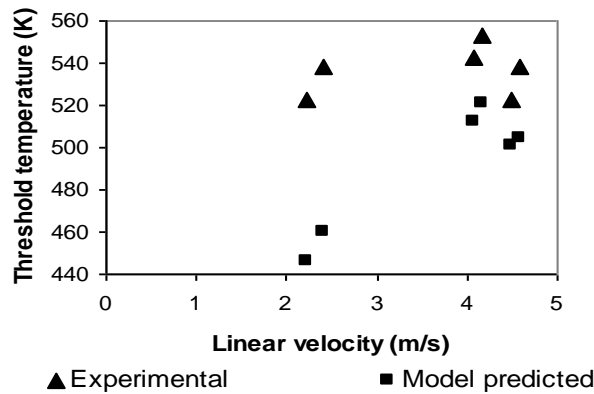
Figure 8: Experimental threshold conditions compared with Yeap model predictions

3.3.2   Suppression term as a function of shear stress and equivalent velocity

The best fittings were obtained using Yeap's model, but with the suppression term amended to include shear stress rather than average fluid velocity:

$$\frac{dR_f}{dt} = \frac{A_m\, C_f\, u T_s^{2/3}\, \rho^{2/3} \mu^{-4/3}}{1 + B_m\, u^3 C_f^{\,2} \rho^{-1/3} \mu^{-1/3} T_s^{\,2/3} \exp(E/RT_s)} - C_m\, \tau_w$$

Given that fouling most likely starts in the region of minimum shear stress, it is this stress which should determine the fouling behaviour. Accordingly, the minimum value of shear stress for a given velocity is used in the modified model when fitting the data. As the velocity and velocity related parameters, Re and C_f, are strictly defined for round tubes in Yeap's model, the average linear velocity cannot be used directly for a tube with inserts. Hence, the concept of equivalent velocity is introduced. It is defined to be the velocity in a bare tube that gives the same wall shear stress in a tube of the same internal diameter fitted with inserts and operating at a different average fluid velocity. The shear stress and velocity data are obtained from the CFD simulation. Figure 9 shows the equivalent velocity plot for the 19 mm id tube fitted with a medium density insert. The Re and C_f values are then calculated based on the equivalent velocity. The parameter values that give the best fittings are 52100 (kJ/mol), 7.93×10^{-10} (kg$^{2/3}$K$^{1/3}$ m$^{5/3}$(kW)$^{-1}$s$^{-1/3}$ h^{-1}), 1.80×10^{-5} (m$^{13/3}$kg$^{-2/3}$ s$^{8/3}$ K$^{-2/3}$), 1.60×10^{-5} (m$^{6/5}$K s$^{4/5}$ K$^{-2/3}$ (kW)$^{-1}$ h^{-1}) for E, A, B, and C, respectively. These parameter values are within the ranges reported by

Yeap et al. [4]. The parameter E, which is commonly regarded as the activation energy, lies within the range reported previously [6].

■: Velocity; ¤: Shear stress
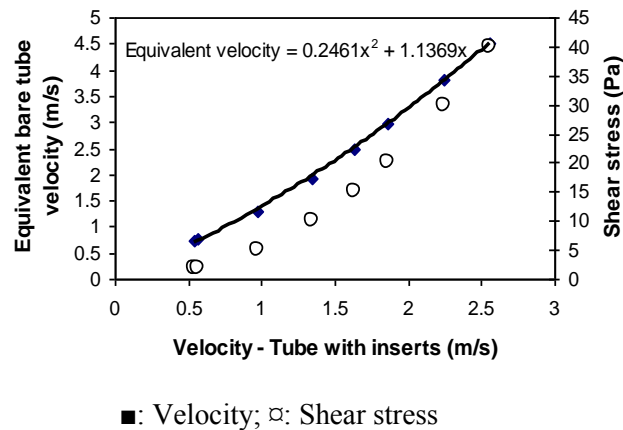
Figure 9: Equivalent velocity of the 19 mm id tube flow with the medium density insert

Figure 10 shows the fitting of the modified model to the experimental data. The quality of the model fittings is significantly better than that using the linear velocity version of the original Yeap model (Figure 7). As shown in Figure 11, the modified model fits the bare tube experimental data very well. For the case of tube fitted with the insert, the model fits the experimental fouling data reasonably well, as shown in Figure 12.
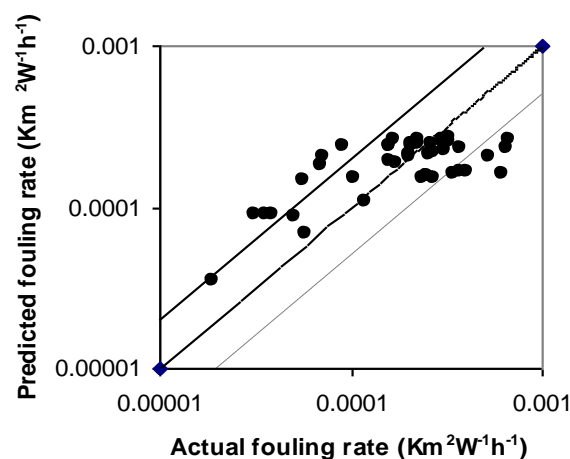
Figure 10: Experimental threshold conditions compared with modified Yeap model predictions

The model predicted threshold temperatures are obtained as the solution of the modified fouling model equation when the fouling rate is set to zero. The actual velocities are shown in *Table 2* and the equivalent velocity for the tube fitted with the insert is obtained using the correlation shown in Figure 9. Figure 13 shows the excellent comparison between the modified model predictions and the experimental threshold conditions. This figure clearly shows that there is now a unique boundary that divides the field into fouling and non-fouling regions, something that the original Yeap model is unable to do. This threshold plot is invaluable in the design of heat exchangers which are subject to fouling.
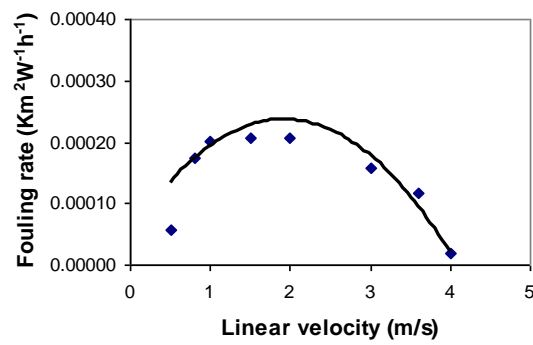
Symbols: Experimental data; Line: Model fitting

Figure 11: Comparison of bare tube experimental data and the modified model predictions at a constant wall temperature (523K)
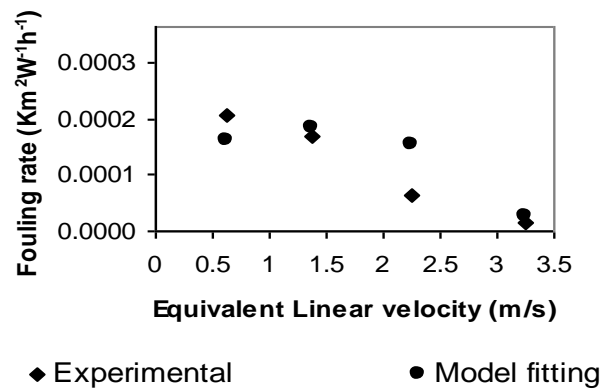
◆ Experimental   ● Model fitting

Figure 12: Comparison of the insert experimental data and the modified model predictions at a constant wall temperature (523K) for the tube fitted with the medium density insert
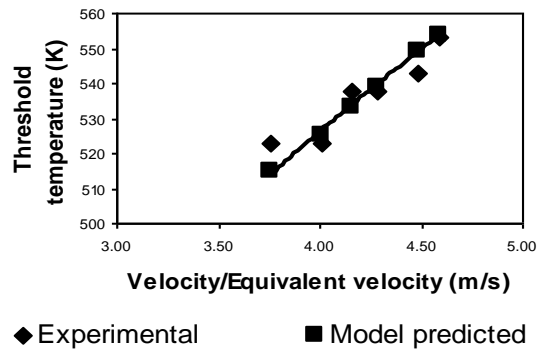
◆Experimental   ■ Model predicted

Figure 13: Threshold conditions – temperature versus velocity/equivalent velocity

The concept of equivalent velocity has been shown to be invaluable in extending the Yeap bare tube model to cope with the situation when a hiTRAN® insert is fitted inside a round tube. Hence, it ought to be possible to extend the scope of application of any good bare round tube fouling model to more complex geometries, not only to tubes fitted with inserts but also to non-round flow channels, etc. Moreover, the concept makes it possible to use fouling data generated using simple test rigs for a preliminary prediction of the fouling threshold conditions in a heat exchanger which comprises more complex geometries. Success depends on a viable approach to determine the wall shear stress distribution and CFD is an invaluable tool in this respect.

4   Conclusions and further work

Fouling models that have been developed for simple round tubes cannot be applied directly to more complex geometries, including heat transfer inserts, non-round channels, etc, because the wall shear stress plays a crucial role not only in the fouling process itself but also in the determination of the threshold conditions below which fouling does not take place. Given the practical difficulty in measuring experimentally the wall shear stress in the case of complex geometries, CFD provides a relatively simple alternative provided that the simulated results can be validated using experimental data. In this paper, the concept of equivalent velocity is developed such that a fouling model developed for bare round tubes can be extended for use with more complex geometries. It has been demonstrated, for example, that Yeap's model [4] can be adapted successfully to correlate the data of Maya crude oil fouling in both a bare round tube and a tube fitted with a hiTRAN® insert [6, 9]. Moreover, the fouling threshold conditions for both cases can be predicted successfully, auguring well for the development of successful strategies to mitigate the highly energy consuming fouling problem [4, 9]. Further investigation of the effect of the inserts on the pressure drop may be needed to determine the practical scope for insert application. No information is currently available to determine whether fouling could take place on the surface of inserts. However this could form part of further work.

Nomenclature

A	model parameter
B	model parameter
C	model parameter
C_f	Fanning fraction factor
C_m	model parameter
E	activation energy, kJ/mol
k	turbulent kinetic energy, m^2/s^2
R	universal gas constant, 8.314 J/mol K
r	radial coordinate
Re	Reynolds number
R_f	fouling resistance, m^2 K/kW
T_s	surface temperature, K
t	time, s
u	average flow velocity, m/s
z	axial position, m
ε	dissipation rate of turbulent energy, m^2/s^3
μ	fluid dynamic viscosity, Pa.s
ρ	fluid density, kg/m^3
τ_w	wall shear stress, Pa
φ	cylindrical coordinate

References

[1] D.I. Wilson, G.T Polley and S. J. Pugh, Ten years of Ebert, Panchal and the "threshold fouling" concept, Proc. 6th International Conference on Heat Exchanger Fouling and Cleaning: Challenges and Opportunities, Editors Hans Müller-Steinhagen, M. Reza Malayeri and A. Paul Watkinson, Engineering Conferences International, Kloster Irsee, Germany, 2005, pp. 25-36.

[2] W. Ebert and C. B. Panchal, Analysis of Exxon crude-oil, slip-stream coking data, Engineering Foundation Conference on Fouling Mitigation of Heat Exchangers, California, 18–23 June 1995.

[3]   N. Epstein, A model of the initial chemical reaction fouling rate for flow within a heated tube and its verification, Proc 10th International Heat Transfer Conference, Institution of Chemical Engineers, Rugby, 1994, Vol. 4, pp. 225-229.

[4]   B. L. Yeap, D. I. Wilson, G. T. Polley and S. J. Pugh, Mitigation of crude oil refinery heat exchanger fouling through retrofits based on thermo-hydraulic fouling models. TransIChemE Part A, 82 (2004), pp. 53-71.

[5]   B. D. Crittenden, S. A. Hout and N. J. Alderman, Model experiments of chemical reaction fouling, Trans. IChemE Part A, 65 (1987), pp. 165-170.

[6]   B. D. Crittenden, S. T. Kolaczkowski, T. Takemoto and D. Z. Phillips, Crude oil fouling in a pilot-scale parallel tube apparatus, *Heat Transfer Engineering*, 30 (2009), pp. 777-785.

[7]   B. D. Crittenden., S. T. Kolaczkowski and T. Takemoto, Use of in-tube inserts to reduce fouling from crude oils, AIChE Symp Series, Vol. 89 (No. 295) (1993) pp. 300-307.

[8]   J. M. Ritchie and P. Droegemueller, Application of tube inserts in heat exchangers: Benefits of tube inserts, in *Heat exchanger design handbook*, ed. G. F. Hewitt, Begell House, Redding, CT, Section 3.21.2. (2008).

[9]   A. W. Krueger and F. Pouponnot, Heat exchanger performance enhancement through the use of tube inserts in refineries and chemical plants – successful application examples: Spirelf, Turbotal and Fixotal systems. Proc. Eurotherm Conference on Fouling and Cleaning in Heat Exchangers, Schladming, Austria, 2009, pp. 400-406.

[10] T. R. Bott, Potential physical methods for the control of biofouling in water system, Trans. IChemE, Part A, 79 (2001), pp. 484-490.

[11] A. Wills, T. R. Bott, and I. J. Gibbard, The control of biofilms in tubes using wire-wound inserts, Canadian J. Chem. Eng., 78 (2000), pp. 61-64.

[12] J. M. Ritchie, P. Droegemueller, and M. J. H. Simmons, hiTRAN® wire matrix inserts in fouling applications, Heat Transfer Engineering. 30 (2009), pp. 876-884

[13] D. Z. Phillips, Mitigation of crude oil fouling by the use of HiTRAN inserts, PhD Thesis, University of Bath (1999).

[14] Comsol Model library - chemical engineering module, 2006, pp. 230-231.

[15] M. Yang, A. Young and B. D. Crittenden, Modelling of the induction period of crude oil fouling, Proc. Eurotherm Conference on Fouling and Cleaning in Heat Exchangers, Schladming, Austria, 2009, pp. 272-280.

[16] A. Young, S. Venditti, C. Berrueco, M. Yang, A. Waters, H. Davies, S. Hill, M. Millan and B. D. Crittenden, Characterisation of crude oils and their fouling deposits using a batch stirred cell system, Heat Transfer Engineering, in press 2010.

[17] F. A. Holland and R. Bragg, Fluid flow for Chemical Engineers, Edward Arnold, London, 1995, pp. 70-74.

Application of Intensified Heat Transfer for the Retrofit of Heat Exchanger Network

Yufei Wang[§], Ming Pan[§], Igor Bulatov, Robin Smith, Jin-Kuk Kim[*]

Centre for Process Integration, School of Chemical Engineering and Analytical Science, The University of Manchester, Manchester, M13 9PL, United Kingdom

[*] Corresponding author, Tel.: +44 (0)161 306 8755, E-mail: j.kim-2@manchester.ac.uk
[§] They contributed to the work equally.

Abstract

A number of design methods have been proposed for the retrofit of heat exchanger network (HEN) during the last three decades. Although considerable potential for energy savings can be identified from conventional retrofit approaches, the proposed solutions are hardly adopted in practice, due to significant topology modifications required and its engineering complexities during implementation. The intensification of heat transfer for conventional shell-and-tube heat exchangers can eliminate the difficulties of implementing retrofit in HEN which are commonly restricted by topology, safety and maintenance constraints, and includes high capital costs for replacing equipments and pipelines. This paper presents a novel design approach to solve HEN retrofit problems based on heat transfer enhancement. A mathematical model has been developed to evaluate shell-and-tube heat exchanger performances, with which heat transfer coefficients and pressure drops for both fluids in tube and shell sides are obtained. The developed models had been compared with Bell-Delaware, simplified Tinker and Wills-Johnston methods and tested with HTRI[®] and HEXTRAN[®] software packages, which demonstrates that the new model is much simpler but can give reliable results in most cases. For the debottlenecking of HEN, five heuristic rules are proposed to identify the most appropriate heat exchangers requiring heat transfer enhancements in the HEN. The application of this new design approach allows a significant improvement in energy recovery without fundamental structural modifications to the network.

Keywords   heat exchanger network (HEN); retrofit; heat transfer enhancement (HTE); heat exchanger model; heuristics

1   Introduction

Nowadays, the retrofit of heat exchanger network (HEN) is an important way of improving energy efficiency in process industries. An industrial plant may need to be retrofitted several times throughout its lifetime to improve energy efficiency and/or to meet the increased production rate. There are various strategies to achieve energy savings in a retrofit study, for example, reducing the use of utilities, modifying appropriate network topology, upgrading heat transfer units, installing additional heat transfer area, repiping streams and re-assigning heat recovery matches. The retrofit objective is to identify a cost-effective HEN, subject to any design and operating constraints. However, implementing aforementioned retrofit strategies in practice may be difficult, due to constraints related to the topology, safety and maintenance which often exist in a complex HEN. Besides, the capital cost is usually high because of considerable piping and civil works required for the retrofit and potential production losses during process modification.

In recent years, heat transfer enhancement (HTE) techniques have been developed. Polley et al. [1] addressed the application of HTE in the context of process integration. The use of HTE in process integration has many benefits. First, enhanced heat exchangers require less heat transfer area for a given heat duty because of higher heat transfer coefficients. Second, the heat transfer capacity for the given heat exchanger can be increased without changing physical size of the exchanger. Third, the use of HTE can reduce pumping requirement in some cases as enhanced heat exchangers can achieve higher overall heat transfer coefficients under lower velocities which may lead to less friction losses. Using HTE techniques has practical advantages in HEN retrofit, as HTE can avoid physical modification of exchanger itself. The implementation of HTE is a relative simple task that can be

easily achieved within a normal maintenance period when production losses can be kept in a minimum level and the relevant civil works can be also reduced.

Design methods proposed for HEN retrofit can be divided into two groups. The first group of methods are based on pinch analysis [1-4]. The second group of methods are based on mathematical programming [5-9]. Polley et al. [1] applied HTE into the retrofit of heat exchanger network and analyzed the aspects of fouling and pressure drop, but only the potential for using enhancement techniques in the heat recovery systems was discussed without providing systematic procedures for the implementing enhancement in the retrofitting of heat recovery network. Zhu et al. [2] presented a methodology for applying HTE in retrofit, based on network pinch approach. The proposed procedure aims to find out which exchanger should be enhanced and the augmentation level of enhancement. However, the enhancement devices were used only for additional area identified from the network pinch method, without using full benefits of enhanced heat transfer. Asante and Zhu [8] developed a network pinch method for retrofit scenarios and Smith et al. [3] further improved the method by considering multi-segmented stream data. They combined structural modifications and cost optimisation in a single step to achieve cost-effective design.

It is very common to use mathematical programming methods for HEN retrofit. Yee and Grossmann [5] presented a systematic procedure for the retrofit design of HEN. They proposed a design method using superstructure that includes all the possible structural scenarios, and formulated an optimisation framework as mixed-integer nonlinear programming (MINLP) model. Sorsak and Kravanja [6] proposed an MINLP optimisation model for HEN retrofit, in which the selection of different exchanger types, such as, double pipe exchangers (DP), shell and tube exchangers (ST), and plate and frame exchangers (PF), was made simultaneously. Since their extended model considered different types of exchangers, feasibility of heat transfer throughout the HEN is strongly dependent on the choice of exchanger types, which limits the extent of heat recovery. For example, in counter-flow heat exchangers, the outlet temperature of the cold stream can be higher, due to geometry-characteristics of exchangers. When multiple tube passes are used for ST exchangers, the flow arrangement combines the counter and co-current flows, and consequently, the feasibility of heat transfer is limited by those flow patterns in the exchangers. To overcome this problem, additional constraints were specified for ST exchangers in their model. Ponce-Ortega et al. [7] presented a new MINLP model for HEN synthesis with consideration of phase change in heat exchangers. Although benefits of mathematical programming have been exploited, the application of these methods was limited when the problem size is large and rigorous exchanger models are to be used.

Although various studies and methodologies have been proposed for HEN retrofit, most of works assume constant heat transfer coefficients and neglect fluid pressure drops, which is not suitable for practical application and retrofit, because heat transfer coefficients and fluid pressure drops vary with design. Furthermore, very expensive costs associated modifications and implementation, are not fully considered in most existing methods, and typical industrial problems are usually too big to be effectively solved with available HEN synthesis methods.

To avoid the aforementioned disadvantage, this paper proposes a novel approach for HEN retrofit through heat transfer enhancement. In our approach, a detailed model for heat exchanger has been developed for calculating heat transfer coefficients and pressure drops in heat exchangers, and then five heuristic rules based on expertise and knowledge in the process engineering communities have been proposed to identify suitable heat exchangers for employing enhanced heat transfer techniques in the HEN. Finally, the retrofit problems can be dealt with without involving complex calculations. In addition, the characteristics of real-world engineering problems imposed on the retrofit of HEN are considered, such as variable heat transfer coefficients, pressure drop constraints, varying stream thermal properties and detailed geometry of heat exchangers. New design methodology aims to maximise energy saving without topology modifications, for example, repiping and resequencing, and the introduction of new additional heat exchange, and hence, no structural options other than intensified heat transfer is considered.

The paper will address, first, a problem statement for rigorous heat exchanger modelling, which is then followed by the descriptions of a new model for shell-and-tube exchanger, and heuristic rules for HEN retrofit. Afterwards, the detailed heat exchanger model proposed in this paper will be validated, and then a case study of a large scale HEN retrofit problem is presented and solved with the proposed approach.

2   Problem statement

Since shell-and-tube heat exchanger is most widely used in process industries, it is assumed that heat recovery in the paper is based on heat transfer through shell-and-tube exchanger type. The heat transfer coefficient and pressure drop of each individual heat exchanger in the network are calculated by new model proposed in this paper. Before evaluation of detailed performance of heat exchanger, the overall configuration of HEN must be known, and thus, the problem to be addressed in this paper is based on the following information and assumptions.

It is assumed that the following information is given:
  a. Matches between hot streams and cold streams.
  b. The current use of utilities for heating and cooling in the existing HEN.
  c. Stream data (i.e., flowrates, inlet temperature and outlet temperature, density, specific heat capacity, viscosity, thermal conductivity and fouling coefficient).
  d. Tube-side geometry of heat exchanger (i.e., tube length, tube inner diameter, number of tube, number of tube passes, tube wall conductivity and nozzle inner diameters of tube-side).
  e. Shell-side geometry of heat exchanger (i.e., tube outer diameter, tube pitch, tube layout angle, shell inner diameter, number of shell passes, baffle spacing, baffle cut, shell-bundle clearance and nozzle inner diameters of shell-side).

The design methodology for retrofitting HEN is required:
  a. To identify suitable heat exchangers for heat transfer enhancement.
  b. To calculate heat transfer coefficients of heat exchangers before and after enhancement.
  c. To calculate pressure drops of tube and shell sides for heat exchangers before and after enhancement.
  d. To minimise the use of utilities for heating and cooling in the retrofitted HEN.

The aim with our design approach is to utilize heat transfer enhancements and consequently to reduce the energy consumptions of HEN in which no topology modification is needed. To derive the proposed approach for HEN retrofit, the following assumptions and strategies are made:
  a. Heat exchange between streams in liquid phase is only considered.
  b. The type of shell-and-tube heat exchanger considered is AES, namely, front head type is channel and removable cover (A), shell type is one pass shell (E), and rear head type is floating heat with backing device (S).
  c. The baffle type is single segmental.
  d. Baffle cut varies 20% to 50%.
  e. Tube layout angle is 90°.
  f. Tube insert, hiTRAN® (produced by Cal Gavin Ltd), is used for heat transfer enhancement. Heat transfer coefficient and pressure drop of hiTRAN® can be obtained from software hiTRAN.SP® (supported by Cal Gavin Ltd) [10].

Although one type of heat transfer enhancement and its enhancement on tube-side is only considered for HEN retrofit in this paper, the proposed design approach is generic enough to be used for accommodating other enhancement methods (e.g. twisted-tap tube inserts, coiled wire tube inserts, helical baffles, etc) as well as other retrofit options, including heat transfer enhancements with both tube and shell sides and suitable topology modifications based on the network pinch approach.

3   Modelling of shell-and-tube heat exchanger

For predicting heat exchanger performances, it is necessary to calculate the overall heat transfer coefficient, and pressure drop for both fluids in tube and shell side. Understanding of fluid behaviour

in the tube side is relatively straightforward, and well-known correlations, such as Colburn correlation [11], Dittus-Boelter correlation [11] and plain tube pressure drop method [12] are sufficiently accurate for tube-side calculations. The methods commonly used for shell-side calculation include Bell-Delaware method [13], Developed Delaware method [14], Chart method [15], simple Delaware method [16], simplified Tinker method [17] and Wills-Johnston method [18]. However, those available methods for shell-side often results in significantly different heat transfer coefficients and pressure drops, compared with commercial software (e.g. HTRI®), which has been accepted and widely used in the process industries. Therefore, this study had been carried out to respond this fundamental need for developing more reliable model for estimating performance of shell and tube exchanger.

In the new model, heat transfer coefficients and pressure drops of tube-side are calculated firstly,and then improved models of Chart method [15] and simple Delaware method [16] are used for shell-side calculations, the overall heat transfer coefficient, logarithmic mean temperature difference (*LMTD*), *LMTD* correction factor (FT), and overall heat transfer area are addressed in sequence. A number of literature, for example [12], are available for describing geometrical details of shell-and-tube heat exchangers and their schematic diagram required in the calculations of heat transfer and pressure drops.

3.1   Tube-side heat transfer coefficient

To calculate tube-side heat transfer coefficient, the velocity (v_i), Reynolds number (Re_i), and Prandtl number (Pr_i) of tube side have to be obtained first, as shown in Equations (1) to (3), where D_i is tube inner diameter; $\overline{m}_i$ is the mass flowrate of tube-side fluid; n_p and n_t are the number of tube passes and tubes, respectively. For tube-side fluid properties, specific heat capacity (C_{pi}), viscosity (μ_i), fluid density (ρ_i), and thermal conductivity (k_i) are evaluated at average bulk fluid temperature, and these values are assumed to be known.

$$v_i = \frac{\overline{m}_i\left(n_p / n_t\right)}{\rho_i\left(\pi D_i^2 / 4\right)} \tag{1}$$

$$\mathrm{Re}_i = D_i v_i \rho_i / \mu_i \tag{2}$$

$$\mathrm{Pr}_i = C_{Pi}\mu_i / k_i \tag{3}$$

Equation (4) shows the correlation of tube-side Nusselt number (Nu_i) based the Dittus-Boelter correlation [11], in which some of original parameters for cooling had been updated.

$$Nu_i = \begin{cases} 0.024\,\mathrm{Re}_i^{0.8}\,\mathrm{Pr}_i^{0.4} & \text{for heating} \\ 0.023\,\mathrm{Re}_i^{0.8}\,\mathrm{Pr}_i^{0.4} & \text{for cooling} \end{cases} \qquad \mathrm{Re}_i \geq 10^4 \tag{4}$$

$$Nu_i = 0.116\left(\mathrm{Re}_i^{2/3} - 125\right)\mathrm{Pr}_i^{1/3}[1 + \left(D_i / L\right)^{2/3}] \qquad 2100 < \mathrm{Re}_i < 10^4 \tag{5}$$

$$Nu_i = 1.86\left[\mathrm{Re}_i\,\mathrm{Pr}_i\left(D_i / L\right)\right]^{1/3} \qquad \mathrm{Re}_i \leq 2100 \tag{6}$$

where L is tube length.

Then, tube-side heat transfer coefficient (h_i) can be calculated:

$$h_i = \left(k_i / D_i\right) \times Nu_i \tag{7}$$

3.2   Tube-side pressure drop

Tube-side pressure drop is contributed by three major elements, pressure drop due to fluid friction in straight sections of tube ($\triangle P_{fi}$), pressure drop due to tube entrance, exit and return losses ($\triangle P_r$), and pressure drop in nozzles ($\triangle P_{ni}$).

The pressure drop due to friction loss ($\triangle P_{fi}$) is based on Darcy friction factor (f_i) [12].

$$f_i = 0.4137\,\text{Re}_i^{-0.2585} \qquad\qquad \text{Re}_i \geq 3000 \tag{8}$$

$$f_i = 64/\text{Re}_i \qquad\qquad\qquad \text{Re}_i < 3000 \tag{9}$$

$$\Delta P_{fi} = \frac{n_p f_i L \rho_i v_i^2}{2 g_c D_i} \tag{10}$$

where g_c is unit conversion factor which is equal to $1.0\ \text{kg·m/(N·s}^2)$.

Equations (11)-(13) presents the pressure drop related to the tube entrance, exit and return losses ($\triangle P_r$) [12].

$$\alpha_r = 2n_p - 1.5 \qquad\quad \text{for turbulent flow} \tag{11}$$

$$\alpha_r = 3.25 n_p - 1.5 \quad\ \ \text{for laminar flow} \tag{12}$$

$$\Delta P_r = \frac{0.5\alpha_r \rho_i v_i^2}{g_c} \tag{13}$$

To estimate the pressure drop in nozzles ($\triangle P_{ni}$), inlet and outlet nozzles should be considered separately, as shown in Equations (14) to (21) [12].

$$v_{ni,inlet} = \frac{\overline{m}_i}{\rho_i\left(\pi D_{ni,inlet}^2 / 4\right)} \tag{14}$$

$$\text{Re}_{ni,inlet} = \frac{D_{ni,inlet} v_{ni,inlet} \rho_i}{\mu_i} \tag{15}$$

$$\Delta P_{ni,inlet} = \frac{0.375 N_S \rho_i v_{ni,inlet}^2}{g_c} \qquad \text{for turbulent flow} \tag{16}$$

$$\Delta P_{ni,inlet} = \frac{0.75 N_S \rho_i v_{ni,inlet}^2}{g_c} \qquad \text{for laminar flow} \tag{17}$$

where $v_{ni,inlet}$ is the velocity of inlet nozzle in tube side, $D_{ni,inlet}$ is the inner diameter of inlet nozzle in tube side, N_S is the number of shell passes, and $\triangle P_{ni,inlet}$ is the pressure drop of inlet nozzle in tube side.

$$v_{ni,outlet} = \frac{\overline{m}_i}{\rho_i\left(\pi D_{ni,outlet}^2 / 4\right)} \tag{18}$$

$$\text{Re}_{ni,outlet} = \frac{D_{ni,outlet} v_{ni,outlet} \rho_i}{\mu_i} \tag{19}$$

$$\Delta P_{ni,outlet} = \frac{0.375 N_S \rho_i v_{ni,outlet}^2}{g_c} \qquad \text{for turbulent flow} \tag{20}$$

$$\Delta P_{ni,outlet} = \frac{0.75 N_S \rho_i v_{ni,outlet}^2}{g_c} \qquad \text{for laminar flow} \tag{21}$$

where $v_{ni,outlet}$ is the velocity of outlet nozzle in tube side, $D_{ni,outlet}$ is the inner diameter of outlet nozzle in tube side, and $\triangle P_{ni,outlet}$ is the pressure drop of outlet nozzle in tube side.

The pressure drop in nozzles ($\triangle P_{ni}$) can be presented as:

$$\Delta P_{ni} = \Delta P_{ni,inlet} + \Delta P_{ni,outlet} \tag{22}$$

Based on equations (8) to (22), overall tube-side pressure drop ($\triangle P_i$) is obtained.

$$\Delta P_i = \Delta P_{fi} + \Delta P_r + \Delta P_{ni} \tag{23}$$

3.3 Shell-side heat transfer coefficient

Ayub [15] proposed a chart method to calculate shell-side heat transfer coefficient in a single segmental shell-and-tube heat exchanger. This method was based on a chart which was a graphical represenation of wide range of actual exchanger data. He also demonstrated that the results from this method agreed well with HTRI®. However, as shell-side heat transfer coefficient information is only presented in a chart without numerical correlations, and the chart method cannot be readily applied in a mathematical simulation and optimisation studies. Therefore, several new correlations, Equations (30) and (31), are set up in this section, based on the chart presented by Ayub [15]. As shown in Ayub's work, shell-side heat transfer coefficient (h_0) can be calculated from:

$$h_0 = \frac{F_s F_p F_L k_0^{2/3} \left(C_{p0}\mu_0\right)^{1/3}}{D_0} \tag{24}$$

where $F_P = 0.85$, $F_L = 0.90$, and D_0 is tube outer diameter. Shell-side fluid properties, specific heat capacity (C_{p0}), viscosity (μ_0), fluid density (ρ_0), and thermal conductivity (k_0) are evaluated at average bulk fluid temperature.

Factor F_z is defined as:

$$F_z = \rho_0 D_0 v_{h0} / \mu_0 \tag{25}$$

$$v_{h0} = \frac{\overline{m}_0}{\rho_0 S_{hm}} \tag{26}$$

where $\overline{m}_0$ is the mass flow rate of shell-side fluid; v_{h0} is the velocity of shell-side fluid used for calculating heat transfer coefficient; and S_{hm} is the shell-side crossflow area for calculating v_{h0}.

S_{hm} of 90° tube layout angle is calculated as:

$$D_{otl} = D_s - L_{sb} \tag{27}$$

$$N_{PT,90°} = even\left\lceil \frac{D_{otl} - D_0}{P_T} \right\rceil \tag{28}$$

$$S_{hm,90°} = B\left[\frac{D_s - N_{PT,90°} P_T - D_0}{2} + N_{PT,90°}\left(P_T - D_0\right) \right] \tag{29}$$

where function $even\lceil X \rceil$ returns the largest even number not larger than X, L_{sb} is the diameter clearance between shell and tube bundle, D_{otl} is bundle outer diameter, P_T is tube pitch, and B is central baffle spacing.

The relationship of factors F_s, F_z and baffle cut (B_c) is given in the chart proposed by Ayub [15], in which F_s is the function of F_z and B_c. The correlations of F_s, B_c and F_z are formulated as:

$$F_s = -9.2223F_z^2 + 76.78F_z + 17.793, \qquad F_z \le 2 \tag{30}$$

$$F_s = 34.4783F_z^{0.6633}B_c^{-0.5053}, \qquad 2 < F_z \le 1000 \tag{31}$$

3.4 Shell-side pressure drop

Simplified Delaware method [16] uses less empirical equations, but provides accurate results [12], compared to other methods, for the wide operaing range of shell-side diameter and flow velocity. Simplified Delaware method [16] is a relatively simple method, but only suitable for 20% baffle cut scenarios. In this section, new additional correlations of shell-side cross-flow area (Equations (33) and (34)) and the relationships between pressure drop and baffle cut (Equations (43) to (45)) are added to

guarantee that simplified Delaware method can be used for a larger baffle cut. Shell-side pressure drop consists of the pressure drop due to fluid friction in straight section of shell ($\triangle P_{f0}$), and the pressure drop in nozzles ($\triangle P_{n0}$).

Equation (32) is based on simplified Delaware method, which presents the pressure drop in one central baffle spacing when baffle cut is 20% ($\triangle P_{fb,20\%Bc}$).

$$\Delta P_{fb,20\% Bc} = \frac{f_0 D_s \rho_0 v_{p0}^2}{2 g_c D_e} \tag{32}$$

where f_0 is shell-side friction factor, D_e is equivalent diameter, and v_{p0} is the velocity of shell-side fluid used for calculating pressure drop.

Similar to the estimation of shell-side heat transfer, v_{p0} depends on S_{pm} (the shell-side cross-flow area) when calculating pressure drop and S_{pm} also varies with different tube layout angles:

For 90° tube layout angle:

$$S_{pm,90°} = B \left[\frac{D_s - D_{otl}}{2} + \frac{D_{otl} - D_0}{P_T} \left(P_T - D_0 \right) \right] \qquad D_s \leq 0.7 \ m \tag{33}$$

$$S_{pm,90°} = B \left[D_s - D_{otl} + \frac{D_{otl} - D_0}{P_T} \left(P_T - D_0 \right) \right] \qquad D_s > 0.7 \ m \tag{34}$$

Then, the velocity of shell-side fluid (v_{p0}) can be calculated as:

$$v_{p0} = \frac{\overline{m_0}}{\rho_0 S_{pm}} \tag{35}$$

Equations (36) to (40) present the equivalent diameter (D_e), related Reynolds number (Re_0) and friction factors.

$$D_e = \frac{4 \left(P_T^2 - \pi D_0^2 / 4 \right)}{\pi D_0} \qquad \text{for square pitch} \tag{36}$$

$$Re_0 = \frac{D_e \rho_0 v_{p0}}{\mu_0} \tag{37}$$

$$f_0 = 144[f_1 - 1.25 (1 - B / D_s)(f_1 - f_2)] \tag{38}$$

$$f_1 = (0.0076 + 0.00653543 D_s) Re_0^{-0.125} \qquad D_s = 0.7 \ if \ D_s \geq 0.7 \ m \tag{39}$$

$$f_2 = (0.0016 + 2.2835 \times 10^{-3} D_s) Re_0^{-0.157}, \qquad D_s = 0.59 \ if \ D_s \geq 0.59 \ m \tag{40}$$

The pressure drop in straight section of shell with 20% baffle cut ($\triangle P_{f0,20\%Bc}$) can be determined in Equations (41) and (42).

$$\Delta P_{f0,20\% Bc} = (n_b - 1) \Delta P_{fb} + R_s \Delta P_{fb} \tag{41}$$

$$R_s = (B / B_{in})^{1.8} + (B / B_{out})^{1.8} \tag{42}$$

where R_s is the correction factor for unequal baffle spacing, B is central baffle spacing, B_{in} and B_{out} are inlet and outlet baffle spacing, respectively.

To consider the pressure drop in straight section under different baffle cuts ($\triangle P_{f0}$), new correlations are proposed in Equations (43) to (45).

$$\Delta P_{f0} = \Delta P_{f0,20\% Bc} \left(B_c / 20\% \right)^{-0.26765}, \quad 20\% < B_c \leq 30\% \tag{43}$$

$$\Delta P_{f0} = \Delta P_{f0,20\% Bc} \left(B_c / 20\% \right)^{-0.36106}, \quad 30\% \leq B_c < 40\% \tag{44}$$

$$\Delta P_{f0} = \Delta P_{f0,20\% Bc} \left(B_c / 20\% \right)^{-0.58171}, \quad 40\% \leq B_c \leq 50\% \tag{45}$$

The pressure drop in shell-side nozzles can be determined in the same correlations as calculating the pressure drops in tube-side nozzles.

$$v_{n0,inlet} = \frac{\overline{m}_0}{\rho_0 \left(\pi D_{n0,inlet}^2 / 4 \right)} \tag{46}$$

$$\text{Re}_{n0,inlet} = \frac{D_{n0,inlet} v_{n0,inlet} \rho_0}{\mu_0} \tag{47}$$

$$\Delta P_{n0,inlet} = \frac{0.375 N_S \rho_0 v_{n0,inlet}^2}{g_c} \qquad \text{for turbulent flow} \tag{48}$$

$$\Delta P_{n0,inlet} = \frac{0.75 N_S \rho_0 v_{n0,inlet}^2}{g_c} \qquad \text{for laminar flow} \tag{49}$$

where $v_{n0,inlet}$ is the velocity of inlet nozzle in shell side, $D_{n0,inlet}$ is the inner diameter of inlet nozzle in shell side, N_S is the number of shell passes, and $\triangle P_{n0,inlet}$ is the pressure drop of inlet nozzle in shell side.

$$v_{n0,outlet} = \frac{\overline{m}_0}{\rho_0 \left(\pi D_{n0,outlet}^2 / 4 \right)} \tag{50}$$

$$\text{Re}_{n0,outlet} = \frac{D_{n0,outlet} v_{n0,inlet} \rho_0}{\mu_0} \tag{51}$$

$$\Delta P_{n0,outlet} = \frac{0.375 N_S \rho_0 v_{n0,outlet}^2}{g_c} \qquad \text{for turbulent flow} \tag{52}$$

$$\Delta P_{n0,outlet} = \frac{0.75 N_S \rho_0 v_{n0,outlet}^2}{g_c} \qquad \text{for laminar flow} \tag{53}$$

where $v_{n0,outlet}$ is the velocity of outlet nozzle in shell side, $D_{n0,outlet}$ is the inner diameter of outlet nozzle in shell side, and $\triangle P_{n0,outlet}$ is the pressure drop of outlet nozzle in shell side.

The pressure drop in nozzles ($\triangle P_{n0}$) can be presented as:

$$\Delta P_{n0} = \Delta P_{n0,inlet} + \Delta P_{n0,outlet} \tag{54}$$

Based on above equations, shell-side pressure drop ($\triangle P_0$) is obtained.

$$P_0 = \Delta P_{f0} + \Delta P_{n0} \tag{55}$$

3.5   U, LMTD, FT and A

The overall heat transfer coefficient (U) can be calculated with Equation (56), where k_{tube} is tube conductivity; R_{Di} and R_{D0} are fouling resistances of tube side and shell side, respectively.

$$U = \left[\frac{D_0}{h_i D_i} + \frac{D_0 \ln \left(D_0 / D_i \right)}{2 k_{tube}} + \frac{1}{h_0} + \frac{R_{Di} D_0}{D_i} + R_{D0} \right]^{-1} \tag{56}$$

Before logarithmic mean temperature difference (*LMTD*) is considered, the outlet temperature of shell side ($T_{0,outlet}$) is set as an initial estimated value, and then this will be iterated and updated accordingly, and the outlet temperature of tube side ($T_{i,outlet}$) can be calculated based on energy balances.

$$\overline{m}_0 C_{p0}\left(T_{0,outlet} - T_{0,inlet}\right) = \overline{m}_i C_{pi}\left(T_{i,outlet} - T_{i,inlet}\right) \tag{57}$$

where $T_{0,inlet}$ is the inlet temperature of shell side, and $T_{i,inlet}$ is the inlet temperature of tube side.

LMTD is the mean temperature difference between the two fluid streams, which is shown in Equation (58).

$$LMTD = \frac{\left|T_{0,inlet} - T_{i,outlet}\right| - \left|T_{0,outlet} - T_{i,inlet}\right|}{\ln \dfrac{\left|T_{0,inlet} - T_{i,outlet}\right|}{\left|T_{0,outlet} - T_{i,inlet}\right|}} \tag{58}$$

In multi-tube-pass heat exchangers, the flow pattern includes both counter and co-current flows and, therefore, the mean temperature difference is not equal to the logarithmic mean when tube passes are more than one, and the correction factor of *LMTD* (*FT*) is used [12].

$$R = \frac{T_{0,inlet} - T_{0,outlet}}{T_{i,outlet} - T_{i,inlet}} \tag{59}$$

$$P = \frac{T_{i,outlet} - T_{i,inlet}}{T_{0,inlet} - T_{i,inlet}} \tag{60}$$

For $R \neq 1$:

$$\alpha = \left(\frac{1 - RP}{1 - P}\right)^{1/N_s} \tag{61}$$

$$S = \frac{\alpha - 1}{\alpha - R} \tag{62}$$

$$FT = \frac{\sqrt{R^2 + 1}\ln\left(\dfrac{1 - S}{1 - RS}\right)}{(R-1)\ln\left[\dfrac{2 - S\left(R + 1 - \sqrt{R^2 + 1}\right)}{2 - S\left(R + 1 + \sqrt{R^2 + 1}\right)}\right]} \tag{63}$$

For R = 1:

$$S = \frac{P}{N_s - (N_s - 1)P} \tag{64}$$

$$FT = \frac{S\sqrt{2}}{(1-S)\ln\left[\dfrac{2 - S\left(2 - \sqrt{2}\right)}{2 - S\left(2 + \sqrt{2}\right)}\right]} \tag{65}$$

Based on above calculation, the overall heat transfer area can be determined in two ways. One is based on the geometry of heat exchanger (*A*), and the other is based on the overall heat transfer coefficient (*A'*). They are presented in Equations (66) and (67), respectively.

$$A = n_t \pi D_0 L_{eff} \tag{66}$$

where L_{eff} is the tube effective length.

$$A' = \frac{\overline{m}_0 C_{p0} \left| T_{0,inlet} - T_{0,outlet} \right|}{U \times FT \times LMTD} \tag{67}$$

3.6   Iteration

Since the outlet temperature of shell side ($T_{0,outlet}$) is assumed, the overall heat transfer area based on this temperature (A') is not usually identical to the overall heat transfer area based on heat exchanger geometry (A). For this reason, an iteration loop from Equations (57) to (67) is proposed to find a suitable outlet temperatures of shell side until the values of A and A' are converged, which is usually converged after several iterations.

4   Heuristic rules for HEN retrofit with HTE

In this paper, HEN retrofit problems considers aspects of the reduction in the use of utilities, number of heat exchangers to be enhanced, enhancement details of each heat exchanger and pressure drop constraints. As there are a large number of potential exchanger enhancement options included in a HEN, estimating the efficiency for all these options is not straightforward. Moreover, safety and operability play an important role in the decision for retrofitting. These factors are qualitative in nature, and although they cannot be expressed explicitly, they must be traded off against other design requirements. To solve complex and large-scale problems, solution strategies for solving optimisation problems can be benefited by considering heuristic rules [19-21]. In this section, several heuristic rules are proposed for HEN retrofit to identify the exchangers to be enhanced.

4.1   Rule 1: searching for exchangers in utility path

Candidates are those exchangers which may increase heat recovery in a HEN after heat transfer enhancements are implemented. Bsaed on pinch method, only if an exchanger is on utility path, the consumption of utility can be reduced by increasing the duty of exchanger without changing the target temperature of streams [22-24]. If it is desired to retrofit the network without any topology modifications, changing the duty of exchangers through utility path is the only way. So, first of all, the candidates should be on utility path. Figure 1 is used to illustrate the procedure of searching exchangers in utility path. As shown in Figure 1, every exchanger is on a utility path. After checking utility path, there are, in general, many candidate exchangers to be further examined. The exchangers on the same stream with a utility exchanger can affect the duty of the utility exchanger directly. And these exchangers should be selected. For example, if a reduction of hot utility is required, exchangers 1, 2, 4 and 5 should be selected to the next step analysis, because all of these exchangers are involved to raise the temperature of the cold stream (C2).
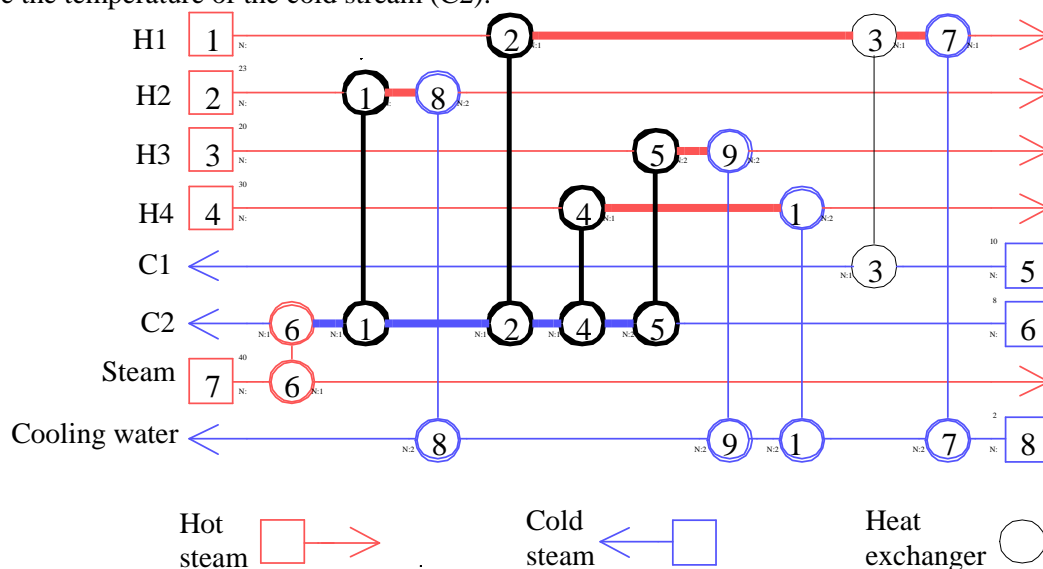
There are four utility paths: exchangers 6, 1 and 8; exchangers 6, 2 and 7; exchangers 6, 4 and 10; exchangers 6, 5 and 9.

Figure 1: A heat exchanger network

4.2   Rule 2: sensitivity analysis

After heat exchangers are selected with Rule 1, sensitivity tables presented by Kotjabasakis and Linnhoff [25] is used to quantify impact of heat transfer intensity on utility consumption of the HEN. Sensitivity table is based on a simple heat transfer equation[2] , in which only stream data and network structure are needed.

Assume that the inlet temperature of cold utility in a HEN is the response parameter, the change of temperatures for utility exchangers related to utility path will be known, when the UA value (heat transfer coefficient, U, multiplied by area, A) of candidate exchangers is changed. The best candidate exchanger can be found if its response parameter has high sensitivity. As shown in Figure 2, exchanger 2 is a good candidate, since with 25% increment of UA value, the inlet temperature of cold utility almost increase 4ºC. On the contrary, exchanger 3 is not a good candidate because, with 25% increment of UA value, the inlet temperature of utility increases slightly. Sensitivity analysis is the key basis of the proposed work, which can help to indentify the exchangers with large energy saving potential.
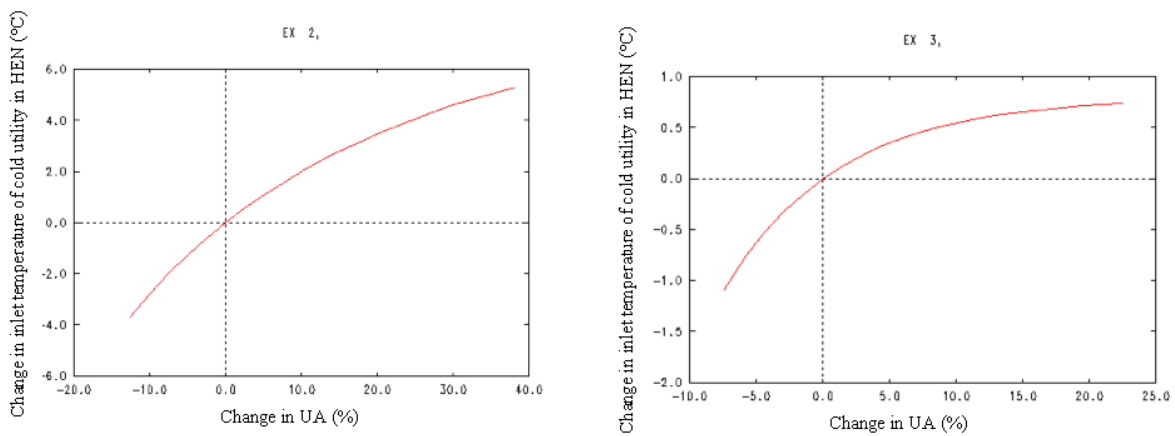
Figure 2: Sensitivity graphs of exchangers 2 and 3
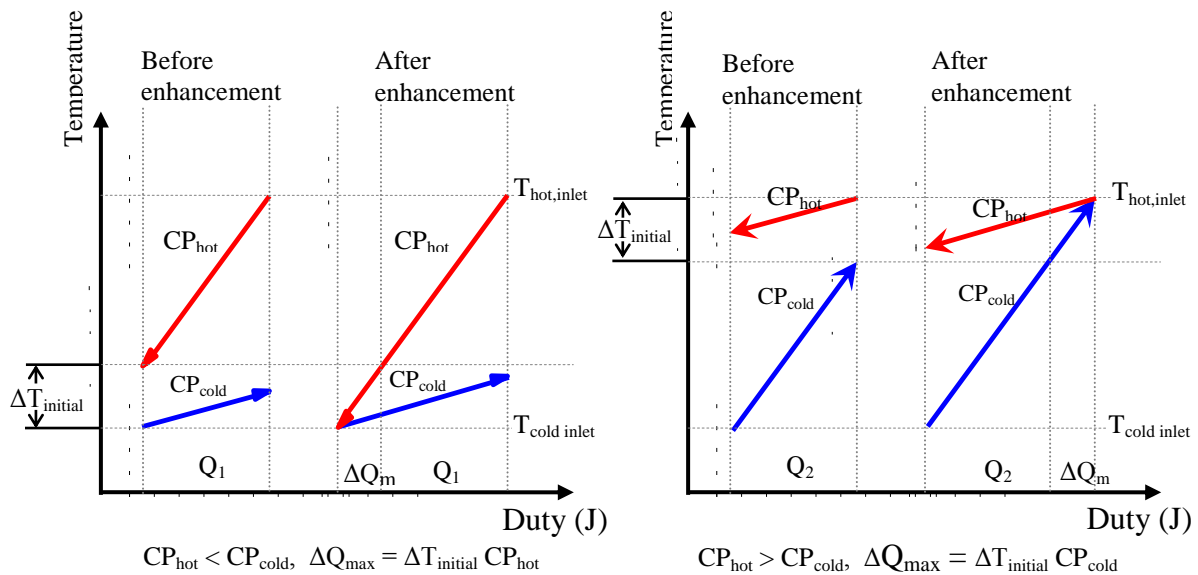
Figure 3: Maximum heat recovery in a heat exchanger

To explain why high sensitivity exchanger can be a good candidate, Figure 3 is used to shows the maximum heat recovery in a heat exchanger, where the red line indicates the hot stream, and the blue

---

[2] $Q = U \cdot A \cdot \Delta T_{LM}$, where Q is the overall heat transfer load, U is overall heat transfer coefficient, A is heat exchanger area, ΔT_{LM} is the log-mean temperature difference.

line indicates the cold stream. In the figure, the slope of line is the reciprocal value of CP (heat-flow capacity which is the multiplication between heat capacity and flowrate) for each stream, and the equation of maximum heat recovery in an exchanger is given as:

$$\Delta Q_{max} = \Delta T_{initial} CP_{min} \qquad (94)$$

where ΔQ_{max} is the maximum heat recovery, $\Delta T_{initial}$ is the initial temperature difference between the inlet of high CP stream and the outlet of low CP stream, and CP_{min} is CP value of the stream that has lower CP in the exchanger.

From equation (94), energy saving depends on CP_{min} and $\Delta T_{initial}$. If a heat exchanger on utility path is enhanced, then for the exchanges between the enhanced one and utility exchanger, the heat transfer is reduced, due to small heat transfer driving force. In other word, the exchanger with large CP_{min} and $\Delta T_{initial}$, and close to utility exchanger can be a high sensitivity heat exchanger.

4.3   Rule 3: checking pinching match
From the network concept presented by Asante and Zhu [8], it can be noted that pinching match is the bottleneck of heat recovery network. A pinching match is defined as an exchanger match where the temperature approach between hot and cold streams unavoidably tends towards a limiting value as the heat recovery in the HEN is increased. Normally, the pinching match will have a very small heat transfer temperature difference. When the heat recovery of the network is further to be increased, heat transfer temperature difference for the pinching match will go towards zero. If a pinching match is a downstream[3] exchanger of the candidate, then the candidate is not promising.

4.4   Enhancing several candidates simultaneously
Sometimes, only enhancing one exchanger may not achieve considerable energy savings. Normally, with Rules 1, 2 and 3, more than one good candidate can be identified and this provides a good opportunity for further improvement in the energy recovery. It is obvious that when one candidate is enhanced, all of its downstream exchangers will be affected. Therefore, after an exchanger is enhanced, sensitivity analysis is applied again to all candidate exchangers to find the next best one.

4.5   Rule 4: enhancing pinching match
Sometimes, no good candidate for the heat transfer enhancement exists, or potential for energy savings from enhancing promising candidates may be very low. In this situation, enhancing pinching match can be considered. As low driving force for heat transfer in pinching match is bottleneck for the enhancement of candidate exchanger, enhancing pinching match can be a good option to compensate the loss of heat transfer driving force after the candidates are enhanced. Based on the heuristic rules 1-5, suitable candidates in HEN are selected, and the detailed performances of these exchangers before and after enhancement can be calculated with the developed heat exchanger model. The procedure of the proposed approach is shown in Figure 4.

5   Case studies
The semi-rigorous heat exchanger model developed in this paper is validated at first. Then, an industrial-scale HEN retrofit problem is presented and applicability and robustness of the proposed retrofit approach is demonstrated.

5.1   Performance evaluation of heat exchanger model
The proposed heat exchanger model are compared with three models, namely, Bell-Delaware [13], simplified Tinker [17] and Wills-Johnston [18] and two commercial software, namely, HTRI® and HEXTRAN®. The details of methods used in the models are presented in *Table 1*. *Tables 2* and *3* show stream properties and geometry details of heat exchangers used in Examples 1-10.

---

[3] For this study, if a stream exited from exchanger A goes into exchanger B, then exchanger B is located in the downstream of exchanger A.
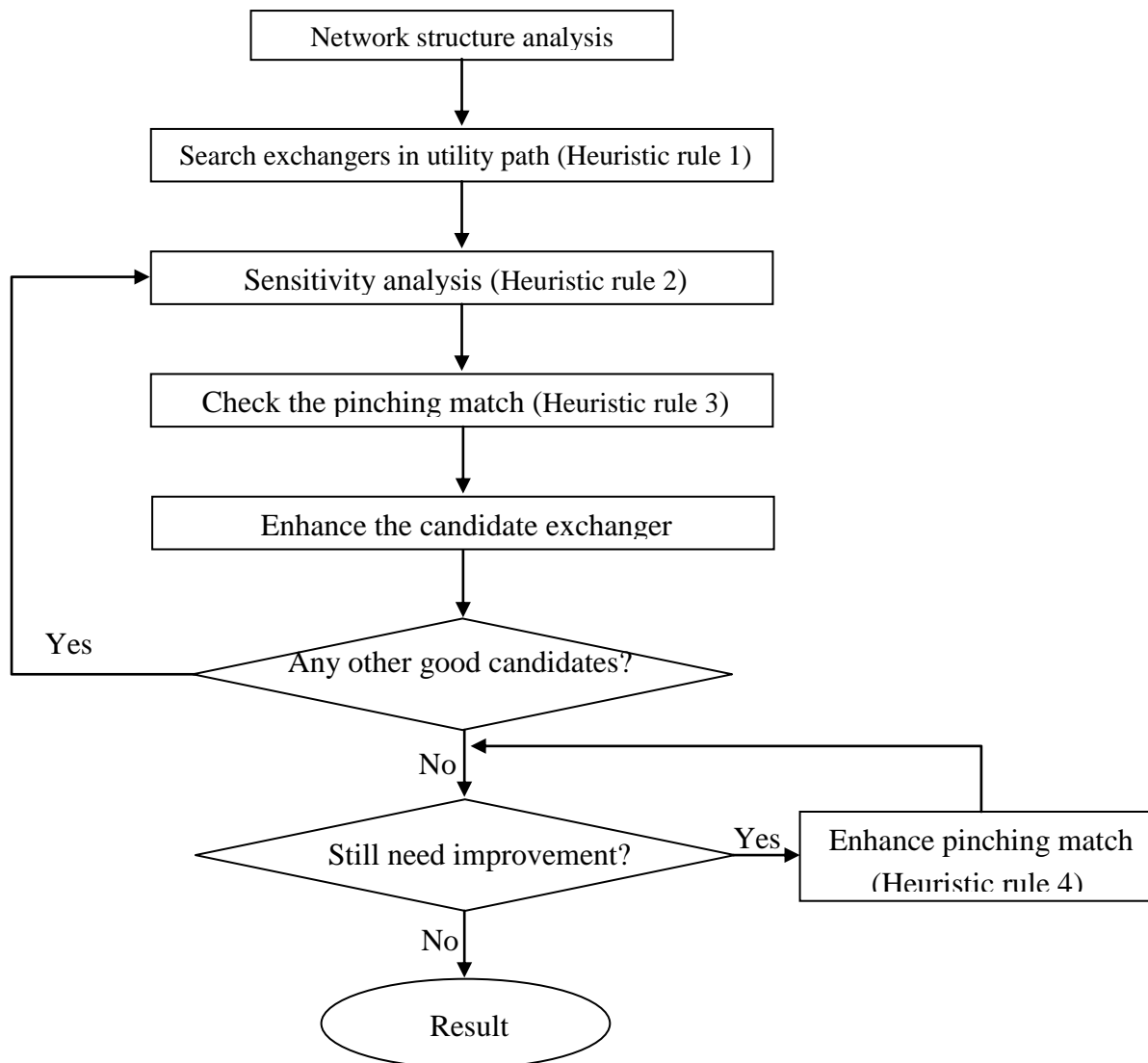
Figure 4: Procedure of the proposed retrofit approach

Table 1
Method details of the compared models

| Model | Tube side | | Shell side | |
	Heat transfer method	Pressure drop method	Heat transfer method	Pressure drop method
M1	Colburn correlation	Plain tube pressure drop	Bell-Delaware	Bell-Delaware
M2	Dittus-Boelter correlation	Plain tube pressure drop	Developed Bell-Delaware	Simplified Tinker
M3	Dittus-Boelter correlation	Plain tube pressure drop	Developed Bell-Delaware	Wills–Johnston
New	Modified Dittus-Boelter correlation	Plain tube pressure drop	Modified Chart	Modified simple Delaware

Table 2
Stream data and geometry of heat exchangers: Examples 1-5

	Example 1		Example 2		Example 3		Example 4		Example 5	
	Shell-side	Tube-side	Shell-side	Tube-side	Shell-side	Tube-side	Shell-side	Tube-side	Shell-side	Tube-side
Streams										
Specific heat C_P (J/kg·K)	2470	2052	4272	642	4179	4179	2135	2428	2273	2303
Thermal conductivity k (W/m·K)	0.137	0.133	0.685	0.085	0.633	0.623	0.123	0.106	0.08	0.0899
Viscosity μ (mPa·s)	0.40	3.60	0.17	0.20	0.62	0.71	2.89	1.2	18.93	0.935
Density ρ (kg/m^3)	785	850	910	635	991	994	820	790	966	791
Flow rate m_i (kg/s)	5.675	18.917	16.11	109.47	192.72	385.4	75.22	19.15	46.25	202.54
Inlet temperature T_{in} (°C)	200.0	38.0	150.0	207.0	48.0	33.0	51.7	210.0	227.0	131.0
Fouling resistance (m^2·K/W)	0.00035	0.00053	0.0001	0.0005	0.0007	0.0004	0.00035	0.00035	0.00176	0.00053
Geometry of heat exchanger										
Tube pitch PT (m)		0.03175		0.032		0.025		0.0254		0.03125
Number of tubes n_t		124		296		3983		528		612
Number of tube passes n_p		4		2		2		6		2
Tube length L (m)		4.27		2.4		9		5.422		6
Tube effective length L_{eff} (m)		4.17		2.24		8.821		5.219		5.903
Tube conductivity k_{tube} (W/m·K)		51.91		51.91		51.91		51.91		51.91
Tube pattern (tube layout angle)		90°		90°		90°		90°		90°
Tube inner diameter D_i (m)		0.0212		0.02		0.015		0.0148		0.02
Tube outer diameter D_0 (m)		0.0254		0.025		0.019		0.0191		0.025
Shell inner diameter D_s (m)		0.489		0.7		1.9		0.771		0.965
Number of baffles n_b		41		15		16		18		25
Baffle spacing B (m)		0.0978		0.14		0.5		0.2584		0.22
Inlet baffle spacing B_{in} (m)		0.127		0.14		0.66		0.4132		0.3117
Outlet baffle spacing B_{out} (m)		0.127		0.14		0.66		0.4132		0.3117
Baffle cut B_c		20%		20%		25%		22%		20%
Inner diameter of tube-side inlet nozzle $D_{i,inlet}$ (m)		0.1023		0.3		0.438		0.128		0.336
Inner diameter of tube-side outlet nozzle $D_{i,outlet}$ (m)		0.1023		0.3		0.438		0.128		0.336
Inner diameter of shell-side inlet nozzle $D_{0,inlet}$ (m)		0.0779		0.15		0.337		0.259		0.154
Inner diameter of shell-side outlet nozzle $D_{0,outlet}$ (m)		0.0779		0.25		0.337		0.259		0.154
Shell-bundle diametric clearance L_{sb} (m)		0.059		0.074		0.023		0.074		0.069

Table 3
Stream data and geometry of heat exchangers: Examples 6-10

	Example 6		Example 7		Example 8		Example 9		Example 10	
	Shell-side	Tube-side	Shell-side	Tube-side	Shell-side	Tube-side	Shell-side	Tube-side	Shell-side	Tube-side
Streams										
Specific heat C_P (J/kg·K)	2477	2503	2505	1993	2512	2240	2555	2265	2430	4223
Thermal conductivity k (W/m·K)	0.076	0.08	0.093	0.103	0.089	0.091	0.083	0.091	0.0865	0.6749
Viscosity μ (mPa·s)	4.53	0.67	0.26	3.76	0.33	1.1	0.5	1.05	1.8	0.296
Density ρ (kg/m³)	937	748	662	846	702	801	743	798	786	957
Flow rate m_i (kg/s)	32.24	130.288	71.3	202.54	76.92	405.1	17.657	202.542	60.23	23.9
Inlet temperature T_{in} (°C)	293.0	196.0	194.0	44.0	227.0	112.0	265.0	121.0	170.0	77.0
Fouling resistance (m²·K/W)	0.00176	0.00088	0.00053	0.00053	0.00053	0.00053	0.00053	0.00053	0.00088	0.00053
Geometry of heat exchanger										
Tube pitch PT (m)		0.03125		0.03125		0.03125		0.03125		0.025
Number of tubes n_t		538		650		1532		407		582
Number of tube passes n_p		2		2		2		2		4
Tube length L (m)		6		5.7		9		5.5		7.1
Tube effective length L_{eff} (m)		5.9		5.6		8.85		5.45		7.062
Tube conductivity k_{tube} (W/m·K)		51.91		51.91		51.91		51.91		51.91
Tube pattern (tube layout angle)		90°		90°		90°		90°		90°
Tube inner diameter D_i (m)		0.021		0.02		0.02		0.021		0.015
Tube outer diameter D_0 (m)		0.025		0.025		0.025		0.025		0.019
Shell inner diameter D_s (m)		0.914		1.1		1.5		0.9		0.8
Number of baffles n_b		24		14		17		29		20
Baffle spacing B (m)		0.232		0.35		0.489		0.18		0.33
Inlet baffle spacing B_{in} (m)		0.286		0.5227		0.539		0.205		0.4
Outlet baffle spacing B_{out} (m)		0.286		0.5227		0.539		0.205		0.4
Baffle cut B_c		20%		24.4%		38%		20%		40%
Inner diameter of tube-side inlet nozzle $D_{i,inlet}$ (m)		0.3048		0.3		0.337		0.337		0.154
Inner diameter of tube-side outlet nozzle $D_{i,outlet}$ (m)		0.3048		0.3		0.337		0.337		0.154
Inner diameter of shell-side inlet nozzle $D_{0,inlet}$ (m)		0.1541		0.3		0.255		0.102		0.203
Inner diameter of shell-side outlet nozzle $D_{0,outlet}$ (m)		0.1541		0.3		0.255		0.102		0.203
Shell-bundle diametric clearance L_{sb} (m)		0.068		0.082		0.071		0.067		0.066

Table 4
Modelling Results: Examples 1-3

	Tube-side temperature (ºC)	Shell-side temperature (ºC)	Tube-side pressure drop (kPa)	Shell-side pressure drop (kPa)	Tube-side heat transfer coefficient (W/(m²·K))	Shell-side heat transfer coefficient (W/(m²·K))	Overall heat transfer coefficient U (W/(m²·K))
Example 1							
M1	38~69	200~115	70.0	7.1	885.0	901.1	286.3
M2	38~72	200~105	70.0	10.5	1207.1	1400.7	365.5
M3	38~73	200~104	70.0	8.9	1207.1	1583.2	376.8
New Model	**38~73**	**200~104**	**70.0**	**12.1**	**1207.1**	**1508.9**	**372.5**
HTRI	**38~72**	**200~105**	**71.2**	**12.5**	**1299.3**	**1473.5**	**380.4**
HEXTRAN	38~70	200~112	69.6	14.7	886.2	1274.5	315.7
Example 2							
M1	207~189	150~168	31.5	7.3	2212.6	5594.1	656.8
M2	207~188	150~169	31.5	7.8	2466.0	8623.3	713.5
M3	207~188	150~169	31.5	5.5	2466.0	9704.5	720.1
New Model	**207~188**	**150~169**	**31.5**	**7.9**	**2275.4**	**8541.3**	**692.0**
HTRI	**207~189**	**150~169**	**39.8**	**7.9**	**2161.4**	**7884.5**	**674.5**
HEXTRAN	207~189	150~170	31.5	8.2	2112.1	8587.4	684.8
Example 3							
M1	33~38	48~38	28.6	65.0	4967.7	6400.5	602.0
M2	33~38	48~38	28.6	37.9	5754.6	11419.4	642.0
M3	33~38	48~38	28.6	26.0	5754.6	12155.0	644.0
New Model	**33~38**	**48~38**	**28.8**	**53.4**	**5754.6**	**5788.6**	**608.7**
HTRI	**33~38**	**48~38**	**29.7**	**45.0**	**5644.0**	**5791.8**	**609.2**
HEXTRAN	33~38	48~38	29.3	38.5	5014.5	6667.6	605.1

Table 5
Modelling Results: Examples 4-6

	Tube-side temperature (ºC)	Shell-side temperature (ºC)	Tube-side pressure drop (kPa)	Shell-side pressure drop (kPa)	Tube-side heat transfer coefficient (W/(m²·K))	Shell-side heat transfer coefficient (W/(m²·K))	Overall heat transfer coefficient U (W/(m²·K))
Example 4							
M1	210~106	52~82	87.7	96.0	1117.3	1414.2	370.1
M2	210~102	52~83	87.7	70.2	1130.8	1934.6	400.3
M3	210~102	52~83	87.7	56.9	1130.8	2090.3	406.6
New Model	**210~102**	**52~83**	**87.8**	**92.7**	**1393.8**	**1471.1**	**408.7**
HTRI	**210~100**	**52~83**	**86.8**	**97.7**	**1470.0**	**1534.0**	**422.0**
HEXTRAN	210~106	52~82	84.9	99.4	1117.2	1434.1	371.5
Example 5							
M1	227~195	131~138	55.6	47.3	1574.9	313.6	154.8
M2	227~189	131~140	55.6	30.9	2030.9	536.8	201.8
M3	227~188	131~140	55.6	26.9	2030.9	572.5	206.7
New Model	**227~191**	**131~139**	**55.6**	**65.8**	**2030.9**	**433.3**	**185.2**
HTRI	**227~193**	**131~139**	**59.2**	**76.4**	**2060.6**	**371.7**	**173.3**
HEXTRAN	227~189	131~140	56.3	52.4	1574.8	570.9	199.1
Example 6							
M1	293~256	196~205	26.0	24.0	1248.2	442.1	164.9
M2	293~251	196~206	26.0	16.7	1595.5	681.3	197.5
M3	293~250	196~206	26.0	14.1	1595.5	735.3	201.8
New Model	**293~253**	**196~206**	**26.0**	**29.0**	**1595.5**	**562.2**	**186.1**
HTRI	**293~254**	**196~206**	**27.9**	**31.1**	**1604.7**	**500.5**	**178.9**
HEXTRAN	293~253	196~206	26.3	23.4	1248.1	636.0	186.0

Table 6
Modelling Results: Examples 7-10

	Tube-side temperature (°C)	Shell-side temperature (°C)	Tube-side pressure drop (kPa)	Shell-side pressure drop (kPa)	Tube-side heat transfer coefficient (W/(m²·K))	Shell-side heat transfer coefficient (W/(m²·K))	Overall heat transfer coefficient U (W/(m²·K))
Example 7							
New Model	**44~69**	**194~137**	**63.1**	**30.9**	**1134.1**	**1613.2**	**336.9**
HTRI	**44~70**	**194~135**	**59.1**	**27.8**	**1310.5**	**1717.8**	**359.7**
HEXTRAN	44~68	194~141	64.4	27.9	816.5	2036.3	306.0
Example 8							
New Model	**112~130**	**227~141**	**69.5**	**20.0**	**1583.2**	**844.3**	**310.5**
HTRI	**112~130**	**227~142**	**73.5**	**17.5**	**1616.9**	**745.7**	**297.6**
HEXTRAN	112~130	227~141	71.3	12.8	1217.5	991.7	304.8
Example 9							
New Model	**121~131**	**265~160**	**83.8**	**16.5**	**2463.1**	**980.7**	**369.6**
HTRI	**121~131**	**265~162**	**91.2**	**20.5**	**2494.3**	**900.6**	**358.2**
HEXTRAN	121~131	265~161	84.1	17.0	1898.9	1066.2	361.3
Example 10							
New Model	**77~119**	**170~141**	**26.1**	**43.0**	**7568.7**	**738.7**	**321.0**
HTRI	**77~120**	**170~140**	**26.8**	**38.4**	**7363.2**	**809.1**	**333.3**
HEXTRAN	77~120	170~140	25.6	35.7	7145.2	853.3	339.7

As shown in *Tables 4* to *6*, stream temperatures, heat transfer coefficients and pressure drops calculated from the proposed model are similar to values obtained by HTRI® and HEXTRAN® in most cases. Three models considered in this paper (M1, M2 and M3) may give significantly different results, compared with HTRI® and HEXTRAN®. As shown in the tube-side results from the developed model, HTRI® and HEXTRAN®, major difference is in heat-transfer coefficients. The developed model and HTRI® method usually give higher values than HEXTRAN® which may use Colburn correlation (i.e. Nu = 0.023Re^{0.8}Pr^{1/3}) [11] to calculate tube-side heat-transfer coefficient. Compared with Equation (4), the Colburn correlation uses a smaller factor to calculate Nusselt number (Nu_i). For calculating pressure drop, plain tube pressure drop method [12] is used, the values predicted by the proposed model have reasonably a good agreement with those from HTRI® and HEXTRAN®.

In shell-side calculations, the developed model and HTRI® give similar values in most examples. HEXTRAN® uses different correlations for the heat transfer coefficient and friction factor of ideal tube bank, while HTRI® includes a large number of empirical parameters for heat transfer and flow resistance, and with many adjustable parameters, HTRI® model can provide a good representation of the experimental data for shell-side heat transfer and pressure drop [12]. From Examples, it has been demonstrated that the proposed model can be used in process engineering and design practice with confidence for predicting heat exchanger performance.

5.2   HEN retrofit with HTE

Figure 5 presents an existing preheat train for a crude oil distillation column in a refinery plant. The retrofit objective is to reduce the hot utility (H13) consumption, namely, reduce the heat duty of heat exchanger 30 (target exchanger). The initial data of the HEN can be found in *Table 7*. Based on these data, the proposed heuristic rules can be utilized to find suitable heat exchangers for enhancement.

From Rule 1: Heat exchangers 4, 23, 24, 26, 27, 28 and 29 locating in the same path with the target exchanger are selected for performing sensitivity analysis. From Rule 2: Figure 6 presents the sensitivity graphs for all the selected exchangers. Exchanger 24, 26 and 28 with high sensitivity are regarded as good candidates, exchangers 27 and 29 are normal candidates, and exchangers 4 and 23 are bad candidates with low sensitivity. As having large CP_{min} and there is only one exchanger between exchanger 28 and target utility exchanger, exchanger 28 is the beat candidate. From Rule 3: Exchangers 20, 22 and 23 are pinching match in the HEN. Pinching match of Exchanger 20 is in the downstream of promising candidate Exchanger 24, therefore, Exchanger 24 is constrained by the pinching match.
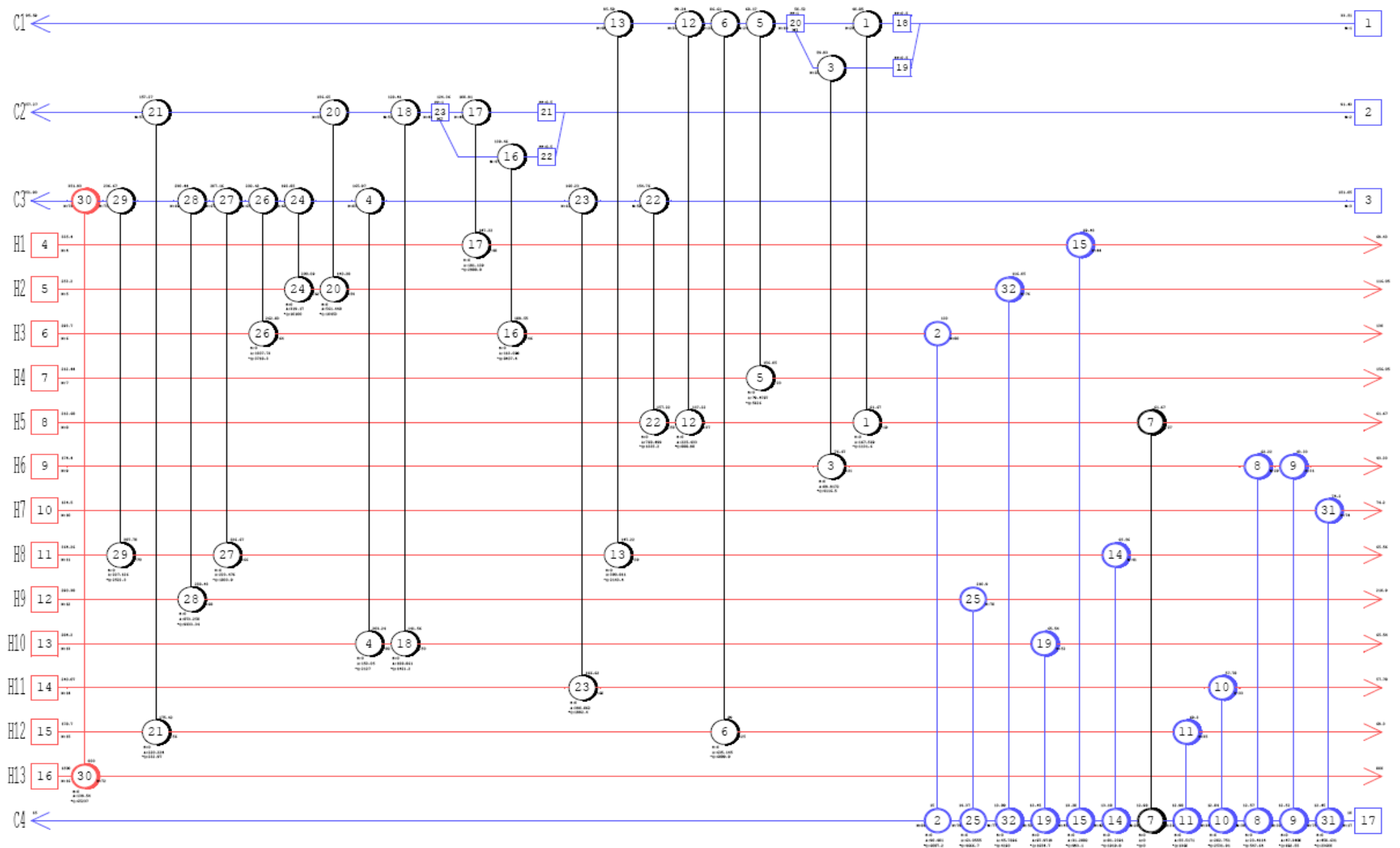
Figure 5: A HEN for case study

Table 7
Data of HEN in the case study

Exchanger	Initial situation				Enhancement situation			
	U (kW/m²·K)	Area (m²)	ΔT_{ln} (°C)	Duty (kW)	U (kW/m²·K)	Area (m²)	ΔT_{ln} (°C)	Duty (kW)
1	0.1400	167.6	48.2	1132	0.1400	167.6	48.2	1132
2	0.4690	90.4	143.4	6087	0.4690	90.4	140.3	5954
3	0.6270	89.9	73.0	4117	0.6270	89.9	73.0	4117
4	0.1850	153.0	75.2	2128	0.1850	153.0	75.1	2127
5	0.5720	97.4	100.9	5626	0.5720	97.4	100.9	5626
6	0.2040	653.1	45.7	6090	0.2040	653.1	45.6	6087
7	0.3540	13.3	43.3	204	0.3540	110.6	5.2	204
8	0.4130	23.4	56.6	548	0.4130	23.4	56.6	548
9	0.4130	47.3	35.4	693	0.4130	47.3	34.8	680
10	0.0990	282.8	90.4	2532	0.0990	282.8	90.4	2532
11	0.3730	55.5	65.7	1360	0.3730	55.5	65.7	1360
12	0.0842	225.4	46.8	889	0.0842	225.4	46.8	889
13	0.0628	380.8	89.6	2143	0.0628	380.8	91.3	2183
14	0.2720	81.2	86.9	1920	0.2720	81.2	87.7	1937
15	0.3520	31.3	90.2	993	0.3520	31.3	90.2	993
16	0.6730	113.1	110.5	8408	0.6730	113.1	109.0	8295
17	0.1280	191.1	122.2	2989	0.1280	191.1	122.2	2989
18	0.1880	188.9	40.0	1421	0.1880	188.9	40.2	1427
19	0.2000	97.9	84.5	1655	0.2000	97.9	84.3	1651
20	**0.3210**	**1338.4**	**24.3**	**10450**	**0.4290**	**1338.4**	**18.2**	**10440**
21	0.0527	220.2	20.1	233	0.0527	220.2	20.4	237
22	0.0752	768.5	23.1	1335	0.0752	768.5	23.1	1335
23	0.1430	390.9	35.6	1992	0.1430	390.9	35.6	1992
24	**0.2190**	**1003.3**	**46.0**	**10100**	**0.2860**	**1003.3**	**41.8**	**11994**
25	0.3520	63.1	210.3	4667	0.3520	63.1	195.2	4333
26	**0.1700**	**1308.0**	**16.7**	**3718**	**0.1870**	**1308.0**	**16.3**	**3981**
27	0.1950	223.5	42.1	1834	0.1950	223.5	42.2	1838
28	**0.2110**	**1003.3**	**44.1**	**9333**	**0.2728**	**1003.3**	**39.4**	**10783**
29	0.1260	227.1	88.1	2522	0.1260	227.1	85.6	2449
30 (hot utility)	0.5710	139.5	819.0	**65240**	0.5710	139.5	791.4	**63040**
31	0.5710	458.6	90.1	23600	0.5710	458.6	90.1	23600
32	0.8020	45.8	114.1	4190	0.8020	45.8	92.1	3384
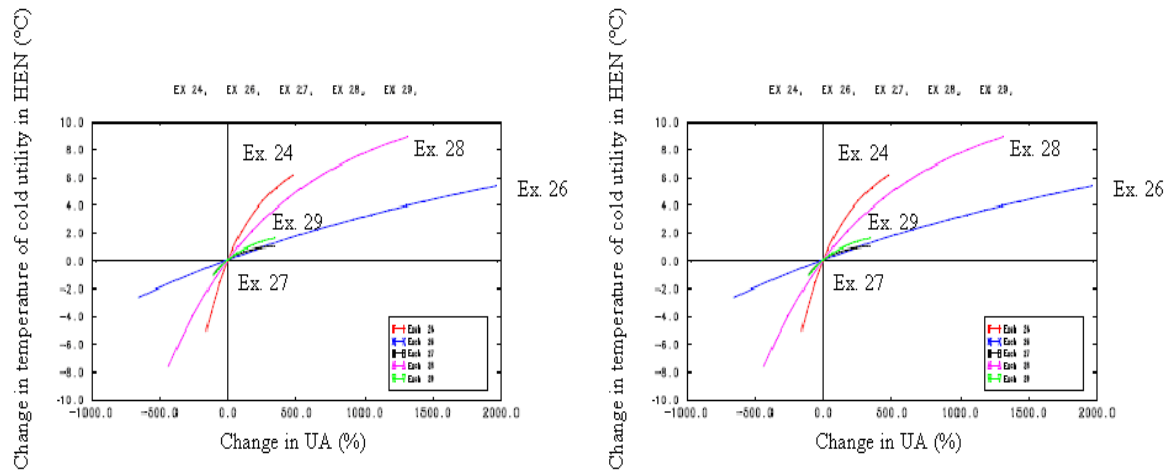
Figure 6: Sensitivity graphs of exchangers in the case study

Table 8
Stream data and geometry of heat exchangers 20, 24, 26 and 28 in the case study

	Heat Exchanger 20		Heat Exchanger 24		Heat Exchanger 26		Heat Exchanger 28	
	Shell-side	Tube-side	Shell-side	Tube-side	Shell-side	Tube-side	Shell-side	Tube-side
Fluids	H2	C2	H2	C3	H3	C3	H9	C3
Specific heat C_P (J/kg·K)	2394	2310	2597	2444	2965	2526	2832	2609
Thermal conductivity k (W/m·K)	0.096	0.090	0.095	0.085	0.062	0.078	0.071	0.074
Viscosity μ (mPa·s)	0.67	0.90	0.44	0.80	0.10	0.69	0.30	0.57
Density ρ (kg/m^3)	773	789	734	766	556	751	638	733
Flow rate m_i (kg/s)	73.1	160.2	73.1	153.7	40.6	153.7	63.4	153.7
Inlet temperature T_{in} (°C)	200.0	128.4	253.2	166.0	293.7	192.9	290.4	207.2
Fouling resistance (m^2·K/W)	0.00006	0.00036	0.00120	0.00072	0.00221	0.00080	0.00117	0.00088
Geometry of heat exchanger								
Tube pitch PT (m)		0.03125		0.03125		0.03125		0.03125
Number of tubes n_t		1532		1532		650		1532
Number of tube passes n_p		2		2		1		2
Tube length L (m)		11.3		8.5		5.5		8.5
Tube effective length L_{eff} (m)		11.1		8.3		5.3		8.3
Tube conductivity k_{tube} (W/m·K)		51.91		51.91		51.91		51.91
Tube pattern (tube layout angle)		90°		90°		90°		90°
Tube inner diameter D_i (m)		0.02		0.02		0.02		0.02
Tube outer diameter D_0 (m)		0.025		0.025		0.025		0.025
Shell inner diameter D_s (m)		1.5		1.5		1.1		1.5
Number of baffles n_b		20		16		9		18
Baffle spacing B (m)		0.49		0.49		0.52		0.49
Inlet baffle spacing B_{in} (m)		0.95		0.57		0.71		0.57
Outlet baffle spacing B_{out} (m)		0.95		0.57		0.71		0.57
Baffle cut B_c		20%		20%		40%		20%
Inner diameter of tube-side inlet nozzle $D_{i,inlet}$ (m)		0.336		0.336		0.3		0.336
Inner diameter of tube-side outlet nozzle $D_{i,outlet}$ (m)		0.336		0.336		0.3		0.336
Inner diameter of shell-side inlet nozzle $D_{0,inlet}$ (m)		0.255		0.255		0.3		0.255
Inner diameter of shell-side outlet nozzle $D_{0,outlet}$ (m)		0.255		0.255		0.3		0.255
Shell-bundle diametric clearance L_{sb} (m)		0.074		0.074		0.082		0.074
Maximum pressure drops in shell and tube side (KPa)		100		100		100		100

From the results of sensitivity table, exchanger 24, 26 and 28 are good candidates. From Rule 3, exchanger 24 is constrained by pinching match exchanger 20 and exchanger 28 is the best candidate without being contrained by a pinching match. Exchanger 28 should be enhanced first, and then after applying sensitivity table again, exchanger 26 is the next best candidate after the enhancement of exchanger 28. After the enhancement of both exchangers 26 and 28, there is no good candidate left from the results of sensitivity table. Rule 4 is now applied to check whether further energy saving can be made. From the results of previous rules, exchanger 24 is a good candidate constrained by a pinching match exchanger 20. So, according to rule 4, both exchanger 24 and exchanger 20 are enhanced. From heuristic methodology: Exchangers 20, 24, 26 and 28 are enhanced with hiTRAN®, a tube-insert using for the enhancement of tube-side and produced by Gal Gavin Ltd.

To estimate the enhancement performances of the four exchangers, the detailed data of the heat exchangers should be given, as shown in *Table 8*. In *Table 9*, the overall heat transfer coefficient for each enhanced exchanger increases within the maximum pressure drop constraints. From *Table 7*, exchangers 20, 24, 26 and 28 are selected to be enhanced, which achieves 2.2 MW of heat duty reduction in exchanger 30, leading to 3.4% of overall energy saving. It should be emphasised that this saving has been made without any additional topology modification of the network.

Table 9
Tube-side heat transfer enhancement for heat exchangers 20, 24, 26 and 28 in the case study

	Example 20		Example 24		Example 26		Example 28	
	Shell-side	Tube-side	Shell-side	Tube-side	Shell-side	Tube-side	Shell-side	Tube-side
	H2	C2	H2	C3	H3	C3	H9	C3
New model								
Pressure drop $\triangle P$ (KPa)	24.1	14.7	20.6	11.25	5.1	8.1	19.2	11.1
Film coefficient h (W/m^2·K)	975	822	1117	824	753	961	979	894
Overall heat transfer coefficient U (W/m^2·K)		321.4		219.1		169.8		211.1
HTRI								
Pressure drop $\triangle P$ (KPa)	23.6	15.1	23.6	11.8	3.7	9.3	17.4	11.7
Film coefficient h (W/m^2·K)	981	839	1267	842	765	982	1014	906
Overall heat transfer coefficient U (W/m^2·K)		325.6		225.9		171.1		213.4
Heat transfer enhancement of tube side								
Pressure drop $\triangle P$ (KPa)	24.1	88.5	20.6	98.6	5.1	95.2	19.2	96.5
Film coefficient h (W/m^2·K)	975	1684	1117	2778	753	1954	979	3827
Overall heat transfer coefficient U (W/m^2·K)		428.5		286.0		191.3		272.8

6   Conclusion

Selecting suitable exchangers for enhancement is an efficient way to solve large-scale HEN retrofit problems. This paper presents a new approach for HEN retrofit with HTE. First of all, a mathematical model has been developed to predict shell-and-tube heat exchanger performances, with which heat

transfer coefficients and pressure drops for both fluids in tube-side and shell-side can be estimated with satisfactory accuracy. And then, five heuristic rules have been proposed to screen candidates for heat transfer enhancement of exchangers in HEN, which can reduce problem complexity significantly. In contrast to the available design methods, the proposed retrofit approach provides realistic solutions for HEN retrofit based on intensified heat transfer with substantial energy saving without topology modification of HEN.

Acknowledgements

References

[1]   Polley GT, Reyes Athie CM, Gough M. Use of heat transfer enhancement in process integration. Heat Recovery Systems and CHP 1992; 12(3): 191-202.

[2]   Zhu X, Zanfir M, Klemes J. Heat transfer enhancement for heat exchanger network retrofit. Heat Transfer Engineering 2000; 21(2): 7-18.

[3]   Smith R, Jobson M, Chen L. Recent development in the retrofit of heat exchanger networks. Chemical Engineering Transactions 2009; 18: 27-32.

[4]   Li BH, Chang CT. Retrofitting heat exchanger networks based on simple pinch analysis. Industry and Engineering Chemistry Research 2010; 49: 3967-3971.

[5]   Yee TF, Grossmann IE. A screening and optimization approach for the retrofit of heat exchanger networks. Industry and Engineering Chemistry Research 1991; 30 (1): 146-162.

[6]   Sorsak A, Kravanja Z. MINLP retrofit of heat exchanger networks comprising different exchanger types. Computers and Chemical Engineering 2004; 28: 235-251.

[7]   Ponce-Ortega JM, Jiménez-Gutiérrez A, Grossmann IE. Optimal synthesis of heat exchanger networks involving isothermal process streams. Computers and Chemical Engineering 2008; 32: 1918-1942.

[8]   Asante NDK, Zhu XX. An automated approach for heat exchanger network retrofit featuring minimal topology modifications. Computers and Chemical Engineering 1996; 20: S7-S12.

[9]   Kovac KA. Optimization of an industrial retrofitted heat exchanger network, using a stage-wise model. Energy 2010 (In press); doi:10.1016/j.energy.2010.09.016.

[10] Cal Gavin Ltd. hiTRAN® thermal systems: changing fluid dynamics and harnessing the benefits. Technical report of Cal Gavin Ltd, 2009.

[11] Bhatti MS, Shah RK. Turbulent and transition convective heat transfer in ducts, in Handbook of Single-Phase Convective Heat Transfer, S. Kakac, R. K. Shah, and W. Aung, eds., Wiley, New York, 1987; Chap. 4.

[12] Serth RW. Design of shell-and-tube heat exchangers, in Handbook of Process Heat Transfer Principles and Applications, R. W. Serth, eds., Elsevier Ltd, 2007; Chap. 5.

[13] Taborek J. Shell-and-tube heat exchangers, in Heat Exchanger Design Handbook, Hemisphere Publishing Corp., New York, 1988; Vol. 3.

[14] Gnielinski A, Zukauskas A, Skrinska A. Banks of plain and finned tubes, in Heat Exchanger Design Handbook, Hemisphere Publishing Corp., New York, 1998; Vol. 2.

[15] Ayub ZH. A new chart method for evaluating single-phase shell side heat transfer coefficient in a single segmental shell and tube heat exchanger. Applied Thermal Engineering 2005; 25: 2412-2420.

[16] Kern DQ, Kraus AD. Extended Surface Heat Transfer, McGraw-Hill, New York, 1972.

[17] ESDU Ltd. Baffled shell-and-tube heat exchangers; flow distribution, pressure drop and heat transfer coefficient on the shell side, ESDU International Ltd, London, 1984.

[18] Wills MJN, Johnston D. A New and Accurate Hand Calculation Method for Shell-side Pressure Drop and Flow Distribution, Proc. 22nd National Heat Transfer Conference, American Society of Mechanical Engineers, 1984; 36: 67-79.

[19] Pan M, Qian Y, Li X. A novel precedence-based and heuristic approach for short-term scheduling of multipurpose batch plants. Chemical Engineering Science 2008; 63: 4313-4332.

[20] Pan M, Li X, Qian Y. New approach for scheduling crude oil operations. Chemical Engineering Science 2009; 64: 965-983.

[21] Pan M, Li X, Qian Y. Continuous-time approaches for short-term scheduling of network batch processes: Small-scale and medium-scale problems. Chemical Engineering Research and Design 2009; 87: 1037-1058.

[22] Linnhoff B, Townsend DW, Boland D, Hewitt GF, Thomas BEA, Guy AR, Marsland RH. A User Guide on Process Integration for the Efficient Use of Energy, IChemE, Rugby, UK, 1982.

[23] Linnhoff B, Hindmarsh E. The Pinch Design Method of Heat Exchanger Networks. Chemical Engineering Science 1983; 38: 745-763.

[24] Varbanova PS, Klemesb J. Rules for paths construction for HENs debottlenecking. Applied Thermal Engineering 2000; 20(15): 1409-1420.

[25] Kotjabasakis E, Linnhoff B. Sensitivity Tables for the Design of Flexible Processes (1)-How Much Contingency in Heat Exchanger Networks is Cost-Effective. Chemical Engineering Research and Design 1986; 64(a): 197-211.

Track 1 Section 2

Industrial Applications

Potential Energy Savings by Application of the Novel CRIMSON Aluminium Casting Process

Xiaojun Dai, Mark Jolly[*]

School of Mechanical Engineering, University of Birmingham, Edgbaston, Birmingham, B15 2TT, United Kingdom

* Corresponding author. Email: m.r.jolly@bham.ac.uk; Tel: +44(0) 121 414 7355; Fax: +44(0) 121 414 4168

Abstract

Compared with its output the casting industry uses a disproportionate amount of energy as a result of the inefficient processes used. This paper presents the melting processes that are used in one of the traditional foundries and identifies the energy burdens associated with them. A comparison is then made with the novel CRIMSON process to demonstrate where energy savings can be made. An actual case or casting sample is investigated to demonstrate the advantage of energy saving in novel CRIMSON method which will help the foundry industry in reduction of energy cost and promote competitiveness in the production of high end casting components.

Keywords   energy saving; aluminium casting; melting; CRIMSON

1   Introduction

The metal casting industry is naturally very energy intensive. Energy consumption in foundry mainly depends on electricity gas and oil. It is estimated that the energy required in melting and heating in a typical metal casting facility is 60 % to 75 % of the total energy used in the facility [1].The energy efficiency of any metal casting facility depends largely on the efficiency of its melting and heat treating operations. In conjunction with the two operations, over 60 % of the total process energy costs are represented in a typical casting facility [2]. Therefore, there are huge opportunities for metal casting industry to adopt the best energy solutions which will offer the great energy saving potential. To improve the energy efficiency of these operations will have an important effect on reducing the manufacturing cost and promote the competitiveness. For example, by implementing some cutting-edge technology such as the CRIMSON method in aluminium alloy casting will take advantage of such opportunities.

The CRIMSON (Constrained Rapid Induction Melting Single Shot Up-Casting) method was co-invented by researchers and engineers of University of Birmingham and a local company, - N-Tec Ltd. The aim is to reduce the energy consumption and to improve the casting quality within light-metal shape casting industry. The method's main philosophy is that foundries, using an induction furnace, need only to melt the quantity of metal required to fill a single mould in a closed crucible rather than large batches that use unnecessary energy and create more rejects. The closed crucible, then, is transferred to a station and the melted metal is push up using a computer controlled anti-gravity filling method to fill the mould. Due to a feature of rapid melting, transfer and filling in the new method, the holding time of melted metal is minimised, a drastic energy saving is achieved and in the mean time the possibility of hydrogen absorption and formation of surface oxide film are reduced to a great extent [3]. In this paper, the traditional melting and casting processes from one local company are investigated and they are compared with the novel method. The calculation and analysis of energy consumption are completed to see what the difference between the current melting processes and the novel method. Then, the potential energy saving for the novel method can be found. This comparison is only one of a number being carried out under the auspices of an EPRSC project whereby 4 traditional casting processes will be benchmarked for their energy usage and scrap rates.

2   Audit the energy consumption of melting processes in traditional foundry

Energy audit is the definition for "a thorough mapping of energy and water use, all beneficial saving possibilities, and the renewable form of energy usable possibilities of the building and the production process carried out by experts" [4]. Usually, energy used in foundry will be electricity, gas, oil and other forms. In this paper, we mainly focus on the energy consumption of melting processes, other energy consumption issues will be investigated later in our research project. The energy burden of the melting and holding processes is a large part of the total energy used in the foundry. Figure 1 gives an estimate of the process-specific energy profile of the metal casting industry based on tacit energy and it was calculated by converting delivered energy data, obtained from published energy reports, to tacit energy (Tacit energy is a term used to describe an energy value that equals the combination of onsite energy consumption, the process energy required to produce and transmit/transport the energy source, and feedstock energy). Melting and holding stands out above all other process areas with an estimated 72 percent of the metal casting industry tacit energy consumption [5].
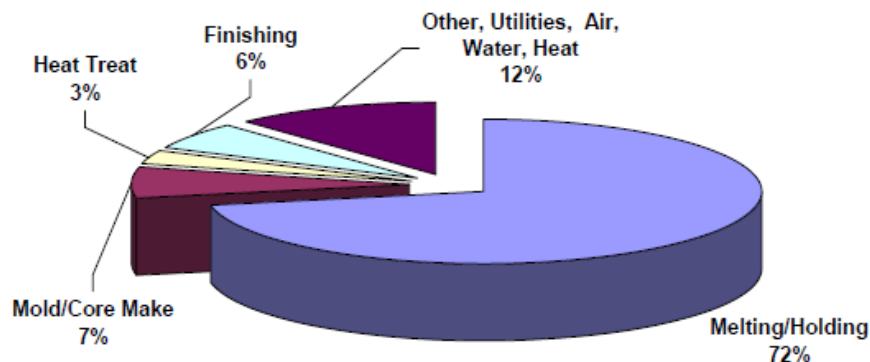
Figure 1: Typical metal casting tacit energy profile by process

In UK, most of the foundry use electricity, gas and oil as the fuel in the melting processes. Traditionally, the majority of foundries melt the alloys to be cast first and then hold the melted alloys in a furnace for long time, sometimes for the duration a full shift. The purpose of holding the molten alloys is to pour the moulds in batches. This process planning method is convenient and flexible for the foundry personnel to operate in normal circumstances. However, for every hour the metal is held energy is unnecessarily. Theoretically, the quantity of energy required for melting one tonne of aluminium to a superheat of 100 $^\circ$C is calculated to be 1.1 GJ/tonne (~306 KWh/tonne) [3]. Figure 2 [3] shows the flow chart of foundry process where the energy loss at each stage is indicated. In the worst cases for each stage, the figure of the final energy cost could be 182 GJ/tonne (~50.6 MWh/tonne) [3]. In the current research project, a specific casting has been identified and the energy consumption is audited by comparing the traditional melting process and the new process.

Traditional foundry ingot is supplied in what are called "pigs" and are roughly trapezoidal in cross section (Figure 3(a)). For the new process a circular cross section direct chill (DC) cast billets (Figure 3(b)) would be required in order obtain the best efficiency of heating with the RF induction coil. The latter route has an added benefit in also being a metal of higher quality. Traditionally produced foundry ingot is cast in a turbulent fashion which inherently produces poor quality metal to start with thus starting with DC cast billet is an immediate advantage. It is not possible at this stage to purchase small volumes of DC cast foundry alloy billet. For this project it was necessary to re-cast the traditional ingot into billets after treating the melt to reduce the oxide content. In order to make a comparison of the traditional processes with the new process route the initial casting of the stock has been left out of the energy audit for both routes. In other words the starting point has been chosen as the metal in solid billet or ingot form required by the process. This can be justified by specifying that if the new process were adopted by the industry it would only be feasible if the starting stock was foundry alloy in billet form of the correct diameter.
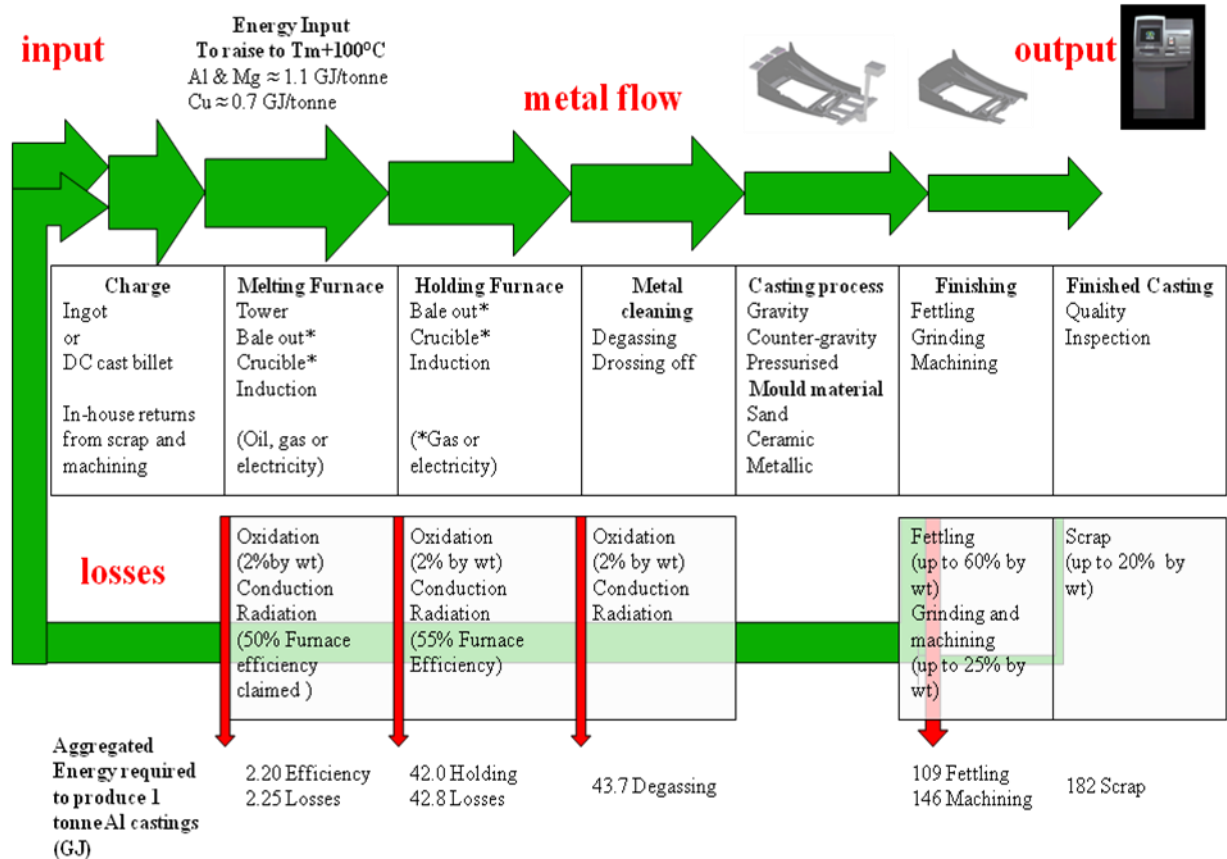
Figure 2: Flow chart of aluminium foundry processes with estimated energy losses at each stage (The cycle is treated as a closed loop and discounts the embedded energy within the casting ingot supplied by the primary industry)

| Figure 3(*a*): Traditional foundry ingot | Figure 3(*b*): DC Cast billet |

3   Case investigation - Grainger & Worrall Co. Ltd.

One of the foundries for producing high end casting components in Grainger & Worrall (G&W) Ltd. is currently using one type of melting furnace (Figure 4) with combining melting process where the primary melting area can be called a melting area and gas is used to melt aluminium ingot, then the melted aluminium alloy flowing along an inclined channel to a refining area where an electric resistance furnace is used. The refined liquid aluminium alloy is held in the electric resistance furnace. "Pouring" is carried out using an electromagnetic pump to pump the liquid metal to the mould. This is called the "Cosworth" process. In this foundry, there are two furnaces using this kind of combining melting processes for producing two types of aluminium alloys-A354 and A357. The capacity of both

furnaces is 4 tonne. The holding time for each furnace is up to 4-5 days. The overheating temperature of A354 aluminium alloy is 760 °C. The pouring temperature of the melted Al alloy is 700 °C. G&W is currently using traditional sand casting processes to produce normal casting components and the Cosworth casting process is especially selected to produce high quality components. A "Test bar" mould has been selected to use novel method to examine its energy consumption. The design of the "Test bar" with a runner system is shown in Figure 5 which has a profile of 530 mm length x 390 mm width x 100 mm height with a weight of 4 kg. [6]
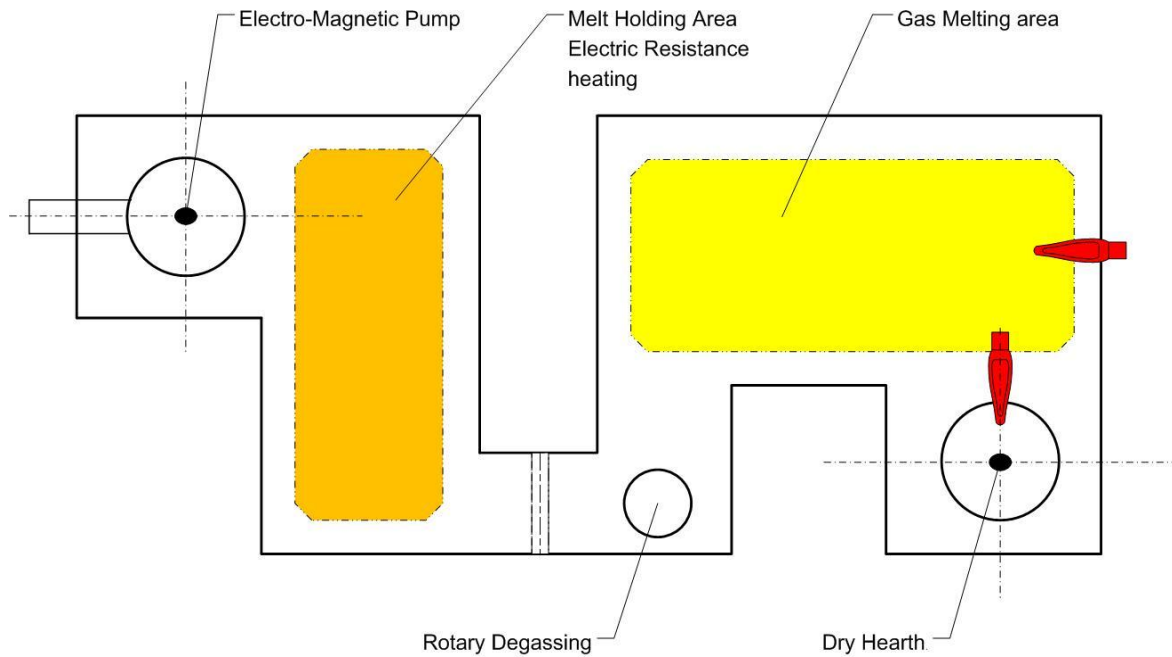
Figure 4: The schematic plan of the furnace in G&W Ltd
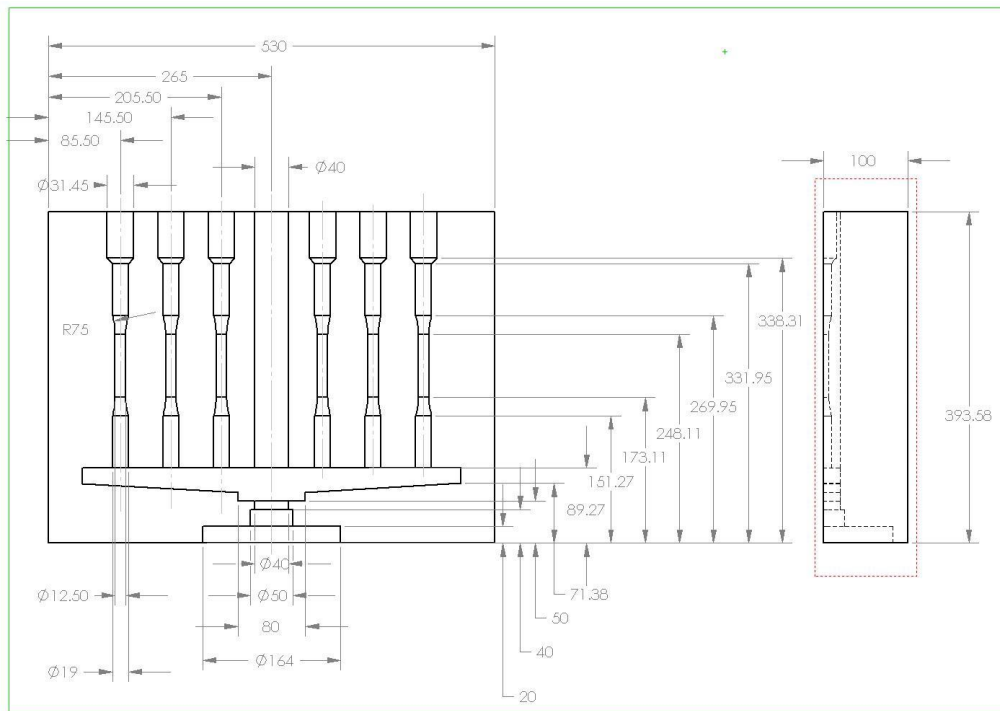
Figure 5: The structure of the "Test bar" with runner system [6]

3.1 Calculation of energy consumption of melting process

Without considering the chemical reaction, slag formation and other heat losses, the theoretical calculation of energy for heating A354 aluminium alloy to 760 °C is as follows [7]:

$$Q = m\,C_{m1}(T_m - T_1) + Q_f + m\,C_{m2}(T_2 - T_m) \qquad (2.1)$$

Here, Q is the heat that is needed to heat and melt the Al alloys;

m is the mass of the Al alloy;

C_{m1} is the specific heat for solid A354 Al alloys, 1.07 kJ.kg^{-1}.°C^{-1} [7];

C_{m2} is the specific heat for liquid A354 Al alloys, 1.05 kJ.kg^{-1}.°C^{-1} [7];

T_m is the melting temperature of A354 Al alloys, 596 °C [8];

T_1 is the environment temperature, 20 °C;

T_2 is the superheat temperature, 760 °C;

Q_f is the heat of fusion, 389 kJ.kg^{-1}.°C^{-1} [8];

3.1.1 Calculation of the gas consumption

In this case, the gas is used to heat the Al alloys to its melting point 596 °C and melt the alloys.

Therefore, the heat Q_1 for heating and melting the Al alloys can be calculated as:

$$Q_1 = m\,C_{m1}(T_m - T_1) + Q_f \qquad (2.2)$$
$$Q_1 = 1.07(596 - 20) + 389 = 1005 \text{ kJ. kg}^{-1}$$

3.1.2 Calculation of the electricity consumption

In this case, the electricity is used to overheat the melted Al alloys to 760 °C. Therefore, the heat Q_2 for overheating the Al alloys can be calculated as:

$$Q_2 = m\,C_{m2}(T_2 - T_m) \qquad (2.3)$$
$$Q_2 = 1.05(760 - 596) = 172 \text{ kJ. kg}^{-1}$$

3.1.3 Total energy consumption

Combining Q_1 and Q_2, the total theoretical energy consumption Q_{t1} for melting A354 Al alloys to 760 °C is:

$$Q_{t1} = Q_1 + Q_2 = 1005 + 172 = 1177 \text{ kJ. kg}^{-1} = 327 \text{ kWh. tonne}^{-1} \qquad (2.4)$$

During the heating and melting processes of Al alloys, the actual energy consumption in a furnace is higher than the value of theoretical calculation due to the heat losses from conduction, radiation, convection, drossing and oxidation etc. It is estimated [9] that the thermal efficiency is 7~19 % for a crucible furnace using natural gas, 59 ~76 % for an induction furnace using electricity. (The average values of the thermal efficiency are selected in this case: $\eta_1 = 13\ \%$ for the gas; $\eta_2 = 67.5\ \%$ for electricity.)

The energy consumption at G&W where the Cosworth process is applied was investigated where both gas and electricity are included and the usages are recorded in *Table 1*. It should be pointed out that power measurement may link with the day or night rate. Here, only the energy consumption (kJ.kg-^{1}or MJ.kg^{-1}) is measured and the cost which linking with the rate is not considered in this measurement.

Table 1
Actual consumption of gas and electricity in G&W Ltd where the Cosworth process is applied

Energy type	Energy consumption	Energy density by mass ($MJ.kg^{-1}$)
LPG (propane) [10]	(0.7 m^3.tonne^{-1}) 65.31 kJ.kg^{-1}	49.6
Electricity	(2800 kWh.tonne^{-1}) 10.08 MJ.kg^{-1}	--------

From *Table 1*, the total actual energy consumption Q_{t2} for melting A354 Al alloys in G&W can be calculated as follows:

$$Q_{t2} = 0.7 \times 49.6 \times \frac{10^6}{3600} + 2800 = 9644 + 2800 = 12444 \text{ kWh.tonne}^{-1}$$
$$= 44.80 \text{ MJ.kg}^{-1}$$

The thermal efficiency of using the LPG for melting the alloys:

$$\eta_1' = 1005 \div 9644 = 10.4 \%$$

The thermal efficiency of using the electricity for holding the melt:

$$\eta_2' = 172 \div 2800 = 6.14 \%$$

4 Audit energy consumption of new process
4.1 The novel casting facility

The structure of the novel casting process facility is indicated in Figure 6,

Where the Up-caster's features are as follows:

a. High power Induction furnace (275 KW): it is used to quickly heat and melt the metal to the required pouring temperature. Usually each time, a billet of the required size and calculated amount of metal is put in, also the composition of the billet should be consistent with the casting component that will be poured and produced;

b. Up-caster: when the crucible with the melted metal inside is ready, it is moved and cramped in the right position in Up-caster and a mould is located on the top of pouring position, a piston in the Up-caster will raise and push the melted metal in the crucible into the mould;

c. Computer-controlled operation table of the Up-caster: the movement of the piston in Up-caster is automatically controlled by the pre-programmed computer program;

d. Mould transfer stop: after pouring, cooling down and solidification, the mould can be moved to the transfer stop, waiting for lifting and cleaning;
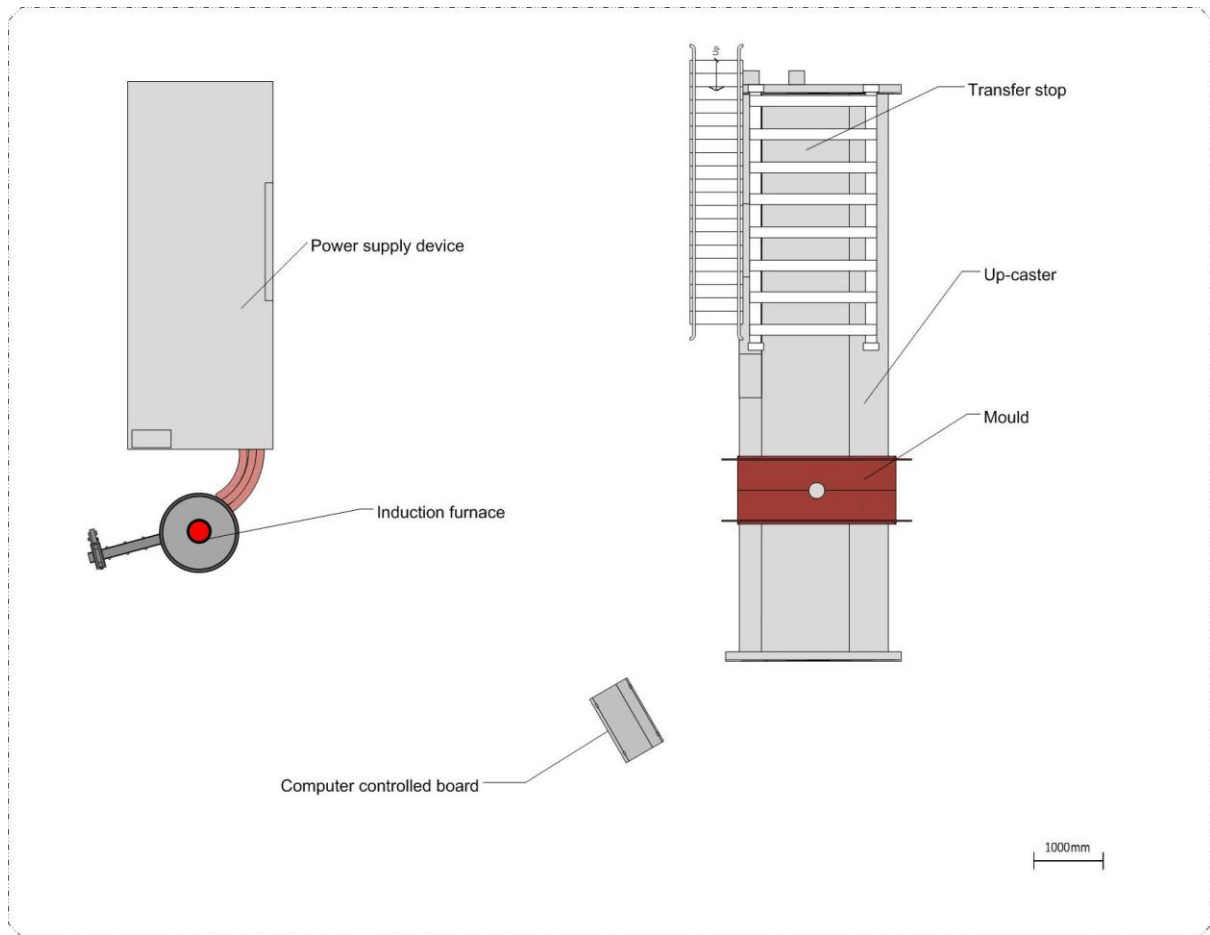
Figure 6: The schematic plan of the new casting process facility

4.2   Calculation of energy consumption of novel casting method

Experimental parameters for casting the "Test bar" mould in the new casting facility are given in *Table 2*:

Table 2

Experimental parameters for the "Test bar" in the new casting process facility

Experiment parameter	Value	Note
Weight of metal charge	4 kg	
Melt temperature	729°C	Using thermal couple
Melting time	2 minutes	
Injection time of Up-caster	10 Seconds	
Holding time	20 Seconds	
Solidification time	28 Seconds	
Measured energy consumption for melting the charge	7.92 MJ (2.2 KWh)	

The theoretical energy consumption Q_{t3} for heating the A354 alloy to 729 °C can be calculated using equation 2.1.

$$Q_{t3} = m\,C_{m1}(T_m - T_1) + Q_f + m\,C_{m2}(T_2 - T_m) = 1145\,\text{kJ. kg}^{-1} = 318\,\text{kWh. tonne}^{-1}$$

The energy consumption measured during the melting was 1.98 GJ.tonne^{-1} (550 kWh.tonne^{-1}) (*Table 2*). The thermal efficiency of the induction furnace can be calculated from these two figures and is given below:

$$\eta_c = \frac{1145}{1980} \times 100\% = 57.8\,\%$$

5   Comparison and discussion of energy consumption between traditional foundry and the new casting method

The normal thermal efficiency (average $\eta_1 = 13\,\%$) of crucible furnace for melting Al alloys using gas and the thermal efficiency ($\eta_1' = 10.4\,\%$) of furnace using LPG at G&W are in the normal range 7~19 % although it is a bit lower than the expected average value (13 %). The difference in the thermal efficiency ($\eta_2' = 6.14\,\%$) of holding furnace using electricity at G&W with the normal thermal efficiency ($\eta_2 = 59 \sim 76\,\%$) of an induction furnace was a much larger than expected. This suggests that there are great savings to be made in identifying why these poor efficiencies exist. If it were possible to replace the large holding and melting furnaces at G&W by single shot melting then melting efficiencies could be improved by upwards 40%. Thus reducing production cost.

During the "Test bar" experiment using the new up-casting facility, the thermal efficiency η_c was calculated as $57.8\,\%$ which is close to the normal thermal efficiency of an industrial induction furnace ($\eta_2 = 59 \sim 76\,\%$). The reason for the heat loss in up-casting process facility can be attributed to radiation, conduction and convection between the melt and the surrounded environment. When melting the same weight of the Al alloys, G&W used 22.6 times more energy than the new casting facility. It is estimated that 42.8 GJ.tonne^{-1} (11.9 MWh.tonne^{-1}) can be saved for producing every tonne of A354 casting alloys when using the new process.

Further reasons for recommending choosing the new casting method and as opposed to using crucible furnace in G&W are: a crucible furnace is less expensive melting method for melting Al alloys which is popular in foundry due to its easy for tapping and charging different alloys. However, the thermal efficiency of the crucible furnace is far lower (7~19 %) than the new casting method (57.8 %), and the temperature of the melted alloys is difficult to control. It has been proved in the case of G&W where the thermal efficiency is only 10.4 %. Furthermore, the new up-casting method uses a quick pouring method as soon as the alloy is heated to the casting temperature, avoiding using holding furnace or needing holding time, reduces the potential energy waste. In the mean time, due to the rapid melting and filling processes, the possibility of producing the oxide film on the surface of the melted Al alloys and the potential time for hydrogen ingress are drastically reduced. Therefore, the quality of the casting can be assured.

6   Conclusions and future work

Comparing the thermal efficiency and energy consumption of melting processes between the traditional foundry and the novel melting method, both the theoretical calculation and the experiment results give the following conclusion: the new method is an advanced method for saving energy in the casting industry. If the traditional foundries in the study could use the novel melting method instead of their usual method, the estimated energy savings could be of the order of 43 GJ.tonne^{-1} (11.9 MWh.tonne^{-1}) for A354 alloy. This would drastically reduce their production cost by about

£904 pounds.tonne^{-1} (7.6 p.kWh^{-1}). This will become more important in the intensively competitive market of the future.

The other aspects of the energy consumption for the whole foundry will be further considered in the research project which is not only consider the melting process, but also include casting and other relevant processes.

References
[1] V.J. Saha, Energy Efficiency Improvement in Melting Furnaces, Report, World Foundrymen Organisation, 2010.
[2] R. Eppich, R.D. Naranjo., Implementation of Metal Casting Best Practices, Report of U.S. Department of Energy, 2007.
[3] M. Jolly, Energy Saving in the Foundry Industry by Using the "CRIMSON" Single Shot UP-Casting Process, 2010 TMS Annual Meeting & Exhibition, Febuary 14-18, 2010, Seattle, WA.
[4] M. Seppanen, Foundrybench-D3 Description of common energy analysis methods, tools and reporting templates appropriate for the purpose of the project, Report, 2009.
[5] J.F.Schifo, J.T. Radia., Theoretical/Best Practice Energy Use in Metalcasting Operations, KERAMIDA Environmental, Inc. Indianapolis, May 2004.
[6] J. C. Geelin, M. Lovis & M.R. Jolly, SIMULATION OF TENSILE TEST BARS: DOES THE FILLING METHOD MATTER?, Symposium on Simulation of Aluminum Shape Casting Processing, TMS2006 March 2006, Warrendale, PA, Eds Q. Wang, M.J.M Krane and P.D Le.
[7] C. Schmitz, Handbook of aluminium recycling: Fundamentals, Mechanical Preparation, Metallurgical Processing, Plant Design, Vulkan-Verlag GmbH, Germany, 2006.
[8] MatWed MATERIALS PROPERTY DATA, http://www.matweb.com/search/MaterialGroupSearch.aspx
[9] BSC, Incorporated, Advanced Melting Technologies: Energy Saving Concepts and Opportunities for the Metal Casting Industry, Report, U.S. Department of Energy, 2005.
[10] Wikipedia-Energy density: http://webcache.googleusercontent.com/search?q=cache:COLNRlCHJmUJ:en.wikipedia.org/wiki/Energy_density+lpg+density&cd=2&hl=en&ct=clnk&gl=uk&client=firefox-a

Significant Thermal Energy Reduction in Lactic Acid Production Process

Iqbal M. Mujtaba[a]*, Elmahboub A. Edreder[b], Mansour Emtir[c]

[a] School of Engineering, Design and Technology, University of Bradford, West Yorkshire, BD7 1DP, United Kingdom
[b] Libyan Petroleum Institute, P.O. Box 6431, Tripoli, Libyan Arab Jamahiriya.
[c] National Oil Corporation, P.O. Box 2655, Tripoli, Libyan Arab Jamahiriya

* Corresponding Author. Tel: +44 1274 233645   Email: I.M.Mujtaba@bradford.ac.uk

Abstract

Lactic acid is widely used as a raw material for the production of biodegradable polymers and in food, chemical and pharmaceutical industries. The global market for lactic acid is expected to reach 259 thousand metric tons by the year 2012. For batch production of lactic acid, the traditional process includes the following steps: (i) esterification of impure lactic acid with methanol in a batch reactor to obtain methyl lactate (ester), (ii) separation of the ester in a batch distillation, (iii) hydrolysis of the ester with water in a batch reactor to produce lactic acid and (iv) separation of lactic acid (in high purity) in a batch distillation. Batch reactive distillation combines the benefit of both batch reactor and batch distillation and enhances conversion and productivity (Taylor and Krishna, 2000; Mujtaba and Macchietto, 1997). Therefore, the first and the last two steps of the lactic acid production process can be combined together in batch reactive distillation (Figure 1) processes. However, distillation (batch or continuous) is an energy intensive process and consumes large amount of thermal energy (via steam). This paper highlights how significant (over 50%) reduction in thermal energy consumption can be achieved for lactic acid production process by carefully controlling the reflux ratio but without compromising the product specification. In this paper, only the simultaneous hydrolysis of methyl lactate ester and the separation of lactic acid using batch reactive distillation is considered.

Keywords   Lactic acid; hydrolysis; batch reactive distillation; optimization; reflux ratio policy; energy reduction

1   Introduction

Taylor and Krishna [1] provided a comprehensive list of research on the use of Reactive Distillation (batch and continuous) system for producing many useful products/chemicals via a number of chemical reactions and distillations.

1.1   Lactic acid production process

Esterification of impure lactic acid with methanol has been considered by several researchers in the past to obtain methyl lactate ester which is then separated by distillation. The distilled ester is then hydrolyzed into pure lactic acid (Figure 1).

Choi and Hong [3] used two reactors and two batch distillation columns to carry out the esterification and hydrolysis reactions and achieved relatively pure lactic acid. Kim *et al.* [4] considered a batch reactive distillation with esterification and hydrolysis for the recovery of lactic acid and studied the dynamics of batch reactive distillation of lactic acid in terms of instantaneous rate of esterification reaction. They also compared semi-batch operation with the batch mode with continuous feeding of methanol. Kumar *et al.* [5] explored and investigated batch reactive distillation strategy involving experimental esterification and hydrolysis reaction for recovery of pure lactic acid. They studied the effect of operating parameters such as feed concentration, mole ratio; catalyst loading, and boilup rate on the recovery of lactic acid.

Li *et al.* [6] considered the esterification of diluted lactic acid with methanol in a reactor followed by hydrolysis of methyl lactate in continuous column to achieve pure lactic acid. Kumar *et al.* [7] carried

out both experiments and simulation of a continuous reactive distillation process for esterification of lactic acid and hydrolysis of methyl lactate to get pure lactic acid.

1.2   This work

It is clear from the previous researches that most of the work has been focused on experiments or simulation to recover lactic acid. No work has focused on the thermal energy requirement or discussed about the possibility of energy saving in lactic acid production process. Therefore, this is the main focus of this paper. Here, energy minimisation (or savings) is achieved via minimisation of production time which is obtained by optimising reflux ratio in a batch reactive distillation process. Successive Quadratic Programming (SQP) based techniques [8] is used for solving the optimisation problem.
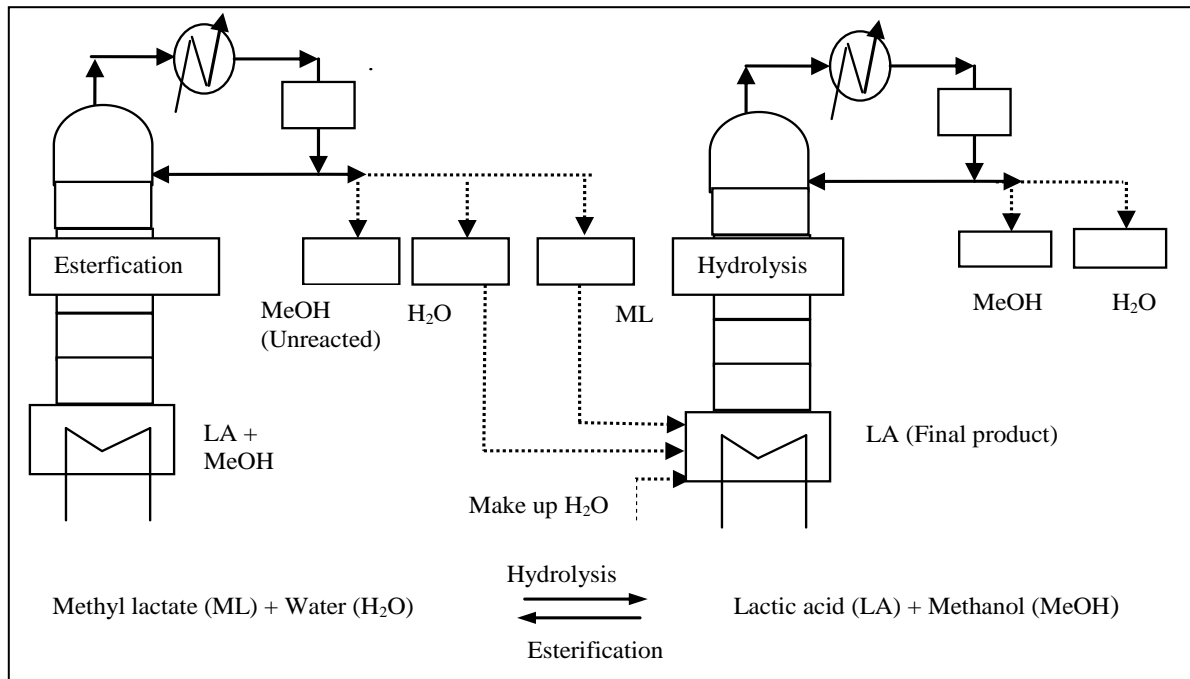
Figure 1: Lactic acid production process by batch reactive distillation

2   Energy consumption

Traditionally, the most popular type of batch distillation column is conventional (regular) batch column (CBD) as shown in Figure 1. It consists of a bottom receiver/reboiler, rectifying column (either a tray or packed column) placed over the reboiler, connected to a total condenser or a partial condenser system and distillate receivers. In this column, the charge is loaded into the reboiler at the beginning of the process and heated to its boiling point. Vapour flows upwards in the column and condenses at the top. After some time, a part of the overhead condensate is withdrawn continuously as distillate, and the other part is returned to the column section as reflux (note: the ratio of the liquid being refluxed to the column and the condenser vapour load defines the internal reflux ratio which is used in the work).

The liquid in the reboiler is increasingly depleted of the more volatile components and the boiling point of the mixture gradually increases. Also, as the amount of liquid in the reboiler decreases, the concentration of high-boiling components increases. In batch distillation literature [8, 9], it can be found that a batch distillation column operates under the following modes:

a. Mode 1 - Constant reboiler duty (Q): Heat supply (usually in the form of steam) to the reboiler is constant over the batch time (production time). In this mode, the vapour boilup rate gradually decreases as the boiling point gradually increases (note the latent heat of vaporisation is higher for high-boiling component compared to that of a low boiling component).

b. Mode 2 - Constant vapor boilup rate (V): In this mode, the heat supply to the reboiler gradually increases to maintain the constant vapour boilup rate. This is due to increase of the latent heat of vaporization of the reboiler mixture.

c. Mode 3 - Constant condenser vapour load (V_c): In this mode, the vapour load to the overhead condenser is kept constant. Also, in this mode the heat supply to the reboiler (Q_r) gradually increases.

The total energy requirement over the batch time (i.e. over the production time) for any of these operating modes can be given by:

Mode 1: $Q_{Total} = Q \times t_f$ (1)

Mode 2: $Q_{Total} = V \int_0^{t_f} \lambda dt$ (2)

Mode 3: $Q_{Total} = \int_0^{t_f} Q_r dt$ (3)

Where, λ is the instantaneous value of the latent heat of vaporization which is a function of reboiler composition which changes as the batch progresses in time. Q_r is the instantaneous value of the heat supply needed to maintain constant V_c. Note, V_c is always smaller than V and depends on the mass transfer rate and column pressure drop. Whatever the mode of operation is chosen, clearly, the amount of energy savings is directly dependent on the reduction in batch time without compromising the product specification.

3   Production period

Generally the production period starts when distillate removal from the process is begun. The operation in the product period and its duration depends on the requirements of the product. This period can be operated under the following conditions:

- Policy-1: The start-up period is ended when the desired distillate purity is reached. Product take off is started and the product is collected at constant composition by varying the reflux ratio until a specified amount of distillate has been collected. This type of operation is known as "variable reflux operation" or "constant distillate composition operation". In this mode of operation the reflux ratio is such that always produces on-specification material.
- Policy-2: The total reflux start-up period is ended when the unit reaches it steady state. Product is collected at some constant finite reflux ratio until the accumulated product composition reaches its desired purity. This type of operation is known as "constant reflux operation". Under this operation mode the column is operated on a fixed reflux ratio for the whole fraction (cut), producing better than specification material at the beginning and distillate below specification at the end of the fraction.

The above two types of operation policies are referred to as "conventional" method of operation in the literature although none of them addresses the issue of energy consumption or energy savings. Note, the second type of operation is the easiest from control point of view and is the most used in industries [8, 9].

4   Energy reduction

As mentioned in section 2, minimisation of batch time will minimise the total energy consumption of the process. Therefore, a third type of operation (Policy-3) which is a trade off between the above two types of operation (described in section 3) will be considered in this work where an optimal reflux ratio policy will be chosen so that a given amount of lactic acid product with a given purity can be achieved in minimum time to minimise the energy consumption of the process. Operating Policy-2

will also be considered in this work to demonstrate significant energy savings between Policy-2 and Policy-3. Note, Masoud and Mujtaba [10] utilised operating Policy-3 in Inverted Batch Distillation column to study the impact of this operation policy on the design and energy consumption of process for binary (no-reactive) separations. Note, huge literature is available which demonstrates how reflux ratio minimises batch time for a given design of the column and for a fixed vapour load operation. Readers are directed to Mujtaba [8] and Diwekar [9] for a comprehensive review on this.

In this work, the hydrolysis reaction is considered for the lactic acid production. For a given amount of lactic acid product with a range of lactic acid purity (from 0.8 to 0.95 molefraction of lactic acid) *minimum time* optimisation problems are formulated incorporating a mathematical model for the batch reactive distillation process within gPROMS software [11]. The lactic acid being the heaviest in the reaction mixture, reflux ratio policy plays an important role in removing the light product methanol from the system while ensuring the presence of both reactants in the reaction zone to maximise the conversion to lactic acid. Therefore, for a given column configuration (in terms of number of stages), the minimum operation time is obtained by optimising the reflux ratio profile. The optimisation problem can be described as:

given: the column configuration, the feed mixture, condenser vapour load, product purity and the amount of bottom product (lactic acid).
determine: optimal reflux ratio which governs the operation
so as to minimise: the operation time.
subject to: equality and inequality constraints (e.g. model equations).

Mathematically, the Optimisation Problem (OP) can be represented as:

$$
\begin{array}{ll}
\underset{R(t)}{Min} & t_f \\
\text{s.t.} & \\
\text{Process Model Equations} & \text{(equality constraints)} \\
B = B^* & \text{(inequality constraint)} \\
x_3^* \leq x_3 \leq +\varepsilon & \text{(inequality constraint)}
\end{array}
\tag{4}
$$

Where B, x_3 are the amount of bottom product (lactic acid) and composition at the final time t_f, (* denotes that the B and x_3 are specified), $R(t)$ is the reflux ratio profile which is optimized. ε is the small positive number of the order of 10^{-3}. The process model in the form of differential algebraic equations (DAE) (see section 5) acts as equality constraint to the optimization problem.

Single and multiple reflux ratio strategies are used, yielding an optimal reflux ratio policy. Single reflux ratio policy will represent operating Policy-2 described in section 3. For multiple reflux ratio policy, the total batch time is divided into multiple intervals. Within each interval, the reflux ratio (assumed constant) and the interval length are optimized. The optimisation problems results in a Non Linear Programming (NLP) problem, which is solved using an SQP-based optimization technique available within gPROMS [11].

5   Process model

A schematic diagram of batch reactive distillation column is shown in Figure 2 and a dynamic model for the process is shown in Figure 3 [12].

Condenser and Accumulator

V_1, y_1

L_1, x_1

V_{j+1}, y_{j+1}

L_{j-1}, x_{j-1}

Plates

V_j, y_j

L_i, x_i

V_N, y_N

Reactor /Reboiler
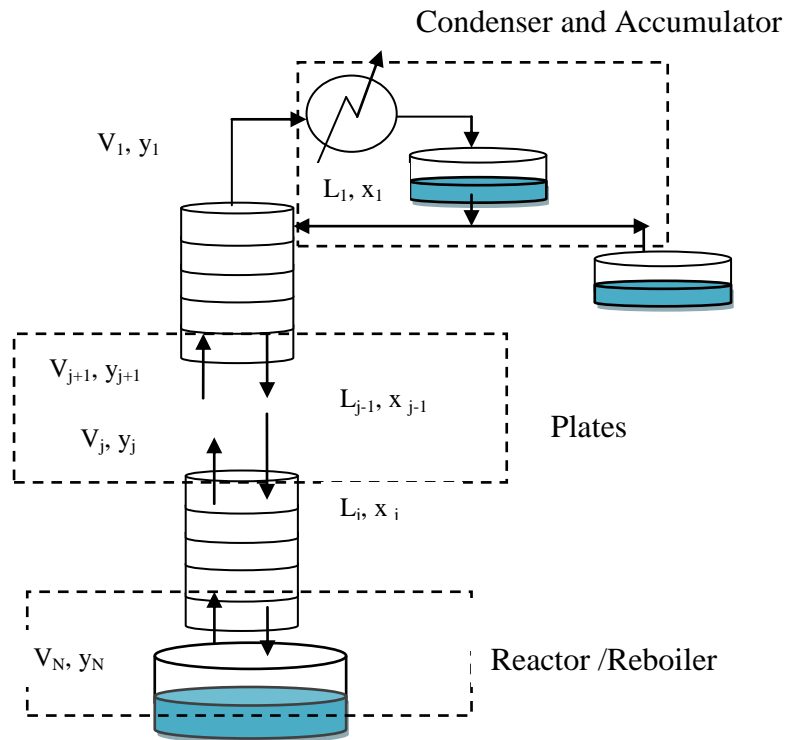
Figure 2: Conventional Batch Reactive Distillation Column

Internal Plates, j = 2, N-1

Total Mass Balance:

$$0 = L_{j-1} + V_{j+1} - L_j - V_j + \Delta n_j H_j$$

Component Mass Balance:

$$H_j \frac{dx_{ji}}{dt} = L_{j-1} x_{j-1,i} + V_{j+1} y_{j+1,i} - L_j x_{ji} - V_j y_{ji} + r_{ji} H_j$$

Energy Balance:

$$0 = L_{j-1} h^L_{j-1} + V_{j+1} h^V_{j+1} - L_j h^L_j - V_j h^V_j$$

Equilibrium:

$$y_{ji} = K_{ji} x_{ji} ,$$

Restrictions:

$$\sum y_{ji} = 1$$

Relations defining physical properties:

$$K_{ji} = K_{ji}(y_j, x_j, T_j, P)$$

$$h^L_j = h^L_j(x_j, T_j, P) , \quad h^V_j = h^V_j(y_j, T_j, P)$$

$$r_{ji} = r_{ji}(k_{ji}, x_{ji}) , \quad \Delta n_j = \sum r_{ji}$$

Condenser and Distillate Accumulator: j=1

Accumulator Total Mass Balance:

$$\frac{dH_a}{dt} = L_D$$

Component Mass Balance:

a) Accumulator:

$$H_a \frac{dx_a}{dt} = L_D(x_{D,i} - x_{a,i})$$

b) Condenser Holdup Tank

$$H_c \frac{dx_{Di}}{dt} = V_2 y_{2,i} + \eta_{1,i} H_c - (V_2 + \Delta n_1 H_c) x_{Di}$$

Energy Balance:

$$0 = V_2 h^V_2 - (V_2 + \Delta n_1 H_c) h^L_1 - Q_c$$

Other Equations:

$$L_1 = R(V_2 + \Delta n_1 H_c) , \quad L_D = (V_2 + \Delta n_1 H_c)(1 - R)$$

$$T_1 = T_1(x_{D,i}, P) , \quad h^L_1 = h^L_1(x_{D,i}, T_1, P)$$

Reboiler: j = N

Total Mass Balance:

$$\frac{dH_N}{dt} = L_{N-1} - V_N + \Delta n_N H_N$$

Component Mass Balance:

$$H_N \frac{dx_{Ni}}{dt} = L_{N-1}(x_{N-1,i} - x_{Ni}) - V_N(y_{Ni} - x_{Ni})$$
$$+ r_{Ni} H_N - \Delta n_N H_N x_{Ni}$$

Energy Balance:

$$0 = L_{N-1}(h^L_{N-1} - h^L_N) - V_N(h^V_N - h^L_N) + Q_R$$

Figure 3: Model Equations

5.1   Chemical reaction and kinetics

The hydrolysis reaction of methyl lactate (ester) can be expressed as:

$$\text{Methyl lactate (1)} + \text{Water (2)} <=> \text{Lactic acid (3)} + \text{Methanol (4)} \qquad (5)$$

| *Boiling Point (K)* | *417.15* | *373.15* | *490.15* | *337.15* |

A quasi-homogeneneous (QH) activity ($a_i = \square_i x_i$) based kinetic model is used [13] and can be written as:

$$-r = 1.65 \times 10^5 \exp(\frac{-50.91}{RT})a_1 a_2 - 1.16 \times 10^6 \exp(\frac{-48.52}{RT})a_3 a_4 \qquad (6)$$

5.2   Vapor-liquid equilibrium (VLE)

K-values (VLE constants) are computed from (Eq. 7) where γ_i is computed from UNIQUAC equation. The vapor pressure (P^{sat}) of pure components is calculated by using Antoine's equation. The UNIQUAC binary interaction parameters and Antoine parameters were taken from Sanz *et al.* [14].

$$K = \gamma_i P_i{}^{sat} / P \qquad (7)$$

The Antoine parameters are given in *Table 1*. Volume and area parameters for the UNIQUAC equation were taken from the data bank of HYSYS and are also given in *Table 1*. The UNIQUAC binary interaction parameters are given in *Table 2*.

Vapour phase enthalpies are calculated using empirical equations from Holland [15]. The physical and thermodynamic properties data and enthalpy equations for all pure components are given in *Table 3* and *Table 4*.

Table 1
Antoine parameters and area and volume parameters

Component	A	B	C	r	q
Methyl Lactate (*1*)	7.24147	2016.46	-32.104	5.95005	5.01723
Water (*2*)	7.0436	1636.909	-48.230	0.92000	1.39970
Lactic Acid(*3*)	7.51107	1965.7	-91.021	5.27432	4.47617
Methanol (*4*)	7.21274	1588.63	-32.5988	1.4311	1.4320

Table 2
Binary interaction parameters for UNIQUAC equation

	Aij/K	Aji/K
Methanol-Water	-192.6	325.0
Methanol-Methyl lactate	866.6	-164.4
Methanol - Lactic acid	322.59	17.14
Water – Methyl lactate	-20.05	325.31
Water- Lactic acid	-84.80	-26.1
Methyl lactate- Lactic acid	367.14	-302.09

Table 3
Physical and thermodynamic properties for pure components

	Methyl Lactate (1)	Water (2)	Lactic acid (3)	Methanol (4)
Tc (K)	584.0	647.3	627.0	512.6
M.wt	104.11	18.02	90.08	32.04
λ_1 (KJ/kmol)	38177	40651	54670	35290
T_b (K)	417.95	373.15	490.0	337.8

Table 4
Vapour enthalpy equations for all pure components

$$h_1^V = 104.11 \times (0.0 - 2.9834 \times 10^{-1}T + 3.4219 \times 10^{-3}T^2 - 2.43350 \times 10^{-6}T^3$$
$$+ 1.0223 \times 10^{-9} \; T^4 - 1.7705 \times 10^{-13}T^5)$$

$$h_2^V = 2.32 \times (0.1545871 \times 10^5 + 0.8022526 \times 10(T \times 1.8) - 0.4745722 \times 10^{-3}(T \times 1.8)^2$$
$$- 0.6878047 \times 10^{-6}(T \times 1.8)^3 - 0.1439752 \times 10^{-9} \; (T \times 1.8)^4)$$

$$h_3^V = 90.0784 \times (0.0 - 3.77592 \times 10^{-2}T + 2.41939 \times 10^{-3}T^2 - 1.38409 \times 10^{-6}T^3$$
$$+ 4.8395 \times 10^{-10} \; T^4 - 7.68398 \times 10^{-14}T^5)$$

$$h_4^V = 2.32 \times (0.1174119 \times 10^5 + 0.7121495 \times 10(T \times 1.8) + 0.5579442 \times 10^{-2}(T \times 1.8)^2$$
$$- 0.4506170 \times 10^{-6}(T \times 1.8)^3 - 0.2091904 \times 10^{-10} \; (T \times 1.8)^4)$$

Where h^V is in kJ/kmol and T is in °K.

The liquid and vapour enthalpies (h^L, h^V) which constitute the energy balance equations in the process model (Figure 3) are usually expressed as a function of liquid/vapour mole fractions, temperature and pressure. The liquid phase enthalpies are calculated by subtracting the latent heat of vaporisation from the vapour enthalpies.

$$h_j^V = \sum y_i h_i^V \tag{8}$$

$$h_j^L = \sum x_i (h_i^V - \lambda_i) \tag{9}$$

Where λ_i is the latent heat of vaporisation (kJ/kmol) of component i.

6   Case study
6.1   Specifications
Hydrolysis reaction and separation of Lactic Acid is carried out in a 10 stages column (including condenser and reboiler). The column is operated with energy consumption Mode 3 with condenser vapour load (V_c) of 2.5 (kmol/hr). The total column holdup is 4 % of the initial feed. Fifty percent of the total holdup is taken as the condenser hold up and the rest is equally divided in the plates. The initial charge to the reboiler is 5 kmol. The feed composition <Methyl Lactate (1), Water (2), Lactic acid (3), Methanol (4)> is : <0.5, 0.5, 0.0, 0.0>. It is assumed that the mixture in the reboiler, in the plates and in the condenser are at the boiling point at time t = 0 (beginning of the process). There is no pre-assigned period of total reflux operation. The column only runs at total reflux if it is demanded by the optimiser. The total amount of desired lactic acid product (in the reboiler) is 2.5 kmol with purity of lactic acid varying from 0.8 to 0.95 (molefraction).

Two types of reflux ratio policies are adopted to show how these policies affect the energy consumption of the process without compromising the product specifications. These are: (i) traditional constant reflux ratio Policy-1; (ii) time optimal reflux ratio Policy-3. Note, however, in Policy-1 instead of selecting a random constant reflux ratio, the reflux ratio is optimised to minimise the batch time. In Policy-3, the batch time is discretised into 2, 3 and 4 intervals and the reflux ratio is assumed to be constant in each intervals. For each interval, both the reflux ratio and the interval length are optimized to minimise the overall batch time.

6.2   Results and discussions
Table 5 summarises the optimisation results for Policy-1, in terms of constant (but optimal) reflux ratio, conversion of methyl lactate to lactic acid, minimum operating time and the total energy consumption for a range of product purity. *Tables 6-8* summarise the optimisation results for Policy-3 where time dependent reflux ratio is used.

The results of *Tables 5-8* show that as the demand on lactic acid purity increases (from 0.8 to 0.95 molefraction), high reflux ratio operation, longer batch time, increased energy consumption are required to keep the reactants together to convert to more of the desired product (lactic acid). Interestingly, with Policy-1, product purity of 0.95 molefraction was not at all achievable with very high reflux ratio and very long batch time such as 200 hrs. Single constant reflux ratio was not able to simultaneously remove methanol from the system and keep the reactants (methyl lactate and water) together to have more conversion to lactic acid. However, with reflux ratio Policy-3 (*Tables 6-8*), product purity of 0.95 was achievable. Low reflux ratio in the first interval was able to remove the methanol from the system quickly while the higher reflux ratios in subsequent intervals helped keeping the reactants together in the systems for further reaction.

Table 5
Summary of optimisation results using reflux Policy-1

Purity of Lactic acid, x_3^* (molefraction)	Minimum Batch Time, t_f (hr)	Optimum Reflux Ratio	Conversion %	Total Energy Q_{Total} (mkJ)
0.80	14.88	0.933	77.7	1.722
0.90	46.04	0.973	86.9	5.429
0.95*	*	*	*	*

*no results obtained

Table 6
Summary of optimisation results using reflux Policy-3 (2 intervals)

x_3^*	t_1, R_1	t_f, R_2	Conversion %	Q_{Total} (mkJ)
0.80	9.54, 0.914	13.72, 0.957	77.7	1.588
0.90	8.66, 0.922	23.95, 0.979	87.9	2.822
0.950	10.55, 0.935	44.73, 0.990	92.5	5.318

Note: t_1 = length of interval 1, R_1, R_2 = Reflux ratio in interval 1 and 2

Table 7
Summary of optimisation results using reflux Policy-3 (3 intervals)

x_3^*	t_1, R_1	t_2, R_2	t_f, R_3	Conversion %	Q_{Total} (mkJ)
0.800	2.33, 0.813	2.00, 0.907	11.27, 0.945	77.8	1.305
0.900	4.86, 0.886	3.74, 0.950	21.90, 0.980	88.1	2.581
0.950	6.24, 0.909	11.09, 0.975	37.82, 0.992	92.9	4.497

Table 8
Summary of optimisation results using reflux Policy-3 (4 intervals)

x_3^*	t_1, R_1	t_2, R_2	t_3, R_3	t_f, R_4	Conversion %	Q_{Total} (mkJ)
0.800	0.500, 1.00	2.11, 0.800	2.63, 0.918	10.80, 0.935	77.9	1.250
0.900	0.420, 1.00	2.70, 0.835	3.88, 0.937	20.09, 0.976	88.3	2.368
0.950	0.540, 1.00	2.93, 0.848	8.79, 0.964	34.17, 0.989	93.3	4.063

Figure 4 shows the total energy consumption profile for different product purity and for different reflux ratio policies. Cleary with the increase of product purity, the total energy consumption increases exponentially (Policy-3, with 2-4 intervals). For example, with increase in product purity from 0.8 to 0.9 molefraction (12.5% increase), the increase in total energy consumption with Policy-3 (2 intervals) is 77.7%. However, with increase in product purity from 0.9 to 0.95 molefraction (5.5% increase), the increase in total energy consumption with Policy-3 (2 intervals) is 88.4%. This is due to having comparatively higher reflux ratio and longer batch time to ensure further reaction to satisfy product purity (compare the reflux ratio profile at different purity in *Table 6* and also in *Tables 7* and *8*). Also note, for high product purity (0.95 molefraction), the column required to operate almost near to total

reflux ratio (R=1) for a longer period in order to keep the reactants together for further reaction and in order to transport lighter components up the column from the reboiler.
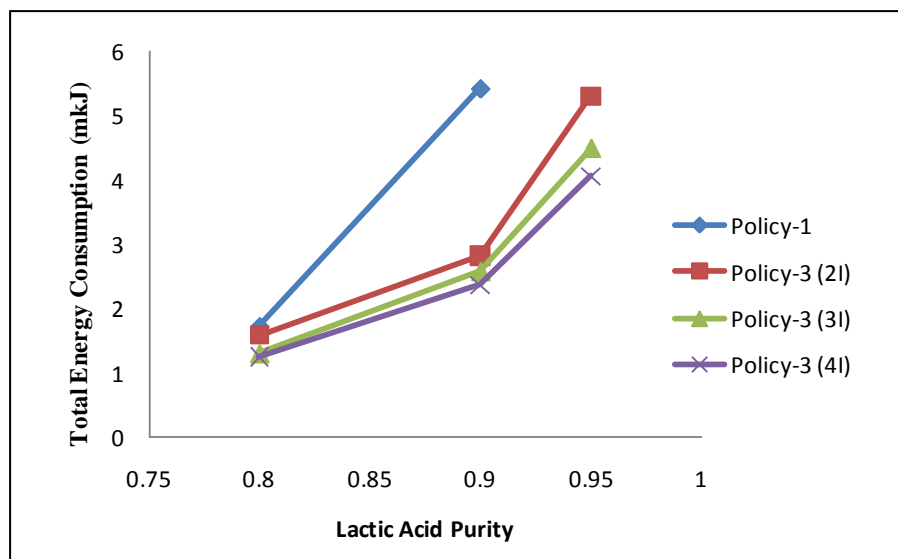
Figure 4: Total Energy Consumption Profile

For the same product purity, significant reduction in batch time and total energy consumption are possible by selecting appropriate operation strategy in terms of reflux ratio policies. For example, for product purity 0.9 molefraction, a batch time reduction of 56.4% and an energy reduction of 56.4% are possible by having 4 interval reflux ratio policy (*Table 8*) compared to 1 interval reflux ratio policy (*Table 5*). For the same product purity, even a 2 interval reflux ratio policy (*Table 6*) reduces 48% energy consumption.

For high product purity such as 0.95 molefraction, reduction in energy consumption of 24% is possible when 4 interval reflux ratio policy (*Table 8*) is adopted compared to 2 interval reflux ratio policy (*Table 6*). Note, 1 interval reflux ratio policy (*Table 5*) does not even achieve the product with the desired specifications.

Unlike esterification reaction in conventional batch reactive distillation (Figure 1) where the reaction product (Methyl lactate ester) is the lightest, the hydrolysis reaction considered in this work produces the reaction product (lactic acid) which is the heaviest in the mixture. The column has to always operate at high reflux ratio so that both the reactants (methyl lactate and water) are available in the reaction zone (reboiler and stages). Low reflux ratio operation will separate the reactants from the system and will thus lower the conversion. Multi-reflux ratio operation (Policy-3) enjoys more freedom to balance between the conversion and product purity.

6.3   Conclusions

The opportunity for thermal energy reduction in lactic acid production in batch reactive distillation process is investigated here. For a given mode of heat supply to the distillation column, minimizing the production time (i.e. batch time) without compromising the product specifications offers potential reduction in thermal energy consumption. For a given column configuration (i.e. number of stages), reflux ratio policy determines the product amount, quality and batch time.

A dynamic optimization problem incorporating a process model is formulated to minimize the batch time subject to constraints on the amount and purity of lactic acid. Piecewise constant reflux ratio profile (with single and multiple time intervals) is considered for exploring the potentials for thermal energy reduction. A series of minimum time optimisation problems was solved with different values of lactic acid purity ranging from 0.8 to 0.95 molefraction and the impact of time dependant reflux ratio policy on the thermal energy consumption are analyzed.

It is observed that about 56% reduction in thermal energy is possible for certain product specification by operating the column with multi-reflux ratio strategy instead of operating the column with traditional single-reflux ratio strategy. It is also observed that 95% purity of lactic acid was not achievable with single-reflux ratio operation policy as the policy was not able to keep the reactants together for a longer period in the column to have further conversion to lactic acid to satisfy the product purity. Multi-reflux operation policies enjoyed additional freedom to have the balance between the conversion and the product purity while reducing significant amount of energy consumption.

Finally, the methodology to calculate the energy requirement and to explore the scope of energy savings as presented in this work is general and is applicable to other reaction system. Also energy minimization is achieved in this work via minimization of production time. Readers are directed to other methods of energy optimisation, for example, Marshman et al. [16] achieved energy optimisation for a pulp and paper mill via total cost minimization.

Nomenclature

L_D	distillate flow rate (kmol/hr)
H_a, H_c	accumulator and condenser holdup respectively (kmol)
H_j, H_N	plate and reboiler holdup respectively (kmol)
h^L, h^V	liquid, vapour enthalpy (kJ/kmol)
L, V	liquid, vapour flow rates in the column (kmol/hr)
N	number of plates
Q_C, Q_R	condenser or reboiler duty (kJ/hr)
T, P	temperature (K), pressure (bar)
K	vapour-liquid equilibrium constant
r	reaction rate
t	batch time (hr)
R_1, R_2, etc.	reflux ratio in time interval 1, 2, etc.
t_1, t_2, etc.	length of interval 1 2 , etc., hr
x, y	liquid or vapour composition (mole fraction)
x_a	accumulated distillate composition (mole fraction)
x_D	instant distillate composition (mole fraction)
Δn	change in moles due to chemical reaction
D	amount of product (kmol)
R	reflux ratio

Superscripts and subscripts

i	component number
j	stage number

References

[1] Taylor R, Krishna R. Modelling of reactive distillation-Review. Chem Eng Sci 2000;55:5183-5229.
[2] Mujtaba IM, Macchietto S. Efficient optimisation of batch distillation with chemical reaction using polynomial curve fitting techniques. Ind Eng Chem Res 1997;36:2287-2296.
[3] Choi J, Hong WH. Recovery of lactic acid by batch distillation with chemical reaction using ion exchange resin. J Chem Eng Japan 1999;32:184–189.
[4] Kim JY, Kim YJ, Hong WH, Wozny G. Recovery process of lactic acid using two distillation columns. Biotechnol Bioprocess Eng 2000;5:196-201.
[5] Kumar R, Mahajani SM, Nanavati H, Noronha SB. Recovery of lactic acid by batch reactive distillation. J Chem Technol Biotechnol 2006;81:1141-1150.
[6] Li MA, Yang Z, Jichu Y. Purification of lactic acid by heterogeneous catalytic distillation using ion-exchange resins. Chinese J Chem Eng 2005;13: 24- 31.
[7] Kumar R, Nanavati H, Noronha SB, Mahajani SM. A continuous process for the recovery of lactic acid by reactive distillation. J Chem Technol Biotechnol 2006;81:1767-1777.

[8]   Mujtaba IM. Batch distillation: Design and operation. London: Imperial College Press; 2004

[9]   Diwekar UM. Batch Distillation. Simulation, Optimal Design and Control, New York: Taylor & Francis; 1995

[10] Masoud AZ, Mujtaba IM. Effect of operating decisions on the design and energy consumption of Inverted Batch Distillation column. Chem Prod Proc Mod 2009;4(1), Article 35:1-10

[11] gPROMS. Introductory User Guide, Process System Enterprise Ltd (PSE). 2004

[12] Edreder EA, Mujtaba IM, Emtir, MM (2009). Optimisation of Design, Operation and Scheduling of Batch Reactive Distillation Process with Strict Product Specification and Fixed Product Demand using gPROMS, Comput Aided ChemEng 2009; 26:411-415.

[13] Sanz MT, Murga R, Beltran S, Cabezas JL, Coca J. Kinetic study for the reactive system of Lactic Acid esterification with methanol: Methyl lactate hydrolysis. Ind Eng Chem Res 2004;43: 2049-2053.

[14] Sanz MT, Beltran S, Calvo B, Cabezas JL. Vapor Liquid Equilibria of the Mixtures involved in the esterification of lactic acid with methanol. J Chem Eng Data 2003;48:1446-1452.

[15] Holland CD. Fundamentals of Multicomponent Distillation. New York: McGraw-Hill. 1981.

[16] Marshman DJ, Chmelyk T, Sidhu MS, Gopaluni RB, Dumont GA. Energy optimization in a pulp and paper mill cogeneration facility. Applied Energy 2010;87:3514–3525

Sequential Modelling of Thermal Energy: New Potential for Energy Optimisation in Papermaking

Puya Afshar [a*]**, Martin Brown** [a]**, Paul Austin** [b]**, Hong Wang** [a]**, Timofei Breikin** [a]**, Jan Maciejowski** [b]

[a] Control Systems Centre, School of Electrical and Electronic Engineering, The University of Manchester, Manchester, M13 9PL, United Kingdom
[b] Cambridge University Engineering Department, Trumpington Street, Cambridge, CB2 1PZ, United Kingdom

* Corresponding author. Email: puya.afshar@manchester.ac.uk; Tel. +44(0) 161 306 4665; Fax. + 44(0) 161 306 4665

Abstract
Papermaking is known as an energy-intensive, but not always efficient industry. This is at least partly due to the fact that the majority of papermaking technologies and procedures were established at a time when energy was both cheap and plentiful. A considerable fraction of the energy required for papermaking is consumed in removing water by the use of steam in the paper machine's drying section. It is also known that even a small reduction in steam use can result in a significant reduction in production costs and environmental effects. To date, a great deal of research has been undertaken, aimed at improving the performance of the drying section by making more efficient use of dryer steam. This paper investigates a new approach to reducing thermal energy use in paper making by seeking to enhance the amount of water removed in sections of the machine prior to the drying section. The proposed method is focused on sequential modelling of the effect of vacuums used in the forming section on the thermal energy consumption in the drying section. The primary models explain how different vacuum pressures can affect the flow of water from the sheet in the forming section whilst the secondary models describe the effect of increased drainage on the steam requirements in the dryer. Operational data from a UK paper mill are used to illustrate the proposed method. The models developed can have subsequent application to optimising the use of thermal energy in paper making.

Keywords   energy auditing; thermal energy modelling; sequential processes

1   Introduction

Papermaking is an energy-intensive operation, due at least in part to the fact that most of the associated machinery and production procedures were designed at a time when energy was both cheap and plentiful. Recent statistics from the UK Department of Energy and Climate Change compare the energy consumption figures of different sectors of the UK's manufacturing industry. *Table 1* summarises the aggregated oil equivalent energy used across several major industries of the UK in 2008 [1]. As the summary shows, papermaking is the fourth biggest energy consumer in the UK's manufacturing industry.

Table 1
Aggregated energy use in various sectors of UK industry in 2008

Industry	*Thousand tonnes of oil equivalent*
Chemicals	*5,540*
Food and beverages	*3,591*
Mineral products	*2,553*
Pulp and paper	*2,226*
Mechanical engineering	*1,488*

It is also believed that energy is the third highest cost in the papermaking process, accounting for approximately 8 % of turnover. According to UK government statistics summarised in *Table 2*, in 2008 UK papermaking used on average 4MWhr per tonne of paper made.

Table 2
UK Energy Use in Papermaking branches

Paper Type	Specific Energy (MWhr/t)
Newsprint	*3-4*
Packaging board	*2-3*
Fine papers	*4-8*
Tissues	*5-6*
UK Average	**4**

The rising costs of energy and an increasing awareness of the environmental footprint of the paper industry have focussed attention on the crucial importance for paper mills of energy optimisation in order to maintain their financial sustainability as well as to meet customer satisfaction. So far, attention has been drawn to improved heat recovery schemes [2], and to the application of more energy-efficient equipment such as Variable Speed Drives (VSDs) wherever drive technology has been required [3]. Although these approaches have proved to be effective in reducing energy use, they imply significant financial overheads. In this regard, less attention has been drawn to alternative approaches that may prove to be at least as viable commercially, such as improved utilisation and extension of the functionality of existing resources. With better exploitation of the existing data, more comprehensive understanding of the process and energy consumption models can be obtained. This understanding can then be employed to develop advanced techniques to control the process in such a way as to meet energy optimisation objectives while also maintaining variables within specified limits. This type of process awareness can be obtained by appropriate use of existing Distributed Control Systems (DCS) in order to improve the energy efficiency of the process. The proposition underlying much of our current work is that by exploiting the potential of automation technology and implementing integrated optimisation algorithms the energy efficiency of the overall operation may be improved at more feasible cost.

The main requirement for implementing such a proposition is acquiring suitable insights relating to the process, production, and the consumption of energy. This approach is often referred to as energy auditing. In an energy audit existing plant information is utilised to locate the sections of the plant where the largest proportions of mill-wide energy are consumed. Subsequently, data analysis is performed to determine the process variables which have significant effects on energy usage. The results are then evaluated to identify a number of feasible approaches to reducing energy use. The ultimate goal of energy optimisation based on process data is to tune a group of process settings in such a way as to *(a)* enhance product quality and *(b)* reduce energy consumption. This approach to optimisation requires a set of process and performance models that can predict reliably the consequences of energy optimisation plans prior to online application. Modelling can be based solely on the process' operational data (black-box modelling), on first-principle mathematical models, or on a combination of both approaches (grey-box modelling). If they can be developed, first principle models have the advantage of accuracy; however, they are often difficult to obtain due to unmeasured uncertainties, unknown process interactions, and the large number of unknown parameters and coefficients to be determined, or time varying process dynamics. On the other hand, although black-box models are easier to obtain, their validity may be limited to the range of specific training data. That is, extrapolation is usually not possible to operating points beyond the training data [4].

Considering the papermaking industry, the majority of existing energy optimisation approaches which are based on modelling and advanced control have focused on improving the efficiency of the drying section. This has included using advanced control techniques to tune the steam pressure (or flow) more precisely. For instance, [5] and [6] employ the black-box approach to develop a non-linear neural network model of the drying section by considering air temperature and initial web moisture content as inputs and final paper moisture content and finished paper temperature as outputs. Also, a paper quality model developed using the black-box approach has been developed in [7] to model the variations of the stiffness and tensile strength of paper. By employing the black-box modelling approach, this paper aims at global (mill-wide) identification of the potential opportunities for

improving quality and for more efficient use of energy. It also provides a means of predicting the consequences of optimisation, prior to online application.

There are two main features associated with the approach introduced in this paper:

- As papermaking is comprised of sequentially linked processing units, it is difficult to develop a single model explaining the dynamic relationship of the process and performance measures. A chain of models needs to be developed and considered so that the effect of intermediate processing units on energy and (or) quality can be studied.
- As the approach applies black-box modelling, models can be sensitive to data quality. That is, measurement noise, parameter uncertainties and process variability can considerably affect the reliability of the models. This can be tackled by effective noise filtering and, more importantly, by gathering high quality (persistently exciting) data from the plant.

This paper is organised as follows. In section 2, the papermaking process is briefly introduced. In section 3, an overview of energy auditing is presented. Also in this section, a MATLAB™-based software tool called 'DataExplorer', developed for Exploratory Data Analysis (EDA), is briefly introduced. In section 4 the results of data exploration in two UK-based commercial paper mills are presented, together with suggestions for other possible energy reduction scenarios. Section 5 presents the idea of sequential modelling in papermaking. Finally, concluding remarks are made in section 6.

2   Introduction to papermaking

During the process of papermaking, virgin, de-inked, or recycled fibres alongside different fibrous materials and fillers are used as raw materials and additives. Roughly speaking, papermaking is the art of appropriately mixing the raw materials at the correct consistency and moisture content and de-watering the spread suspension to form the final sheet. The paper and paperboard making process is usually comprised of several sections, depicted in Figure 1: Stock Preparation, Stock Approach, and various Paper Machine sections.
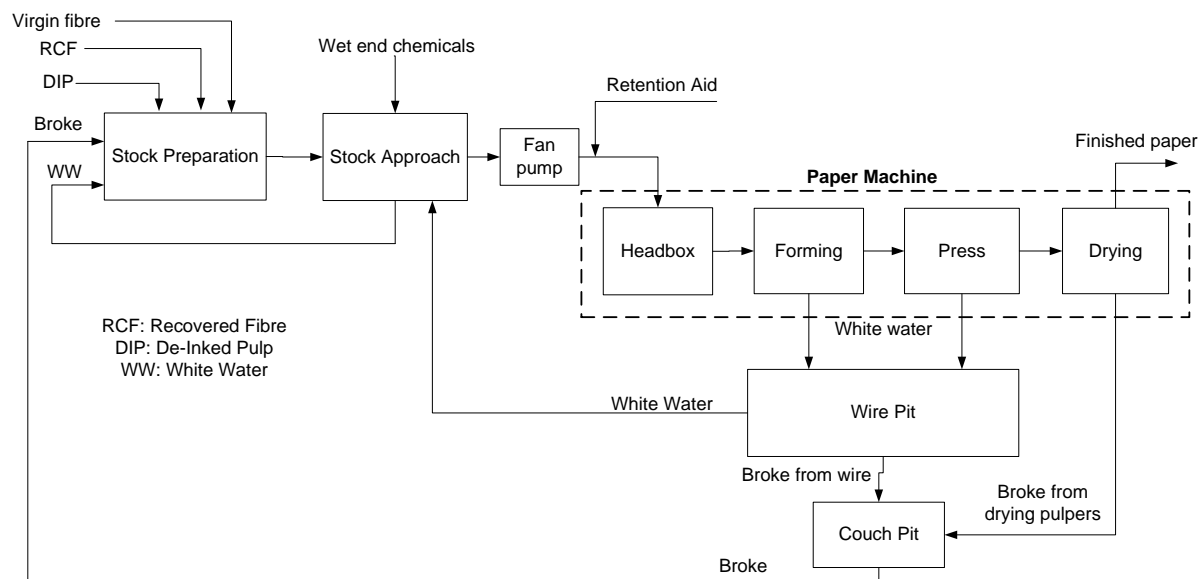
Figure 1: Schematic diagram of a typical paper mill

2.1   Stock preparation system

In the stock preparation section Virgin Fibre, De-Inked Pulp (DIP), Recovered Fibre (RCF), returning White Water (WW) and Broke are processed to produce a thick stock for the paper machine. In this section the fibres are first disintegrated, then cleaned, modified, and mixed to prepare the raw material suitable for the paper machine. The quality of prepared thick stock usually has a determining effect on the quality of the finished paper. Generally, in the stock preparation section the fibres are purified

mechanically by means of refiners, screens, centrifugal cleaners, and multi-stage filters. The stock is then pumped to storage and mixing chests which act as buffers to ensure the continuity of supply to the paper machine. Depending on the paper grade to be produced, prepared stock types are proportionately mixed in the mixing tanks to the required fibre consistency [8].

2.2   Stock approach system

The stock approach system is designed to ensure that the stock delivered to the paper machine's headbox has appropriate properties. For example, the amount of dissolved air in the stock must be regulated. Air removal, which is one of the two most important functions of the stock approach system, is realised using a deculator vessel and a number of vacuum pumps located near the headbox fan pump. Also, as solids retention can be problematic in high speed and low grade machines, certain polymers known as retention aids are usually added in the stock approach system to enhance retention, by tuning the electrical charge of the white water and its turbidity [8].

2.3   Paper machine

As shown in Figure 1 the paper machine consists of the headbox, which suspends the fibres onto the wire and creates uniform distribution of fibres across the wire, as well as the forming, press and drying sections, which remove moisture from the web by vacuum-assisted de-watering, mechanical pressing, and steam-assisted heating, respectively. The most common machine design is the Fourdrinier in which the sheet is formed onto a continuous horizontal wire. Recently, twin wire formers (gap formers) have been used for web formation in which the fibre suspension is fed between two wires operating at the same speed where the water is drained in two directions. In gap formers the diluted stock is injected directly into the gap between the two wires. Gap formers have proved to be very effective in reducing the two-sidedness of the finished paper, an effect that typically characterises sheets formed on a Fourdrinier. The water drains through the wire by vacuum –assisted foils, loadable blade units, and curved suction boxes. Once the sheet solids are high enough, around 15% - 20 %, the web can be sent to the press and then the drying sections. As the paper web travels through the press section, it is squeezed between felts at between two and four press 'nips' which are loaded to quite high pressures and there are also a number of vacuum sections; on leaving the press, the sheet's moisture content is typically about 50%. Then a series of cylinders filled with superheated steam is used to further dry the sheet to about 5%-10% moisture content. In the majority of cases, most of the heat used for drying passes through the hood as moistened exhaust air. The temperature of the exhaust air is normally 80 - 85 °C and its humidity is typically 140-160 gH_2O/kg. The final paper is then rolled in the reel section [8].

3   Energy auditing: a data exploration approach

Any systematic efforts aimed at energy reduction must begin with an investigatory phase to determine existing levels of energy consumption. This is more formally called energy auditing, which consists of three main stages, namely:

- Obtaining adequate knowledge of the existing energy consumption profile of the site
- Identifying the factors that have an effect on energy consumption
- Recognising cost-effective energy-saving opportunities [9, 10]

3.1   A review of energy auditing in papermaking

Based on the steps listed above, a number of energy auditing applications have been reported. For instance, the use of bio-fuels in Combined Heat and Power (CHP) plants within paper mills has been studied in [11]. The authors suggest three main methods for energy conservation, namely Pinch Analysis ([12] and [13]), knowledge-based techniques, and numerical optimisation; these are also known as process integration techniques [13]. The authors have concluded that efforts to conserve energy in papermaking should be focused on excess energy (i.e. steam dumping) [11]. A similar approach has been applied for a waste management project on a 9 t/day paper machine in Vietnam. The authors mention that to determine electrical energy use, parameters such as power demand, loading data, and power factor are needed. Regardless of the energy source, energy and material

balances are required for each section of the production process, in order to determine the overall energy consumption [14].

Apart from the auditing efforts mentioned above, attention has been paid to efficient drying control, knowing it to be the main consumer of mill energy. By rebuilding the whole drying section of one of Stora Enso's North American paper mills, Aue *et al.* provided a feasibility study through installation of control software called the Dryer Management System™ [15]. The important fact about the above audit method is that the authors established an assessment criterion that considered a dryer inefficient if the temperature difference between the sheet and dryer surface was less than $25^{o}C$. In their solution, the authors proposed maximising this temperature difference in order to maximise the heat transfer rate between the two and thus improving dryer efficiency. Investigation has revealed that in the papermaking process, more than 80% of mill-wide energy use is concentrated in the drying section. In spite of this significant usage, the drying section removes less than 1% of sheet moisture. However, the forming section, which removes more than 90% of sheet water, consumes a small fraction of mill-wide energy use. Figure 2 shows the proportion of water removal and energy consumption in the forming, press, and drying sections of a typical paper machine.
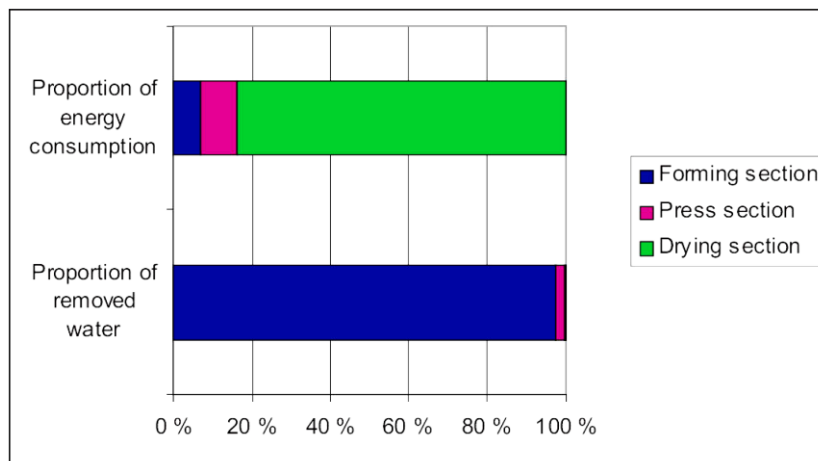
Figure 2: Water removal and energy consumption in a typical paper mill [9]

Also as a part of energy auditing, the major energy consumers are examined in terms of the type of operation and energy source. This analysis is summarised in Figure 3.
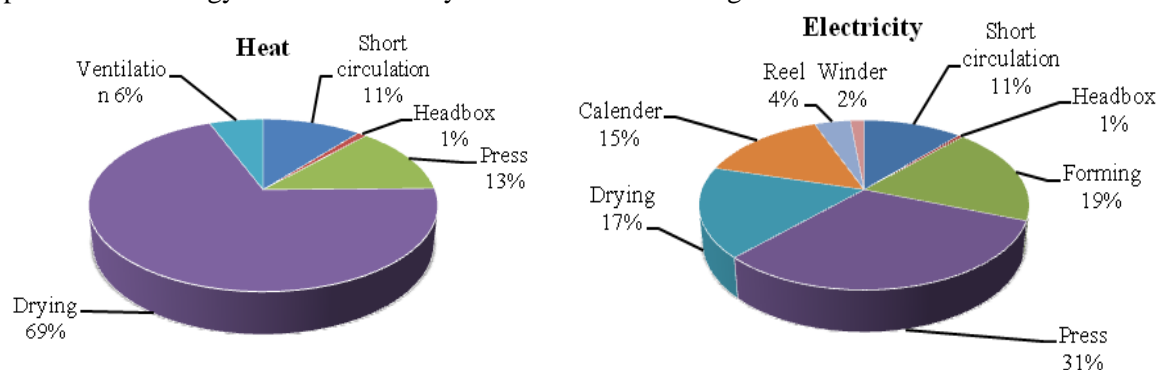
Figure 3: Energy consumption by sub-processes and energy source (data from [16])

Evidently, the main usage of energy in papermaking is in the form of heat - drying and process heating are the most energy-intensive operations within a paper mill. It is also worth mentioning that in terms of electricity usage, press, forming and drying sections are the most energy-intensive units. This is an important finding since it can direct energy conservation studies towards optimisation of drying, pressing, and forming. Previously, efforts have been made to reduce a mill's energy consumption by

improving pumping, compression and even lighting [17]. Although these measures can contribute considerable energy reduction, the study proves them to be less significant than reductions resulting from improving de-watering operations.

As mentioned earlier, some preliminary knowledge about the operation is required in order to determine effective energy optimisation scenarios. Often the only sources of information about the plant are the operational data obtainable from the DCS. This can be carried out by manual data explorations, which can help to discover certain arbitrary aspects of the data. For this purpose, a MATLAB-based tool called "DataExplorer" has been developed which is briefly explained in the next section.

3.2 Exploratory data analysis (EDA) tool: DataExplorer

In the current project, it is desired to perform data analysis, and later modelling and optimisation, within the MATLAB™ environment. DataExplorer has been constructed as a MATLAB toolbox equipped with a Graphical User Interface (GUI), shown in Figure 4.
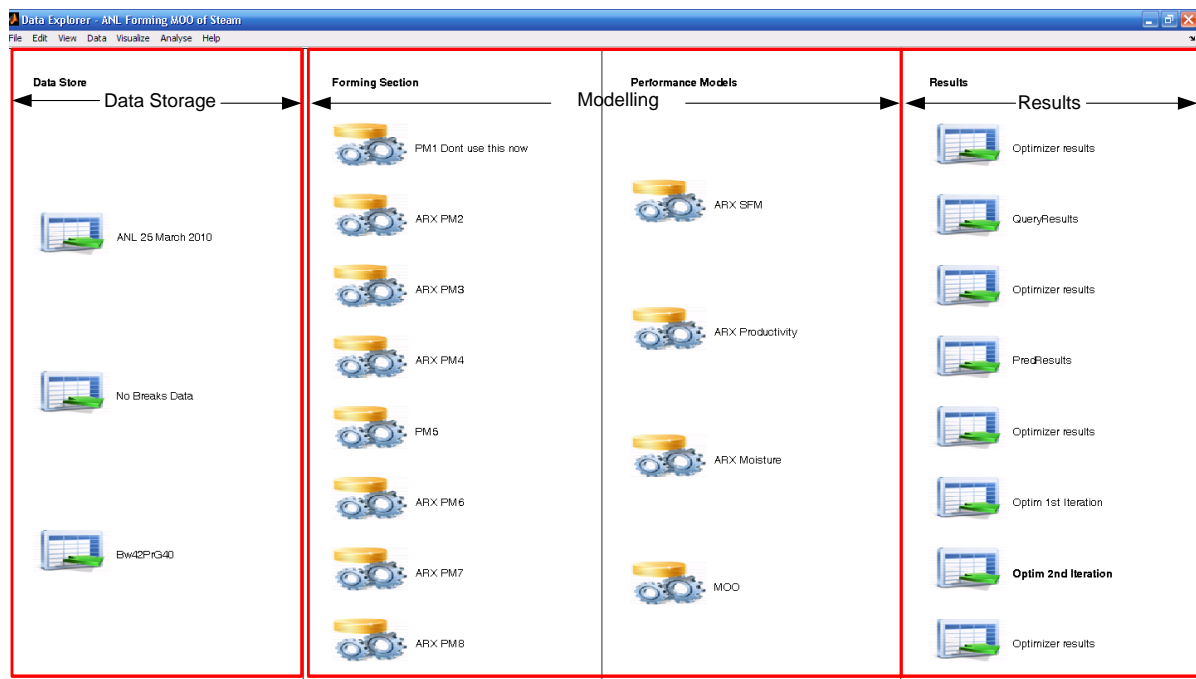
Figure 4: GUI of the DataExplorer tool

Within its GUI environment, DataExplorer provides three main capabilities: data storage, modelling (and optimisation), and the presentation of results. In the data storage area, the operating data can be loaded and prepared for analysis. Often the operating data include points corresponding to machine sheet breaks and other irregular events, but it is usual practice to exclude such data points from the data set used for analysis and modelling. Appending the datasets corresponding to consecutive days is part of the functionality available in the data storage section. Also, the data may be filtered to focus the analysis on specific product conditions (e.g. a specific paper grade, moisture content, etc). Furthermore, DataExplorer can provide views to selected signals' histograms; time series, linear regression, spectral analysis, and also 2-D scatter plots. DataExplorer is able to categorise the operating data based on the physical sections in the mill, e.g. wet end, forming section, press section, etc. In its modelling area, DataExplorer provides functionality for sequential modelling of the process systems and it facilitates local multi-objective optimisation of the process' sequential process models. The results area is mainly associated with demonstrating/visualising the results of the modelling or optimisation obtained in the modelling area.

4   Auditing results and energy reduction opportunities
In this section, results of the data exploration of two UK paper machines are presented.

4.1   Detecting important production features
Looking at operating data gathered over a 6 day period during March 2010 from a newsprint and from a board machine, the first observation, confirming natural expectations, was that the total steam consumption of the paper machine depends directly on the basis weight, higher grades requiring greater energy to dry the sheet. In the case of the board machine, it has also been observed that the sheet is typically considerably over dried. As is shown in Figure 5, the moisture set-point error suggests that over the period of study, different grades (whose grammages range between 100 and 220 gsm) have been over-dried by an average of 0.31%. This implies inefficient use of steam in the drying section which provides an obvious energy reduction opportunity.
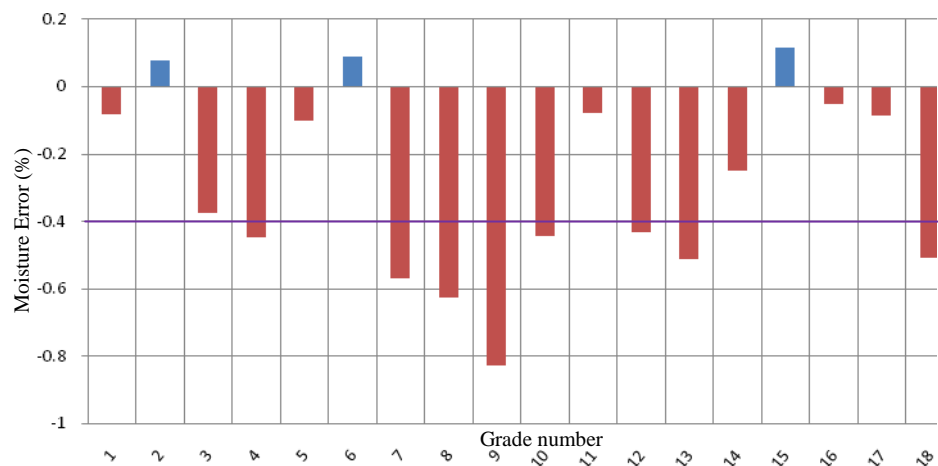
Figure 5: Over-drying of finished products in a board machine

Another tool to analyse the data is linear regression which helps to quantify the dependency of energy consumed on particular process variables.

4.2   Identifying linear correlations
As already noted, the forming and press sections remove the greatest amounts of water from the sheet while consuming considerably less energy than the drying section. Therefore, it was considered worthwhile to investigate the energy reduction opportunities these sections might facilitate for the dryer. *Table 3* summarises the coefficient of correlation (R^2) and standard deviations of the residuals corresponding to a linear regression test on data from the forming section of the newsprint machine.

Table 3.
Dependence of dryer steam use on forming water flowrates

Flowrate (l/min)	R^2	Standard Deviation
Multi-foil shoe chamber #2	0.7648	1.0707
Curved suction box	0.3592	1.7673
Outer wire	0.1675	2.0144
Couch Roll #1	0.1449	2.0415
Multi-foil shoe chamber #1	0.0741	2.1244
HIVAC	0.0642	2.1357

Table 3 suggests the existence of a linear relationship between steam flow to the paper machine and the flowrate of water draining from at least certain portions of the forming section. A similar exploration performed in the press section suggested a significant linear relationship between the vacuum pressure applied to the pressing rolls and steam flow to the paper machine. More specifically,

Figure 6 shows that increasing water flow from the 2nd multi-foil shoe chamber of the gap-former can reduce the steam flow to the machine (left). It also suggests that intensifying the vacuum pressure on the Transfer Roll in the press section can reduce the total steam demand of the paper machine (right).
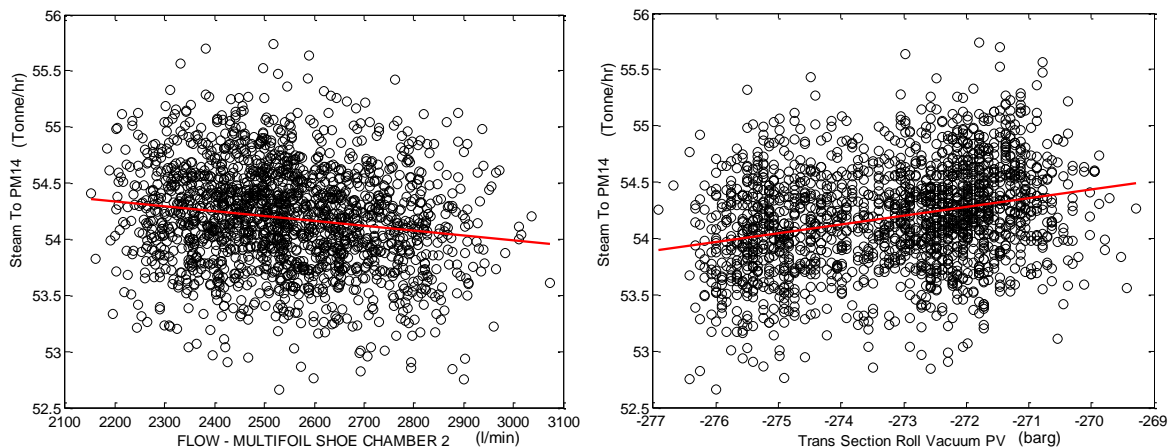
Figure 6: Linear regression: steam demand and drainage (left), and steam demand and press vacuum

4.3   Considering consequences of steam saving

As a part of energy auditing, any energy saving proposal must be carefully examined for any possible conflict with product quality or raw material requirements; these considerations must be borne in mind when evaluating the results of linear regression tests. For example, Figure 7 shows the correlation between sheet ash and total steam flow to the newsprint machine (left) as well as retention aid dosage and total steam flow to the newsprint machine (right).
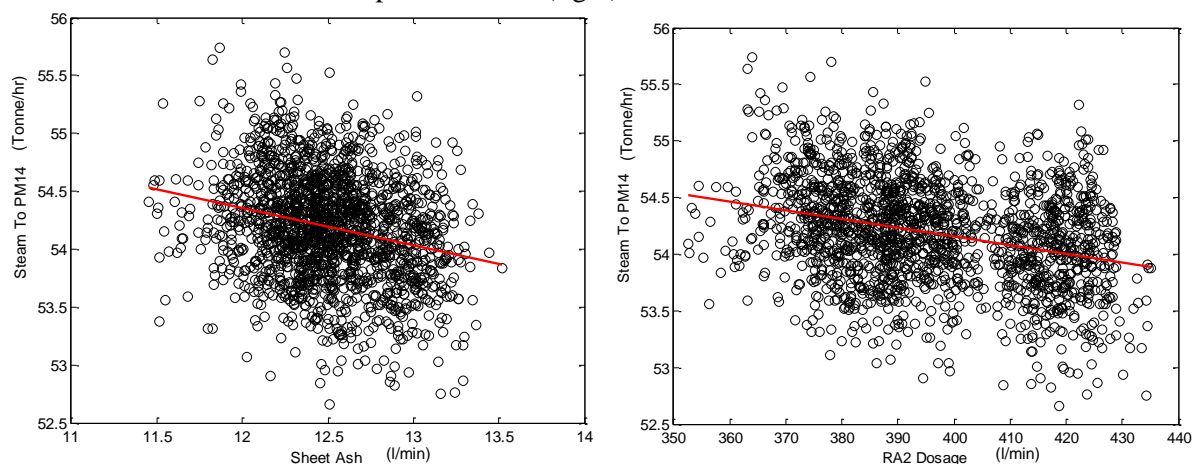
Figure 7: Linear regression: machine's steam flow and sheet ash (left), steam flow and RA dosage

The test suggests that as sheet ash is increased steam consumption is reduced. However, there is an upper limit for sheet ash beyond which sheet strength will be impaired and also reduced printability may result. It is also evident that as the dosage rate of this particular retention aid is increased steam use will decrease, but of course increased use of dosage chemicals implies increased cost. This highlights the importance of considering possibilities for energy reduction in the context of a multi-criteria optimisation problem. It is worthwhile mentioning that modelling is a challenging task due to the presence of several interfering signals (e.g. measurement and environmental noises or even other variables overlooked due to univariate analysis). The common practice in modelling industrial processes is an iterative process involving filtering the measurements, and consulting with process experts to count for unforeseen parameters affecting the models.

4.4   Proposals for energy reduction

Based on the results obtained from the data exploration, a series of energy reduction proposals can be prepared. These are summarised in this section.

4.4.1   Improving drainage

Assume that headbox consistency is 0.9%, and sheet moisture is 88% at the couch roll, 50% at the entry to the dryer and 8% at the reel. If it possible to reduce sheet moisture to the dryer by 5%, the weight of water to be removed in the dryer from what remains of the 100g of thin stock laid onto the wire by the headbox reduces from 0.822g to 0.658g. That is, a 20% reduction in dryer load results from a 5% reduction in the moisture content of the sheet entering the dryer. The notion of presenting a drier sheet to the dryer is consistent with the results of the audit presented in Section 4.2, which suggested that increasing the vacuum-assisted de-watering in the forming and press sections would be a key means of reducing dryer steam use.

4.4.2   Eliminating over-drying of the sheet

Consider the steam benefit of raising the reel moisture target by 1%, in relation to the 100g of stock laid onto the wire. By raising the moisture target by 1%, when the dryer feed moisture content was 50%, the dryer steam demand would diminish by 1.34%. That is, a 1% increase in the moisture target results in a 1.34% reduction in dryer steam demand [18].

5   Sequential modelling for process & thermal energy associated with vacuum pressure

A model-based optimisation scenario requires solving polynomial or state equations obtained from a number of models which represent the behaviour of the plant. As shown in Figure 8, a typical paper machine is formed of interconnected sub-systems (processing units) linked in series. Therefore, it is necessary to consider sequential modelling of these systems. In this section, a sequential modelling strategy that can be used for optimising energy use on paper machines is briefly introduced.
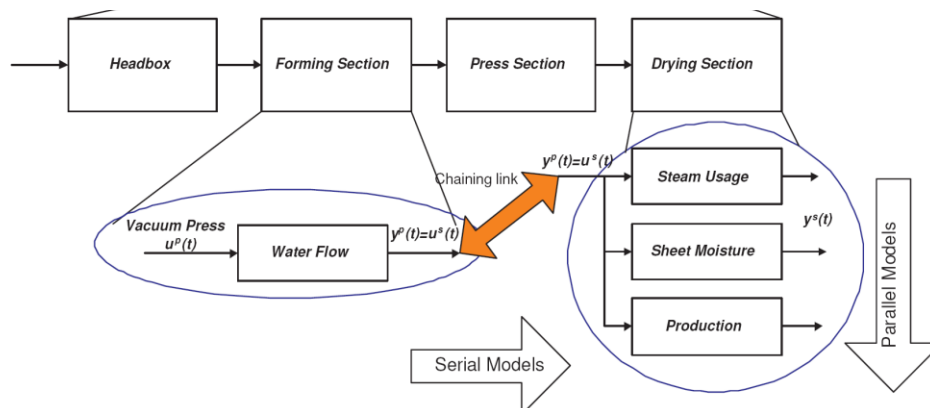
Figure 8: Serial and parallel chains of process/performance models in a paper machine

5.1   Modelling thermal energy of steam

Assuming the drying section is an adiabatic system, the energy content of the steam can be modelled using energy balance equations. The most important factor of an energy balance in the dryer is the internal energy (enthalpy), which is a non-linear function of the working pressure and temperature and is usually obtained from steam tables which present the thermodynamic properties of steam. To model the steam energy usage of the paper machine, the flowrate, pressure and temperature of steam and/or condensate to and from the dryer are required. These variables are often available from the DCS database. Assuming negligible pressure drops across the valves, the following energy balance holds for the drying section:

$$E = \int \left[Q_{Steam\_in}\, h_{Steam\_in} - Q_{Cond\_out}\, h_{Cond\_out} \right] dt. \qquad (1)$$

where Q and h represent the flowrate and enthalpy, respectively, and E is the total thermal energy consumed in the drying section. Automatic enthalpy calculation is performed in our DataExplorer software tool. The ultimate goal of the modelling is to find process settings which reduce energy use

while maintaining the desired paper quality. As for the optimisation strategy discussed in Section 4.4.1, it is necessary to establish a link between the energy used in creating vacuums for drainage and the flow of water draining from the forming and press sections (see Figure 8). This is discussed in the next section.

5.2 Modelling steam flow variations caused by drainage

According to the discussions in Section 4, drainage in the forming and press sections has a causative effect on steam flow in the drying section. Therefore, draining water flow is taken to be a primary input to the Steam Flow Model (SFM). Also, other process measurements such as headbox flow or fibre consistency are considered as primary measured inputs to the SFM. The drainage itself is determined by the amount of water removed from the sheet in the forming and press sections and is caused by the vacuum pressure applied to the vacuum boxes, rolls, and felts in these sections. Therefore, the drainage is modelled through a set of parallel Process Models (PM) in the forming and press sections. Applying the same concepts to a Condensate Flow Model (CFM), the proposed modelling scheme is shown in Figure 9.
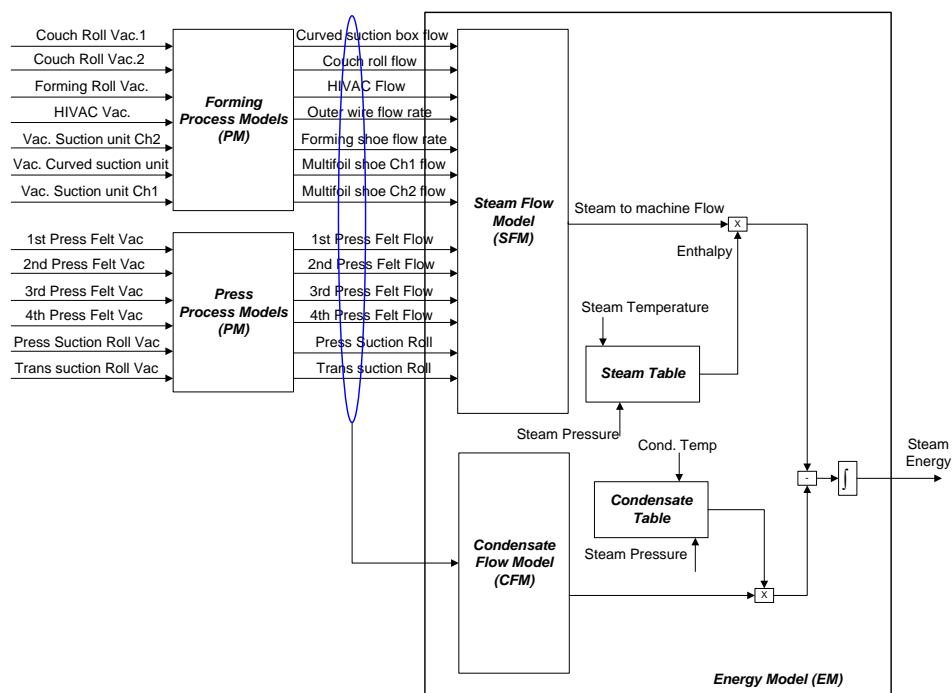
Figure 9: Sequential modelling proposed for energy optimisation in papermaking.

As noted in section 4, the effect of any suggested energy reduction strategies on the production quality parameters must be carefully examined prior to the application of the optimisation algorithms. As for the current project, the moisture content has been considered as Product Quality Models (PQM). Linear models have been sought, with Auto-Regressive eXogenous (ARX) structure and have been trained by The Least Squares (LS) algorithm [4]. These models will in turn be used for multi-objective process optimisation purpose. Figure 10 illustrates the link between process measurements, sequential modelling framework, and parallel coordinates plots which help to explore linkages between process measurements and performance indices. As the figure implies, the operational data (represented as histograms) are first explored and ranked based on their correlation with the performance indices (quality and energy). The parallel coordinate plots can be used to establish one's expectations of the outcomes of the subsequent optimisation.
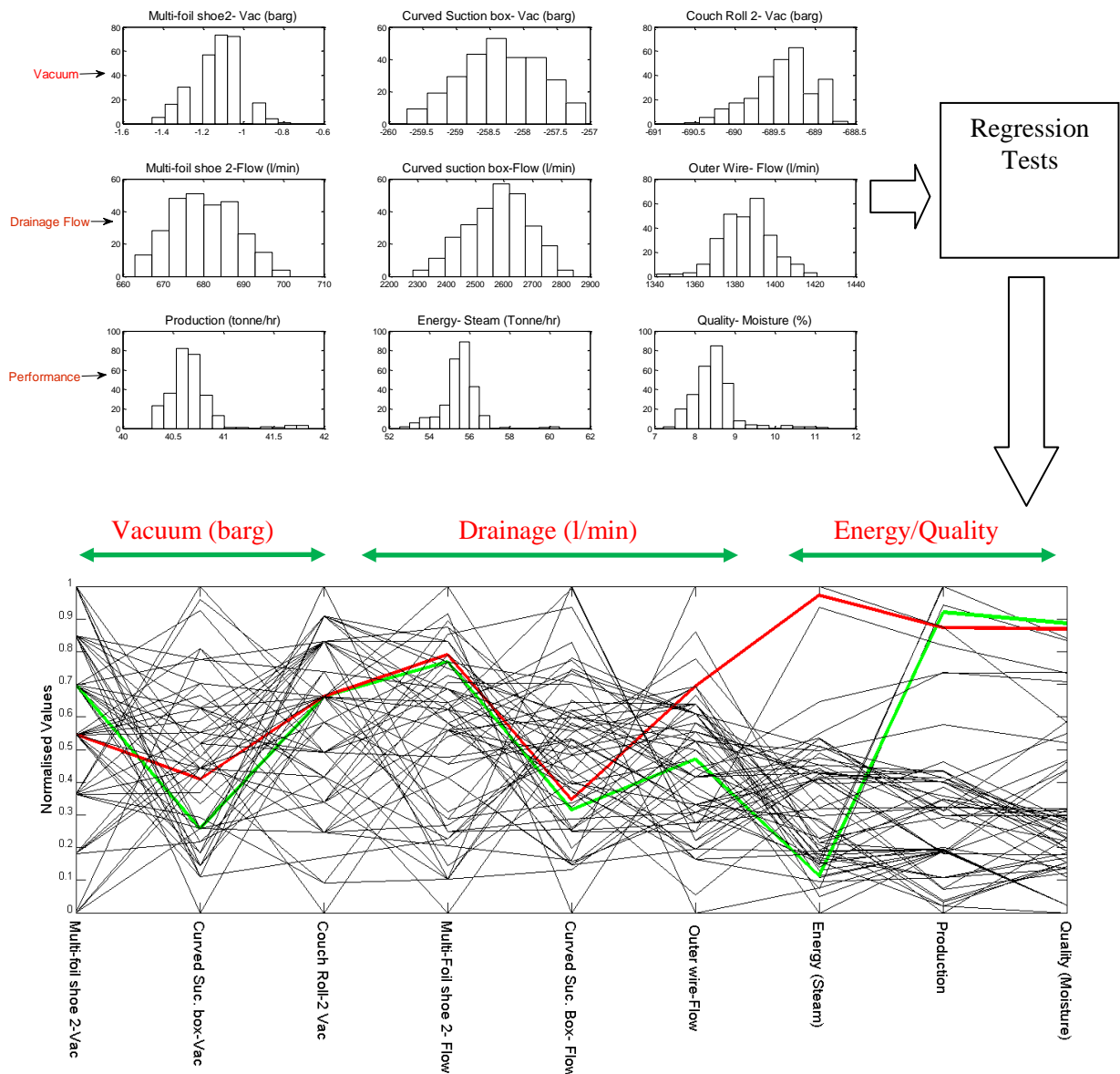
Figure 10: Normalised parallel coordinates graph for selected variables of the chained models

As shown in the figure, the red trend line indicates an inefficient operation where high productivity and quality were achieved with very high energy consumption, whereas the green line shows an operation with considerably more efficient energy usage and (slightly) better productivity and quality. Evidently, releasing the vacuum at 'Multi-foil Shoe #2' and intensifying it at the 'Curved Suction Box' can result in more efficient operation. Naturally, when there are enough historical data available, visual analyses can do a search to reveal the conditions in which the operating parameters satisfied the objectives. However, the restriction of these methods is that they are obviously limited to the past operating conditions and cannot provide a figure of future behaviour. With the use of sequential models, however, the process conditions can be estimated beyond the historical data. In this context, in order to achieve reliable optimisation results, the uncertainty inherent in the extrapolation must be carefully quantified and examined.

6   Conclusions and future work

This paper proposes a potential pathway for reducing thermal energy consumption in papermaking through sequential modelling of process and energy metrics. As part of a comprehensive thermal energy demand reduction initiative being undertaken in two commercial UK-based paper mills, this

paper first identifies the key process variables which can reduce thermal energy consumption by a data-based energy audit operation. For exploratory data analysis, a MATLAB-based software tool "DataExplorer" was developed at the University of Manchester. The energy auditing has revealed that at least for the two machines of the study, improving drainage and eliminating over-drying of the sheet provide two important opportunities for thermal energy reduction in the papermaking industry. As a requirement for model-based process optimisation, the energy, steam flow, vacuum-assisted drainage, and product quality have been modelled through linear sequential dynamic models. The fundamentals of this approach will be used in future for multi-objective optimisation of energy and quality parameters. The optimisation algorithms will provide a set of recommendations for changing the vacuum pressure set-point in the forming and press sections to achieve a reduction in thermal energy demand.

Acknowledgements

References

[1] I. MacLeay, K. Harris, A. Annut, Digest of UK Energy Statistics , A Nat. Stat publication, 2009.

[2] P. Sivil, P., P. Ahita, M. Taimisto, Thermodynamic simulation of dryer section heat recovery in paper machines, App. Therm Eng., (25) 2005, pp 1273-1292.

[3] M. Barnes, Practical Variable Speed Drives and Power Electronics, Elsevier Ltd, 2003.

[4] L. Ljung. System Identification Toolbox 7 Users Guide. TheMathWorks, Inc., 3 Apple Hill Drive, 7th edition, 2010.

[5] B. Huang and A.S.Mujumdar. Use of neural network to predict industrial dryer performance. Juornal of Drying Technology, 11:525–541, 1993.

[6] F. Cubillos and Reyes. A. drying of carrots in a fluidized bed. ii. design of a model based on a modular neural network approach. Journal of Drying Technology, 21:1185–1196., 2003.

[7] J. Lampinen and O. Taipale. Optimization and simulation of quality properties in paper machine with neural networks. In In Proceedings of the IEEE International Conference on Neural Networks, Orlando, Florida, June 2729, 1994.

[8] G.A. Smook, Handbook for Pulp and Paper Technologies, Angus Wilde Publications, Vancouver, 2nd Edition, 1992

[9] S. Siitonen, , P. Ahtila, Possibilities of reducing CO_2 emissions in the Finnish forest industry, Tech report, Finnish Forest Ind. Fed., 2002.

[10] Motiva, Process industry energy analysis. Phase 1: Guidelines for auditing, 2000.

[11] L. Kilponen, Improvement of pulp mill energy efficiency in integrated pulp and paper mill, Master's Thesis, Dep. Mech Eng, Helsinki Univ. Tech, 2000.

[12] J. Nygaard, Energy audits in the pulp and paper industry, 411(84):150–176, 1984.

[13] A.P. Rossiter, Waste minimization through process design. McGraw-Hill Inc., 1995.

[14] V.T. Anh, Cleaner production audit in the pulp and paper industry: A case study in Vietnam, Master's thesis, Asian Ins. Tech. Bangkok, Thailand, 1996.

[15] J. Aue, S. Pierce, Energy audit uncovers major energy savings for paper mill, In Proc. 27th Industrial Energy Technology Conference, 2005.

[16] H.Oinonen, Recent Advances in Pulp and Paper Technology, Wochenblatt für Papierfabrikation, (3,4), August 2009, pp 100-114

[17] Caddett . CADDETT brochure R163, 1993. Project number SE-93-002, 1993.

[18] P. Austin, J. Mack, M. McEwan, P. Afshar, Improved Energy Efficiency in Papermaking Using Advanced Process Control, in Proc. 64th APPITA Annual Conf.,18-21 April 2010, Melbourne, Australia.

Modelling of Energy Flows in Potato Crisp Frying Processes

Hongwei Wu, Hussam Jouhara, Savvas Tassou[*], Tassos Karayiannis

School of Engineering and Design, Brunel University, Uxbridge, Middlesex, UB8 3PH, United Kingdom

* Corresponding author. Email: savvas.tassou@brunel.ac.uk; Tel. +44(0) 1895 266865; Fax. + 44(0) 1895 269803

Abstract

Food frying is very energy intensive and in industrial potato crisp production lines frying is responsible for more than 90% of the total energy consumption of the process. This paper considers the energy flows in crisp frying using a First Law of Thermodynamics modelling approach which was verified against data from a potato crisp production line. The results indicate that for the frying process considered, most of the energy used is associated with the evaporation of water present in the potato and on the surface of potato slices. The remainder is from evaporation of frying oil and air of the ventilation system and heat losses from the fryer wall surfaces by convection and radiation. The frying oil is heated by an industrial gas furnace and the efficiency of this process was calculated to be 84%. The efficiency of the overall frying process which was found to be of the order of 70% can be improved by employing exhaust heat recovery and optimising other operating and control parameters such as exhaust gas recirculation.

Keywords   frying processes; energy consumption; heat recovery; potato crisp; modelling of frying processes

1   Introduction

Energy consumption is a significant contributor to greenhouse gas (GHG) emissions and global warming. In its efforts to reduce emissions of greenhouse gases and dependence on imported fossil fuels the European Union has set an indicative objective to reduce its primary energy consumption by 20% by 2020 compared to projected 2020 energy consumption [1]. The UK Government has set even more ambitious targets. The Climate Change Act 2008 enacts a legal obligation for Government to reduce GHG emissions by 34% compared to 1990 levels by 2012 and by at least 80% by 2050 [2]. The Energy White Paper published in 2007 sets out a framework of measures to address these challenging targets and energy efficiency is one of them [3]. Energy efficiency is of particular importance to the process industries due to the rapid rises in energy costs in the last few years and the volatility of energy prices. Energy costs may also represent a significant proportion of the overall production costs in various process sectors and energy efficiency can offer one of the best approaches to increasing profitability even in what are perceived as mature and energy efficient processes.

Energy efficiency can be achieved in a number of ways including improving the efficiency of equipment and unit operations, heat recovery and process integration. Over the last 30 years considerable research and development effort has been devoted to these fields. Process integration and optimisation involves a number of techniques and methodologies that can be applied in a systematic manner to facilitate the selection or modification of processing steps in large processing plants to minimise energy consumption and resource use. Amongst the most common process integration techniques are pinch analysis, exergy and thermodynamic analysis of specific equipment and processes, and mathematical programming techniques, which can be used to simulate and optimise the process or part of the process using techniques such as neural networks and genetic algorithms [4,5]. Pinch analysis is a structured approach which can be used to identify inefficiencies in energy use in industrial processes. It has been applied to large plants particularly in the petrochemical industry and a number of case studies on its application exist both in the petrochemical and food industries [6]. Successful application of the technique, however, requires considerable expertise that very often is not available within the organisation and so, to date, application of pinch analysis has not been applied widely outside the petrochemical industry.

Nomenclature

A	surface area of fryer casing, m^2	ov	oil evaporation
c_p	specific heat, kJ/kg K	$o,2$	oil in foul gas
CV	calorific value, kJ/m^3	$o,13$	oil in potato crisp
$\dot{E}$	energy, kW	ps	potato slice solid
h_{fg}	latent heat, kJ/kg	pw	water in potato slices
$\dot{m}$	mass flow rate, kg/s	s	potato solid
$\dot{Q}_{loss}$	heat loss, kW	$s,9$	potato solid in raw potato slices
T	temperature, K	$s,13$	potato solid in potato crisp
U	heat transfer coefficient, kW/m^2 K	SY	system
V	volume, m^3	$total$	total energy input
X	composition percentage, %	tw	transmittion through external wall
		v	vapour
Greek Letters		$v,2$	water vapour in foul gas
		w	water
η	efficiency, %	$w,9$	water in raw potato slices
ρ	density, kg/ m^3	$w,13$	water in potato crisp
		1	fuel
Subscripts		2	foul gas
a	air	3	combustion air
act	actual	4	recycling exhaust gas
amb	ambient	5	combustion product
$a,2$	air in foul gas	6	exhaust gas
b	boiling water	7	oil outlet
c	combustion products	8	air flow
CHE	combustor and heat exchanger	9	raw potato slices
fo	frying oil	10	surface water of raw potato slices
HE	heat exchanger	11	oil return
in	inlet	12	fines removal
o	oil	13	potato crisp
out	outlet	14	oil inlet

Exergy analysis which is based on the Second Law of Thermodynamics allows the consideration of losses not only in the energy but also the energy quality in complex systems and can thus provide useful information where energy can be saved [7]. An extension of exergy analysis is thermoeconomics which includes costs and the resources needed to effect energy savings. Thermoeconomic analysis has been gaining in popularity in recent years but its application for plant monitoring and optimisation presents difficulties in the identification of the independent variables that characterise the behaviour of the process. For this reason, where the main interest is the practical analysis of the behaviour of thermal systems, the application of models based on the thermodynamic description of the system is the preferred method with many researchers. This is because this approach relies on the use of properties and performance variables that are well known and accepted by industry and are widely used for the monitoring of industrial processes. This paper uses thermodynamic modelling based on the First Law as a first step in the analysis of the energy flows in crisp frying.

The food and drink industry is the single largest manufacturing sector in the EU in turnover and employment. It is also the largest manufacturing sector in the UK, contributing 14.2% of manufacturing's gross value added (GVA) and employing some 470,000 people. The greenhouse gas footprint of the UK food chain is in the region of 160 MtCO2e and food manufacturing is responsible for around 13 MtCO$_2$e and primary energy consumption of 42 TWh [2]. In food manufacturing approximately 68% of the energy is used by fuel fired boilers and direct heating systems for process

and space heating. From the remainder, 16% is electrical energy used by electric motors, 8% is used by electric heating, 8% by refrigeration equipment and the remainder 2% by air compressors [8].

Potato product manufacturing and preservation is one of the larger contributors to food manufacturing emissions at 0.71 MtCO2e or 5.5% of total [9]. Crisp manufacture in the UK is estimated to be around 220,000 tonnes per year and is responsible for around 0.18 $MtCO_2e$. This was estimated from a recent study by a major crisp manufacturer in the UK which indicated that approximately 34% of the emissions from the production of crisps is from the manufacturing process and that 1 ton of potato crisps is responsible for 2.3 tons of CO_2e emissions [10].

In the production of potato crisps, frying consumes more than 80% of the total processing energy requirement so the greatest potential for energy savings is offered by design and control optimisation to minimise heat input to the potato slices and reduce thermal losses [11]. Frying is a complex processing operation and optimisation entails short frying times, high product quality and reasonable costs [12,13]. Numerous research investigations on deep-fat frying modelling have been carried out [14-21]. Many of these have considered and combined heat and mass transfer principles to describe the temperature and moisture content profiles of the product [17, 18] whilst others have concentrated on empirical [14, 16] and semi-empirical [19] relationships for heat and mass transfer. The majority of the reported research on frying processes to date, however, has concentrated mainly on the physical and chemical changes occurring in the food item under the influence of high temperature and prolonged heating. Very limited work has been done to include energy requirements and energy efficiency in industrial frying processes even though this is of significant importance both in terms of GHG emissions and economic competitiveness [20, 21]. To this end this paper presents a simplified analysis of the key processes using energy balance equations based on the First Law of thermodynamics. The primary aim is to provide a first approximation of the energy flows and efficiency of the frying process in order to identify opportunities for energy conservation measures.

2   Potato crisp frying

A typical potato crisp production line is illustrated schematically in Figure 1. As can be seen, the bulk hopper holds the potatoes for the line while a conveyor feeds potatoes from the hopper, at a controlled rate to correspond to changes in feed rates in the frying line. From the hopper, the potatoes enter the de-stoning and wash unit where they are washed and any stones present removed by a store removal conveyor. The washed potatoes are then transferred by another conveyor to the peeler. The peeler which is normally a disc with gritted surface peels the potatoes as it rotates. The peelings are washed down by a water jet into a drainage channel below the peeler where they are removed by a drum washer. The potatoes are then inspected and sorted, by size, before entering the slicer where they are cut into slices of 2-3 mm in thickness. The diameter of the slices can vary but normally fall within the range 30-40 mm.
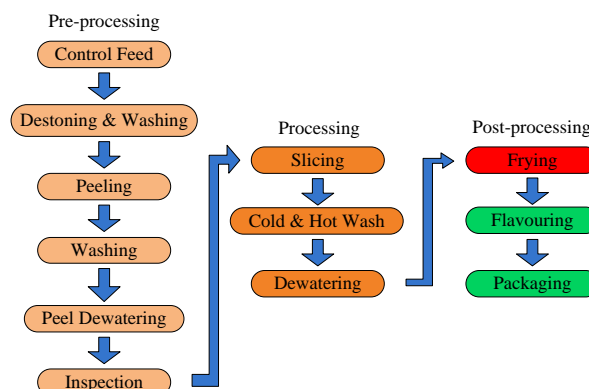
Figure 1: Flow diagram of industrial fried potato crisp production line

The potato slices are then transported to the cold wash rinsing unit where they are rinsed with cold water to remove starch solids. The cold water is subsequently destarched and re-used on the process

line for potato cleaning. Following the cold wash, the potato slices enter the hotwash stage, where hot water removes sugars and other water soluble solids from the slices. The washed potato slices then enter a dewatering stage where surface water is removed, normally with warm air blown over the potatoes, before the slices enter the fryer. Removal of water from the slices ensures that the frying process is faster and more energy efficient since less energy will be required to evaporate the water from the potato slice surface.

On entering the fryer, the slices are submerged in hot oil flow which enters the fryer at temperatures in the range 170-190 °C. The rate of flow of potato slices through the fryer is controlled by the moisture content of the potato after the fryer which is normally kept below 2% by weight. The crisps then travel along cooling and transportation belts, where they are salted, flavoured and vacuum-packed.

3   Frying system

The frying system is designed to transfer energy, produced by combustion, to heat oil (sunflower oil) which is circulated through the fryer. The system can be divided into three main parts, combustor, heat exchanger and fryer as illustrated in Figure 2. In the combustor, a gas burner burns natural gas with fresh air and foul gas (vapours from the fryer) to produce products of combustion at approximately 702 °C. In some cases exhaust gas recirculation can be used to increase turbulence, provide surface cooling and reduce emissions. The products of combustion then flow through a heat exchanger to heat up the frying oil that is re-circulated through the fryer.
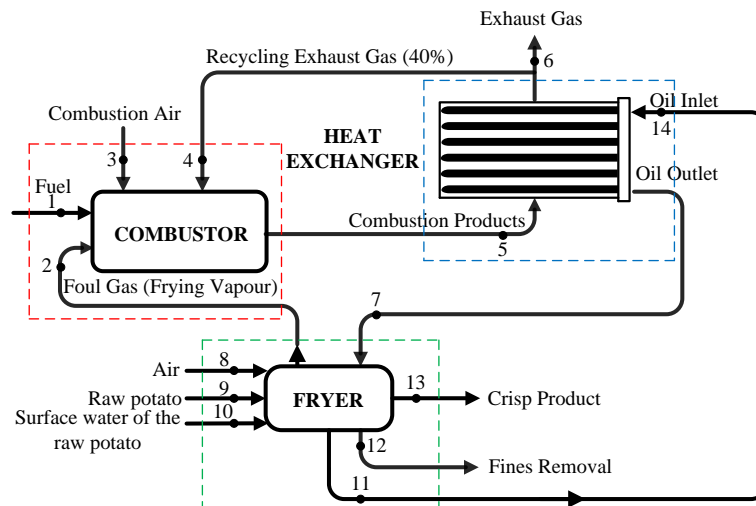
Figure 2: Schematic diagram of flow through the combustor, heat exchanger and fryer (frying system)

3.1   Combustor

For complete combustion in the chamber, air-fuel ratio of 16.5:1 was assumed giving 20% excess air. The combustor is well insulated and this minimizes heat loss to the ambient to an insignificant amount compared to the total energy input. Referring to Figure 3, the energy balance in the combustor is given by:
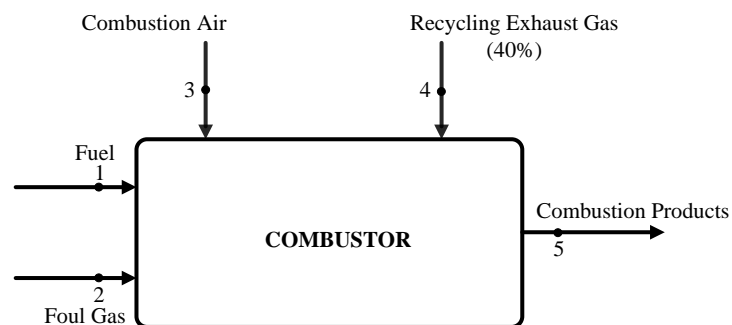
Figure 3: Schematic diagram of flow through the combustor

$$\dot{E}_1 + \dot{E}_2 + \dot{E}_3 + \dot{E}_4 = \dot{E}_5 \tag{1}$$

where,

$\dot{E}_1$ is energy input by the combustion of fuel given by:

$$\dot{E}_1 = \dot{m}_1 \cdot CV_1 / \rho_1 \tag{2}$$

where m_1, CV_1 and ρ_1 are the mass flow rate, calorific value and density of fuel, respectively.

$\dot{E}_2$ is energy input to combustor by the foul gas given by:

$$\dot{E}_2 = c_{p2} \cdot \dot{m}_2 \cdot T_2 \tag{3}$$

$\dot{E}_3$ is energy input by combustion air calculated from:

$$\dot{E}_3 = c_{p3} \cdot \dot{m}_3 \cdot T_3 \tag{4}$$

$\dot{E}_4$ is energy input to combustor by recirculated exhaust gas determined from:

$$\dot{E}_4 = c_{p4} \cdot \dot{m}_4 \cdot T_4 \tag{5}$$

$\dot{E}_5$ = energy in the products of combustion before the heat exchanger given by:

$$\dot{E}_5 = c_{p5} \cdot \dot{m}_5 \cdot T_5 \tag{6}$$

3.2   Heat exchanger

The heat exchanger transfers heat from the exhaust gases to the frying oil. The heat exchanger in the current study is of the U-tube cross-counterflow type. The energy flows in the heat exchanger are illustrated in Figure 4.
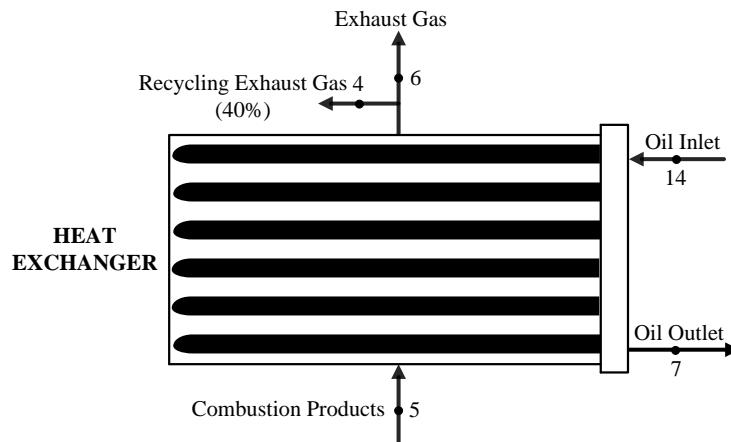
Figure 4: Schematic diagram of flow through the heat exchanger

Energy balance on the heat exchanger gives:

$$(\dot{E}_5 + \dot{E}_{14}) = (\dot{E}_7 + \dot{E}_4 + \dot{E}_6) \tag{7}$$

where:

$\dot{E}_6$ is energy in the exhaust gas given by:

$$\dot{E}_6 = c_{p6} \cdot \dot{m}_6 \cdot T_6 \tag{8}$$

$\dot{E}_7$ = energy in oil leaving the heat exchanger:

$$\dot{E}_7 = c_{po} \cdot \dot{m}_7 \cdot T_7 \tag{9}$$

$\dot{E}_{14}$ is energy of oil at inlet to the heat exchanger:

$$\dot{E}_{14} = c_{po} \cdot \dot{m}_{14} \cdot T_{14} \tag{10}$$

The first law efficiency for the heat exchanger can be written as follows:

$$\eta_{HE} = \frac{\dot{E}_7 - \dot{E}_{14}}{\dot{E}_5 - (\dot{E}_4 + \dot{E}_6)} \tag{11}$$

where η_{HE} is the energy efficiency of heat exchanger.

The combined combustor and heat exchanger energy efficiency can be calculated from:

$$\eta_{CHE} = \frac{\dot{E}_7 - \dot{E}_{14}}{\dot{E}_1} \tag{12}$$

3.3   Fryer

Figure 5 shows a schematic diagram of the various mass flows in the fryer. The energy analysis of the fryer assumed: (i) a steady flow process; (ii) the heat required for chemical reactions is small compared to the heat required to evaporate the water; (iii) constant water and air specific heats.
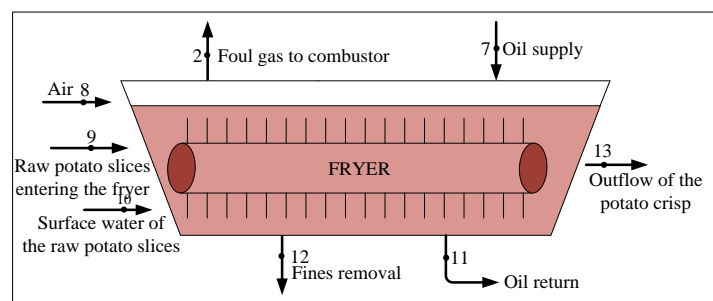
Figure 5: Mass flow balance in the industrial crisp frying process

The general equation for the conservation of mass in the frying process is given by:

$$\sum \dot{m}_{in} = \sum \dot{m}_{out} \quad \text{or} \quad \dot{m}_7 + \dot{m}_8 + \dot{m}_9 + \dot{m}_{10} = \dot{m}_2 + \dot{m}_{11} + \dot{m}_{12} + \dot{m}_{13} \tag{13}$$

where $\dot{m}_{in}$ and $\dot{m}_{out}$ represent the total inlet and outlet mass flows of the fryer respectively; $\dot{m}_2$ is the mass flow rate of foul gas, $\dot{m}_7$ is the mass flow rate of supplied oil, $\dot{m}_8$ is the mass flow rate of air, $\dot{m}_9$ is the mass flow rate of raw potato slices, $\dot{m}_{10}$ is the mass flow rate of surface water associated with the raw potato slices, $\dot{m}_{11}$ is the mass flow rate of oil return, $\dot{m}_{12}$ is the mass flow rate of fines removal and $\dot{m}_{13}$ is the mass flow rate of crisp product.

In addition, the mass conservation equations of each species can be determined as follows:

3.3.1   Frying oil

$$\dot{m}_7 = \dot{m}_{11} + \dot{m}_{12} + \dot{m}_{o,2} + \dot{m}_{o,13} \tag{14}$$

where

$$\dot{m}_{o,2} = \dot{m}_2 \cdot X_{o,2} \tag{15}$$

$$\dot{m}_{o,13} = \dot{m}_{13} \cdot X_{o,13} \tag{16}$$

$\dot{m}_{o,2}$ and $\dot{m}_{o,13}$ are the mass flow rates of oil in foul gas and potato crisp, respectively. $X_{o,2}$ is the percentage of oil in the foul gas by mass and $X_{o,13}$ is the percentage of oil in potato crisp by mass.

3.3.2   Potato solid

$$\dot{m}_{s,9} = \dot{m}_{s,13} \tag{17}$$

where

$$\dot{m}_{s,9} = \dot{m}_9 \cdot X_{s,9} \tag{18}$$

$$\dot{m}_{s,13} = \dot{m}_{13} \cdot X_{s,13} \tag{19}$$

$\dot{m}_{s,9}$ and $\dot{m}_{s,13}$ are the mass flow rates of potato solid in raw potato slices and potato crisp, respectively. $X_{s,9}$ is the percentage of potato solid in raw potato slices by mass and $X_{s,13}$ is the percentage of potato solid in potato crisp by mass.

3.3.3   Water

$$\dot{m}_{w,9} + \dot{m}_{10} = \dot{m}_{v,2} + \dot{m}_{w,13} \tag{20}$$

where

$$\dot{m}_{w,9} = \dot{m}_9 \cdot X_{w,9} \tag{21}$$

$$\dot{m}_{v,2} = \dot{m}_2 \cdot X_{v,2} \tag{22}$$

$$\dot{m}_{w,13} = \dot{m}_{13} \cdot X_{w,13} \tag{23}$$

$\dot{m}_{w,9}$ is the mass of water in the raw potato slices, $\dot{m}_{v,2}$ is the mass of water vapour in the foul gas, and $\dot{m}_{w,13}$ is the mass of water in the crisp product respectively. $X_{w,9}$ is the percentage of water in raw potato slices by mass (wet basis), $X_{v,2}$ is the percentage of water vapour in foul gas by mass and $X_{w,13}$ is the percentage of water in potato crisp by mass.

3.3.4   Air

$$\dot{m}_8 = \dot{m}_{a,2} \tag{24}$$

where

$$\dot{m}_{a,2} = \dot{m}_2 \cdot X_{a,2} \tag{25}$$

$\dot{m}_{a,2}$ is the mass flow rate of air in the foul gas and $X_{a,2}$ is the percentage of air in the foul gas by mass.

The general form of the energy equation of the fryer can be expressed in a rate form as

$$\dot{E} = \dot{E}_{ps} + \dot{E}_{pw} + \dot{E}_{ov} + \dot{E}_a + \dot{E}_{tw} \tag{26}$$

where

$\dot{E}$ is total energy input to the fryer.

$\dot{E}_{ps}$ is energy needed for raw potato slice solid heating during the whole frying process given by:

$$\dot{E}_{ps} = c_{ps} \cdot \dot{m}_{s,9} \cdot (T_{13} - T_9) \tag{27}$$

where c_{ps} is the specific heat of the potato slice solid, T_{13} is the temperature of the potato crisp and T_9 is the temperature of the raw potato slice solid.

$\dot{E}_{pw}$ is energy needed for heating and evaporation of the water contained in the raw potato slices and can be determined from:

$$\dot{E}_{pw} = \left[c_{pw} \cdot (T_b - T_9) + h_{fg_w} \right] \cdot (\dot{m}_{w,9} + \dot{m}_{10} - \dot{m}_{w,13}) \tag{28}$$

where c_{pw} is the specific heat of water, T_b the boiling temperature of water and h_{fg_w} the latent heat vaporization of free water.

$\dot{E}_{ov}$ is energy needed for oil evaporation given by:

$$\dot{E}_{ov} = h_{fg_o} \cdot \left(\dot{m}_7 - \dot{m}_{11} - \dot{m}_{12} - \dot{m}_{o,13}\right) \tag{29}$$

where h_{fg_o} is the latent heat of oil.

$\dot{E}_a$ is energy needed for heating the air entering the fryer calculated from:

$$\dot{E}_a = c_{pa} \cdot \dot{m}_8 \cdot \left(T_2 - T_8\right) \tag{30}$$

where c_{pa} is the specific heat of air and T_8 is the temperature of air.

$\dot{E}_{tw}$ is energy transmitted through the external wall of the fryer to the environment determined from:

$$\dot{E}_{tw} = U \cdot A \cdot \left(T_{fo} - T_{amb}\right) \tag{31}$$

where U is the overall heat transfer coefficient of the casing of the fryer, A is surface area of the casing, subscript fo denotes the frying oil. T_{amb} is the average ambient temperature for the location at which the system under consideration operates. In this analysis T_{amb} was assumed to be 25 °C.

Substituting Eqs. 27 to 31 into Eq. 26, gives:

$$\dot{E} = c_{ps} \cdot \dot{m}_{s,9} \cdot \left(T_{13} - T_9\right) + [c_{pw} \cdot \left(T_b - T_9\right) + h_{fg_w}] \cdot \left(\dot{m}_{w,9} + \dot{m}_{10} - \dot{m}_{w,13}\right) + c_{pa} \cdot \dot{m}_8 \cdot \left(T_2 - T_8\right) +$$
$$h_{fg_o} \cdot \left(\dot{m}_7 - \dot{m}_{11} - \dot{m}_{12} - \dot{m}_{o,13}\right) + U \cdot A \cdot \left(T_{fo} - T_{amb}\right) \tag{32}$$

To solve Eq. 32, several parameters need to be defined. These parameters were directly measured or estimated from a commercial crisp frying system in service and are listed in *Table 1*. The data relate to the period December 2009 to March 2010.

Table 1
Parameters for the developed model.

Symbol	Value or expressions	Source	Symbol	Value or expressions	Source
A	45 m^2	measured	$\dot{m}_{12}$	0.02 kg/s	assumed
c_{pa}	1.006 kJ/kg K		$\dot{m}_{13}$	$\dot{m}_9 \cdot X_{s,9}/X_{s,13}$ kg/s	calculated
c_{ps}	1.3 kJ/kg K	measured	T_{amb}	298.0 K	measured
c_{pw}	4.18 kJ/kg K		T_{fo}	446.0 K	measured
$h_{fg\,w}$	2256.7 kJ/kg		T_2	375.9 K	measured
$h_{fg\,o}$	300.0 kJ/kg	measured	T_8	$T_8 = T_{amb}$	
U	1.4×10^{-3} kW/m^2 K	[21]	T_9	333.0 K	measured
$\dot{m}_2$	1.07 kg/s	assumed	T_{13}	423.0 K	assumed
$\dot{m}_7$	62.73 kg/s	measured	$X_{o,13}$	30.3%	measured
$\dot{m}_8$	0.04 kg/s	assumed	$X_{o,2}$	0.13%	calculated
$\dot{m}_9$	1.1 kg/s	measured	$X_{s,9}$	20.0%	measured
$\dot{m}_{10}$	0.054 $\dot{m}_9$ kg/s	measured	$X_{v,2}$	98.8%	calculated
$\dot{m}_{11}$	62.57 kg/s	assumed	$X_{w,13}$	1.6%	measured

4   Results and discussion
4.1   Analysis of fryer
Figure 6 shows a comparison between predicted daily energy consumption from the model and data obtained from the plant over the four month period December 2009 to March 2010. The average quantity of surface water during a sampling period was found to be 5.4% by weight (wet basis) of the potato slice and the initial water content of the potatoes was assumed to be 80% by weight. The surface water on the potato slices was determined by randomly sampling potato slices just before entry to the fryer and weighing them. The slices were then dried with a water absorbing towel before they were re-weighted. The percentage surface water was then determined as the difference between the average weight of wet and dried slices divided by the average weight of wet slices.
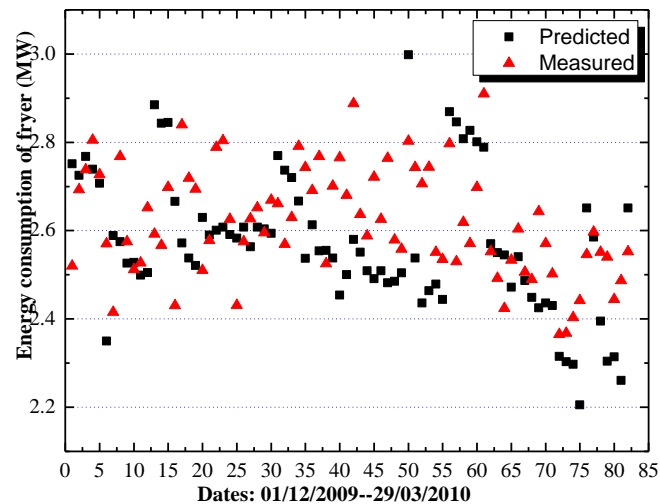
Figure 6: Comparison between measured and predicted energy consumption of the fryer

The model assumes steady state conditions during the period whereas in the real process there are fluctuations in the throughput and energy consumption which depend on a large number of operational and control factors. Despite this, it can be seen that in general there is a good agreement between the predicted and actual energy consumption. The maximum error is around 13%.

The average energy requirement of the fryer was found to be 2574 kW. Using the data in *Table 1*, and a final moisture content for the crisps of 1.5% by weight it was determined from the model that approximately 90% of this energy was used for the evaporation of water from the potato slices. The other energy losses are quite small by comparison with energy input to the ventilation air representing 2% of total, energy input to potato solid 0.9% and energy lost through the external walls by convection 0.4%.

The moisture content of potatoes will depend, among others, on their variety and growing conditions. To investigate the effect of moisture content on the energy consumption, 3 different initial moisture contents, 60%, 70% and 80% were considered. Figure 7 shows the variation of the energy consumption of the fryer as a function of raw material flow rate and moisture content. It can be seen, as expected, that the energy consumption is a linear function of the raw material flow rate. It can also be deduced that the energy consumption is also a linear function of the potato moisture content. At a raw material flow rate of 1.0 kg/s, increasing the moisture content from 70% to 80% increased the energy input to the process from 2322 kW to 2574 kW which represents a 10% increase.

Even though before entering the fryer the potato slices are normally dewatered using one of a variety of methods not all the water is removed and this contributes to the energy consumption of the fryer. The impact of surface water on energy consumption is shown in Figure 8 for surface water percentages of between 4% and 10% by weight. It can be seen that surface water increases the energy input to the process almost linearly. At a raw material mass flow rate of 1.0 kg/s, and surface water of

4% the energy input to the fryer is 2541 kW. Increasing the surface water to 10% increases the energy input to 2686 kW which represents a 145 kW (6%) increase.
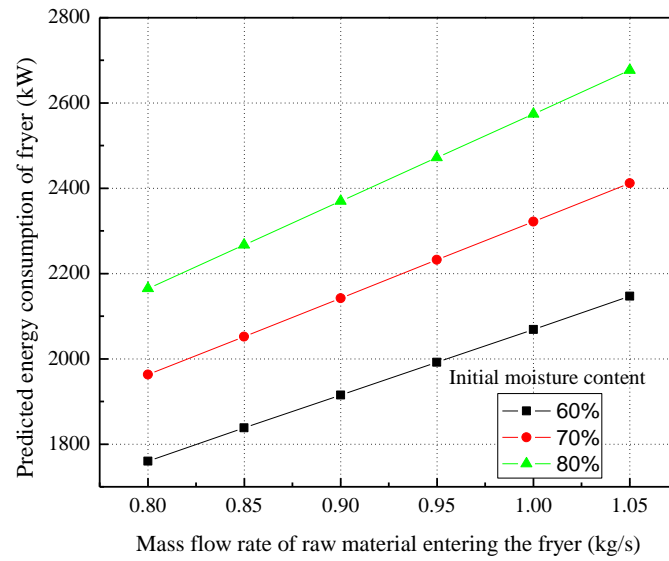
Figure 7: The effect of initial moisture content of raw material on the predicted energy consumption
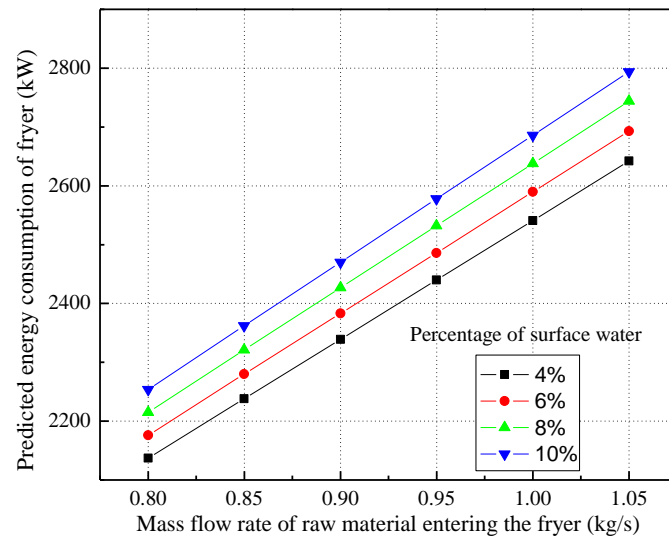
Figure 8: Predicted energy consumption at different percentages of raw materials surface water

The energy required by the fryer is provided by the combustor and oil heat exchanger. To optimise the whole process it is essential to appreciate the efficiency of the various sub-processes in the system.

4.2   Analysis of heat exchanger
The heat lost to the ambient through the exhaust gases.

$$\dot{Q}_{loss} = \dot{E}_6 = (\dot{E}_5 - \dot{E}_4) - (\dot{E}_7 - \dot{E}_{14})$$

Based on the fact that $\dot{m}_7 = \dot{m}_{14}$, $c_{p4} = c_{p6}$ and $T_4 = T_6$

$$\dot{Q}_{loss} = \dot{m}_5 \cdot (c_{p5} \cdot T_5 - c_{p4} \cdot T_4) - \dot{m}_7 \cdot c_{po} \cdot (T_7 - T_{14}) = 622 \text{ kW} \tag{33}$$

The First Law efficiency of the heat exchanger can be calculated from Eq.(11):

$$\eta_{HE} = \frac{\dot{E}_7 - \dot{E}_{14}}{\dot{E}_5 - (\dot{E}_4 + \dot{E}_6)} = \frac{2597}{3249} = 79.9\% \qquad (34)$$

The energy efficiency of the combined combustor and heat exchanger can be determined from Eq.(12):

$$\eta_{CHE} = \frac{\dot{E}_7 - \dot{E}_{14}}{\dot{E}_1} = \frac{c_{po} \cdot \dot{m}_7 \cdot (T_7 - T_{14})}{\dfrac{\dot{m}_1 \cdot CV_1}{\rho_1}} = \frac{2597}{3076} = 84\% \qquad (35)$$

The above compares well with studies on industrial steam boilers reported by Saidur et. al. [22] which indicated efficiencies of between 72% and 94%.

4.3   Overall frying system efficiency

The energy efficiency of the overall frying system (η_{SY}) can be determined from:

$$\eta_{SY} = \frac{\text{energy in products}}{\text{total energy input}} = \frac{\dot{E}_{ps} + \dot{E}_{pw} + \dot{E}_{o,13}}{\dot{E}_{total}} \qquad (36)$$

where $\dot{E}_{ps}$, $\dot{E}_{pw}$ and $\dot{E}_{o,13}$ are the quantities of energy needed for raw potato heating, water heating and evaporation, and oil absorption, respectively. E_{total} is the total energy input of the whole system. Using the data in *Tables 1* and *2*,

$$\dot{E}_{o,13} = c_{po} \cdot \dot{m}_{o,13} \cdot T_{13} = 116 \qquad \text{kW}$$

(37)

$$E_{total} = E_1 + E_3 = \frac{\dot{m}_1 \cdot CV_1}{\rho_1} + c_{p3} \cdot \dot{m}_3 \cdot T_3 = 3440 \, \text{kW} \qquad (38)$$

therefore,

$$\eta_{SY} = \frac{\dot{E}_{ps} + \dot{E}_{pw} + \dot{E}_{o,13}}{\dot{E}_{total}} = \frac{25 + 2264 + 116}{3440} = 69.9\% \qquad (39)$$

Table 2

Combustor and heat exchanger operating data.

Symbol	Value or expressions	Symbol	Value or expressions
c_{po}	2.34 kJ/kg K	$\dot{m}_5$	3.28 m^3/s
c_{p4}	1.08 kJ/kg K	T_3	298 K
c_{p5}	1.54 kJ/kg K	$T_4 = T_6$	473 K
CV_1	40,120 kJ/m^3	T_5	975 K
$\dot{m}_1$	0.061 kg/s	T_7	445.8 K
$\dot{m}_3$	1.21 kg/s	T_{14}	427.9 K
$\dot{m}_4$	1.19 m^3/s	ρ_1	0.8 kg/m^3

The above indicates that with an overall efficiency of only around 70% there are opportunities to reduce the energy consumption of frying processes. Despite the fact that the overall efficiency of combustor and heat exchanger was determined to be 84%, 622 kW were rejected to the ambient with the exhaust gases. Some of this heat can be recovered and used in a number of ways to reduce the energy input to the crisp production line or the fryer itself.

5   Conclusions

This paper presented a thermodynamic analysis of potato crisp frying. The analysis is based on data from a crisp production line and a First Law modelling of the frying process. The results indicated that the overall efficiency of the frying system investigated was of the order of 70%. The major energy requirement of the process is for the evaporation of water contained in the potatoes and on the surface of the slices which represents over 90% of the energy input in the fryer. The energy in the exhaust gases to the atmosphere is also significant, of the order of 622 kW compared to 3440 kW energy input to the combustor. Some of this heat can be recovered and used in a number of ways such as preheating the combustion air to the combustor or to heat water in the hot wash system of the production line.

Exhaust gas recirculation to the combustor has an impact on the effectiveness of the heat exchanger and the energy available in the exhaust for heat recovery. Future investigations will address in detail the influence of this control parameter as well as effective ways of recovering and utilising energy in the exhaust gases.

Acknowledgements

References

[1]   Siitonen S., Tuomaala M., Suominen M., Ahtila P. Implications of process energy efficiency improvements for primary energy consumption and CO2 emissions at the national level. Applied Energy. 2010; 87(9):2928–2937.

[2]   HM Government, Department of Environment Food and Rural Affairs (Defra). Food 2030 strategy, January 2010, 81 pgs.
http://www.defra.gov.uk/foodfarm/food/pdf/food2030strategy.pdf

[3]   DTI (Department of Trade and Industry), 2007. Meeting the Energy Challenge, A White Paper on Energy, 343 pgs. http://www.berr.gov.uk/

[4]   Wang Z., Zheng D., Jin H. Energy integration of acetylene and power polygeneration by flowrate-exergy diagram. Applied Energy. 2009; 86(3):372-379.

[5]   Al- Kawari, ME. Pinch technology: an efficient tool for chemical-plant energy and capital-cost saving. Applied Energy. 2000; 65(1-4):45-49.

[6]   Lee SC., Ng DKS., Foo DCY., Tan RR. Extended pinch targeting techniques for carbon-constraint energy sector planning. Applied Energy. 2009; 86(1):60-67.

[7]   Uson S., Valero A., Correas L., Energy efficiency assessment and improvement in energy intensive systems through thermoeconomic diagnosis of the operation. Applied Energy. 2010; 87(6):1989-1995.

[8]   DECC (Department of Environment and Climate Change), Energy consumption in the UK: industrial data tables. 2010 update.
http://www.decc.gov.uk/en/content/cms/statistics/publications/ecuk/ecuk.aspx

[9]   FDF (Food and Drink Federation) 2006. Defra Public Consultation on Draft Food Industry sustainability Strategy, Overall Comments, 6 pgs. https://www.fdf.org.uk/responses/CCWG-031-10.pdf

[10] PEPSICO Environmental Sustainability Report, 2008.
http://www.pepsico.co.uk/purpose/environment/environment-resources-library#asset/98

[11] Mellema M. Mechanism and reduction of fat uptake in deep-fat fried foods. Trends Food Sci. Technol 2003;14(9):364-73.

[12] Krokida MK, Oreopoulou V, Maroulis ZB, Marinos-Kouris D. Deep fat frying of potato strips-quality issues. Drying Technol. 2001a;19(5):879-935.

[13] Krokida MK, Oreopoulou V, Maroulis ZB, Marinos-Kouris D. Effect of osmotic dehydration pretreatment on quality of french fries. J. Food Eng. 2001b;49(4):339-45.

[14] Gamble MH, Rice P, Selman JD. Relationship between oil uptake and moisture loss during frying of potato slices from c.v. record U.K. tubers. Int. J. Food Sci. Tech. 1987;22(3):233-41.

[15] Gamble MH, Rice P. The effect of slice thickness on potato crisp yield and composition. J. Food Eng. 1988;8(1):31-46.

[16] Rice P, Gamble MH. Technical note: Modelling moisture loss during potato slice frying. Int. J. Food Sci. Tech. 1989;24(2):183-7.

[17] Farkas BE. Modelling immersion frying as a moving boundary problem. Ph.D. Thesis. Davis, USA: University of California, 1994.

[18] Moreira RG, Palau J, Sun X. Deep-fat frying of tortilla chips: an engineering approach. Food Tech. 1995a;49(4):146-50.

[19] Mittelman N, Mizrahi S, Berk Z. Heat and mass transfer in frying, chap. 2. In: Engineering and Food. McKenna, B. M. (ed.). Elsevier Applied Science Publishers, 1984.

[20] Rywotycki R. The effect of fat temperature on heat energy consumption during frying of food. J. Food Eng. 2002;54(3):257-61.

[21] Rywotycki R. A model of heat energy consumption during frying of food. J. Food Eng. 2003;59(4):343- 47.

[22] Saidur R., Ahamed J.U., Masjuki, H.H., Energy, exergy and economic analysis of industrial boilers. Energy Policy. 2010;38(5):2188-97.

Novel Model Reduction Techniques for Refinery-Wide Energy Optimization

Taoufiq Gueddar, Vivek Dua [*]

Centre for Process Systems Engineering, Department of Chemical Engineering
University College London, Torrington Place, London WC1E 7JE United Kingdom

* Corresponding author. Email: v.dua@ucl.ac.uk;Tel.: +44 (0) 20 7679 0002 ; Fax: +44 (0) 20 7383 2348

Abstract

The oil refining industry mainly uses Linear Programming (LP) modelling tools for refinery optimization and planning purposes, on a daily basis. LPs are attractive from the computational time side; however these models have limitations such as the nonlinearity of the refinery processes is not taken into account. In addition, building the LP model can be an arduous task that requires collecting large amounts of data. The main aim of this work is to develop approximate models to replace the rigorous ones providing a good accuracy without compromising the computational time, for refinery optimization. The data for deriving approximate models has been generated from rigorous process models from commercial software, which is extensively used in the refining industry. In this work we present novel model reduction techniques based upon optimal configuration of artificial neural networks to derive approximate models and demonstrate how these models can be used for refinery-wide energy optimization.

Keywords   refinery-wide optimization; artificial neural network; MINLP; model reduction

1   Introduction

The oil refinery remains a key component of the global oil production and distribution process. It consists of an industrial process plant where crude oils are processed and refined into more valuable petroleum products [1]. These products should meet certain commercial specifications before being shipped to the domestic and international markets. The oil refining industry is currently facing new challenges. In fact, there is a change in fuel demand towards lighter products, as well as a change in the quality of crude oils. Furthermore, environmental restrictions are leading to tighter fuel specifications that require refiners to either invest in new refinery technologies or use better crude feedstock to improve the quality of the products downstream. Challenges from the operational point of view include the selection of crude oils to be fed to the refinery in order to achieve higher margins and to meet the final product specifications, impacting the cost per barrel.

  The complexity of oil refineries operations makes the operations decision making process an extremely difficult task, especially when uncertainty in feed specifications, product demand and economic parameters is involved [2]. Refinery wide optimization is a key requirement to overcome these challenges to achieve a high standard of performance and to stay competitive within the market [3]. Through refinery-wide optimization optimal refinery crude feed mixture as well as gasoline and distillates blending can be achieved [4]. It can also be used to minimize low-value fractions and quality giveaway whilst ensuring a better energy management, which is becoming of increasing importance in process industries [5].

LP models are routinely used to optimize refinery operations and work processes such as crude acquisition, final product blending and product sales as well as assess new investment opportunities. For such important financial decisions it is crucial to have models that are as accurate and robust as possible. However it is well known that LP models are usually built using process data from different units. Getting hold of plant data with the required range of physical process data is very difficult. Actual data with the needed range of physical properties is even more difficult to obtain. LPs are attractive from the computational point of view but their main drawback is the lack of consistency and

accuracy. This is in contrast to rigorous process simulators. They are more accurate and based on kinetic nonlinear models which are complex and large, therefore difficult to optimize. Within the Oil refining industry, there are in fact different rigorous simulation packages available. These softwares are able to simulate the refinery units with accuracy. However these packages are mainly used for process design, unit monitoring, and energy management. Attempts to achieve Refinery-wide optimization with rigorous simulators have not been very successful. In this work the objective is to replace rigorous simulator with neural networks models [6]. The Artificial neural network (ANN) models have two key properties, first they can capture highly nonlinear characteristics of a process, and secondly they are much simpler than the rigorous process model. The first property allows to retain the accuracy of the process and second property is important from computational point of view. Mixed Integer programming techniques were used to further simplify the structure of the ANN models to reduce the computational effort and maintain the models.

The rest of the paper is organised as follows. In section 1.1 – 1.4 an introduction to the refinery operations, feedstocks and products is presented. In section 2 refinery-wide optimization and refinery configurations are discussed. In the section 3 the refinery mathematical model is formulated. In Section 4, artificial neural networks model reduction techniques are presented. Results of the ANN modelling are discussed in section 5. In section 6 refinery model optimization results are discussed.

1.1   Refinery operations overview

The crude oil after being shipped to the refinery is firstly processed through a desalter preheated with the downstream Crude and Vacuum units products before being heated in a fired heater. It is then fed to the atmospheric crude distillation unit (CDU) to be fractioned into: LPG (liquefied petroleum products), Naphtha, kerosene, atmospheric gas oil, and atmospheric residue (Figure 1). The residue is sent to the vacuum distillation tower and separated into vacuum gas oil and a vacuum residue. The vacuum residue can be used as a feedstock to a delayed coker unit to produce fuel gas, coker naphtha, and coker gas oil and coke [1].

The visbreaker is another thermal cracking process that can use the Vacuum Residue (VR) as a feedstock. In the refineries where no deep conversion units are available, the VR is sold as a heavy fuel oil or as bitumen. The atmospheric gas oil and light vacuum gas oils as well as the coker gas oil are used as feedstocks for the fluid catalytic cracking (FCC) or hydrocracking units. These units crack the heavy molecules into lower molecular weight compounds boiling in the naphtha and distillates cut ranges.

The products from the hydrocracker are saturated. The unsaturated catalytic cracker products are saturated and improved through processing into hydrotreating and/or reforming units. The straight run naphtha cut from the crude distillation unit is sent to a Naphtha splitter that separate the naphtha full range into a light and heavy naphtha streams. The light naphtha cut from the naphtha splitter, coker and cracking units are used as a feedstock to the isomerisation unit to upgrade the research octane numbers and motor octane numbers by increasing the branching of the paraffinic chains. The heavy naphtha cuts from the crude distillation unit, coker, and cracking units are fed to the reformer in order to improve their octane numbers. The reformate product from the catalytic reformer is blended along with other products, into regular and premium gasoline for sale. The gas produced in the crude unit, coker, and cracking units is separated in the gas plant into fuel gas, liquefied petroleum gas (LPG), unsaturated hydrocarbons (propylene, butylenes, and pentenes), normal butane, and isobutane. The fuel gas is used in the fired heaters. The normal butane can be blended into gasoline or LPG. The unsaturated hydrocarbons and isobutane are sent to the alkylation unit for processing. The middle distillates from the crude unit, coker, and cracking units are blended into diesel and jet fuels.
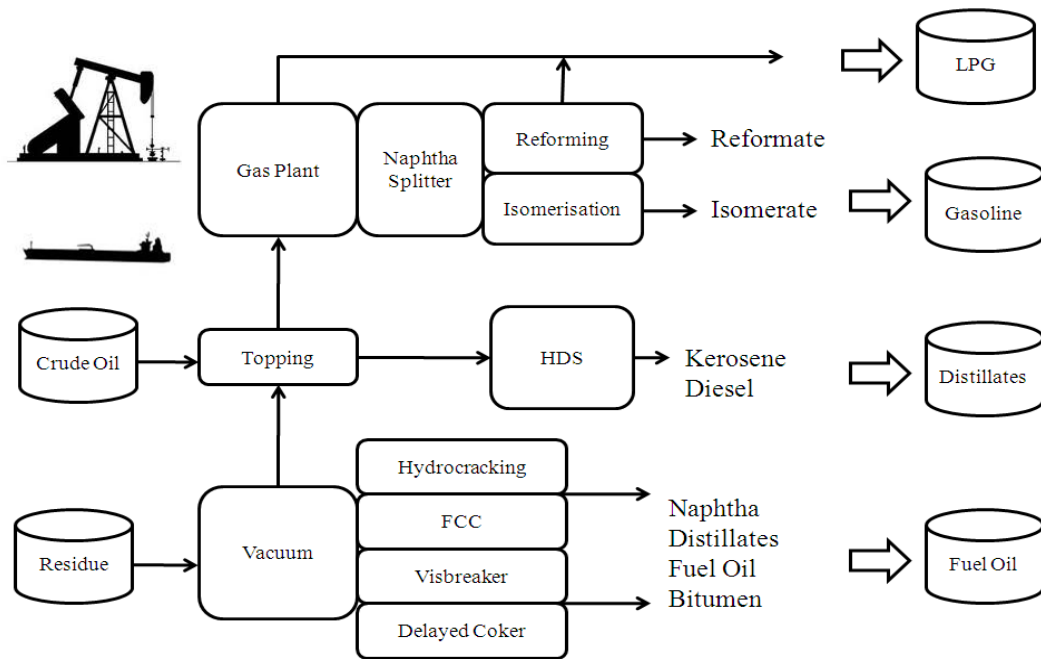
Figure 1: Refinery flowsheet

1.2   Refinery products

The main products of an oil refinery are: gasoline, diesel, jet fuel, fuel oil and kerosene. Each of these products consists of a blend of several different streams produced by the various refinery processes to meet final specifications. These products are then stored in a tank farm on the refinery premises before being delivered to retail markets. Delivery may be via pipeline to area distribution terminals, or through loading onto tanker trucks for direct delivery to retail outlets.

1.3   Refinery feedstocks

The main feedstock for oil refineries is crude oil, even though some refineries do process synthetic crude oils and natural gas liquids [1]. The main characteristics of the crude oil are:

1.3.1   API gravity:

The density of crude oils is expressed in terms of API gravity rather than specific gravity. The API gravity is an indicator of the heaviness of the crude, the lower the API the heavier the crude. The units of API gravity are °API and can be calculated from specific gravity by the following:

$$^{\circ}API = \frac{141.5}{Specific\ \ gravity} - 131.5$$

Usually high API crudes have a larger economical value than low API crudes as they can yield more valuable products.

1.3.2   Sulphur content:

The sulphur content is expressed as a weight percent of the sulphur, typically the sulphur content varies between 0.1% and 5%. Crude oil with greater than 0.5% sulphur generally requires more extensive hydrotreatment processing than those with lower sulphur content.

1.4   Product blending

Refinery final products as well as feeds to various process units are obtained through blending several components or streams. For the final products, the purpose of blending is to control the quality and to ensure that they respect the commercial specifications. For the gasoline blend to meet the

specifications, refineries usually blend reformate, isomerate, FCC gasoline, butane, MTBE/ETBE and other streams. Blending can also be driven by an optimization of the process unit capacity utilization. While many properties blend linearly on a weight or a volume basis, some other properties blend non-linearly. Hence, it is a common practice to use a blending index of the same property that can be blended linearly.

2 Refinery–wide optimization

The complexity of oil refineries leaves no doubt that a mathematical optimization approach is required to support the decisions that a refiner has to make with regards to crude oils purchasing, production planning, and operation strategies. These decisions include unit severities (the severity is a measure of the intensity of overall reaction conditions in a chemical reaction e.g. reactor outlet temperature in a Fluid Catalytic Cracking), operating and products blending as well as future investments inside the refinery and/or a petrochemical complex.

2.1 Crude acquisition

Crude oil acquisition decision will depend mainly on the type of the crude, the quantity, the availability on time and the type of contract (spot or term). To make the right judgment the refiner has to take into consideration the crude oil characteristics and this includes the physical properties (API, sulphur content, Watson K factor, Distillation data, etc) as well as the market price. Since different crudes can yield different intermediate product throughputs it is important to know the process constraints within each unit of the refinery such as the capacity limits and the utilization of the refinery units. In addition to this, some refineries are only able to handle certain type of crudes. In fact, simple refineries where no conversion units are available are designed for light crudes yielding mainly Gasoline, Kerosene and Diesel, while the heavy residue with a lower market value is a minor production of the refinery. On the other hand, conversion refineries have the ability of processing heavier cheap crude oil and upgrade them into valuable light products. In these modern refineries the heavy residue cut is upgraded into lighter products, which leads to a better utilization of the crude as well as the units. Also, these refineries have much more operational flexibility. The domestic demand can also dictate the type of the crude that a refiner has to process as some types of crudes can have good yields of a specific product but not the other. Usually the refiner runs multiple feeds to meet the constraints listed above while maximising energy efficiency and profit margin.

2.2 Refinery configurations

Each refinery has its own unique configuration which is determined by the process equipment available, the connections between the units, crude oil characteristics, operating costs, and product demand. The optimum flow pattern of various process streams in any refinery is set by economical considerations and no two refineries are identical in their operations.

2.2.1 Topping refinery

The topping refinery is composed essentially of the crude distillation tower that fractionates the crude oil into 5 cuts: light ends, Naphtha, kerosene, Diesel and the atmospheric residue for fuel oil production. When there were no strict restrictions on the products, the topping refinery was sufficient to meet the industrial and domestic needs of oil products. However, because there has been a continual change in the product and emissions specifications, this has meant that products have to be cleaner or/and environmental compliant and more efficient for industrial and vehicle use, thus the topping refinery is no longer suitable. There are only few of this kind that are still in operation at this current time. However this type of refinery can provide the intermediate product for further processing in other refineries when they have shortage in their products or purely for economical reasons.

2.2.2 Hydroskimming refinery

These types of refineries are more complex than the topping refinery as they have the ability of hydrotreating the naphtha and the distillates products in the hydrodesulphurisation units. In these units catalytic hydrodesulphurisation reactions take place with the use of hydrogen feedstocks to remove the sulphur from the hydrocarbon molecules. This is a key process that helps refineries achieve the low sulphur specifications on Naphtha, Diesel and kerosene. These types of refineries also have a

reforming unit. By making aromatics from naphthenic feed, it increases research octane number and motor octane number and meets the specifications required by the vehicle engine vendors. This refinery however still yields significant amounts of low value fuel oil.

2.2.3 Conversion refinery

Conversion refinery does have a vacuum distillation tower available to separate the crude unit residue into vacuum gas oil and vacuum residue. The vacuum gasoil is then processed in a catalytic cracking or a hydrocracking process to upgrade it into more distillate and gasoline products.

The vacuum residue can be routed to a visbreaker or delayed coking units. Also, since products are traded in volume the cracking units add value by increasing quantity through volume expansion (the cracking reactions lead to producing lighter products with a lower gravity than the feed, hence the volume is augmented through the cracking units) in addition to producing higher priced products than feed. For the same crude, a conversion refinery will have greater flexibility in product mix than the previous type of refineries. However, this type of refineries requires a large capital investment project.

3   Refinery optimization model
3.1   Constraints

All process plants operate within suitable process constraints which determine the operating conditions as well as the types and throughputs of the feedstocks. The plants are also expected to meet domestic and export demands for different products. Refineries have a large set of constraints that have to be met during operations. The types of constraints found in a refinery process model are:

3.1.1   Equality constraints

Rigorous simulator solves a large set of nonlinear equations, representing material and energy balances with zero degree of freedom. These equations will be replaced by simpler ANN model equations:
- Material and energy balances for each unit and for the refinery as a whole.
- Stream property balances: in some units, it is important to control some qualities at the front of the unit to ensure a safe and efficient operation for the unit. For the FCC unit, it is common to control the metals in the feed as the reactor catalysts can only tolerate a specific concentration. Any values beyond these limits can disrupt the operations and may lead to a loss in the profit margin.

3.1.2   Inequality constraints

The process specifications are what an optimizer (positive degrees of freedom) can take into account:
- Blending specifications: the final products have to be produced in conformity with the commercial specifications. The specifications depend on the region and/or the country as well as the season (e.g. summer and winter specifications).
- Process unit capacities: Each unit will operate within maximum and minimum capacity constraints.

3.2   Variables

Variables are the important factors or quantities for which best operating values are sought in the refinery model. Typically variables include Crude oil, chemicals, natural gas and final products additives. Flowrates of feeds and products, products physical properties. Blending qualities and quantities are other variables to consider in the model as well. We can also include energy consumptions/productions to account for energy/operating costs. Integer variables may be used when a discrete decision have to be made (number of crudes to be processed, number of units running, etc).

3.3   The objective function

The objective function is a weighted combination of refinery variables that is to be optimized (maximized or minimized). It may include: feedstock costs, operating costs and sales prices of products. The objective function usually represents the refinery gross margin or net refinery margin. However, rather than maximising profit, refiners can minimise operating costs.

3.4   Mathematical formulation of the refinery-wide optimization problem

An artificial neural network model will be developed to approximate the Topping refinery rigorous simulator. The equations representing the ANN model will then be used within the refinery optimization problem to replace mass and energy balances of the topping refinery. The ANN modelling will be discussed in depth in section 4 and appendix A.

Consider the following proposed general formulation for an ANN based Topping refinery optimization model:

$$\max M = \sum_{i=1}^{N_P} SP_i\, ZB_i \ - \ \sum_{k=1}^{N_{CR}} CP_k\, ZC_k \qquad \text{(Refinery gross margin) (1)}$$

Subject to:

$$Z_{i,k} = Y_{i,k} ZC_k, \quad i = 1,...,N_p \quad k = 1,...,N_{cr} \qquad \text{(Individual product flows) (2)}$$

$$ZB_i = \sum_{k}^{Ncr} Z_{i,k}, \quad i = 1,...,N_p \qquad \text{(Blend i of the products i from different crudes) (3)}$$

Capacity limits:

$$CAP^{LB} \le \sum_{k}^{Ncr} ZC_k \le CAP^{UB} \qquad \text{(Capacity limit of the refinery) (4)}$$

Blending equations:

$$QB_{i,wt} = \frac{\sum_{k=1}^{Ncr} SPG_{i,k} Z_{i,k} Q_{i,k,wt}}{\sum_{k}^{Ncr} SPG_{i,k} Z_{i,k}}, \quad i = 1,...,N_P \qquad \text{(Property Blending – weight properties) (5)}$$

$$Q_{B,vol} = \frac{\sum_{k=1}^{Ncr} Z_{i,k} Q_{i,k,vol}}{\sum_{k}^{Ncr} Z_{i,k}}, \quad i = 1,...,N_p \qquad \text{(Property Blending – volume properties) (6)}$$

$$QB_{i,idx} = \frac{\sum_{k=1}^{Ncr} SPG_{i,k} Z_{i,k} Q_{i,k,idx}}{\sum_{k}^{Ncr} SPG_{i,k} Z_{i,k}}, \quad i = 1,...,N_p \qquad \text{(Property Blending – index properties) (7)}$$

Commercial Specifications on final products:

$$QB_{i,vol}^{LB} \le QB_{i,vol} \le QB_{i,vol}^{UB}, \quad i = 1,...,Np \qquad \text{(Lower and upper bounds s on volume properties) (8)}$$

$$QB_{i,wt}^{LB} \le QB_{i,wt} \le QB_{i,wt}^{UB}, \quad i = 1,...,Np \qquad \text{(Lower and upper bounds s on weight properties) (9)}$$

$$QB_{i,idx}^{LB} \le QB_{i,idx} \le QB_{i,idx}^{UB}, \quad i = 1,...,Np \qquad \text{(Lower and upper bounds s on index properties) (10)}$$

Process simulator:
Mass and energy balances (later replaced by Artificial Neural networks Model)
A neural networks model is developed using training and testing data from a rigorous simulator. They are integrated within the refinery-wide optimization model and are acting like a simulator.

Model description:
In the above equations, (1) – (10), *Np* is the number of products, *Ncr* is the number of crude feedstocks, *ZB* the refined products flows and *ZC* the purchased crudes flows. *SPi* and *CPk* represent the product selling prices and crude purchase costs respectively. *Zi* is the throughput for the different refined products. *Yi,cr* is the yield for product *i* from processing crude k. *ZBi* is the blend quantity of product i quantities *Qi,wt*, is the weight quality for product i, index *vol* is for the volume qualities and *idx* is for the blending indexes. *QB* is the quality of the Blend B.

In this formulation, the objective function in equation (1) is the gross refinery margin which is simply the multiplication of the refined products prices per unit and the products productions minus the multiplication of the crudes prices per unit and the purchased capacities. Equation (2) calculates the flows of the different products using the unit yields for each crude. In equation (3) the quantities of the same product from different crudes are summed –up as a blend product. Inequality (4) is the capacity constraint of the refinery that limits the sum of the crudes throughputs that can be processed into the refinery. In (5)-(7) the product blend qualities are blended linearly for volume, weight and index blended properties. The specifications for the different products are given by equations (8)-(10). The reduced ANN equations will be discussed more in depth in the next section.

4   Artificial neural networks

Artificial neural networks (ANN) are very efficient in approximating complex nonlinear systems [7, 8] and have been widely used for solving many engineering problems [9, 10, 11, and 12]. The ANN consists of a network structure of neurons, where neurons are nonlinear, unbounded, parameterized functions. Variables are given in the form of inputs to the neurons which use its internal activation function to calculate outputs (Figure 2).

4.1   Nonlinear formulation:

Each input has an assigned weight. The output of the neuron will be calculated by using a nonlinear combination of the inputs, and the weights. The computation of the synaptic weights can be achieved through the process of learning. The objective of the learning is to calibrate the network with a set of data for which we know the input and the corresponding output [13]. The learning process is achieved solving the following Nonlinear Programming (NLP) problem:

$$\min_{a,b,w,h,W,B,u} E_1 = \sum_{k=1}^{N_o} (\hat{u}_k \quad u_k)^2 \qquad \text{(ANN prediction error objective function) (11)}$$

Subject to:

$$a_j^1 = \sum_{i=1}^{N_x} w_{ji}^1 x_i + b_j^1, \quad j = 1,...,N_n \qquad \text{(Activation variables of the first hidden layer) (12)}$$

$$h_j^l = tanh(a_j^l), \quad l = 1,...N_h \qquad \text{(Nonlinear transformation of activation variables) (13)}$$

$$a_j^l = \sum_{i=1}^{N_n} w_{ji}^l h_j^{l\ 1} + b_j^l, \qquad j = 1,...,N_n, \quad l = 2,...,N_h$$

(Activation variables of the remaining hidden layers) (14)

$$u_k = \sum_{i=1}^{N_n} W_{ki} h_j^{N_h} + B_k, \quad k = 1,...,N_o \qquad \text{(ANN Output) (15)}$$

Where x_i denotes the input values to the network, $i = 1,...,Nx$ is the number of inputs, N_n linear combinations of these inputs gives the activation variables, a_j^l, where N_n is the number of nodes in the hidden layer, the superscript 1 denotes the index of the first hidden layer, w_{ij} are the weights and b_j the biases. These activation variables are then transformed non-linearly to provide h_j^l, the output of a hidden layer; note that nonlinear transformations other than tanh are also used in the literature. h_j^l, the output of a hidden layer then becomes the input to the next hidden layer. The outputs from the last hidden layer $h_j^{N_h}$ are then combined to provide the outputs, u_k. N_0 is the number of nodes in the output layer and w_{ki} and B_k are the weights and biases respectively. Let $\hat{u}_k$ denote the desired output, the training of the network can then be formulated as minimization of the error function, E_1. For simplicity in presentation, u_k, $\hat{u}_k$, a_j^l, h_j^l and x_i represent vectors for all the points in the training data set.

4.2 Data generation

To build the ANN model, Petrosim® a refinery simulator that is extensively used in the industry has been used. The first step was to build a short cut model for the crude distillation model (DISTOP) and a rigorous tray to tray model. Due to the difficulty in converging the tray to tray model, for each crude type and a given operating cut points we first run the short cut distillation model to predict the flowrates of the different cuts. These production rates will be then used, if needed, as an initial guess in the tray to tray model.
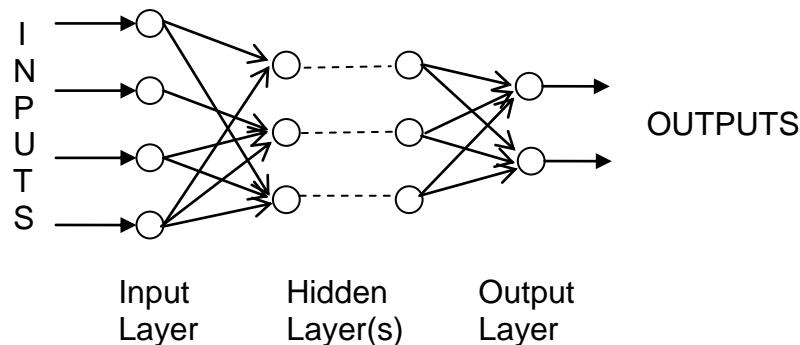
Figure 2: Artificial neural network

4.2.1 Tray to tray model

For tray-to-tray modelling it is assumed that the column is operating at steady-state. The model takes into consideration mass and energy balance and vapour-liquid equilibrium (VLE).

A general stage in a column is represented in Figure 3. F is the stage feed stream, L is the Liquid stream travelling to stage below (j+1), V is the Vapour stream travelling to stage above (j-1), and LSD is the Liquid side draw from stage, VSD is the Vapour side draw from stage and Q is Energy stream entering stage.
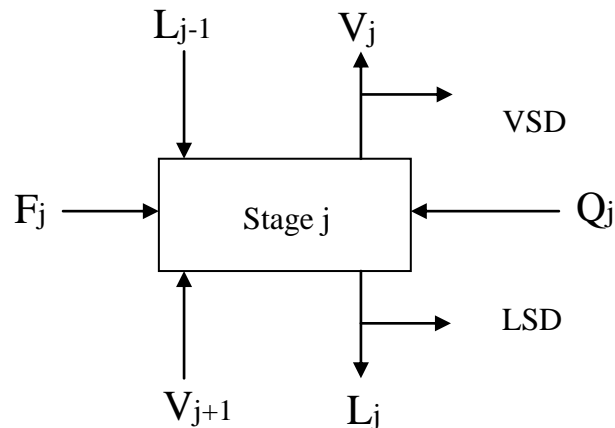
Figure 3: Representation of a generic stage in the column

To simulate the tray-to-tray model of the column, following data was specified:

- Reboiler and condenser pressure: the tray to tray model uses this information to determine the operating pressure of each stage in the distillation column.
- Feeds: These must be completely specified using pressure, temperature / vap fraction and a flowrate.
- Number of trays.

The side strippers for kerosene, light diesel and heavy diesel are connected to the main column. The main purpose of the side strippers is to remove the remaining light hydrocarbons by injecting steam or using a reboiler. Some of the properties are also controlled in the side strippers. The pumparounds are also modelled to induce condensation of vapours (column set-up data available in Appendix B). The whole flowsheet is shown in Figure 4.
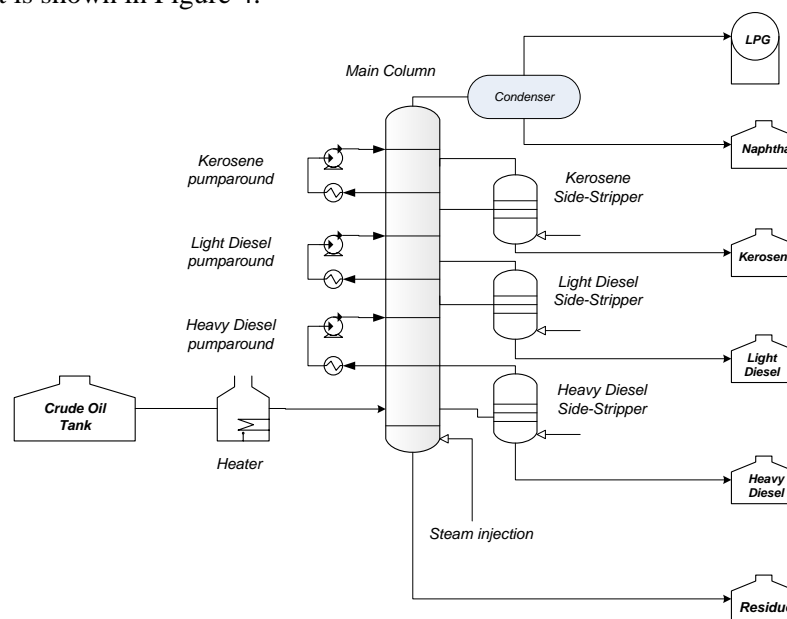
Figure 4: Rigorous tray-to-tray column flowsheet

4.2.2   Data generation process

To be able to produce an approximate ANN model representing rigorous tray-to-tray system which can be used later in the refinery optimization cases, a number of steps have been undertaken from the selection of the crude oils that will be used as potential feedstocks of the refinery to obtaining the reduced ANN model ready to be used for refinery-wide optimization. Figure 5 summarizes the steps below.

In the conventional ANN learning method the number of neurons and interconnections are fixed. Model reduction (Steps 5 and 6) is achieved by reducing overparameterization of the ANN by removing redundant nodes and interconnections while the training error is kept under a defined limit. This is achieved by using mixed integer nonlinear programming techniques. In many cases the MIPANN prediction has actually improved compared to the conventional ANN. The simplified configuration will also result in reduced computational effort for computing the outputs for given inputs, e.g. where ANN is used as property and yields prediction correlation for refinery units. Refinery optimisation problems are complex and large where computational performance can be an issue. Since we are using the ANN approximate models instead of the rigorous ones in the optimization problems, any further structure reduction with reduced computational effort and without compromising the performance of the network, is highly desirable.

1. *Selection of the crudes:* The Crude basket contains 37 crudes. We made sure that these crudes are representative of the different types of crudes available in production. This includes sour and sweet crudes as well as light and heavy crudes. We also looked at acid and non acid crudes. In refinery studies only a limited number will be required though.

2. *Rigorous simulation*: Consists of processing the selected crudes through the CDU flowsheet while varying the TBP cut points so we can capture the yields and products change as function of the cut points. For each crude each TBP cut point is varied while the two other cut points are kept fixed. Note that the advantage of using the rigorous simulation is that we are not limited on the number of points we can have. Therefore in case of non satisfactory prediction results we can decide to increase the number of generated points in this phase.

3. *Data Generation and scaling:* Before the training of the ANN, the data from the simulator (the input and desired output values) need to be scaled in order to achieve a better estimation of the ANNs internal parameters. Scaling is achieved by dividing each input and output data value from Petrosim® by the maximum value within the dataset of that variable. All the data values were scaled in the [0, 1] interval.

4. *NLP Network Training:* The first step consists of solving a Non-Linear Program using the SNOPT solver. The objective of this program is to train the ANN without proceeding with any structure reduction. The ANN is trained by minimizing the objective function E1 which is the Sum of Squared Errors (SSE) between the predicted outputs from the ANN and the desired outputs obtained from the simulator.

5. *MINLP Nodes Reduction (MIPANN):* The completion of step 4 will allow the reduction to be initialized by identifying a tolerable error value above the E1 value achieved by NLP training. This Program (refer to appendix A) will minimize a new objective variable E2 (total number of nodes), whilst keeping the training error under the chosen tolerable error for E1. In this way, the number of nodes within the network is reduced while keeping the accuracy of the network within the allowable range.

6. *MINLP Interconnection Reduction (MIPANN):* This program will first enforce the weights of unused nodes to zero. The next step is to minimise a new objective function ERR3 which is the sum of the interconnection binary variables from the inputs to the hidden layer nodes and from the hidden layer to the outputs. The network error is also kept under the chosen error. These operations along with step 6 are carried out in a loop where the weights are initialised randomly during each iteration, the loops stops when the prediction MSE (Mean Square Error) is under the MSE target. We can also run the loop for several iterations (50 in this case) and select the best configuration among the different runs.

7. *NLP Training with the optimised structure:* This program is the same as in the step 4. But in this step we use the optimised structure by fixing the binary variables on their optimum values found earlier.

8. *Validation test:* Steps 6 are 7 carried out in a loop where the weights are initialised randomly during each iteration. Also for each run SSE are calculated using testing data. The loop stops when the prediction MSE is under the MSE target. We can also run the loop for several iterations (50 in this case) and select the best configuration among the different runs.
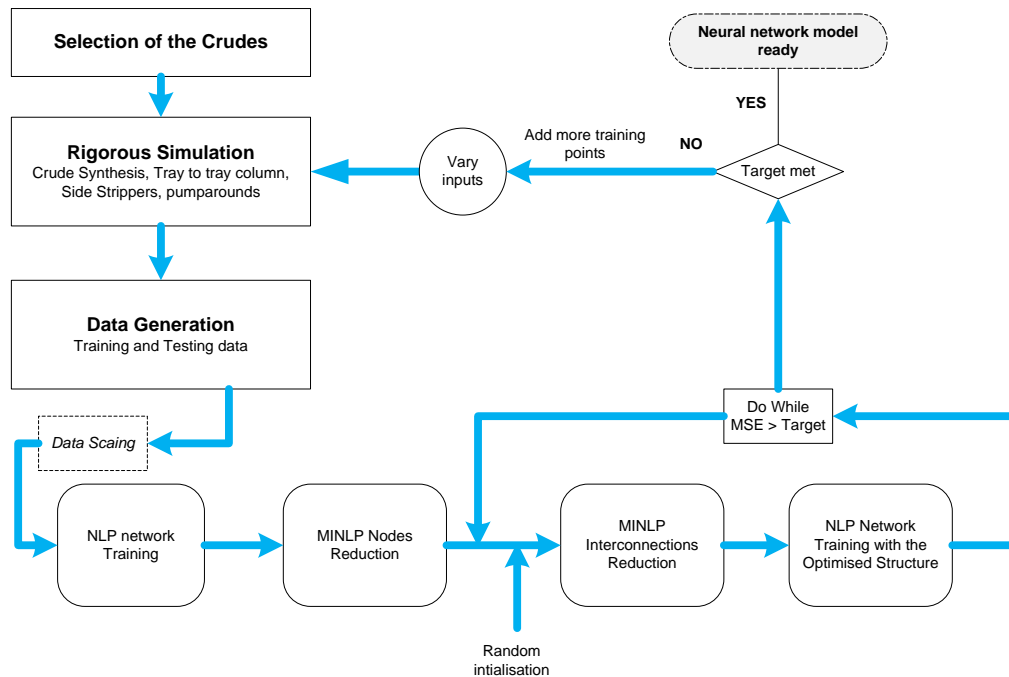
Figure 5: Model reduction process

5   ANN modelling results

The training and validation, node reduction and interconnection reduction programs were modelled in

GAMSIDE [14] and run using the SBB and SNOPT solvers for MINLP and NLP formulations respectively. Global optimality [15] issues were not addressed in this paper.

Because of the complexity of the crude oil separation the prediction of the products properties as well as the yields has been broken down into different networks. Variables of the same type /magnitude are grouped within the same network. Overall 8 neural networks are modelled and optimised. The results of the ANN modelling are presented in *Table 1* and *Table 2*.

Table 1

Initial ANN Structure

Network	System	Inputs	Outputs	Initial Nodes	Inter-Connections (IC)
1	Specific Gravities	9	4	15	195
2	Yields	9	4	20	260
3	Paraffins & Naphthenes %	8	2	15	150
4	RON and MON	10	2	15	180
5	Viscosity index	9	1	20	200
6	Distillates Properties	10	5	10	150
7	Metals	5	2	10	70
8	Temperatures	9	2	20	220

Table 2

Summary of ANN reduction results

Network	System	Reduced Nodes	Reduced IC	% Reduction on Nodes	% Reduction on IC	SSE	Prediction MSE
1	Specific Gravities	2	26	87%	87%	7.60E-02	3.32E-04
2	Yields	4	52	80%	80%	5.48E-01	9.40E-03
3	Paraffins and Naphthenes %	4	39	73%	74%	8.07E-01	7.08E-03
4	RON and MON	2	15	87%	92%	5.34E-01	4.68E-03
5	Viscosity index	2	20	90%	90%	2.72E-02	4.78E-04
6	Distillates properties	4	60	60%	60%	3.51E+00	1.23E-02
7	Metals	2	14	80%	80%	5.92E-02	5.19E-04
8	Temperatures	4	19	80%	91%	5.22E-02	4.58E-04

5.1   Temperature prediction network

The initial network was given as a single hidden layer containing 10 nodes. Using the MINLP Model Reduction method (MIPANN), the resultant architecture is shown below in Figure 6, containing 4 nodes and 19 interconnections.
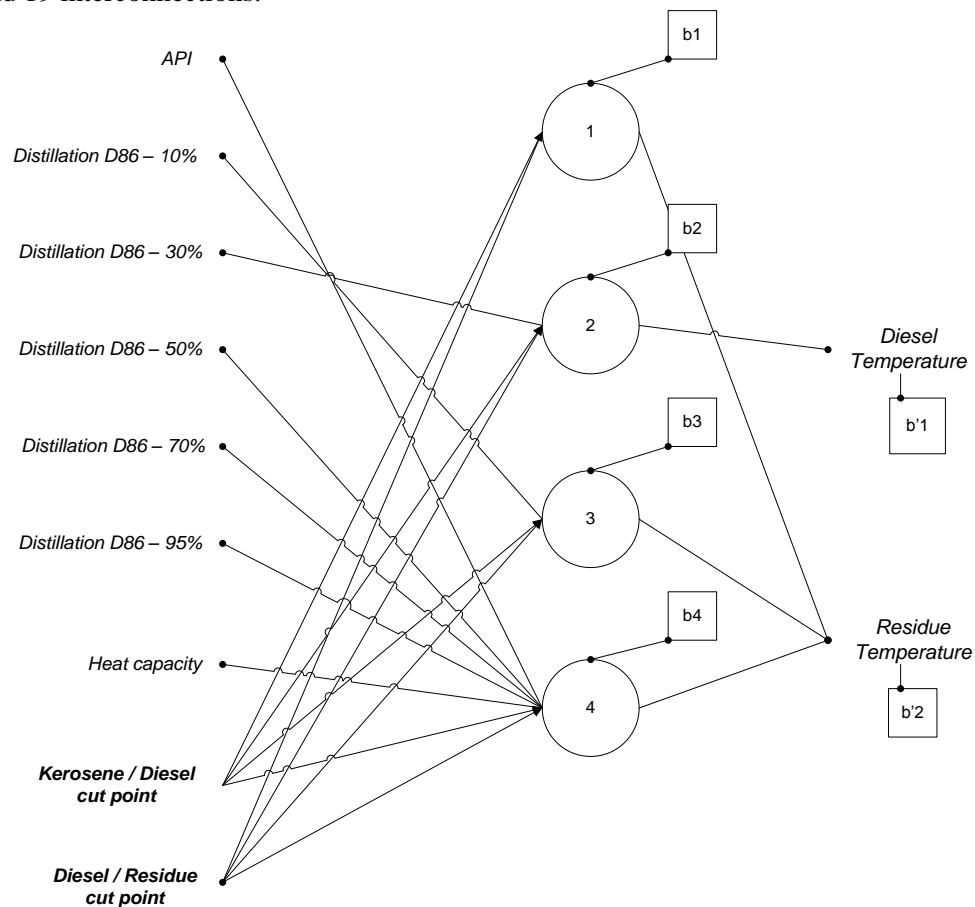
Figure 6: Temperature prediction reduced network

6   Model optimization results

The ANN model developed in section 5 for topping refinery is used to predict the product yields and properties for specific crudes for different cut points. It is also used to carry process optimization and optimal feedstock selection studies.

6.1   Gross product worth calculation (GPW)

The GPW is a method of valuation of crude oils based on the fractionation yields. The traditional 5-cut model is based on the primary fractionation yields of:

1. LPG valued as LPG
2. Naphtha valued as Naphtha
3. Kerosene valued as Jet
4. Gasoil/Diesel valued as Diesel
5. Atmospheric Residue valued as Fuel Oil

The reduced ANN topping refinery model has been used to predict the yields of the Minas crude which will be used along with product prices to calculate the GPW. The standard 5-cut method cut points have been used (*Table 3*).

Table 3
Standard cut points for GPW method

Crude Cuts	TBP cut point (Deg C)
LPG	C3/C4
Naphtha	C5-149
Kerosene	149-232
Diesel	232-369
Residue	369 +
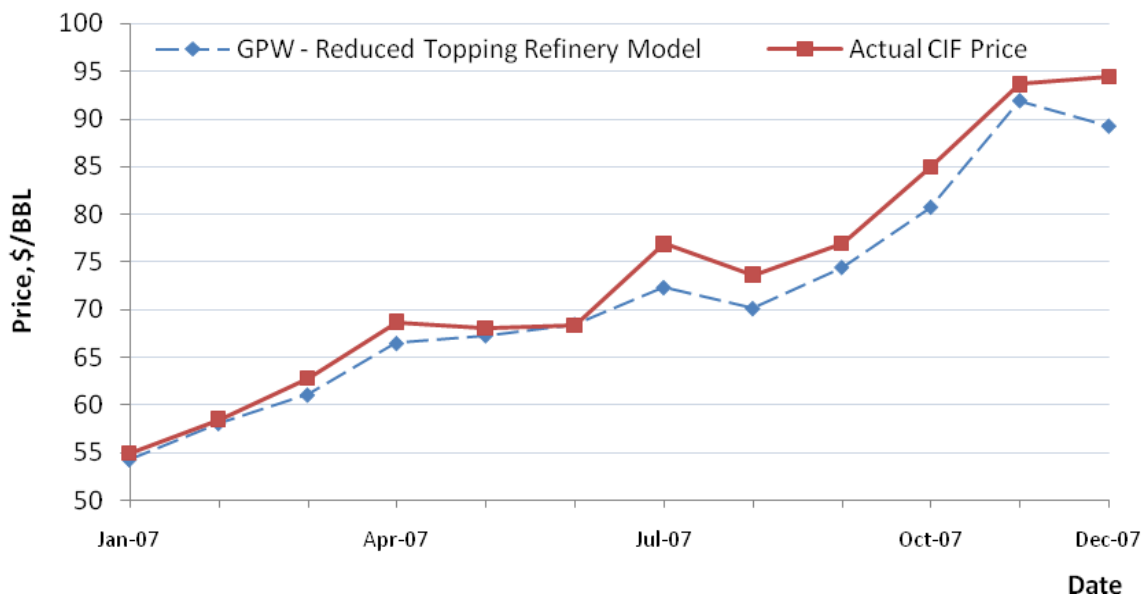
Figure 7: GPW prediction against Crude CIF price for Minas (Year 2007)

The GPW for the refinery purchasing the crude must be greater than the actual CIF (Cost insurance and Freight) value otherwise there is no incentive to buy the crude. Since the GPW model represents a relatively simple refinery configuration: GPW-5 is effectively a topping refinery. As a consequence it may be seen from Figure 7, that for the majority of the time period, the GPW is below the CIF price. As the 'complexity' of the Refinery is increased, for example by reforming naphtha to gasoline and conversion of residue to distillates, we would expect the difference between the GPW of a high API crude and a low API crude to decrease.

6.2   Crude selection

The crude oil characteristics have a considerable impact on the yield structure of a refinery, hence on its economical performance. Also, a refinery design can only handle crudes within a limited range. For these reasons, prior to any approval for crude to be processed in a refinery, a rigorous process to analyse crude suitability for processing into the refinery has to take place. The refinery model is used in the example below to optimise the crude feedstock composition subject to specifications of some refined products. The crude basket contains both heavy and light sweet and sour crude with different distillation volumes as well. This will ensure that the specifications will be met by optimally blending the crudes. The cut points are fixed for this particular case.

6.2.1   Products Specifications

While we are optimising crude feedstock selection we want to ensure that the refined products meet certain specifications. Below a set of specifications that have to be met for Naphtha : Research Octane number (RON), aromatics content (ARO) and specific gravity(SPG), Kerosene : Smoke point (Smk), Diesel : Specific gravity and Cetane index(CET) and the Residue (volume Flow).

$$RON_{Naphtha} \geq 45$$
$$ARO_{Naphtha} \leq 7\%$$
$$SPG_{Naphtha} \leq 0.74$$
$$Smk_{Kerosene} \geq 25$$
$$CET_{Diesel} \geq 50$$
$$SPG_{Diesel} \leq 0.86$$
$$Z_{Residue} \leq 50\,kbpd$$

The crude selection program for a given crude oil characteristics as highlighted in the *Table 4* as well as the CIF prices of each crude resulted in the optimal feedstock composition as shown in *Table 5*. The refinery optimization selects Minas as the most attractive crude economically however running Minas only will not allow us to meet the products specifications. For that reason different crudes will have to be processed to meet the different specifications while the gross margin is kept at optimum. Note that two crudes, Arabian Heavy and Gippsland, have not been selected. And we can see a negative Marginal values allocated to them. The marginal value expresses the changes in the objective function which is the gross margin. These marginal values are nothing but the Lagrangian multipliers allocated to the volume flows of these two crudes.

$$\lambda_{ARH} = \frac{dM}{dZ}\bigg|_{ARH} = -2.845$$
$$\lambda_{GPS} = \frac{dM}{dZ}\bigg|_{GPS} = -0.946$$

Table 4
Crudes Properties for crude selection case

Crude Properties	Urals (URL)	Minas (MINI)	Arabian Heavy (ARH)	Forcados (FORI)	Gippsland (GPS)	Shengli (SHG)	Tapis (TAP)
API	*31.7*	*35.4*	*27.8*	*29.8*	*46.9*	*23.1*	*44.8*
Sulphur (ppm)	*1.32*	*0.07*	*2.75*	*0.2*	*0.11*	*0.64*	*0.03*
Distillation D86 – 30%	*223*	*282*	*239*	*243*	*128*	*361*	*165*
Distillation D86 – 50%	*322*	*378*	*354*	*297*	*189*	*478*	*247*
Distillation D86 – 95%	*615*	*681*	*705*	*523*	*415*	*656*	*449*
Watson K factor	*11.5*	*12.1*	*11.4*	*11.3*	*11.7*	*11.6*	*11.9*
Prices $/BBL	*94.0*	*100.5*	*88.1*	*100.34*	*101.1*	*85.1*	*104.2*

Table 5
Optimal feedstock composition

Crude	Lower Bound	Optimal	Upper Bound	Marginal Value
MIN1	*0*	*73.474*	*100*	-
FOR1	*0*	*13.916*	*100*	-
ARH	*0*	*0*	*100*	*-2.845*
GPS	*0*	*0*	*100*	*-0.946*
TAP	*0*	*3.074*	*100*	-
URL	*0*	*3.324*	*100*	-
SHG	*0*	*6.213*	*100*	-

Table 6
Optimal products physical properties

Quality	Lower Bound	Optimal	Upper Bound	Marginal Value
Nap.SPG	-	0.74	0.74	18009.175
Nap.RON	45	49.063	-	9
Ker.Smk	25	25	-	-82.988
Dsl.SPG	-	0.839	0.86	-
Dsl.Cet	50	78.448	-	-
Dsl.SPG	-	0.839	0.86	-
Res	-	50	50	31.999

This means that should these two crudes to be processed in this topping refinery, a Refiner will loose 2.845 k$/ day by using Arabian heavy and 0.946 k$/day by using Gippsland. Residue Flow has a positive marginal value (see *Table 6*). This tells us that by allowing this constraint to be relaxed by 1 kbpd (1000 barrels per day) than we can make an extra 31.99 k$ /day. These are valid in the neighbourhood of the optimal solution.

6.3   MINLP crude selection

The classical crude selection problem gives the feedstock fraction among the studied crude oils. But more realistically only a limited number of crudes will be selected. The idea of this case is to model a discrete crude selection through an MINLP problem [16, 17].

Based on the previous refinery model formulation in section 3, the following equations will be added to solve the crude selection MINLP problem:

$$\sum_{i}^{Ncr} Ycr_i \leq NCS$$

$$LB.Ycr_i \leq CR_i \leq UB.Ycr_i$$

$$Ycr_i = \{0,1\}^{Ncr}$$

$$UB = 100$$

$$LB = 1E - 6$$

NCS is the maximum number of crudes that should be considered for the crude selection problem. UB is a large number (100), LB is a small number (1E-6) and Ycr is a binary variable indicating whether or not crude is selected. We solved this problem, by fixing NCS to 4. SBB was used to solve this problem.

Minas and Gippsland are the optimal crude selections for this problem:

$$
\begin{aligned}
Ycr \text{ (Minas)} \quad &= 1 \\
Ycr \text{ (Gippsland)} \quad &= 1 \\
ZC \text{ (Minas)} \quad &= 86.65 \text{ kbpd} \\
ZC \text{ (Gippsland)} \quad &= 13.35 \text{ kbpd}
\end{aligned}
$$

The MINLP crude selection formulation can be particularly relevant for the refineries with a limited storage capacity which may limit the blending opportunities resulting from a feedstock optimisation Problem.

6.4   Operating conditions optimization

In this section, we are interested in optimising the operating conditions for a specific crude feedstock. The TBP distillation cut points are the operating conditions used within the model. The variation of these variables will impact the yields and the qualities for each of the refined products. The cut points that were fixed in the previous case studies are now relaxed:

$$140 \leq \ NK \ \leq \ 170 \qquad \text{Naphtha / Kerosene cut point, Deg C}$$

$$220 \leq \ KD \ \leq \ 250 \qquad \text{Kerosene / Diesel cut point, Deg C}$$

$$340 \leq \ DR \ \leq \ 375 \qquad \text{Diesel / Residue cut point, Deg C}$$

Table 7
Prices set for operating conditions optimization

Cases	Case 1	Case 2	Case 3	Case 4	Case 5
LPG	70.01	76.01	76.01	76.01	76.01
Naphtha	88.67	89.67	89.67	89.67	89.67
Kerosene	121.37	124.37	124.37	124.37	124.37
Diesel	123.75	118.75	118.75	118.75	118.75
Residue	81.32	75.32	75.32	75.32	75.32
Constraints					
Kerosene	-	-	-	-	SUL <0.3%
Diesel	-	-	SUL < 1.5%	-	-
Residue	-	-	-	CCR < 13%	-

Five cases are considered for optimisation. In the first case the objective is to optimise the gross margin subject to cut points variation without any constraints on the physical properties. In the case 2-

5, the price set is changed and extra constraints are considered for different products. In fact for diesel and kerosene a sulphur upper limit is considered. Also, for the residue the Carbon Conradson will have an upper bound in case 4.

For case 1 the cut points of the most valuable products which are in this case Kerosene and Diesel are maximised. As a result the Naphtha/ kerosene cut point is at the lower bound and the diesel/residue cut point at the upper bound. Low value products are then minimized. The kerosene/diesel cut point will also depend on the crude yields of these two products. Two approaches are in competition: producing a low value material that is large in quantity or more of a product higher in value but with less quantity. In this case the optimal cut point is 236.

In case 2 the kerosene becomes more valuable than Diesel and as a result the Kerosene is maximised against Diesel. The kero/diesel cut point is at its upper bound.

In case 3, regardless of the economical attractiveness of producing Kerosene, the optimisation lowers the Kero/diesel cut point at minimum. Also because of the limit on sulphur on the Diesel, extra kerosene (with low sulphur content) is taken into the Diesel to dilute the sulphur content. The same happens in case 5 where the sulphur limit is on the kerosene. In case 4 the diesel/ residue cut point is adjusted to satisfy the Carbon Conradson constraint on the Residue. All results are summarised in *Table 8*.

Table 8
Operating conditions optimization results for the cases 1-5

Cases	Case 1	Case 2	Case 3	Case 4	Case 5
Naphtha/Kero	140	140	168	140	140
Kero/Diesel	236	250	220	250	233
Diesel/ Residue	380	380	380	362	380

6.5   Energy efficiency optimisation

Based on Crude quality and cut points the temperature prediction ANN model will predict the temperatures of the diesel and residue streams. The chemistry of the crude will obviously impact the heat capacities and thermal properties of the different cuts [18]. This network will then capture for each crude how these properties and temperatures will change when the kero/diesel and diesel/residue cut points are changed. A preheat train is modelled in Petrosim® as 6 heat exchangers to predict the temperature before the furnace (CIT: coil inlet temperature). The UAs of the two main heat exchangers are calculated based on the geometry of the heat exchangers as well as the physical properties, where *U* is the overall heat transfer coefficient and *A* is the heat exchange area. Different runs were performed to generate a set of data that has been used to generate a polynomial correlation that predicts the Furnace duty (Gcal/hr) against residue and diesel yield, diesel and residue temperatures as well as the crude API.

$$Q_{duty} = f(Y_{Res}, Y_{Dsl}, API, T_{Dsl}, T_{Res})$$
$$= -27.72\ Y_{Res} + 22.67\ Y^2_{Res} - 4.83\ Y^3_{Res} + 0.57\ Y_{Dsl} - 15.65\ Y^2_{Dsl} - 4.15\ Y^3_{Dsl}$$
$$+ 4.83 Y_{Dsl} Y_{Res} + 0.003\ API - 0.0108 T_{Dsl} - 0.0054\ T_{Res} + 23.2$$

The Figure 8 shows the calculated duty against the duty calculated in Petrosim for the same crude oil and operating conditions.
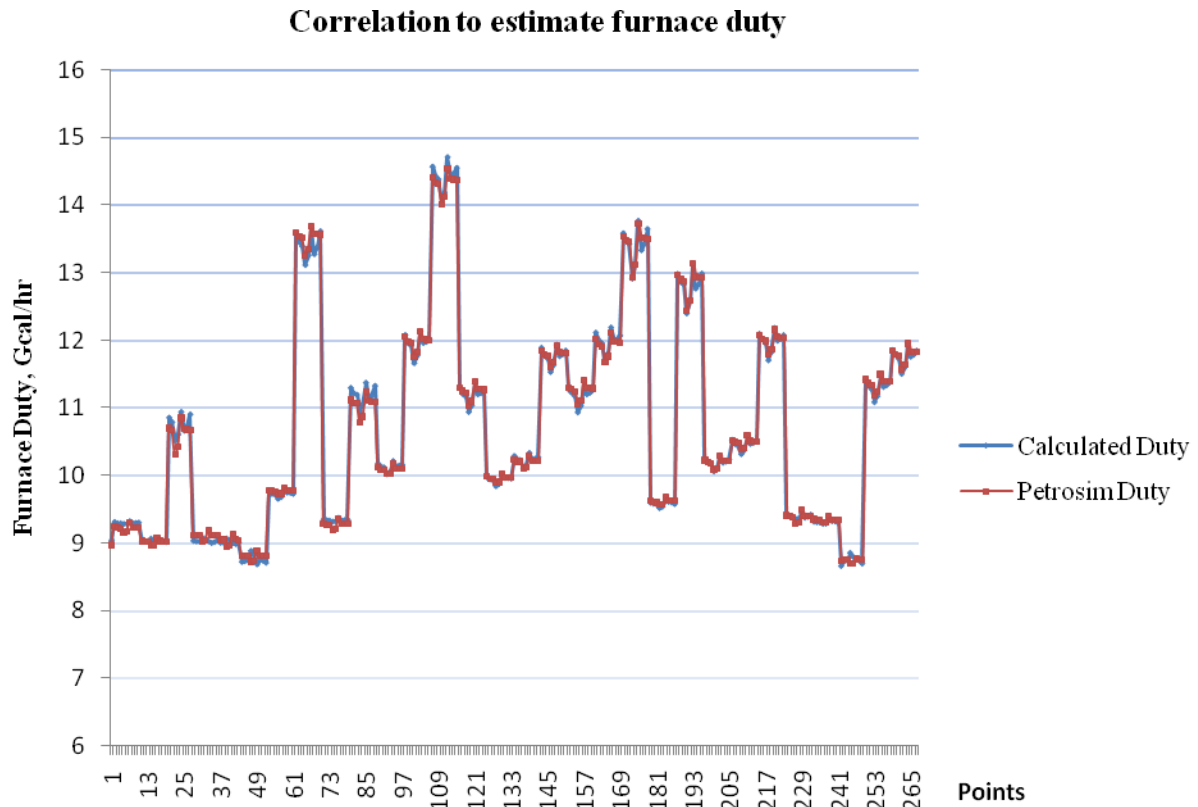
Figure 8: Correlation against rigorous simulator duty

Heat transfer takes place between the bulk fluids over a number of regimes. These are divided into five areas: The hot side film between the bulk fluid and the tube wall, the fouling layer existing on the hot side of the tube wall, the metal surface of the tube wall, the fouling layer existing on the cold side of the tube wall and the cold side film between the bulk fluid and the tube wall
Each zone provides a resistance to heat flow.

The reciprocal of the resistance is the heat transfer coefficient:

$$\frac{1}{U_o} = \frac{1}{h_{ts}} + f_{ts} + wall\ resist + f_{ss} + \frac{1}{h_{ss}}$$

Where:

$$h = \frac{k_w}{D_H} Nu \quad,\quad Nu = 0.023\ Re^{0.8}\ Pr^n \ \text{(Dittus-Boelter correlation)} \quad \text{and} \quad Pr = \frac{Cp\,\mu}{k}$$

Where U_o the Overall Heat Transfer, h_{ts} tube side film heat transfer, f_{ts} Tube side fouling factor, f_{ss} the Shell side fouling factor and h_{ss} the Shell side film heat transfer. Nu is the Nusselt number, Re the Reynolds number and Pr the Prandtl number. The UA's are calculated for the two main heat exchangers of the preheat train which represent 70% of the overall duty of the preheat train.

Since the temperature outside the furnace (inlet of the CDU) is fixed, the change of the products temperature will impact the duty of the furnace (Figure 9), hence the energy requirement for this unit. Optimising the crudes selection will then take into consideration the energy factor as well as the emissions magnitude. We know that the emissions are directly correlated to the duty of the heater; therefore the crude selection problem that classically looks at the yields only can also take into account a limit on emissions as well as the energy costs. (Emissions limit is not addressed in this paper)
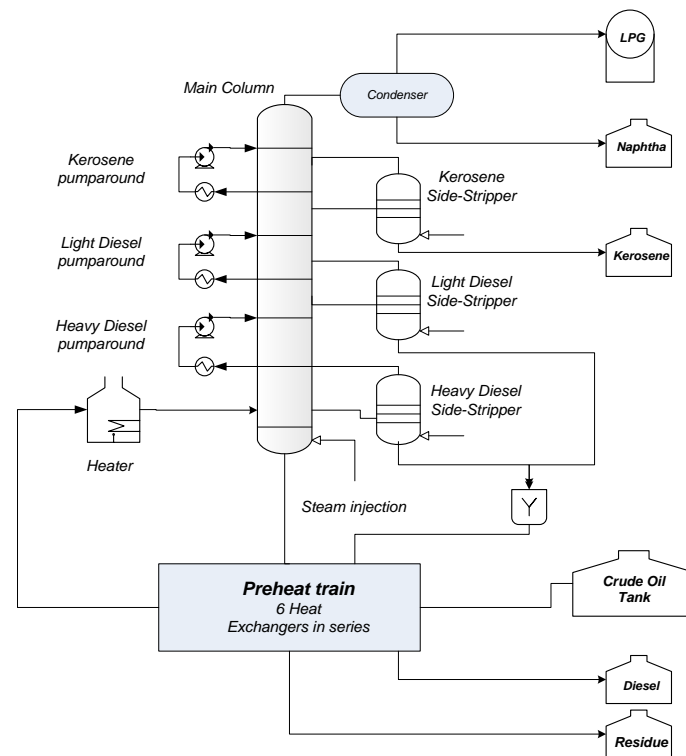
Figure 9: Heat integration to preheat crude oil feed

In the previous examples we have been considering a gross margin based on crude and refined products prices only. We believe that the energy cost is the most predominant operating cost in the refinery that will mainly depend on the operating conditions and the chemistry of the crude oil.

The objective now is to include the energy cost when we optimise the refinery feedstocks and to be able to minimise energy consumption independently from profit.

It is important to note that usually heavy crudes are economically more attractive and have a high heat capacity however they yield into less diesel and gasoline than lighter crudes. There is clearly a conflict between yields and energy. The refinery optimization model with the integration of the preheat train captures the economical impact of each option.

6.5.1   Optimal operating conditions for energy minimization

In this case we consider a blend of *Escravos, Mondo* and *Shengli* crudes as feedstock for a topping refinery. The feedstock composition is as follows: 40% of *Escravos*, 40% of *Mondo* and 20% of *Shengli.* Initially the cut points were set by the products properties specifications and by products prices. The topping cut points will impact the flows and physical properties of the refined products. The temperatures profile in the preheat train will change as a result of this with a direct effect on the Coil inlet temperature of the furnace. A better heat recovery in the preheat train will maximise the CIT which will reduce the duty of the fired heater and achieve a lower energy operation whilst meeting the products specifications of the refined products.

Energy minimization through optimal operating conditions:

$$\min \; Op = Pw.Q_{duty}$$

$Subject\ to:$

$Mass\ and\ Energy\ balances$

$(through\ MIPANN\ models)$

$$ZC_{Escravos} = 40\,kbpd$$

$$ZC_{Mondo} = 40\,kbpd$$

$$ZC_{Shengli} = 20\,kbpd$$

$$130 \le C_{nk} \le 160$$

$$220 \le C_{kd} \le 230$$

$$340 \le C_{dr} \le 355$$

$$Q_{duty} = f(Y_{Res}, Y_{Dsl}, API, T_{Dsl}, T_{Res})$$

Where Op is the operating cost which is in our case the furnace duty multiplied by the unit price (Pw) and *f* is the polynomial correlation for Heater duty calculation.

The results in *Table 9* indicate a 7.5% energy savings for a given feedstock selection through optimisation of the cut points using the reduced models integrated within the refinery-wide model.

Table 9
Optimal cut points for energy minimisation

Optimum cut points	Normal operation	Minimum energy mode	Energy savings
Naphtha/Kero	160	130	-
Kero/Diesel	225	227	-
Diesel/Residue	340	375	-
Furnace Duty, Gcal/h	10.7	9.9	7.50%

6.5.2   Optimal feedstock for energy minimisation

We consider 4 crudes as potential feedstocks for a topping refinery *(Arabian Heavy, Shengli, Cinta, and Mondo)*. The cut points are assumed to be fixed: Naphtha/Kerosene at 155C, Kerosene/Diesel at 230 C and Diesel/Residue at 355 C. These correspond to a normal operation cut points. The aim is to reduce the energy consumption by optimally mixing the crudes. As shown in Figure 10 the crudes selected for this study have different refined product yields as well as heat transfer coefficients. The cut points and the potential feedstocks information is sent to the refinery-wide energy model that consists of the reduced neural ANN models developed earlier using the rigorous simulator data. The optimisation problem formulated below is a minimisation of the operating cost which in this case is mainly the heat duty of the furnace. The optimal feedstock composition is computed (*Table 10*) and it is fed back to the simulator to recalculate the energy duty for the corresponding crude mix.
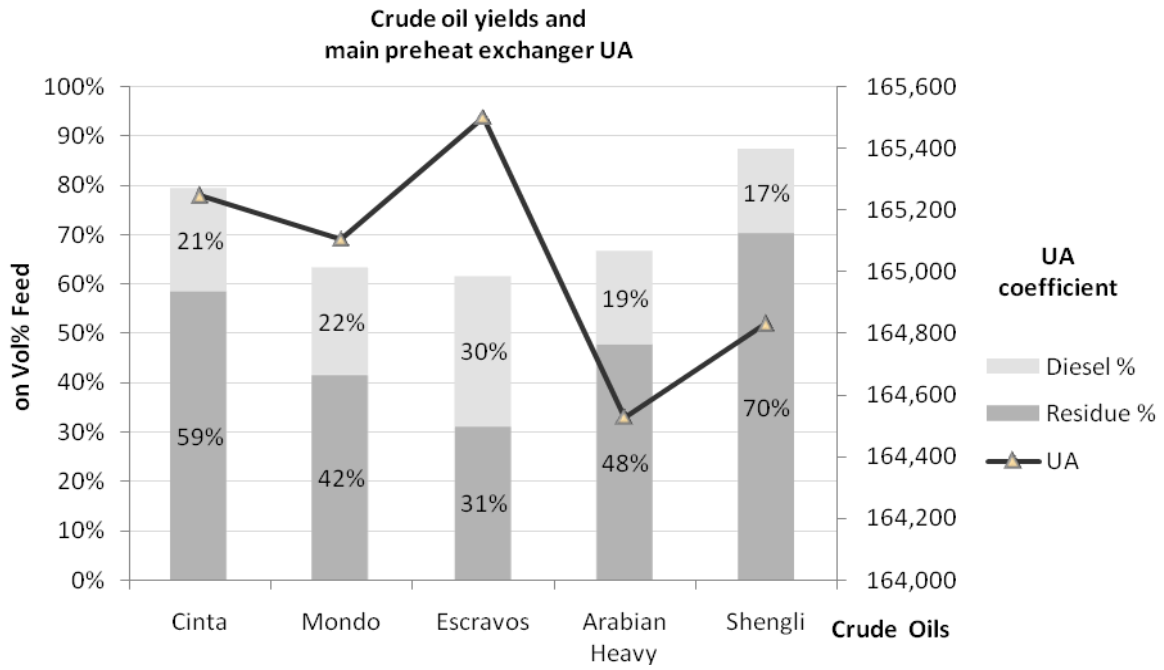
Figure 10: Crude oil yields and UA for the main heat exchanger

Energy minimization through optimal feedstock selection:

$$min\ Op = Pw.Q_{duty}$$

Subject to :

Mass and Energy balances
(through MIPANN models)

$$CAP^{LB} \leq \sum_{k}^{Ncr} ZC_k \leq CAP^{UB}$$

$$C_{nk} = 155$$

$$C_{kd} = 230$$

$$C_{dr} = 355$$

$$Q_{duty} = f(Y_{Res}, Y_{Dsl}, API, T_{Dsl}, T_{Res})$$

Table 10

Optimal feedstock selection for energy minimisation

Crude oil feedstocks	Normal operation	Minimum energy mode	Energy savings
Cinta, kbpd	5.0	5.0	-
Arabian Heavy, kbpd	5.0	5.0	-
Mondo, kbpd	66.0	5.0	-
Shengli, kbpd	24.0	85.0	-
Funace Duty, Gcal/h	9.69	8.87	8.4%
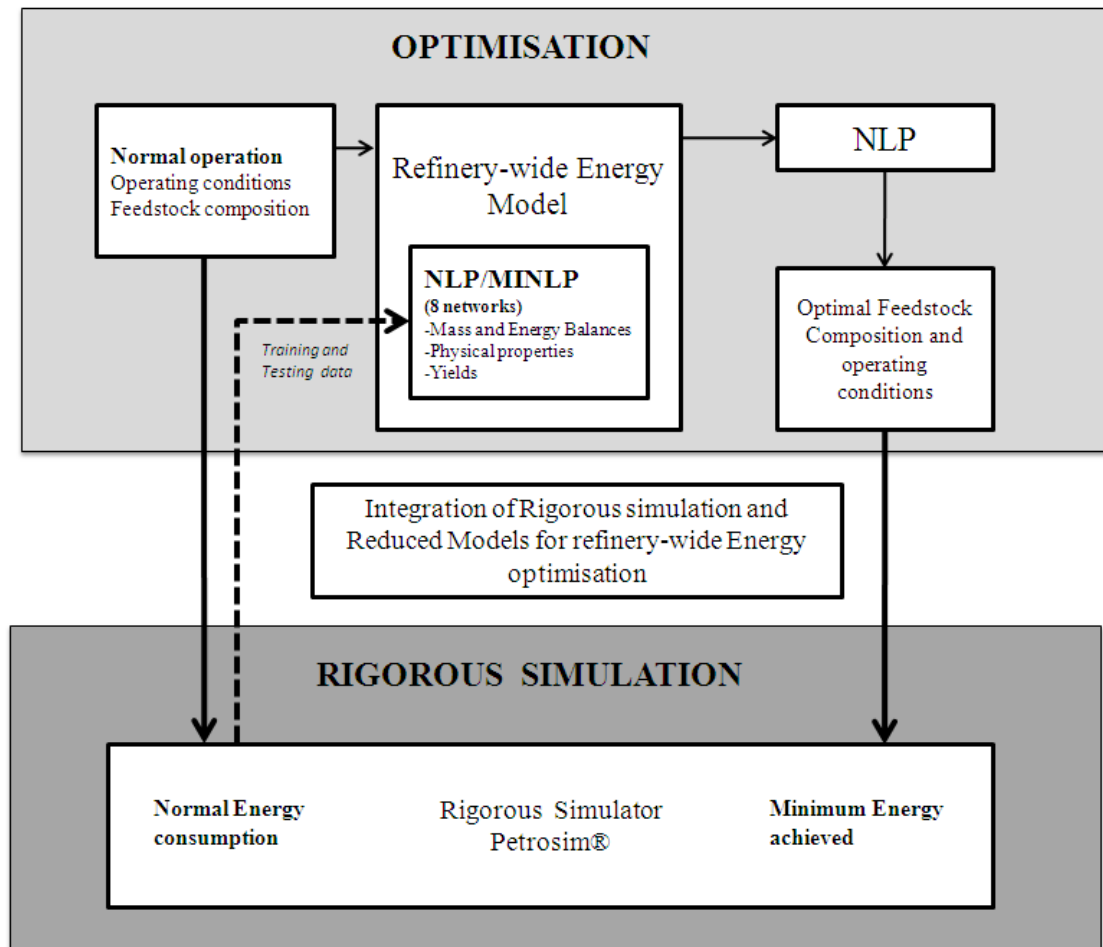
Figure 11: Integration of Rigorous simulation and reduced models for refinery-wide energy optimisation

The results of this case have been verified by simulating the Topping refinery and the preheat train with the optimum feedstock composition as inputs in Petrosim® as shown in Figure 11 and reported in *Table 11*.

Table 11

Optimisation results verified by rigorous simulation

	Normal operation			Minimum energy mode		
Crude oil feedstocks	GAMS	Petrosim®	Error	GAMS	Petrosim®	Error
Cinta, kbpd	5.0	5.0	-	5.0	5.0	-
Arabian Heavy, kbpd	5.0	5.0	-	5.0	5.0	-
Mondo, kbpd	66.0	66.0	-	5.0	5.0	-
Shengli, kbpd	24.0	24.0	-	85.0	85.0	-
Funace Duty, Gcal/h	9.69	9.585	1.1%	8.875	8.793	0.9%

Both the normal operation and the minimum energy mode feedstock composition have been verified by the rigorous simulator to calculate accurately the heat duty of the furnace. This approach allowed finding an optimum crude selection that minimises the Furnace duty in a much reduced computational time (CPU = 0.217 s) while the simulator failed to find any optimal solution and would require

extensive efforts to converge. Also, the duty predicted by the reduced model implemented in GAMS is very close to the duty rigorously calculated in Petrosim® (Figure 11).

7   Conclusion

A novel model reduction technique based on an optimized Artificial Neural Networks configurations approach has been presented for refinery optimisation. The basic idea is to use a rigorous simulator to generate a set of data that is used to train and to test the neural networks. This is done through modelling the existence of nodes and interconnections by introducing 0-1 binary variables and minimizing the sum of these binary variables. These result in a reduced configuration that still satisfies the error criteria specified by the user and is automatically obtained by removing redundant nodes and interconnections from the network. The key advantage of the MIPANN approach is having reduced models that are easy to implement and maintain for a complex refinery. The usefulness of the proposed approach was demonstrated by using the topping refinery model for feedstock selection, process optimization and energy minimization cases. Future work will focus on global optimization of the MIPANN formulation as well as the consideration of uncertainty in the refinery optimization problems.

References

[1] J.H. Gary, G.E. Handwerk, Petroleum Refining: Technology and Economics, Third ed., Marcel Dekker, New York, 1994.

[2] V. Dua, K.P. Papalexandri, E.N. Pistikopoulos, Global optimization issues in multiparametric continuous and mixed-integer optimization problems, Journal of Global Optimization. 30 (2004) 59-89.

[3] D. Slaback, J.Riggs, The inside-out approach to refinery-wide optimization, Industrial and Engineering Chemistry. 46 (2007) 4645- 4653.

[4] C. Mendez, I. Grossmann, I. Harjunkoski, P. Kabore, A simultaneous optimization approach for off-line blending and scheduling of oil-refinery operations, Computer and Chemical Engineering. 30 (2006) 614 – 634.

[5]   M. Georgiadis, E. S. Kikkinides, E. Pistikopoulos (Editors) Energy Systems Engineering. Process Systems Engineering (E. Pistikopoulos, M. Georgiadis, V. Dua - series editors), vol. 5, Wiley, 2008.

[6] T. Gueddar, V. Dua, Refinery-Wide Optimization by using Novel Model Reduction Techniques (manuscript in preparation), Computers and Chemical Engineering, (2010)

[7] K. Hornik, M. Stinchcombe and H. White, Multilayer feedforward networks are universal approximators, Neural Networks. 2 (1989) 359-366.

[8] V. Venkatasubramanian and K. Chan, A neural network methodology for process fault diagnosis, AIChE J. 35 (1989) 1993-2002.

[9] W. Kim, J. Lee, UNIK-OPT/NN: Neural Network based Adaptive Optimal Controller on the Optimization Models, Decision Support Systems. 18 (1996) 43-62.

[10] D.M. Himmelblau, Accounts of experiences in the application of artificial neural networks in chemical engineering, Industrial & Engineering Chemistry Research. 27 (2008) 5782-5796.

[11] M.A. Hussain, L.S. Kershenbaum, Implementation of inverse-model-based control strategy using neural networks on a partially simulated exothermic reactor, Transactions of the Institution of Chemical Engineers. 78 (2000) 299.

[12] M. A. Hussain, C. W. Ng, N. Aziz and I. M. Mujtaba, Neural network techniques and application in chemical process control system , Intelligent system techniques and applications, CRC Press. 5 (2002) 326-362

[13] V. Dua, A mixed-integer programming approach for optimal configuration of artificial neural networks, Chemical Engineering Research and Design. 88 (2010) 55-60.

[14] A. Brooke, D. Kendrick, A. Meeraus, R. Raman, GAMS: a user's guide, GAMS development corporation, Washington, 1998.

[15] R. Karuppiah, K. Furman, I. Grossmann, Global optimization for scheduling refinery crude oil operations, Computer and Chemical Engineering. 32 (2008) 2745-2766.

[16] C.A. Floudas, Nonlinear and mixed-integer optimization, Oxford University Press, New York, 1995.

[17] V. Kosmidis J. Perkins, E. Pistikopoulos, A mixed integer optimization formulation for the well scheduling problem on petroleum fields, Computer and Chemical Engineering. 29 (2005) 1523 – 1541.

[18] K. Papalexandri, D. Patsiatzis, E. Pistikopoulos, L.Ebbesen, Heat integration aspects in crude preheats refinery section, Computers and Chemical Engineering. 22 (1998) 141 – 148.

Appendices

Appendix A: MINLP formulation

Consider the following proposed general Mixed-Integer Programming formulation for ANN (MIPANN):

$$\min_{a,b,w,h,W,B,u,y,\delta} E_4 = P_1 E_1 + P_2 E_2 + P_3 E_3 \tag{A1}$$

Subject to:

$$a_j^1 = \sum_{i=1}^{N_x} w_{ji}^1 x_i + b_j^1, \quad j=1,\ldots,N_n \tag{A2}$$

$$h_j^l = \tanh(a_j^l), \quad l=1,..N_h \tag{A3}$$

$$a_j^l = \sum_{i=1}^{N_n} w_{ji}^l h_j^{l-1} + b_j^l, \quad j=1,\ldots,N_n, \quad l=2,\ldots,N_h \tag{A4}$$

$$u_k = \sum_{i=1}^{N_n} W_{ki} h_j^{N_h} + B_k, \quad k=1,\ldots,N_o \tag{A5}$$

$$-M \cdot y_j^l \le a_j^l \le M \cdot y_j^l \quad j=1,\ldots,N_n, l=1,\ldots,N_h \quad \text{(Existence/non-existence of Nodes)} \tag{A6}$$

$$-M \cdot \delta_{ji}^1 \le w_{ji}^1 \le M \cdot \delta_{ji}^1 \quad j=1,\ldots,N_x \quad \begin{array}{l}\text{(Existence/non-existence of}\\ \text{Interconnections from Input Layer)}\end{array} \tag{A7}$$

$$-M \cdot \delta_{ji}^l \le w_{ji}^l \le M \cdot \delta_{ji}^l \quad j=1,\ldots,N_n, l=2,\ldots,N_h \quad \begin{array}{l}\text{(Existence/non-existence of}\\ \text{Remaining Interconnections)}\end{array} \tag{A8}$$

$$E_1 = \sum_{k=1}^{N_o} (\hat{u}_k - u_k)^2 \quad \text{(ANN Prediction Error)} \tag{A9}$$

$$E_2 = \sum_{l=1}^{N_h} \sum_{j=1}^{N_n} y_j^l \quad \text{(Number of Nodes)} \tag{A10}$$

$$E_3 = \sum_{l=1}^{N_h} \sum_{j=1}^{N_n} \sum_{i=1}^{N} \delta_{ji}^l \quad \text{(Number of Interconnections)} \tag{A11}$$

$$E_1 \le \varepsilon \quad \text{(Upper Bound on Prediction Error)} \tag{A12}$$

$$u_k^{LO} \le u_k \le u_k^{UP}, \quad k=1,\ldots,N_o \quad \text{(Example of a Typical Process Constraint)} \tag{A13}$$

In this formulation, the objective function has been augmented to include E_2 and E_3 representing the number of nodes and interconnections respectively. P_1, P_2 and P_3 are positive penalty weights on the

three objectives, E_1, E_2 and E_3. To systematically analyze various objective functions two of the three penalty weights are fixed to zero. If $P_2 = P_3 = 0$, then the above formulation reduces to the original formulation presented in section 1. If $P_1 = P_2 = 0$, then the objective is to minimize the number of interconnections and if $P_2 = P_3 = 0$, then the number of nodes is minimized. Equations (A2)-(A5) are the same as those in section 4.1and repeated here for the sake of completeness. The existence and non-existence of a node is modeled through equation (A6) where M is a large positive number, y_j^l is the vector of 0-1 binary variables. Note that if $y_j^l = 1$ then a_j^l is unrestricted whereas if $y_j^l = 0$ then $a_j^l = 0$ which implies that j^{th} node of the lth hidden layer does not exist. The total number of nodes is summed and modeled through equation (A10). The existence and non-existence of the interconnections is modeled by equations (A7) and (A8) where δ_{ji}^l are the 0-1 binary variables. Summation of 0-1 binary variables, E_3, is given by equation (A11). Equation (A12) allows specifying an upper bound, ε, on E_1, so that when E_2 and E_3 are being minimized the predictability of the network is within a specified tolerance. Note that an engineering judgment must be used in specifying the value of ε. If the data is highly noisy, a very small value of ε will over-fit the noise and the network will have poor generalization. A very high value of ε, on the other hand, will result in worsening of the accuracy of the network predictions. The value of ε must therefore be selected by considering the target application of the network and the quality of the data available for the training. The Equation (A13) ensures that the output, u, lies between certain lower and upper bounds, u^{LO} and u^{UP} respectively; these bounds are usually available from the engineering knowledge of a given system.

Appendix B: Column set-up tables

Table B1

Crude oil Feed conditions

Property	Value
Temperature	376.0 °C
Pressure	1.5 bar
Mass flow rate	88257.8 kg/h

Table B2

Crude distillation setup

Property	Value
Condenser Pressure	*1.5 bar*
Condenser Pressure Drop	*0.5 bar*
Bottom Stage Pressure	*2.0 bar*
Condenser Temperature estimate	*50 °C*
Top stage temperature estimate	*130 °C*
Bottom stage temperature estimate	*350 °C*
Number of Stages	*48*

Table B3

Steam injections

Refined Product	Flow rate (SI)
Kerosene SSteam	1361 kg/ h
Diesel SSteam	907 kg/ h
HGO SSteam	1814 kg/ h

Table B4
Side strippers setup

Side Strippers (SS)	Kero SS	Diesel SS	HGO SS
Draw Stage	16	28	39
Return Stage	15	27	38
Number of Stages	8	6	6
Configuration	Steam Stripped	Steam Stripped	Steam Stripped
Product Stream	Kerosene	Light Diesel	HGO
Steam Stream	Kerosene Steam	Diesel SSteam	HGO SSteam

Table B5
Energy consumptions comparison

Crude	Gippsland	Cinta	Kuito
Minimum Energy (Qmin), Gcal/h	14.996	7.253	7.36
Diesel Yield	0.215	0.165	0.27
Residue Yield	0.138	0.626	0.537
API	46.9	32.8	21.5
Price, $/BBL	101.12	94.58	83.26

Computational Fluid Dynamics (CFD) Investigation of Air Flow and Temperature Distribution in a Small Scale Bread-Baking Oven

Zinedine Khatir [a*], Joe Paton [a], Harvey Thompson [a], Nik Kapur [a], Vassili Toropov [a,b], Malcolm Lawes [a], Daniel Kirk [c]

[a] School of Mechanical Engineering, University of Leeds, LS2 9JT, United Kingdom
[b] School of Civil Engineering, University of Leeds, LS2 9JT, United Kingdom
[c] Spooner Industries Ltd, Ilkley, LS29 8JB, United Kingdom

* Corresponding author. Email: Z.Khatir@leeds.ac.uk; Tel. +44(0) 113 343 2197; Fax. + 44(0) 113 234 9679

Abstract
Experimental and computational fluid dynamics (CFD) analyses of the thermal air flow distribution in a 3-zone small scale forced convection bread-baking oven are undertaken. Following industrial bread-making practise, the oven is controlled at different (constant) temperatures within each zone and a CFD model is developed and validated against experimental data collected within the oven. The CFD results demonstrate that careful selection of the flow model, together with implementation of realistic boundary conditions, give accurate temperature predictions throughout the oven. The CFD model is used to predict the flow and thermal fields within the oven and to show how key features, such as regions of recirculating flow, depend on the speeds of the impinging jets.

Keywords   bread-baking oven; heat transfer; fluid flow; CFD modelling; experiments

1   Introduction
Bread is an important food product that has been consumed worldwide for several millennia [1]. Commercial bread baking is a complex process of simultaneous heat, water and water vapour transport within the dough/bread in which heat is supplied by a wide variety of indirect-fired and direct-fired forced convection ovens [2]. The former, which rely on radiation from heated elements within the oven, have traditionally been used in commercial bread baking, however the latter have recently been increasing in popularity since they can also offer greater levels of thermal efficiency. Energy use in the process industries is currently an area where a significant amount of research is being conducted. A typical oven may bake between 1000 and 3000 loaves per hour, per m width. Previously, energy use for the production of bread has been estimated to be in the region of between 5 and 10 MJ/ kg [3]. Just below half of the energy use in a bakery is consumed in the baking oven [4].

Forced convection ovens are the focus of the present study and are based on hot air jet impingement technologies that have been used extensively in order to dry coated products, paper and textiles [5]. Within forced convection baking ovens, heat is transferred to the dough/bread via conduction, convection and radiation and the relative importance of each mode is determined by the baking temperatures and speeds of the impinging air jets [6]. For low air speeds, radiation is often the predominant mode of heat transfer, while convection is much more important for higher air speeds [7]. Most previous studies of forced convection baking ovens have tended to focus on regimes with relatively low air speeds, where radiative heat transfer is also influential [8-11]. In contrast this paper presents a combined experimental and computational investigation of the thermal air flows that arise in an example of an industrial forced convection oven with higher air speeds, for which convective heat transfer is predominant [12,13]. Lastly though this is beyond the scope of the present work, it is worth mentioning there have been attempts to understand the internal processes in the bread resulting from heat flux into it [14,15].

Rising energy costs and changing legislation are bringing the need for more efficient baking processes into much sharper focus. This will require greater scientific understanding of how to manipulate oven design and baking conditions to give energy efficient designs whilst maintaining the quality of the product. Computational Fluid Dynamics (CFD) is increasingly being used to improve the efficiency of

baking processes[16,17]. For example, CFD has been used recently to predict successfully the complex air circulation patterns resulting from air input and extraction in biscuit baking ovens, Mirade *et al* [18], and to provide the engineering insight needed to reduce overall energy consumption in a commercial baking process [11]. Wong *et al* [19] later demonstrated that simpler, 2D flow baking flow models are capable of predicting the temperature distribution in ovens accurately and can be very useful in practical oven design.

Crucially though, since air flows within forced convection ovens are highly turbulent in the region of the nozzles, it is very important to validate CFD predictions against experimental data before using CFD for baking process optimization. Accordingly, the objectives of this study are (i) to describe the development and experimental validation of a CFD model of the thermal air flows in an industrial, high speed forced convection baking oven; (ii) to use the CFD model to study the effect of operating parameters on the associated flow distributions inside the oven. This is a necessary first step towards the use of CFD for detailed baking process and oven design optimization.

2 Bread-baking oven and experimental setup
2.1 Description of the bread-baking oven
The oven analysed is a scaled-down replica of the type of industrial direct-fired, forced convection ovens widely used in industry (Figure 1). The oven length is 9 m, 1 m width and 1.5 m height. Jet impingement nozzles (arrays of round nozzles) direct hot air above and below the product at high velocity, which is controlled through the use of dampers. The oven is split into three zones each with a burner, each zone having two sections. The burner set points are $T^1_{norm}=1$, $T^2_{norm}=107\%$ T^1_{norm} and $T^3_{norm}=105\%$ T^1_{norm} respectively.
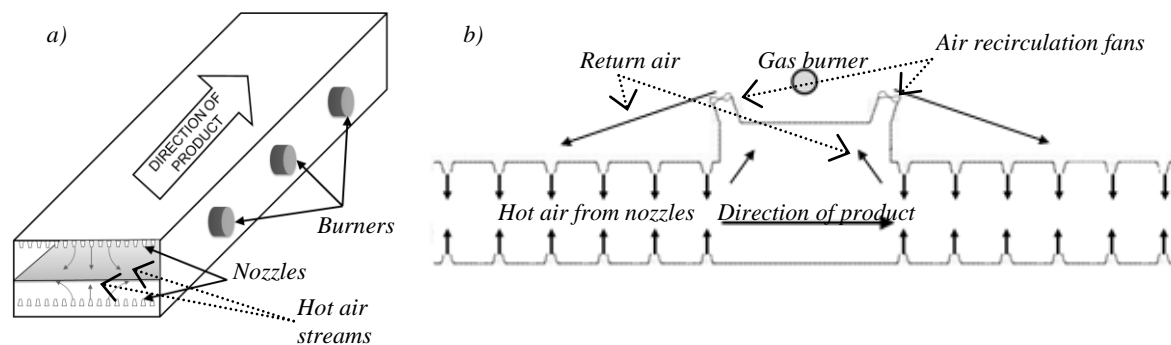
Figure 1: Three-zone direct fired oven: *a)* Overview of the oven; *b)* Simplified schematic showing the mechanism for distributing air through the nozzles for a single zone

2.2 Experimental setup
Data with which to validate the CFD models was obtained by performing a series of experiments to measure temperature distribution and velocity profiles throughout the oven. Temperature was monitored using K-type thermocouples connected to a TC-Link® 6 Channel Wireless Thermocouple Node (Microstrain, Inc.) which logged air temperature at 5 positions through the oven every 10 seconds (see Figure 2). In addition, in order to measure the air temperature at the nozzles, K-type thermocouples were attached to selected nozzles at the nozzle exits with connections external to the oven. Once the oven reached set-point temperature a C9001 Thermometer (Comark Ltd.) displayed an instantaneous temperature reading. K-type thermocouples have a typical operating range of -50 to 300 °C and have accuracy of ±0.3% + 2 °C in the operating range used for this study (RS Components Ltd).

Velocity distributions were inferred from pressure readings obtained using a handheld 922 Airflow Meter Micromanometer (Fluke Corporation), which measured instantaneous pressures at the nozzle exit in a cold oven, i.e. with the oven burners off but with the fans running. In addition, air velocities into and out of the oven ends once hot are measured using a handheld Speedtech SM-18 Anemometer (SkyMate Inc.).
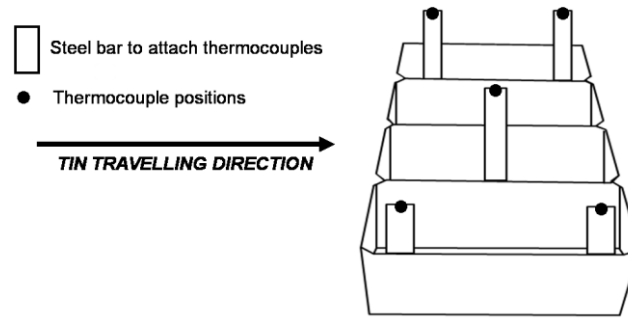
Figure 2: Tin schematic with points labelled for temperature measurements

2.3   Experimental results

Normalised temperature distributions $T_{norm}= T/T_1$ (i.e. T_1 is the burner's setpoint temperature for zone 1) for points located at H/D = 1.43, 2.86 and 4.29 along the oven x/D, where D is the nozzle diameter, H the distance below the top nozzles and x the distance along the oven, are depicted in Figure 3. Results show the temperature in zone 1-2 steadily climbs towards burner set point as the bread travels through the oven, and that temperature in the remaining two zones is uniform. In terms of control of the process this is an important factor since this directly impacts on the product quality. Agreement of the normalised burner temperature set points ($T^1_{norm}=1$, $T^2_{norm} =107\%$ T^1_{norm} and $T^3_{norm}=105\%$ T^1_{norm}) and the actual recorded temperature across the zones is also good, with the largest variation taking place in zone 1.
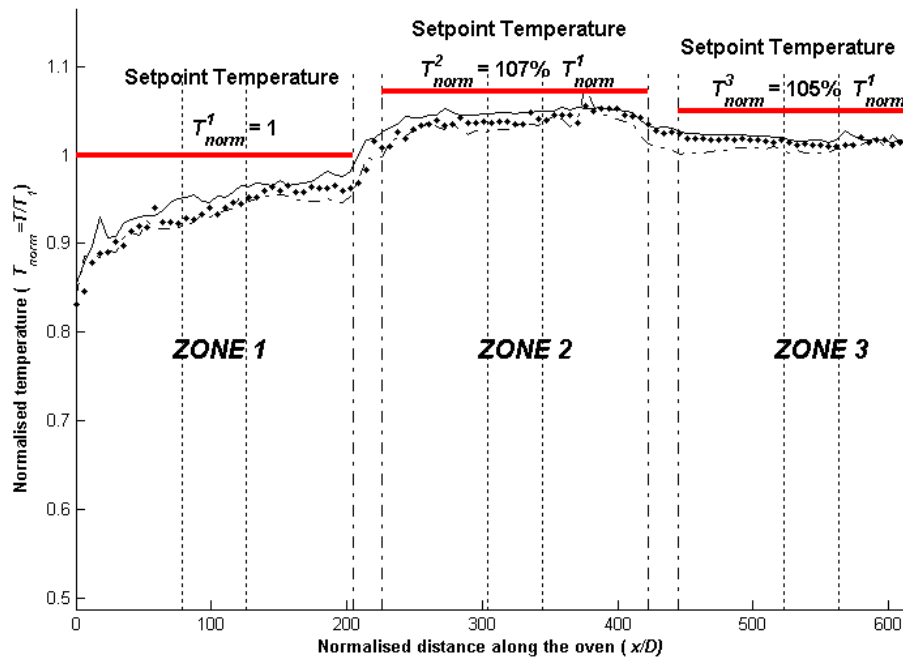
Figure 3: Normalised air temperature ($T_{norm}=T/T_1$) profile through the oven (x/D)
for H/D = 1.43 (—), 2.86 (-.-) and 4.29 (---)

Zone 1 corresponds to the first third of the oven and its normalised temperature ranges from 90% to 101%. Zone 2, 214-428 normalised distance along the oven, has a temperature varying from 103% to 105%. Finally zone 3 which entails the last 214 normalised length of the oven has temperature ranging from 103 to 90%. Air temperature reaches a peak of 106%, at a normalised distance of 380 from the oven entrance (see Figure 3). There is no dependence on air temperature with relation to distance beneath the nozzles due to the strong turbulent mixing within the oven.

The distributions of normalised velocity magnitudes $v_{norm}=v/v_{ref}$, where v_{ref} is the nozzles' velocity, at the top and bottom nozzles for the various zones are plotted in Figure 4. Velocity for the top nozzles is generally larger than that for the bottom nozzles. This is largely due to the location of the recirculation

fans, which are above the top banks of nozzles. The air supply to the bottom nozzles travels around the baking chamber and up through a U-bend in the supply ducts, which causes a drop in pressure and therefore velocity. Results point out a peak in air velocity at the middle of each section of a zone for the top nozzles. This is the case for each of the 3 zones. This is due to the internal air flow within the ducts and the balance of pressure drop down the plenum that feeds the nozzles with that through the nozzles.
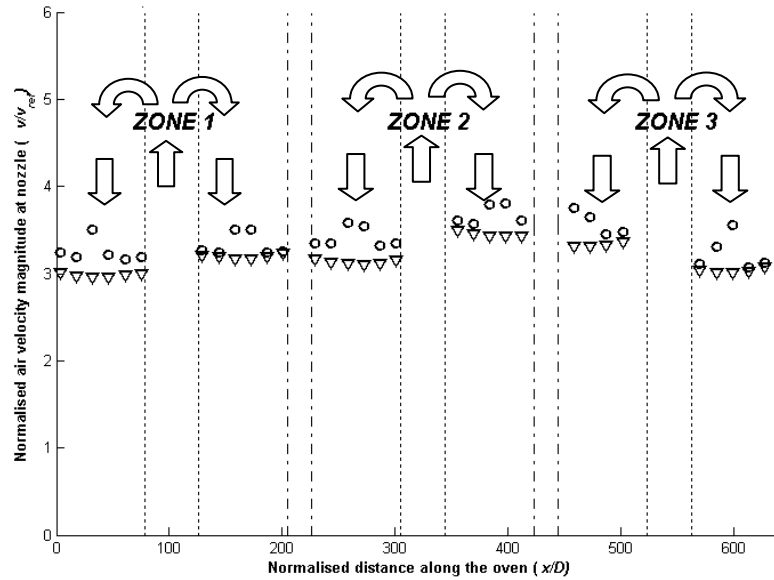
Figure 4: Normalised air velocity distribution through oven: (○○○) top nozzles, (∇∇∇) bottom nozzles. The arrows show the internal air distribution pattern: the location of the recirculation fan is shown within each zone by the up-arrow, the return air is split into two and distributed through two banks of nozzles per zone (down arrow)

3   CFD model development
3.1   Mathematical modelling
The air flow in the oven chamber is turbulent, as confirmed by the estimation of the Reynolds number, *Re,* based on a typical inlet air jet inlet velocity of v_{ref} m/s and *D* mm diameter nozzle. Previous studies have successfully used Reynolds Averaged Navier-Stokes (RANS) models to predict the air flows in baking ovens. The continuity and momentum equations written in the RANS format are:

$$\frac{\partial \rho}{\partial t} = \frac{\partial}{\partial x_i}(\rho u_i) \tag{1}$$

$$\frac{\partial}{\partial t}(\rho u_i) + \frac{\partial}{\partial x_i}(\rho u_i u_j) = -\frac{\partial p}{\partial x_i} + \frac{\partial}{\partial x_j}\left[\mu\left(\frac{\partial u_i}{\partial x_j} + \frac{\partial u_j}{\partial x_i} - \frac{2}{3}\delta_{ij}\frac{\partial u_l}{\partial x_l}\right)\right] + \rho \vec{g} + \frac{\partial}{\partial x_i}\left(-\rho \overline{u_i' u_j'}\right) \tag{2}$$

where ρ and u_i are the air density and velocity components in the ith coordinate direction x_i respectively, *p* is pressure and $\vec{g}$ is the acceleration due to gravity. Buoyancy forces are considered by using a weakly compressible formulation where density depends on temperature, but not on pressure. The ideal gas law with constant pressure (1.013 x 10^5 Pa) was used to define density. The last term of Eq. (2) represents the turbulent stresses that requires additional closure equation(s) to be solved. Various turbulent models have been proposed for the closure equations in baking applications, including the standard *k–ε* model (Norton and Sun [16,17]). In the 2-D model presented in this work where v_{ref} is based on an equivalent 2-D flow rate into the oven, the turbulence is described with two additional variables *k* (turbulent kinetic energy) and ε (turbulent dissipation) that enables the computation of the turbulent stress and the turbulent viscosity. The realizable *k–ε* model is an improvement of the standard *k– ε* model that can be useful for flows in complex geometries, and consists of the following two transport equations (Boulet *et al* [7]):

$$\frac{\partial}{\partial t}(\rho k) + \frac{\partial}{\partial x_j}(\rho k u_j) = \frac{\partial}{\partial x_j}\left[\left(\mu + \frac{\mu_t}{\sigma_k}\right)\frac{\partial k}{\partial x_j}\right] + G_k + G_b - \rho\varepsilon \tag{3}$$

$$\frac{\partial}{\partial t}(\rho\varepsilon) + \frac{\partial}{\partial x_j}(\rho\varepsilon u_j) = \frac{\partial}{\partial x_j}\left[\left(\mu + \frac{\mu_t}{\sigma_\varepsilon}\right)\frac{\partial\varepsilon}{\partial x_j}\right] + \rho C_1 S_\varepsilon - \rho C_2 \frac{\varepsilon^2}{k + \sqrt{\nu\varepsilon}} + C_{1\varepsilon}\frac{\varepsilon}{k}C_{3\varepsilon}G_b \tag{4}$$

In Eq. (3), the terms G_k and G_b represent the turbulence energy production by means of the velocity gradient and the buoyancy effects. The negative term represents the energy dissipation. For Eq. (4), the first production term (the second term on the right-hand side of Eq. (4)) is related to the spectral energy transfer (and does not contain the term G_k). The turbulent viscosity μ_t is obtained from the turbulent energy k and the dissipation. The terms σ_k, σ_ε, C_1, C_2, $C_{1\varepsilon}$, $C_{3\varepsilon}$ are model parameters, (Boulet et al [7]) with the following given values $\sigma_k = 1.0$, $\sigma_\varepsilon = 1.2$, $C_1 = \max[0.43, \frac{\eta}{\eta+5}]$, $\eta = S\frac{k}{\varepsilon}$,

$S = \sqrt{2S_{ij}S_{ij}}$, $C_2 = 1.9$, $C_{1\varepsilon} = 1.44$ and $C_{3\varepsilon} = \tanh\left|\frac{v}{u}\right|$ where v is the component of the flow velocity parallel to the gravitational vector and u is the component of the flow velocity perpendicular to the gravitational vector.

The energy equation is also solved and takes the form:

$$\frac{\partial}{\partial t}(\rho C_p T) + \frac{\partial}{\partial x_i}(u_i \rho C_p T) = \frac{\partial}{\partial x_j}\left(\lambda\frac{\partial T}{\partial x_j}\right) \tag{5}$$

where C_p, T and λ are the specific heat capacity, temperature and thermal conductivity of the air, respectively. Equations (1)-(5) are solved computationally using ANSYS FLUENT 12.0.1. Results obtained using the standard and realizable k–ε models are compared and found to be very similar. All results presented here have been obtained using the realizable k–ε model.

3.2 Boundary conditions

A single zone of the oven geometry shown in Figure 5 and is composed of flow openings and walls. For flow openings a combination of velocity inlet and pressure outlet types are used, with temperature defined along the walls. *Tables 1a* and *1b* summarise the boundary conditions.

Table 1a
General boundary conditions

Modelled equation	Inlet	Outlet	Wall
Energy	$T=T_{inlet}$ (from measurements) $V_{jet}=v_{ref}$ m/s, $V_{in}=0$–0.17 v_{ref} m/s	$T=T_{outlet}$ (from measurements)	$T=T_{wall}$ (from measurements
Momentum	$V_{out}=0$ m/s	$P = 0$ Pa	No-slip
Turbulence	$I=5\%$ and $l_{scale}=0.01$	$I=5\%$ and $l_{scale}=0.01$	Wall function

Table 1b
Normalised nozzle jets temperature boundary conditions in % ($T_{norm}=T/T_1$)

Nozzle jets number	1	2	3	4	5	6	7	8	9	10	11	12
Top	91.6	92.0	92.6	93.4	94.0	94.7	97.5	98.3	98.6	99.4	100.0	100.8
Bottom	97.5	98.6	99.1	99.2	99.2	99.2	99.2	99.4	99.6	99.8	100.0	100.0

3.3   CFD Grid
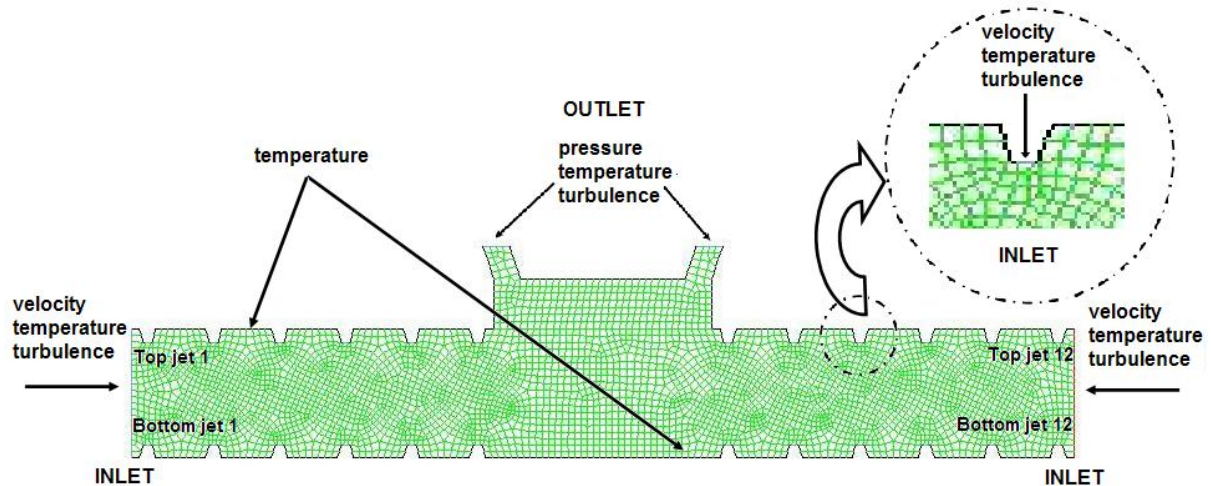
Figure 5: Geometry of an oven zone baking chamber, showing a typical CFD mesh and indicating the boundary conditions

The study focused on the inside baking chamber of the first zone of the small scale industrial oven. Figure 5 shows a schematic diagram of the oven structure. In production, the oven would be loaded with product, however for simplicity the experiments and CFD analyses were carried out with the oven empty. The mesh geometry was designed and generated using Gambit version 2.4.6, mesh generation software available within ANSYS FLUENT.

4   Computational validation and results

Grid sensitivity tests were performed using the three different meshes summarised in *Table 2*. The coarsest mesh did not reproduce the distribution as observed with Cases 2 and 3. All results reported subsequently have been obtained using the Case 2 mesh.

Table 2
Information on the grids in the sensitivity tests

	Case 1 (coarsest)	Case 2	Case 3 (finest)
Cells	4090	18045	40078
Faces	8421	36579	81010
Nodes	4332	18535	40933

2D Steady state computations have been performed. The temperature predictions show good agreement with the experimental temperature measurements (Figure 6) for different distances under the top nozzles, namely at $H/D = $ 1.43, 2.86 and 4.29 below the top the nozzles. The error bars in Figure 6 have been computed from 25 measured values for each location along the oven length using standard statistical variance analysis by $\sigma/\sqrt{25}$, where σ denotes the standard deviation of the data series. The error due to the thermocouples' accuracy $\pm 0.3\% + 2$ °C has been accounted for as well.
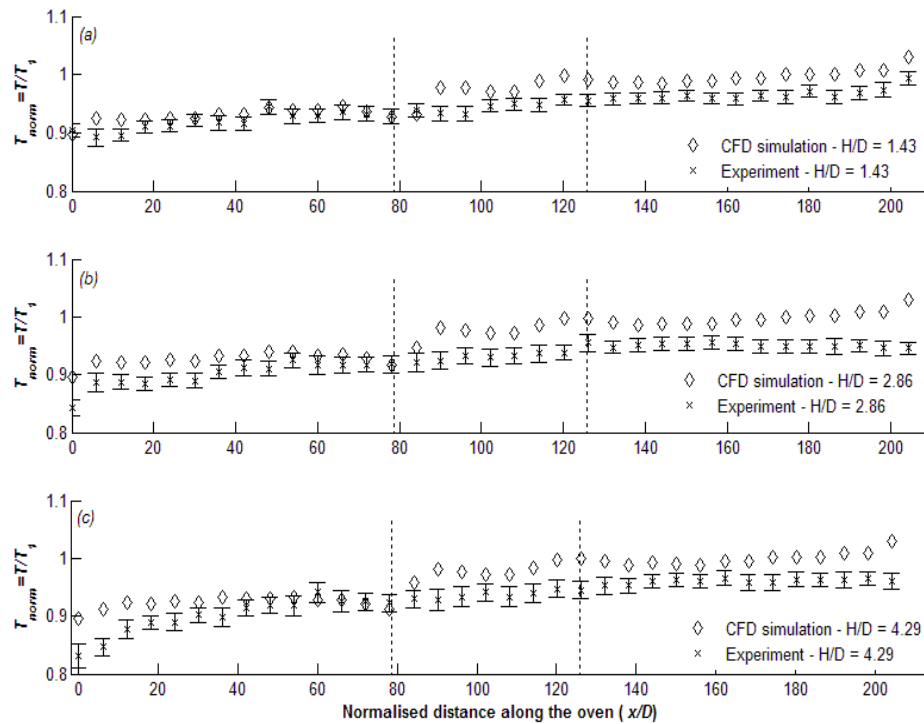
Figure 6: Comparison between CFD predictions (◊◊◊) and experimental measurements (xxx) of the normalised air temperature profile at various points below the top nozzles within zone 1 of the baking oven located at *H/D = a)* 1.43; *b)* 2.86 and *c)* 4.29

As presented in *Table 3*, comparing the modelled temperature profile to the measured temperature at $H/D = $ 1.43, 2.86 and 4.29 below the top nozzles, leads to an average relative error of 3.5 %, while the average coefficient of correlation and RMS error between the modelled values and the measured values are 0.91 and 3.6% respectively.

Since the uniformity of the temperature distribution is an important design goal in a baking oven in order to ensure predictable product properties, Figure 7 presents the simulated normalised temperature distribution $T_{norm}=T/T_1$ in the form of a temperature contour plot in Zone 1 of the oven where the burner's temperature is set at T_1. This shows that the normalised temperature is uniformly spread between 90 to 103% from the inlet to outlet of this zone with an average temperature of 97.5%. Note also that in the region located between H/D=5.71 and H/D= 14.3 where the bread is usually baked temperature shows only a 2% deviation from the burner's set temperature T_1. The second bank of nozzles within this zone have a temperature much closer to T_1, since the entrance effects at the oven inlet will have died away. This demonstrates the capability of the CFD model to predict temperature distribution within the oven, which has an important influence on final bread quality.

Table 3
Relative and root mean square (RMS) error compared to the measured temperature [%] together with coefficient of correlation: Case 2 in Table 1

	Distance below the top nozzles (H/D)	1.43	2.86	4.29
Relative Error		2.54	4.16	3.8
Coefficient of correlation		0.92	0.92	0.90
RMS Error		2.8	4.2	3.9

The corresponding air flow fields are shown in Figures 8 and 9(*b*) with the velocity vector field and stream function respectively when the jet velocity is nominally set at v_{ref} m/s. These demonstrate the existence of multiple recirculation zones and complex vortex dynamics characteristics within the

oven. The high velocities within the return air are as a result of the geometry around the burner (and typical of those velocities found in practice), but have no effect on the flow field within the oven.
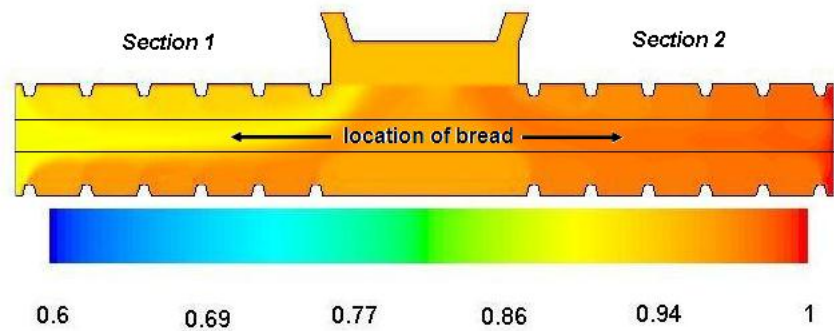
Figure 7: Contour plot of normalised temperature ($T_{norm}=T/T_1$) throughout zone 1 of the industrial small-scale bread baking oven. The location of where the bread would be baked along the oven is also indicated
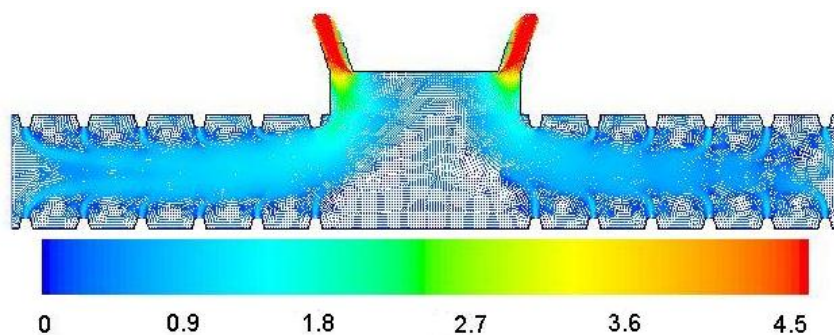
Figure 8: Normalised air flow patterns ($v_{norm}=v/v_{ref}$) throughout zone 1 of the industrial small-scale bread baking oven
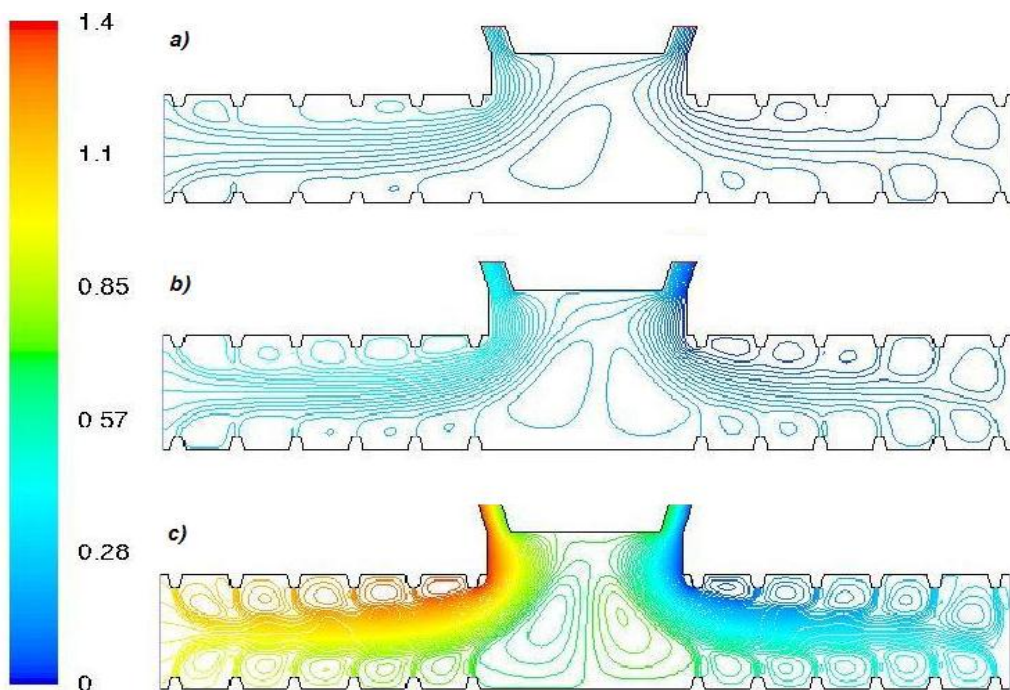
Figure 9: Normalised streamlines of air flow (kg/s) throughout zone 1 of the industrial small-scale bread baking oven at various nozzle jets velocity: *a)* $0.5v_{ref}$ m/s, *b)* v_{ref} m/s and *c)* $3v_{ref}$ m/s

The CFD model allows a much deeper investigations into the flow field. To this effect further simulations are performed by changing the jets velocity to see the impact on the air flow distribution. Figures 9 and 10 show the results when the jet velocity is varied from $0.5v_{ref}$ to $3v_{ref}$ m/s.

The streamlines of air flow in Figure 9 clearly emphasizes that an increase in jets velocity causes an increase in the strength of the vertical structures (as well as the flow rates). The velocity magnitude at the centre line throughout the oven (i.e. H/D=10) is depicted in Figure 10 for the three jet velocities. These velocities have been scaled as a function of the inlet jet velocity. This shows that with higher velocities, there is more fluctuations within the oven, in general support of the increased velocity seen in Figure 9.
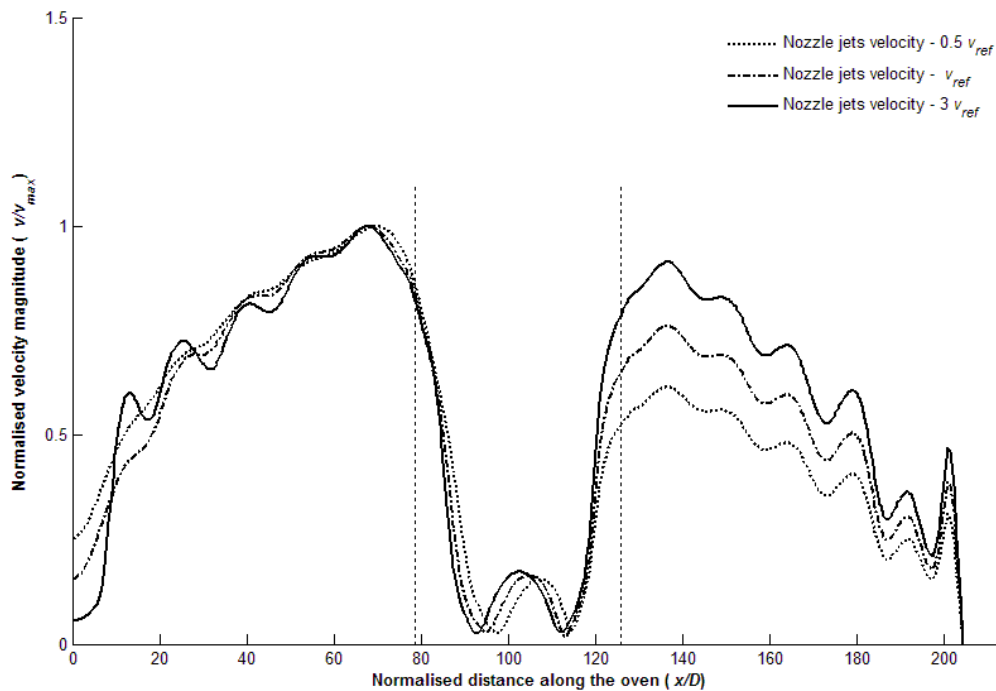
Figure 10: Normalised velocity magnitude at the centre line of the baking chamber (i.e. H/D=10) at various nozzle jets velocity: (**...**) $0.5v_{ref}$ m/s, (–•–) v_{ref} m/s and (——) $3v_{ref}$ m/s

It is important to be able to predict these velocity variations since they can lead to corresponding variations in heat transfer during the bread baking process that can influence bread quality [12-16].

5   Conclusions

Due to the complexity of thermal air flows in baking ovens, CFD models require careful validation before they can be used for practical oven design. This paper has demonstrated that combining RANS turbulence modelling with realistic boundary conditions enables CFD models to be developed for forced convection ovens with high speed impinging air jets. This is capable of providing valuable insight into key baking issues such as temperature uniformity that are difficult to measure experimentally. This is a necessary first step towards the development of a CFD bread baking design optimization tool that can be used to optimize energy efficiency and/or product quality in practical baking applications.

References

[1]   A. Mondal and A.K. Datta, Bread baking - A review. Journal of Food Engineering, 86(4) (2008) 465-474.

[2]   M.R. Zareifard, M. Marcotte, and M. Dostie, A method for balancing heat fluxes validated for a newly designed pilot plant oven. Journal of Food Engineering, 76(3) (2006) 303-312.

[3]   G.A. Beech, Energy Use in Bread Baking. Journal of the Science of Food and Agriculture, 31(3) (1980) 289-298.

[4]   A. Thumann and D.P. Mehta, Handbook of energy engineering, 6th. Fairmont Press, Lilburn, GA; Boca Raton, FL, 2008.

[5]   Ikin, J.B., Thompson, H.M. Drying-air induced disturbances in multi-layer coating systems, Chemical Engineering Science, 62 (2007), 6631-6640.

[6]   H. Martin, Heat and Mass Transfer between Impinging Gas Jets and Solid Surfaces. Advances in Heat Transfer, 13(1977) 1-60.

[7]   M. Boulet, B. Marcos, M. Dostie and C. Moresoli, CFD modeling of heat transfer and flow field in a bakery pilot oven. Journal of Food Engineering, 97(3) (2010) 393-402.

[8]   P. Verboven, N. Scheerlinck, J. De Baerdemaeker, and B.M. Nicolai, Computational fluid dynamics modelling and validation of the temperature distribution in a forced convection oven. Journal of Food Engineering, 43(2) (2000) 61-73.

[9]   P. Verboven, N. Scheerlinck, J. De Baerdemaeker, and B.M. Nicolai, Computational fluid dynamics modelling and validation of the isothermal airflow in a forced convection oven. Journal of Food Engineering, 43(1) (2000) 41-53.

[10] N. Therdthai, W.B. Zhou, and T. Adamczak, Two-dimensional CFD modelling and simulation of an industrial continuous bread baking oven. Journal of Food Engineering, 60(2) (2003) 211-217.

[11] N. Therdthai, W.B. Zhou, and T. Adamczak, Three-dimensional CFD modelling and simulation of the temperature profiles and airflow patterns during a continuous industrial baking process. Journal of Food Engineering, 65(4) (2004) 599-608.

[12] D. Kocer, N. Nitin and M. Karwe, Applications of CFD in Jet Impingement Oven, in: Da-Wen Sun (Ed.), Computational Fluid Dynamics in Food Processing, CRC Press, 2007, pp. 469–485.

[13] E. E.M. Olsson and C. Trägårdh, CFD Modeling of Jet Impingement during Heating and Cooling of Foods, in: Da-Wen Sun (Ed.), Computational Fluid Dynamics in Food Processing, CRC Press, 2007, pp. 487–503.

[14] D.R. Jefferson, A.A. Lacey, and P.A. Sadd, Crust density in bread baking: Mathematical modelling and numerical solutions. Applied Mathematical Modelling, 31(2) (2007) 209–225.

[15] A. Ousegui, C. Morsoli, M. Dostie and B. Marcos, Porous multiphase approach for baking process - Explicit formulation of evaopration rate. Journal of Food Engineering, 100 (2010) 535-544.

[16] T. Norton and D.-W. Sun, Computational fluid dynamics (CFD) - an effective and efficient design and analysis tool for the food industry: A review. Trends in Food Science & Technology, 17(11) (2006) 600-620.

[17] T. Norton and D.-W. Sun, An overview of CFD Applications in the Food Industry, in: Da-Wen Sun (Ed.), Computational Fluid Dynamics in Food Processing, CRC Press, 2007, pp. 1–41.

[18] P.S. Mirade, J. D. Daudin, F. Ducept, G. Trystram and G. Clement, Characterization and CFD modelling of air temperature and velocity profiles in an industrial biscuit baking tunnel oven. Food Research International, 37(10) (2004) 1031-1039.

[19] S.Y. Wong, W.B. Zhou, and J.S. Hua, CFD modeling of an industrial continuous bread-baking process involving U-movement. Journal of Food Engineering, 78(3) (2007) 888-896.

Track 2 Section 2

Process Modelling

Physical and Operating Conditions Effects on Silica Gel/Water Adsorption Chiller Performance

Ahmed R. M. Rezk, Raya K. Al-Dadah

Department of Mechanical Engineering, University of Birmingham, Birmingham Edgbaston, B15 2TT, United Kingdom

Corresponding author. Email: r.k.al-dadah@bham.ac.uk; Tel. +44 (0) 121-4143513,

Abstract

Adsorption refrigeration systems are commercially developed due to the need of replacing the conventional systems which utilise environmentally harmful refrigerants and consume high grade electrical power. This paper presents the key equations necessary for developing a novel empirical lumped analytical simulation model for commercial 450kW two-bed silica gel/water adsorption chiller incorporating mass and heat recovery schemes. The adsorption chiller governing equations were solved using MATLAB® platform integrated with REFPROP® to determine the working fluids thermo-physical properties. The simulation model predicted the chiller performance within acceptable tolerance and hence it was used as an evaluation and optimisation tool. The simulation model was used for investigating the effect of changing fin spacing on chiller performance where changing fin spacing from its design value to minimum permissible value increased chiller cooling capacity by 3.0% but decreased the COP by 2.3%. Furthermore, the effect of generation temperature lift on chiller performance and the feasibility of using it as a load control tool will be discussed. Genetic Algorithm optimisation tool was used to determine the optimum cycle time corresponding to maximum cooling capacity, where using the new cycle time increased the chiller cooling capacity by 8.3%.

Keywords   adsorption chiller; silica gel/water; empirical simulation

1   Introduction

Heat powered adsorption cooling systems are becoming increasingly considered for applications where cooling is required and low grade heat (temperature as low as $55^{o}C$) is available. Applications for such systems include combined cooling, heating and power (CCHP) system employed in many industrial and commercial applications [1] and sustainable building climatisation using solar energy as heat source [2, 3]. Adsorption cooling systems is a promising solution for more environmentally friendly system [4]. In an adsorption cooling system, a solid adsorbent that has high affinity to the refrigerant is used to move the refrigerant from the evaporator pressure to the condenser pressure by means of adsorption effect during adsorbent bed cooling followed by desorption effect during heating. During the last few decades, several adsorbing materials were investigated including silica gel/water, zeolite/water and activated carbon or activated carbon fibres/ammonia, methanol, ethanol or R134a. For water chilling applications, silica gel/water adsorption pair has the advantages of the excellent physical and thermal properties of water (high latent heat of evaporation, high thermal conductivity, low viscosity, thermally stable in wide range of operating temperature and the compatibility with wide range of materials) and good adsorbing properties of silica gel (high adsorption/desorption rate, low generation heat and low generation temperature). Silica gel/water adsorption pair can be classified as the best adsorption pair for chilling applications and activated carbon/R134a is the best for refrigeration applications, with the main drawback of R134a is its global warming potential [5].

Adsorption refrigeration systems modelling is a primary tool for design and optimisation of these machines [6]. There are many modelling techniques which were used to simulate the adsorption refrigeration systems such as lumped-parameter simulation technique [7-10], lumped analytical simulation technique [11-21], dynamic simulation technique [22-25] and distributed-parameter simulation technique [26]. Object oriented simulation tool such as MODELICA was also used by [27] to simulate the adsorption refrigeration units. All these simulation techniques present the overall heat transfer coefficient for adsorbent beds, evaporator and condenser as constant values. That limits the prediction capability of the effect of any physical change on the adsorption chiller performance,

especially the adsorbent bed. This paper presents the key equations to develop a novel empirical lumped analytical simulation model for a commercial 450kW two-bed silica gel/water adsorption water chiller. The chiller utilises heat and mass recovery schemes. The importance of such type of simulation technique is highlighted by investigating the influence of fin configuration on chiller performance.

Operating conditions significantly affect adsorption chiller performance. One of the most important operating conditions is the operating temperatures [28-31]. The time required for different operating modes (adsorption/desorption, mass recovery and heat recovery) also influences chiller performance [32-34]. However, most of the currently published work on the effect of operating conditions are based on parametric runs of chosen parameters and the need for using a global optimisation technique to obtain the optimum parameters is essential [12]. Genetic Algorithm (GA) one of the robust population-based global optimisation tools was used to determine the global optimum parameters. GA repeatedly modifies a population of individual solutions using three rules namely; selection, crossover and mutation. Over successive generations, the population evolves toward an optimal solution. GA has the advantage over standard optimization algorithms of the ability to solve a variety of problems of discontinuous, non differentiable, stochastic, or highly nonlinear objective functions.

This paper aims at studying the influence of operating temperatures on chiller performance and the feasibility of using regeneration temperature lift as a control tool. Also the effect of cycle time for different operating modes (ads/des, mass recovery and heat recovery) on chiller performance, and the use of GA to determine the optimum cycle time using the cooling capacity as an objective function will be described.

2   System description

Figure 1 shows a schematic diagram of the simulated two-bed adsorption chiller and *Table 1* shows the various operating modes of the chiller. Each adsorbent bed is connected to the evaporator or condenser by flap valves operated by the pressure difference between heat exchangers during adsorbing or desorbing respectively. On the other hand, the flow of cooling and heating water through the heat exchangers at different operating modes is controlled by 12 pneumatic valves.
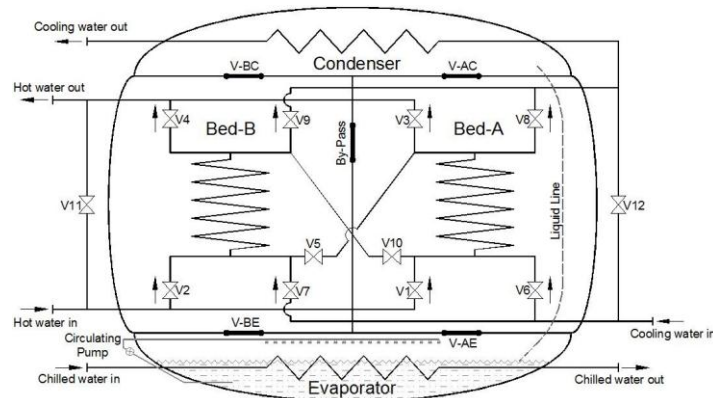
Figure 1: Diagram for simulated two-bed cycle adsorption heat pump

Physically, the adsorbent bed heat exchanger is constructed from plain copper tubes with aluminium rectangular fins and silica gel granules are packed to fill the gaps between fins. The evaporator and condenser are shell and tube heat exchangers where the refrigerant flows on the shell side and the secondary fluid (water) flows inside the tubes. The condenser heat exchanger is constructed from plain copper tubes while the evaporator is constructed from externally enhanced high efficiency finned copper tubes (GEWA-B)[®].

Table 1
Chiller cyclic operation modes and valving

Mode	B-A	B-B	V-AE	V-AC	V-BE	V-BC	BP	V1	V2	V3	V4	V5	V6	V7	V8	V9	V10	V11	V12
A-Ads/Dses	HW	CW	X	O	O	X	X	O	X	O	X	X	X	O	X	O	X	X	X
B-Mass Recovery	NF	NF	X	X	X	X	O	X	X	X	X	X	X	O	O	X	O	O
C-Heat Recovery	CW	CW	X	O	O	X	X	X	X	X	X	O	O	X	X	O	X	O	X
D- Ads/Dses	CW	HW	O	X	X	O	X	X	O	X	O	X	O	X	O	X	X	X	X
E-Mass Recovery	NF	NF	X	X	X	X	O	X	X	X	X	X	X	O	O	X	O	O
F-Heat Recovery	CW	CW	X	X	X	X	X	X	X	X	X	X	O	O	X	O	O	X

HW=hot water, CW=cooling water, NF=no flow, X=close, O=open

3   Simulation model

The simulation model of the adsorption system was constructed from four sub-models describing the performance of evaporator, condenser, adsorber and desorber. The four sub-models were linked together taking into account the various operating modes. Equations 1-3 present the energy balance equations for adsorbent bed, evaporator and condenser respectively, where the adsorbent, adsorbate and heat exchanger metal are assumed to be momentarily at the same temperature. Equation 4 presents the refrigerant mass balance in the evaporator taking into account no flow condition in case of heat and mass recovery.

$$\left(\zeta M_{bed-w} C_w(T_{bed}) + M_{sg} w_{sg} Cp_{ref}(T_{bed}) + M_{sg} C_{sg} + M_{bed-met} C_{bed-met}\right) dT_{bed}/dt = (1-\zeta) \sum_{n=1}^{n=N_{bed}} dUA_{bed-n} \times LMTD_{bed} \quad (1)$$

$$+ (\phi \bullet \partial)\left[\gamma\{h_g(T_{Hex}) - h_g(P_{Hex}, T_{bed})\} + (1-\gamma)\{h_g(P_{Hex}, T_{Hex}) - h_g(P_{bed}, T_{bed})\}\right]M_{sg}\, dw_{sg}/dt + \phi M_{sg} \Delta H_{sg}\, dw_{sg}/dt$$

$$\left[Cp_{ref,f}(T_{evap})M_{ref,evap} + C_{evap-met}M_{evap-met}\right] dT_{evap}/dt = UA_{evap} \times LMTD_{evap}$$
$$+ \phi\left[h_{ref,evap,in} - h_{ref,evap,out}\right]M_{sg}\, dw_{sg}/dt + dE_{pump}/dt \quad (2)$$

$$\left[Cp_{ref,l}(T_{cond})M_{ref,cond} + C_{cond-met}M_{cond-met}\right] dT_{cond}/dt = UA_{cond} \times LMTD_{cond}$$
$$+ \phi\left[(h_{ref,cond,l} - h_{ref,cond,g}) + Cp_{ref}(T_{cond} - T_{bed})\right]M_{sg}\, dw_{sg}/dt \quad (3)$$

$$dM_{ref,f,evap}/dt = -\phi \cdot M_{sg}\left(dw_{des}/dt + dw_{ads}/dt\right) \quad (4)$$

Where M (kg), C (kJ kg^{-1} K^{-1}), Cp (kJ kg^{-1} K^{-1}), T (K), LMTD (K), P (kPa), h (kJ kg^{-1}), w (kg$_w$ kg$_{sg}^{-1}$), ΔH_{ads} (J/kg) and t (s) are the mass, specific heat, specific heat at constant pressure, temperature, log mean temperature difference, pressure, specific enthalpy, uptake value, isosteric heat of adsorption, and time respectively. The subscripts bed, evap and cond refer to adsorbent bed (ads/des), evaporator and condenser condition respectively and w, sg, ref and met refer to water, silica gel, refrigerant and metal respectively. Subscripts g, f, refer to fluid vapour and liquid condition respectively and Hex refers to the heat exchanger that interconnect with the adsorbent bed.

A group of flags (ζ, ϕ, ∂, γ) were used to enable or disable some of the equation terms based on the operating mode as shown in *Table 2*. The rate of adsorption was evaluated using linear driving force kinetic model (LDF), where water vapour can reach all silica gel granules and the inter-particle mass transfer resistance can be neglected, equation 5.

$$\frac{dw}{dt} = \left(15 D_{so}/R_p^2\right)\exp\left(-E_a/RT\right)\left(w^* - w\right) \quad (5)$$

Where R_p (m), D_{so} (m^2 s^{-1}), E_a (J mol^{-1}), R (J mol^{-1} K^{-1}) and w* (kg$_w$ kg$_{sg}^{-1}$) are particles radius, pre-experimental constant, activation energy, universal gas constant and equilibrium uptake respectively.

Table 2
Simulation model switching flags

Mode	Flag ζ	Flag ϕ	Flag ∂	Flag γ
Ads-evaporation	0	1	1	1
Des-condensation	0	1	0	0
Mass recovery	1	0	1	0
Heat recovery	0	0	1	0

Adsorption isotherms describe the amount of refrigerant that should be contained in the adsorbent pores at equilibrium conditions. There are many correlations that have been used to calculate the adsorption isotherms for different types of adsorbent materials. Freundlich model which was modified by Saha (1995) to give more precise fitting of the experimental data for silica gel/water pair was used to determine the adsorption isotherms [11]. Equations 6-8 present the modified Freundlich model and all constants are furnished in *Table 3*.

$$w^* = A(T_{ads})\left[P_{sat}(T_{ref})/P_{sat}(T_{ads})\right]^{B(T_{ads})} \tag{6}$$

$$A(T_{ads}) = A_0 + A_1 T_{ads} + A_2 T_{ads}^2 + A_3 T_{ads}^3 \tag{7}$$

$$B(T_{ads}) = B_0 + B_1 T_{ads} + B_2 T_{ads}^2 + B_3 T_{ads}^3 \tag{8}$$

Where, A_{0-3} and B_{0-3} are constants. Equations 9-10 present the methodology of evaluating incremental overall conductance of the adsorbent bed (dUA_{bed}) and the overall conductance of evaporator and condenser heat exchanger respectively ($UA_{evap-cond}$) based on different thermal resistance R. Simulation model governing equations are solved using MATLAB® platform using ODE45 solver to compile the differential equations simultaneously and materials thermo-physical properties are evaluated by REFPROP® software. More detailed description of calculating the heat transfer thermal resistance can be found in [5].

$$dUA_{bed} = 1/R_{w,bed} + R_{tube,bed} + R_{o,bed} \tag{9}$$

$$UA_{evap-cond} = 1/R_{w,evap-cond} + R_{tube,evap-cond} + R_{ref,evap-cond} \tag{10}$$

The interface thermal contact resistance between two different materials depends on contact area, voids area, filling material and thermal conductivity for both materials [35]. Contact thermal resistance between zeolit granules and heat exchanger metal surface was experimentally investigated by [36]. Due to the negligible effect (1.5% difference in contact resistance value) of the difference in thermal conductivity of silica gel (0.198W/mK) and zeolite (0.097W/mK) on the contact thermal resistance [35], Equations 11-13, were used in the model. These equations are polynomial expressions with minimum R-squared value of 0.986 for the thermal contact resistance measured by [36] for three different zeolite granules sizes 50, 100 and 200 mesh corresponding to 0.297, 0.149 and 0.074 mm respectively.

$$R_{contact,\#50} = 0.0013 T_{bed}^2 - 0.1773 T_{bed} + 8.6221 \tag{11}$$

$$R_{contact,\#100} = 0.0012 T_{bed}^2 - 0.1624 T_{bed} + 7.6785 \tag{12}$$

$$R_{contact,\#200} = 0.0008 T_{bed}^2 - 0.1214 T_{bed} + 6.422 \tag{13}$$

Table 3
Parameters value of the simulation model

Constant	value	Constant	value	Constant	value
A_o	-6.5314	B_o	-15.587	D_{so}	3.625E-3
A_1	0.72452E-1	B_1	0.15915	E_a	4.2 E4
A_2	-0.23951E-3	B_2	-0.50612E-3	R_p	0.16 E-3
A_3	0.25493E-6	B_3	0.53290E-6	ΔH_{ads}	2.939 E6

3.1 Performance indicators

To evaluate adsorbent bed thermal performance two performance parameters were used; namely heat capacity ratio HCR and number of transfer unit NTU. HCR is the ratio between the thermal capacity of silica gel to that of the adsorbent bed metal, equation 11. Higher HCR means higher heat absorbed by silica gel compared to metal that directly enhances chiller COP. NTU is a dimensionless parameter whose magnitude influences adsorbent bed heat transfer performance, equation 12. It is noteworthy to mention that enhancement of HCR and NTU improve adsorbent bed overall performance.

$$HCR = M_{sg}C_{sg}/M_{met}C_{met} \tag{11}$$

$$NTU = UA_{bed}/\dot{m}_w C_w \tag{12}$$

To evaluate adsorption chiller overall performance four indicators are used; namely cooling capacity 'Q_{evap}' equation 13, heating load 'Q_{heat}' equation 14, coefficient of performance 'COP' equation 15, Carnot coefficient of performance 'COP_{carnot}' equation 16 and chiller efficiency 'η' equation 17.

$$Q_{evap} = \int_0^{t_{cycle}} \dot{m}_{chw}C_w \left(T_{chw,in} - T_{chw,out}\right)dt \Big/ t_{cycle} \tag{13}$$

$$Q_{heat} = \int_0^{t_{cycle}} \dot{m}_{hw}C_w \left(T_{hw,in} - T_{hw,out}\right)dt \Big/ t_{cycle} \tag{14}$$

$$COP = Q_{evap}/Q_{heat} \tag{15}$$

$$COP_{Carnot} = \left[\left(\overline{T}_{ads} - \overline{T}_{des}\right)/\overline{T}_{des}\right] \times \left[\overline{T}_{evap}/\left(\overline{T}_{ads} - \overline{T}_{evap}\right)\right] \tag{16}$$

$$\eta_{chiller} = COP/COP_{Carnot} \tag{17}$$

Where $\dot{m}$ (kg s^{-1}) presents secondary fluid mass flow rate and subscripts chw, hw refer to chilled water and hot water respectively.

3.2 Chiller simulation model results

Figure 2, compares the predicted chilled, cooling and heating water outlet temperatures and their actual analogous values which were supplied by the manufacturer based on the same average inlet conditions. *Table 4* presents the average percent deviation (APD) and absolute average percent deviation (ABS-PD) for cooling, heating and chilled water outlet temperatures for the test results shown in Figure 2. The deviation between the predicted COP, heating load and cooling capacity are also presented. It is known that the predicted value of thermal simulation model can be accepted if the absolute average percent deviation is below 30%, [37]. *Table 4*, and Figure 2, indicate clearly the good agreement between the model and experimental results. *Table 5* presents the absolute average percent deviation for average cooling, heating and chilled water outlet temperature in addition to cooling capacity, heating power and COP for additional experimental runs. It can be seen that the maximum absolute percent deviation calculated based on steady state cycle is 17.8%.
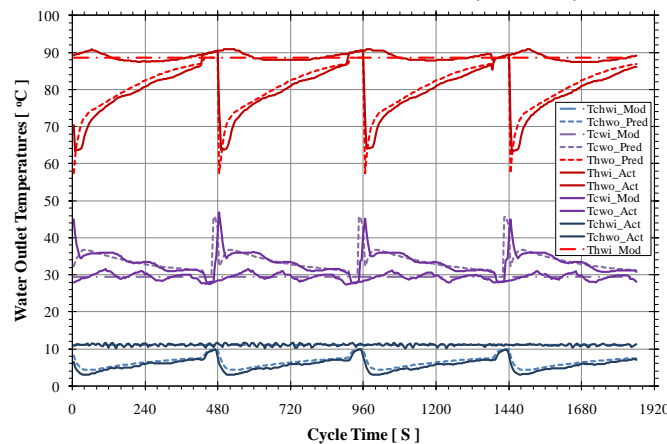
Figure 2: Comparison between predicted data and actual data

Table 4
Simulation model deviation analysis (m•$_{hw}$=1100 L/min, m•$_{cw}$=4000 L/min, m•$_{chw}$=1180 L/min)

Term	APD	ABS-PD	Term	APD	ABS-PD
$T_{hw,o}$	-1.6%	2.4%	Q_{evap}	12.9%	12.9%
$T_{cw,o}$	-1.1%	3.4%	Q_{heat}	10.9%	10.9%
$T_{chw,o}$	-16.5%	16.5%	COP	2.8%	2.7%

Table 5
Simulation model deviation analysis at one steady state cycle

Term	RUN-1		RUN-2		RUN-3		RUN-4		unit
m•$_{hw}$	1100		1100		1100		2200		l/min
m•$_{cw}$	4000		4000		4000		4000		l/min
m•$_{chw}$	1180		1180		1180		1320		l/min
$T_{hw,i,av}$	88.6		89.0		88.8		88.2		°C
$T_{cw,i,av}$	29.5		29.4		29.4		29.2		°C
$T_{chw,i,av}$	11.1		11.1		11.1		11.1		°C
Deviation analysis (actual o/p temperature & ABS-PD)									
$T_{hw,o}$	79.7	1.6	80.1	1.5	79.9	1.6	83.3	0.9	°C & %
$T_{cw,o}$	33.4	0.9	33.4	0.8	33.3	1.0	33.6	0.0	°C & %
$T_{chw,o}$	5.8	12.3	5.7	13.1	5.7	13.3	5.8	15.7	°C & %
Q_{heat}	650	10.3	654	9.9	652	9.9	704	10.6	°C & %
Q_{cool}	439	13.1	446	13.6	444	13.5	487	17.8	°C & %
COP	0.68	3.7	0.68	3.9	0.68	3.8	0.69	7.8	°C & %

4 The effect of fin spacing on adsorption chiller performance

To improve heat and mass transfer performance in the adsorbent bed the following factors need to be considered: (1) Improving the overall heat transfer coefficient U and heat transfer area A in order to improve the overall conductance of the adsorbent bed UA significantly affect the heat transfer performance and the adsorption kinetics; (2) Increasing the fins height increases the silica gel thickness over heat exchanger tubes and decreases adsorbent bed permeability; (3) Changing the fins configuration affects the metal mass of the adsorbent bed, which affects the overall performance of the adsorption chiller.

The simulation model was used to investigate the effect of fin spacing on the performance of adsorption chiller with the amount of silica gel kept constant and operating temperature of 11, 29.5 and 88.5^{o}C for chilled, cooling and heating water respectively and ads/des, mass recovery and heat recovery time of 430, 30 and 20 seconds respectively. As fin spacing changed, fin configuration (height and/or width) changed in order to accommodate the same amount of silica gel, Figure 3(*a*). It was observed that changing the fin width does not affect bed HCR or NTU in case of heating and cooling, Figures 3(*b*), 4(*a*) and 4(*b*) respectively. Therefore fin height was kept constant and fin width varied to keep the mass of silica gel constant without affecting the bed permeability.

Decreasing fin spacing results in increasing the number of fins which will increase bed NTU but reduces its HCR due to increasing the surface area and the mass of metal in the bed. Increasing the adsorbent bed heat transfer performance by means of fin spacing reduction enhances the adsorption kinetics and hence chiller cooling capacity, Figure5. In contrast, the reduction in the bed HCR increases chiller heating capacity to heat up the increased metal mass, Figure5, these trends confirmed by [25, 38]. However, the rate of cooling capacity increase is lower than the rate of heating capacity increase which causes chiller COP to decrease by reducing fin spacing. To sum up, changing fin spacing from design value to minimum permissible value can increase the chiller specific cooling capacity by 3%, but decrease chiller COP by 2.3% due to the increase of heating capacity by 5.4%.

(*a*)   (*b*)
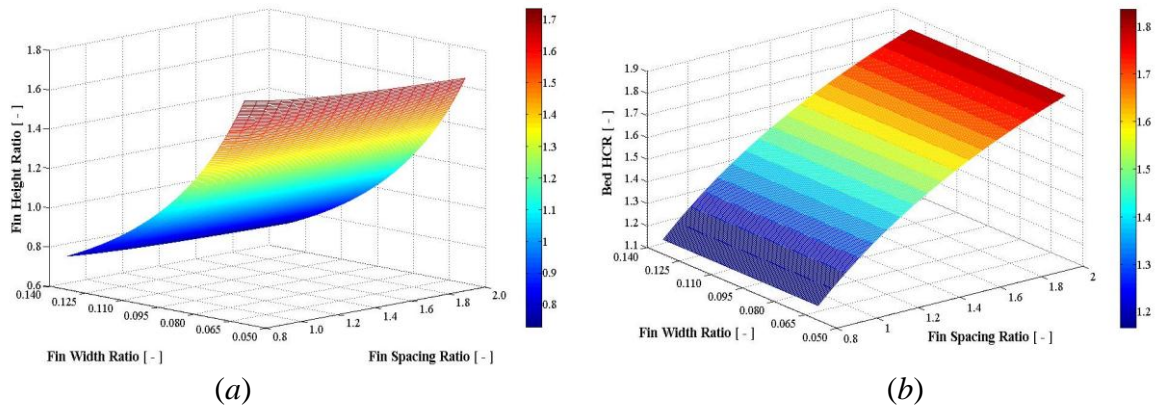
Figure 3: Fin height and HCR versus fin configuration

(*a*)   (*b*)
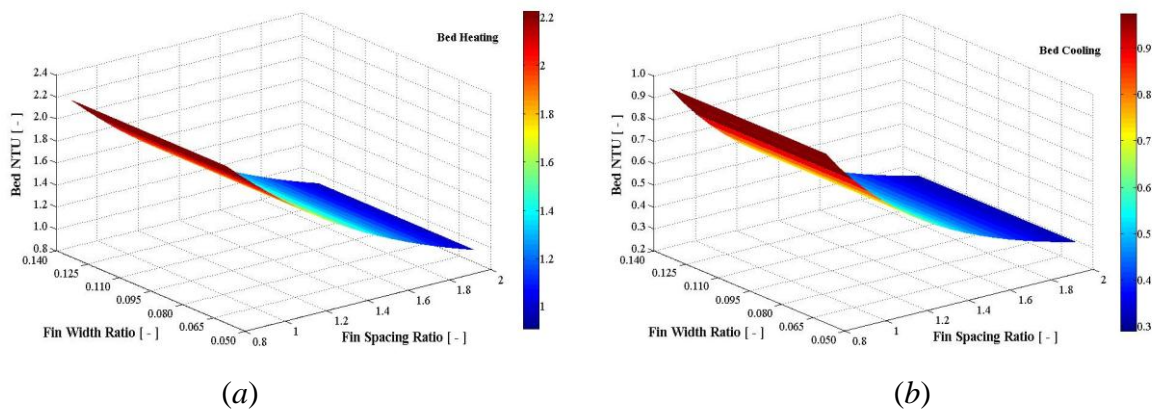
Figure 4: Bed NTU versus fin configuration (*a*) bed heating (*b*) bed cooling
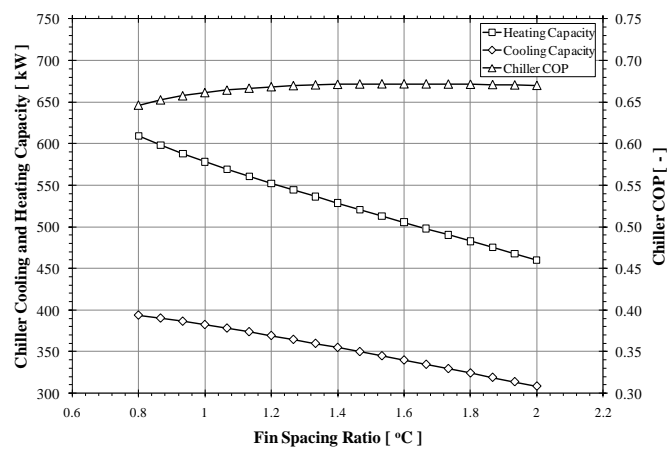
Figure 5: The effect of fin spacing on chiller performance

5   Operating temperatures

Operating temperatures influence adsorption chiller performance. Lowering cooling water inlet temperature not only increases cooling capacity, but also enhances adsorption chiller COP, due to the significant increase in adsorption rate. Increasing heating water temperature also enhances chiller cooling capacity due to enhancing desorption rate. The difference between the heating water temperature and the cooling water temperature is termed as the generation temperature lift [11]. Figure 6 presents the change in chiller cooling capacity versus generation temperature lift at various cooling water inlet temperatures at fixed ads/des, mass recovery and heat recovery times. As the generation temperature lift increases chiller cooling capacity increases.
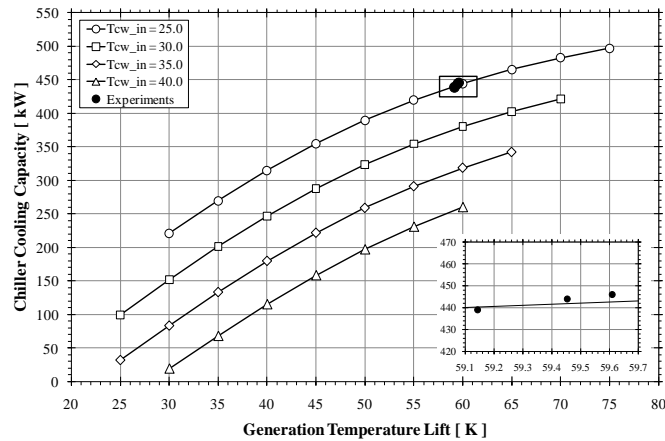
Figure 6: The effect of generation temperature lift on chiller cooling capacity

Figure 7 presents the variation in chiller COP and chiller efficiency versus generation temperature lift. It can be seen that at low cooling water temperature, the chiller COP and efficiency decrease with increasing the generation temperature lift over the tested range. However, at higher cooling water temperature (T_{cw}>30°C), the chiller COP initially increases to a certain point and then remains relatively constant with increasing the generation temperature lift. On the other hand, the chiller efficiency after reaching maximum point decreases with increasing the generation temperature lift. The decrease in chiller efficiency at low generation temperature lift and high cooling water temperature is due to the insufficient refrigerant circulation required to generate the cooling power. On the other hand, the decrease in chiller efficiency at high temperature lift is due to the increase in heat losses [21].

Chiller COP and efficiency behaviours encourage using generation temperature lift as a load control tool. For example, at cooling water temperature of 35°C, the chiller cooling capacity increased almost linearly (from 180 to 342kW) with increasing the generation temperature lift (from 40 to 65K). The reduction in chiller COP (from 0.63 to 0.60) and efficiency (from 0.68 to 0.52) are relatively small.

6   Cycle time
During the physical adsorption process, the solid adsorbent adsorbs the refrigerant from the evaporator container to develop a cooling effect by means of refrigerant evaporation. The heat generated due to the adsorption process is removed to sustain the adsorption process and maintain the cooling effect. However for specific adsorption time, the rate of adsorption decreases with increasing the amount of refrigerant adsorbed until the bed becomes saturated with refrigerant. Hence the cooling

(*a*)   (*b*)
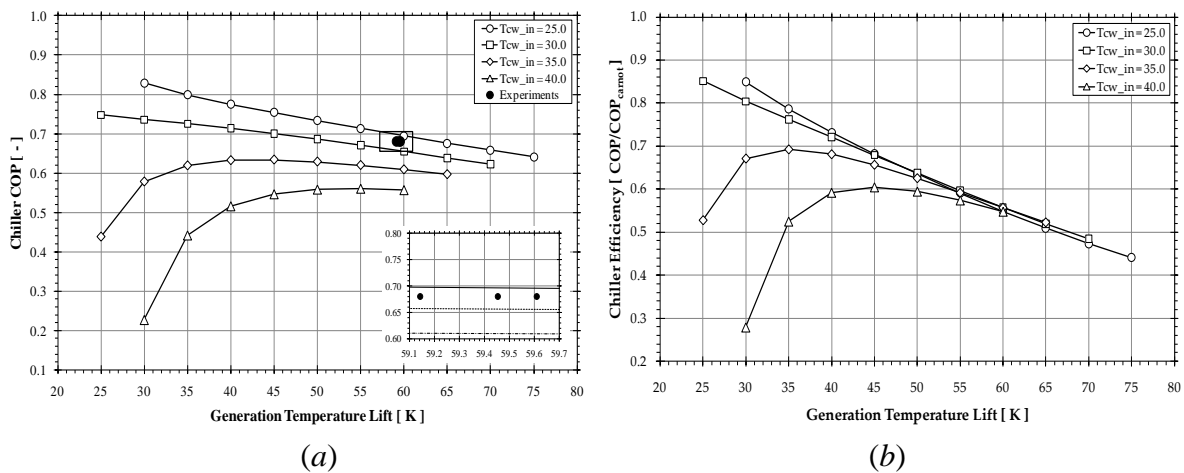
Figure 7: The effects of generation temperature lift on chiller (*a*) COP and (*b*) Efficiency

effect reduces with increasing the adsorption time. The adsorbent bed is regenerated by heating and the desorbed refrigerant is condensed and passed back to the evaporator to repeat the aforementioned process. As the adsorption time increase, the heating load decreases and hot water outlet temperature approaches the inlet temperature. This will increase the COP but decrease the cooling capacity.

Continuous cooling is achieved by using two beds, where one bed is connected to the evaporator in adsorption mode and the other bed to the condenser in desorption mode. Before reversing adsorption and desorption modes sufficient time period is required to preheat/precool the adsorption/desorption beds to avoid premature connection between the hot bed and evaporator which results in momentary desorption of adsorbed refrigerant and undesirable reduction in instantaneous cooling capacity. In the simulated adsorption chiller the switching period is divided into mass and heat recovery periods. It is noteworthy that during switching period there is no interconnection between adsorbent beds and evaporator/condenser where no cooling effect can be achieved anymore. As a result, appropriate switching time can improve the cooling capacity and COP of the adsorption chiller.

Figure 8 presents the effect of changing ads/des and mass recovery time periods simultaneously on chiller cooling capacity for different heat recovery times using constant operating temperature given in section 4. It is observed that as ads/des time period increases, chiller cooling capacity increases sharply, reaches a maximum at certain time and then decreases gradually. Within the investigated range, it was observed that the cooling capacity at maximum point in Figure 9(*a*), 9(*b*) and 9(*c*) produces 6.1 and 0.4% higher and 5.7% lower values compared to the reference operating times given in section 4.

GA is used to calculate the optimum values for ads/des, heat recovery and mass recovery times that achieve the maximum cooling capacity, which is the optimisation objective function. GA is a subclass of evolutionary algorithms that based on the natural selection processes that drive the biological evolution. The algorithm starts the first iteration with initial random population for each parameter to get a set of individuals ($N_{population}$ X $N_{parameter}$). This population is used for calculating the corresponding objective function values. A new generation is then developed to be used as a new population in next iteration using a selection function based on three rules named; elite selection, crossover and mutation. The individuals that achieved the best objective function values in the current generation and granted to survive to the next generation are elite individuals. Crossover enables the algorithm to extract the best individuals and recombine them into potential superior individuals using a specified crossover fraction. The mutation rule replaces the remaining population with randomly selected new ones. Crossover fraction of 1 does not enhance the solution where the new generation is just a new combination of the initial population. However, crossover fraction of zero gets the new generation based on mutation only which diverge the solution.

GA is applied to determine global optimum operating times within a specific range that could include the optimum combination that maximize the cooling capacity. The range of times used were 250-450 seconds for ads/des time period, 10-50 seconds for mass and heat recovery time periods. The number of population for each individual parameter is selected to be 20 while the number of elite count is 2, the crossover fraction is 0.8 and the rest of individuals are managed by mutation rule. These were

(*a*)   (*b*)   (*c*)
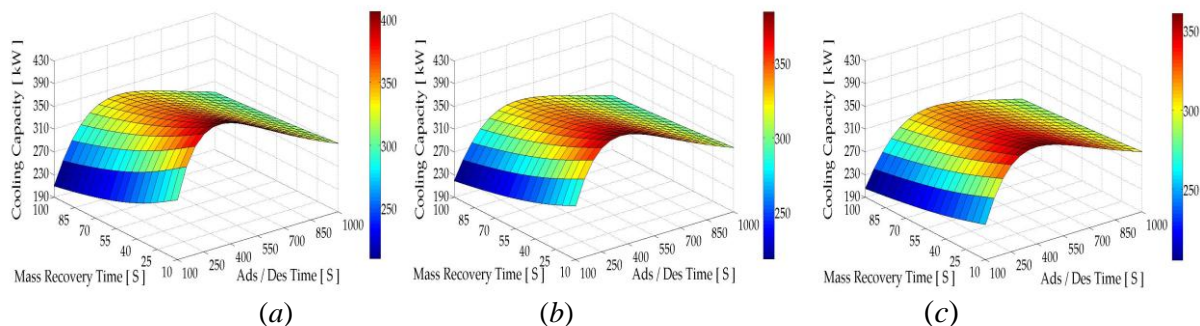
Figure 8: The effect of Ads/Des and mass recovery time period on chiller cooling capacity

(*a*) t*heat recovery*=20s (*b*) t*heat recovery*=60s (*c*) t*heat recovery*=100s

recommended by Mathwork GA Manual® [39]. After 30 iterations the GA solver stopped, where no more improvement in the solution in terms of objective function value, average diversity and best, worst and mean score. The determined optimum ads/des, mass recovery and heat recovery time period values are 345, 12 and 14 seconds respectively. Chiller cooling capacity at the new cycle time increased by 8.3% and COP reduced from 0.66 to 0.60 compared to their analogues values while chiller working at reference operating cycle times.

7   Conclusions

The presented simulation model predicted the performance of commercial 450kW adsorption water chiller with good accuracy. The model is a global model that has the ability to investigate the effect of various physical parameters on the performance of the adsorption chiller. This advantage is highlighted by investigating the effect of fin spacing on chiller performance, where chiller cooling capacity increases by 3% by reducing fin spacing from its design value to the minimum permissible value.

Chiller operation conditions such as operating temperature and cycle time directly influence chiller performance. Operating temperature can be used as a load control tool to mange chiller operation in case of part load with high efficiency. Cycle time can be used to improve chiller performance to get more cooling and GA is used to determine the global optimum cycle time corresponding to the maximum cooling capacity, where chiller cooling capacity can be increased by 8.3%.

References

[1]   S Li , JY Wu, Theoretical research of a silica gel-water adsorption chiller in a micro combined cooling, heating and power (CCHP) system. App Energy. 86 (2009) 958-967.

[2]   H Luo, R Wang , Y Dai, The effects of operation parameter on the performance of a solar-powered adsorption chiller. App Energy. 87 (2010) 3018-3022.

[3]   CJ Chen, RZ Wang, ZZ Xia, Study on a compact silica gel-water adsorption chiller without vacuum valves: Design and experimental study. App Energy. 87 (2010) 2673-2681.

[4]   DB Riffel, U Wittstadt, FP Schmidt, Transient modeling of an adsorber using finned-tube heat exchanger. Int J Heat Mass Transfer. 53 (2010) 1473-1482.

[5]   RK Aldadah , ARM Rezk. Empirical Simulation Model of Silica Gel/Water Adsorption Chiller. ASME-ATI-UIT, Thermal and Enviromental Issues in Energy Systems. 2010. Sorrento, Italy.

[6]   A Freni, B Dawoud, F Cipiti. Finite Element-Based Simulation of The Heat and Mass Transfer Process Through an Adsorbent Bed in an Adsorption Heat Pump/Chiller. ASME-ATI-UIT, Conference on Thermal and Environmental Issues in Energy Systems. 2010. Sorrento, Italy.

[7]   HT Chua, KC Ng, A Malek, Modeling the performance of two bed, silica gel-water adsorption chiller. Int J Ref. 22 (1999) 194-204.

[8]   EC Boelman, BB Saha , T Kashiwagi, Parametric study of a silica gel-water adsorption refrigeration cycle - the influence of thermal capacitance and heat exchanger UA-Values on cooling capacity, power density and COP. ASHRAE Trans. 103, Part 1 (1997) 139-148.

[9]   X Wang , HT Chua, Two bed silica gel-water adsorption chillers: An effectual lumped parameter model. Int J Ref. 30 (2007) 1417-1426.

[10] JY Wu , S Li, Study on cyclic characteristics of silica gel-water adsorption cooling system driven by variable heat source. Energy. 34 (2009) 1955-1962.

[11] BB Saha, EC Boelman , T Kashiwagi, computer simulation of a silica gel-water adsorption refrigeration cycle - the influence of operating conditions on cooling output and COP. ASHRAE Trans. 101 (1995) 348-357.

[12] T Miyazaki , A Akisawa, The influence of heat exchanger parameters on the optimum cycle time of adsorption chillers. Appl Therm Eng. 29 (2009) 2708-2717.

[13] A Akahira, KCA Alam, Y Hamamoto, Mass recovery adsorption refrigeration cycle--improving cooling capacity. Int J Ref. 27 (2004) 225-234.

[14] T Miyazaki, A Akisawa, BB Saha, A new cycle time allocation for enhancing the performance of two-bed adsorption chillers. Int J Ref. 32 (2009) 846-853.

[15] AS Uyun, A Akisawa, T Miyazaki, Numerical analysis of an advanced three-bed mass recovery adsorption refrigeration cycle. Appl Therm Eng. 29 (2009) 2876-2884.

[16] MZI Khan, KCA Alam, BB Saha, Performance evaluation of multi-stage, multi-bed adsorption chiller employing re-heat scheme. Renewable Energy. 33 (2008) 88-98.

[17] Y Hamamoto, KCA Alam, BB Saha, Study on adsorption refrigeration cycle utilizing activated carbon fibers. Part 2. Cycle performance evaluation. Int J Ref. 29 (2006) 315-327.

[18] MZI Khan, BB Saha, KCA Alam, Study on solar/waste heat driven multi-bed adsorption chiller with mass recovery. Renewable Energy. 32 (2007) 365-381.

[19] BB Saha, S Koyama , T Kashiwagi, waste heat driven dual-mode, multi-stage, multi-bed regenerative adsorption system. Int J Ref. 26 (2003) 749-757.

[20] MZI Khan, KCA Alam, BB Saha, Study on a re-heat two-stage adsorption chiller - The influence of thermal capacitance ratio, overall thermal conductance ratio and adsorbent mass on system performance. Appl Therm Eng. 27 (2007) 1677-1685.

[21] BB Saha, EC Boelman , T Kashiwagi, Computational analysis of an advanced adsorption-refrigeration cycle. Energy. 20 (1995) 983-994.

[22] BB Saha, A Chakaborty, S Koyama, A new generation cooling device employing CaCl2-in-silica gel-water system. Int J Heat Mass Transfer. 52 (2009) 516-524.

[23] S Vasta, A Frazzica, G Maggio. Simulation of a small size solar assisted adsorption air conditioning system for residential application. Heat Powered Cycles. 2009. Berlin.

[24] G Maggio, LG Godeeva, A Freni, Simulation of a solid sorption ice-maker based on the novel composite sorbent "lithium chloride in silica gel pores". Appl Therm Eng. 29 (2009) 1714-1720.

[25] G Cacciola, G Restuccia , GHW van Benthem, Influence of the adsorber heat exchanger design on the performance of the heat pump system. Appl Therm Eng. 19 (1999) 255-269.

[26] X Wang , HT Chua, A comparative evaluation of two different heat-recovery schemes as applied to a two-bed adsorption chiller. Int J Heat Mass Transfer. 50 (2007) 433-443.

[27] M Schicktanz , T Núñez, Modelling of an adsorption chiller for dynamic system simulation. Int J Ref. 32 (2009) 588-595.

[28] WS Chang, CC Wang , CC Shieh, Design and performance of a solar-powered heating and cooling system using silica gel/water adsorption chiller. Appl Therm Eng. 29 (2009) 2100-2105.

[29] YL Liu, RZ Wang , ZZ Xia, Experimental performance of a silica gel-water adsorption chiller. Appl Therm Eng. 25 (2005) 359-375.

[30] J Di, JY Wu, ZZ Xia, Theoretical and experimental study on characteristics of a novel silica gel-water chiller under the conditions of variable heat source temperature. Int J Ref. 30 (2007) 515-526.

[31] Rd Boer, S Smeding , S Mola. Silica gel-water adsorption cooling prototype system for mobile air conditioning. Heat powered cycles. 2009. Technische Universtat Berlin.

[32] ZZ Xia, RZ Wang, DC Wang, Development and comparison of two-bed silica gel-water adsorption chillers driven by low-grade heat source. Int J Thermal Science. 48 (2009) 1017-1025.

[33] RE Critoph , SJ Metcalf, Specific cooling power intensification limits in ammonia-carbon adsorption refrigeration systems. Appl Therm Eng. 24 (2004) 661-678.

[34] CJ Chen, RZ Wang, ZZ Xia, Study on a silica gel-water adsorption chiller integrated with a closed wet cooling tower. Int J Thermal Science. 49 611-620.

[35] JP Holman, ed. *Heat Transfer*. 1990, Library of Congress Cataloging

[36] D Zhu , S Wang, Experimental investigation of contact resistance in adsorber of solar adsorption refrigeration. Solar Energy. 73 (2002) 177-185.

[37] LM Chamra , PJ Mago, Modeling of condensation heat transfer of refrigerant mixture in micro-fin tubes. Int J Heat Mass Transfer. 49 (2006) 1915-1921.

[38] G Cacciola , G Restuccia, Progress on adsorption heat pumps. Heat Recovery Systems and CHP. 14 (1994) 409-420.

[39] *Genetic Algorithm and Direct Search toolbox for use with matlab*: The Mathworks.

Operation Window and Part-Load Performance Study of a Syngas Fired Gas Turbine

Fen He[a], Zheng Li[a*], Pei Liu[a], Linwei Ma[a], Efstratios N. Pistikopoulos [b]

[a] State Key Laboratory of Control and Simulation of Power System and Generation Equipment, Department of Thermal Engineering, Tsinghua University, Beijing 100084, China
[b] Centre for Process Systems Engineering, Department of Chemical Engineering, Imperial College London, London SW7 2AZ, United Kindom

* Corresponding author. Email: lz-dte@tsinghua.edu.cn; Tel. +86(0) 10 627 957 35; Fax. + 86(0) 10 627 957 36

Abstract
Integrated coal gasification combined cycle (IGCC) provides a great opportunity for clean utilization of coal while maintaining the advantage of high energy efficiency brought by gas turbines. A challenging problem arising from the integration of an existing gas turbine to an IGCC system is the performance change of the gas turbine due to the shift of fuel from natural gas to synthesis gas, or syngas, mainly consisting of carbon monoxide and hydrogen. Besides the change of base-load performance, which has been extensively studied, the change of part-load performance is also of great significance for the operation of a gas turbine and an IGCC plant.

In this paper, a detailed mathematical model of a syngas fired gas turbine is developed to study its part-load performance. A baseline is firstly established using the part-load performance of a natural gas fired gas turbine, then the part-load performance of the gas turbine running with different compositions of syngas is investigated and compared with the baseline. Particularly, the impacts of the variable inlet guide vane, the degree of fuel dilution, and the degree of air bleed are investigated. Results indicate that insufficient cooling of turbine blades and a reduced compressor surge margin are the major factors that constrain the part-load performance of a syngas fired gas turbine. Results also show that air bleed from the compressor can greatly improve the working condition of a syngas fired gas turbine, especially for those fired with low lower heating value syngas. The regulating strategy of a syngas fired gas turbine should also be adjusted in accordance to the changes of part-load performance, and a reduced scope of constant TAT (turbine exhaust temperature) control mode is required.

Keywords   gas turbine; part-load performance; syngas; modelling

1   Introduction
Integrated coal gasification combined cycle (IGCC) provides a great opportunity for clean utilization of coal whilst maintaining the advantage of high energy efficiency of gas turbines. A challenging problem arising from the integration of a standard natural gas fired gas turbine to an IGCC system is the performance change of the gas turbine due to the shift of fuel from natural gas to synthesis gas, or syngas, mainly consisting of carbon monoxide and hydrogen. Gas turbines (GT) are typically designed and optimized for operation with standard fuel, for instance, natural gas, of which the lower heating value (LHV) is much larger than that of syngas. For a syngas fired gas turbine, more syngas is required in the combustion system, and the inlet pressure of the turbine should also be increased to obtain a higher gas flow rate. However, if the pressure ratio gets too high, there are risks of encountering compressor instability and insufficient cooling of turbine blades.

Measures such as air bleed and fuel dilution are commonly adopted in a syngas fired gas turbine [1-2]. Air bleed refers to extracting air from a gas turbine compressor, and using it in an air separation unit (ASU). The scheme with a portion of compressed air extracted from the gas turbine to the ASU while the remaining part supplied by auxiliary air compressor is also referred to as integration. In this paper, we define air bleed ratio and integration degree as follows:

$$\text{Air Bleed Ratio} = \text{Air to ASU from GT} / \text{Air at GT Inlet} \tag{1}$$

$$\text{Integration Degree} = \text{Air to ASU from GT} / \text{Total Air To ASU} \qquad (2)$$

Air bleed and integration reduce the amount of gas flowing through the turbine expander, therefore reduces the extent of modifications required to accommodate increased volumetric flow through the expander and fuel systems. However, the present experience with IGCC plant recommends a maximum of 50 percent of integration, on grounds of reliability and availability. It is not a goal of this paper to optimize the integration of the gas turbine and the ASU, although several papers have shown that 25-30 percent of the integration degree provides the best balance between maximizing plant output and efficiency without compromising plant availability or reliability[3-4]. In a typical IGCC plant, the entire amount of air needed at the ASU is about 20 to 25 percent of the GT inlet air flow, mostly depending on the oxygen assumption of the gasifier. Thus 25 to 30 percent of the integration degree requires approximately five to seven percent of the air bleed ratio from the gas turbine.

Fuel dilution refers to injecting compressed nitrogen from the ASU into fuel gas before combustion. The nitrogen injection is also beneficial to reduction of NOx emissions and power augmentation [5].

Although applications of syngas fired gas turbines in IGCC power plants and polygeneration energy systems[6-9] have been extensively studied, they are mainly focused on the full load performance[1][10-16], and research on the part-load performance of a syngas fired gas turbine is still limited[17]. This paper presents a mathematical model for the simulation of the part load performance of a gas turbine fired with different types of fuels. This model is capable of quantifying variation in the performance of a gas turbine over a wide load range, and evaluating control strategies for part load operation. Particularly, impacts of variable inlet guide vane (VIGV), degree of fuel dilution, and degree of air bleed on the GT performance are also presented.

2   Gas turbine modelling

2.1   Turbine model

An illustrative flow sheet of a gas turbine with air-cooling arrangement is shown in Figure 1. Its key functional units are a compressor, a combustion chamber and a turbine expander. Other components such as diffusers, intake and exhaust pipes are illustrated as pressure loss valves. Two streams of the turbine coolant flow, taken from the compressor exit, mix with the hot combustion gas: one in front of the turbine inlet and the other behind the first vane. The one entering before the first vane is assumed to do work in the rotor, while the other is not [18].
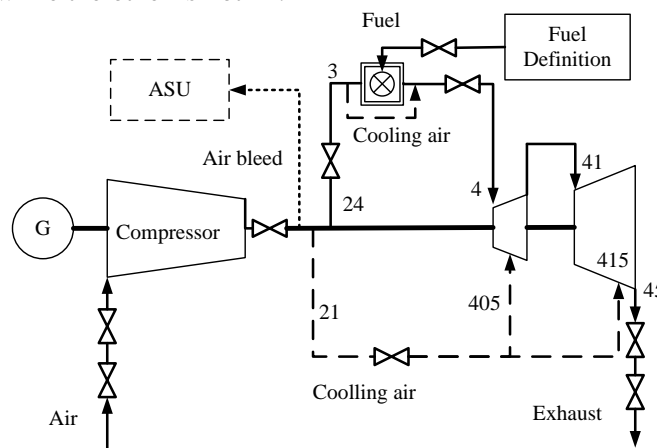
Figure 1: An illustrative flow sheet of a gas turbine with air-cooling arrangement

The most mature syngas firing technology has been applied in E-class gas turbines. Operating parameters of an standard E-class gas turbine at ISO condition are shown in *Table 1*, which provide a basis for the modelling and analytical work delivered in this paper.

Table 1
Operating parameters of an E-class gas turbine at design point: ISO condition

Output (MW)	Compressor pressure ratio	Turbine inlet temperature (^{o}C)	Turbine exhaust temperature (^{o}C)	Exhaust mass flow (kg/s)	Net efficiency (%)
166.5	17.6	1100	524	533	35.7

Compressor and turbine characteristic maps are used in the off-design calculation. The surge margin of a compressor is defined by equation (3)[10]

$$\text{Surge Margin} = (PR_{\text{Surge}} - PR_{\text{Operation}}) / PR_{\text{Operation}} \tag{3}$$

where PR represents the compression ratio.

Assuming the flow is choked at the nozzle of the turbine, the turbine flow characteristics can be described by the constant flow function as shown in Equation (4), which is a reasonable assumption even for considerably low pressure ratios [10,18-19].

$$\frac{\dot{m}\sqrt{TR}}{p\sqrt{\gamma}} = \frac{\dot{m}_0\sqrt{T_0 R_0}}{p_0\sqrt{\gamma_0}} \tag{4}$$

where $\dot{m}$ is the turbine inlet mass flow rate，p is the turbine inlet pressure, T is the turbine inlet hot gas temperature, R is the gas constant, γ is the adiabatic exponent of the hot gas, and the subscript "0" denotes the design-point value. The off-design turbine efficiency variation is estimated as follows[20].

$$\eta_t = \eta_{t0}\left(1 - 0.5\left(\sqrt{\Delta h_{s,t0} / \Delta h_{s,t}} - 1\right)\right) \tag{5}$$

where η_t is the polytropic efficiency of the turbine, $\Delta h_{s,t}$ is enthalpy drop through the turbine during an isentropic process, and the subscript "0" denotes the design-point value.

Flame temperature is defined as the adiabatic temperature in the combustion chamber. The hot gas temperature is defined as the combustor exit temperature, *i.e.*, the temperature of the mixture of combustion products and cooling air.

To pursue high cycle efficiency, advanced heavy industry gas turbines are designed with very high turbine inlet temperature, which makes turbine cooling necessary. In advanced GT designs, film cooling for the turbine blade is accomplished by air extracted from the compressor. The air exits from the blades through a large number of small holes forming a film that partially shields the blades from the hot gases, then the air mixes with the hot gas. The blade cooling has significant impact on the GT performance and lots of research has been performed on cycle analysis of the cooled turbine[20-26]. Detailed cooling analysis can be complex, however, with the aim at exploring the GT operation window and highlighting the load regulation strategy for a specified gas turbine, a much simplified approach is used here. Based on basic heat transfer equations, the coolant fraction (the ratio of the coolant mass flowrate from compressor outlet $\dot{m}_{cl}$ to the hot gas mass flowrate $\dot{m}_g$) can be expressed by equation (6):

$$\dot{m}_{cl} / \dot{m}_g = 1.5 m^* St_g (c_{p,g} / c_{p,cl})(A_{sg} / A_g) \tag{6}$$

$c_{p,g}/c_{p,cl}$ is the specific heat capacity ratio of the hot gas to the coolant. A_{sg}/A_g is the area ratio of blade heat transfer surface to the hot gas cross section, typically ranging from 20 to 40. St_g is the Stanton number. m^* is expressed in terms of three parameters as shown in Equation (7): blade cooling effectiveness ε_0, film cooling effectiveness ε_f, and the cooling efficiency η_{cl}. ε_0 is fully specified by the gas and coolant temperature(T_g and T_{cl}), and the allowable blade temperature T_{bl} restrained by the blade material.

$$m^* = \varepsilon_f + \eta_{cl}^{-1}(1-\varepsilon_0)^{-1}(\varepsilon_0 - \varepsilon_f) \tag{7}$$

$$\varepsilon_0 = (T_g - T_{bl})(T_g - T_{cl})^{-1} \tag{8}$$

Equations (6)~(8) correlate the total amount of coolant flow with a given blade temperature and the level of blade cooling technology. Blade cooling calculation is applied only to the first stage vane, where the most serious condition occurs and the largest portion of total coolant flow is consumed. The distribution of the coolant directed to and after the first vane is carefully tuned to match the manufacture data of the GT performance at its nominal point as much as possible. Values of key parameters regarding the coolant calculation are listed in *Table 2*. At off-design operation, the distribution of the coolant flows keeps unchanged while the total amount of the coolant m_{cl} is calculated by the coolant temperature T_{cl}, the pressure difference between the coolant extraction point at the compressor outlet p_{cl} and the turbine inlet pressure p_{cl}', as shown in Equation (9):

$$\frac{m_{cl}}{p_{cl}}\sqrt{\frac{T_{cl}}{2(1-p_{cl}/p_{cl}')}} = const \tag{9}$$

Table 2
Values for key parameters

Film cooling effectiveness	Cooling efficiency	A_{sg}/A_g	Blade temperature C
0.4	0.7	20	850

2.2   Boundary conditions and fuel specification

At any operating point, a gas turbine should satisfy certain boundary conditions to guarantee a safe operation. These boundary conditions jointly identify the engine operation window[17]. Key operational boundary conditions of a gas turbine considered in this work are summarised as follows:

   a. Turbine blade temperature should never exceed its design-point value;
   b. Compressor outlet temperature should never be 40°C higher than its design-point value;
   c. Turbine exhaust temperature should never be 30°C higher than its design-point value;
   d. The compressor should always have a sufficient surge margin.

When a gas turbine is fired with syngas, the syngas is usually diluted by nitrogen to stabilize the combustion and suppress NOx formation. To investigate the impact of the syngas composition and its heating value on the operation characteristics of a gas turbine, gas turbines fired with four kinds of syngas are studied. The composition of each syngas variant is shown in *Table 3*. No. 1 undiluted CO-rich syngas represents a typical fuel composition derived from Shell coal gasification process. No.3 shows a typical composition when CO_2 capture process is added to the IGCC plant. Both No.1 and No.3 fuel can be diluted to 7000 kJ/kg with nitrogen, referred to as 'diluted CO-rich' and 'diluted H_2-rich' respectively.

Table 3
Composition and lower heating value of four typical syngas fuels

	No. 1 Undiluted CO-rich	*No. 2* Diluted CO-rich	*No. 3* Undiluted H₂-rich	*No. 4* Diluted H₂-rich
N_2 (Vol.%)	6.22	39.65	6.23	52.08
CO_2 (Vol.%)	1.01	0.65	1.13	0.58
H_2O (Vol.%)	0.15	0.10	0.44	0.22
CH_4 (Vol.%)	0.03	0.02	0.03	0.02
H_2 (Vol.%)	30.87	19.87	87.77	44.85
CO (Vol.%)	61.72	39.72	4.40	2.25
LHV(kJ/kg)	12397	7000	42212	7000

3   Results and discussion
3.1   Performance of a natural gas fired gas turbine

The mathematical model introduced in Section 2 is established on EES (Engineering Equation Solver)[27]. The operation window of a natural gas fired gas turbine is firstly obtained as a baseline, and the main performance parameters are highlighted in the operation window as shown in Figure 2. All the temperature data in Figure 2 indicate the temperature departure (unit: ^{o}C) from its nominal value at ISO condition. Turbine inlet temperature (TIT) is represented by the red lines, blade temperature T_{bl} by black lines, compressor outlet temperature (TK2) by pink dashed lines, and the turbine exhaust temperature (TAT) by purple lines. The blue line of 'VIGV 0' refers to the VIGV position at design-point set, whilst 'VIGV -30' refers to its fully closed position when the compressor inlet mass flow is reduced by 30 percent.

Although the gas turbine operating point can be uniquely identified by the flame temperature and VIGV, there remains a possibility that different combinations of the flame temperature and VIGV may lead to the same power output, which suggests that within a certain load arrange there are different load control modes to reach the same load.
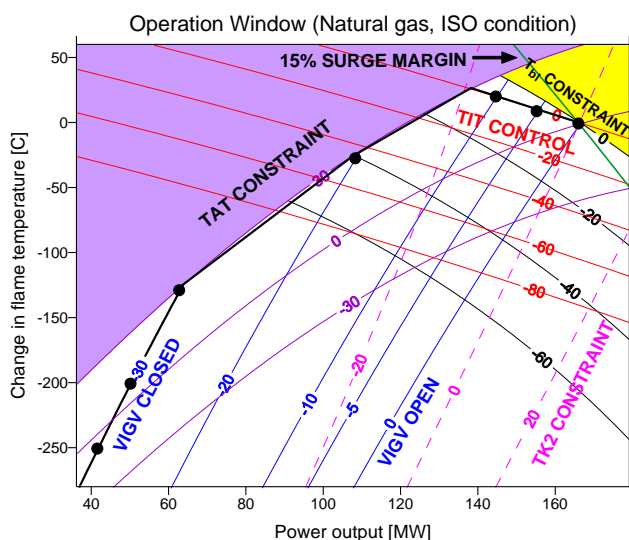
Figure 2: GT Operation window with natural gas   Figure 3: GT Unloading diagram with natural gas
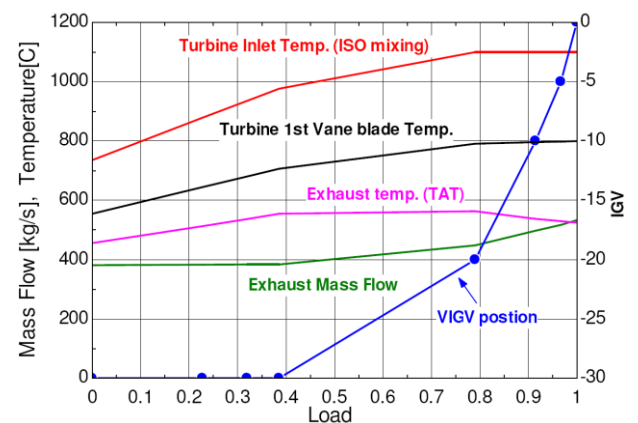
The area without shadow in Figure 2 represents the feasible gas turbine operating region. To prevent the deterioration of the gas turbine efficiency in part load operation, the TIT should be maintained as high as possible, *i.e.*, it is desirable to operate a gas turbine along the upper border of its operation window. The variations of gas turbine performance parameters along this upper boarder are shown in

Figure 3. When the load of a gas turbine drops from 100 percent to 80 percent, the constant TIT control mode applies. Only VIGV control is necessary, and then the TIT maintains the same value until the TAT reaches its maximum value. When further reduction of the load is required from 80 percent to 40 percent, the VIGC has to be turned down, and the flame temperature should also be reduced, *i.e.*, a constant TAT control mode.

3.2   Performance of a diluted CO-rich syngas fired gas turbine

The operation window of a diluted CO-rich syngas fired gas turbine is shown in Figure 4(*a*). It can be seen that the gas turbine operating point at full load is determined by two contour lines: 'VIGV 0' and $\Delta Tbl = 0$, where the flame temperature is reduced by as much as $60^{\circ}C$ from its nominal value at design point.
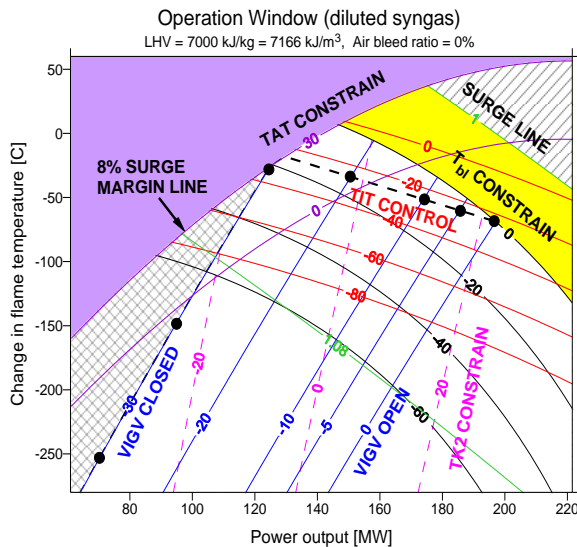
Figure 4(*a*): Operation window of a diluted CO-rich syngas fired gas turbine without air bleed
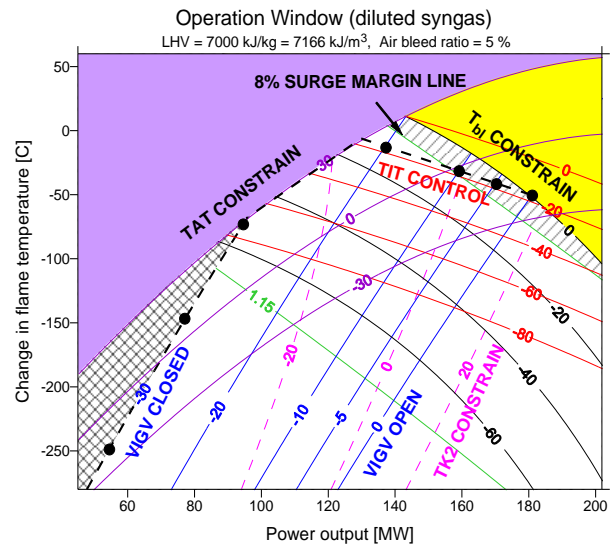
Figure 4(*b*): Operation window of a diluted CO-rich syngas fired gas turbine with five percent air bleed

The necessity of a lower flame temperature is the result of the combined effect of increased heat flux and higher coolant temperature. Firstly, due to a lower LHV and constant air flow, an increased fuel mass flow rate is required to maintain an identical flame temperature, and both the hot gas flow and the heat flux to the turbine expander increase. Secondly, due to the limited swallowing capacity of the turbine, the rise in hot gas flow rate can only be achieved by increasing the pressure ratio, and this results in an increase in the temperature of the coolant flow extracted from the compressor. As can be seen in Figure 4(*a*), if the gas turbine is operated with the same turbine blade temperature as its design-point set, the flame temperature, represented by the y axis, has to be greatly reduced. As a result, the TIT drops by about $22^{\circ}C$. It is also obvious that the gas turbine operating point moves closer toward its surge line, mainly due to significantly increased pressure ratio. Another consequence is that TAT drops by about $20^{\circ}C$, which is mainly affected by the increased turbine expansion ratio. In addition, the gas turbine output is increased by 16.6 percent compared with its design-point value.

Different from the operating strategies for natural gas fired gas turbines, the regulation scope of constant TIT control mode is broader, while that of the constant TAT control mode is narrowed. Figure 4(*a*) indicates that TAT almost reaches its maximum value at lower load with constant TIT control mode, and the VIGV is already at its fully closed position, leaving less space for constant TAT control mode.

Figure 4(*b*) presents a mode where five percent of compressed air from the compressor is used in the turbine, which is a common strategy in a partially integrated IGCC process. As a result, the surge margin of the compressor is enlarged compared with that in Figure 4(*a*). In addition, the constraint of

the blade temperature is slightly relieved, so the flame temperature does not have to be reduced as much as in Figure 4(*a*). The drop of TIT temperature is also smaller. When the gas turbine is operated at its full capacity, the power output increases by eight percent from design-point value. The scope of constant TAT control mode is valid from 53 percent load to 72 percent load, larger than one without air bleed.

3.3   Performance of an undiluted CO-rich syngas fired gas turbine

Performance of an undiluted CO-rich syngas fired gas turbine is shown in Figure 5(*a*) and Figure 5(*b*). Compared with the operation of a diluted CO-rich syngas fire gas turbine, a larger operation window is observed. Firstly, turbine blade cooling is remarkably enhanced. To prevent overheat of the turbine blades, a smaller reduction (about 10°C) in TIT is required at full load for a gas turbine without air bleed, and this number is only about 5°C for a gas turbine with five percent air bleed. Secondly, the compressor surge margin is enlarged. The surge margin is more than eight percent for a gas turbine without air bleed, and about 15 percent for one with air bleed. Thirdly, the valid scope of a constant TAT control mode is extended: ranging from 51 percent load to 77 percent load for a gas turbine without air bleed, and from 39 percent to 78 percent for one with air bleed. This implies that the exhaust gas can remain at a relatively high temperature in a wider load range. This is beneficial to improving the efficiency of a downstream heat recovery steam generator (HRSG).
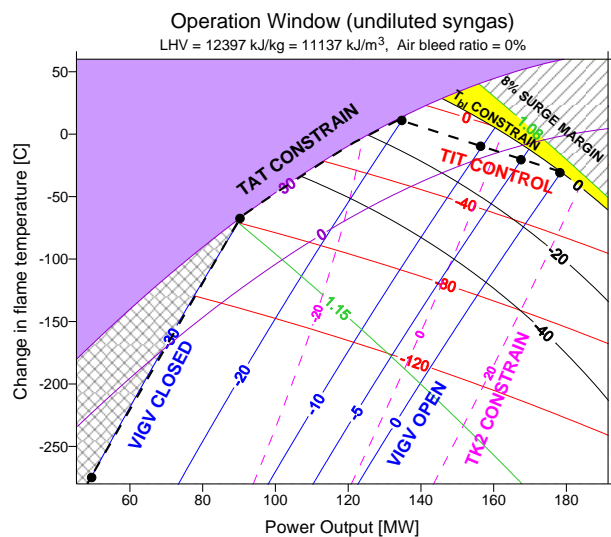
Figure 5(*a*): Operation window of an undiluted CO-rich syngas fired gas turbine without air bleed
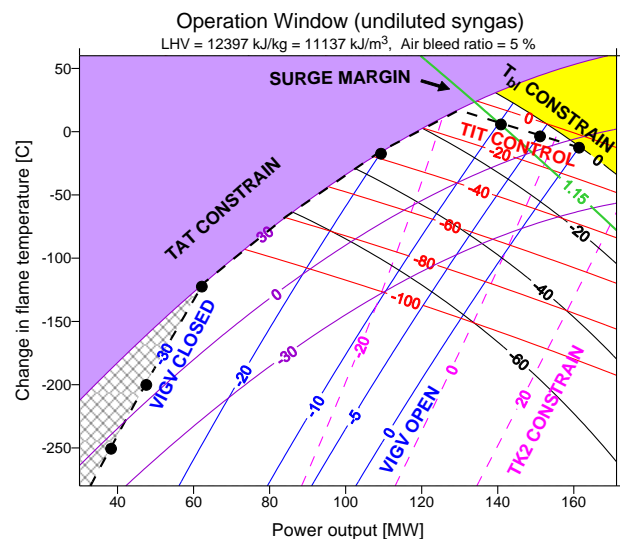
Figure 5(*b*): Operation window of an undiluted CO-rich syngas fired gas turbine with five percent air bleed

However, if operated with undiluted syngas, a gas turbine has limited potential to enhance its power output, since the undiluted fuel has a higher LHV and thus a smaller mass flow rate is required compared to the diluted cases. From the viewpoint of power output, an important implication can be drawn that in a partially integrated IGCC system, where air is bleed from the compressor to feed the ASU, nitrogen is recommended to be injected to the gas turbine as a dilute stream.

3.4   Performance of a H_2-rich syngas fired gas turbine

The operation window of an undiluted hydrogen-rich syngas fired gas turbine is shown in Figure 6. This operation window is similar to the one of a natural gas fired gas turbine, mainly due to a similar heating value of undiluted H_2-rich syngas and natural gas.

From the viewpoint of gas turbine operation it would be preferred to use undiluted H_2-rich syngas, as can be seen from Figure 6; however, in practice N_2 diluent is necessary on ground of current GT combustor design. The operation window of a diluted H_2-rich syngas fired gas turbine without air bleed is shown in Figure 7(*a*), and the operation window of one with five percent air bleed is shown in Figure 7(*b*). Again, the operation point at full load is determined by two contour lines: 'VIGV 0'

and $\Delta Tbl = 0$. Considering the fact that the H_2-rich syngas is diluted to the same level as shown in Figure 4, with a LHV of 7000 kJ/kg, the difference of performance is mainly caused by the change of syngas composition.
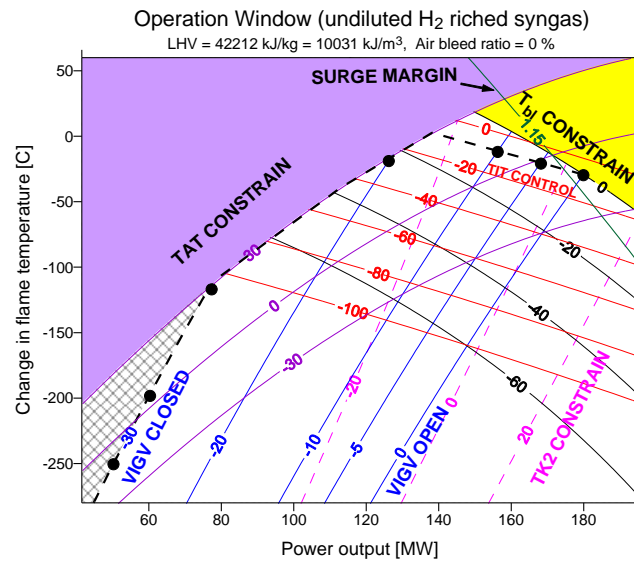
Figure 6: Operation window of an undiluted H_2-rich syngas fired gas turbine without air bleed
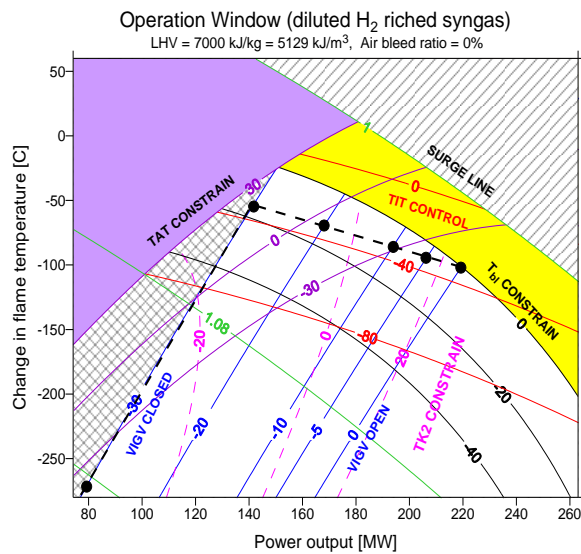
Figure 7(*a*): Operation window of a diluted H_2-rich syngas fired gas turbine without air bleed
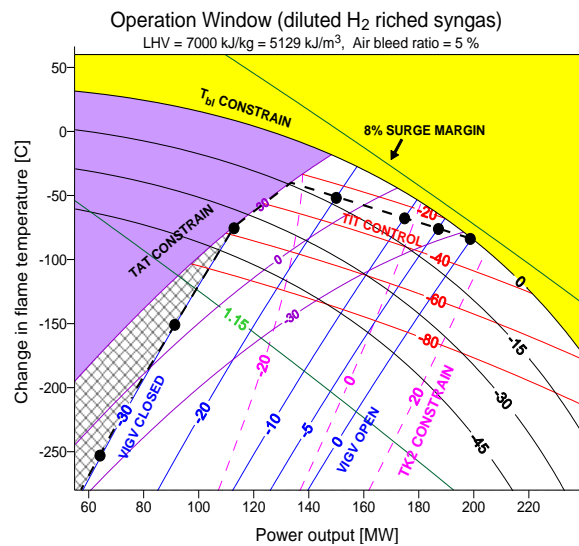
Figure 7(*b*): Operation window of a diluted H_2-rich syngas fired gas turbine with five percent air bleed

Compared with Figure 4, diluted CO-rich cases, the operation points of a diluted H_2-rich syngas fired gas turbine deviate further from its design points, although the measure of air bleed can still improve the operating conditions. The flame temperature of a H_2-rich syngas fired gas turbine is further reduced to maintain the same turbine blade temperature. Besides, a diluted H_2-rich syngas fired gas turbine has a larger power output at full load.

Compared with diluted CO-rich fuel, the hydrogen content in this case has both positive and negative impacts on the power output of a gas turbine. It is found that the positive effect dominates the power output in this case. On one hand, hydrogen has a high specific heating value, which tends to reduce the hot gas mass flow and the power output of the gas turbine. On the other hand, the increase in hydrogen content leads to a higher water vapour content in the hot gas, hence a higher specific heat capacity. This increase enhances the capability of the gas turbine to do work at an identical TIT. In addition, the

increased moisture content results in a smaller polytropic exponent, which also contributes to a higher power output of the turbine expander.

Similar to the operating strategies of an undiluted CO-rich syngas fired gas turbine, the regulation scope of the constant TAT control mode is substantially squeezed in Figure 7(*a*). However, it can be effectively broadened by the measure of air bleed as shown in Figure7(*b*).

4   Conclusions

A mathematical model for part-load behaviour study of a gas turbine is introduced in this paper. Performance simulations of a gas turbine running on four typical types of syngas with and without air bleed are presented. Key findings of the gas turbine performance are summarized in terms of an operation window, featuring:

- The active constraints of a typical syngas fired gas turbine comprise insufficient cooling of turbine blades and reduced compressor surge margin. With reduced heating value of the syngas, lower flame temperature and lower TIT temperature have to be taken, leading to significant departure of the operating points from the design points.
- The load regulation strategy of a syngas fired gas turbine is similar to that of a natural gas fired gas turbine, but the scope of the constant TAT control mode is much narrower.
- Air bleed from the compressor/ GT integration is beneficial in that it draws the mass flow ratio between the compressor and turbine expander closer to its design-point value. This effect is more obvious for cases with extensive fuel dilution. However, this advantage diminishes for undiluted fuel variant. The GT operation window with undiluted syngas requires lower reduction in TIT temperature and has a comparatively larger surge margin. Considering that GT air side integration is known as one main reason for the low availability of today's IGCC plants, a concept with undiluted syngas and without air bleed /GT integration could be a preferred option.
- The gas turbine operating points with diluted H_2-rich syngas have larger departure from its design points than those with CO-rich syngas, when the fuel is required to diluted to identical LHV. This suggests that operation with diluted H_2-rich syngas is more difficult. As suggested in the operating window with undiluted H_2-rich syngas, it should be noted that the possibility to burn undiluted H_2-rich fuel would greatly support the CO_2 captured IGCC plants. The prime challenge therefore is to be seen in the combustion system.

References
[1] H.C. Frey, Y. Zhu. Improved system integration for integrated gasification combined cycle (IGCC) systems. Environment Science and Technology. 2006, 40: 1693–1699.
[2] A.R. Smith, J. Klosek. A review of air separation technologies and their integration with energy conversion processes. Fuel Processing Technology. 2001, 70(2): 115–134.
[3] Robert F. Geosits and Lee A. Schmoe. IGCC – The Challenges of Integration. Proceedings of GT2005 ASME Turbo Expo 2005: Power for Land, Sea, and Air, Reno, NV, June 2005.
[4] Jaeger Harry. Plant Design Net Rated 644 MW and 38% HHV on Low Rank Coal, Gas Turbine World, March-April 2006.
[5] C. Lee, S.J. Lee, Y. Yun. Effect of air separation unit integration on integrated gasification combined cycle performance and NOx emission characteristics. Korean Journal of Chemical Engineering. 2007, 24(2): 368–373.
[6] P. Liu, D.I. Gerogiorgis, E.N. Pistikopoulos. Modeling and optimization of polygeneration energy systems. Catalysis Today. 2007, 127(1-4): 347-359.

[7]   P. Liu, E.N. Pistikopoulos, Z. Li. A mixed-integer optimization approach for polygeneration energy systems design. Computers & Chemical Engineering. 2009, 33(3): 759–768.

[8]   P. Liu, E.N. Pistikopoulos, Z. Li. A multi-objective optimization approach to polygeneration energy systems design. AIChE Journal. 2010, 56 (6): 1218-1234.

[9]   P. Liu, E.N. Pistikopoulos, Z. Li. Decomposition based stochastic programming approach for polygeneration energy systems design under uncertainty. Industrial & Engineering Chemistry Research. 2010, 49 (7): 3295-3305.

[10] J.J. Lee, Y.S. Kim, K.S. Cha, T.S. Kim, J.L. Sohn, Y.J. Joo. Influence of system integration options on the performance of an integrated gasification combined cycle power plant. Applied Energy. 2009, 86(9): 1788–1796.

[11] Z. Li, W. Ni, H. Zheng, L. Ma. Polygeneration energy system based on coal gasification. Energy for Sustainable Development. 2003, 7(4): 57–62.

[12] J.G. Wimer, D. Keairns, E.L. Parsons, J.A. Ruether. Integration of gas turbines adapted for syngas fuel with cryogenic and membrane-based air separation units: issues to consider for system studies. Journal of Engineering for Gas Turbines and Power. 2006, 128: 271–280.

[13] F. Emuna, M. Gadallaa, T. Majozib, D. Boerc. Integrated gasification combined cycle (IGCC) process simulation and optimization. Computers & Chemical Engineering. 2010, 34(3): 331–338.

[14] M.C. Carbo, D. Jansen, J.W. Dijkstra, J.P. van Buijtenen, A.H.M. Verkooijen. Pre-combustion decarbonisation in IGCC: gas turbine operating window at variable carbon capture ratios. Energy Procedia. 2009, 1(1): 669–673.

[15] Antonio Giuffrida, Matteo C. Romano, Giovanni G. Lozza. Thermodynamic assessment of IGCC power plants with hot fuel gas desulfurization. Applied Energy. 2010, 87(11): 3374–3383.

[16] D. Sánchez, R. Chacartegui, J.M. Muñoz, A. Muñoz, T. Sánchez. Performance analysis of a heavy duty combined cycle power plant burning various syngas fuels. International Journal of Hydrogen Energy. January 2010; 35(1):337-345.

[17] Y.S. Kim, J.J. Lee, T.S. Kim, J.L. Sohn, Y.J. Joo. Performance analysis of a syngas-fed gas turbine considering the operating limitations of its components. Applied Energy. 2010, 87(5): 1602–1611.

[18] Performance prediction and simulation of gas turbine engine operation for aircraft, marine, vehicular, and power generation. Technical report RTO-TR-AVT-036, Research and Technology Organisation North Atlantic Treaty Organisation, February 2007.

[19] P. Fletcher, P.P. Walsh. Gas Turbine Performance, 2nd ed., Blackwell Science Ltd., 2002.

[20] T.S. Kim, S.T. Ro. Effect of control modes and turbine cooling on the part load performance in the gas turbine cogeneration system. Heat Recovery Systems and CHP. 1995, 15(3): 281-291

[21] O. Bolland, J.F. Stadaas. Comparative evaluation of combined cycles and gas turbine systems with water injection, steam injection, and recuperation. Journal of Engineering for Gas Turbines and Power. 1995, 117: 138–145.

[22] B. Facchini, G. Ferrara, L. Innocenti. Blade cooling improvement for heavy duty gas turbine: the air coolant temperature reduction and the introduction of steam and mixed steam/air cooling. International Journal of Thermal Sciences. 2000, 39(1): 74–84.

[23] J. H. Horlock, D.T. Watson, T.V. Jones. Limitations on gas turbine performance imposed by large turbine cooling flows. Journal of Engineering for Gas Turbines and Power. 2001, 123:487–494.

[24] K. Jordal. Modeling and performance of gas turbine cycles with various means of blade cooling. PhD thesis, 2001, Lund University, Sweden.

[25] M.H. Albeirutty, A.S. Alghamdi, Y.S. Najjar. Heat transfer analysis for a multistage gas turbine using different blade-cooling schemes. Applied Thermal Engineering. 2004, 24(4): 563–577.

[26] S.O. Sanjay, B.N. Prasad. Influence of different means of turbine blade cooling on the thermodynamic performance of combined cycle. Applied Thermal Engineering. 2008, 28(17–18): 2315–2326.

[27] F-Chart. EES Engineering Equation Solver for Microsoft Windows Operating Systems, 2005.

Condensing Boiler Applications in the Process Industry

Qun Chen*, Karen Finney, Hanning Li, Xiaohui Zhang, Jue Zhou, Vida Sharifi, Jim Swithenbank

SUWIC, Department of Chemical & Process Engineering, Sheffield University, United Kingdom

*Corresponding author. Email: q.chen@sheffield.ac,uk; Tel. +44(0) 114 222 7563; Fax. + 44(0) 114 222 7501

Abstract
Major challenging issues such as climate change, energy prices and fuel security have focussed the attention of process industries on their energy efficiency and opportunities for improvement. The main objective of this research study was to investigate technologies needed to exploit the large amount of low grade heat available from a flue gas condensing system through Industrial Condensing Boilers. The technology and application of industrial condensing boilers in various heating systems were extensively reviewed. As the condensers require site-specific engineering design, a case study was carried out to investigate the feasibility (technically and economically) of applying condensing boilers in a large scale district heating system (40 MW). The study showed that by recovering the latent heat of water vapour in the flue gas through condensing boilers, the whole heating system could achieve significantly higher efficiency levels than conventional boilers. In addition to waste heat recovery, condensing boilers can also be optimised for emission abatement, especially for particle removal. Two technical barriers for the condensing boiler application are corrosion and return water temperatures. Highly corrosion-resistant material is required for condensing boiler manufacture. The thermal design of a "Case Study" single pass shell-and-tube condensing heat exchanger/condenser showed that a considerable amount of thermal resistance was on the shell-side. Based on the case study calculations, approximately $4900m^2$ of total heat transfer area was required, if stainless steel was used as a construction material. If the heat transfer area was made of carbon steel, then polypropylene could be used as the corrosion-resistant coating material outside the tubes. The addition of polypropylene coating increased the tube wall thermal resistance, hence the required heat transfer area was approximately $5800m^2$. Net Present Value (NPV) calculations showed that the choice of a carbon steel condenser ensured cash return in a relatively shorter period of time (i.e. 2 years) when compared to a stainless steel condenser (i.e. 5 to 7 years). Moreover, the NPV for the stainless steel was more sensitive to the change of the interest rate.

Keywords   condensing boiler; heat pump; heat recovery; district heating system; process industry

1   Introduction
Flue gases from waste to energy plants often contain 15-40% of the fuels' heat content. This heat is available over the range of temperature from 30°C to 250°C although the upper level may often be lower. Though waste heat can be recovered, little effort has been made to do this, as it can be difficult to utilise low-temperature heat and counteract corrosion. However, modern condensing natural gas fired domestic boilers are designed to recover this energy by use of suitable materials that avoid corrosion of the wet heat transfer surfaces [1]. In the case of domestic heating, the boiler efficiency is typically increased from 75% to 90% i.e. the cost/energy saving is about 15% and there is a corresponding reduction in CO_2 emissions [2].

Industrial combustion systems are used predominantly for process heating or power production. The combustion usually takes place in a steam boiler fitted with a super-heater and economiser. These are followed by an air heater to preheat the combustion air, and its exit temperature is maintained above the acid dew point to avoid corrosion from the condensate and to ensure buoyancy of the flue gases. However, the industrial situation is now changing with the progressive requirement to use scrubbers and filters to remove acids and particulates from the exhaust, and it is timely to assess the new situation. Similarly to domestic condensing boilers, by the use of suitable materials (PTFE, aluminium, etc) the exhaust could be cooled to about 30°C with the recovery of both latent and

sensible heat. In the case of natural gas, which contains a significant proportion of hydrogen in the molecule, this heat represents about 15% of the energy. In the case of biomass such as wood chips, this heat represents 6-8% of the fuel calorific value due to the hydrogen in the fuel and up to half the calorific value of the raw fuel due to its 50% moisture content. Thus recovery of energy by condensing the flue gases can recover both the energy due to the moisture in the feed and the water due to the hydrogen content of the fuel. The fact that one device can recover both components suggests that this is a preferable strategy to drying the feed and using two separate devices.

Sheffield University Waste Incineration Centre (SUWIC) has conducted an extensive literature review of industrial condensing boilers, looking into various technologies and the associated costs. In addition, extensive calculations have been carried out as part of a case study to investigate the thermal design of a condensing boiler in a large scale district heating plant (40 MW). This paper presents the results obtained from the above studies.

2   Industrial condensing boilers and their applications

Combustion in air yields water vapour and CO_2. Conventional boilers transfer most of the sensible heat of this reaction to hot water or steam, whereas condensing designs capture the latent heat – the energy released by condensing the vapour; extracting this heat achieves higher efficiencies.

2.1   Flue gas condensers

The application of condensers to recover latent heat from flue gas is wider than stand-alone gas-fired condensing boilers, for power plants and commercial/industrial facilities. In general, there are two types of condensers: indirect and direct contact. Indirect contact condensers recover the latent heat by passing gas through condensing heat exchangers [3]. These can be sub-categorised into pipe condensers, lamella condensers and combi condensers [4]. The second option, direct contact condensers, consist of a vapour-conditioning chamber and a counter-current spray chamber, in which small droplets of cool liquid come into contact with the hot flue gas, providing a non-fouling heat transfer surface. The droplets cool, condense and remove water vapour. To improve contact between the spray and gas, the chamber may be equipped with packing. This offers high heat transfer and water recovery capabilities.   Such condensers require site-specific engineering design and an understanding of their effects on the system.

2.2   Advantages of condensing boilers
2.2.1   Latent heat recovery
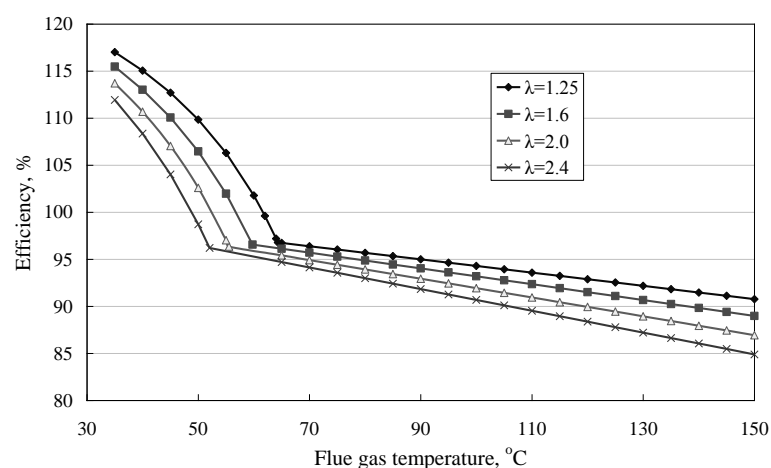
Figure 1: Theoretical efficiency of a boiler/condenser changing with exit flue gas temperature

Latent heat recovery is the most significant advantage of condensing boilers, greatly improving thermal efficiency. Figure 1 shows this for a wood chip boiler with a condensing heat exchanger at different excess air ratios (λ). The fuel (wood chips) used in the boiler has 50% moisture content. As shown, the heat exchanger recovers the latent heat of the moisture when it is condensed, resulting in

efficiencies exceeding 100% with reference to the lower heat value of the fuel. On the other hand, increasing λ decreases the vapour partial pressure in the gas and lowers its dew point; more sensible heat is carried by non-condensable gas, less vapour is condensed under higher λ and at the same temperature, higher λ lead to lower efficiencies.

2.2.2   Emission abatement

Flue gas condensers can also reduce flue gas emissions, providing several environmental benefits. The condensate forms a constant film that can remove large particles and dissolve most of the highly dissociated inorganic matter, such as sulphuric acid, chlorides, etc [5]. Combustion generates fine particles, contributing significantly to energy sector emissions [6]. Sipula *et al*. [7] studied emissions of 4 wood chip-fired district heating units. All were equipped with cyclones to remove coarse particles. One had a condensing flue gas scrubber, which removed 44% of PM_1 and 84% of total solid particles, resulting from thermophoresis (induced by the temperature gradient between the gas and the surface) and diffusiophoresis (caused by steam condensing on cool surfaces). Other separation mechanisms include inertial impaction and gravitational settling for large particles and Brownian diffusion for small particles. Particle sizes grew inside the scrubber, causing a shift in the particle size distribution [7].

2.3   Technical barriers of condensing boilers and potential solutions
2.3.1   Corrosion

Corrosion by corrosive combustion products causes cracks in low-temperature steel heat exchangers, where mechanical stresses are high [8]. Microscopic analyses reveal inter-granular corrosion, showing complete material grains becoming detached. The amount and composition of condensate needs to be known to avoid this [8,9]. To reduce corrosion and capture latent heat, condensing boilers need corrosion-resistant fabrication materials, careful installation and sophisticated controls. The specialised materials and terminal units are expensive and the installation costs are higher than conventional boilers [10]. Characterised by austenitic/ferritic material and high Cr, Mo and N contents, a typical material is high-performance steel. The most important material property is high thermal conductivity, as it increases heat transfer.

2.3.2   Return water temperature

Return Water Temperature is the critical factor in the operation of heating systems [10]. Heat sinks are required to capture latent heat, which determines the boiler efficiency; less vapour is condensed at high temperatures, decreasing efficiency [11]. The return water serves as a heat sink in district heating systems; moisture condensation from the gas requires them to be cooled below their dew point, 55-65°C for natural gas. The return water temperature from a central heating system must be about 30°C. This requires an under-floor heating system or a high surface area of the radiators in the building. Similar considerations apply to district heating schemes if the latent heat of the moisture is to be recovered from the flue gases.

If the return water is not cool enough to directly serve as a heat sink, heat pumps can be coupled with condensing boilers in the application. A heat pump is a device that moves heat from a low temperature 'source' to a higher temperature 'sink'. There are two main types: compression and absorption heat pumps. A compression heat pump is composed of a compressor, expansion valve and heat exchangers (evaporator and condenser) with a volatile working fluid circulating through the components in a closed circuit. In the evaporator, the heat source heats and evaporates the working liquid. The vapour is compressed to a higher pressure and temperature and enters the condenser, where it condenses to give off heat. The high-pressure fluid returns to its original state, expanding to the evaporator pressure, and enters the evaporator. The compressor is usually driven by an electric motor or by a combustion engine. Thermally-driven absorption heat pumps utilise liquids/salts to absorb working fluid vapour; water-LiBr is the most common working fluid-absorbent pair. Fluid compression is achieved thermally in a solution circuit that consists of an absorber, solution pump, generator and expansion valve.

Figure 2 shows a typical application of a flue gas condenser with a heat pump to recover heat from flue gases. The coolant in the condensing boiler works between 25 and 35°C, much lower than the return water temperature. It serves as the heat source of the heat pump which pumps the heat from the condenser to the return water. This system is simple but the high energy consumption and capital costs are drawbacks.
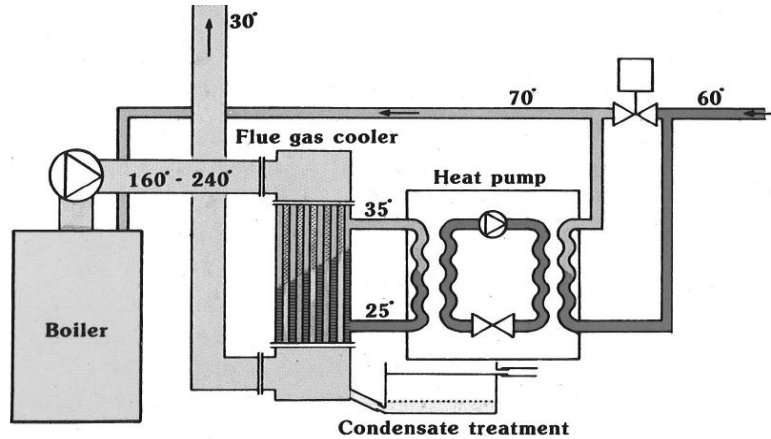
Figure 2: Flue gas condenser with a heat pump (Fagersta Energetics AB)

2.4   Applications of condensing boilers in heating systems

Table 1
Examples of condensing boiler application in heating systems

Plant	Plant capacity	Capacity of condensers/heat pumps
Sodra Nas Vimmerby Energi AB Biomass District Heating Plant, Sweden	10MW	2MW condenser
Kraftvarmeværk Waste Incineration Plant, Denmark	3.3MW$_e$/10.6MW$_{th}$	1MW condenser & 17GWh/y absorption heat pumps
Davamyran Heat and Power Plant	350GWh$_{(th)}$/80GWh$_{(e)}$ per annum	11MW condenser & 11.4 MW heat pumps
Vestforbranding Waste to Energy Plant, Denmark	400GWh$_{(th)}$/140GWh$_{(e)}$ per annum	13MW condenser

Although most district heating schemes in the UK presently use delivery and return water temperatures of about 120°C and 70°C respectively, some European district heating schemes do utilize the latent heat in the flue gas through industrial condensing boilers and heat pumps. *Table 1* presents some of successful examples of the application (OPET CHP/DH project and Götaverken Miljö AB).

3   Thermal design of a flue gas condenser for a biomass heating plant – a case study
In general the decision (based on economic feasibility) to integrate a condensing boiler into a heat system is mainly case-dependent. In this study, thermal design of a flue gas condenser (condensing heat exchanger) was carried out for an existing large scale biomass heating plant. The aim was to investigate various technical and economic issues in relation to the condensing boiler application.

3.1   Plant description and conditions
Few examples of application of condensing boiler technology in the process industries have been reported in the literature. The plant chosen for this case study is one of the largest biomass-fired heating stations in Finland [12]. The wood chip fuel for the plant is mainly logging residue from final felling of spruce-dominant forests, other forestry residues and by-products from sawmills. Wood chips are burned in a fluidised-bed boiler. The output of the boiler is 40MW at full fuel feed, and the temperature of flue gases after the boiler is approximately 150°C. The flue gases are then led to an

electrostatic precipitator (ESP) for removing particles from the flue gases with efficiency > 99%. The amount of ash separated from the ESP is about 800 t/a. After the electric precipitator the flue gases are led into the condensing plant. In the flue gas condensing plant, the temperature of flue gases is decreased to 35°C and the most of water vapour is condensed to water. About 12MW of district heat capacity is produced at the condensing plant. This increases the derived thermal efficiency to as high as 118% with reference to the lower heating value of the input fuel. Finally, the flue gases are led through a 60m high stack to the open air.

The properties of the fuel are listed in *Table 2* [13]. The average moisture content of the wood chips is 50% and the lower heating value of the fuel is as low as 8.16MJ/kg. The fuel input for this plant is approximately 19.4tonnes/hr. As a result, the flue gas contains 12.1% CO_2, 24.4% H_2O, 3.2% O_2 and 60.3% N_2. The dew point of the flue gas is 64.3°C.

Figure 3 shows the process diagram for the plant. *Table 3* lists the conditions for each stream (as shown in Figure 3) in the system. These main properties of the relevant streams in the process were evaluated based on mass and energy balances. In this simplified calculation, the heat losses due to heat dissipation and incomplete combustion of fuel were not considered. The heat loss of the flue gas in the ESP was also neglected. As shown in *Table 3*, the preheated feed water is heated from 55°C up to 140°C under the pressure of 16bar in the fluidised bed boiler. The hot water is sent to district heating consumers for heating buildings and yards. Generally, the heating system in the buildings consists of water radiator system and the return water temperatures are between 35–40°C [14]. In this case study, the return water temperature is assumed to be about 30°C. The return water is preheated in the condensing plant using the recovered latent heat of water vapour and sensible heat of the flue gas. The total heat output of the plant is 52MW$_{th}$, and the yield of energy is about 300 GWh/a for an annual operating time of 7000 hours.
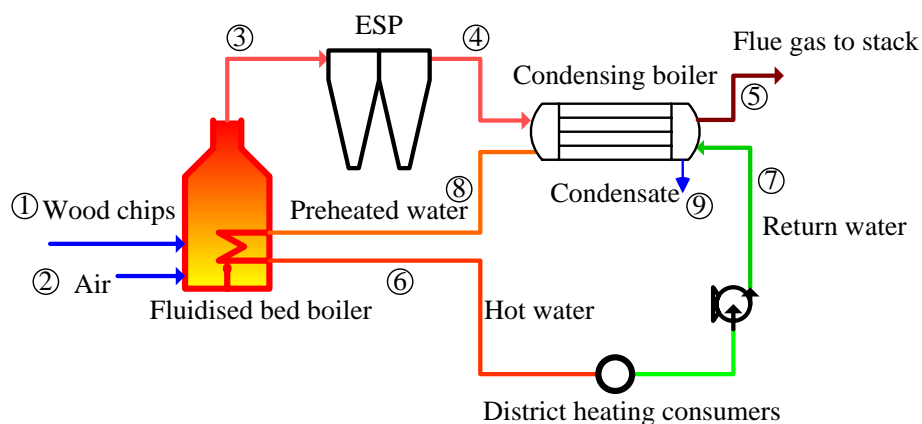
Figure 3: Process diagram for the heating plant

Table 2
Properties of the fuel input for the heating plant

	Dry basis	As received
C	51.2	25.6
H	6.1	3.05
N	0.3	0.15
O	40.9	20.45
Ash	1.5	0.75
Moisture	-	50.0
GCV, MJ/kg	20.1	10.05
NCV, MJ/kg	-	8.16

Table 3
Calculated process parameters for the heating plant

Stream No.	Pressure, bar	Temperature, °C	Mass flow rate, kg/s	Enthalpy, kJ/kg
1	1	20	5.4	-17.2
2	1	20	20.9	-5.15
3	1	150	26.3	146.7 (+388.4)*
4	1	150	26.3	146.7 (+388.4)
5	1	35	23.0	10.6 (+92.1)
6	16	140	111.6	590.0
7	16	30	111.6	128.0
8	16	55	111.6	231.7
9	1	35	3.32	42.4

* Data in the parentheses are the potential latent heat of the moisture in the flue gas

3.2   Heat exchanger selection

An indirect-contact condensing boiler mainly consists of heat exchangers containing heat transfer elements and fluid distribution elements. In this case study an E type shell (TEMA notation [15]) single tube-pass shell-and-tube exchanger was chosen as the main component for the flue gas condenser due to its relative simplicity. The other reason for this choice is that tubular heat exchangers are designed for high pressure differences between the fluids and are primarily used for liquid-to-liquid and liquid-to-phase change (condensing or evaporating) heat transfer applications [16].

The flue gas was assumed to be on the shell side with the return water on the tube side. In the condensing heat exchanger, the outside diameter of plain tubes was assumed as 25.4mm. Generally, smaller diameter tubes lead to higher heat transfer coefficients and thus the heat exchange can be more compact. However, this may also result in higher pressure drop across the exchanger. As the ratio of the tube pitch to tube outside diameter for most shell-and-tube heat exchangers varies between 1.25 and 2.0, the ratio was assumed to be 1.75 in this case study. Other properties and dimensions of the heat exchanger are summarised in *Table 4*.

Table 4
Dimensions of the condensing boiler

Heat exchanger type	Single tube pass, countercurrent shell-and-tube exchanger (E type shell)
Tube outside diameter, d_o (mm)	25.4
Tube inner diameter, d_i (mm)	22.9
Pitch, p_t/d_o	1.75
Total tube number, N	1024
Tube layout	Rotated square
Shell inner diameter, D_s (mm)	2090
Shell thickness, δ_s (mm)	14
Baffle type	Single-segmental
Baffle spacing, B (mm)	1776
Baffle cut	25%

Generally, carbon steel and stainless steel are the most common materials for industrial heat exchangers. In this case study, Stainless steel 316 and carbon steel (<0.5% C) were chosen for comparison purposes. The aim was to investigate their impacts on the thermal design of a condensing boiler and their associated cost implications. As the flue gas from wood fuel combustion contains corrosive products, such as nitric oxides, chloride, and sulphate/sulphite, the material used to make the shell and tubes must be corrosion resistant. Stainless steel is a good corrosion-resistant material whereas carbon steel rusts quickly when exposed to the air and moisture. Thus in order to use carbon steel in the condensing boiler, the outer surface of the tubes and the inner surface of the shell must be coated or lined with a corrosion resistant material for protection purposes. In this study,

polypropylene (PP) was chosen as the coating material for its low cost, excellent resistance to corrosion and easy fabrication. The melting of polypropylene occurs over a specific range. Isotactic PP has a melting point of 171°C. Commercial isotactic PP has a melting point that ranges from 160 to 166°C, depending on atactic material and crystallinity [17].

3.3 Condensation curve and log mean temperature difference (LMTD)

Figure 4 shows the equilibrium condensation curve for the flue gas, where the equilibrium gas temperature is plotted versus the difference of the specific enthalpy of the mixture from the outlet, assuming a constant pressure throughout. As shown, the tube-side temperature changes linearly whereas the temperature variations in the shell-side show a de-superheating zone together with condensation occurring in the presence of non-condensable gases. According to the shell-side temperature variations, the diagram can be divided into zones where the temperature curves on both sides are almost linear. In Figure 4, the condensation curve is divided into four zones, as shown by the vertical dashed lines as zone boundaries. Zone I represents the de-superheating of the flue gases in which the flue gas temperature decreases linearly. At the boundary B, the water vapour in the flue gas begins to condense. Over each zone, the temperature difference (T_s-T_t) varies linearly with the amount of heat transferred from the shell-side to the tube-side.
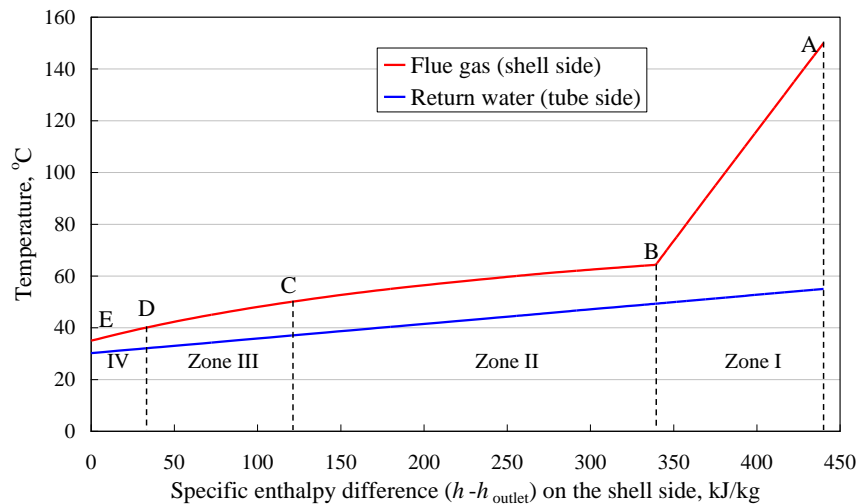
Figure 4: Condensation curve for the flue gas

In this case study, the LMTD method is employed for the thermal design of the condensing heat exchanger. For each zone, the temperature difference (ΔT_{LM}) between the shell and tube sides can be calculated by,

$$\Delta T_{LM} = \left(\Delta T_I - \Delta T_{II} \right) \big/ \ln \left(\Delta T_I / \Delta T_{II} \right) \tag{1}$$

where ΔT_I and ΔT_{II} are temperature differences between both sides at the boundaries of each zone. It represents the maximum driving force for heat transfer when two fluid streams are in countercurrent flow on the shell and tube sides respectively. In practical, as the heat exchanger was designed in cross-flow, which is different from true countercurrent flow, the true mean temperature difference differs from the LMTD by a factor (F), as follows [16],

$$F = \frac{\ln \left[(1-RP)/(1-P) \right]}{(R-1)\ln \left[1 + (1/R)\ln (1-RP) \right]} \tag{2}$$

where $R = (T_{s1}-T_{s2})/(T_{t2}-T_{t1})$ is the heat capacity rate ratio and $P = (T_{t2}-T_{t1})/(T_{s1}-T_{s1})$ is the thermal effectiveness.

Table 5
LMTD and the thermal duty for each zone in Figure 4

	LMTD, °C	*F*	Heat transfer rate, MW
Zone I	43.3	0.971	2.652
Zone II	14.0	0.865	5.757
Zone III	10.3	0.935	2.296
Zone IV	6.2	0.966	0.865

Table 5 shows the calculated LMTD, factor F and the thermal duty for each zone of the condensation curve. As the water vapour condenses out, the equilibrium condensing temperature is decreased. As a result, the temperature difference between the shell and tube sides is reduced.

3.4 Heat transfer coefficients

The thermal design of the condensing boiler aims to estimate adequate surface area of the heat exchanger to handle the required thermal duty. Thus heat transfer coefficients needs to be evaluated before the size of the condensing boiler can be calculated. As the flue gas contains non-condensable gas components, the heat transfer in the condensation process is more complex than for a pure vapour condensation [18]. This case study employed the Silver equilibrium method to calculate the heat transfer coefficients for the condensing heat exchanger because of its simplicity and wide application in engineering design practice [19, 20].

3.4.1 Tube-side heat transfer coefficient

On the tube-side, the Reynolds number (Re) of the water flow ranges from 7×10^3 to 1.2×10^4. Consequently, the correlation (Nusselt number) obtained under fully developed turbulent flow in smooth tubes can be used to calculate the tube-side heat transfer coefficient [21],

$$Nu_t = \frac{h_t d_i}{\lambda_t} = \frac{(f/2)(\mathrm{Re}-1000)\mathrm{Pr}}{1+12.7(f/2)^{1/2}\left(\mathrm{Pr}^{2/3}-1\right)} \tag{3}$$

where λ_t is the thermal conductivity of the water on the tube-side, d_i is the inner diameter of the tubes, h_t is the tube-side heat transfer coefficient, Pr is the Prandtl number and f can be expressed as,

$$f = (1.58\ln\mathrm{Re} - 3.28)^{-2} \tag{4}$$

3.4.2 Shell-side heat transfer coefficient

On the shell-side, the heat resistances in the shell-side consist of those of the condensate film and the cooling of the sensible heat of the flue gases. For the heat transfer coefficient of the gas stream (h_g) in the shell side, the following correlation can be used [19],

$$Nu_{s,g} = h_g D_e / \lambda_g = 0.27\,\mathrm{Re}_{De}^{0.63}\,\mathrm{Pr}_g^{0.34} \tag{5}$$

where λ_g is the thermal conductivity of the gas mixture and D_e is the equivalent diameter calculated along (instead of across) the long axes of the shell.

In addition to the thermal resistance of the gas stream ($1/h_g$), there exist the resistance of the condensate film in Zones II − IV (as shown in Figure 4). Nusselt treated the case of laminar film condensation of a quiescent vapour on an isothermal horizontal tube. The analysis yields the average heat transfer coefficient (h_m) outside the top tube upstream as follows [21],

$$Nu_{s,l} = h_m d / \lambda_1 = 0.728 \left[\frac{\rho_1 (\rho_1 - \rho_g) g i_{lg} d^3}{\mu_1 (T_{sat} - T_w) \lambda_1} \right]^{1/4} \tag{6}$$

where ρ_l, λ_l, and μ_l are the density, thermal conductivity and viscosity of the condensate, respectively, i_{lg} is the latent heat, T_{sat} and T_w are the saturation temperature and the tube wall temperature, respectively. Including the inundation effect in the tube bundles, the average coefficient for a vertical column of N tubes ($h_{m,N}$) compared to the coefficient for the first tube (i.e., the top tube in the row) is

$$h_{m,N} = N^{-1/4} h_m \tag{7}$$

3.4.3 Fouling and thermal resistance of tube wall

It is certain that fouling may occur inside and/or outside the tubes in the condensing boiler. Although fouling is time dependent, only a fixed value can be assumed during the design stage. Inside the tubes, the feed water to the boiler should be chemically treated. However, outside the tubes, the flue gas contains ultrafine particles and trace acid gases. Thus the condensate on the shell-side may contain some amounts of solid and liquid contaminants. Consequently, the fouling resistances inside and outside the tubes ($R_{f,i}$ and $R_{f,o}$) were chosen as 0.000176 m²K/W and 0.00176 m²K/W [15]. The thermal resistance of the stainless steel tube wall is 6.55×10^{-5} m²K/W whereas for the carbon steel tubes coated with polypropylene, the thermal resistance is approx. 9.23×10^{-4} [22] due to the low thermal conductivity of the polypropylene.

3.4.4 Overall heat transfer coefficient

The local overall heat transfer coefficient (U) from the shell side to the tube side can be written as

$$1/U = 1/h_t + R + 1/h_{s,ef} \tag{8}$$

where R is the thermal resistance due to the tube wall and fouling, and h_{ef} is an effective shell-side heat transfer coefficient. When condensation occurs, this effective coefficient is obtained by [19],

$$1/h_{s,ef} = 1/h_{m,N} + q_g / q / h_g \tag{9}$$

where q is the total heat flux from the shell side to the tube side and q_g is the sensible heat flux from the non-condensable gas components.

Based on the above equations, the overall heat transfer coefficients at the boundaries of each zone (U_a and U_b) can be calculated. A mean overall heat transfer coefficient (U_m) for each zone can thus be obtained by weighed average method or arithmetic mean [18].
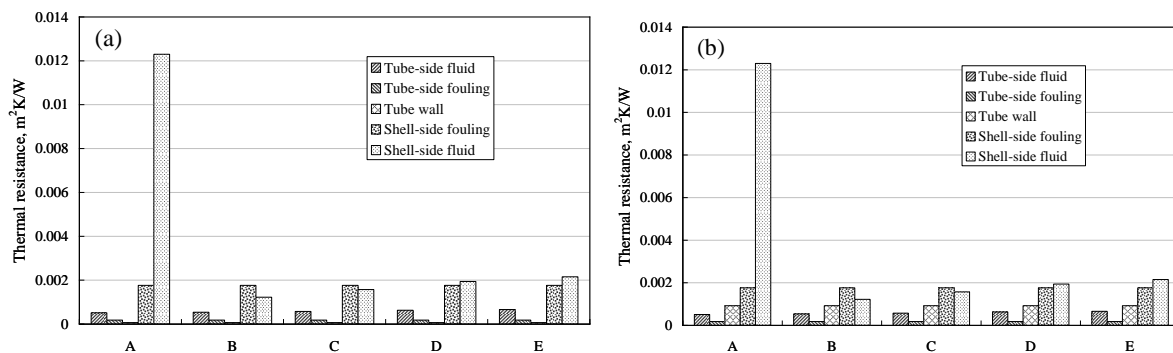
Figure 5: Thermal resistances in the stainless steel (*a*) and carbon steel (*b*) condensing boilers

In both condensing boilers, the thermal resistances in the tube-side (including the fluid and fouling) are relatively small, whereas the shell-side resistances contribute approximately 60 – 90% of the total resistance (Figure 5). As can be seen, in Zone I where no condensation occurs, the thermal resistance of the shell-side flue gas flow is the dominant factor. When the condensate film forms around the tubes, the thermal resistance of the shell-side fluid decreases and the shell-side fouling becomes a major contributor to the total thermal resistance. Due to the low thermal conductivity of PP, the thermal resistance of the tube wall in the carbon steel condenser is much higher than for the stainless steel. *Table 6* summarises the overall heat transfer coefficients for each zone.

Table 6
The overall heat transfer coefficients for each zone (W/m^{2}K)

	Stainless Steel Condenser	Carbon steel condenser
Zone I	68.5	64.7
Zone II	253.7	207.6
Zone III	229.9	191.0
Zone IV	213.4	180.0

3.5 Size of the condenser and the pressure drops

Once the heat transfer rates (Q), LMTD (θ_{LM}) and the mean overall heat transfer coefficients (U_m) for each zone have been obtained, the heat transfer area (A) for each zone can be calculated from,

$$A_j = Q_j / \left(U_{m,j} \theta_{LM,j} \right) \tag{10}$$

where the subscript j refers to the zone number. *Table 7* lists the lengths (L) of the tubes and the total heat transfer areas (based on the outer diameter of the tubes). The results show that the heat flux (Q/A) for a unit heat transfer area in the condensing boiler is around 1.5–2.5kW/m^2. This range is close to the performance of flue gas condensers available in the market [23] and also agrees well with the results obtained by Cortina [24] who designed a flue gas condenser for biomass boilers.

Table 7
Size of the condensing boiler

	Stainless Steel Condenser	Carbon steel condenser
Tube length in Zone I, m	12.17	12.90
Tube length in Zone II, m	27.87	34.06
Tube length in Zone III, m	14.31	17.22
Tube length in Zone IV, m	8.94	10.61
Total tube length (L)	63.30	74.79
Surface area (A), m^2	4918.9	5811.5
Q/A (kW/m^2)	2.34	1.98

The estimation of pressure drops of the fluids flowing through the condenser is crucial to determine the pumping power or fan work input, the provision of which contributes additional capital costs and operating costs for the condensing boiler. On the tube-side, the frictional pressure drop (Δp_t) can be expressed as [21],

$$\Delta p_t = 0.316 \text{Re}^{-0.25} \left(L/d_i \right) \left(\rho u_m^2 / 2 \right) \tag{11}$$

where um is the mean fluid velocity. On the shell-side, the pressure drop depends on the number of tubes the fluid is passing through in the tube bundle between the baffles as well as the length of each crossing. The pressure drop can be calculated by [21],

$$\Delta p_s = \exp\left(0.576 - 0.19\ln\text{Re}\right)\left(\frac{G_s}{A_s}\right)^2 \frac{(N_b+1)D_s}{2\rho D_e}\left(\frac{\mu_w}{\mu_b}\right)^{0.14} \tag{12}$$

where G_s is the mass flow rate of the flue gas, A_s is the tube-bundle cross-flow area, and N_b is the number of baffles.

Calculation results show that, for the stainless steel condensing boiler, the tube-side pressure drop is 3.2kPa where as the shell-side pressure drop is approx. 28.4kPa. Due to the longer tube length, the pressure drops for the carbon steel condenser are higher: 3.8kPa on the tube side and 34.1kPa on the shell-side. Consequently, the required pump power (tube-side) is 0.43kW for the stainless steel condenser and 0.50kW for the carbon steel condenser, whereas the powers of the fan (shell-side) are 828.3kW and 993.4kW respectively.

3.6   Cost estimation and profitability

The cost and profitability were calculated for the condensing boiler only. The overall total cost consists of the equipment cost, installation cost, operating and maintenance (O&M) costs. The capital costs for the condensing boiler were estimated based on the algorithms developed by Couper [22]. The O&M costs for the condensing boiler mainly include the electricity consumption for the pump and fan, chemical treatment for the condensate, fouling removal in the condensing boiler, etc. As little useful information is found in the literature about the maintenance costs for such a condensing boiler, an estimated value of 6% of the fixed capital cost per year [22, 25] was used for fouling treatment and other maintenance costs.

Table 8 summaries the costs and financial benefits for both types of condensing boilers. As stainless steel is more expensive, the capital cost for the stainless steel condenser is about 2.5 times higher than the carbon steel condenser. Due to the higher operating costs (mainly the electricity consumption for the fan) in the carbon steel condenser, the total operating and maintenance costs for both condensers are relatively the same. Due to corrosion, the expected life for a carbon steel heat exchanger is usually 5 years much shorter than a stainless steel one (10-15 years) [28]. Therefore, the Net Present Value (NPV) was calculated over a period of 5 years for the carbon steel condensing boiler and the 10 year period for the stainless steel condenser, as shown in Figure 6. As can be seen, the choice of a carbon steel condenser ensures cash return in a relatively shorter period of time compared to a stainless steel condenser. Moreover, the NPV for the stainless steel is more sensitive to the change of the interest rate.

Table 8
Costs and revenue for the condensing boiler

		Stainless steel condenser	Carbon steel condenser
Capital costs	Boiler cost ($)	2,562,000	902,000
	Installed factor	1.9	2.2
	Installed boiler cost ($)	4,868,000	1,984,000
	Fan cost ($)	40,000	44,000
	Capital cost in total ($)	4,908,000	2,028,000
O&M costs	Electricity rate ($/kWh) [26]	0.1	0.1
	Electricity ($/year)	580,300	695,800
	Chemical treatment expense ($/m^3) [27]	0.45	0.45
	Condensate treatment cost ($/year)	37,600	37,600
	Maintenance cost factor (%)	6	6
	Maintenance cost ($/year)	294,480	121,680
Benefit	Wood chips saving (t/h)	5	5
	Wood chips cost ($/tonne)	60	60
	Fuel cost saving ($/year)	2,100,000	2,100,000
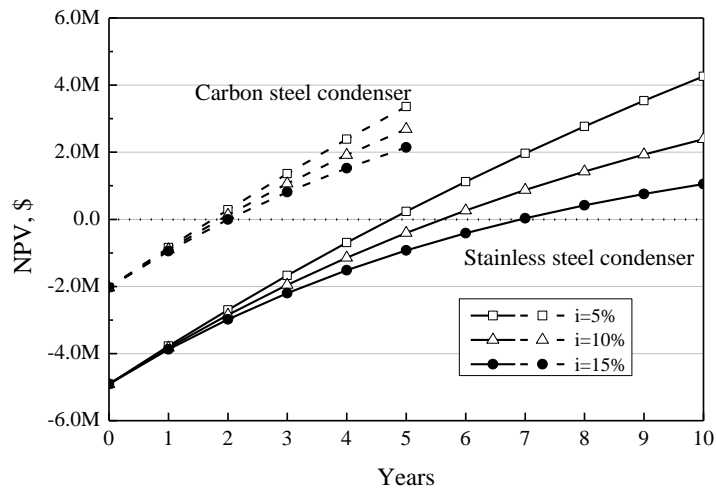
Figure 6: NPV for the carbon steel condenser and the stainless steel condenser
(i: the interest rate)

5   Conclusions

In this paper, the thermal design of a single pass shell-and-tube flue gas condenser showed that a considerable amount of thermal resistance was on the shell-side. This includes fouling, gas phase convective resistance and vapour film interface resistance. The average heat flux per unit heat exchanger area in the designed condenser ranges from 1.5 to 2.5 kW/m^2. Approximately 4900m^2 of total heat transfer area is required, if stainless steel is used as a construction material. If the heat transfer area is made of carbon steel, then polypropylene could be used as the corrosion-resistant coating material outside the tubes. The addition of polypropylene coating increases the tube wall thermal resistance, hence the required heat transfer area will be approximately 5800m^2. Net Present Value (NPV) calculations showed that the choice of a carbon steel condenser ensured cash return in a relatively shorter period of time (i.e. 2 years) when compared to a stainless steel condenser (i.e. 5 to 7 years). Moreover, the NPV for the stainless steel was more sensitive to the change of the interest rate.

References
[1]   Comakli K. Economic and environmental comparison of natural gas fired conventional and condensing combi boilers. J Energ Inst 2008; 81:242–6.
[2]   Weber C, Gebhardt B, Fahl U. Market transformation for energy efficient technologies – success factors and empirical evidence for gas condensing boilers. Energy 2002; 27:287–315.
[3]   EERE Information Center. Considerations When Selecting a Condensing Economizer, http://www1.eere.energy.gov/industry/bestpractices/pdfs/steam_26b.pdf, accessed in May, 2010.
[4]   Nederhoff E. A flue gas condenser for energy saving. Grower 2003; 58:42–3.
[5]   Green DW, Perry RH. Perry's Chemical engineers' handbook. New York: McGill-Hill; 2008.
[6]   Grohn A, Suonmaa V, Auvinen A, Lehtinen KEJ, Jokiniemi J. Reduction of fine particle emissions from wood combustion with optimized condensing heat exchangers. Environ Sci Tech 2009; 43:6269–74.
[7]   Sippula O, Hokkinen J, Puustinen H, Yli-Pirila P, Jokiniemi J. Particle emissions from small wood-fired district heating units. Energy & Fuels 2009; 23:2974–82.

[8] Huijbregts WMM, Leferink RGI. Latest advances in the understanding of acid dewpoint corrosion: corrosion and stress corrosion cracking in combustion gas condensates. Anti-Corros Method M 2004; 51:173–88.

[9] Kiang YH. Predicting dew points of acid gases. Chemical Engineering 1981; 127.

[10] Consortium for Energy Efficiency (CEE). A market assessment for condensing boilers in commercial heating applications. Boston, M.A.; 2001.

[11] Doherty PS, Srivastava N, Riffat SB, Tucker R. Flue gas sorption heat recovery – experimental test and modelling results. J Energ Inst 2006; 79:2–11.

[12] http://www.tekes.fi/opet/, accessed in March, 2008

[13] Demirbas A. Biohydrogen: for future engine fuel demands. London: Springer; 2009.

[14] Hasan A, Kurnitski J, Jokiranta K. A combined low temperature water heating system consisting of radiators and floor heating. Energ Buildings 2009; 41:470–9.

[15] Tubular Exchanger Manufacturers Association. Standards of the tubular exchanger manufactures association. 8th ed., New York: TEMA; 1998.

[16] Shah RK, Sekulic DP. Fundamentals of heat exchanger design. Hoboken: John Wiley & Sons; 2003.

[17] Maier C, Calafut T. Polypropylene: the definitive user's guide and databook. New York: Plastic Design Library; 1998.

[18] Butterworth D. Steam power plant and process condensers. In: Kakac S. editors. Boilers, evaporators and condensers, Hoboken: John Wiley & Sons; 1991, p. 571–633.

[19] Chisholm D. Developments in heat exchanger technology – 1. London: Applied Science Publishers; 1980.

[20] Marto PJ. Heat transfer in condensation. In Kakac S. editors. Boilers, evaporators and condensers, Hoboken: John Wiley & Sons; 1991, p. 525–70.

[21] Kakac S, Liu H. Heat exchangers: selection, rating, and thermal design. 2nd ed. CRC Press; 2002

[22] Couper JR. Process engineering economics. New York: Marcel Dekker; 2003.

[23] Thermeta Service BV. Flue gas condenser. http://www.thermeta.nl/documents/FLDR_EKA0705.03-EN.pdf. Accessed in July 2010.

[24] Cortina M. Flue gas condenser for biomass boilers (Master Thesis). Lulea University of Technology. 2006.

[25] Sinnott RK. Chemcial engineering design. 4th ed. Oxford: Elsevier Butterworth-Heinemann; 2005.

[26] Department of Energy and Climate Change (DECC). Quarterly energy prices, March 2010. ISSN 1475-6544. http://www.berr.gov.uk/files/file50355.pdf, accessed in May 2010.

[27] Spirax Sarco, The steam and condensate loop book. Spirax-Sarco; 2007.

[28] Jegede FO, Polley GT. Capital cost targets for networks with non-uniform heat exchanger specifications, Computers & Chem Eng 1992; 16:477–95.

Dynamic Modelling of a Two-Phase Thermofluidic Oscillator for Efficient Low Grade Heat Utilization: Effect of Fluid Inertia

Roochi Solanki, Amparo Galindo, Christos N. Markides*

Department of Chemical Engineering, Imperial College London, South Kensington Campus, London SW7 2AZ, United Kingdom

* Corresponding author. Email: c.markides@imperial.ac.uk; Tel. +44 (0)20 759 41601

Abstract

In this paper, a promising heat engine technology capable of utilizing low grade heat is examined. Based on a two-phase thermofluidic oscillator concept, the novelty and advantage of this particular system lie in its use of phase change and its lack of reliance on inertia to sustain oscillations, though it is recognized that inertia will always be present in any physical manifestation of the engine. The system is analysed using lumped linearized one-dimensional network models, both with and without inertia, based on thermoacoustic principles and extending these to account for phase change. The gain (temperature difference between source and sink heat exchangers) and frequency at which marginal stability (desirable continuous oscillations) can be achieved is calculated. The effects of the load resistance (fluid drag) and fluid inertia, as well as of the flow resistance due the feedback valve on the marginal stability gain, frequency and exergetic efficiency of the system are investigated. It is found that an increase in feedback resistance leads to a need for a higher gain for oscillatory behaviour to be achieved. In addition, even though an increase in either the resistance or inertia in the load, or the feedback resistance at low values of these variables has almost no effect on the required gain and the oscillation frequency of the system, an increase in these variables can lead at higher values to increased gains and reduced frequencies. A reduced feedback resistance and greater load inertia can also lead to considerably higher efficiencies, while increasing the load resistance allows for an increase in efficiency until a maximum is reached, after which the efficiency decreases again. The validity of certain approximations made previously is considered, and it is shown that these must be made with care. The results from this study can be used for the improved design and optimization of such oscillators, and similar systems.

Keywords   electrical analogy; two-phase; thermofluidic oscillator; heat engine; efficiency; low grade heat

1   Introduction

The maximum theoretical thermal efficiency (the Carnot limit) attainable by a heat engine, and hence also the ability of a thermodynamic power-generating system to produce useful work, increases monotonically as the temperature at which the source heat is available increases. For this reason, historically, the area of power generation has been dominated by the utilization of high grade (i.e. temperature) heat, which almost exclusively involves the combustion of fossil fuels. With ever-increasing environmental concerns of harmful emissions and climate change, but also of energy security in the light of finite resources of common fossil fuels, it is becoming increasingly important to consider alternative clean and efficient energy solutions. In this paper we investigate an interesting new technology capable of converting low grade heat (e.g. solar energy or waste heat) to useful work, as proposed in Refs. [1–3]. The 'Non-Inertive-Feedback Thermofluidic Engine' (NIFTE) has been demonstrated to operate across temperature differences between the heat source and the ambient as low as 50°C [1].

The NIFTE is an unsteady heat engine, within which persistent and regular thermodynamic (pressure, temperature, etc.) oscillations are generated and sustained by steady external conditions. The oscillations are driven by and give rise to heat and fluid flows, from which power can be extracted. The thermodynamic cycle of the NIFTE involves the evaporation and condensation of its working fluid, so the NIFTE may also be considered a two-phase realization of a class of devices known as 'thermofluidic oscillators'. Recently, considerable attention has been drawn to the suitability of thermofluidic

oscillators for low grade heat utilization, and the potential reliability and cost advantages that arise from their lack of moving parts relative to conventional engines. Single-phase (gas cycle) thermofluidic oscillators include Sondhauss tubes [4,5], standing [6,7] and travelling [8] wave thermoacoustic engines, and liquid-piston Stirling (Fluidyne) engines [9–11].

It was claimed in Ref. [2] that one particular advantage of the NIFTE is that it does not (by design) rely on fluid inertia to operate. This independence from inertia implies that bulky tuning lines and resonators become unnecessary, allowing the system an increased capability of sustaining pressure oscillations with large amplitudes, which is vital for the achievement of high power densities. However, any real system will encompass inertial effects to some extent, and further, inertia in the load is not a variable left open to the designer, but something that must be taken into account during the design stage. Understanding the effects of finite inertia is crucial for the optimized design of the next generation of these novel and complex systems, both in terms of enhanced efficiency and performance.

In Smith [1–3] a simple, but useful model for the dynamic behaviour of the NIFTE was proposed, following Backhaus and Swift [8], Ceperley [12] and Huang and Chuang [13]. This approach, also employed and extended in the current study (details in Section 2), involves spatially lumped and first order linear sub- models for each sub-component of the NIFTE. The sub-models are then interconnected to derive a complete model for the whole device. The linearization allows analogies to be drawn with electrical components, thus enabling a representative network to be constructed for the NIFTE. The network employed in Refs. [1– 3] contains resistive and capacitive components, with the former accounting for viscosity, fluid drag and thermal resistance, and the latter for gravity and compressibility. However, it does not contain inductive components, and as such cannot capture finite inertive effects that embody (fluid) inertial phenomena.

The original 'non-inertive model' was validated against experimental data with partial success. For example, in Ref. [2] good predictions of the *trends* of the NIFTE's oscillation frequency f_0 and temperature gain k (related to the spatial temperature gradient in the heat exchangers) required for operation were obtained by adjusting a parameter that was not measured, specifically the feedback valve resistance R_f, in order to obtain the best fit between model predictions and experimental data. However, this fit was performed by the inclusion of R_f into a term that was then scaled. Since the behaviour of the NIFTE is very sensitive to this parameter, this may have led to a situation whereby even though the trends of f_0 and k were captured, the actual values for R_f necessary to achieve this, which were hidden by its grouping with other parameters, were unrealistic. Here, we evaluate all linear parameters, including R_f, directly from experimental variables.

Furthermore, the model's predictions of the variations in the NIFTE's oscillation frequency due to changes in the load did not correlate well with experimental observations [2, 3]. It was proposed that this is probably due to a transition in the mode of evaporation in the HHX from pool boiling to flash boiling, which is not accounted for in the model, as well as a breakdown of the assumption that the specific volume of the vapour is much greater than that of the liquid. It is important to ascertain whether this discrepancy can in fact be explained by reference to inertial effects. A major objective of the current work is to examine the applicability of a full lumped linear 'inertive model' of the NIFTE that includes resistive, capacitive and inductive components, and to compare key results with those from the non-inertive model. To the best knowledge of the authors, the model of the NIFTE presented in this paper is the first application of linear network analysis including inertia to any two-phase oscillator.

2   Methods and materials
2.1   Description and operation of an existing NIFTE
An existing NIFTE prototype is described in detail elsewhere [1–3], but briefly and referring to Figure 1, it consists of a network of interconnected chambers and tubes, and two solid (aluminium) heat exchanger blocks (4,5). At the top (4) the hot heat exchanger (HHX) receives heat from an external heat source (not shown) and transfers this to the engine's working fluid (in this work, *n*-pentane). Directly below this (5)

the cold heat exchanger (CHX) rejects heat from the working fluid to an external heat sink (not shown). This arrangement is used to establish a temperature difference between the two heat exchanger blocks ΔT_{HX}.
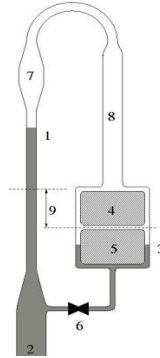
Figure 1: Diagram of the NIFTE taken from Ref. [1]. Component 2 is connected to the load line (denoted by subscript 'l'), 4 (hot) and 5 (cold) are heat exchanger blocks ('th'), 6 is the feedback valve ('f'), 7 is the power cylinder ('p'), and 8 the displacer cylinder ('d'). Levels 1 and 3 are the working fluid vapour-liquid interfaces in the power (left) and displacer (right) cylinders respectively. The combined vapour space above Levels 1 and 3 is assumed to be an adiabatic vapour chamber ('ad')

The NIFTE will operate when the temperatures of the HHX and CHX become higher and lower, respectively, than the boiling point of the working fluid. During operation, evaporation takes place when the vapour-liquid interface (Level 3) in the displacer cylinder (8) contacts the HHX, whereas condensation takes place when Level 3 contacts the CHX (as in Figure 1). It is important to note that the two heat transfer processes do not occur simultaneously, but in a periodic alternating manner as Level 3 oscillates vertically within the displacer cylinder (8) from one heat exchanger block to the other. The NIFTE is a positive displacement machine. It produces fluid displacement (hydraulic) work by transforming: (i) the generated volume of working fluid (from liquid to vapour) during the evaporation phase (that flows up through 8 and down into 7) into a pressurization and positive (downwards) displacement stroke of Level 1 out of the power cylinder (7) and into the load (2); followed by, (ii) the reduced working fluid volume during the condensation phase into a suction and negative (upwards) displacement stroke of Level 1 into the power cylinder (7) from the load (2).

2.2   Analysis, determination of marginal frequency and gain

Our goal at this stage is to extend the analysis in Refs. [1–3] in order to formulate an *inertive* model for the NIFTE, and to represent this with an LRC circuit, that is, an electrical circuit with inductors (L), resistors (R) and capacitors (C). To this end the dominant heat or fluid flow process undergone inside each sub-component of the NIFTE is firstly identified and modelled linearly to first order. Spatial variations are eliminated by averaging. Analogies are then drawn between the physical variables of pressure (P) and voltage (E), volumetric flow rate (U) and current (I), temperature (T) and voltage (E), and entropy rate ($\dot{S}$) and current (I). The analogies are used to transform the simplified NIFTE equations involving the thermal-fluid variables into a suitable network of electrical elements. We use governing equations that describe the dynamics of three types of components: (i) a resistor $\Delta E = RI$, (ii) a capacitor $I = C\Delta\dot{E}$; and (iii) an inductor $\Delta E = L\dot{I}$, where ΔE is the potential difference across the component and I is the current through it. Thus, a resistance to heat or fluid flow is represented by a resistor R_i; hydrostatic pressure (i.e. gravitational potential energy) of a liquid and adiabatic compressibility of a vapour are represented by capacitors C_i; and liquid inertia (gas inertia is neglected) is represented by an inductor L_i.

As seen in Figure 2 the resulting full inertive model of the NIFTE features four inductors, which can capture, to first order, the effects of inertia in the load 'l', power cylinder 'p', displacer cylinder 'd' and feedback line 'f'. It can be reduced to the non-inertive model presented in Refs. [1–3] simply by setting $L_i = 0$, though we will show that key improvements arise from the inclusion of inertia in the full model. The physical variables used to evaluate each electrical component in Figure 2 are presented in *Table 1*. The

'nominal' values and investigated ranges of all variables contained in the parameter expressions in *Table 1* can be found in *Table 2*. The nominal values are based on the configuration of the existing NIFTE as described in Refs. [1–3], while the ranges describe reasonable incremental design perturbations from the existing NIFTE, always leading to an acceptable and realistic configuration that we deem as practically achievable in the short term.
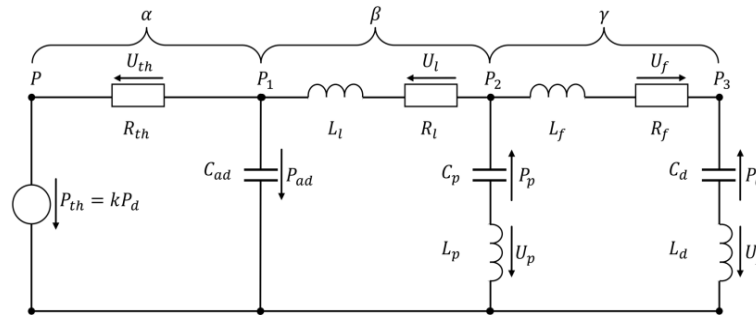
Figure 2: Circuit diagram of the NIFTE, where k is the feedback gain, R_i is a resistance, C_i is a capacitance, L_i is an inductance, P_i is a pressure and U_i is a volumetric flow-rate. Subscript 'th' denotes the thermal domain (i.e. interactions with the HHX and CHX), 'ad' the adiabatic domain, 'l' the load, 'p' the power cylinder, 'd' the displacer (heat exchanger) cylinder, and 'f' the feedback line and valve

Table 1
Electrical analogies in the NIFTE and relations for resistance, capacitance and inductance

Electrical element	Thermal-fluid effect	Parameter expression
Resistance (R)	Thermal resistance	$R_{th} = \rho_{g,eq} T_{eq} s_{fg} / h A_s (dT/dP)_{TP}$
	Load flow resistance (viscous/pressure drag)	$R_l = 128 \mu_w l_l / \pi d_l^{\ 4}$
	Feedback valve flow resistance (drag)	$R_f = 128 \mu_{pen} l_f / \pi d_f^{\ 4}$
Capacitance (C)	Vapour compressibility	$C_{ad} = V_{g,eq} / \gamma P_{eq}$
	Power cylinder hydrostatic capacitance	$C_p = A_p / \rho_{pen} g$
	Displacer cylinder hydrostatic capacitance	$C_d = A_d / \rho_{pen} g$
Inductance (L)	Load inertia (fluid mass)	$L_l = \rho_w l_l / A_l$
	Power cylinder inertia	$L_p = \rho_{pen} l_p / A_p$
	Displacer cylinder inertia	$L_f = \rho_{pen} l_f / A_f$
	Feedback tube inertia	$L_d = \rho_{pen} l_d / A_d$

Hence, for example, in the absence of inertial effects the resistance to fluid flow (drag) in the load is modelled as $P_l = P_2 - P_1 = (128 \mu_w l_l / \pi d_l^{\ 4}) U_l = R_l U_l$. In other words, it is assumed that the volumetric flow-rate through the load is proportional to the pressure that can be generated across it by the NIFTE. This is a reasonable approximation for viscous flow in a smooth pipe at laminar Reynolds numbers Re and low Womersley parameters Wo (i.e. low frequencies) when the flow is quasi-steady, such that $\Delta P / (\rho U^2 / 2)(l/d) = 64/Re$. At higher frequencies the inclusion of inertia in the form of the first order inductive component L_l (as shown in Figure 2) is necessary to account for changes in the amplitude and the phase of P_l relative to U_l [14], resulting in $P_l = P_2 - P_1 = (R_l + j\omega L_l) U_l$.

Table 2
Nominal values and investigated ranges of variables in Table 1

Variable	Nominal value	Investigated range	Units
g	9.81	-	m/s^2
l_l	1	0.01 to 30	m
l_p	0.55	0.2 to 2	m
l_f	0.15	0.05 to 0.5	m
l_d	0.26	0.2 to 2	m
d_l	0.01	0.003 to 0.1	m
d_f	0.005	0.001 to 0.05	m
A_l	7.85×10^{-5}	7.07×10^{-6} to 7.85×10^{-3}	m^2
A_p	4.52×10^{-4}	1.96×10^{-5} to 7.85×10^{-3}	m^2
A_f	1.96×10^{-5}	7.85×10^{-7} to 1.96×10^{-3}	m^2
A_d	4.48×10^{-3}	9.71×10^{-5} to 7.34×10^{-3}	m^2
P_{eq}	1.01×10^5	-	Pa
$V_{g,eq}$	1.94×10^{-4}	2.37×10^{-5} to 2.25×10^{-5}	m^3
T_{eq}	309	-	K
ρ_{pen}	621	-	kg/m^3
$\rho_{g,eq}$	2.98	-	kg/m^3
ρ_w	998	-	kg/m^3
s_{fg}	1.16×10^3	-	J/kg.K
γ	1.09	-	-
μ_{pen}	2.18×10^{-4}	-	kg/m.s
μ_w	1.00×10^{-3}	-	kg/m.s
$(dT/dT)_{TP}$	28.9×10^{-5}	-	K/Pa
h	4.61×10^3	1.00×10^3 to 2.00×10^4	W/m^2.K
A_s	1.60×10^{-3}	1.07×10^{-4} to 1.22×10^{-1}	m^2

The governing relations of the three elemental electrical components are considered in the Laplace domain. The impedances Z of a resistor, capacitor and inductor are $Z_R = R$, $Z_R = 1/sC$ and $Z_R = sL$, respectively. A quantity of interest is the total impedance $Z_{TOT} \equiv P_{th}/U_{th}$ of the overall circuit in Figure. 2, where P_{th} and refer to the input pressure and flow-rates to the system from the heat exchanger due to phase change heat transfer. An expression for Z_{TOT} is obtained by adding contributions from all impedances around the circuit, after taking into account series and parallel connections, leading to,

$$Z_{TOT} = R_{th} + (sC_{ad} + (Z_l + (Z_{fd} + Z_p^{-1})^{-1})^{-1})^{-1},$$

(1)

where $Z_{fd} = R_f + s(L_f + L_d) + 1/sC_d$, $Z_p = sL_p + 1/sC_p$ and $Z_l = R_l + sL_l$. Further, three important transfer functions are

$\alpha = P_1/P = 1 - R_{th}/Z_{tot}$,
$\beta = P_2/P_1 = 1 - Z_l(1/\alpha Z_{tot} - sC_{ad})$, and
$\gamma = P_3/P_2 = 1/(1 + Z_f/Z_d)$.

Since all aforementioned components are linear, the complete network is also linear and can only display one of three possible stability behaviours: stable, with any perturbation decaying exponentially to zero; marginally stable, with sustained oscillations of constant amplitude; or unstable, with perturbations growing exponentially. However, in the real (physical) system the output will not grow exponentially if the gain is increased above the marginal stability limit. Experimental evidence reveals that the system output

saturates and attains a new oscillatory operating state characterized by (nonlinear) limit-cycle behaviour. Thus, we focus on the gain required for marginal stability as this is the lowest gain that will give sustained engine operation. An internal feedback process can be seen in Figure. 2. The relation $P_{th} = kP_d$ on the far left describes the heat transfer (both evaporation in the HHX and condensation in the CHX, which are assumed symmetric) from the heat exchanger blocks within the displacer cylinder as a function of the vertical position of the vapour-liquid interface in the same cylinder. Specifically in this model, a constant temperature gradient is established along the lengths of the HHX and CHX blocks, and the gain k is proportional to this spatial temperature gradient $(dT/dy)_{HX}$. Thus, k also scales with the temperature difference ΔT_{HX} between the two blocks. At low gain (i.e. low temperature gradient), the NIFTE is stable. As the temperature gradient is increased, for example by increasing the supply of heat to the HHX, a point of marginal stability is reached, from which the NIFTE can be made unstable if the temperature gradient is increased even further. We are interested here in the performance of the NIFTE at marginal stability.

In order to evaluate any characteristic property of the system, the frequency at which marginal stability occurs, which is associated with desirable continuous oscillations, must first be evaluated. Once this has been found each function can be evaluated at $s = j\omega_0$, where ω_0 is the marginal stability frequency. Any transfer function relating any two thermodynamic variables of the system will have 5 poles: 2 complex conjugate pole pairs and 1 purely real pole. At zero gain the NIFTE model as presented in Figure. 2 will be stable, with all poles having negative real parts thus representing a dynamic behaviour consisting of a superposition of oscillations enveloped by decaying exponentials. As the gain is increased the closed loop system reaches a point of marginal stability, which occurs when one conjugate pole pair lies exactly on the imaginary axis. The imaginary part of this pair is equal to the frequency at which the system oscillates, $s = \pm j\omega_0$. The remainder of the poles of the system must lie in the negative real plane, such that their transient behaviour recedes.

To find the gain and frequency at marginal stability, the complete system was imported into Matlab, and the `sisotool` function was used. The closed loop feedback gain k at which marginal stability occurs can be found by moving the square points in the right window such that one pair of poles lie purely on the imaginary axis. The value of the compensator in the left window is the closed loop feedback gain. The frequency can be read directly by examining the pair of poles on the imaginary axis.

2.3 Calculation of exergetic efficiency

A key quantity of interest is the efficiency of the NIFTE device at marginal conditions. We present results of exergetic (or second law) efficiency η_{ex}, which is defined as the time-averaged power dissipated in the load over the time-averaged exergy (also equal to the time-averaged availability) input rate to the system,

$$\eta_{ex} = \frac{\overline{P_l(t)U_l(t)}}{\overline{T_{HX}(t)\dot{S}_{th}(t)}} = \frac{\overline{P_l(t)U_l(t)}}{\overline{P_{th}(t)U_{th}(t)}} = \frac{|P_l(j\omega)U_l(j\omega)|}{|P_{th}(j\omega)U_{th}(j\omega)|} = \left|\frac{P_l}{P_{th}}\right|\frac{|1/Z_l|}{|1/Z_{tot}|},$$
(2)

where T_{HX} is the heat exchanger temperature at the locality of phase change, $\dot{S}_{th}$ is the entropy input to the system due to the heat transfer associated with the phase change, P_l and P_{th} are the load and input pressures respectively, and U_l and U_{th} are the load flow-rate and input flow-rate (due to phase change). Note that in Eq. (2) we show both the time domain and Laplace domain representations of the different variables, the latter of which is used in the calculations with $\omega = \omega_0$. In the final equality, from which η_{ex} is actually evaluated, we have made use of the relationship between P_l and U_l ($P_l = Z_l U_l$), and that between P_{th} and U_{th} ($P_{th} = Z_{TOT}U_{th}$). Finally, it can be shown that the transfer function between the pressure across the load and the input pressure is also given by $P_l/P_{th} = \alpha(1 - \beta)$.

3 Results and discussion
3.1 Comparison of the model with and without inductances
In previous work [1–3], inductances (i.e. inertia) were assumed to be negligible everywhere. Here, the effect of including finite inductances is investigated by comparing the inertive model's predictions

against those obtained by setting all inductances to zero. Importantly, all other parameters were varied within acceptable physical limits. In the following sections we focus on the effects of the resistance to flow in the feedback tube (R_f), the resistance to flow in the load (R_l), and the inertia of the liquid in the load (L_l), on the behaviour and performance of the system. The data was generated parametrically, with each parameter perturbed independently and all others set to a nominal value.

3.1.1   Required gain or heat exchanger temperature gradient

In Figure 4(a) the effects of R_f, R_l and L_l on the required feedback gain k for marginal stability are shown. The required gain k is directly proportional to the required temperature gradient along the heat exchanger blocks $(dT/dy)_{HX}$, and scales with the temperature difference ΔT_{HX} between the two blocks. The lines on these plots can be considered stability limits at which the system is marginally stable. Below the lines the system is stable, whereas above them it is unstable. Similarly, in Figure 4(b) the effects of R_f and R_l on the required gain are shown, but with all inductances set to zero.
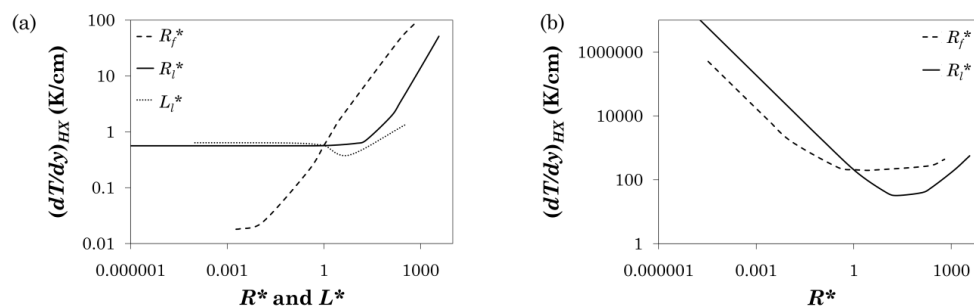
Figure 4: Stability plots. Effect of perturbing the main parameters R_f (dashed line), R_l (solid line) and L_l (dotted line) on the value of $(dT/dy)_{HX}$ required for marginal stability; (a) with inductances, and (b) without inductances

The most striking feature of Figure 4 is the fact that the inclusion of inertia leads to results that are not only entirely different in magnitude, but also in the trends they reveal and, by extension, the design rules they imply. In Figure 4(b) an increase in resistance leads to a decrease in the required $(dT/dy)_{HX}$ for operation, which is very desirable given the goal of utilizing heat at low temperature. However, in Figure 4(a) a general increase is seen in the required $(dT/dy)_{HX}$ as the resistances are increased. In the case of R_f this is monotonic, but in the case of R_l (and also L_l) there is a wide range over which the necessary $(dT/dy)_{HX}$ is independent of the load. Furthermore, the values of $(dT/dy)_{HX}$ in Figure 4(b) are unrealistically high, whereas Figure 4(a) contains more realistic values.

3.1.2   Oscillation frequency

In Figure 5(a) the effects of R_f, R_l and L_l on the NIFTE oscillation frequency f_0 with inertia are shown, and in Figure 5(b) these effects are seen in the absence of inertia. Experimental measurements have shown f_0 to be of the order of 0.1–0.2 Hz [1] for the range of parameters used in the present study.
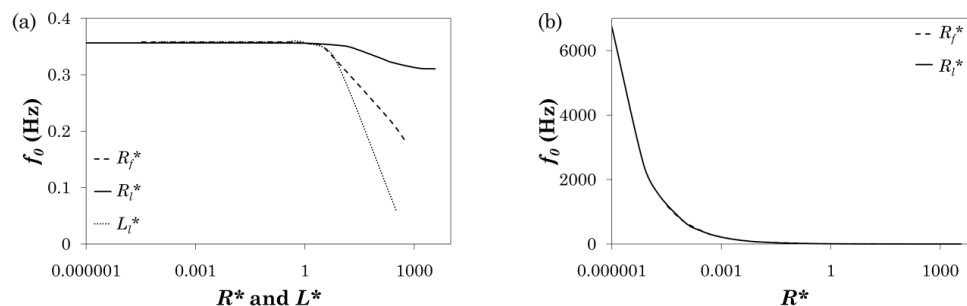
Figure 5: Effect of R_f (dashed line), R_l (solid line) and L_l (dotted line) on oscillation frequency; (a) with, and (b) without inductances

In both figures f_0 decreases with increasing resistance or inductance. Yet, in Figure 5(b) a sharp decrease with increasing resistance is seen, followed by a plateau at large resistance values. The frequency range is large and unrealistic except for extremely high resistances. In Figure 5(a) on the other hand, changes in R_f, R_l and L_l are not seen to affect the frequency over a large parameter space. At very high values of these parameters f_0 does indeed decrease, as expected qualitatively from the non-inertive model.

3.1.3   Exergetic efficiency

In Figure 6 the effects of R_f, R_l and L_l on η_{ex} are shown, both with and without inertia. The inertive and non-inertive values of η_{ex} are significantly different. Clearly the presence of inertia in the load L_l leads to higher (and more realistic) efficiencies. Experimental measurements have shown η_{ex} to be up to 10% [1] over the range of parameters used in the present study. In both models we can see that an increase in R_l leads to an in increase in η_{ex} until a maximum is reached after which η_{ex} decreases again. However, the effect of R_f is contradictory. In the inertive model an increase in R_f leads to a strong reduction in η_{ex}, the exact opposite of which is observed when inertia is neglected. This is an important finding, of great interest to the designer.
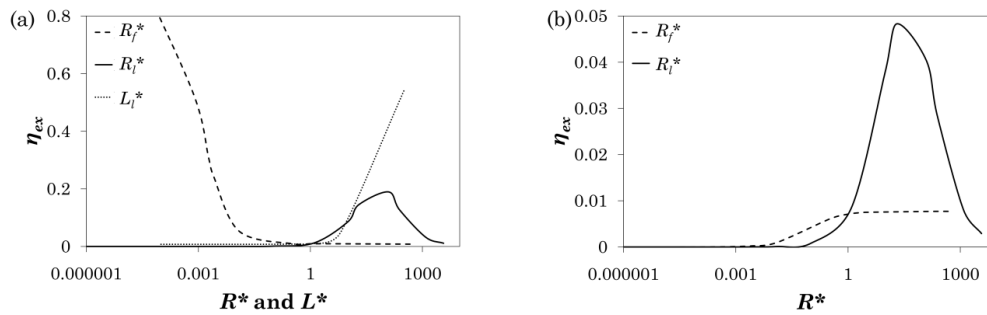
Figure 6: Effect of perturbing load parameters R_l (dashed line) and L_l (solid line), and R_f (dotted line), on the exergetic efficiency η_{ex} of the system; (a) with, and (b) without inductances

Summarizing briefly, the results shown in Figures 4, 5 and 6 suggest that the inclusion of inertia leads to a more realistic model, capable of returning values that are comparable to the values observed experimentally [1, 2]. They also suggest that although the NIFTE does not rely on inertia, its presence can lead to significant improvements in performance, and to a change in the predicted behaviour of the system (even qualitatively) that must be taken into account in any model.

3.2   Simplifying approximations

For the network in Figure 2 it was stated in a previous study [1] that, after neglecting inductances and subject to a few reasonable approximations, ω_0 can be evaluated from,

$$\omega_0 = 2\pi f_0 = \sqrt{\frac{R_{th} + R_l}{R_{th} R_f R_l C_{ad} C_d}}.$$

(3)

The validity of these approximations, which are: (i) $|P_1/P_2| \gg 1$, (ii) $|P_1/P_3| \gg 1$, and (iii) $|U_f/U_l| \ll 1$, is investigated in this section. Starting from nominal values, each system parameter was changed to two 'high' and 'low' (but still practically achievable) values with all other parameters unchanged. Recall from Section 2.2 that practically achievable values for each parameter were chosen as representations of reasonable incremental perturbations from the existing physical NIFTE [1–3], always leading to an acceptable and realistic design. The nominal value of each parameter can be found in *Table 3*, and the results from the parametric study are shown in *Table 4*.

Table 3
Calculated nominal values for the parameters in Table 1

Electrical Parameter	Nominal value	Investigated range	Units
R_{th}	5.02×10^8	3.27×10^7 to 6.74×10^9	kg/m^4.s
R_l	4.08×10^6	4.08×10^0 to 1.51×10^{10}	kg/m^4.s
R_f	2.13×10^6	7.10×10^1 to 4.44×10^9	kg/m^4.s
C_{ad}	1.76×10^{-9}	1.87×10^{-9} to 1.46×10^{-7}	m^4.s^2/kg
C_p	7.43×10^{-8}	3.22×10^{-9} to 1.29×10^{-6}	m^4.s^2/kg
C_d	7.35×10^{-8}	1.59×10^{-8} to 1.21×10^{-6}	m^4.s^2/kg
L_l	1.27×10^7	8.50×10^3 to 6.40×10^6	kg/m^4
L_p	3.77×10^5	7.90×10^3 to 3.16×10^7	kg/m^4
L_f	4.74×10^6	1.27×10^3 to 4.24×10^9	kg/m^4
L_d	1.80×10^5	1.58×10^4 to 3.95×10^8	kg/m^4

Table 4
Selection of perturbed values for parameters R_{th}, R_l, R_f, C_{ad}, C_p, C_d and showing the frequencies obtained from the non-inertive model and results from Eq. (3) and approximations (i) $|P_1/P_2| \gg 1$, (ii) $|P_1/P_3| \gg 1$, and (iii) $|U_f/U_l| \ll 1$ in Section 3.2

Para-meter	Perturbed Value	Frequency (Hz)		Approximations		
		Non-inertive Model	From Eq. (3)	$\left\|\dfrac{P_1}{P_2}\right\| \gg 1$	$\left\|\dfrac{P_1}{P_3}\right\| \gg 1$	$\left\|\dfrac{U_f}{U_l}\right\| \ll 1$
R_{th}	3.3×10^7	1.2×10^3	8.2×10^2	2.3×10^0	2.2×10^0	2.4×10^0
	6.7×10^9	6.7×10^0	4.7×10^0	2.2×10^0	2.2×10^0	2.4×10^0
R_l	4.1×10^0	6.7×10^3	4.7×10^3	2.1×10^0	2.0×10^0	2.4×10^0
	1.5×10^{10}	6.1×10^{-1}	4.3×10^{-1}	3.0×10^3	9.0×10^3	4.8×10^{-1}
R_f	7.1×10^1	1.2×10^3	8.2×10^2	1.1×10^0	1.0×10^0	4.5×10^1
	1.3×10^9	4.1×10^{-1}	1.9×10^{-1}	4.3×10^{-1}	4.8×10^1	8.8×10^{-3}
C_{ad}	6.4×10^{-10}	1.1×10^1	7.9×10^0	2.2×10^0	2.2×10^0	2.4×10^0
	1.5×10^{-7}	1.0×10^0	5.2×10^{-1}	6.9×10^0	2.9×10^0	1.3×10^0
C_p	3.2×10^{-9}	2.4×10^1	4.8×10^0	2.7×10^0	3.9×10^1	1.7×10^0
	2.0×10^{-3}	4.8×10^0	4.8×10^0	3.8×10^1	1.4×10^3	7.5×10^{-2}
C_d	4.2×10^{-8}	8.30×10^0	6.3×10^0	3.9×10^0	2.0×10^0	1.9×10^0
	1.2×10^{-6}	4.9×10^0	1.2×10^0	1.4×10^0	5.4×10^0	3.2×10^0

Specifically, from the second and third columns it can be seen that the approximate result for the oscillation frequency f_0 from Eq. (3) captures the order of magnitude for this variable as evaluated from the non-inertive model, though discrepancies of up to a factor of 5 can be seen. This discrepancy is investigated further in Figure 7. We note that C_p is absent from Eq. (3) due to the assumption that $|U_f/U_l| \ll 1$. It can be seen in *Table 4*, as well as in Figure 7(*a*), that at large values of C_p this assumption holds true. At low values of C_p however, the assumption is far from valid, and therefore Eq. (3) will fail to agree with the prediction of f_0 from the non-inertive model to an acceptable degree. Returning to *Table 4*, the last three columns reveal that the approximations are not generally valid.

Therefore expressions such as Eq. (3) based on these approximations may also not be valid in general, and should be used with care.
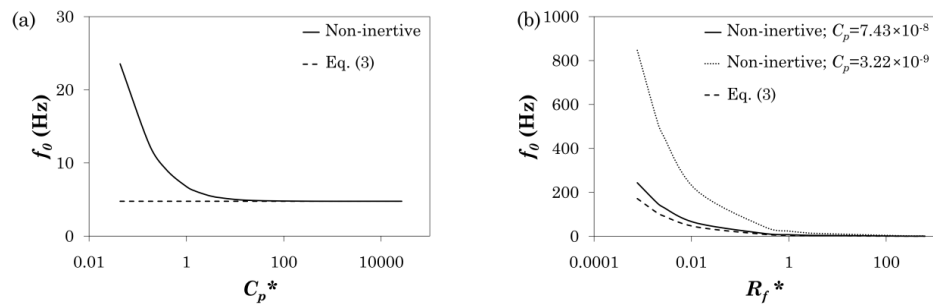
Figure 7: Effect of (a) C_p and (b) R_f, on f_0 from the non-inertive model and comparison with prediction from Eq. (3). The dashed lined represents the results from Eq. (3), and the solid and dotted lines represent results at $C_p = 7.43 \times 10^{-8}$ and $C_p = 3.22 \times 10^{-9}$ m^4.s^2/kg, respectively
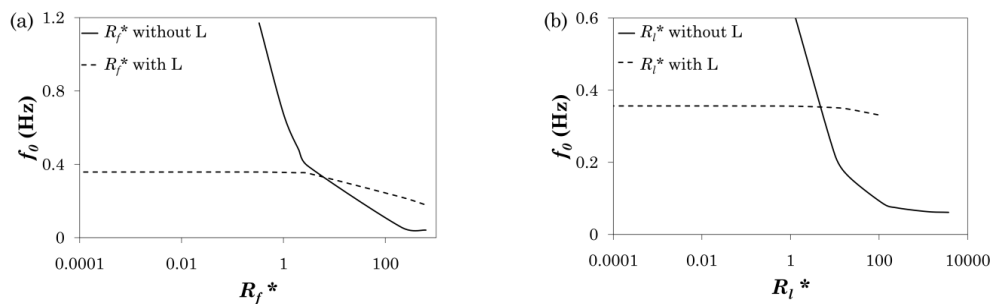
Figure 8: Effect of inertia on the variations in f_0 due to (a) R_f and (b) R_l, with nominal $C_p = 7.43 \times 10^{-8}$ m^4.s^2/kg, where the dashed and solid lines are results from the model with and without inductances, respectively. In the non-inertive case we plot $f_0/10$

The different predictions of f_0 are considered more closely in Figure 7(b) and Figure 8. From Figure 5 we are aware that the use of nominal values results in great differences between inertive and non-inertive predictions of f_0. In order to compare further the two models we modify the nominal value of C_p to 7.43×10^{-8} m^4.s^2/kg. Interestingly, the non-inertive prediction of the effect of R_f on f_0 is both: (i) in close agreement with Eq. (3), as seen in Figure 7(b); and also (ii) in relatively good agreement with the inertive prediction in Figure 8(a), except at low R_f. However, even in this case, there remains a deviation in the predictions of the effect of R_l on f_0 between the non-inertive and inertive models, the latter of which are considerably more realistic. It is possible that inertia is responsible for the model-experiment discrepancy observed in Ref. [2], although other factors are probably also playing a role.

4 Conclusions

In this paper we complement previous investigations carried out on the NIFTE thermofluidic oscillator [1–3] in which all inertial effects were neglected. When comparing predictions from an inertive model with those from a non-inertive model, significant differences are found. Further, the predictions from the non-inertive model diverge significantly from experimental observations. We conclude that inertia may constitute an important factor in the modelling of this system. Specifically, the effects of: (i) fluid flow drag (resistance) and inertia in the load; as well as (ii) feedback valve drag, on the marginal gain (minimum temperature difference between the source and sink heat exchangers necessary for operation), frequency and exergetic efficiency of the NIFTE are investigated. Increases in load resistance and inertia have little effect on the gain and oscillation frequency at lower values of resistance and inertia, though at higher values they result in increased gain and reduced frequency. These observations are not in accordance with corresponding non-inertive model predictions. Moreover the gain and frequency predictions in the absence of inertia are quantitatively unphysical. Of interest to the designer is the

finding that decreasing the feedback valve resistance or increasing the load inertia lead to increases in efficiency, while an increase in load resistance leads to an in increase in efficiency until a maximum is reached, after which the efficiency decreases again. Finally, when the non-inertive model was developed, certain approximations were made which are shown not to be true generally in describing the system over a range of conditions. In conclusion, it is found that difficulties in the early stage modelling of this system, and hence in our ability to gain a better understanding of its behaviour and performance, can in many cases be overcome by the introduction of inertia.

Acknowledgements

References

[1]   Smith TCB. Power dense thermofluidic oscillators for high load applications. Energy conversion engineering. IECEC 2004: Proceedings of the 2nd International Energy Conversion Engineering Conference; 2004 Aug 16-19; Providence (RI), USA. Reston (VA): AIAA; 2004. p. AIAA-2004-5758 1–15.

[2]   Smith TCB. Asymmetric heat transfer in vapour cycle liquid-piston engines. Stirling Engine. ISEC 2005: Proceedings of the 12th International Stirling Engine Conference and Technology Exhibition; 2005 Sept 7-9; Durham, UK. Durham: Durham University; 2005. p. 302–14.

[3]   Smith TCB. Thermally driven oscillations in dynamic applications [PhD thesis]. Cambridge: University of Cambridge; 2006.

[4]   Sondhauss C. Ueber die schallschwingungen der luft in erhitzten glasröhren und in gedeckten pfeifen von ungleicher weite. Ann Phys. 1850;79:1–38. German.

[5]   Feldman KT. Review of the literature on Sondhauss thermoacoustic phenomena. J Sound Vib. 1968;7:83–9.

[6]   Wheatley J, Hofler T, Swift GW, Migliori A. An intrinsically irreversible thermoacoustic heat engine. J Acoust Soc Am. 1983;74:153–70.

[7]   Wheatley J, Hofler T, Swift GW, Migliori A. Experiments with an intrinsically irreversible acoustic heat engine. Phys Rev Lett. 1983;50:499–502.

[8]   Backhaus S, Swift GW. A thermoacoustic-Stirling heat engine: detailed study. J Acoust Soc Am. 2000;107:3148–66.

[9]   Goldberg LF, Rallis CJ. A prototype liquid-piston free-displacer Stirling engine. Energy conversion engineering. IECEC 1979: Proceedings of the 14th Intersociety Energy Conversion Engineering Conference; 1979 Aug 5-10; Boston (MA), USA. Washington (DC): ACS; 1979. p. 1103–8.

[10] West CD, Pandey RB. Laboratory prototype Fluidyne water pump. Energy conversion engineering. IECEC 1981: Proceedings of the 16th Intersociety Energy Conversion Engineering Conference; 1981 Aug 9-14; Atlanta (GA), USA. New York (NY): ASME; 1981. p. 1916–8.

[11] Elston MJ, Lurie MS, Rallis CJ, Kilgour DB. Further development of the Fluidyne liquid-piston engine. Energy conversion engineering. IECEC 1982: Proceedings of the 17th Intersociety Energy Conversion Engineering Conference; 1982 Aug 8-12; Los Angeles (CA), USA. New York (NY): IEEE; 1982. p. 1755–60.

[12] Ceperley PH. A pistonless Stirling engine–the traveling wave heat engine. J Acoust Soc Am. 1979;66:1508–13.

[13] Huang BJ, Chuang MD. System design of orifice pulse-tube refrigerator using linear flow network analysis. Cryog. 1996;36:889–902.

[14] Ünsala B, Rayb S, Durst F, Ertunça Ö. Pulsating laminar pipe flows with sinusoidal mass flux variations. Fluid Dyn Res. 2005;37:317–33.

Computational Fluid Dynamic Investigation of Liquid Rack Cooling in Data Centres

Ali Almoli [a], Adam Thompson [a], Nikil Kapur [a], Jonathan Summers [a], Harvey Thompson [*a], George Hannah [b]

[a] Institute of Engineering Thermofluids, Surfaces & Interfaces (iETSI), School of Mechanical Engineering, University of Leeds, Leeds, LS2 9JT, United Kingdom
[b] Airedale Air Conditioning Ltd, Leeds, United Kingdom

* Corresponding author. Email: h.m.thompson@leeds.ac.uk; Tel. +44(0) 113 343 2136; Fax. + 44(0)113 343 2150

Abstract
Relying on thermal air management in a data centre is becoming less effective as heat densities from the Information Technology (IT) equipment continue to rise. Direct liquid cooling is more efficient at transferring the waste heat, but requires liquid loops passing as close as possible to the heat source. A new computational fluid dynamics (CFD) strategy is developed for data centre scenarios where a liquid loop heat exchanger is attached at the rear of server racks (back doors), which can avoid the need to separate the cold and hot air streams in traditional hot/cold aisle arrangements. The effectiveness of additional fans in the back door heat exchangers is investigated using the three-dimensional CFD model of a simplified three-aisle, six-rack data centre configuration.

Keywords   data centres; liquid cooling; heat transfer; CFD modelling

1   Introduction

The rapidly increasing energy demand of data centres is presenting industry and governments with an energy supply problem. It is clear that the current roadmap of higher density servers with no radical changes in computing technology on the horizon will lead to year-on-year increases in energy requirements since data centre power consumption has doubled in the last 5 years and is likely to double again in the next 5 years to over 100 billion kWh [1]. Within the UK, the issue of thermal management in data centres is becoming critical since power supply is becoming restricted in key data centre locations such as London Docklands, The Thames Valley and Manchester [2].

There are two main inefficiencies leading to such enormous energy requirements: the Information Technology (IT) hardware inefficiencies and the cooling requirements, each accounting for roughly 40% of the total energy usage, with the result that each kWh of energy for data processing requires a further kWh for cooling. The energy-efficient design of data centres is a truly multi-disciplinary problem. IT load inefficiencies can be addressed by improved semiconductor technologies [2] and server virtualisation, while cooling of the electronics in data centres can be achieved in a number of ways, by far the most popular at present being via cold air, but there is a trend to adopt direct liquid cooling [3] of the servers by, for example tube and fin heat exchangers attached to the back of the server rack or, yet to be fully utilised, dielectric liquid immersion cooling and on-chip spray cooling [4].

In this paper we focus on thermal air flow management and cooling in data centres, issues which are particularly challenging since Computer Room Air Conditioning (CRAC) systems have to maintain temperatures and humidity levels in narrow bands in order to avoid catastrophic data losses due to over-heating servers, hygroscopic dust or electric discharge failures. Strategies are usually based on the separation of hot and cold air via a layout of hot and cold aisles, but efficiencies can be gained with either of the two aisles contained. The CRAC units usually supply cold air into Data Centres through raised floor tiles and the cold air passes through the server racks, cools the electronic equipment and emerges from the back of the servers as a hot air stream. Computational Fluid Dynamics (CFD) is increasingly being used to improve air flow design in such systems [5,6]. The objectives of this paper are to: (i) develop a new CFD modelling strategy to investigate the effectiveness of liquid loop heat exchangers mounted to the rear of the IT server racks, referred to as a

back door cooler, and (ii) apply the CFD model to a simplified three-row, six-rack high-density data centre scenario where the back door cooler either contains a series of fans (active) or no fans (passive), the latter relying entirely on the fans in the servers to push the air through the back door cooler.

2   CFD modelling of thermal air flow in data centres
2.1   Mathematical model
Although Computational Fluid Dynamics (CFD) is now used to analyse and design thermal air flows in Data Centres, they are still largely unverified with respect to the accuracy of their thermal predictions for large Data Centres [6]. In addition, the modelling methodologies adopted for the all-important flow through server racks have not been described adequately [1], making comparison with previous studies extremely difficult. In this paper we briefly describe a modelling methodology for the thermal air flow in Data Centres with a particular focus on the representation of the server racks and back door cooling units.

Thermal air flows in Data Centres are usually complex, recirculating air flows characterised by a hierarchy of different length scales. A typical Reynolds number, Re, based on an air inlet velocity from the supply vents of 1m/s and a rack length scale of 2.4m, leads to an estimated Re$\approx 10^5$ indicating the turbulent flow regime. Most previous CFD studies of Data Centre air flows have used Reynolds Averaged Navier-Stokes (RANS) models, see e.g. the very recent study of Cho *et al* [1]. The governing continuity and momentum equations, written in the RANS format, are:

$$\nabla.\underline{U} = 0 \tag{1}$$

$$\frac{\partial \underline{U}}{\partial t} + \nabla.\left(\underline{U}\,\underline{U}\right) = \frac{1}{\rho}\nabla.\left(\underline{\underline{\sigma}} - \rho\overline{\underline{U}'\,\underline{U}'}\right) + \frac{1}{\rho}\underline{S} \tag{2}$$

where $\underline{\underline{\sigma}} = -P\underline{\underline{I}} + \mu\left(\nabla(\underline{U}) + [\nabla(\underline{U})]^T\right)$ is the Newtonian stress tensor and μ is the air viscosity, ρ its density (defined using the ideal gas law with constant pressure 1.013 x 10^5 Pa), $\underline{U}$ and $\underline{U}'$ are the average and turbulent fluctuation velocity vectors respectively, P is the pressure and $\underline{\underline{I}}$ is the unit tensor. The vector $\underline{S}$ represents the additional momentum sources, which will be discussed in greater detail below, and the $-\rho\overline{\underline{U}'\,\underline{U}'}$ term is the so-called Reynolds stress tensor that requires additional model equations.

Following Cho et al [1], the CFD models developed here use the standard *k*–ε model where the turbulence is described with two additional variables *k* (turbulent kinetic energy) and ε (turbulent dissipation). This model requires the flow to be fully turbulent, which may not be the case in all areas of the air flow within the data centre, but the model is well tested and popular for flows that have complex geometries and heat transfer. Clearly, more detailed investigations into the most appropriate turbulence modelling approaches are required, however this issue is not pursued here. The two transport equations are:

$$\frac{\partial k}{\partial t} + \nabla.\left(k\,\underline{U}\right) = \frac{1}{\rho}\nabla.\left(\frac{\mu_t}{\rho_k}\nabla(k)\right) + \frac{2\mu_t}{\rho}S_{ij}.S_{ij} - \varepsilon \tag{3}$$

$$\frac{\partial \varepsilon}{\partial t} + \nabla.\left(\varepsilon\,\underline{U}\right) = \frac{1}{\rho}\nabla.\left(\frac{\mu_t}{\rho_\varepsilon}\nabla(\varepsilon)\right) + C_{1\varepsilon}\frac{\varepsilon}{k\rho}2\mu_t S_{ij}.S_{ij} - C_{2\varepsilon}\frac{\varepsilon^2}{k} \tag{4}$$

with the turbulent viscosity defined via

$$\mu_t = \rho C_\mu \frac{k^2}{\varepsilon}$$

(5)

and the S_{ij} terms are the deformation tensor. Five empirical constants ρ_k, ρ_ε, $C_{1\varepsilon}$, $C_{2\varepsilon}$, and C_μ in equations (3)-(5) are set equal to 1, 1.3, 1.44, 1.92, and 0.09 respectively (Boulet *et al* [7]).

The energy equation is also solved and takes the form:

$$\frac{\partial T}{\partial t} + \nabla.(TU) = \nabla.\left(\left(\frac{v}{\text{Pr}} + \frac{v_T}{\text{Pr}_T}\right)\nabla(T)\right) + \frac{1}{\rho C_p} S_Q$$

(6)

where T and v are the temperature and dynamic viscosity respectively and Pr is the Prandtl number defined by

$$\text{Pr} = \frac{v}{\alpha} \text{ where } \alpha = \frac{k}{\rho C_p},$$

(7)

k is the thermal conductivity and C_p is the air's specific heat transfer capacity. The subscript T indicates the turbulent flow and S_Q is the source term of the energy equation, described below.

2.2 Server rack and back door cooler modelling

The simplified data centre configuration considered is shown in Figure 1. It consists of two rows of three server racks where cold air is supplied from six floor vents into a cold aisle, passes the rack mounted IT equipment (servers), absorbs the heat generated by them, and the resultant hot air flows into a hot aisle. Many data centres recirculate the hot air that flows into the hot aisle through CRAC units that cool the air before it flows back out into the cold aisle through the supply vents. In this paper we investigate cases where liquid loop heat exchanger units are attached to the back of the servers so that the hot air is cooled before it flows into the 'hot' aisle.
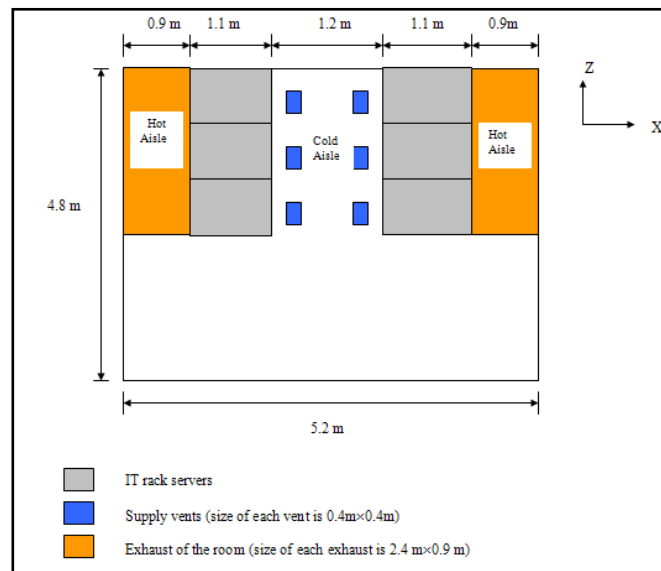
Figure 1: Plan view of three-aisle, six rack data centre

Previous CFD studies of data centre air flows that have appeared in the literature have provided very little explanation of the way the flow through server racks are modelled. These omissions make it very difficult to carry out detailed comparison with previous CFD studies.

The modelling strategy adopted here is summarised in Figure 2. The cold aisle is represented by region B, where the inlet air velocity and temperature is specified at each of the supply vents and the governing RANS, continuity, energy, k and ε equations are solved simultaneously. The region to the left of region B is composed of a server rack (rack 1), back door cooler (back door cooler 1) and a hot aisle (region A). In practice, rack 1 forms a complex geometrical obstacle to the air passing through it and the processors act as sources of thermal energy into the air stream [5]. Previous CFD studies of flow through the servers have ignored the small-scale geometric features and modelled them in a highly averaged sense [6]. In the present study we treat the rack as a porous medium by defining the following source terms in the momentum and energy equations respectively:

$$\underline{S} = \underline{\underline{K}}\,\underline{U} \quad \text{and} \quad S_Q = \frac{Q_{rack}}{V_{rack}} \tag{8}$$

where $K_{ij} = -\dfrac{\mu}{\alpha_{ij}}$ and α_{ij} are elements of the permeability tensor. The coordinate system and hence

the momentum source terms are aligned with the principal axes of the porous medium and therefore the elements in K_{ij} are zero apart from the diagonal ones, K_{11}, K_{22} and K_{33} (see [8]). Note that the momentum source term assumed here is linear; however more complex nonlinear models for porous media flows [9] can be imposed if necessary.

In equation (8) α_{11} is the permeability of the rack in the direction of flow (front to back), Q_{rack} is the rate of heat generation inside the rack and V_{rack} is the volume of the rack. The other two non-zero α_{ij} terms are set to 10^{-20} m^2 to ensure that flow is primarily through the servers from front to back. In practice, α_{11} can be estimated experimentally by measuring the pressure drop across the rack for a range of flow rates, but its value would be dependent on the type of IT equipment. The rate of energy generation by the IT equipment can be estimated at a particular server load from manufacturers' specifications. Results presented here have used an estimated $\alpha_{11} = 1.8 \times 10^{-5}$ m^2, which is calculated by equating the pressure drop in a Hagen-Poiseuille flow in a pipe whose diameter is equal to the hydraulic diameter of a typical 1U server. The heat load and the source term for each case are shown below in Table 1.

Table 1
Heat load per rack and the source term.

Heat load per rack (kW)	Source term per rack (W/m^3)
15	7102.2
25	11837
30	14204.5

Each server rack is split into four sections representing a cluster of rack servers or a blade cluster of approximately 10U. Since the air flow through the rack is aided by server fans at its rear (indicated by the left orange line in Figure 2) this is modelled by a pressure drop across the rear rack boundary, which is given as a cubic polynomial in terms of the speed of air flow normal (given by vector $\hat{\underline{n}}$) to the boundary and is based on a Comair Rotron fan [10],

$$V = \underline{U}.\hat{\underline{n}} \quad \text{and}$$

$$\Delta P = 948.4 - 131.39V + 16.2V^2 - 1.154V^3 \qquad \text{(for the three lower server clusters)}$$

$$\Delta P = 1481.87 - 164.23V + 16.2V^2 - 0.923V^3 \qquad \text{(for the upper server cluster)}$$

The relationship between the fan speed and the pressure drop can be expressed as $\dfrac{P_1}{P_2} = \left(\dfrac{N_1}{N_2}\right)^2$,

where N_1 and N_2 are the first and second fan speeds (RPM) respectively and P_1 and P_2 are static pressure (Pa) at these fan speeds respectively.

The hot air emerging from the rear of rack 1 passes into an air gap within which the same RANS, continuity, energy, k and ε equations as in region B, are solved. The air then flows into the back door cooler 1, which constitutes a further obstruction to the air flow and which is again modelled by an additional porous medium by adding the source term in equation (8). In the illustrative results presented here, the permeability values, α_{ij}, for the back door cooler are set to the same values as for the racks.

The energy removing properties of the back door cooler are modelled by treating it as a radiator which removes energy from the air stream at a rate given by

$$\dot{Q}_{bdc} = \dot{m}\, h\big(|\underline{U}|\big) A (T_{ref} - T_{air})$$

where $\dot{m}$ is the mass flow rate of air across the back door cooler, $h(|\underline{U}|)$ and A are its average convective heat transfer coefficient at airspeed $|\underline{U}|$ and cross-sectional surface area respectively, T_{air} is the temperature of the air stream and T_{ref} is the set point temperature of the back door cooler. In practice the heat transfer coefficient, h, for the back door cooler will be a function of air speed through the cooler. The required empirical relationship of the form $h(|\underline{U}|)$ can be determined by using experimental measurements of the difference between air on and air off temperatures as a function of air speed. For a fin and tube heat exchanger there is plenty of evidence that the Nusselt number (and hence heat transfer coefficient $h(|\underline{U}|)$) is a function of Reynolds number (see e.g. [11,12]). The relationship used for the CFD results presented here is based on the curve in Figure 3.

Back door cooler 1 is an example of a *passive* back door cooler since the air flow through it is not driven by mechanical means, but relies on the pressure generated by the fans of the IT equipment. Back door cooler 2, however, is an example of an *active* back door cooler which has additional fans at its rear to increase the speed of air flow through the back door cooler. Although this clearly requires additional energy to power the fans, it can be seen from Figure 4 that the increased air flow will lead to a higher average heat transfer coefficient, and hence higher heat extraction rate, from the air stream.

3   Results and Discussion

The CFD model for the server rack in a simplified data centre configuration as described above is solved using the commercial CFD package, ANSYS FLUENT 12.0.1. Within the CFD mesh, surfaces and volumes are represented using quadrilateral and hexahedral elements respectively. Results were obtained on grids using between 70000 and 420000 cells, and mesh independent results are presented here using a mesh with 87884 cells. Steady state solutions were obtained using the pressure based method for solving the governing equations using the default relaxation factors. A brief analysis of the effectiveness of both the active and passive back door coolers is presented below.
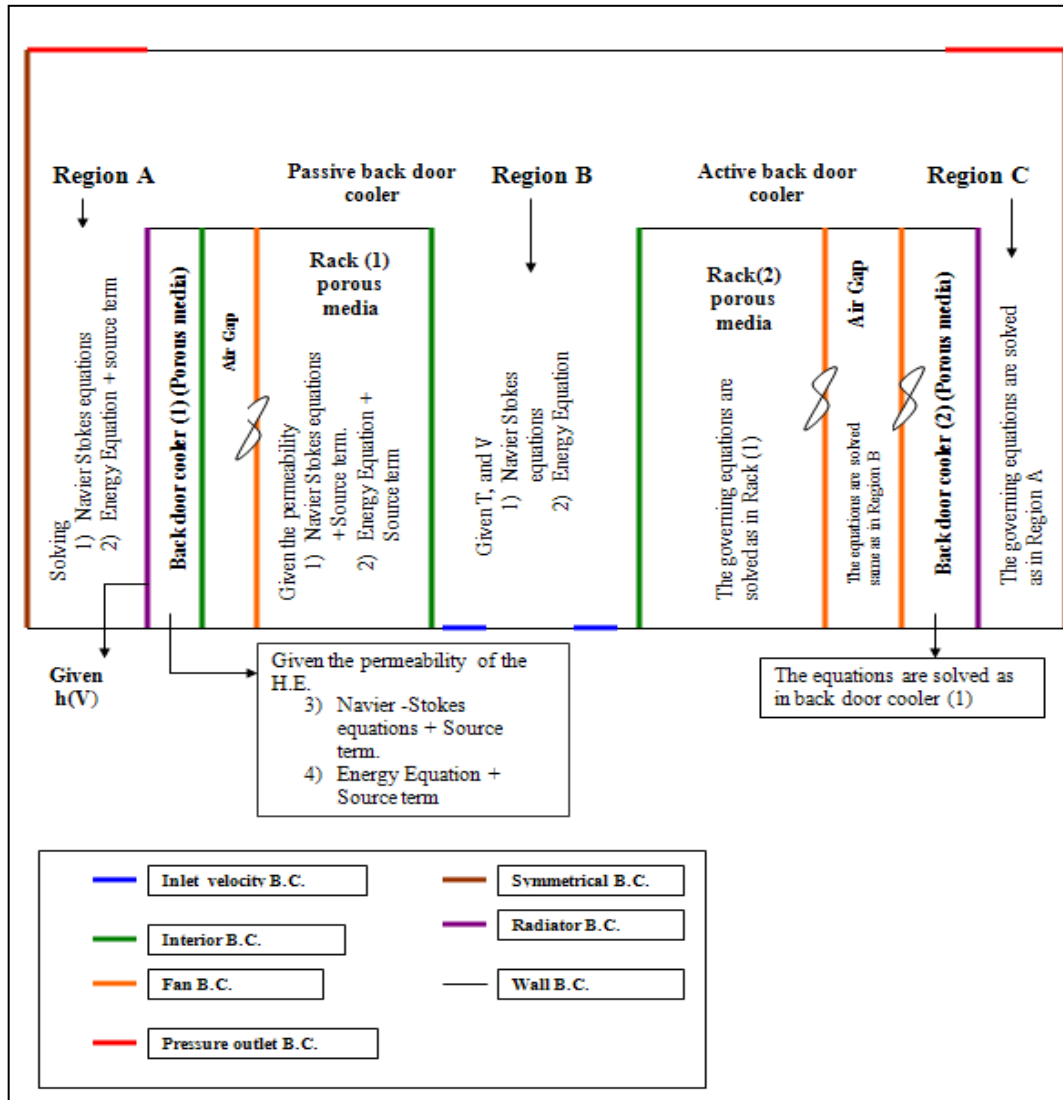
Figure 2: The solution procedure of the governing equations and the boundary condition
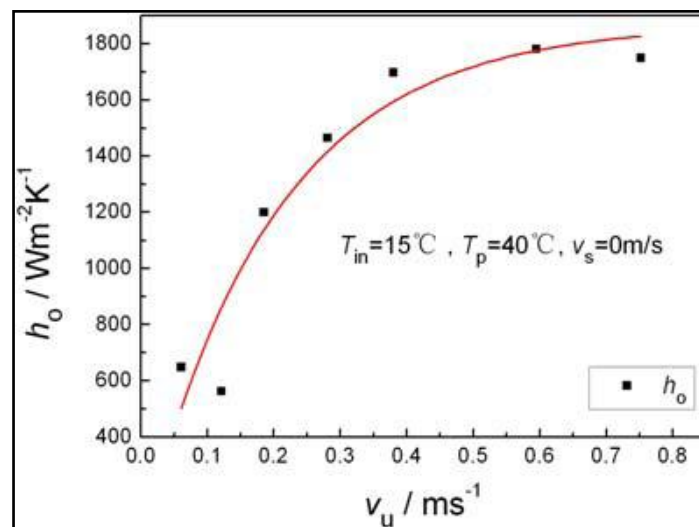
Figure 3: The air side convective heat transfer coefficient for different speed values [12]

3.1 Air flow within the data centre

Air enters the data centre via the floor vents where an inlet temperature, T_{IN}, is maintained by the CRAC unit supplying cool air to the under floor plenum. The cool air rises in the cold aisle, which is in front of the server racks and is then drawn through the server racks, where it is heated by the IT loads within the servers and then passes into the hot aisles at the back of the two rows of servers. Finally the hot air in the hot aisles is extracted via the outlet vents in the roof of the simplified data centre. Figure 4 (left) shows the air flow via colour coded velocity vectors and it is possible to see that the air speeds are greatest in front of the servers where the air is propelled into the room through the flow tiles, and in the case of active back doors, the air speeds to the rear of the server racks is increased by the additional fans in the back door cooler. Figure 4 (right) shows the corresponding temperature distribution.
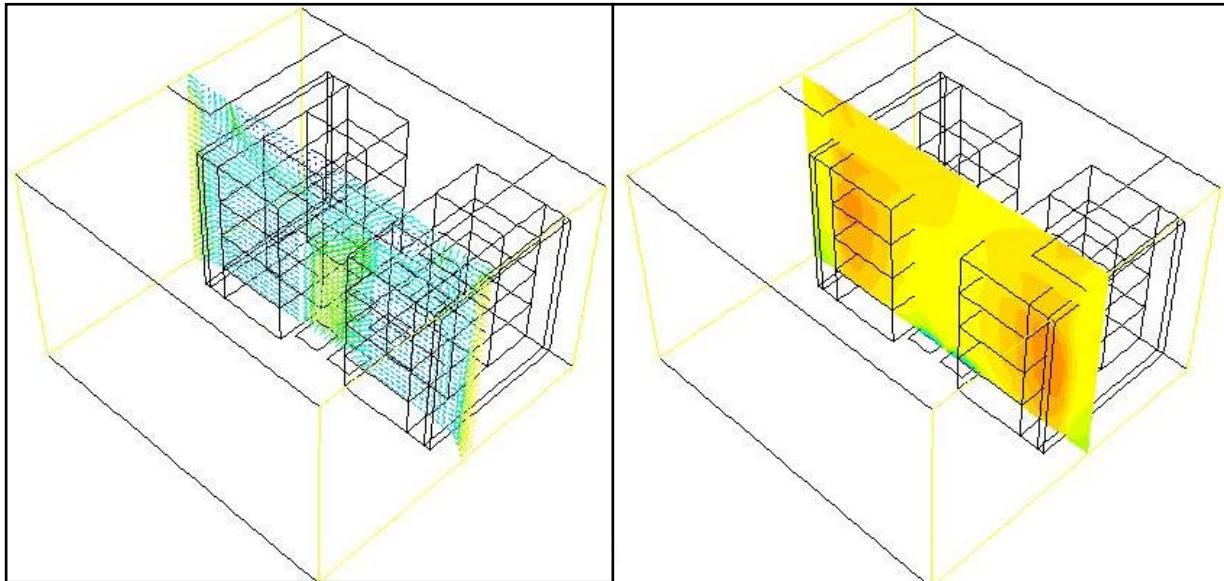
Figure 4: Velocity profile (left), colour indicates airflow magnitude with yellow being the highest speed; and temperature profile (right), blue for cool and red for hot for the active back door cooler at 30 kW.

3.2 Comparison of passive and active back door coolers.

Table 2 shows an example of how the use a back door cooler can reduce the cooling load for a CRAC unit. The data shown is for a case in which each rack adds 30kW of thermal power into the air streams. When CRAC units are used without the assistance of a back door cooler, all of the heat transferred into the air stream has to be removed by the CRAC unit, namely 180kW (6 racks at 30kW each).

Table 2
Effect of using back door coolers on the cooling load of CRAC units with six 30kW racks, where
$\dot{m}_{CRAC}$ *and* $\dot{m}_{BD}$ *are the mass flow rate through the CRAC and back door respectively.*

Configuration	Heat load on CRAC	Heat load on back door
CRAC	180 kW	0 kW
CRAC + passive	$\dot{m}_{CRAC}C_p(T_{OUT}-T_{IN})=14.5kW$	$\dot{m}_{BD}C_p(T_{B4}-T_{AFTER})=164.8kW$
CRAC + active	$\dot{m}_{CRAC}C_p(T_{OUT}-T_{IN})=11.5kW$	$\dot{m}_{BD}C_p(T_{B4}-T_{AFTER})=170.8kW$

When the passive back door coolers are used, these remove approximately 165kW from the air streams with the result that the load on the CRAC units is reduced to only 14.5kW. Finally, when an active back door cooler is used, the higher heat transfer coefficient that results from higher air speeds through it enables the load on the CRAC units to be reduced further to only 11.5kW. Clearly the precise values of these benefits will depend critically on the back door cooler specifications. The cost

benefit analysis of using liquid cooling via the back door scenarios will need to take account of the need to reduce the temperature of the water before it returns to the rear of the rack, but there are benefits in using liquid in that its specific heat capacity is much greater than air and the temperature ranges could make use of free cooling in certain geographical locations.

Table 3

The intake and exhaust temperatures (T) for both active (black curves) and passive (red curves) back door coolers for different heat loads (kW).

Heat dissipation load (kW)	Rack intake temperature	Rack exhaust temperature
15 kW		
25 kW		
30 kW		

Table 3 shows CFD predictions of the rack intake and exhaust temperatures for the passive and active back door cooler specifications described earlier, for heat dissipation rates of 15, 25 and 30kW per rack. As expected, the exhaust air temperatures leaving the active back door cooler are lower than those associated with the passive cooler. For the parameters used here, the exhaust temperatures with

the active back door cooler are typically between 1 and 2^oC less than for the passive case with a heat dissipation load per rack of 30kW.

4   Conclusions

Relying solely on air as the primary heat transfer medium in data centres is becoming increasingly problematical due to inexorable increases in power densities from IT equipment. Although CFD is increasingly being used to improve air flow design in data centres, few details of the means by which the all-important flow through server racks is modelled have appeared in the literature to date. This is an important omission since it makes comparison and validation with other studies difficult. A new CFD methodology has been developed for simulating data centre scenarios where a liquid loop heat exchanger is attached at the rear of the server racks. This enables the potential benefits of liquid back door cooling versus traditional air cooling in terms of reduced load on the CRAC units to be assessed against the need to cool the recirculating water, which could in principle be achieved by free cooling in cold climates. The additional benefits of using active versus passive back door cooling can also be assessed by comparing the further reduced load on the CRAC units against the energy needed by the active back door cooler's fans. Detailed validation of the CFD methodology is required before it can be used in practical data centre design scenarios.

References

[1]   J. Cho, T. Lim, B. Sean Kim, Measurements and predictions of the air distribution systems in high compute density (Internet) data centers, Energy & Buildings, 41 (2009) 1107-1115.

[2]   R. Cushing, J. Doherty, Next Generation Data Centres, MSC Business Development Ltd, 2009.

[3]   T.Cader, L.Westra, V.Sorel, and A.Marquez. Liquid cooling in Data Centers. ASHRAE Transactions 2009, Vol 115, pt 1, 231-241.

[4]   S.S. Anandan, V. Ramalingam, Thermal management of electronics: a review of literature, Thermal Science, 12(2) (2008), 5-26.

[5]   J. Choi, Y. Kim, A. Sivasubramaruam J. Srebric, Q. Wang, J. Lee. A CDF-based tool for studying temperature in rack-mounted servers, IEEE Transactions on Computers 57(8) (2008), 1129-1142.

[6]   S.K. Shrivastava, M. Iyengar, B.G. Sammakia, R. Schmidt J.W. VanGilder, Experimental-numerical comparison for a high-density data center: hot spot heat fluxes in excess of $500W/ft^2$, IEEE Transactions on Components and Packaging Technologies, 32(1) (2009), 166-172.

[7]   M. Boulet, B. Marcos, M. Dostie and C. Moresoli, CFD modeling of heat transfer and flow field in a bakery pilot oven, J. Food Engineering, 97(3) (2010), 393-402.

[8]   A.C. Liakopoulos, Darcy's coefficients of permeability as symmetric tensor of second rank, J. Hydrological Sciences, 10(3) (1965), 41-48.

[9]   J. Bear. Dynamics of Fluids in Porous Media. Dover Books. 1988.

[10]   [10] Comair rotron company. Fan specification based on Tarzan AC - TNE2A – 020174 (http://www.comairrotron.com).

[11] L.H. Tang, M. Zeng and Q.W. Wang. Experimental and numerical investigation on air-side performance of fin-and-tube heat exchangers with various fin patterns. Experimental Thermal and Fluid Science 33 (2009) 818–827

[12] C.S. Dai, Y.Chen, and J.Z Zhao. An experimental simulation on the heat transfer characteristics of downhole heat exchanger. 2009.

Identifying and Quantifying Energy Savings on Fired Plant Using Low Cost Modelling Techniques

Robert Tucker [a*], John Ward [b]

[a] Zerontec Energy Consultancy, Stratford-upon-Avon CV37 6PQ
[b] Faculty of Advanced Technology, University of Glamorgan, Pontypridd, CF37 1DL

* Corresponding author. Email: robertjtucker@zerontec.com; Tel./Fax. +44(0)1789 298659

Abstract

Combustion in fired heaters, boilers and furnaces often accounts for the major energy consumption on industrial processes. Small improvements in efficiency can result in large reductions in energy consumption, CO_2 emissions, and operating costs. This paper will describe some useful low cost modelling techniques based on the ZONE method to help identify energy saving opportunities on high temperature fuel-fired process plant.

The ZONE method has for many decades, been successfully applied to small batch furnaces through to large scale reheating furnaces, glass tanks, boilers and fired heaters on petrochemical plant. ZONE models can simulate both steady-state furnace operation and more complex transient operation typical of a production environment. These models can be used to predict thermal efficiency and performance, and more importantly, to assist in identifying and predicting energy saving opportunities such measures as:

- Improving air/fuel ratio and temperature controls
- Improved insulation
- Use of oxygen or oxygen enrichment
- Air preheating via flue gas heat recovery
- Modification to furnace geometry and hearth loading

There is also increasing interest in the application of refractory coatings for increasing surface radiation in fired plant. All of the techniques can yield savings ranging from a few percent upwards and can deliver rapid financial payback, but their evaluation often requires robust and reliable models in order to increase confidence in making financial investment decisions. This paper gives examples of how low cost modelling techniques can be applied to improve confidence in implementing energy efficiency improvements, whilst safeguarding manufacturing output and quality.

Keywords   heat transfer; modelling; radiation; combustion; furnaces

1   Introduction

Modelling is applied in many fields ranging from climate and weather forecasting to predicting the performance of the stock market. In the field of energy conservation on industrial processes, modelling can provide reliable assessments of the losses and the potential for improved efficiency and performance. Unfortunately, the benefits afforded by modelling are often ignored on the basis that models are too expensive or complex to apply, and that it is often simpler and quicker to rely on engineering experience and simple "rules-of-thumb". For example, application of large computational fluid dynamic programmes can involve prohibitively large expense in expertise and computing resources. However, simpler mathematical models can provide an alternative approach, which can be equally powerful when evaluating a number of alternative options for improving plant performance. Rhine [1], Mullinger [2] and Baukal [3] all describe techniques for mathematical modelling of industrial combustion plant. Many of the techniques described are based on the ZONE method first originally developed by Hottel [4].

The energy efficiency of high temperature plant can have a major impact on the unit cost of production. Often the fuel burnt in a furnace or fired heater accounts for the major source of energy consumption within a manufacturing process. Measures such as flue stack heat recovery and improvements to the insulation and controls, have to be carefully applied to ensure that product quality and productivity are not adversely affected. The potential risk to production is often used as a reason for not investing in improved energy saving measures. This paper gives examples of how low cost modelling techniques can be applied to improve confidence in implementing energy efficiency improvements, whilst safeguarding manufacturing output and quality. A general description of the ZONE modelling technique will first be described. This will then be followed by description of its application to examples of industrial furnaces and fired heaters.

2   Background to the ZONE method

To improve thermal efficiency, a furnace should be designed to ensure maximum heat is transferred to the load surface and that the heat losses through the walls and in the gases leaving the process are minimised. Thermal radiation is usually the dominant mode of heat transfer in high temperature industrial combustion equipment. Radiation is emitted from the hot combustion products on account of the CO_2 and H_2O in the combustion products, and this radiation is transmitted, reflected and absorbed within the furnace chamber. The complex interchange of radiation in a furnace can be modeled using the ZONE method.

In the ZONE method, the radiating enclosure is subdivided into a number of isothermal surface and volume elements (zones). A total energy balance is formulated around each surface or volume zone (i) which includes terms for:

- radiation leaving i
- radiation arriving at i from all other zones j in the enclosure
- enthalpy flow in and out of volume zone i due to flow of the combustion products
- heat release due to combustion in volume zone i
- convection to and from contiguous surface and volume zones

The radiation interchange is written in terms of radiation exchange factors. The net radiation flux between any two zones is proportional to these factors and to the absolute temperatures to the fourth power. The factors are a function of the geometric orientation and radiative properties (emissivities) of the zones. The radiation from the hot combustion products is a function of their emissivity. These gases are not grey and include spectrally absorbing (and emitting) bands interspersed with clear non-participating bands or 'windows' in the spectrum. In the ZONE models described in this paper, the gases are represented by the *weighted-sum-of-grey-gases* model first introduced by Hottel [4].

In its simplest form, a single gas zone can be used to represent the furnace chamber. This is often referred to as the *single well-stirred zone* (WSZ) *model*. The radiation interchange factors between a single gas zone and a load and a wall surface can be derived from simple algebraic expressions. This simple model, involves only three temperatures (combustion products, wall and load surface) and can provide a very powerful technique for evaluating energy savings.

If there is a significant temperature gradient through the furnace, such as within a continuous steel reheating furnace, then a *long furnace* (LF) *model* can be applied. This entails a series of linked well-stirred zones with for example a wall surface and a load surface surrounding each gas zone. A typical configuration of a long furnace model is shown in Figure 1.

The long furnace model simulates the temperature profile of the load as it moves through the furnace in counter-current flow to the hot combustion products. Such models are able to predict:

- The specific fuel consumption
- The flue gas temperature and losses
- The heat losses to the refractory walls and hearth

- ▪ The internal and surface load temperatures at discharge and during the heating process
- ▪ The internal wall temperatures
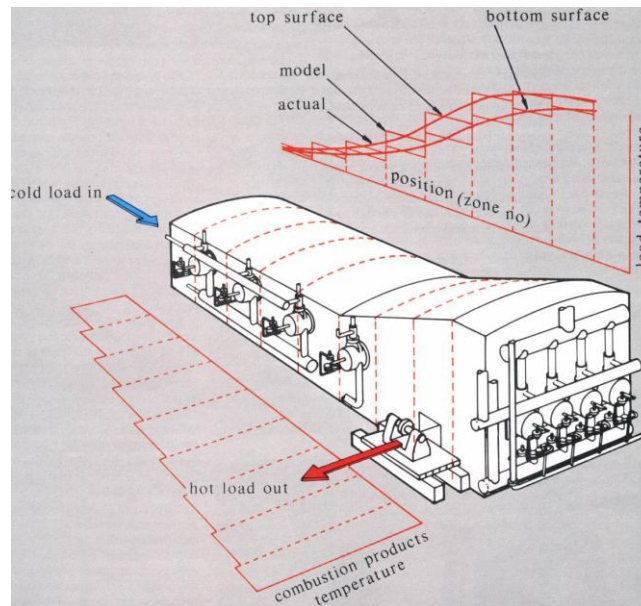
Figure 1: A long furnace model representation of a small-scale steel-reheating furnace

Both the WSZ and LF models can provide a complete heat balance on a furnace, which is often the crucial first step in identifying opportunities for fuel saving. In larger furnaces there may be considerable variations in temperature across the length, width and height of the system and in these situations multi-zone two and three-dimensional zone models may be appropriate as described by Correia [5].

Some simple examples of applications will now be described starting with the WSZ model, followed by the LF model applied to both steady-state and transient furnace applications.

3   Application of the WSZ model

The single well-stirred gas zone model provides a valuable first step to evaluate energy saving options on fuel-fired furnaces and heaters. A version has been developed in Visual Basic, which requires negligible computing resources. The model only requires the wall and load surface areas and the chamber volume to be specified. The radiation interchange between the gases and load plus any convective heat transfer is calculated, and the fuel input rate is derived which satisfies the following energy balance equation on the furnace:

Heat in fuel + Heat in air = Heat to load + Heat loss in flue gases + Heat loss through walls

3.1   A small continuous furnace

Predictions for a natural gas furnace of hearth area 5 x 5m and height 2m were prepared. The base case assumed an excess air level of 25% with an exhaust gas temperature of 1250°C, and a load surface temperature of 900°C. The model predicts a thermal efficiency of 29.6% net. This may be representative of a steady-state metal heat treatment or metal melting application. The WSZ model was applied to evaluate a number of energy saving opportunities. The results are shown in *Table 1*.

The priority should be to reduce the excess air level, if this can be done without detriment to the safe operation of the plant, emissions or to product quality. Controlling excess air may be achieved though better burner air-fuel ratio control, or by preventing air ingress into the furnace by pressure control and sealing of gaps and doors. The fuel saving achieved, then reduces the cost of subsequent measures. For example if recuperation is applied, the size and installed cost of the equipment is reduced because smaller heat exchangers can be used.

Table 1
Prediction of fuel saving opportunities on a small continuous furnace

	Flue gas O_2 % dry	O_2 conc. v/v %	Air preheat T ^{o}C	Exhaust gas T ^{o}C	Fuel input kW_{net}	Efficiency %$_{net}$	Fuel saving %
Base case[1]	4.6	21	15	1250	6049	29.6	-
Reduced xsa[2]	1.1	21	15	1243	4578	39.1	24.3
Recuperator[2]	1.1	21	383	1243	3427	52.3	43.3
Regenerator[2]	1.1	21	875	1243	2512	71.4	58.5
Oxy-enriched	1.1	25	15	1236	3729	48.1	38.4
Oxy/gas	1.1	95	15	1216	2224	80.7	63.2

[1] Excess air = 25% ; [2] Excess air reduced to 5%

On high temperature plant, where flue losses are significant, oxygen enrichment or oxy-gas firing can achieve substantial savings. The cost savings in reduced fuel consumption has to be greater than the cost of supplying the oxygen. Hence, it is important to minimise fuel consumption before applying oxygen. In this example, oxygen has been supplied at a rate that gives the same flue gas oxygen concentration (1.1%). The level has to be set to ensure safe operation of the plant. In the oxy/gas case above, a total of 0.049 kg/s of natural gas is saved by supplying 0.177 kg/s oxygen. To break even, the cost/kg of oxygen must be less than 27% of the cost/kg of natural gas. The same break even cost ratio applies for the oxygen enriched combustion case.

In the case of reducing excess air or applying oxygen, the predicted flue gas temperature is reduced because the radiant emissivity of the gases is improved (owing to the high concentrations of CO_2 and H_2O).

3.2 A fired heater

Fired heaters account for the major energy consumption and carbon emissions on refineries and petrochemical plant. They usually comprise a high temperature radiant box in which combustion occurs. The hot gases radiate to a series of tubes containing high-pressure hydrocarbon fluids. On most large fired heaters, the hot flue gases leaving the radiant section are passed across a convective tube bank to further heat the hydrocarbon fluids.. On modern plant the heat in the flue gases may then be further recovered to preheat the combustion air or to generate steam.

Safety is critical in these applications because of the serious consequences in the event of a release of high-pressure feedstock. The temperature at the top of the radiant section is often referred to as the bridge wall temperature (BWT). During operation, this must be maintained below a certain value to avoid overheating and potential failure of the tubes.

A schematic of a typical fired heater with convective tube bank and air preheater is shown in Figure 2.

Over the last three decades, there has been a considerable interest in the application of coatings on the refractory walls of fuel-fired furnaces for energy savings. It is claimed that these special coatings raise the emissivity of the surface and improve the radiative heat transfer and hence the thermal efficiency of the process. Products under various brand names are commercially available and can be applied by trowel or spray gun to the surface of hard face refractory or ceramic fibre walls. However, energy savings claims resulting from these products are often difficult to verify because of the variable nature of plant operation. It has also been difficult to forecast the savings on different applications because most thermal design models for heat transfer in furnaces fail to show any influence of wall emissivity. This is due to the limitations of most models rather than the capability of the coating products.
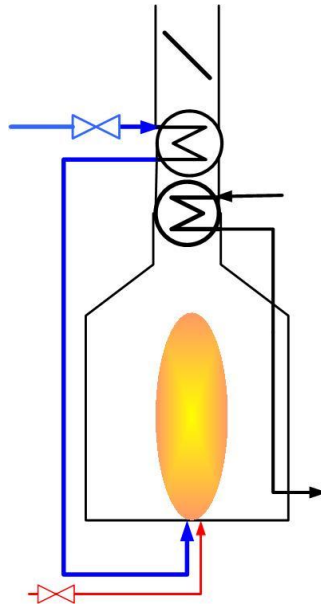
Figure 2: A schematic arrangement of a typical fired heater

Docherty [6] and Elliston [7] independently showed that if the combustion products are assumed to be grey, then changing the wall emissivity in an enclosed furnace, has no effect on overall predicted heat transfer. This is because in general, for an adiabatic wall, these simple models do not distinguish between radiation that is absorbed and re-radiated, and radiation that is reflected at the wall surface. By introducing a non-grey gas to represent more realistically the combustion products in the furnace, both authors identified improvements when emissivity was raised. The radiation model used in the ZONE method uses a non-grey gas combustion model (the *weighted sum of grey gas model*) and is therefore able to predict the increase in radiant heat transfer with surface emissivity.

A WSZ model has been applied to simulate the heat transfer enhancement in the radiant section of a typical fired heater. The heater parameters are:

Fuel type:	Natural gas
Excess air:	20%
Thermal input:	6907 kW_{net}
Tube area:	110m^2
Exposed wall area:	152m^2
Radiant section load:	3187 kW
Convection section load:	3098 kW

The flue gas temperature downstream of the convection section is 162°C and flue losses represent just 7.1% of the net thermal input.

The wall emissivity in the model was then changed from 0.5 to 0.93 to simulate application of a high emissivity coating. The results are shown in *Table 2*. In Case 1, the total process load is held constant, and the model predicts the fuel saving. A negligible saving is predicted. This is because the heater is already running at over 90% net thermal efficiency, and so there is little additional energy available to extract from the combustion products. However, the model is able to predict a potential increase in productivity, which could have a significant impact on overall plant performance. In case 1 the model predicts a reduction in BWT of 15°C, which results from the improved radiative heat transfer. There is a small increase in heat transfer in the radiant section. The model can be applied to determine the increase in thermal duty that could be achieved if the BWT were restored to 1000°C (Case 2). This assumes that the convection section is also enlarged to maintain the same heat recovery effectiveness. In this case the production can be increased by 12% without exceeding a BWT of 1000°C. In practice

it may not be feasible to enlarge the convection section. In this case, the flue gas temperature downstream of the convection bank will increase, resulting in a loss of efficiency. However, production is still predicted to increase by over 6%.

Table 2
The predicted performance of a fired heater with a high emissivity wall coating

CASE	ε = 0.5		ε = 0.93	
	Base case	1	2	3
	Base case	Const.Q process	Constant Bridge wall T Fixed convection section effectiveness	Constant Bridge wall T Fixed convection heat transfer
Flue gas T, ^{o}C	163	161	163	258
Bridge wall T, ^{o}C	1000	985	1000	1000
Fuel input kWnet	6907	6903	7713	7713
Qrad, kW	3187	3245	3574	3574
Qconv, kW	3094	3038	3455	3097
Qwall, kW	132	132	133	133
Qflue, kW	495	488	552	910
Qprocess, kW	6281	6283	7028	6671
Production increase %			11.89%	6.21%
Efficiency overall %	90.94%	91.02%	91.12%	86.49%

4   Application of the long furnace ZONE model

The ZONE method lends itself well to modelling continuous steel reheating furnaces. The simple zoning arrangement of a LF model represents well the longitudinal temperature profile created by the directional flow of steel through the furnace. A transient version of the LF model can be very useful since most furnaces operate under non-steady-state conditions with variable throughput, changes in load size and scheduled and unscheduled breaks in production. In these models, which are described in detail by Rhine [1], the transient conduction into both the steel billets and the refractory hearth and walls are calculated.
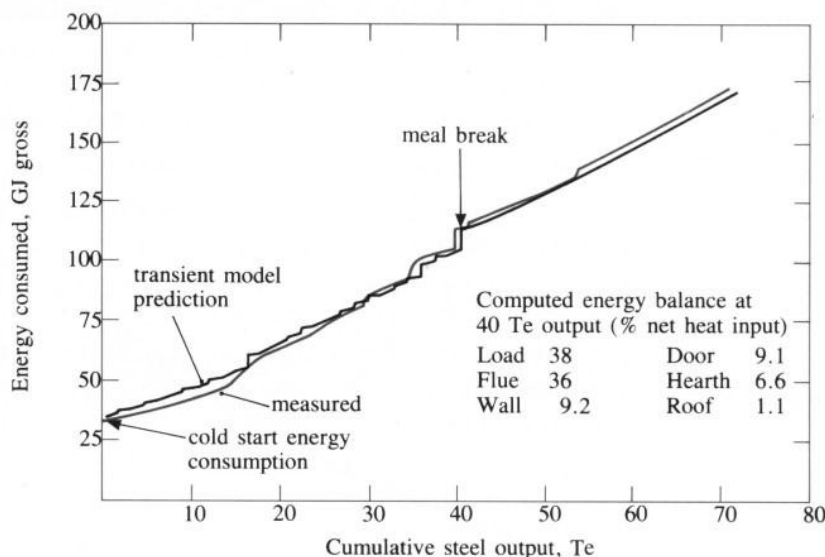
Figure 3: Predicted and measured energy consumption on a continuous steel reheating furnace

The approach has been validated against operating data from a steel-reheating furnace. A comparison of predicted and measured energy consumption is presented in Figure 3.The plant was monitored and

simulated from a cold start, and included a scheduled break in production. As can be seen the predicted consumption closely follows the actual measured values through the trial.

Two applications of these models for steel reheating will now be described.

4.1   A small forging furnace

Figure 4 is an example of a small forging furnace used to reheat 150mm diameter steel bars to 1150°C. There are many similar furnaces used in industry for reheating steel and non-ferrous metals for rolling, forging or heat treatment applications. This study is based on a small furnace in Belarus. The original specification is detailed in *Table 3*. Since this furnace is used in a semi-continuous manner, with repeated cold starts every day, a transient long furnace model was applied [1]. This model simulates the start-up of the furnace from cold. Under such conditions the heat stored in the refractory walls can represent a significant energy loss.

The furnace was represented by an 11-zone LF model with zones of length 0.36m. A time step of 5 seconds was applied to simulate the operation from cold. After 150 minutes, production is simulated with billets leaving from the hot zone 1 and cold billets entering zone 11. The thermal input is modulated to simulate temperature control to maintain furnace roof temperature in zone 1. To maintain desired output, a roof set point temperature of 1220°C was required.

Table 3
Specification of the small forging furnace

Load details:	Size	150mm dia x 280mm length
	Weight	38.6 kg
	Material	Carbon steel
	Output temperature	1150°C
	No.of billets in furnace	22 (850kg)
	Throughput	1000 kg/hr
Furnace construction:	Length	4.1m
	Width	0.93m
	Hearth	Dense refractory brick 2600kg/m^3
	Walls and roof	Insulating firebrick 860 kg/m^3
Burner:	Number	3
	Total max thermal input	54m^3(s)/hr
	Excess air	5%
	Air preheat	285°C
Production schedule:	2.5 hrs to start of forging	
	16 hours production	

Five simulations were carried out as follows:

1) A base case simulation according to current furnace. Unfortunately, there was no metered data so it was not possible to establish the reliability of the predictions.
2) Simulation with the walls and roof replaced with lightweight ceramic fibre.
3) Repeat of case 1) with an improved flue gas recuperator (heat recovery effectiveness increased to 50%)
4) Repeat of case 2) with improved flue gas recuperator
5) Base case but with a single recuperative burner installed at hot end (replacing all existing burners). Flue gas pull back to recuperator = 60%; 40% of combustion products go onto the existing flue.
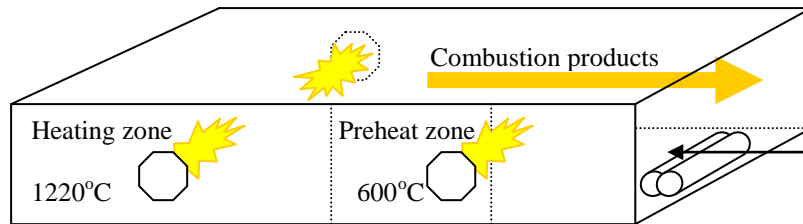
Figure 4: A schematic of the small forge furnace

The predicted results are shown in *Table 4*. T_b is the steel discharge temperature and ΔT is the predicted temperature difference in the steel billet.

Table 4
Predicted results for the forge furnace

Case	Condition	Overall SFC GJ/Te$_{net}$	Saving %	Steady-state SFC GJ/Te$_{net}$	Tb ^oC	ΔT ^oC	kg/hr	eff%$_{net}$
1	Base case	1.728	-	1.39	1154	70	982	53.75%
2	CF walls	1.539	10.94%	1.29	1151	71	983	57.89%
3	Recup 50%	1.467	15.10%	1.19	1156	71	982	62.71%
4	CF walls + Recup 50%	1.33	22.92%	1.19	1154	73	982	62.71%
5	Recuperative burner	1.51	12.50%	1.29	1151	150	836	57.89%

The overall Specific Fuel Consumption (SFC) is the fuel consumption over the entire simulation divided by the tonnes of steel discharge. It includes the energy to start the furnace from cold. The steady-state SFC is based on the last hour of continuous operation and hence is lower.

As can be seen from these predictions, the largest single fuel saving (~15%) is achieved by installing an improved flue stack recuperator (Case 3). Replacing the walls with ceramic fibre gives a fuel saving of around 11%. Combining these options (Case4) gives a saving of ~23%. The preferred option financially is dependent on the cost of installation. However, the model provides reliable prediction of the running cost savings which can be used to derive the financial payback of each option.

The model has also shown that in this application, installing a recuperative burner, although giving a 12.5% fuel saving, may lead to excessive temperature differences in the billets, which may seriously reduce forging quality. This results from the change in heat flux profile along the hearth. Also, the furnace throughput is reduced. This demonstrates how a model can help avoid bad investment decisions.

4.2 Application of heat recovery on a steel reheating furnace

The above application demonstrated how a recuperative burner could lead to poor performance. There are many applications where recuperative and regenerative burners can yield very significant performance benefits. Using a steady-state LF model, a simple study was carried out to compare different options for flue gas heat recovery on a continuous natural-gas fired steel reheating furnace, against performance with no heat recovery. These options were:

- Use of a flue stack recuperator (40% effective)
- Use of regenerative burners with an effectiveness of 70%

The furnace is 18.6m in length and heats steel bars of thickness 88mm to 1100°C with a throughput of 70 Te/hour. The furnace was modelled using a 10-zone LF model. Burners are distributed along the length of the furnace in order to ensure that the steel is adequately 'soaked' before discharge. The original firing profile as shown in the first row in *Table 5* was applied in the model and this predicted a steel temperature distribution through the furnace as shown in Figure 5 resulting in a (top to bottom) temperature difference in the steel at discharge of 56°C. The model was then applied to predict the performance benefits of the different heat recovery options. In the regenerative burner case, 80% of the flue gases are pulled back into the burner to preheat the air. The remaining 20% of products travel to the main flue stack. The firing profile and burner locations had to be adjusted as shown in *Table 5* to ensure that billet temperature difference at discharge was not adversely affected.

Table 5
The assumed firing profiles in a continuous steel reheating furnace

	Zone number (1= discharge zone)								
	1	2	3	4	5	6	7	8	9	10
Base case	7%	0%	50%	43%	0%	0%	0%	0%	0%	0%
End recuperator	7%	0%	50%	43%	0%	0%	0%	0%	0%	0%
Regenerative burner	7%	0%	0%	18%	25%	25%	0%	25%	0%	0%
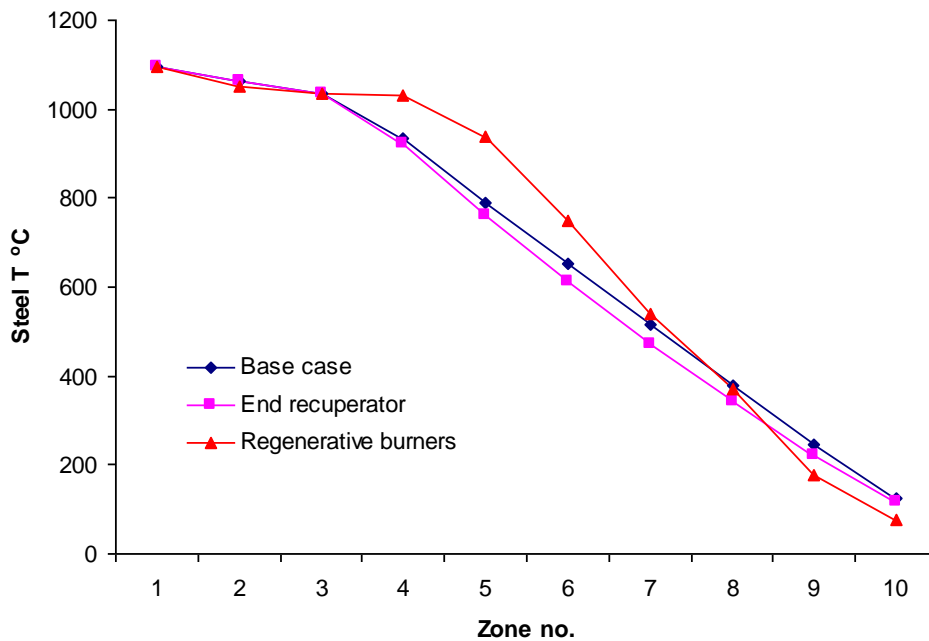
Figure 5: The predicted steel temperature distribution through the furnace

The predicted efficiencies and steel temperature differences are given in *Table 6* below:

Table 6
The predicted results for a continuous steel reheater

	Efficiency %gross	Fuel/Carbon saving %	ΔT $^{\circ}$C
Base case	48.2	-	56
End recuperator	62.8	23.2	59
Regenerative burners	65.9	26.9	51

This final choice depends on the installed cost of an end recuperator compared to installing regenerative burners.

5   Conclusions

This paper has shown how low cost mathematical models based on the ZONE method for computation of radiation exchange in enclosures can be applied to evaluate fuel saving opportunities on a range of high temperature plant. In many applications there are often several opportunities that could be applied. It is important to identify low cost, fast pay-back options that should be given priority. These can then reduce the cost of more expensive solutions. This is demonstrated on a simple furnace where reducing the excess air is given priority. This then reduces the cost of more expensive measures such as flue gas heat recovery or application of oxygen to the combustion process.

In certain situations, fuel saving measures may lead to unexpected reduction in throughput or product quality. When heating thick material such as steel billets or slabs, any impact on the heat flux profile and temperature distribution in the steel has to be carefully evaluated before investment is made. Steady-state and transient long furnace ZONE models can be usefully applied to such situations.

The ZONE model has also been further developed recently to simulate more accurately the spectral absorption and emission bands due to CO_2 and H_2O in the combustion gases [8]. This was then applied to predict the effects of wall emissivity on furnace efficiency. The fuel savings were increased compared to those predicted using the simpler weighted sum of grey gases model.

The ZONE method can also be applied to more complex 2- and 3-dimensional problems. A 3-dimensional ZONE model has recently been applied to simulate different low NOx firing strategies on a glass-melting furnace [9]. Data on the complex flow and combustion fields were provided by computational fluid dynamic simulations and by the use of physical models – in this case using the acid-alkali technique to simulate fuel/air mixing.

References

[1] Rhine J.M. & Tucker R.J. Modelling of gas-fired furnaces and boilers, Mcgraw-Hill, 1990.
[2] Mullinger P. & Jenkins B. Industrial and Process Furnaces, Elsevier, 2008.
[3] Baukal C.E. & Schwartz R.,The John Zink Combustion Handbook CRC Press, 2001
[4] Hottel H.C. & Sarofim A.F. (1967) Radiative Transfer, McGraw Hill
[5] Correia S.A.C, Ward J., Sousa J.L.V.A., "Numerical Prediction of the Transient Operation of a Gas-Fired Reheating Furnace", Proc. ASME Heat Transfer Division, HTD-vol 367, pp 87-94, 2000.
[6] Docherty P. & Tucker R.J. (1985) The influence of wall emissivity on furnace performance, J.Inst.Energy, **59**, pp 35-37.
[7] Elliston D.G., Gray W.A. Hibberd D.F., Ho T-Y, Williams A. (1987), The effects of surface emissivity on furnace performance, J.Inst.Energy, **60**, pp 155-167.
[8] Ward J., Tan C.K., Tucker R.J., Development of a spectral radiation model to predict the transient performance of a metal reheating furnace, Proc. ASME International Mechanical Engineering Congress (2009).
[9] Fricker N., *et al*, "A Multimode Modelling Approach for NOx Reduction on Gas-Fired Glass Melters Through Flame/Furnace Matching", Proc. 16th IFRF Members Conference, - Combustion and Sustainability: New Technologies, New Fuels, New Challenges, Boston, USA, 13 pp., June 2009.

Section 3

Thermal Power

The Effect of Hydrogen Containing Fuel Blends upon Flashback in Swirl Burners

Nicholas Syred[®]*, Mohammed Abdulsada, Tim O'Doherty, Phil Bowen

Gas Turbine Research Centre, Cardiff University, CF24 3AA, United Kingdom

*Corresponding author. E-mail: syredn@cardiff.ac.uk; Tel.+44(0)2920874318

Abstract
Lean premixed swirl combustion is widely used in Gas Turbines and many other combustion Processes due to the benefits of good flame stability and blow off limits coupled with low NOx emissions. Although flashback is not generally a problem with natural gas combustion, there are some reports of flashback damage with existing gas turbines, whilst hydrogen enriched fuel blends, especially those derived from gasification of coal and/or biomass/ industrial processes such as steel making, cause concerns in this area. Thus, this paper describes a practical experimental approach to study and reduce the effect of flashback in a compact design of generic swirl burner representative of many systems. A range of different fuel blends are investigated for flashback and blow off limits; these fuels mixes include methane, methane/hydrogen blends, pure hydrogen and coke oven gas. Swirl number effects are investigated by varying the number of inlets or the configuration of the inlets. The well known Lewis and von Elbe critical boundary velocity gradient expression is used to characterise flashback and enable comparison to be made with other available data.

Two flashback phenomena are encountered here. The first one at lower swirl numbers involves flashback through the outer wall boundary layer where the crucial parameter is the critical boundary velocity gradient, G_f. Values of G_f are of similar magnitude to those reported by Lewis and von Elbe for laminar flow conditions, and it is recognised that under the turbulent flow conditions pertaining here actual gradients in the thin swirl flow boundary layer are much higher than occur under laminar flow conditions. At higher swirl numbers the central recirculation ZONE (CRZ) becomes enlarged and extends backwards over the fuel injector to the burner baseplate and causes flashback to occur earlier at higher velocities. This extension of the CRZ is complex, being governed by swirl number, equivalence ratio and Reynolds Number. Under these conditions flashback occurs when the cylindrical flame front surrounding the CRZ rapidly accelerates outwards to the tangential inlets and beyond, especially with hydrogen containing fuel mixes. Conversely at lower swirl numbers with a modified exhaust geometry, hence restricted CRZ, flashback occurs through the outer thin boundary layer at much lower flowrates when the hydrogen content of the fuel mix does not exceed 30%. The work demonstrates that it is possible to run premixed swirl burners with a wide range of hydrogen fuel blends so as to substantially minimize flashback behaviour, thus permitting wider used of the technology to reduce NOx emissions.

Keywords   flashback; swirl burner; lean premixed; hydrogen

1   Introduction
Lean premixed (LP) combustion is a widely used strategy to decrease undesirable emissions in gas turbines. In LP systems, fuel and air are mixed prior to the combustion chamber to promote mixing, combustion efficiency, uniform temperatures and low NOx. Swirl combustors are almost universally used in some form or other in gas turbine **[1,2]** and numerous other systems. Especially when operated in a LP mode many problems can be encountered including blow off and flashback **[3-5]**.

Using alternative fuels has becomes another option to reduce emissions of CO_2. Hydrogen, hydrogen and other fuel blends can cause major issues with many swirl combustors, because of the considerable variation in flame speed with such fuel blends compared to natural gas. Similar comments apply to process gases such as Coke Oven gas (COG) widely produced in the steel industry. Biomass and coal gasification prototype power plants have performed well, but have not proved to be competitive against conventional boiler technology for power production **[6-8],** primarily

because gas turbine manufacturers have had full order books for conventional units. Demand for systems capable of economically and efficiently producing power and CO_2 for sequestration may well change this. There are many other problems associated with the use of alternative fuels as discussed in **[9]**.

Basically, swirling flows are defined as a flow undergoing simultaneous axial-tangential vortex motion. This flow motion can be generated using swirl vanes or many other methods **[10, 11]**. The main desirable characteristic of swirl combustors is the formation of unattached reverse flow zones (RFZ) and central recirculation zones (CRZ) capable of recycling hot chemically active reactants to substantially enhance flame stability **[5]**. The swirl number (S) is one of the main parameters used to characterize swirling flow. It is defined as the ratio of axial flux of swirl momentum divided by axial flux of axial momentum, divided by the equivalent nozzle radius **[4].** Commonly owing to flow complexities a geometric swirl number (S_g) is used which depends entirely on the geometry of the burner.

Flashback is a problem which has arisen when using LP combustors especially with hydrogen based fuel mixtures. Flashback occurs when the gas velocity becomes lower than the burning velocity due to flame propagation within boundary layer, core flow or because of combustion instabilities **[3, 12-14]**. One important manifestation of the flashback phenomenon is that due to flame propagation in the low velocity region of wall the boundary layer. Flame propagation is thus limited by quenching in the very near wall region **[14]**; for turbulent flow this will be the laminar sub layer. Lewis and von Elbe **[15]** have suggested use of the critical boundary velocity gradient, based on considerations of the velocity gradient G_f at the wall, the laminar flame speed S_L and the quenching distance *dq* ,

$$G_f = \left[\frac{\partial u}{\partial r}\right]_{wall} \lessapprox \frac{S_L}{d_q} \tag{1}$$

Flashback can also occur because of turbulent flame propagation in the core flow. Combustion instabilities have a very considerable effect on system dynamics and can cause flashback due to non-linear interaction of pressure fluctuations, hence periodic heat release and non linear flame propagation **[16].**Finally , flashback in swirl burners can be caused by a phenomena termed combustion induced vortex breakdown (CIVB) due to rapid expansion at the burner exit creating a recirculation zone which acts as a flame holder: the breakdown of this structure can occur due to flow perturbations and chemical reaction effects causing the CRZ and hence flame to propagate upstream into the premixing zone **[17, 18]**

2   Experimental setup

The generic swirl burner was used to examine flame stability limits at atmospheric conditions (1bar, 293K). The was designed and assembled at Cardiff University's Gas Turbine Research Centre (GTRC). A single tangential inlet feeds an outer plenum chamber which uniformly distributes premixed air/fuel to the inserts, eventually into the burner body. A central fuel injector extended through the whole body of plenum and the insert burner. Principally, the fuel injector is used to produce both non-premixed and partially premixed flames; its position is shown in Figures 1 and 2. This simulates many industrial applications where liquid fuels are sprayed through a central fuel injector

Figure1: Exploded view of Swirl Burner
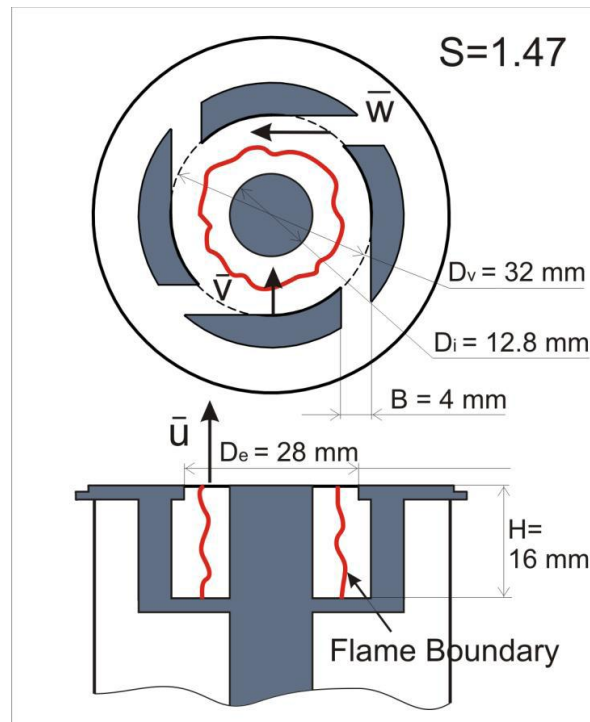
Figure 2: Schematic diagram of Internals of Swirl Burner

Three swirl numbers have been used in the experiments, with the only change in the system being in the exhaust insert with tangential inlets which force flow into the swirl chamber, then exhaust. Three inserts are used with different swirl numbers, achieved by changing the number, length and width of the tangential inlets. The three swirl burners have swirl numbers of : S_I=1.47, S_{II}=1.04, S_{III}=0.8. Based on other work [10, 22] an exhaust nozzle extension 0.5De long was added to the exhaust of two of the inserts. The fuel injector was left in the same position Swirl insert III is very similar to II the only differences lying in the width of the tangential inlets, 5 as opposed to 4 mm (9 inlets used). Swirl insert 1 only has 4 inlets, but operated at a significantly higher swirl number of 1.47, Figure 2. Coriolis flow meters have been used simultaneously to measure the mass flow rate of both fuel and air separately.

3   Results and discussion
Three swirl burners plus five different fuels has been used to establish results, these are summarized in *Tables 1* and *2* below:

Table 1
Swirl Burners and their specifications

Swirl Burner name	I	II	III
Geometrical swirl number	1.47	1.04	0.8
Exhaust Sleeve 0.5 De long	NO	Yes	Yes

Table 2
Fuels Blends and their composition

Fuel Name	%CH_4	%H_2	%CO	%N_2	LHV [MJ/kg]	$T_{max\ adiabtic}$ [K]
Pure Methane	100	0	0	0	50.1	2237
Pure Hydrogen	0	100	0	0	126.1	2406
15%H_2	85	15	0	0	51.6	2245
30%H_2	70	30	0	0	53.7	2253
Coke Oven Gas	25	65	6	4	54.2	2300

Typically the pressure loss coefficient at S_{II}=1.04 is nearly half that at S_I=1.47 and again is about 20% lower again at S_{III}=0.8. Lower pressure drop is a major advantage to designers and operators of gas turbines and other large burners and thus there is a drive to use lower Swirl Numbers, providing the flame stability advantages of the CRZ are not lost. Coke oven gas has been used as a representative process industry fuel gas, which is widely available at steelworks and has the potential to be widely used in power generation in process industry, providing appropriate efficient reliable technology can be developed to utilise it. The system has been tested on a wide range of fuel blends as shown below, *Table 2*. Up to 15 combinations of swirl burner and fuel gases have been used to investigate their effects on the flashback and blow-off characteristics. Fuel characteristics are interesting as they show similar lower heating values and adiabatic flame temperatures. The exception is pure hydrogen with much higher lower heating value, but adiabatic flame temperature about ~100K higher than coke oven gas.

(a) SI=1.47

(b) SII=1.04

(a) SIII=0.8
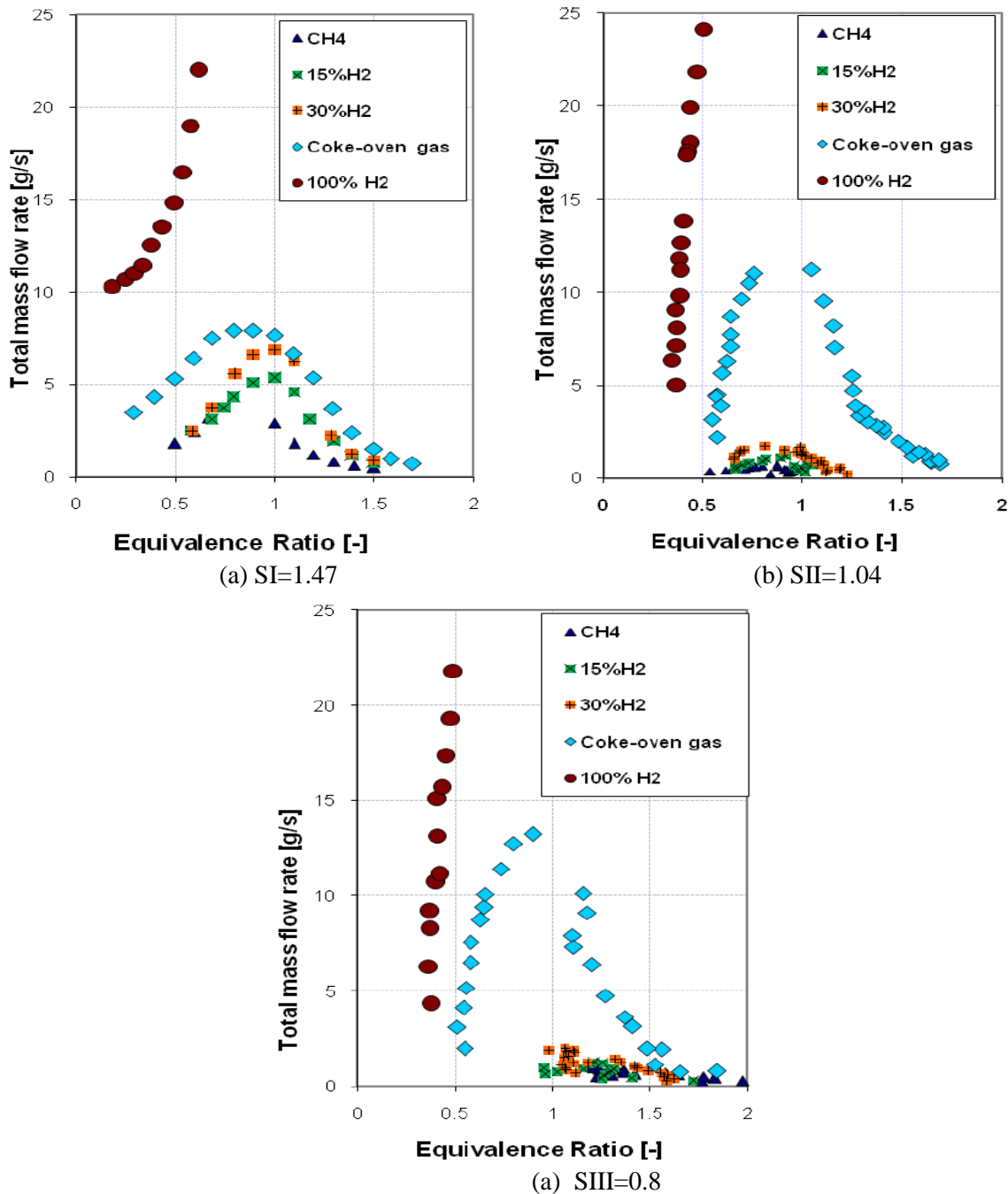
Figure 3: Flashback Limits of the Generic Swirl Burners with three different Swirl Numbers for 5 different fuels. Note: The area under the curve for each fuel is the flashback region, here stable combustion may occur undesirably inside the burner.

Three families of flashback curves are shown in Figure 3 above, one for a swirl number of S_I=1.47, Figure3a, the other at a swirl number S_{II}=1.04, Figure3b and Figure3c for S_{III}=0.8.
Associated flame photographs at conditions just before flashback for pure methane are shown in figures 4a (S_I=1.46) and 4b (S_{II}=1.04).

The comparison is extremely interesting whilst other analysis has revealed different flashback mechanisms for the different swirl numbers [11, 22]. With S_I=1.47 the central recirculation zone (CRZ) extends over the central fuel injector to the base plate for all fuels, with an associated flame front on the CRZ boundary. This is illustrated in Figure2 (and does not happen with S_{II}= 1.04 and S_{III}= 0.8). Flashback occurs when the radial velocity in the swirl level drops to such a level that the near radial flame front can flashback to the inlets and often into the plenum chamber. Conversely with S_{II}=1.04 and S_{II}=0.8 flashback occurs by a different mechanism via flashback in the outer wall boundary layer of the exhaust nozzle, then being controlled by the critical boundary velocity gradient [11, 22] as defined by Lewis and von Elbe [15].

In terms of flashback limits for methane and methane containing up to 30% hydrogen a value of S_{II}=1.04 and S_{III}=0.8 produces flashback which occurs at a mass flow (and hence velocity levels) up to 1/3 of those found for S_I=1.47 for a wide range of equivalence ratios. However with coke oven gas (COG) different effects start to appear as the hydrogen content of the fuel increase beyond 50%. For Swirl Numbers of 0.8 and 1.04 flashback performance is better than S=1.47 for values of equivalence ratio up to 0.6 to 0.65 and mass flows of ~ 7 g/s. Beyond this point for equivalence ratios > 0.65 and < 1.2 a Swirl Number of 1.47 is better by up to 50%. However for LP combustors the aim is to operate around an equivalence ratio of ~ 0. 7 or less and thus this is not a disadvantage. However comparison of the three Swirl Number cases, Figure3 shows that there is a significant change in flashback behaviour moving between a fuel with 30% hydrogen content to one with 65% hydrogen content as with COG. Moving onto the pure hydrogen results similar trends were evident, although the range of equivalence ratios tested was restricted to being below 0.5 and above 2 due to the very large hydrogen and air flow rates required.

More detailed inspection of the results for S_{II}=1.04 and S_{III}=0.8, showed generally both swirlers have virtually identical trends and values with differences being within experimental limits. S_{III}=0.8 is preferred as it gives lower pressure drop.
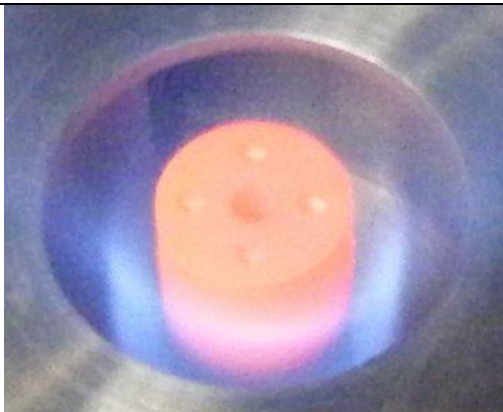
| Figure 4(*a*): Photo of flame surrounding central fuel injector at S_I=1.47, just before radial flashback | Figure 4(*b*): Photo of flame just before flashback through outer wall boundary layer, S_{II}=1.04 |

Another interesting fact of the results was that the peaks of the flashback curves all occurred at weak equivalence ratios as opposed to the expected just on the rich side of stoichiometric. This effect is thought to be due to changes in the recirculation zone occurring as the equivalence ratio approaches 1.

This is also illustrated by Figure5 where all the methane data has been plotted as a function of critical boundary layer gradient at flashback, G_f; also included is laminar data on natural gas. The swirl burners at S_{II} =1.04 and S_{III}=0.8 are flashing back at lower values of G_f than the laminar results (albeit at a higher pressure drop), whilst for S_I=1.46 values of G_f are significantly higher.
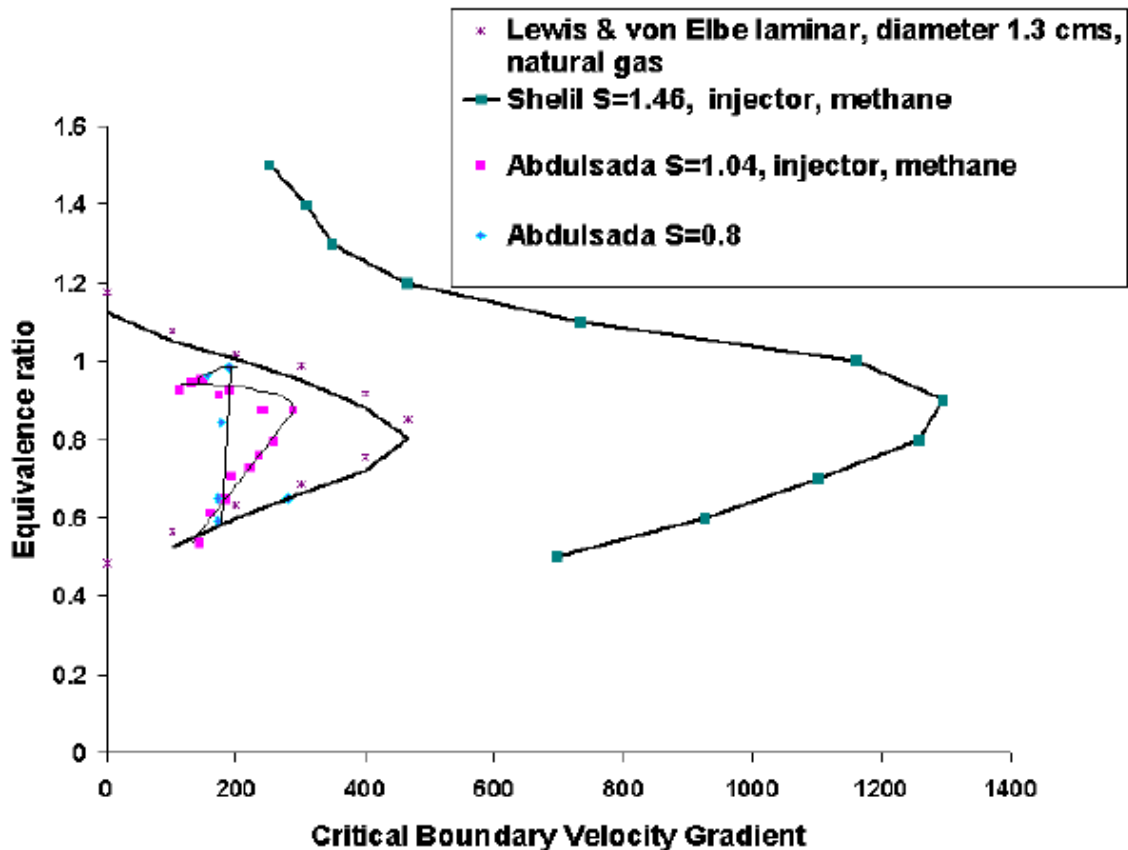
Figure 5: Lewis and von Elbe Critical Boundary velocity Gradient Comparison
for 3 Swirl Numbers and laminar data [15]

Overall S_{III}=0.8 gives the best flashback limits for methane based fuels with hydrogen content up to 30% and for hydrogen based fuels with hydrogen content $\geq$ 65% for equivalence ratios $\leq$ 0.65. However for fuels with hydrogen content in the range 30%$\leq$ H_2 content $\leq$ 65% a more complex picture emerges with overlap of the curves as a function of equivalence ratio and the Critical Boundary velocity gradient being higher at lower swirl Numbers and equivalence ratios ~1Separate tests on blow off limits show that the Swirl Number S=0.8 produces the best results.

 A gas turbine, required to be dual fuelled, with given compressor and turbine system has specific air mass flowrates at given thermal inputs. To produce this thermal input different quantities of fuel and thus equivalence ratio are needed for different fuels such as natural gas, coke oven gas and especially pure hydrogen. When dual fuelling/changeover is needed ideally the operational range of the system between flashback and blow off for two different fuels (such as hydrogen and natural gas) should be such that there is sufficient overlap between the blowoff and flashback limits to enable easy fuel change over. Because of the different stoichometry and heating value, hydrogen containing fuels will always have to be operated at weaker equivalence ratios natural gas fired systems, typically 78% of the natural gas equivalence ratio for pure hydrogen. This infers that the overlap region between the flashback limit and blow off limit of given fuels is crucial in determining whether or not the system can be dual fuelled. *Table 2* indicates that because of similar adiabatic flame temperature and lower heating values fuel gases containing up to 65% hydrogen (as with coke oven gas) with a base fuel of

natural gas can be best accommodated in existing or somewhat modified existing combustion systems.

4   Conclusion

This paper has discussed the flashback limits of three different swirl burners and shown that considerable differences exist. Preference is given to the system with low swirl number as it gives lowest pressure drop. The behaviour of methane based fuels with hydrogen content up to 30% has been shown to follow that of methane as the hydrogen content is increased. However Coke Oven gas shows distinctly different behavioural patterns, as does pure hydrogen which needs to be investigated further

Acknowledgments

References

[1]   Huang, Y., and Yang, V., 2005, "Effect of swirl on combustion dynamics in a leanpremixed swirl-stabilized combustor," Proceedings of the Combustion Institute, 30(2), pp. 1775-1782.

[2]   Sankaran, R., Hawkes, E. R., Chen, J. H., Lu, T., and Law, C. K., 2006, "Direct

[3]   Numerical Simulations of Turbulent Lean Premixed Combustion," Journal of Physics, 46, pp. 38-42.

[4]   Lefebvre, A. H., 1999, Gas Turbine Combustion, Taylor & Francis Group, LLC, Oxon, UK

[5]   Gupta, A. K., Lilley, D. J., and Syred, N., 1984, Swirl Flows, Abacus Press, Tunbridge Wells, United Kingdom.

[6]   Goy, C. J., James, S. R., and Rea, S., 2005, "Monitoring combustion instabilities: E.ON UK's experience," Combustion instabilities in gas turbine engines: operational experience, fundamental mechanisms, and modeling, T. Lieuwen, and V. Yang, eds.,Progress in Astronautics and Aeronautics, pp. 163-175.

[7]   Bagdanavicius A., Bowen P., Syred N., Kay P., Crayford A., Wood J., "Burning Velocities of Alternative Gaseous Fuels at Elevated Temperature and Pressure", 47th AIAA Aerospace Sciences Meeting, Orlando, USA, ref. AIAA-2009-0229, 2009.

[8]   Arias B., Fermoso J., Plaza M., Pevida C., Rubiera F., Pis J., Garcia-Pena F., Casero P., "Production of H2 by Co-gasification of Coal with biomass and petroleum coke", Proceedings of 7th European Conference on Coal Research and Its Applications, Wales, UK, 2008.

[9]   Chiesa, P. Lozza, G. and Mazzocchi, L. "Using hydrogen as gas turbine fuel", J. Eng. Gas Turb. Power **127** (2005), pp. 73–80.

[10] Valera-Medina, A. , Syred, N. Griffiths, A. "Visualisation of isothermal large coherent structures in a swirl burner" combustion and Flame 156(2009) 1723-1734.

[11] Shelil N., Bagdanavicius A, Syred N., Griffiths A., Bowen P, Premixed Swirl Combustion and Flash back Analysis with Hydrogen /Methane Mixture "48th AIAA Aerospace Sciences Meeting, Orlando, USA, ref. AIAA-2010-1169, 2010

[12] Syred N., "A Review of Oscillation Mechanisms and the role of the Precessing Vortex Core (PVC) in Swirl Combustion Systems", Progress in Energy and Combustion Systems, vol. 32, issue 2, pp. 93-161, 2006.

[13] Syred, N., 2007 Springer, " Generation and Alleviation of Combustion Instabilities in Swirling Flow," Advanced Combustion and Aerothermal Technologies, N. Syred, and A. Khalatov, eds., Springer, pp. 3–20.

[14] Plee, S. L., and Mellor, A. M., 1978, "Review of Flashback Reported in Prevaporizing/Premixing Combustors," Combustion and Flame, 32, pp. 193-203.

[15] Lewis, B., and Elebel, G., 1987, Combustion, Flames and Explosions of Gases, Academic Press, New York.

[16] Subramanya, M., and Choudhuri, A., 2007, "Investigation of Combustion Instability Effects on the Flame Characteristics of Fuel Blends," 5th International Energy Conversion Engineering Conference and Exhibit (IECEC) AIAA, St. Louis, Missouri.

[17] Fritz, J., Kroner, M., and Sattelmayer, T., 2004, "Flashback in a Swirl Burner with Cylindrical Premixing Zone," Journal of Engineering for Gas Turbines and Power, 126(2), pp. 276-283.

[18] Kroner, M., Fritz, J., and Sattelmayer, T., 2003, "Flashback Limits for Combustion Induced Vortex Breakdown in a Swirl Burner," Journal of Engineering for Gas Turbines and Power, 125(3), pp. 693-700.

[19] Fluent 6.2 Users Guides. ed. F. Incorporated. 2005: Lebanon, USA.

[20] Zimont, V., et al., An Efficient Computational Model for Premixed Turbulent Combustion at High Reynolds Numbers Based on a Turbulent Flame Speed Closure. J. of Gas Turbines Power, July 1998. 120: p. 526- 532.

[21] Valera-Medina A., Abdulsada M., Shelil N., Syred N., Griffiths A., "Flame Stabilization and Flashback Avoidance using Passive Nozzle Constrictions", IFRF International Meeting, Boston, June 8th-10th, USA, 2009.

[22] Valera-Medina A., Abdulsada M., Griffiths A. J., Bowen, P. J., "Flashback Analysis in Swirl Burners under a variety of Geometrical Conditions, Paper under review for Combustion and Flame, 2010

An Integrated Solar-Cryogen Hybrid Power System

Yongliang Li[1] and Yulong Ding[1,2*]

[1]Institute of Particle Science & Engineering, University of Leeds, Leeds, UK
[2]Institute of Process Engineering, Chinese Academy of Sciences, Beijing, China

*Corresponding author. E-mail: y.ding@leeds.ac.uk; Tel. 0044 (0)1133432747

Abstract

This paper reports a new integrated solar-cryogen hybrid power system that uses solar thermal energy and cryogen as the feedstocks. The system consists of a direct expansion (open cycle) of cryogen from an elevated pressure and a closed-loop Brayton cycle operated at a medium to low pressure. The expansion occurs sequentially in three stages (high pressure, medium and low pressure turbines) using solar heat as the superheating source. The open cycle uses all the three turbines, whereas the closed cycle only uses the medium and low pressure turbines. A solar thermal power system and a cryogen fuelled power system are used as the benchmarks to evaluate the performance of the newly proposed hybrid system and the three systems are optimized using a sequential quadratic programming (SQP) method. The results show that the integrated hybrid system gives far better overall system efficiency and provides over 30% more power output that the summation of the power outputs of the two other systems.

Keywords   cryogenic energy storage; solar thermal power; power system optimization

1   Introduction

Energy and environment are two of the most concerning issues in the current world. For over a century cheap, plentiful fossil energy has been supporting the industrialization and the increasingly higher living standards. However, increasing energy demand particularly in developing countries implies depletion of the fossil fuel resources at a rapid rate. In the meantime, the use of fossil fuels continues to cause environmental degradation. All these call for the use of new and renewable energy resources. Currently, renewable energy contributes to only 11% of the world primary energy and this is expected to increase to 60% by 2070 [1]. Solar energy is one of the most promising clean and non-depleting sources that is able to fulfill the increasing energy demands. Apart from direct heating applications, solar energy can be converted to electrical energy in two main ways. One is through solar cells (photovoltaic technology), which convert the diffuse radiation to electrical energy directly. The other is via an indirect solar thermal route, which converts the solar radiation to thermal energy by means of solar collectors or concentrators and then generating electricity through a conventional thermal process. Solar cells are most suitable for small scale low-power demand, while solar thermal power plant is often the best option for large-scale and grid-connected systems [2; 3].

This work is concerned about improving the indirect power generation via the solar thermal route in a Solar Thermal Power Plant (STPP). The STPP is a conventional power station that obtains all or parts of its thermal energy load by concentrating solar radiation, producing high temperature solar heat to activate a Rankine power cycle. In this process the concentrated solar radiation does not heat the working fluid of the power cycle directly but uses a solar energy carrier, which transport the solar radiation to storage vessel and also transfer the heat to the working fluid. The use of heat carrier has an advantage of more precise control of quality and quantity of vapour of the working fluid according to the needs. In addition, the use of storage and a heat carrier also enables the mass flow rate of the working fluid to be optimized independent of the fluctuations either or both of the load and solar radiation [4; 5]. The stored thermal energy can be used to either pre-heat water/steam in steam cycle power plants [6] or super-heat the steam in combined cycle power plants [7; 8] or even produce steam directly in Direct Steam Generation (DSG) [4; 9]. Generally in these cycles water/steam or other organic liquids are selected as the working fluid and the solar energy is stored in the form of high temperature sensible heat. It is therefore less efficient when taking the behavior of the solar thermal

energy carrier into account due to temperature glide mismatching between the solar thermal energy carrier and the working fluid.

This work is also concerned with efficient extraction of cold energy from cryogens. A cryogen is generally defined as a liquid that boils at below -150°C and contains a considerable amount of cryogenic exergy (thermal energy in the form of extremely low temperature cold) [10]. A lot of efforts have been made in cryogen production (gas liquefaction) processes over the past few decades with fast developments of liquefied natural gas (LNG) industry. For example it is estimated that the amount of LNG imported to China is 20 million tons by end of 2010 [11]. However, efficient recovery of the cryogenic energy is a challenge during the evaporation process without providing some heat to increase the temperature difference. This constitutes the primary motivation of working on integrating the solar thermal and cryogen power systems. This integration, as will be seen later, will provide high overall energy efficiency and alleviate environmental impact of the re-gasification processes of cryogens. In addition, liquid nitrogen/air has recently been proposed for use as a combustion-free fuel as well as an energy carrier for off-peak electricity or even renewable sources [12; 13; 14; 15; 16; 17]. This has led to various theoretical and experimental studies on extracting cryogenic energy using either a direct expansion method or a combined cycle method [10; 11; 18; 19; 20; 21; 22]. These studies reveal that cryogen is a more efficient working fluid than water/steam in extracting thermal heat [10].

In this work, an integrated solar-cryogen hybrid power system is proposed and analyzed. A solar thermal power system and a cryogen fuelled power system are used as the benchmarks to evaluate the performance of the newly proposed integrated system and the three systems are optimized using a sequential quadratic programming (SQP) method. As will be shown later in this paper, the integrated solar-cryogen hybrid system gives far better overall system efficiency.

2   Thermodynamic systems and modelling methodologies
In this section, analyses will be carried out on the three power systems of (i) Solar thermal power system, (ii) Cryogen fuelled power system and (iii) Solar-cryogen hybrid power system, where (i) and (ii) are used as the benchmarks for evaluating the integrated power system proposed in this work.

2.1   Solar thermal power system
A solar thermal power system usually involves focusing sunlight on a small area to create a high-temperature heat source. A thermal energy carrier is often used to transport the heat and pass the heat to the working fluid via a heat exchange system. *Table 1* shows a list of frequently-used high temperature thermal energy carriers [7; 23], which are either pure or mixtures of different thermal fluids.   Figure 1 shows a schematic diagram of the solar thermal power system. The system uses water as the working fluid running on a Rankine cycle and there have been practical applications of the system [9]. The system works in the following way: first solar radiation is concentrated by the parabolic trough or other types of collectors to heat the thermal energy carrier. The high temperature energy carrier superheats high pressure water in heat exchanger 1 (HX1) before entering the high pressure steam turbine (HP). Part of the steam extracted from the HP at an intermediate pressure is reheated by the high temperature energy carrier in heater exchanger (HX2) and then sent to the low pressure steam turbine (LP) for further expansion. The exhaust steam is condensed in the condenser (CD) and then pumped to the regenerator (RG) where it mixes with the outlet steam of the HP. Finally, the condensed steam is pumped to high pressure to complete the closed power cycle. In such a manner the solar thermal energy is used in two levels and the cooled energy carrier is stored in MC and LC respectively.

Table 1
Frequently-used liquid materials for the storage of high temperature sensible heat

Material	Temperature range (K)	Density* (kg/m^3)	Specific heat (J/kg·K)	Thermal energy density (kJ/m^3·K)
Draw salt (50% KNO$_3$+50% NaNO$_3$ by weight)	493 – 813	1733	1550	2686
Molten salt (53% KNO$_3$+40% NaNO$_2$+ 7% NaNO$_3$ by weight)	419 – 813	1680	1560	2620
Liquid sodium	373 – 1033	750	1260	945
Thermal-oil 66	263 – 616	750	2100	1575

*Average density and specific heat in the temperature range given.

HX – Heat Exchanger   CD – Condenser   MC – Intermediate Temperature Carrier Tank

HP – High Pressure Turbine   RG – Regenerator   LC – Low Temperature Carrier Tank

LP – Low Pressure Turbine   P – Pump

SC – Solar Collector   HC – High Temperature Carrier Tank
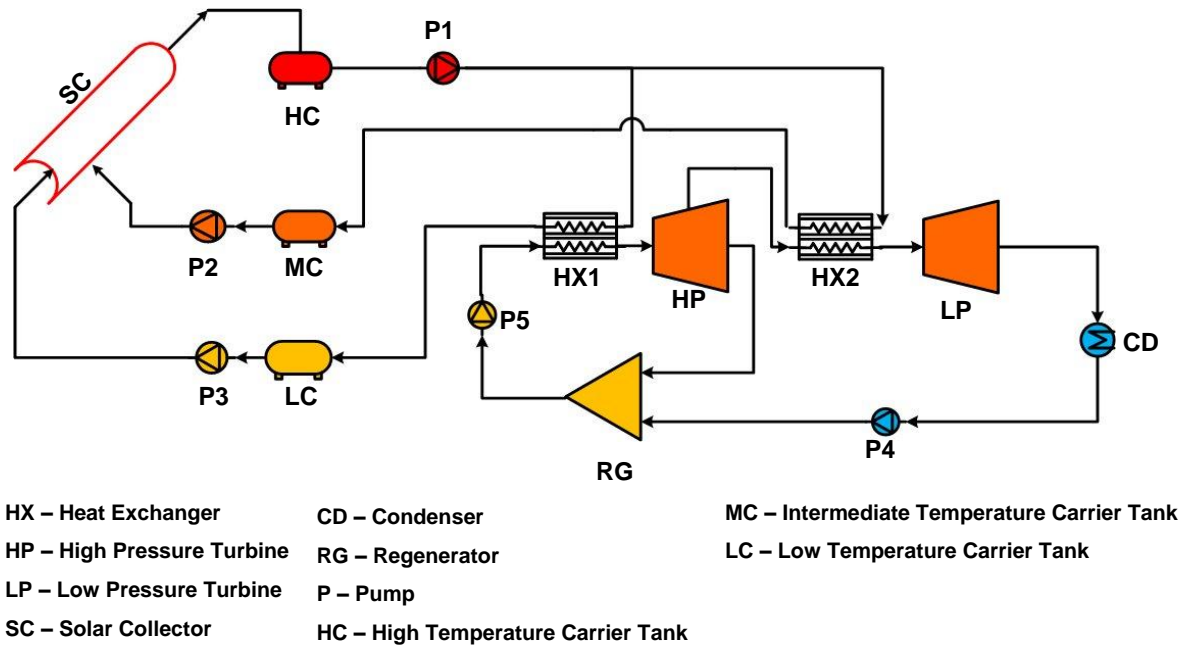
Figure 3: Configuration of a solar thermal power system

The thermal efficiency of a solar collector is given as [24]:

$$\eta_{1,collector}\{T\} = \frac{dQ}{dE} = (\alpha\tau)F + (\alpha\varepsilon)F\frac{\sigma T_c^4}{C^S E_b} - (\varepsilon\bar{\rho})F\frac{\sigma T^4}{C^S E_b} - U_L F\frac{T - T_0}{C^S E_b} \qquad (1)$$

where Q is usable process heat and E is the total irradiance of the collector, $\alpha\tau = \alpha_a\tau_c/[1 - \rho_c(1 - \alpha_a)]$ and α_a is the absorptivity of the absorber, τ_c is the transmissivity of the cover, and ρ_c is the fraction backscattered by the cover, $\alpha\varepsilon = \alpha_a\varepsilon_a/[1 - \rho_c(1 - \alpha_a)]$ and ε_c is the emissivity of the cover, $\varepsilon\bar{\rho} = \varepsilon_a(1 - \rho_c)/[1 - \rho_c(1 - \alpha_a)]$ and ε_a is the emissivity of the absorber, σ is the Stefan–Boltzmann constant, $5.67\times 10^{-8}\text{W/(m}^2\cdot\text{K}^4)$, $\bar{\rho}$ is the average reflectivity, U_L is the heat loss coefficient, F is termed as the fin factor which is close to 1 for a well designed receiver or collector, T is the fluid temperature, T_c is the cover temperature, T_0 is the ambient temperature, C is the concentration ratio, $^S E_b$ is the direct radiation, $^S E_b = {}^S E - {}^S E_d$ with $^S E_d$ the diffusion radiation and $^S E$ the global irradiance, $^S E = f\sigma T_s^4$ with f being the dilution factor which can be assumed to

be wavelength independent. In case of concentrated radiation the diffuse solar part in the incident global radiation can be omitted, one has $^{S}E_{b}=^{S}E$. Integrating Equation (1) from State 1 to State 2, the total irradiance of the collector can be obtained as:

$$E = \int_{T_1}^{T_2} \frac{1}{\eta_{1,collector}\{T\}} dQ \tag{2}$$

The exergy released by the solar irradiance [24]:

$$Ex_{solar} \approx E\left(1 - \frac{4}{3}\frac{T_0}{T_S}(1-0.28\ln f)\right) \tag{3}$$

For a constant specific heat thermal fluid $dQ = d(c_p\dot{m}T) = c_p\dot{m}dT$, then

$$Q = \int_{T_1}^{T_2} dQ = c_p\dot{m}(T_2 - T_1) \tag{4}$$

The exergy transferred to the solar heat carrier is then given as [9]:

$$Ex_Q = Q\left\{1 - \frac{T_0}{T_2 - T_1}\ln\left[\frac{T_2}{T_1}\right]\right\} \tag{5}$$

As a consequence, one has the exergetic efficiency of the collector as follows:

$$\eta_{II,collector} = \frac{Ex_Q}{Ex_{solar}} = \frac{1 - \dfrac{T_0}{T_2 - T_1}\ln\left[\dfrac{T_2}{T_1}\right]}{\dfrac{1}{T_2 - T_1}\displaystyle\int_{T_1}^{T_2}\dfrac{1}{\eta_{1,collector}\{T\}}dT\left(1 - \dfrac{4}{3}\dfrac{T_0}{T_S}(1-0.28\ln f)\right)} \tag{6}$$

The thermodynamic performances of other components of the systems are calculated in the following way. Defining the specific exergy at State i as:

$$\psi_i = (h_i - h_0) - T_0(s_i - s_0) \tag{7}$$

where h is enthalpy, s is entropy and the subscript zero indicates properties at the reference state in P_0 and T_0. The power consumption of the pump is then calculated by:

$$W_{pump} = \dot{m}(\psi_4 - \psi_3)/\eta_{pump} \tag{8}$$

The power output of turbine is:

$$W_{turbine} = \dot{m}(\psi_{inlet} - \psi_{outlet})\eta_{turbine} \tag{9}$$

where η_{pump} and $\eta_{turbine}$ are the efficiencies of pump and turbine respectively.

2.2 Cryogen fuelled power system

If ambient heat is the only source available, a combination of direct expansion and Rankine cycle is the most applicable way to extract the cryogenic energy in a cryogen fuelled power system due to its low power consumption in the compression process [10]. Figure 2 shows such a system with a two-stage direct expansion. The cryogen stored in the storage tank (CT) is first pumped to a high pressure by a cryogenic pump (CP) and then heated gradually in the heat exchanger (HX) and the room heater (RH1) before subject the two-stage expansion process in the high pressure (HP) and low pressure (LP) turbines with inter-heating (RH2). The high grade cold discharged in HX is recovered by liquefying a refrigerant in a Rankine cycle. The liquid refrigerant is pumped and heated in room heater (RH3) to drive the refrigerant turbine (RT) to produce more power. The commonly used refrigerant, propane, is selected as the working fluid for the Rankine cycle in this work. The mathematical formulae for evaluating the thermodynamic performance of the components in this system are similar to those used in the solar thermal power system and will not be repeated here.

CT -- Cryogen Tank	HP – High Pressure Turbine	P – Pump
CP – Cryogenic Pump	LP – Low Pressure Turbine	RH – Room Heater
HX – Heat Exchanger	RT – Refrigerant Turbine	EG – Exhaust Gas
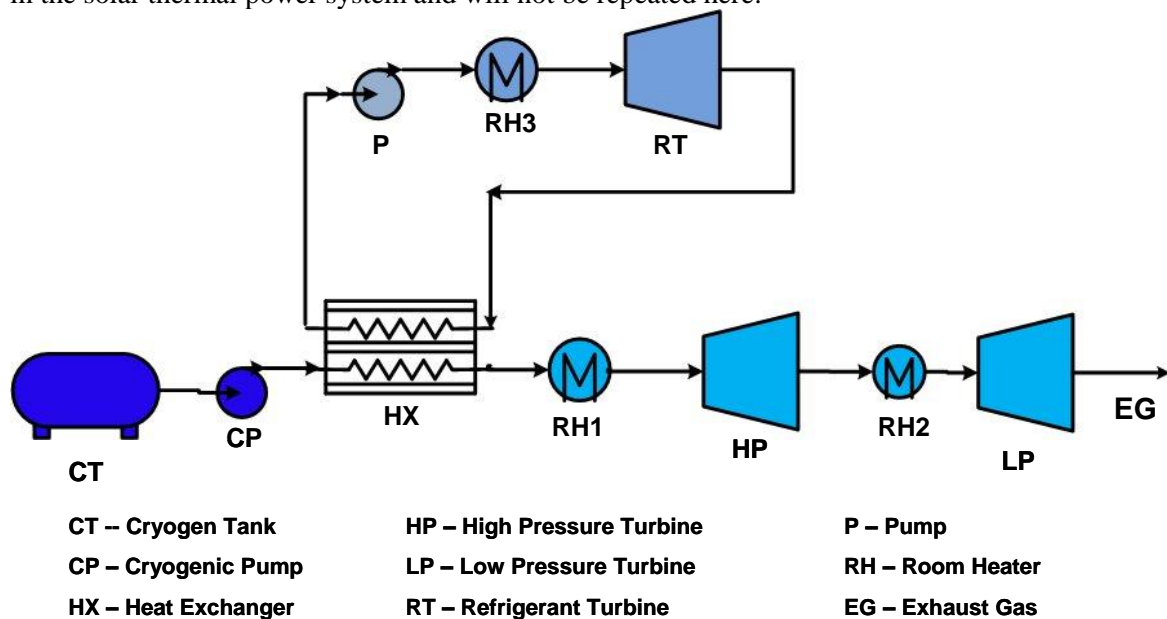
Figure 4: Configuration of cryogen fueled power system

2.3 Solar-cryogen hybrid power system

The hybrid system proposed in this work integrates the solar thermal power cycle and the cryogen fuelled power cycle and the cryogen itself is used as the common working fluid. Figure 3 illustrates such a system. One can see that the hybrid system consists of three parts: an open cycle of cryogen direct expansion, a closed Brayton cycle for a full extraction of cryogenic energy and a solar energy collection and storage unit to capture the solar energy and provide the heating source for both the cycles. In this system the closed Brayton cycle shares the intermediate pressure (IP) and low pressure (LP) turbines with direct expansion cycle to simplify the configuration while the cryogen is also used as the working fluid of the Brayton cycle. The cold energy released by the cryogen direct expansion is recycled by the Brayton cycle through a heat transfer process in HX1. Similarly to the solar thermal power system, the solar thermal energy (the heat source) is extracted at two levels: the superheating process between State 14 and State 16 corresponding respectively to the high temperature and low temperature carriers and the inter-heating process between State 14 and State 15 corresponding respectively to the high temperature and intermediate temperature carriers. Comparing with the solar thermal power system, an additional compressor is added in the hybrid system. The power consumed by the additional compressor is given by:

$$W_{compressor} = \dot{m}(\psi_{12} - \psi_{11})/\eta_{compressor} \tag{10}$$

where $\eta_{compressor}$ is the compressor efficiency.

Figure 5: Configuration of a cryogen-solar hybrid power system

3   Parametric optimisation and system analysis

Based on the power systems detailed in Section 2, parametric optimisation is carried out using a sequential quadratic programming (SQP) method. The following exergy efficiencies are selected as the objective functions for the optimisation:

$$\eta_{solar} = \frac{W_{net}}{W_{liquefaction}} \tag{11}$$

$$\eta_{cryogen} = \frac{W_{net}}{W_{liquefaction}} \tag{12}$$

$$\eta_{hybrid} = \frac{W_{net}}{Ex_{solar} + W_{liquefaction}} \tag{13}$$

where η_{solar}, $\eta_{cryogen}$ and η_{hybrid} are respectively the exergy efficiencies of the solar thermal power system, the cryogen fuelled power system and the solar-cryogen hybrid power system, W_{net} is the net power output (equal to the turbine output power subtracting the power consumed by compression and pumping processes) and $W_{liquefaction}$ is the power consumed by the cryogen production process.

Liquid nitrogen is taken as an example of the working cryogen in the parametric optimization and the solar energy carrier is assumed to have a constant specific heat. Other data used in the simulations are summarized in *Table 2* [9; 24; 25; 26]. The overall optimal performance of the three systems is given in *Table 3*. From table, one can see that the exergy efficiency of the hybrid power system is much higher than the solar thermal and cryogen fuelled power systems – given the same energy source the net output power of the hybrid power system is 1.0118 MW, almost 31% higher than that the summation of output power of both solar thermal and cryogen fuelled power systems.

Table 2
Main assumption for the parametric optimisation

Solar collector	Absorption term coefficient $(\alpha\tau)F$	0.8
	Emission term coefficient $(\alpha\varepsilon)F$	0.8
	Absorber loss term coefficient $(\varepsilon\bar{\rho})F$	0.8
	Convection heat loss coefficient $U_L F$ /Wm^{-2}K^{-1}	20
	Cover temperature T_c /K	300
	The concentration ratio C	40
Cryogenic pump isentropic efficiency η_{pump}		0.75
Turbine isentropic efficiency $\eta_{turbine}$		0.90
Compressor isentropic efficiency $\eta_{compressor}$		0.87
Approach temperature of heat exchanger system ΔT /K		10
The wet vapour quality of steam turbine		>0.9
The effective solar temperature T_s /K		5,777
The dilution factor f		1.3×10^{-5}
Ambient temperature T_0 /K		298.15
Ambient pressure P_0 /Pa		1.01325×10^5
Power consumption of liquid nitrogen production $W_{liquefaction}$ / (kWh/kg)		0.5
The mass flow of liquid nitrogen $\dot{m}_{cryogen}$ / (kg/s)		1.0

Table 3
Overall optimal performances of the three systems

		Solar thermal power system	Cryogen fueled power system	Solar-cryogen hybrid power system
Exergy efficiency (%)		23.89	18.10	27.55
Energy Source	Solar radiation (MW)	2.628	0	2.628
	Liquid nitrogen (kg/s)	0	1.0	1.0
Net output power (MW)		0.4485	0.3259	1.0118

The performance improvement of the hybrid power system comes from more efficient heat transfer processes. This can be demonstrated by the exergy analysis of the energy conservation processes using a graphical representation method named energy utilization diagram (EUD). In the EUD method an intensive parameter called availability factor or energy level (A) is introduced as an indicator of the potential of the energy donated and accepted by the processes [27]:

$$A = \frac{\Delta\psi}{\Delta h} \tag{14}$$

Defining a process that releases energy as an 'energy donor (ED)' and a process that receives energy as an 'energy acceptor (EA)', the exergy loss of the processes can then be given by:

$$EXL = -\sum\Delta\psi_i = \sum\Delta h_i(A_{ed,i} - A_{ea,i}) = \int(A_{ed} - A_{ea})dh \tag{15}$$

By plotting the availability factor of the energy donating and accepting processes against the transferred energy, the amount of exergy loss in the system can be obtained as the area between the two curves.
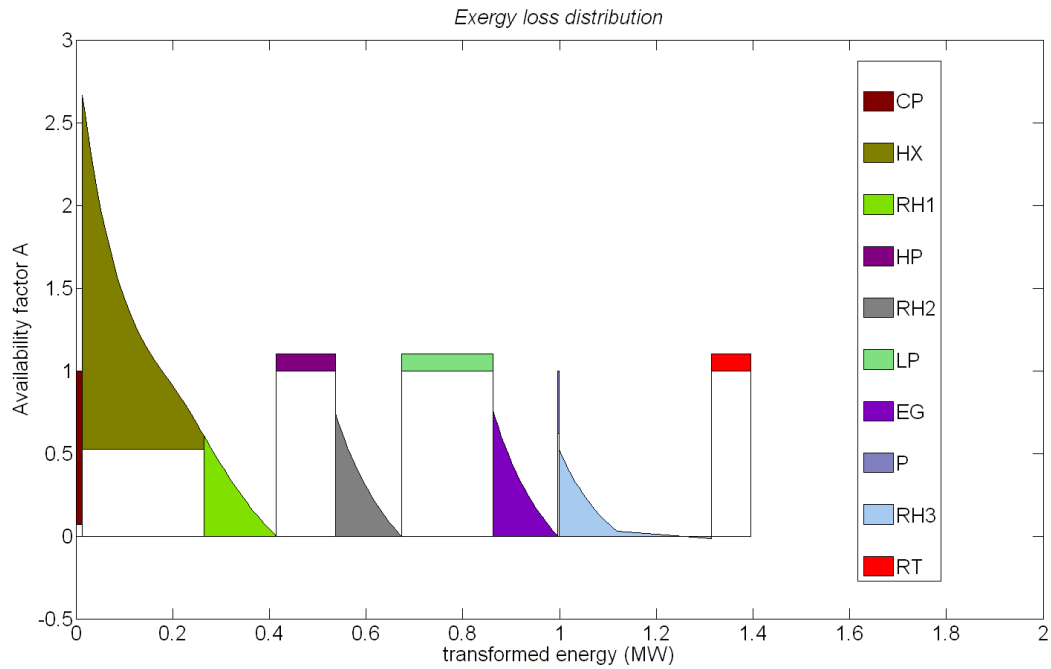
Figure 6: EUD representation of the optimised cryogen fueled power system
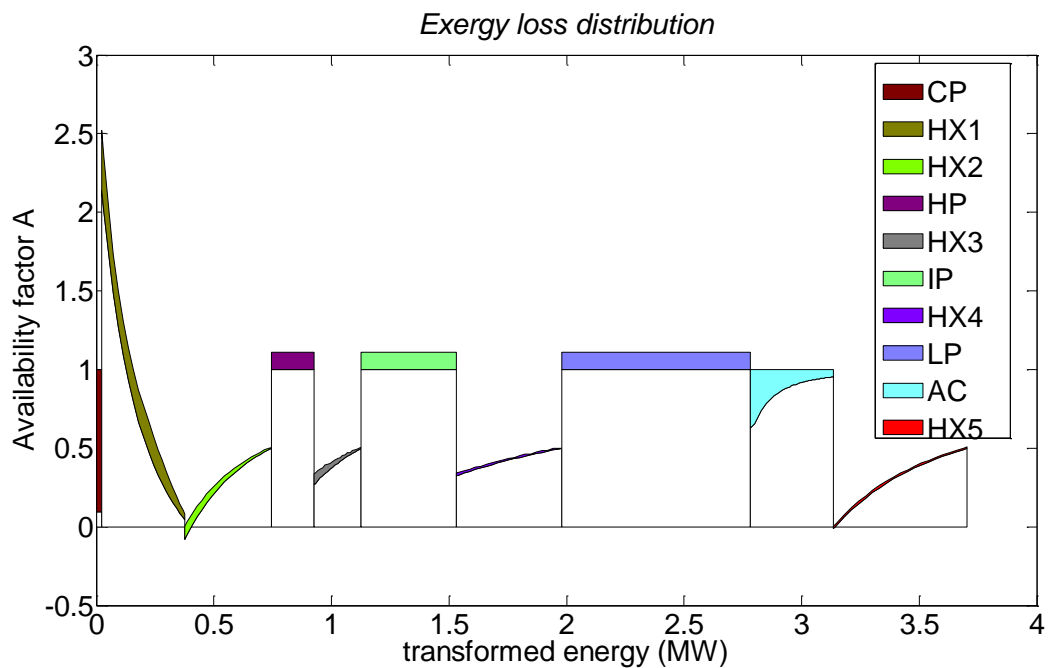
Figure 7: EUD representation of the optimised hybrid power system

Figures 4 and 5 show the EUD representations of the optimised cryogen fuelled and hybrid power systems, respectively. One can see the exergy loss in the heat exchangers and room heaters of the hybrid power system is significantly lower than that in the cryogen fuelled power system. There are two reasons for this. First, the use of the Brayton cycle in the hybrid system enables a much more efficient heat transfer to recover the high grade cold energy due to better temperature glide matching between heat addition and heat rejection. Second, the outlet temperature of the expanded gas is increased as the compressed gas is superheated by the solar thermal energy prior to entering the

turbines. Therefore the exergy loss in the exhaust gas is reduced. Meanwhile, the use of cryogen as the working fluid is beneficial for the solar thermal energy utilization. This can be understood from *Table 4*, which shows that the critical temperatures and pressures of nitrogen are much lower than that of the steam. As a consequence, supercritical cycles are much easily to achieve using the cryogen. Listed in *Table 4* also includes the critical properties of methane, which, as will be discussed in the following section in terms of applications, also gives much better performance than the use of steam as the working fluid.

Table 4
Critical temperature and pressure for water, nitrogen and methane

	Water/Steam	Nitrogen	Methane
Critical temperature (K)	647	126	190
Critical pressure (MPa)	22.06	3.39	4.60

4   Further discussion on the hybrid system

In this section, further discussion will be on (i) selection of thermal energy carrier, (ii) optimal thermal carrier temperature provided by solar heat, (iii) possible commercial position of the hybrid system.

4.1   Selection of thermal energy carrier

The state parameters of the optimised hybrid system are listed in *Table 5*, which shows the highest working temperature is above 600K. This, according to *Table 1*, suggests Thermal-oil 66 could be used the heat carrier fluid and the mass flowrate data in *Table 5* are produced according to the properties of this fluid. The data in *Table 5* also shows that the mass flow rate of heat carrier is 3.6 times that of liquid nitrogen, which should be practically possible. In addition, under the conditions of the hybrid power system, the Thermal-oil 66 has energy density of about 447kJ/kg, which is even higher than most high temperature phase change materials [10]. These make the Thermal oil-66 a competitive thermal energy storage medium for this type of applications.

Table 5
State parameters of the optimal hybrid system

State Number	Mass flow rate (kg/s)	Pressure (Pa)	Temperature (K)
1	1.0	1.0×10^5	77.4
2	1.0	1.5×10^7	84.0
3	1.0	1.5×10^7	275.7
4	1.0	1.5×10^7	593.9
5	1.0	3.9×10^6	406.8
6	1.0	3.9×10^6	593.9
7	2.8	1.3×10^6	441.1
8	2.8	1.3×10^6	593.9
9	1.0	1.0×10^5	298.2
10	1.8	1.0×10^5	298.2
11	1.8	1.0×10^5	94.0
12	1.8	3.9×10^6	294.4
13	1.8	3.9×10^6	593.9
14	3.6	-	603.9
15	2.1	-	451.1
16	1.5	-	304.4

4.2   Optimal thermal carrier temperature provided by solar heat

The optimisation also indicates that the optimal temperature of the heat carrier heated by the solar collectors for the hybrid system is about 600K. This requirement is easily achievable as most of the concentrated solar power plants give a temperature up to 600~700K [28].

4.3   Potential commercial aspects of the hybrid power system

The proposed hybrid system is best suited to locations with (i) cryogen such as LNG and (ii) sunshine. There are a number of places satisfy these criteria, including for example, large scale LNG importing ports in Japan and Southeast coast of China. However, the new system requires a high pressure gas turbine with 15MPa inlet pressure according to the optimisation analyses, which, to our knowledge, cannot be found in commercial market. This is not necessarily a technological challenge in our view as this working pressure is lower than currently available steam turbines and the working temperature is much lower than that of combustion based gas turbines. Another key factor that affects commercial uptake of the hybrid system is economics. Although this is beyond the scope of this work, we expect that capital and running costs for the hybrid power system should be significantly lower than that needed for a solar thermal power system and a cryogen fuelled power system. Bear in mind, the hybrid system provides ~30% more power that the summation of the two systems. It is therefore reasonably optimistic about the commercial future of the proposed hybrid system.

5   Conclusions

A new solar-cryogen hybrid power system is proposed and is compared with a solar thermal power system and a cryogen fuelled power system. Thermodynamic analyses and optimisation are carried on these systems. The results show that the hybrid system provides over 30% more power than the summation of the power outputs of the other two systems. The results also suggest the optimal hot end temperature of the heat carrier heated by the solar collectors be about 600K for the hybrid system.

Acknowledgements

References

[23] A. K Hossain, and O. Badr, Prospects of renewable energy utilisation for electricity generation in Bangladesh. Renewable and Sustainable Energy Reviews 11 (2007) 1617-1649.

[24] N. Lior, Energy resources and use: The present (2008) situation and possible sustainable paths to the future. Energy 35 (2010) 2631-2638.

[25] V. Quaschning, and M.B. Muriel, Solar Power – Photovoltaics or Solar Thermal Power Plants?, Proceeding VGB Congress Power Plants 2001, Brussels, 2001.

[26] V. Morisson, M. Rady, E. Palomo, and E. Arquis, Thermal energy storage systems for electricity production using solar energy direct steam generation technology. Chemical Engineering and Processing: Process Intensification 47 (2008) 499-507.

[27] X.Q. Zhai, and R.Z. Wang, Experimental investigation and performance analysis on a solar adsorption cooling system with/without heat storage. Applied Energy 87 (2010) 824-835.

[28] L. García-Rodríguez, and J. Blanco-Gálvez, Solar-heated Rankine cycles for water and electricity production: POWERSOL project. Desalination 212 (2007) 311-318.

[29] F. Donatini, C. Zamparelli, A. Maccari, and M. Vignolini, High efficency integration of thermodynamic solar plant with natural gas combined cycle, Clean Electrical Power, 2007. ICCEP '07. International Conference on, 2007, pp. 770-776.

[30] M. Horn, H. Führing, and J. Rheinländer, Economic analysis of integrated solar combined cycle power plants: A sample case: The economic feasibility of an ISCCS power plant in Egypt. Energy 29 (2003) 935-945.

[31] Y. You, and E.J. Hu, A medium-temperature solar thermal power system and its efficiency optimisation. Applied Thermal Engineering 22 (2002) 357-364.

[32] Y. Li, H. Chen, and Y. Ding, Fundamentals and applications of cryogen as a thermal energy carrier: A critical assessment. International Journal of Thermal Sciences 49 (2010) 941-949.

[33] X.J. Shi, and D.F. Che, Thermodynamic analysis of an LNG fuelled combined cycle power plant with waste heat recovery and utilization system. International Journal of Energy Research 31 (2007) 975-998.

[34] K. Chino, and H. Araki, Evaluation of energy storage method using liquid air. Heat Transfer—Asian Research 29 (2000) 347-357.

[35] H. Chen, Y. Ding, T. Peters, and F. Berger, A method of storing energy and a cryogenic energy storage system, Highview Enterprises Limited PCT/GB2007/000667, 2007.

[36] C.A. Ordonez, Liquid nitrogen fueled, closed Brayton cycle cryogenic heat engine. Energy Conversion and Management 41 (2000) 331-341.

[37] Y. Li, H. Chen, X. Zhang, C. Tan, and Y. Ding, Renewable energy carriers: Hydrogen or liquid air/nitrogen? Applied Thermal Engineering 30 (2010) 1985-1990.

[38] H. Chen, T.N. Cong, W. Yang, C. Tan, Y. Li, and Y. Ding, Progress in electrical energy storage system: A critical review. Progress in Natural Science 19 (2009) 291-312.

[39] Y. Li, Y. Jin, H. Chen, C. Tan, and Y. Ding, An integrated system for thermal power generation, electrical energy storage and CO2 capture. International Journal of Energy Research (2010) DOI: 10.1002/er.1753.

[40] J.E. Ahern, Applications of the 2nd Law of Thermodynamics to Cryogenics - a Review. Energy 5 (1980) 891-897.

[41] G. Bisio, and L. Tagliafico, On the recovery of LNG physical exergy by means of a simple cycle or a complex system. Exergy, An International Journal 2 (2002) 34-50.

[42] L. Trevisani, M. Fabbri, F. Negrini, and P.L. Ribani, Advanced energy recovery systems from liquid hydrogen. Energy Conversion and Management 48 (2007) 146-154.

[43] F.F. Bai, and Z.X. Mang, Integration of low-level waste heat recovery and Liquefied Nature Gas cold energy utilization. Chinese Journal of Chemical Engineering 16 (2008) 95-99.

[44] J. Szargut, and I. Szczygiel, Utilization of the cryogenic exergy of liquid natural gas (LNG) for the production of electricity. Energy 34 (2009) 827-837.

[45] F. Michael, and B. Borislav, High temperature metal hydrides as heat storage materials for solar and related applications. International Journal of Molecular Sciences (2009) 325-344.

[46] C.J. Winter, R.L. Sizmann, and L.L. Vant-Hull, Solar power plants: Fundamentals, technology, systems economics, Springer-Verlag, Berlin, 1991.

[47] Zhang, and N. Lior, A novel Brayton cycle with the integration of liquid hydrogen cryogenic exergy utilization. International Journal of Hydrogen Energy 33 (2008) 214-224.

[48] H. Chen, and Y. Ding, An Overview of Air Liquefaction and Separation Process, University of Leeds, Leeds, 2007, pp. 42.

[49] T. Srinophakun, S. Laowithayangkul, and M. Ishida, Simulation of power cycle with energy utilization diagram. Energy Conversion and Management 42 (2001) 1437-1456.

[50] A. Fernández-García, E. Zarza, L. Valenzuela, and M. Pérez, Parabolic-trough solar collectors and their applications. Renewable and Sustainable Energy Reviews 14 1695-1721.

An Investigation of a Household Size Trigeneration Running with Hydrogen

Yaodong Wang* [a] , Ye Huang [b], Elijah Chiremba [a], Neil Hewitt [b], Yulong Ding, Jincheng Huang [d], Ruzhu Wang [e], Jingyi Wu [e], Chunqing Tan [f] , Anthony P. Roskilly [a]

[a] Sir Joseph Swan Centre for Energy Research, Newcastle University, United Kingdom
[b] School of Built Environment, University of Ulster, Newtownabbey BT37 0QB, United Kingdom
[c] Institute of Particle Science & Engineering, Leeds University, United Kingdom
[d] Guangxi University, Nanning, Guangxi, China
[e] Shanghai Jiaotong University, Shanghai, China
[f] Institute of Engineering Thermophysics, Chinese Academy of Sciences (IET), Beijing, China

Abstract
This study examined the performance and emission characteristics of a household size trigeneration based on a diesel engine generator fuelled with hydrogen comparing to that of single generation, cogeneration using ECLIPSE simulation software. In single generation simulation, the engine genset is used to produce electricity only and the heat from the engine is rejected to the atmosphere. In cogeneration and trigeneration, in addition to the electricity generated from the genset, the waste heat rejected from the hot exhaust gases and engine cooling system, is captured for domestic hot water supply using heat exchangers and hot water tank; and a part of the waste heat is used to drive absorption cooling in trigeneration. Comparisons have been made for the simulated results of these three modes of operation for hydrogen and diesel. The results prove that hydrogen is a potential energy vector in the future which is a key to meeting upcoming stringent greenhouse gases emissions. The study show that hydrogen has very good prospects to achieve a better or equal performance to conventional diesel fuel in terms of energetic performance, and a near zero carbon emission, depending on the life cycle analysis of the way the hydrogen is produced. The results also show enormous potential fuel savings and massive reductions in greenhouse gas emissions per unit of useful energy outputs with cogeneration and trigeneration compared with that of single generation.

Keywords   hydrogen; trigeneration; household; simulation

1   Introduction

The household energy demand includes three forms of energy simultaneously, namely, electricity, heat and refrigeration. According to the statistics, the energy consumption in the domestic sector makes up more than 25% of all energy used in the UK; it can be split into 23% of electricity consumption and 77% of use for heating and hot water [1]. Refrigeration is also a kind of necessities in the households. The conventional way to provide electricity, heat and cooling in the homes is to purchase electricity from the national grid for powering household electrical appliances including refrigerators and a part of heating such as electrical heaters; and/or generate heat separately in a boiler by burning natural gas or oil. In fact, the average efficiency of the thermal power plants for electricity generation is 37% in the UK [2]. That means around 63% of the energy from the burning of fuels (coal, oil and natural gas), was wasted in the form of low-grade waste heat. At the same time, for heating, the conventional boilers in households mostly using gas as the fuel are of only 60−75% efficiency [1]. Not only is this conventional way to use energy now seen as a very wasteful way of utilising primary energy sources, but also one of the main source of environmental pollution. The use of fossil fuels, upon which most conventional generation systems are based, result in a huge amount of emission of greenhouse gases (GHG) that are believed to cause global warming and climate change. The 'peak oil' situation is premised on the belief that, because fossil fuels are finite, global oil supplies will reach a peak at some point in future after which supplies will start to decrease and never rise again. Therefore, it is necessary to optimise the use of the limited fuel resources in the domestic aspect. The utilisation of the low-grade waste heat from the power generation process for heating and/or cooling/refrigeration will be one of the solutions to save the energy usage. The technology to make use of the 'waste heat' is cogeneration and/or trigeneration. Cogeneration is a system, which

generates power and heat simultaneously with one fuel input only, also called combined heat and power (CHP). Trigeneration, also called Combined Cooling, Heating and Power (CCHP), is the production of useful heat and refrigeration/cooling and electricity from the same energy conversion process. In trigeneration, the mechanical energy from the prime mover is changed into electricity. At the same time the absorption refrigerator generates cooling/refrigeration and heat exchangers generates hot water respectively, from the waste heat sources. These technologies can increase primary energy utilisation efficiency up to over 90%. Trigeneration can therefore lead to substantial energy saving and ultimately significant contribution to the reduction of CO_2 emissions [3].

The principles of the basic components of trigeneration; electricity generation, heat exchange and absorption cooling are not new. It is the combination of them to work in one integrated system that is a relatively new concept and that came into use in the mid 1990's [4]. As trigeneration is a recent development, the number of operating systems worldwide is still small with most plants based on gas turbine or internal combustion engine cycle with absorption type chilling for cold production [5]. Cogeneration, the simultaneous production of heat and power, has a much longer history, dating back over 125 years in the 1880s when steam was the primary source of energy in industry and electricity was just surfacing as a product for power and lighting [6]. Research and application of trigeneration [7 - 13] has been growing fast due to the growing interest in it as a way to increase the efficiency as well as to tackle the climate change.

The majority of existing trigeneration systems is fuelled by natural gas which is also a finite fossil fuel and needs to be substituted by more sustainable alternatives. Alternative fuels that aspire to replace fossil fuels include alcohols, bio-fuels, hydrogen, vegetable oils, biogas and producer gas. Of these, hydrogen has been identified as one of the most prospective and long term renewable and less polluting fuels [14], if the effective way can be found to generate 'renewable hydrogen' to meet our demand. There are many studies on hydrogen as an internal combustion engine fuel [15 – 17]. Van Vorst [15] reviewed early work on hydrogen as an engine fuel dating back from the first recorded use of hydrogen in an internal combustion engine described in the work of Reverend William Cecil in England in the early 1800s. Some research work in the period before the early 1990s has been reviewed by Das [16]. White et al (2006) [17] presented a technical review of hydrogen fuelled internal combustion engines. Ruijven et al [18] presented the potential role of hydrogen in energy systems. Hydrogen emits only a minimum amount of pollutants. These are NO_x from the combustion of nitrogen in the air, particularly at high engine loads; and a very little amount of CO and CO_2 from lubrication oil that may leak into the combustion cylinders. The combustion product of hydrogen is water, which, unlike carbon dioxide and other pollutants from fossil fuels, is not harmful to the environment.

The objective of this study was to investigate the performance, efficiency and emissions of a micro-scale trigeneration based on a diesel engine genset using hydrogen as the fuel in a domestic application, comparing with that of single generation, cogeneration; and compared to that of using original diesel fuel. The study used the ECLIPSE simulation software to model all of the three generations, i.e., single generation, cogeneration and trigeneration.

2   The design of the trigeneration and the computational software

The trigeneration system studied is shown in Figure 1. The design of the system is based on the energy (including electricity and heat) consumptions in the households in the UK [19 – 27]. A diesel engine genset (6.5 kW) is selected for the generation of electrical power; a heat recovery system is designed; an absorption refrigerator is selected for the household trigeneration system. The study is also based on the previous research outcomes, which proved that using hydrogen as a fuel for a diesel engine generator and the use of micro-trigeneration system were feasible [28 –30, 4]. The main components of the micro-trigeneration system are: one Yammar diesel engine genset (YTG6.5S model, rated 6.5kW electrical power output), a heat driven absorption refrigerator and a heat recovery systems including heat exchangers and heat storage tank to recover heat from engine cooling system and exhaust gases. The whole trigeneration system is being built and available for experimental study in laboratory at Newcastle University on different biofuels.
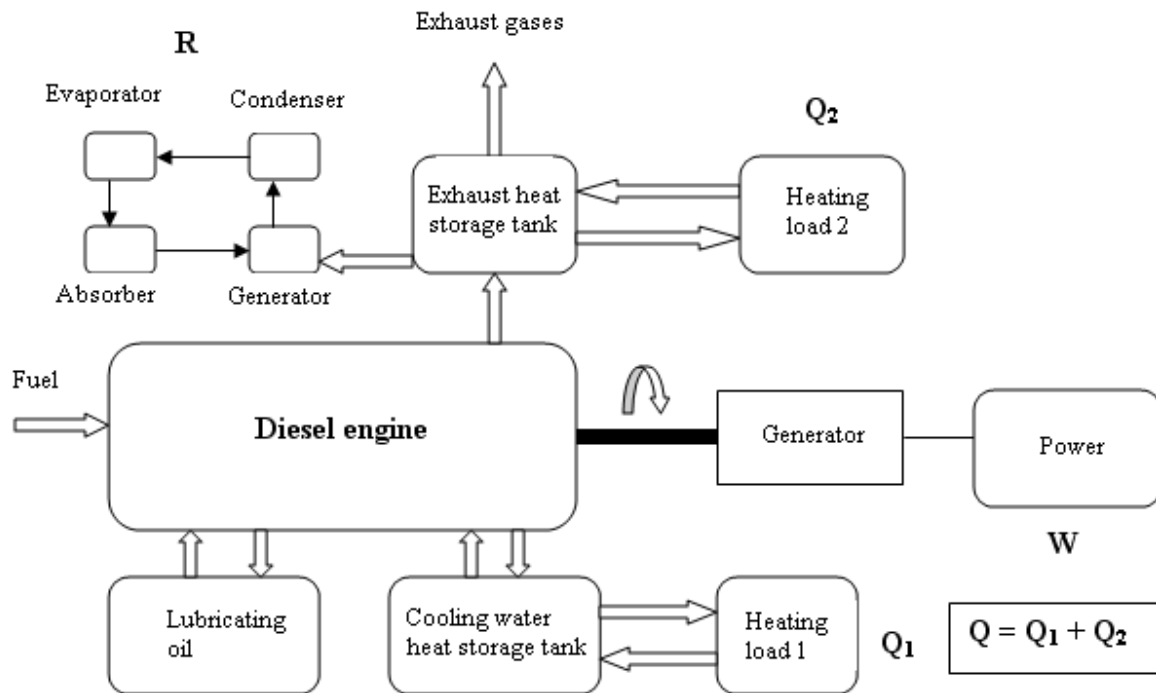
Figure 1: A schematic diagram of the 6.5kWe diesel engine trigeneration system

Previous to the experimental testing, a computational simulation is needed to carry out the initial evaluation of the performance and emissions when the generation system fuelled with hydrogen, comparing with that of original diesel fuel. The performance and emission study of the three generations, namely, single generation, cogeneration (CHP) and trigeneration, are all based on the primary mover – the Yammar genset. The engine test cycles used in the investigation are selected according to the British Standard (EN ISO 8178 4, Reciprocating internal combustion engines, Test cycles for different engine applications), i.e., 10%, 25%, 50%, 75% and 100% of the engine load.

A computational software called ECLIPSE, whose simulation process is shown in Figure 2, is used to simulate the working process of the proposed trigeneration, and the single generation and cogeneration to provide a consistent basis for evaluation and comparison [31, 32]. ECLIPSE was developed for the European Commission and has been used by the Northern Ireland Centre for Energy Research and Technology at the University of Ulster since 1986 [33]. ECLIPSE was successfully used for many European and international projects to implement techno-economic analysis of power systems.

ECLIPSE is a personal-computer-based package containing all of the program modules necessary to complete rapid and reliable step-by-step technical, environmental and economic evaluations of thermodynamic, chemical and allied processes. It is used to carry out the simulation of the whole trigeneration system, including engine working processes, such as air and fuel(s) intake, compression, combustion and expansion, and finally exhaust processes. The software is also used to carry out the simulation of the waste heat recovery system and the absorption refrigeration system in the trigeneration. ECLIPSE uses generic chemical engineering equations and formulae, which keeps the energy and mass in balance, namely, the energy input equals to the energy output; so is the mass. It includes a high-accuracy steam–water thermodynamics package for steam cycle analysis. It has its own chemical industry capital costing program covering over 100 equipment types. The chemical compound properties database and the plant cost database can both be modified to allow new or conceptual processes to be evaluated. A techno-economic assessment study is carried out in stages; initially a process flow diagram is prepared, technical design data can then be added and a mass and energy balance completed. Consequently, the system's environmental impact is assessed, capital and

operating costs are estimated and an economic analysis performed. The proposed trigeneration system is simulated using the function of the energy and mass balance of ECLIPSE.
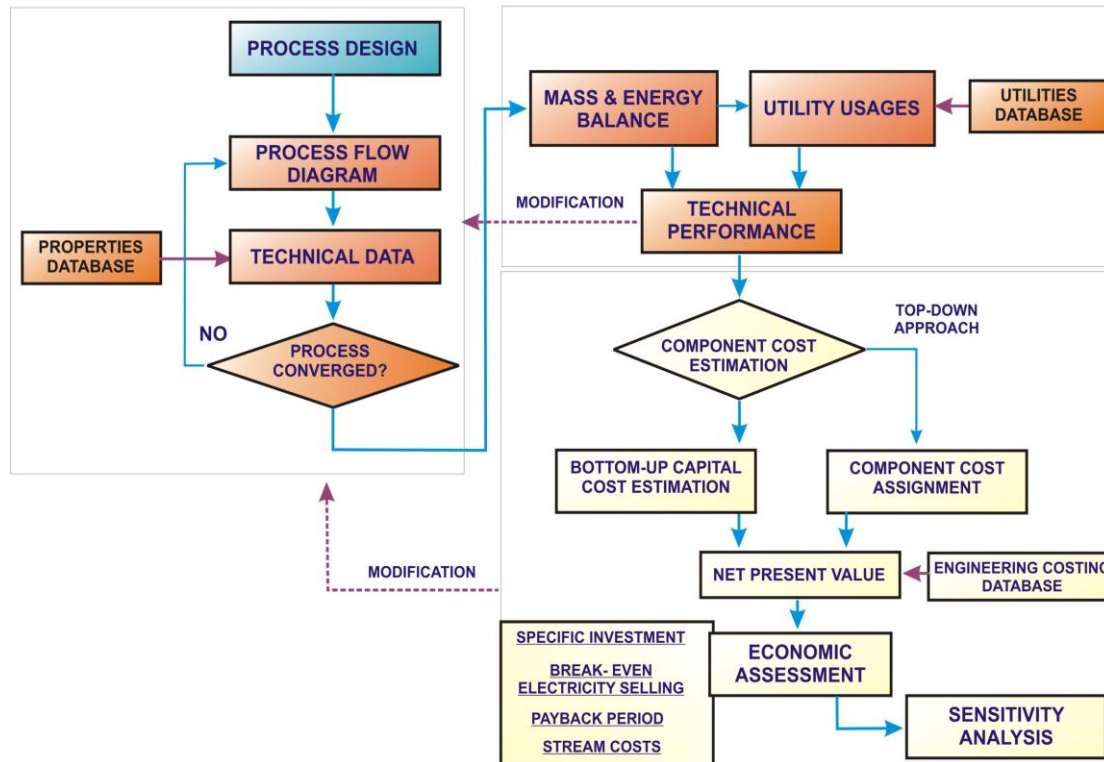
Figure 2: The Simulation Process of ECLIPSE Modelling

3   Results and discussion
3.1   Simulation programmes
The combustion processes of diesel and hydrogen in the engine cylinder in the form of global single step reaction are shown as the following equations:

$$C_{12}H_{26} + 18.5 (O_2 + 3.76N_2) \rightarrow 12\ CO_2 + 13H_2O + 69.56\ N_2 \tag{1}$$

$$2\ H_2 + (O_2 + 3.76N_2) \rightarrow 2H_2O + 3.76\ N_2 \tag{2}$$

The simulations are based on the above equations and the ECLIPSE software is used to carry out the simulation for mass and energy balance in the process. The cases simulated are single generation, cogeneration and trigeneration fuelled with two different fuels – diesel and hydrogen respectively. Figure 3 shows the simulation diagrams of single generation, cogeneration and trigeneration in ECLIPSE.

3.2   Results and discussions
3.2.1   Overall efficiencies and useful energy outputs
The simulation results are shown in the following table and figures. *Table 1* show the results of the six cases when the engine genset runs at full load that the electricity output is 6.5 kW. Figures 4 – 7 show the results when the engine runs at different loads from 10%, 25%, 50%, 75% and 100%.

Figure 4 shows the overall efficiency for single, cogeneration and trigeneration using diesel and hydrogen. It can be seen that for diesel fuel, electrical efficiency is low at low loads, 11% only at the engine 10% of load; and increases gradually to its maximum of about 31% at full load. For hydrogen fuelled case, the electrical efficiency increases from 10% at the engine 10% of load, to 30% at the engine 100% of load. The low efficiency at low loads is because of work that has to be done to overcome frictional forces between the moving parts in the engine, such as the crankshaft with its

bearings, pistons with cylinders. This work to overcome friction is approximately constant for all load conditions. At low load conditions with low fuel feeds, the proportion of the energy input that goes into overcoming friction is higher than at higher load conditions with higher fuel feed. These friction losses caused the lower efficiency at the engine low loads.

(a) Single generation

(b) Cogeneration
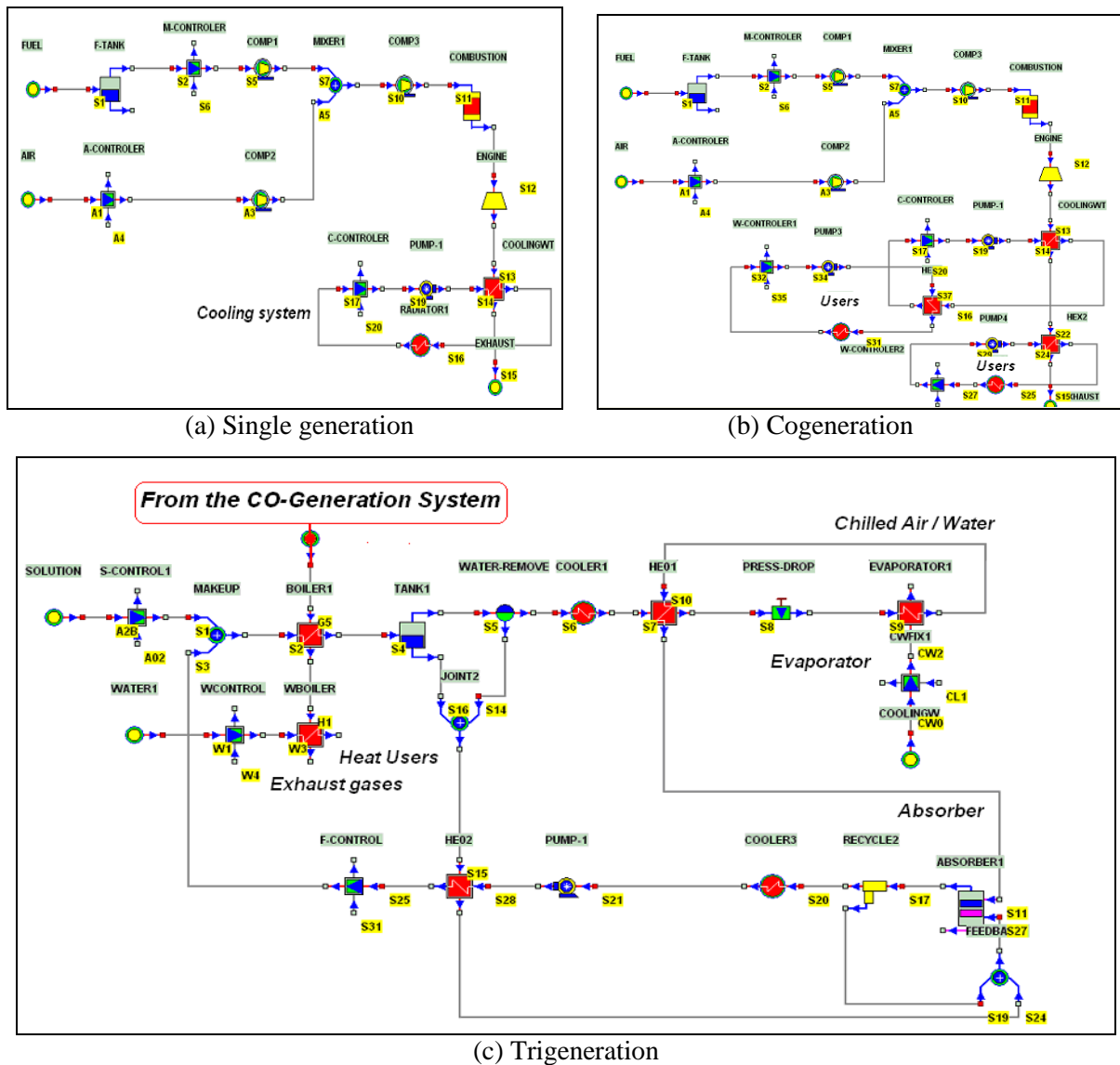
(c) Trigeneration

Figure 3: The Flow Diagram of the three generation systems in ECLIPSE
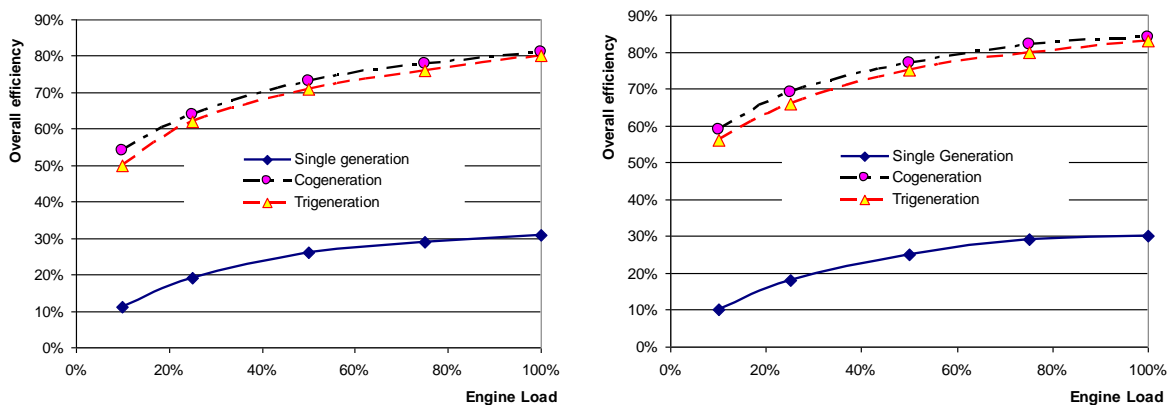
Figure 4: Overall efficiency for Single, Cogeneration and Trigeneration using Diesel & H_2

The cogeneration and trigeneration efficiency start at around 50% at 10% load for diesel; 56% for hydrogen; rising gradually to 80% for diesel and 83% for hydrogen at full load. This represents efficiency increases of about 390% at 10% of engine load to 170% at engine full-load for both cogeneration and trigeneration compared to that of single generation. From the figures and *Table 1*, it can be seen that trigeneration is similar to cogeneration, in terms of the performances and emissions. This is because the refrigerator used in the study is quite small (0.4 kW only), which only consumes very small amount of heat (0.61 kW) from the engine exhaust. But it can also be seen that trigeneration is slightly less efficient than cogeneration. The differences are between 7.4% - 1.23% for diesel fuelled engine; 5.1% - 1.2% for hydrogen fuelled engine. This is due to a part of the waste heat from the engine input into the absorption refrigerator. Notice the fact that the COP of absorption refrigerator is less than 1. This means the refrigeration output is less than the heat input into the absorption refrigerator. This causes less efficient of the trigeneration than that of cogeneration.

Table 1
Technical and Emission Results at Engine Full Load (at 6.5 kW electricity output)

Fuel used	**Diesel**			**Hydrogen**		
Generation	Singlegen*	Cogen	Trigen	Singlegen	Cogen	Trigen
Fuel input (kg/s) x 10^{-3}	0.498	0.498	0.498	0.18	0.18	0.18
LHV (MJ/kg)	42.893	42.893	42.893	120.1	120.1	120.1
Total thermal input (kW_{th})	21.36	21.36	21.36	21.36	21.36	21.36
Electrical output (kWe)	6.53	6.53	6.53	6.50	6.50	6.50
Electrical efficiency (%)	31%	31%	31%	30%	30%	30%
Engine exhaust temperature (^{o}C)	557	557	557	576	576	576
Carbon Dioxide emissions (kg/kWh)	0.855	0.324	0.329	0	0	0
Exhaust gas mass flow (kg/min)	0.7650	0.7650	0.7650	0.7464	0.7464	0.7464
Heat recovered from cooling system and exhaust (kW_{th})		10.7	10.06		11.8	11.15
Total useful energy output (kW) (Electricity + Heat + Refrigeration)	6.53	17.23	16.99	6.50	18.26	18.05
Exhaust temperature at exit of the system (^{o}C)		150	150		150	150
Heat consumption of refrigeration (kW)			0.61			0.61
Refrigeration effect at $-10\ ^{o}C$ (kW)			0.11			0.11
Refrigeration effect at $+5\ ^{o}C$ (kW)			0.29			0.29
COP			0.66			0.66
Overall efficiency	31%	81%	80%	30%	84%	83%

* Singlegen – Single generation, Cogen - Congeneration, Trigen - Trigeneration

For the comparison of the generations run on two fuels, in the case of single generation, the efficiencies of engine fuelled with diesel, are all higher than that of fuelled with hydrogen, from 9.1% at engine 10% load, to 3.2% at the engine full load. As for cogeneration and trigeneration, the engine

efficiency fuelled with hydrogen are all higher than that fuelled with diesel at different engine loads, from 12.0% at 10% of engine load to 3.75% at the engine full load for cogeneration; from 9.3% at 10% of engine load to 3.70% at the engine full load for cogeneration. The reason for that is probably the combustion of diesel and hydrogen in engine are different, the energy from the combustion of hydrogen transferred more heat to the cooling system and the exhaust, therefore reduced the energy changed to electricity.

Figure 5 shows and compares the useful outputs from single generation, cogeneration and trigeneration for each fuel. It can be observed that the useful outputs from trigeneration are less than that of cogenerations fuelled with diesel and hydrogen. As discussed above, this is due to the effect of the COP of absorption refrigerator is less than 1, which effectively reduces the useful energy outputs from the trigeneration, due to the absorption unit uses more heat inputs than the resultant cooling effect.

| (a) Diesel | (b) Hydrogen |
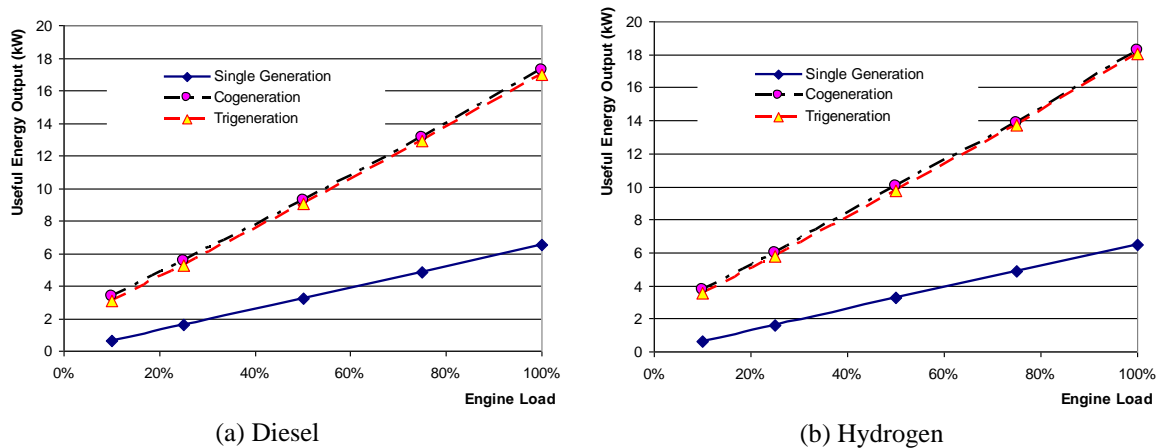
Figure 5: Useful energy output for Single, Cogeneration and Trigeneration using Diesel & H_2

3.2.2 Brake specific fuel consumption (BSFC) and CO2 emissions

BSFC is defined as the rate of fuel consumption per kW of useful energy output in single generation, cogeneration and trigeneration for each fuel. As can be seen from *Table 1* and corresponding Figure 6, for both fuels, the BSFC curves have the same general trends. That is, higher BSFC at low loads for single generation, e.g. 0.791 kg/kWh at the engine 10% load for diesel, 0.292 kg/kWh at 10% of engine load for hydrogen; and gradually the BSFC declines to about 0.275kg/kWh for diesel and 0.100 kg/kWh for hydrogen. This difference in mass per kWh for the two fuels reflects the differences in energy density by mass of the two fuels. The BSFCs for cogeneration and trigeneration, when using both fuels, are much lower compared to those of single generations; and they are almost equal to each other, with that of trigeneration slightly higher, reflecting the slightly lower overall energetic efficiency of trigeneration compared to cogeneration.

From the results in *Table 1* it can be seen that the resulting in CO_2 emissions from the engine for all load conditions when fuelled with hydrogen is zero; while that from diesel decreases with the load increases, i.e., from 2.48 kg (CO_2)/kWh at the engine 10% load to 0.855 kg (CO_2)/kWh at the engine full load, as can be seen in Figure 7. From the results, it can be seen that at low load conditions where single generation is much less efficient, the CO_2 emissions per kWh rise sharply. From the figure, it can also be seen that single generation produces more CO_2 per kWh than cogeneration and trigeneration. Compared to cogeneration, single generation emits 80.4% more CO_2 at 10% of the engine load; to 62.1% more CO_2 at the engine full load. Compared to trigeneration, single generation emits 78.9% more CO_2 at 10% of the engine load; to 61.6% more CO_2 at the engine full load.

(b) Diesel   (b) Hydrogen
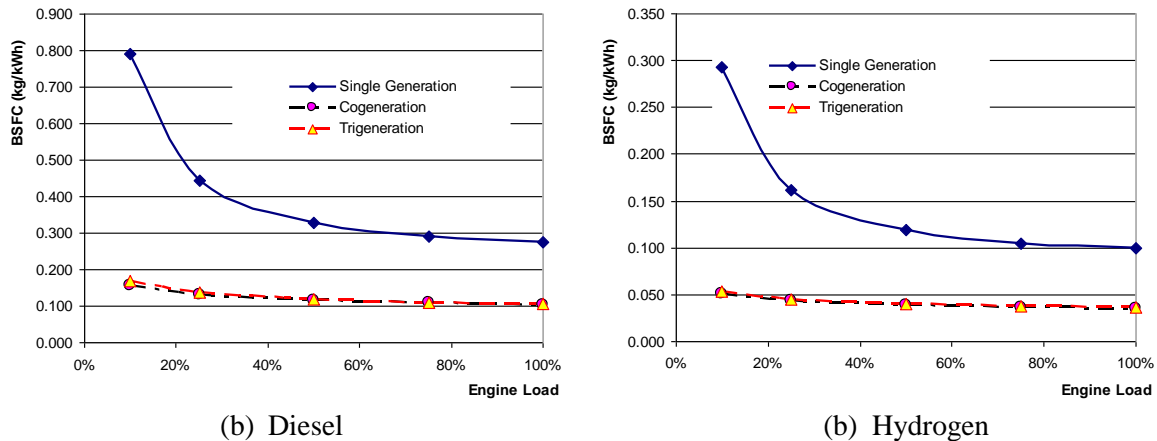
Figure 6: Brake Specific Fuel Consumption (BSFC) for Single, Cogeneration and Trigeneration using Diesel & H_2
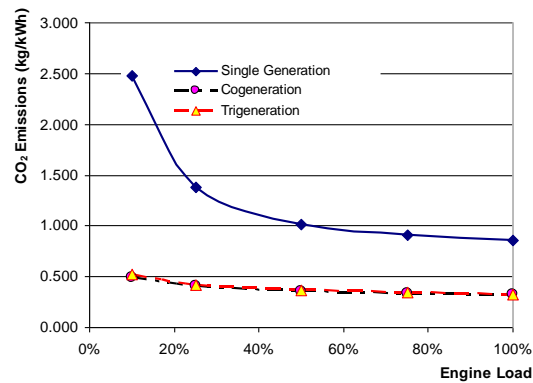
Figure 7: CO_2 Emissions for Single, Cogeneration and Trigeneration using Diesel

4   Conclusions

From the above results and discussions, conclusions can be drawn as follows for the study of the household size trigeneration compared to that of single generation and cogeneration:

- It is feasible to use hydrogen as the fuel to run the domestic micro-trigeneration based on a diesel engine genset.
- The efficiencies of the single generation, trigeneration and cogeneration run by hydrogen are comparable to those run by diesel, respectively.
- The micro-trigeneration has much higher overall efficiency and higher useful energy output than that of single generation.
- The trigeneration produces zero CO_2 emissions when fuelled with hydrogen. This means, if the hydrogen used is from renewable resources, the hydrogen fuelled trigeneration will be a net-zero energy system for the application in households. It has also much lower CO_2 emissions than that of single generation when fuelled with diesel.
- Although the trigeneration has a lower overall efficiency and lower useful energy output than that of cogeneration, it has one more useful refrigeration output using a small part of waste heat from the genset.

References

[1] Parliamentary Office of Science and Technology, Postnote: HOUSEHOLD ENERGY
     EFFICIENCY, October 2005, Number 249,
     http://www.parliament.uk/documents/post/postpn249.pdf

[2] Department of Energy & Climate Change, Digest of United Kingdom Energy Statistics 2009, A
     National Statistics publication, London, TSO, 2009, ISBN 9780115155246

[3] Ge, Y.T., Tassou, S.A., Chaer, I., and Suguartha, N., Performance evaluation of a trigeneration
     system with simulation and experiment. Applied Energy 2009, vol. 86, p.2317-2326.

[4] Lin Lin, Yaodong Wang, Tarik Al-Shemmeri, Tom Ruxton, Stuart Turner, Shengchuo Zeng,
     Jincheng Huang, Yunxin He, Xiaodong Huang; An experimental investigation of a household
     size trigeneration, Applied Thermal Engineering 2007, vol. 27, p.576-585

[5] Khaliq, A., Kumar, R., and Dincer, I., Performance analysis of an industrial waste heat based
     trigeneration system; International Journal of Energy Research; (2009) vol. 33, p.737-744

[6] Onovwiona, H.I., Ugursal, V.I., Residential cogeneration systems: Review of current
     technology, Renewable and Sustainable Energy Reviews, 2006, vol. 10, p.389-431.

[7] Sau Man Lai, Chi Wai Hui, Integration of trigeneration system and thermal storage under
     demand uncertainties, Applied Energy, Volume 87, Issue 9, 2010, Pages 2868-2880

[8] Joan Carles Bruno, Victor Ortega-Lopez, Alberto Coronas, Integration of absorption cooling
     systems into micro gas turbine trigeneration systems using biogas: Case study of a sewage
     treatment plant, Applied Energy, Volume 86, Issue 6, June 2009, Pages 837-847

[9] Z.T. Lian, K.J. Chua, S.K. Chou, A thermoeconomic analysis of biomass energy for
     trigeneration, Applied Energy, Volume 87, Issue 1, January 2010, Pages 84-95

[10] Xiangyu Meng, Fusheng Yang, Zewei Bao, Jianqiang Deng, Nyallang N. Serge, Zaoxiao Zhang,
     Theoretical study of a novel solar trigeneration system based on metal hydrides, Applied
     Energy, Volume 87, Issue 6, June 2010, Pages 2050-2061

[11] Umberto Desideri, Stefania Proietti, Paolo Sdringola, Solar-powered cooling systems: Technical
     and economic analysis on industrial refrigeration and air-conditioning applications, Applied
     Energy, Volume 86, Issue 9, September 2009, Pages 1376-1386

[12] Carlos Rubio-Maya, Javier Uche-Marcuello, Amaya Martinez-Gracia, Angel A. Bayod-Rujula,
     Design optimization of a polygeneration plant fuelled by natural gas and renewable energy
     sources, Applied Energy, In Press, Corrected Proof, Available online 3 August 2010

[13] Nelson Fumo, Pedro J. Mago, Louay M. Chamra, Analysis of cooling, heating, and power
     systems based on site energy consumption, Applied Energy, Volume 86, Issue 6, June 2009,
     Pages 928-932

[14] Saravanan, N; and Nagarajan, GAn experimental investigation of hydrogen-enriched air
     induction in a diesel engine system. In: International Journal of Hydrogen Energy, 2008, vol. 33,
     p.1769-1775.

[15] Van Vorst WMD., Hydrogen fueled transportation, Hydrogen energy System, NATO ASI
     Series, Series E: applied sciences, Vol. 295, 1995. p. 215–40.

[16] Das, L.M. Hydrogen engine: research and development (R&D) programmes in Indian Institute
     of Technology (IIT), International Journal of Hydrogen Energy, 2002, vol.27, p.953-965

[17] White, C.M., Steeper, R.R., Lutz, A.E., The hydrogen-fuelled internal combustion engine: a
     technical review, International Journal of Hydrogen Energy, 2006, vol.31, p.1292-1305

[18] Bas van Ruijven, Detlef, P. van Vuuren, Bert de Vries, The potential role of hydrogen in energy
     systems with and without climate change, International Journal of Hydrogen Energy, 2007,
     vol.32, p.1655-1672.

[19] S. Firth *, K. Lomas, A. Wright, R. Wall, Identifying trends in the use of domestic appliances
     from household electricity consumption measurements, Energy and Buildings 40 (2008) p.926–
     936

[20] Jeremy Cockroft, Nick Kelly, A comparative assessment of future heat and power sources for
     the UK domestic sector, Energy Conversion and Management 47 (2006) p.2349–2360

[21] G. Wood*, M. Newborough, Dynamic energy-consumption indicators for domestic appliances:
     environment, behaviour and design, Energy and Buildings 35 (2002), p.821–841, November
     2002

[22] Geoffrey K.F. Tso , Kelvin K.W. Yau, A study of domestic energy usage patterns in Hong Kong, Energy 28 (2003) p.1671–1682, October 2001

[23] Yigzaw G. Yohanis, Jayanta D. Mondol, Alan Wright, Brian Norton, Real-life energy use in the UK: How occupancy and dwelling characteristics affect domestic electricity use, Energy and Buildings, Volume 40, Issue 6, 2008, Pages 1053-1059

[24] Andrew Wright, Steven Firth, The nature of domestic electricity-loads and effects of time averaging on statistics and on-site generation calculations, *Applied Energy*, *Volume 84, Issue 4*, *April 2007*, *Pages 389-403*

[25] S.R. Allen, G.P. Hammond, M.C. McManus, Prospects for and barriers to domestic micro-generation: A United Kingdom perspective, *Applied Energy*, *Volume 85, Issue 6*, *June 2008*, *Pages 528-544*

I.   Staffell, R. Green, K. Kendall, Cost targets for domestic fuel cell CHP, *Journal of Power Sources*, *Volume 181, Issue 2, 1 July 2008*, *Pages 339-349*

[26] A.D. Peacock, M. Newborough, Effect of heat-saving measures on the CO2 savings attributable to micro-combined heat and power (mCHP) systems in UK dwellings, *Energy*, *Volume 33, Issue 4*, *April 2008*, *Pages 601-612*

[27] J.M. Gomes Antunes, R. Mikalsen, A.P. Roskilly, An experimental study of a direct injection compression ignition hydrogen engine, International Journal of Hydrogen Energy, Volume 34, Issue 15, August 2009, Pages 6516-6522

[28] J.M. Gomes Antunes, R. Mikalsen, A.P. Roskilly, An investigation of hydrogen-fuelled HCCI engine performance and operation, International Journal of Hydrogen Energy, Volume 33, Issue 20, October 2008, Pages 5823-5828

[29] YD Wang, Y Huang, A. P. Roskilly, Trigeneration integrated with absorption enhanced reforming of lignite and biomass, FUEL, vol 88, Issue 10, Oct 2009, Pages 2004-2010.

[30] Williams B C, The development of the ECLIPSE simulator and its application to the techno-economic assessment of clean fossil fuel power generation systems, 1994, DPhil Thesis, Energy Research Centre, University of Ulster, Coleraine, Northern Ireland

[31] Williams B C and McMullan J T, Techno-economic analysis of fuel conversion and power generation systems – the development of a portable chemical process simulator with capital cost and economic analysis capabilities, International Journal of Energy Resources, 1996, Volume 20, Issue 2, p.125–142.

[32] The University of Ulster, ECLIPSE Process Simulator, Energy Research Centre, 1992, Jordanstown, Northern Ireland